Multi-Objective System Optimization of a Mars Atmospheric ISRU Plant

by
Eric Daniel Hinterman

B.S. Chemical Engineering – University of Notre Dame, 2013
M.S. Aeronautics and Astronautics – Massachusetts Institute of Technology, 2018

Submitted to the Department of Aeronautics and Astronautics
in Partial Fulfillment of the Requirements for the Degree of

DOCTOR OF PHILOSOPHY IN AERONAUTICS AND ASTRONAUTICS

at the
MASSACHUSETTS INSTITUTE OF TECHNOLOGY
May 2022

Signature of Author: _____
Department of Aeronautics and Astronautics
May 15, 2022

Certified by: _____
Jeffrey Hoffman
Professor of the Practice, Aeronautics and Astronautics
Dissertation Supervisor

Certified by: _____
Michael Hecht
Principle Investigator, MOXIE
Thesis Committee Member

Certified by: _____
Olivier de Weck
Apollo Program Professor, Aeronautics and Astronautics
Thesis Committee Member

Certified by: _____
Dan Cziczo
Professor and Department Head of Earth, Atmospheric, and Planetary Sciences (Purdue University)
Thesis Committee Member

Accepted by: _____
Jonathan P. How
R.C. Maclaurin Professor of Aeronautics and Astronautics
Chair, Graduate Program Committee

Multi-Objective System Optimization of a Mars Atmospheric ISRU Plant

by

Eric Daniel Hinterman

Submitted to the Department of Aeronautics and Astronautics
on May 15, 2022 in Partial Fulfillment of the
Requirements for the Degree of Doctor of Philosophy in
Aeronautics and Astronautics

Abstract

The Mars Oxygen In-Situ Resource Utilization Experiment (MOXIE) represents the first time that NASA is demonstrating In-Situ Resource Utilization (ISRU) on the surface of another planetary body. MOXIE produces oxygen from atmospheric CO_2 on Mars. It was developed for NASA's Mars 2020 Rover and produces oxygen with greater than 99.6% purity through solid oxide electrolysis. MOXIE is a small fraction of the scale that would be necessary to produce oxygen for use as a propellant for a human Mars mission, assuming that the empty oxygen tank on a Mars ascent vehicle would be filled from a scaled-up MOXIE system.

MOXIE is a small prototype of an ISRU system that would be capable of supporting a crew of six astronauts on Mars. It is unclear, however, how to optimally scale MOXIE and what specific challenges a scaled-up version might face. This dissertation focuses on taking the lessons learned from MOXIE and determining the optimal way to scale it to a full-size system. Specifically, this dissertation defines a systems architecture for an extensible MOXIE system, called the Big Atmospheric MOXIE (BAM), based on the development of a detailed optimization model. The primary subsystems of interest are the solid oxide electrolysis (SOE) stack, the compressor, the liquefaction system, and the heat exchanger. The model has been validated with data from scaled-up SOE cell testing, past MOXIE experiments, and components used in industry.

By understanding the scalability and extensibility of key subsystems in the MOXIE system, it is possible to design a larger, optimized systems architecture model for BAM to support the first human missions to Mars. Producing this optimized, validated systems design of a scaled-up atmospheric ISRU plant for Mars has never been done before under these parameters and is the primary goal of this dissertation.

Table of Contents

Chapter 1: Introduction

1.1 Mars and ISRU

Mars has fascinated humankind for centuries. Detailed observation of Mars began telescopically with Galileo Galilei in 1610. Over the next century, features such as the polar ice caps and tilt of the planet were documented. It was in the 19th century that the first map of Mars was published. An Italian astronomer, Giovanni Schiaparelli, believed he saw straight lines on the surface of the planet, and labeled them "canali". Shiaparelli's intent was to describe channel-like structures, but the word was mistranslated into English as "canals". This gave rise to the widespread imagination of intelligent life on the planet. While the canals were later proven to be nothing more than an illusion, the idea still blossomed into the multi-faceted appeal of Mars that we see today; it is a place that has an intriguing past similar to Earth, it may have or have had life, and it is seen by some as a place to settle humankind in the future.

In-Situ Resource Utilization (ISRU), sometimes called "living off the land", is a concept that has been growing in momentum with humanity's push towards developing a space economy and enabling space exploration [1]. ISRU involves the use of technology to convert materials present at the destination site into useful resources. The early settlers of present-day nations used ISRU to construct their villages and survive, as they were often unable to bring everything they needed with them. In the case of space exploration, any resources derived from ISRU may be useful for life support systems that keep astronauts alive, construction of space structures, generation of propellants, and as energy sources for missions. By obtaining these functionalities with materials found in space, one no longer needs to bring the materials with them from Earth. Currently, it costs several thousand dollars to send one kg of material into Low Earth Orbit (LEO). On top of that, producing 1 kg of propellant on Mars saves 10 – 15 kg in LEO [2]. Therefore, sending enough propellant to Mars for a Mars Ascent Vehicle (MAV), approximately 30 metric tons for a crew of four astronauts, would require on the order of 400 metric tons of mass in LEO. This is the equivalent of billions of dollars in launch costs. For these reasons, development of ISRU technology is critical to the enablement of sustained manned missions into the solar system, as it has the potential to significantly reduce the mass, cost, and risk associated with spaceflight.

ISRU for Mars has been a topic under discussion for decades. Analog experiments have been carried out on Earth to test various ISRU strategies for construction of dwellings, use of perchlorates [3], water purification, and production of oxygen, among others. This dissertation focuses on production of oxygen, which could be used for breathing, rocket propellant, and habitat pressurization. For a 500-sol mission with a crew of six conducting two EVAs per day, the predicted breakdown of oxygen consumption during this theoretical mission is shown in Figure 1.

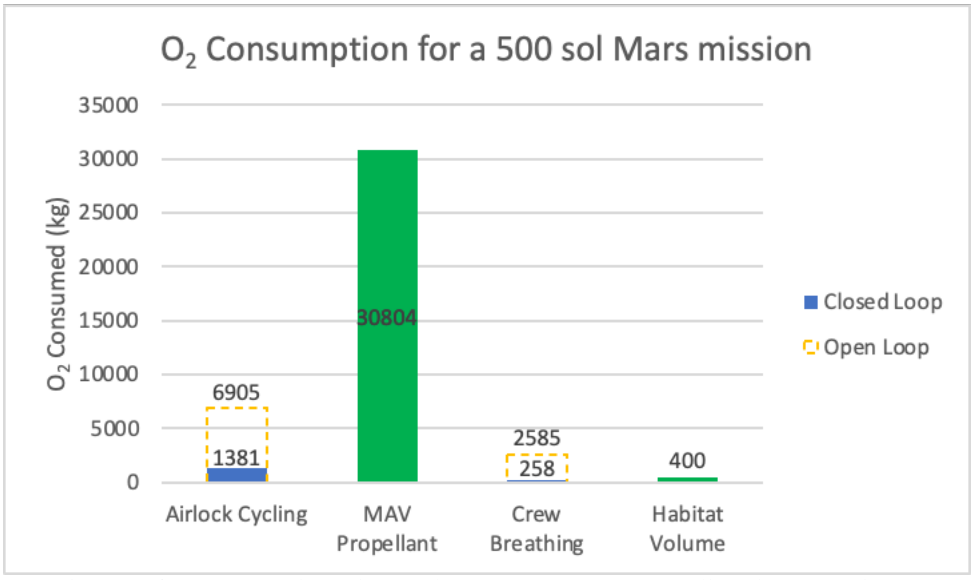

Figure 1: The uses of oxygen in a planned 500-sol Mars mission. MAV propellant dominates the requirements.

A closed-loop design is shown in blue, where 90% of oxygen consumed by breathing is recycled (with a Sabatier process, electrolysis, or photosynthesis) and 80% of airlock gas is recovered (by pumping the gas into the habitat instead of exhausting it to Mars). A completely open-loop design is also shown in dotted orange lines. Systems that are constant in both designs are shown in green. In either scenario, the majority of oxygen required for a crewed Mars mission will be used as MAV propellant.

1.2 MOXIE

This dissertation focuses on the design of a system to produce oxygen from the Martian atmosphere, which is the primary purpose of the Mars Oxygen In-Situ Resource Utilization Experiment (MOXIE). MOXIE is an instrument onboard NASA's Mars 2020 Perseverance rover that produces oxygen from the Martian atmosphere. The Mars atmosphere is an example of a useful resource that can be processed with ISRU technology. It is primarily composed of carbon dioxide, which accounts for approximately 95% of its volume. When electrolyzed to oxygen, it can be used as the oxidizer for a Mars Ascent Vehicle (MAV) that will lift astronauts off the surface of Mars to begin their journey back to Earth. In addition, a portion of the oxygen can be used for breathing as well as for rover and habitation pressure. For context, an image of the Perseverance rover is shown in Figure 2.

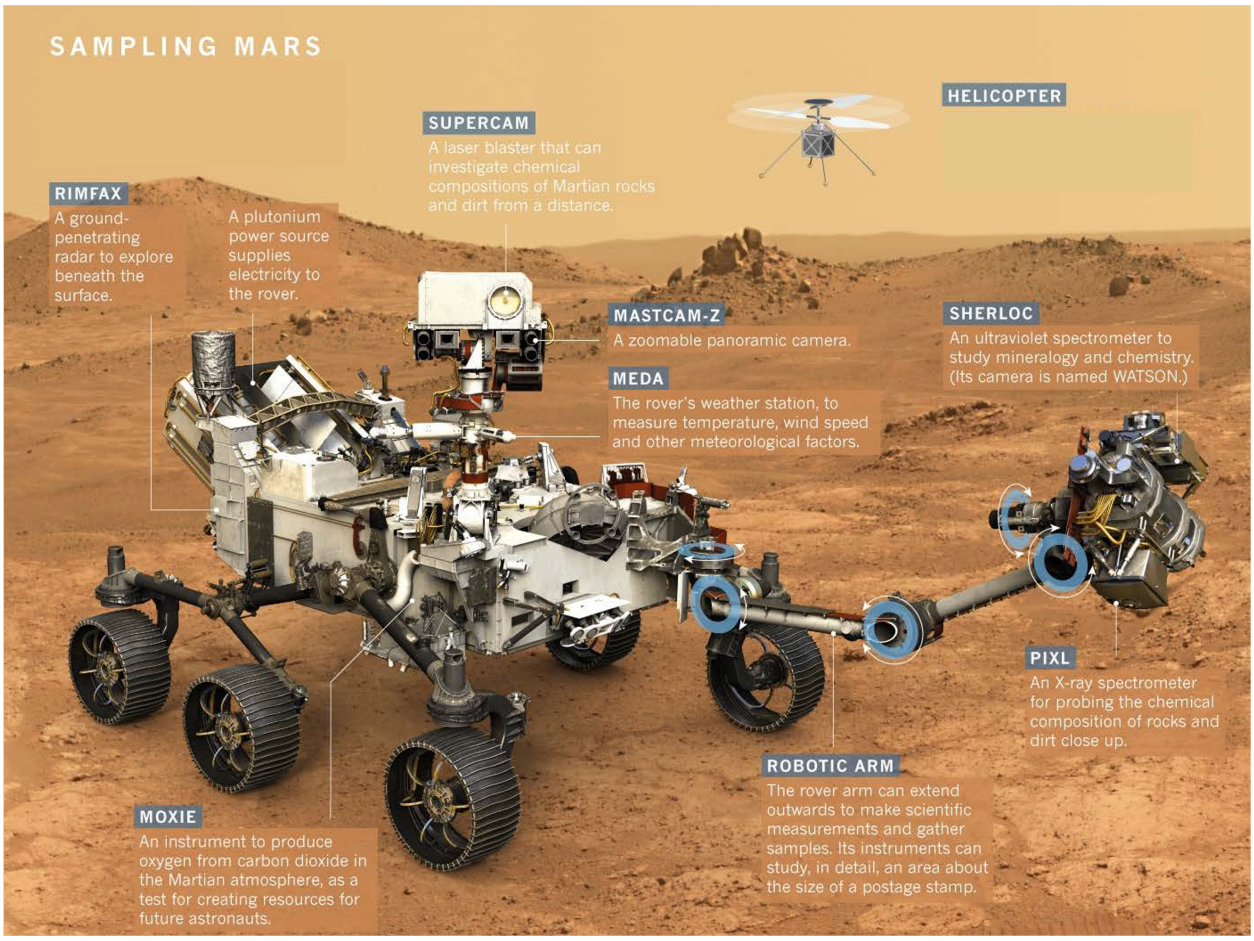

Figure 2: Mars Perseverance rover with majority of major payloads labeled, including MOXIE. Image credit: NASA.

As the image indicates, there are many payloads onboard this Mars rover. These payloads address a number of science objectives, including the continued study of Martian geology, caching samples for a future sample return mission, and the search for life. MOXIE, which produces oxygen, is shown in greater detail in Figure 3.

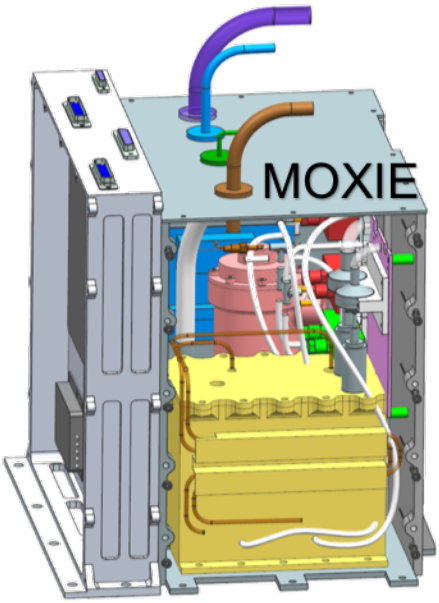

Figure 3: Schematic of MOXIE with front-facing wall cutaway to reveal interior. Credit: JPL

The goal of MOXIE is to demonstrate ISRU technology on Mars that could eventually be used to support a human mission. The development requirements for MOXIE, in the context of the Mars 2020 rover mission, are listed in Table 1.

Table 1: MOXIE top-level mission requirements for Mars 2020 mission

Requirement	Goal	Threshold
Oxygen Production Rate	8 g/hr at 5 Torr, 0°C.	6 g/hr at 5 Torr, 0°C.
Oxygen Purity	99.6%	98%
Number of Cycles	20	10

The threshold requirements for MOXIE are to produce oxygen at a flowrate of 6 grams per hour and at least 98% purity over a minimum of 10 cycles. The following sections will give an overview of MOXIE from a systems level, and then will explore the major components of MOXIE in more detail.

1.2.1 System Overview

MOXIE is primarily composed of three subsystems: the carbon dioxide acquisition and compression (CAC) system, the solid oxide electrolysis (SOXE) system, and the process monitoring and control (PMC) system. Figure 4 is a simplified diagram that shows the subsystems with measured properties (e.g., pressure, temperature, etc.) labeled.

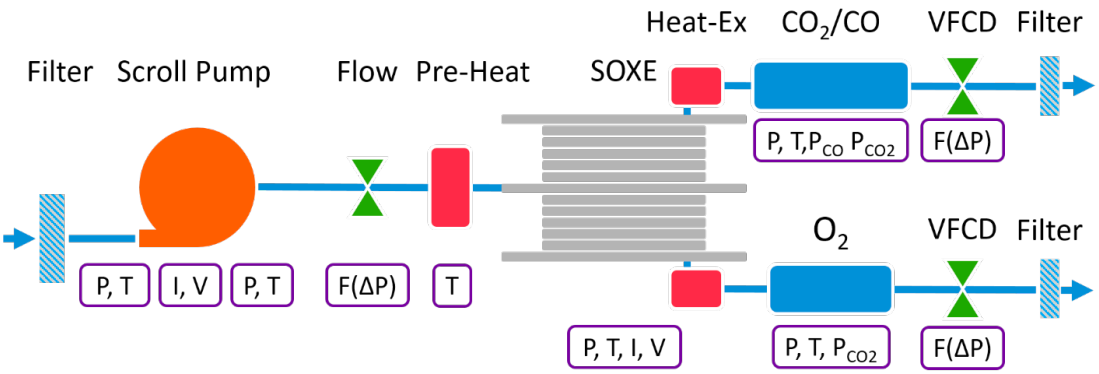

Figure 4: System-level view of MOXIE components, showing major subsystems and end-to-end flow path [4]

These systems, when functioning together, combine to pull in atmospheric gas on Mars, compress it, extract oxygen, measure its composition and production rate, and release the products back into the atmosphere. In a full-scale system, called the Big Atmospheric MOXIE (BAM), the oxygen, and possibly other gas streams, would be captured and stored for use. However, in the case of MOXIE, the primary goal is the demonstration of oxygen production, so the capture and storage of gases is out of scope. An expanded view of MOXIE is shown in Figure 5.

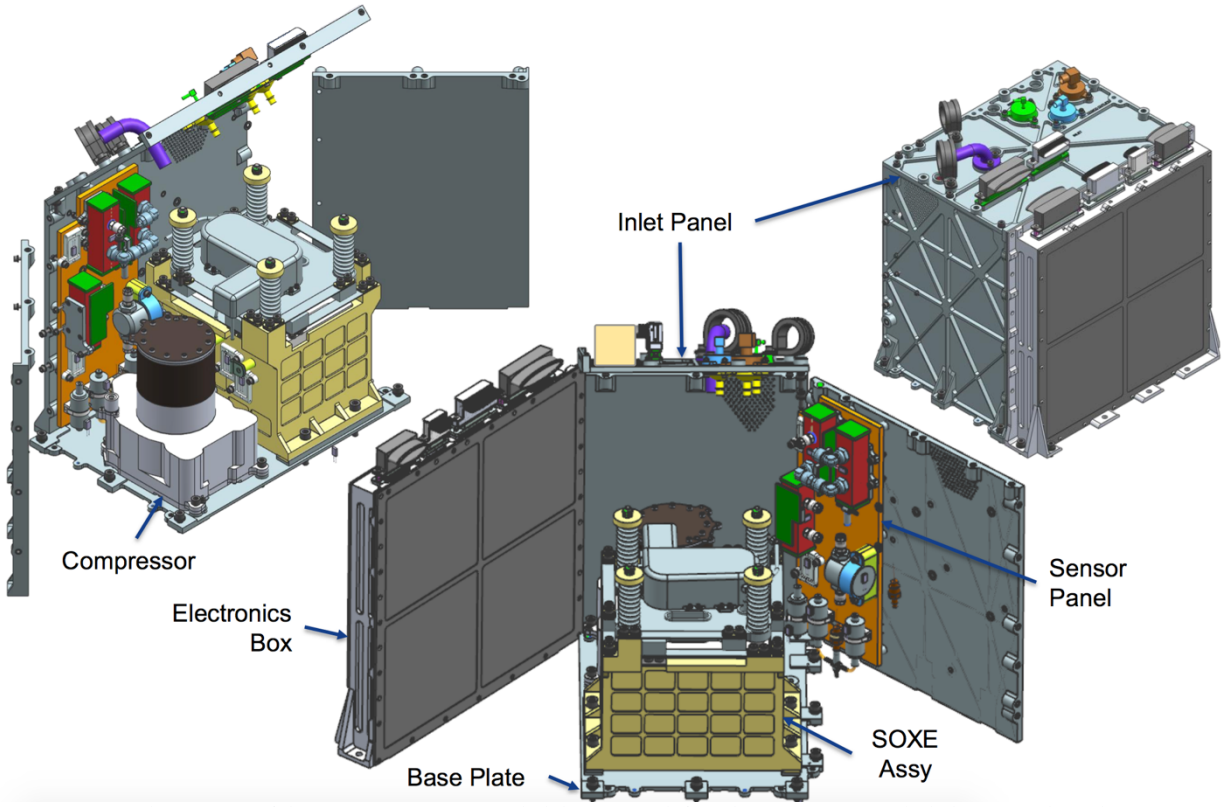

Figure 5: Three views of the MOXIE computer-aided design. On left and in center, an exploded view to show the interior constituents of MOXIE, including the compressor, SOXE assembly, and sensor panel. On right, a view of MOXIE in its flight configuration. Credit: JPL

The compressor occupies most of one side of the assembly, while the SOXE occupies most of the other side. The electronics and sensors are fitted on the walls of the unit.

1.2.2 Carbon Dioxide Acquisition and Compression (CAC) System

The CAC system includes a dust filter covered by a baffle, and a compressor. MOXIE acquires and compresses the Martian atmosphere by means of a scroll pump. A scroll pump is composed of two spiral-like structures superimposed on top of one another. In the case of MOXIE, one of the scrolls is fixed while the other orbits within it. This orbiting motion results in small pockets of gas periodically being compressed and pumped into the system. A cut-away schematic of a scroll pump is shown in Figure 6.

The Martian atmosphere is drawn first through a HEPA filter by the scroll compressor in order to remove dust and particulates that could damage the internal components of MOXIE. The housing for this is shown in Figure 7. As the atmosphere passes through the scroll pump, it is compressed from the ambient pressure on Mars, typically ~7 mbar, to approximately 700 mbar. The final pressure is achieved with a combination of the compression from the pump and downstream Viscous Flow Control Devices (VFCDs) that restrict the exhaust flow. The SOXE is designed to operate at around 700 mbar, and as such, a large portion of the testing and characterization work was done in this pressure range. In terms of flow rate, the compressor was sized for nominal operation of ~55 g/hr inlet flow at room temperature and an external pressure of 7 mbar.

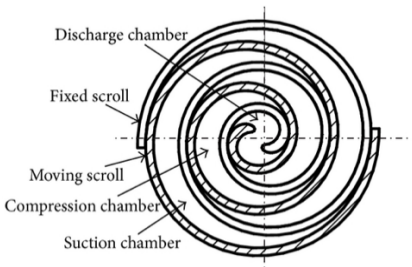

Figure 6: Cutaway schematic of a scroll compressor, the mechanism used by MOXIE for carbon dioxide acquisition and compression [5]

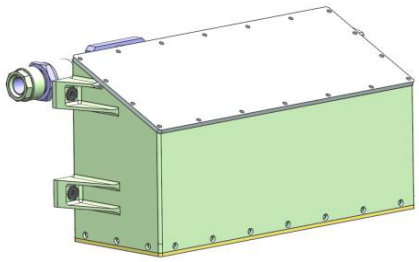

Figure 7: Design of the inlet HEPA filter assembly used on MOXIE to reject dust. Credit: JPL

To control the compressor, the operator inputs a desired RPM, and the compressor's controller adjusts its power input to match that rotational speed setpoint. The scroll compressor is a volumetric pump designed to move a certain volume range of gas through the MOXIE system and is operated between 1500 RPM and 3500 RPM. The compressor for MOXIE was developed by Air Squared Inc. in Broomfield, Colorado. The company has extensive background in scroll pump design and production. While this compressor was developed specifically for MOXIE, scroll pumps in general are well established in the vacuum and HVAC industries.

1.2.3 SOXE

Solid oxide electrolysis technology is used by MOXIE to produce oxygen from carbon dioxide. However, solid oxide electrolysis technology can be used to produce gases other than oxygen as

well. For example, in terrestrial applications such as the nuclear industry, it is used to generate hydrogen gas from water [6]. It can also be used with a mixed stream of water and carbon dioxide to produce synthesis gas, a mixture of hydrogen and carbon monoxide. The Mars-based SOXE inside of MOXIE uses a new application of solid oxide electrolysis: creating oxygen from carbon dioxide without the addition of water. This is referred to as "dry" electrolysis and has been researched and tested extensively for MOXIE in recent years.

The solid oxide electrolysis (SOXE) subsystem on MOXIE is composed of two five-cell stacks of solid oxide cells, one heater for each stack, a gas pre-heater, tubing to transport gases, and insulation and packaging. Each SOXE cell consists of a Scandia-Stabilized Zirconia (ScSZ) electrolyte sandwiched between an electrically conductive cathode and anode. This is shown in Figure 8.

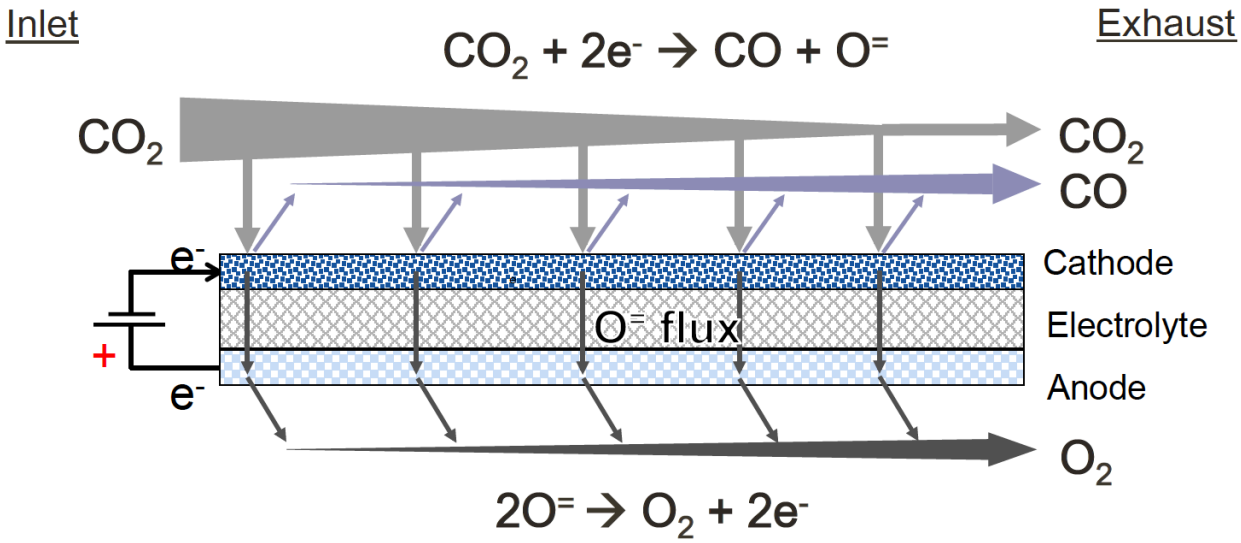

Figure 8: Schematic of SOXE cell and the chemical reaction that it drives. CO_2 flows in and is reduced to CO and oxygen ions. Oxygen ions traverse through the electrolyte under an applied voltage and form O_2 on the anode side of the cell. Credit: JPL

The electrochemical reaction is initiated by the three-phase boundary that exists between the electrolyte, the gas, and the nickel cathode. Under conditions when i) a voltage is applied to the electrolyte, ii) the cell is heated to ~800 °C, and iii) CO_2 is flowed over the cathode, the following net reaction takes place:

$$2CO_2 \rightarrow 2CO + O_2 \quad (1)$$

This reaction takes place over the entire surface of the cathode, as demonstrated in Figure 8. To better understand the reaction, it is necessary to identify the intermediate reactions that lead to the net reaction above. As the CO_2 enters the porous cathode at an elevated temperature, it obtains free electrons from the cathode and is reduced to CO and oxygen ions.

$$2CO_2 + 4e^- \rightarrow 2CO + 2O^{2-} \quad (2)$$

The nickel coating on the cathode enables one of the oxygen atoms to be separated from its original CO_2 molecule, thus forming a CO molecule and a free oxygen ion. This is depicted below.

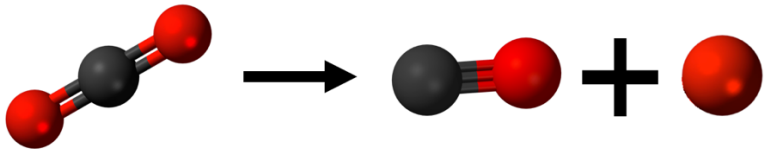

Figure 9: Molecular depiction of CO_2 dissociation into CO and O-

The CO molecule travels along the cell's cathode side and is either exhausted or could be captured and stored. However, the oxygen ions move through the electrolyte under the influence of the electrical potential. The removal of oxygen ions at the cathode-electrolyte interface creates a partial pressure gradient that drives molecules down towards the three-phase boundary and keeps the process moving. Oxygen vacancies in the Scandia-Zirconia structure provide a migration path for the oxygen ions [7]. The anode provides a site for the oxygen ions to reconnect with each other via the following reaction.

$$2O^{2-} \rightarrow O_2 + 4e^- \quad (3)$$

The net reaction becomes that which was presented in Equation (1). The electrons are recycled into the SOXE cell system, and oxygen is produced. The oxygen in MOXIE is measured for quantity and purity and is then vented to the atmosphere, though in a scaled-up version it would be captured, liquefied, and stored for use as rocket propellant and possibly for life support.

The SOXE system on MOXIE consists of 10 cells arranged in two stacks of 5 cells each. A midplate separates the two stacks. Between each pair of cells is an electrically conductive metal plate with grooves that direct gas flow across the cell. Furthermore, glass gaskets line the edge of each layer to prevent leaks from crossing the boundaries of the cells. The stack is held together by a compression fixture. An exploded view of the SOXE stack is shown in Figure 10, followed by a depiction of the stacked SOXE configuration in Figure 11.

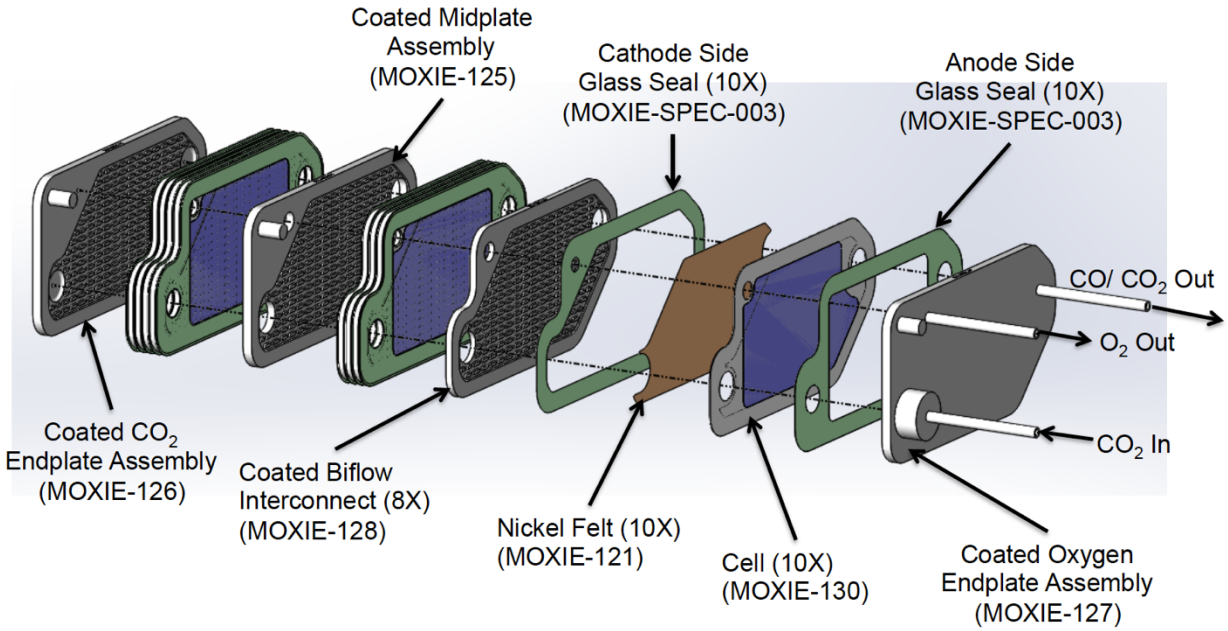

Figure 10: SOXE stack exploded view, showing the various layers included in the MOXIE SOXE. Credit: Ceramatec

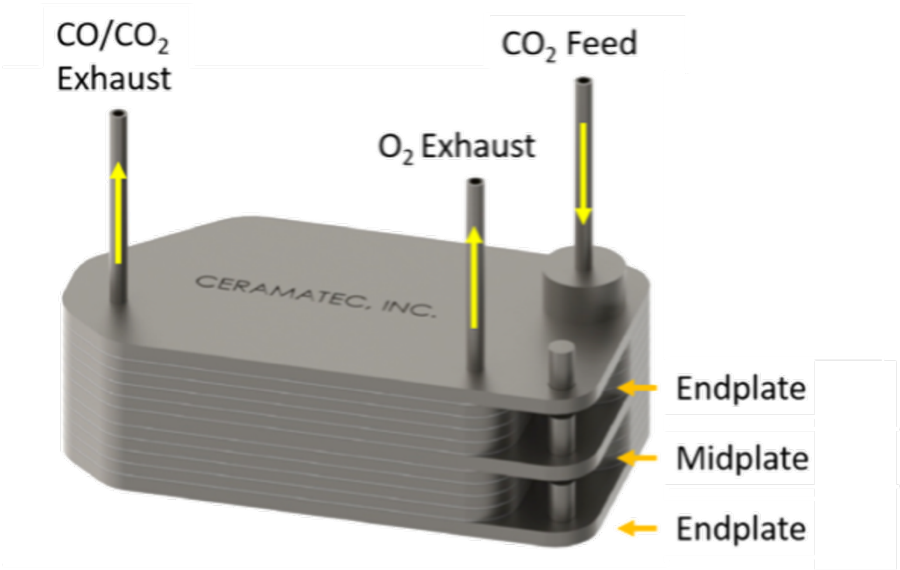

Figure 11: Schematic of SOXE in its stacked configuration, showing endplates, midplates, and gas flow paths. Credit: Ceramatec

The interconnect plates are composed of a chromium-iron-yttrium (CFY) alloy. CFY plates are commonly used as interconnects in solid oxide fuel cells and solid oxide electrolysis cells because, among other beneficial material properties, their coefficient of expansion can be tuned to precisely match that of the electrolyte [8]. This results in uniform expansion and contraction across the SOXE stack during heating cycles, preventing leaks and minimizing structural fatigue.

It is also important to understand the gas flow in and out of the SOXE cell as depicted by Figure 10. The CO_2 flows into the stack and follows a tube that allows it to reach every cell in the stack. As the CO_2 passes over each cell in a parallel configuration, it produces CO on the cathode and, ultimately, O_2 on the anode. It is not possible to achieve 100% conversion of CO_2 into product gases without degradation of the cell, as discussed in Section 2.3.7, resulting in the cathode exhaust being composed of a mixture of CO and unreacted CO_2.

1.2.4 Process Monitoring and Control Subsystem

The process monitoring and control (PMC) subsystem is controlled from an 8051 microcontroller embedded in MOXIE's field programmable gate array (FPGA). Any failure detected by the sensors and control system results in an ordered shutdown of all relevant systems except electronics, followed by a return to an idle state for MOXIE.

A suite of sensors is included in the PMC system, including sensors that measure pressure, temperature, voltage, and gas composition throughout MOXIE. An end-to-end flow diagram for MOXIE showing sensors and transducers is presented in Figure 12. There are five pressure transducers (P1-P5), two CO_2 composition sensors (CS1, CS2), one CO composition sensor (CS3), one oxygen composition sensor (CS4), eighteen in-use temperature sensors (T1-T24) with several spares (T17, T19, T20, T23, T24), current, voltage, and revolution sensors for the

compressor, and current and voltage sensors for the top and bottom stacks of SOXE. Together, these sensors inform the MOXIE Flight Software to ensure safe and effective oxygen production.

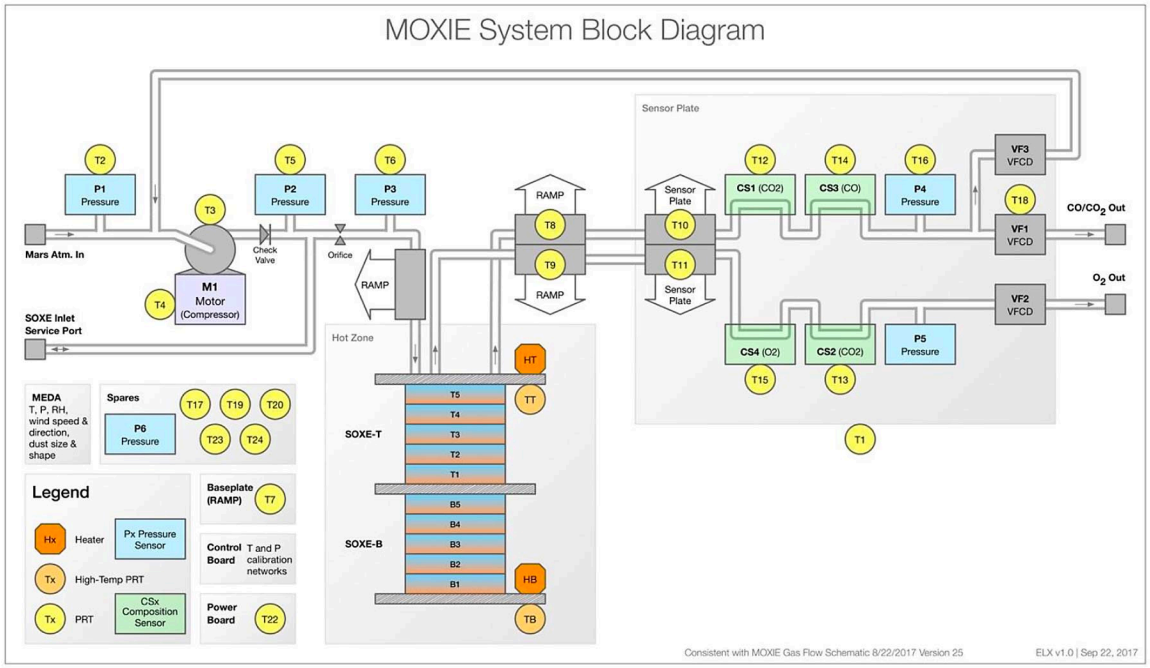

Figure 12: MOXIE end-to-end system with sensors and transducers labeled, showing the full flow-path of gas in the system.

The sensors play a key role in each step of a typical oxygen generation experiment on Mars. The sensors that determine temperature, pressure, voltage, and current are all tied into control loops to maintain the proper setpoints during operation. Five control loops exist for MOXIE: the top and bottom stack voltage controllers, which control the voltage of each electrolysis stack based on readings from current sensors, the top and bottom stack temperature controllers, which control the temperature of each electrolysis stack based on readings from temperature sensors, and the volumetric flow controller, which controls the pressure at the SOXE cathode by adjusting the RPM of the compressor. If the acceptable limit on one of the readings from these sensors is exceeded for a short period of time, MOXIE will autonomously shut down and settle into its IDLE mode to prevent damage to the instrument or the rover.

The four composition sensors onboard MOXIE determine the quantity and purity of oxygen produced and measure the ratio of CO to CO_2 gases. Three of these composition sensors use the nondispersive infrared radiation (NDIR) method, where IR radiation is passed through the gas residing in the sensor's chamber [9]. By analyzing attenuation in certain characteristic frequency bands, the sensors determine the density of the measured gases. These sensors are tuned for CO and CO_2 to provide a measure of the composition of gas leaving the cathode and to search for any CO_2 that may leak through to the anode. The fourth sensor is a luminescence sensor that detects oxygen composition on a scale of 0 – 100% at the anode.

1.3 Dissertation Objectives

MOXIE is the first demonstration of in-situ resource utilization (ISRU) on another planet. It has been extensively tested in Mars-like conditions on Earth and has been operated to produce oxygen several times in the actual Martian environment.

According to the Announcement of Opportunity (AO) from NASA in 2013, the goal of an ISRU instrument on the rover is both to demonstrate that the technology could work on Mars and that it could be scalable for a **future human mission** to Mars:

> A successful precursor mission is both prudent and required before incorporating ISRU into a mission-critical role for either crewed or robotic exploration missions. NASA's Mars 2020 mission presents an ideal opportunity to validate critical ISRU technologies in an extraterrestrial environment.
>
> An ideal investigation would validate the ability of an ISRU system to operate efficiently in varying Martian atmospheric conditions, including both diurnal and seasonal variations. Furthermore, exploration technology investigations should incorporate technologies that are **scalable to support future human missions**.

This dissertation addresses the last part of the AO, the scalability of MOXIE. Broadly, the goals of this research are to use the lessons learned from MOXIE and other ISRU demonstrations to determine the optimal design of the Big Atmospheric MOXIE (BAM) within the defined system bounds, to provide a conceptual design of BAM, and to provide estimates of key performance requirements and characteristics of BAM. The data are validated with laboratory experiments and data: primarily, the testing of solid oxide electrolysis cells under low-pressure operation. A detailed model has been developed and paired with an optimization algorithm to determine the optimal configuration of this scaled-up ISRU system within system bounds and constraints.

The primary contributions of this dissertation are:

1. Designed and developed a detailed and flexible model of a full-scale ISRU system based on MOXIE, called BAM.

2. Created a multi-objective optimization framework to optimize the design of BAM in the context of selected mission parameters.

3. Provided optimized designs of BAM on the basis of power, mass, and reliability.

4. Quantitatively and qualitatively analyzed the impact of changing design variables and mission parameters on the power, mass, and reliability of BAM.

5. Analyzed and modeled three categories of compressors for Mars atmospheric acquisition – cryogenic, sorption, and mechanical – and determined that mechanical compressors offer the lowest mass and lowest power systems.

6. Tested and characterized SOE cells under low-pressure operation, finding that SOE performance is unaffected down to cathode pressures of 150 mbar.

7. Developed a new method for quantifying operational risk, based on a Probabilistic Risk Assessment, and successfully implemented it into the BAM model.

Chapter 2 provides a literature review of Mars ISRU and its relevant technologies. Chapter 3 describes how the optimization problem is formulated for BAM, laying the foundation for the detailed description of system modeling given in Chapter 4. This is followed by Chapter 5, which gives an overview of data that were taken to validate the model, including results of low-pressure operation of SOE cells. Chapter 6 provides results of the model and a discussion of the optimized BAM architecture suggested by the model. Finally, Chapter 7 provides a summary of the contributions of this research and notes on future work. Additional information is given in the Appendices: Appendix A lists all variables used in the model, including values and justifications for constants, Appendix B lists all equations used in the modeling effort, Appendix C contains the SOE data taken for this dissertation at OxEon Energy in North Salt Lake, and Appendix D is a comprehensive list of all MATLAB code used in the model.

Chapter 2: Background and Literature Review

This chapter reviews the literature of Mars exploration, ISRU, SOE, MOXIE, and work that has been done that relates to the extensibility of MOXIE for BAM, a full-scale atmospheric ISRU plant.

2.1 Mars Exploration Overview

Data returned from a multitude of robotic exploration missions of Mars over the past 55 years have increased humanity's knowledge of the planet. The first successful spacecraft to reach Mars and return data was Mariner 4, which was launched in November of 1964. It conducted a fly-by of Mars and returned 21 photos of the planet to Earth. Mariner 6 and Mariner 7 achieved similar feats later in the decade. By coincidence, all three spacecraft flew over cratered areas of Mars, leading to the false conclusion amongst scientists that Mars resembles Earth's Moon [10].

In 1971, Mariner 9 became the first spacecraft to orbit another planet: Mars. What it found was radically different from that which was expected of the supposedly cratered, Moon-like planet. Although a planet-wide dust storm obscured the orbiter's vision of the surface, it still was able to see the peaks of what would later be identified as several dormant volcanoes. Mariner 9 also discovered what we know today as Valles Marineris, the largest canyon in the Solar System [11].

NASA moved into a new category of Mars exploration in 1976 when it successfully landed Viking 1 and Viking 2 on the surface. The Viking landers searched for life and studied the surface and local atmosphere of Mars [12, 13]. One of the key discoveries of the missions was the discovery of unexpected chemical activity in the Martian soil, which might be interpreted as a life signature. However, the scientists also found that several classes of oxidants exist on the surface of Mars that could account for these observations. Subsequent landers have contributed heavily to our knowledge of the planet. The Phoenix lander, for example, arrived in 2008 and confirmed the presence of water ice under the surface of Mars [14].

In 1997, the Pathfinder lander and Sojourner rover touched down on Mars, marking humankind's first mobile mission to the planet's surface. The rover operated for nearly three months, driving a distance of 100 meters and taking pictures of the surface. It carried a single science instrument, the Alpha-Proton X-ray Spectrometer (APXS), which analyzed the chemical composition of the surface and found the rocks it studied to be high in silica, sulfur, and iron [15,16]. Since the success of Sojourner, several rover missions have followed, with each successive mission being larger and more advanced. In 2004, NASA sent twin rovers, Spirit and Opportunity, to the planet. One of their many accomplishments was the discovery of evidence that water had once flowed on the surface of Mars [17]. In addition, Opportunity drove over 28 miles across the surface during its lifetime, vastly expanding the reach of rovers on Mars. In 2012, humankind's most advanced rover to date landed. The Curiosity rover has contributed a plethora of knowledge to our understanding of Mars, including the detection of methane in the atmosphere [18], identification of areas where water had flowed in the past [19], and the discovery of organic compounds [20]. Other countries have also increased our understanding of Mars. In 2014, India sent an orbiter to the planet for the first time, in 2016 ESA's Trace Gas Orbiter entered a successful orbit [21,22], and in 2021 the UAE's Hope orbiter and the Chinese Zhurong Rover arrived at Mars.

NASA's Curiosity rover inspired the hardware design of the most recent major Mars mission, the Mars 2020 Perseverance rover. It landed on Mars in 2021 and hosts MOXIE, the first ISRU experiment that is paving the way for human exploration of the planet.

2.2 In-Situ Resource Utilization

In-Situ Resource Utilization (ISRU) is an important consideration for Mars mission designs, as it can provide propellants, life support oxygen, life support water, habitation pressure, radiation shielding, building blocks for habitats, and more. It can be employed on a robotic mission to fuel a Mars "hopper" vehicle that uses rocket power to repeatedly take off and land while exploring the Mars surface [23]. One of the most common, and possibly most impactful, uses of ISRU that has been studied is the manufacturing of propellant for a Mars Ascent Vehicle. Propellants account for a significant portion of the mass needed for a Mars mission, meaning a reduction in propellant mass that must be sent from Earth results in a significant reduction in landed mass requirements. For each kilogram of propellant produced on Mars, 10 – 15 kg are saved that would have been launched to Mars from Low Earth Orbit (LEO), depending on trajectory design and Entry, Descent, and Landing (EDL) methods used. An example is shown in Figure 13 [24].

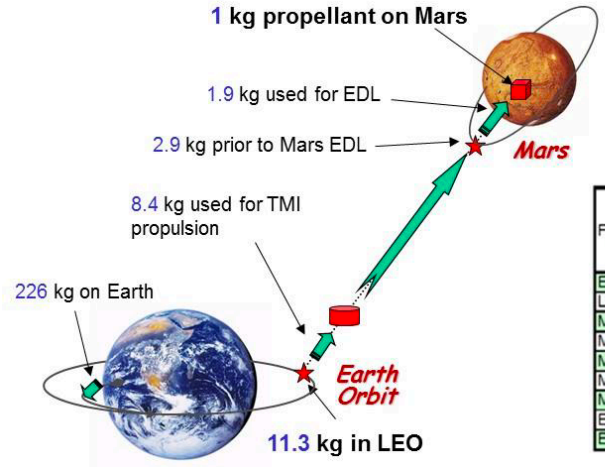

Estimates based on Aerocapture at Mars

From / To->	LEO	Mars Cruise	Mars Orbit	Mars Surface	Mars Ascent	Mars Orbit	Earth Cruise	Earth Orbit	Earth Surface
Earth	20	60	78	148	222	1489	4468	5809	7551
LEO		3	3.9	7.4	11	74	223	290	378
Mars Cruise			1.3	2.5	3.7	25	74	97	126
Mars Orbit				1.9	2.9	19	57	74	97
Mars Surface					1.5	10	30	39	51
Mars Ascent						6.7	20	26	34
Mars Orbit							3	3.9	5.1
Earth Cruise								1.3	1.7
Earth Orbit									1.3

Figure 13: Mars "gear ratios" by mission phase, detailing the mass required to be launched from each phase of the mission to Mars to equal 1 kg of propellant on Mars [24,25]

There are many additional benefits to ISRU apart from mass and cost savings. These include reducing risk through the reduction of number of launches, the ability to extend missions without relying on Earth resupply, enhanced crew safety, and improved crew psychological health from the knowledge that they have tools available to them to increase self-reliance. Many studies have been conducted to design different methods of producing propellant on Mars with ISRU, and these are covered in the following sections.

2.2.1 History of ISRU on Mars

ISRU is a useful option for cost reduction and self-sustainability of a Mars outpost. Desired resources that can be obtained on Mars range from water to building materials to the gases that make up its atmosphere. The lower Martian atmosphere is, on average, composed of 95.3% carbon dioxide, 2.7% nitrogen, 1.6% argon, 0.13% oxygen, and 0.07% carbon monoxide by molar concentration [26]. Many studies have been conducted to explore the possibility of a

human mission to Mars. Notable examples include a 1978 study by Ash, Dowler, et al. [27], the design reference mission architecture from NASA in 2009 [28], and an investigation into the various aspects of human missions to Mars by Rapp in 2015 [29]. It is apparent that one of the greatest impacts on improving the feasibility of a human mission to Mars is the in-situ production of tens of tons of ascent propellants, particularly liquid oxygen. Production of oxygen is central to this dissertation, and several forms of oxygen production on Mars have been studied. Before detailing the method that is explored in this dissertation, it is useful to consider previous oxygen-production concepts.

The Viking program of the late 1970s provided useful information for Mars ISRU studies. The primary scientific objectives of the Viking missions were to obtain high-resolution images of Mars, characterize its atmospheric and surface composition, and search for life [30]. Using data from the orbiters and landers, scientists and engineers were able to begin collecting datasets that would later enable concepts for ISRU [31]. Ash et al. focused on the potential to produce rocket propellant on Mars in 1978 [27]. They compared a variety of fuels, studying the performance and production metrics of CO, H_2, CH_4, CH_3OH, propane, and butane. Their findings were that the atmospheric carbon dioxide, in combination with water, was the most useful resource to produce both CH_4 fuel and liquid oxygen to propel a Mars Ascent Vehicle off the surface. Interestingly, they also found that CO was a viable fuel; however, its performance in terms of specific impulse was too low, making methane the preferential fuel choice. In order to achieve their goal of producing fuel and oxygen, they proposed the following methanation reaction, which would produce rocket fuel in the form of methane along with the oxygen needed for combustion:

$$CO_2 + 4H_2 \xrightarrow{\text{catalyst}} CH_4 + 2H_2O \tag{4}$$

$$2H_2O + 2H_2O \xrightarrow{\text{electrolysis}} 4H_2 + 2O_2 \tag{5}$$

The reaction stoichiometry is written to show how the hydrogen product from the electrolysis reaction can be reused as a reactant for the catalyzed reaction, and the water produce from the catalyzed reaction can be used as a reactant for the electrolysis reaction. Carbon dioxide and water are inputs to the series of reactions, hydrogen serves as an intermediary, and oxygen and methane are produced as products. A schematic of the entire refueling station, as envisioned by the authors, is shown in Figure 14.

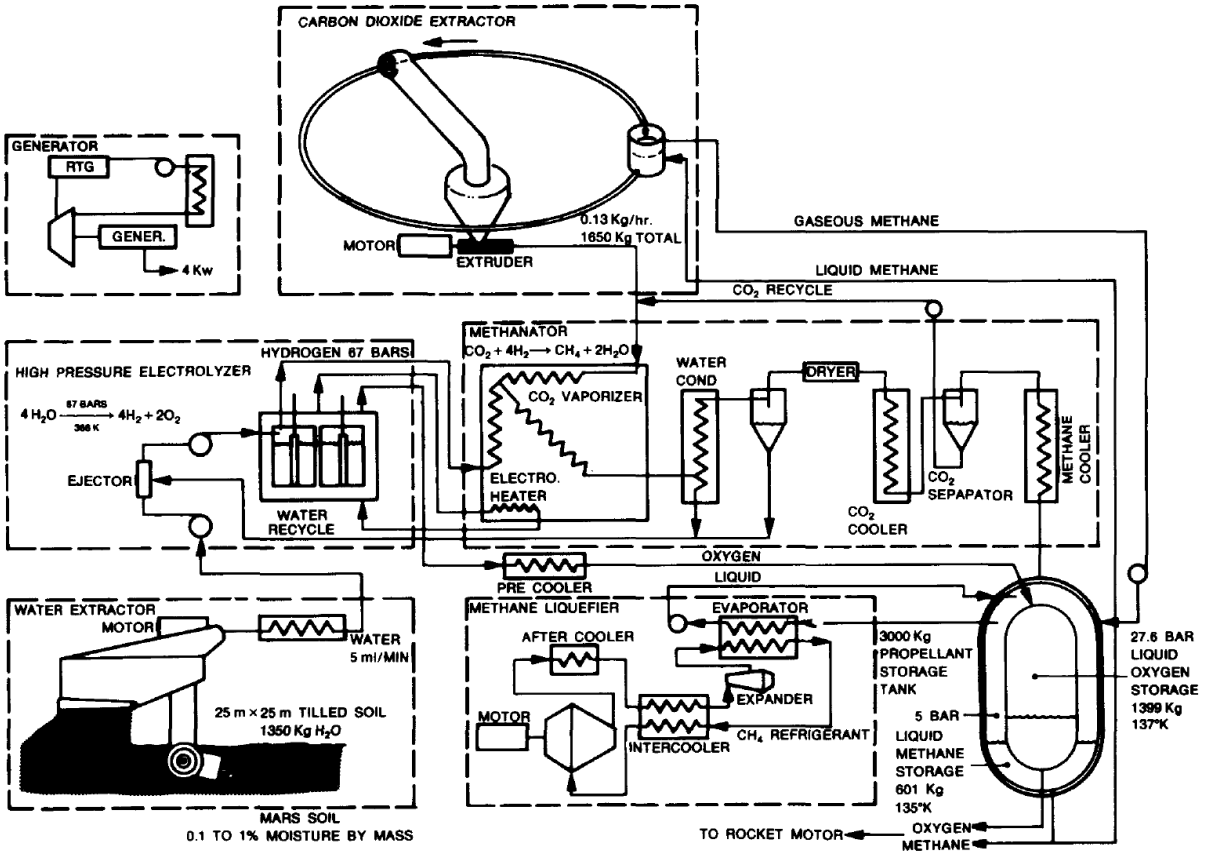

Figure 14: Refueling ISRU station to produce rocket propellant on Mars using local CO_2 and H_2O, as envisioned by Ash et al. (1978)

Ash et al. concluded that using ISRU on Mars to produce rocket propellant could reduce the landed mass required for a human mission by over 50%. Their proposal to produce propellant on Mars from water and carbon dioxide, rather than send it from Earth, was based on an analysis done by Hill and Peterson that showed that propellant mass typically represents between 80% and 90% of ascent vehicle mass [32]. When looking at modern launch vehicles, these numbers remain true and may be higher due to improvements in materials science and manufacturing processes. For example, the Falcon Heavy from SpaceX has a gross weight of 1.42 million kg and a propellant weight of 1.28 million kg, yielding a propellant fraction of 90.1% [33]. With similar numbers in mind, Ash et al. estimated that it would be economically advantageous to produce rocket propellant on Mars as opposed to bringing it from Earth. This is the principle that motivates the MOXIE project and this dissertation.

Ramohalli et al. accepted the above conclusion and expanded on it to form a preliminary ISRU framework for a manned mission in 1989 [34]. While a methane-oxygen propellant system was employed in this architecture, they determined that the methane should be carried from Earth as opposed to being produced on Mars. Primarily, this is because they found that reliability (reducing risk) is the primary driver for Mars mission design. Issues pointed out by the study include the difficulty of storing hydrogen for long durations on Mars and the complexity of recovering water from water ice deposits on Mars. Instead of using both atmospheric carbon dioxide and subsurface water to produce oxygen and methane, therefore, only the oxygen would be produced on Mars in their design. This would still represent substantial cost savings, as

approximately 78% of the rocket propellant mass in a methane-oxygen engine system is oxygen, and the complexity involved with producing methane (e.g., extracting water from the Martian surface) would be eliminated.

Hoffman et al. [35] performed a separate analysis of a combined Sabatier and water electrolysis system to produce oxygen and methane for an ascent vehicle. While many mission designs before them relied solely on the Mars atmosphere and resources brought from Earth for ascent vehicle propellant production, they took a similar approach to the work of Ash et al. from 1978 and explored a design space where water would be available. Indeed, evidence has been growing that substantial quantities of water may be present in large ice sheets beneath the surface, bound in minerals near the surface, and mixed with surface regolith [36]. Their design utilized a Rodriguez Well, similar to systems used near the poles on Earth, to supply water to their ISRU plant from subsurface ice sheets. For a crew of four on a 500-day surface stay mission, the authors determined the requirements for consumables, as shown in Table 2.

Table 2: Mission consumables required, and water required to be harvested from Mars as a supply for these consumables, of a four-crew 500-day Mars mission

	O_2	CH_4	H_2O	Martian H_2O Required
MAV	29,758	8748	N/A	19,683
Life Support	N/A	N/A	24,379	24,379
Mobility	30,276	9936	N/A	22,936
Total	**60,034 kg (~15,891 gallons)**	**18,684 kg (~4,946 gallons)**	**24,379 kg (~6,453 gallons)**	**66,998 kg (~17,735 gallons)**

This mission scenario considered the use of atmospheric carbon dioxide and subsurface water to supply oxygen, methane, and water for the Mars ascent vehicle, but also for life support systems and mobility unit propellant. The water requirements are fairly evenly divided amongst these three.

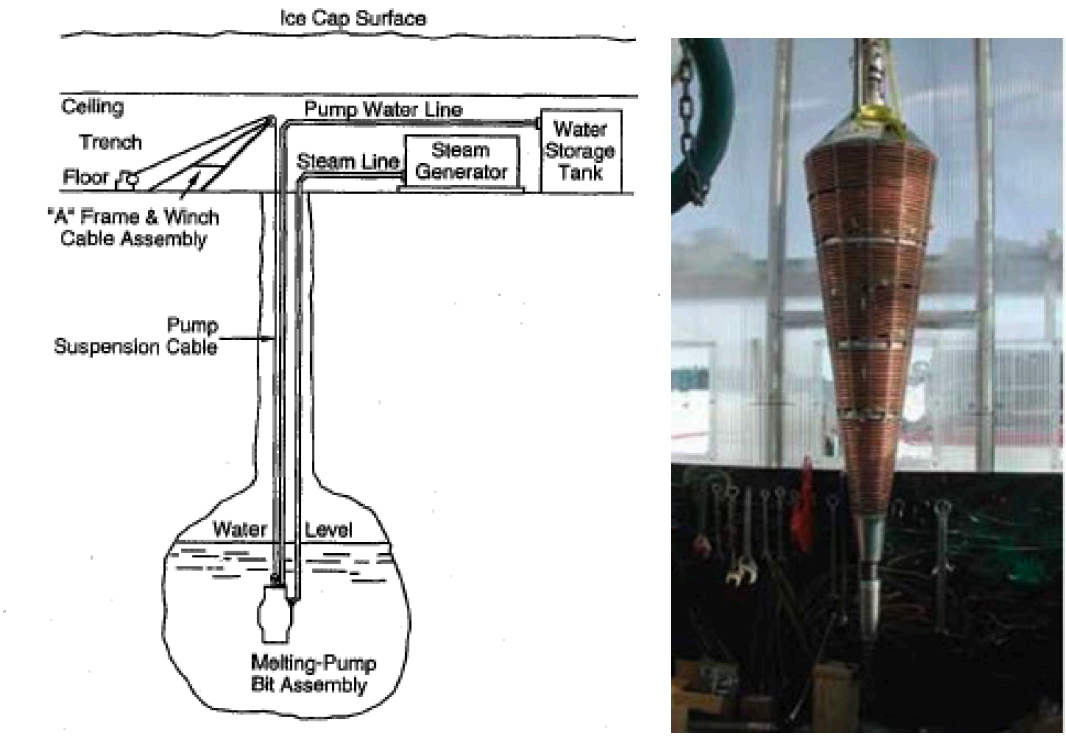

Figure 15: (Left) Rodriguez Well concept for extracting water ice on Mars and (right) a hot fluid drill used to extract water [37]

Figure 15 shows the concept for a Rodriguez Well, where a drill such as a hot fluid drill, which uses a jet of hot water to melt its way through ice, creates a hole and a subsurface well that becomes a reservoir for melted water. Hoffman et al. concluded that the simulation results of the Rodriguez Well show that it is likely a viable approach for ISRU on Mars.

Many studies have also been conducted to determine the usefulness of not only water or carbon dioxide, but of other resources on Mars. For example, Sridhar et al. released a study that analyzed the buffer gas requirements for a Mars mission, concluding that 1.3 metric tons of buffer gas would be lost in airlocks per mission [38]. To counter this, they suggested an adsorption separation unit to separate and compress both the buffer gases (N_2 and Ar) and CO_2 to feed a propellant production plant. In this way, the propellant production would be enabled as normal in these architectures with the added benefit of producing significant quantities of buffer gas to compensate airlock losses.

Robert Zubrin, president of the Mars Society, has also put forth a substantial amount of literature that details various ISRU avenues that one might take when working on Mars. In his 1996 book "The Case for Mars", he devoted multiple chapters to defining the specific ISRU processes that would be beneficial to employ on a manned mission to the planet. He refers to this ISRU as "known and practiced chemical engineering", and all that is needed to land humans on Mars is "present-day technology mixed with some nineteenth-century chemical engineering, a dose of common sense, and a little bit of moxie" [39]. He proposed the same methanation system as Ash et al. [27] to build a methane – oxygen propellant system on Mars from the atmospheric CO_2 and ground-based H_2O. Zubrin recognized that an additional source of oxygen might be necessary to run the MAV engine oxygen-rich, which would increase performance. Additionally, he proposed a second system where hydrogen is brought from Earth to create methane rather than harvesting

it from Martian water reserves. The outputs of this reaction system are also methane and oxygen, but additional oxygen is required to produce the proper oxidizer to fuel ratio for the engine. In order to generate extra oxygen in both of the proposed systems, Zubrin used solid oxide electrolysis to drive the following chemical reaction [39]:

$$2CO_2 \xrightarrow{\text{electrolysis}} 2CO + O_2 \quad (6)$$

This is the same process that MOXIE employs to produce oxygen on Mars.

The closest that a prior Mars ISRU mission had come to flying was the Mars In-situ-propellant-production Precursor (MIP) payload [40]. It was intended to fly onboard the 2001 Mars Surveyor Lander, a planned Mars probe that was canceled in 2000 after failures of both the Mars Climate Orbiter and Mars Polar Lander missions in 1999. MIP was planned to produce oxygen from the Mars atmosphere using a zirconia solid oxide electrolysis cell operated at 750 °C. This was known as the Oxygen Generator Subsystem (OGS). The Mars Atmospheric Acquisition and Compression (MAAC) subsystem was a zeolite adsorption compressor that would selectively adsorb and compress carbon dioxide from the atmosphere. The system would adsorb carbon dioxide over the course of several nights at low temperatures and then, when heated, release the CO_2 at an elevated pressure. Other subsystems of MIP included the Mars Array Technology Experiment (MATE) to measure and test advanced solar cells, the Dust Accumulation and Repulsion Test (DART) to investigate the effects of dust, and the Mars Thermal Environment and Radiator Characterization (MTERC) to measure the night sky temperature and test radiator effectiveness. A subsystem rendering of MIP and the engineering development unit are shown in Figure 16.

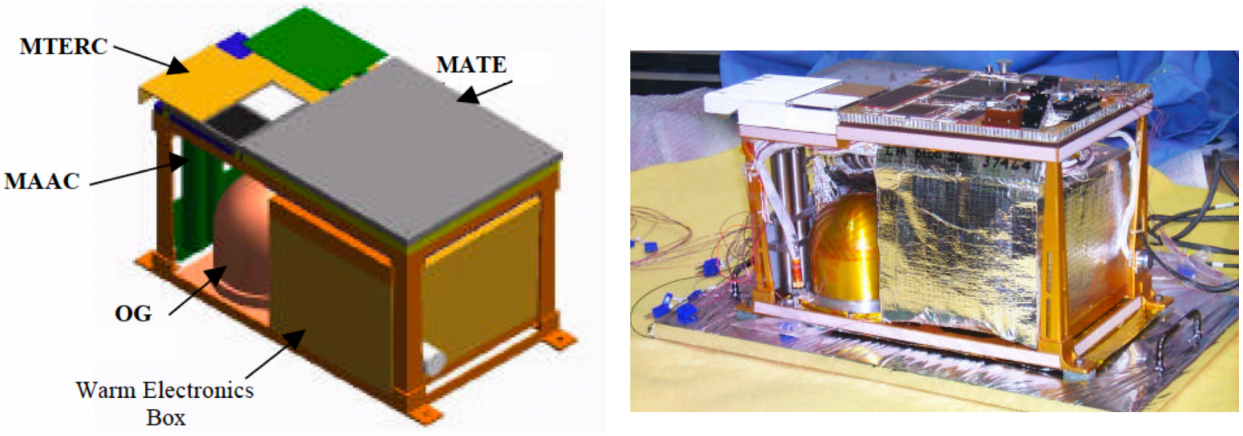

Figure 16: (Left) The Mars ISPP Precursor (MIP) flight demonstration model rendering and (right) the MIP Engineering Development Unit [41]

The MAAC is described in more detail later in this chapter. The goals of the OGS were to produce oxygen at a rate of at least 0.5 sccm (0.043 g/hr) for each run and operate at least 10 times during 90 sols on Mars.

Despite the primary mission being canceled, MIP's development unit and qualification unit underwent extensive testing [42]. The development unit testing included a three-week operation

in a Mars environmental chamber. The qualification unit underwent typical qualification tests and five-day and ten-day simulations in a Mars chamber. Between these tests, several minor problems were uncovered and dealt with, including powdered insulation material loosening from around the MAAC sorbent bed and a leak developing in the MAAC. At the conclusion of the qualification testing, all subsystems passed, and MIP was deemed to have had a successful qualification testing phase. MIP is a good example of an alternate architecture to MOXIE; while both use the same core electrolysis process to produce oxygen, the compression systems and operating parameters are different. The development and testing of systems like MIP and MOXIE are useful technology development steps for the enablement of full-scale ISRU systems to support humans on Mars.

2.2.2 NASA Design Reference Missions and Architecture

An important reference that guides the design of systems like MIP and MOXIE is the series of Design Reference Missions from NASA that detail the agency's strategies for missions to Mars. They are an important reference because they direct NASA's investments and represent the work of a large number of experts at the agency. The NASA Design Reference Mission (DRM) 2.0, published in 1997 [43], detailed high-level plans for an atmosphere-processing ISRU plant. Later, the NASA Design Reference Architecture (DRA) 5.0, published in 2009 [28], expanded on these plans and has been a key driver for recent ISRU system designs. DRA 5.0 is considered an "architecture" rather than a "mission", as it refers to an entire sequence of missions for a human Mars campaign. DRM 2.0 and DRA 5.0 will be briefly explored here, as they have important implications both for ISRU system design as well as overall mission architecture design. DRM 1.0, 3.0, and 4.0 will not be addressed here, as the findings from DRM 1.0 are covered in DRM 2.0, DRM 3.0 represents a continuation of the work from DRM 2.0 and does not represent a final approach to a human Mars mission, and DRM 4.0 was a follow-on to DRM 3.0 that focused on further refinement of system designs. DRM 2.0 and DRA 5.0 are a representative sample of all five of these references.

NASA Design Reference Mission 2.0

The NASA Design Reference Mission 2.0 [43] describes NASA's plan in 1997 for a mission to Mars. It builds off designs presented in the first DRM [44] and explores the concept of operations and technologies needed to send humans to Mars. DRM 2.0 examines a campaign for the first three human missions to Mars. Each mission is located at the same site to establish a base with increasing capabilities. The missions are designed for a crew of six with a fast transit to Mars (4 to 6 months) and a long surface stay of 600 days on Mars. Power would be supplied by two nuclear reactors.

The architecture presented in DRM 2.0 relies on two ISRU plants that produce propellant for the ascent vehicle and water, oxygen, and buffer gases for life support systems. The ISRU system, along with other modules and technologies needed to support humans, would be sent to Mars and confirmed to be functioning on the surface prior to departure of the first flight crew from Earth. The first ISRU plant would be sent prior to the first human launch, and the second would be delivered prior to the second human launch as a backup. Both would be stationed at the same location on Mars.

The requirements laid out by DRM 2.0 for the first ISRU plant are that it would produce 20.2 tons of oxygen, 5.8 tons of methane, 23.2 tons of water, 4.5 tons of breathing oxygen, and 3.9 tons of an inert gas mix made of nitrogen and argon. Further, the system would be required to liquefy and store the materials.

The method of production for these resources would be to use the Martian atmosphere (carbon dioxide, nitrogen, and argon) as a feedstock and combine it with hydrogen brought from Earth. To produce water, oxygen, and methane, a combined Sabatier and water electrolysis process would be used. This is a well-known process on Earth and, in addition to water, would generate a mass ratio of 2:1 of oxygen to methane. However, oxygen-methane rocket engines for Mars ideally operate at a mass ratio of 3.5:1, requiring additional oxygen. To satisfy this requirement, extra oxygen would be produced from carbon dioxide, using solid oxide electrolysis with zirconia cells. Nitrogen and argon would be extracted in an absorption process, though it was not studied in detail for DRM 2.0. A schematic of the ISRU plant is shown in Figure 17.

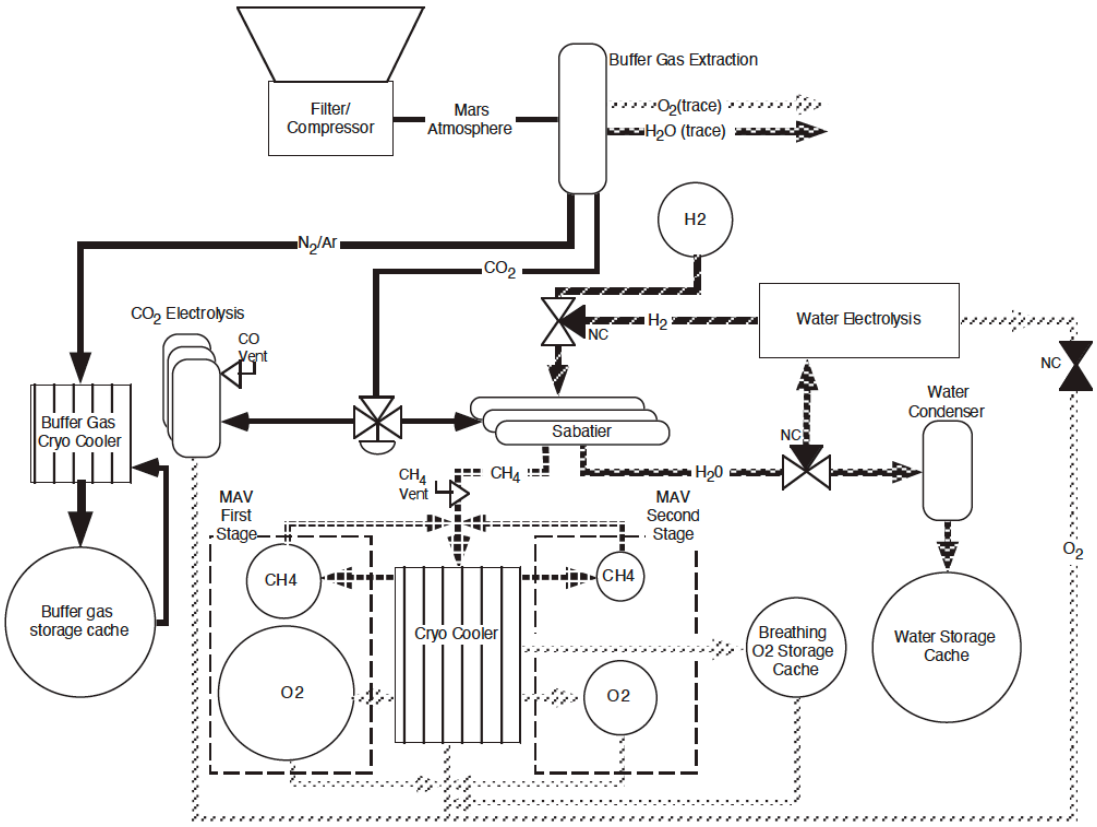

Figure 17: ISRU plant schematic for rocket propellant production on Mars as designed in NASA's DRM 2.0. The design uses CO_2 from the Martian atmosphere in combination with H_2 brought from Earth to produce liquid O_2 and CH_4.

The first ISRU plant sent to Mars would be slightly larger than subsequent plants, as the authors imposed extra requirements on the first plant delivered. Namely, the first plant would be responsible for creating a cache of life support reserves. The authors did not undertake a detailed sizing of the ISRU plants, but estimated mass and power requirements based on prior work in the field. These are given for both plants in Table 3 and Table 4.

Table 3: Production rate, mass, and power estimates for subcomponents of the first ISRU plant in the DRM 2.0 Architecture

Plant Component	Production Rate (per day)	Component Mass (kg)	Component Power (kWe)
Compressor	269.7 kg	716	4.09
CO_2 Electrolysis	53.2 kg O_2	2128	63.31
Sabatier	22.9 kg CH_4	504	1.15
H_2O Electrolysis	27.8 kg H_2O	778	0.00
Buffer Gas Extraction	8.7 kg	23	0.13
Cryogenic Coolers	84.8 kg	653	3.59

Table 4: Production rate, mass, and power estimates for subcomponents of the second ISRU plant in the DRM 2.0 Architecture

Plant Component	Production Rate (per day)	Component Mass (kg)	Component Power (kWe)
Compressor	87.8 kg	233	1.33
CO_2 Electrolysis	18.5 kg O_2	740	22.00
Sabatier	12.4 kg CH_4	272	0.62
H_2O Electrolysis	27.8 kg H_2O	778	5.79
Cryogenic Coolers	30.8 kg	238	2.3

The second ISRU plant represents the 'standard' ISRU plant in this architecture, replicated for subsequent missions. The extra capacity of the first ISRU plant is only needed if the reserves are used.

DRM 2.0 provided a foundation for a Mars mission architecture. While it lacked many details in its ISRU system design, it paved the way for the more detailed ISRU analysis in DRA 5.0.

NASA Design Reference Architecture 5.0

The NASA Design Reference Architecture 5.0 [28] describes a mission architecture that encompasses the first three human missions to Mars. A crew of six is assumed to travel on a conjunction class trajectory, where they would spend 180 days in cruise on the way to Mars, 500 days on the surface, and 180 days in cruise on the way back to Earth. Power would be supplied by surface fission reactors for both the crew requirements and the ISRU system. A key difference from DRM 2.0 is that each mission would be located at a different site on Mars in an effort to expand the diversity of scientific discoveries across the missions. A concept of operations for the mission is shown in Figure 18.

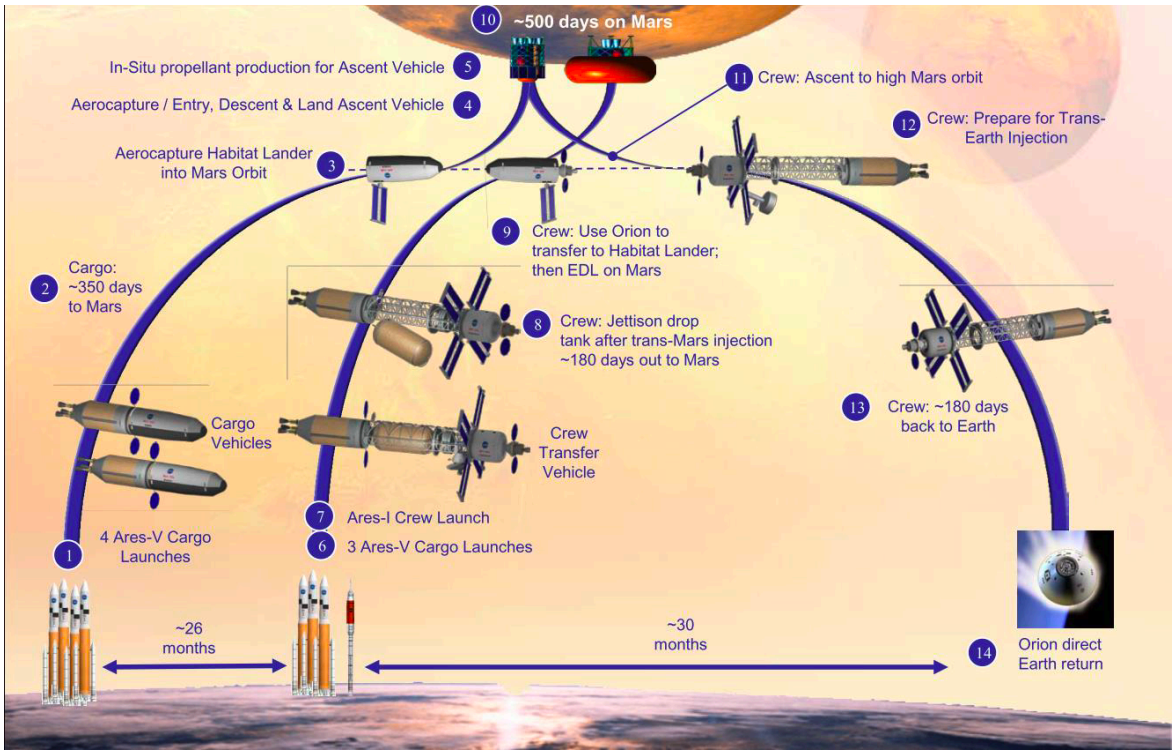

Figure 18: Concept of Operations for the first human mission to Mars as designed in NASA's Mars Design Reference Architecture 5.0. Seven cargo launches are followed by the first crew launch.

A top-down trade tree was used as a systems engineering tool to systematically understand all possible mission combinations under the given set of constraints. This is shown in Figure 19.

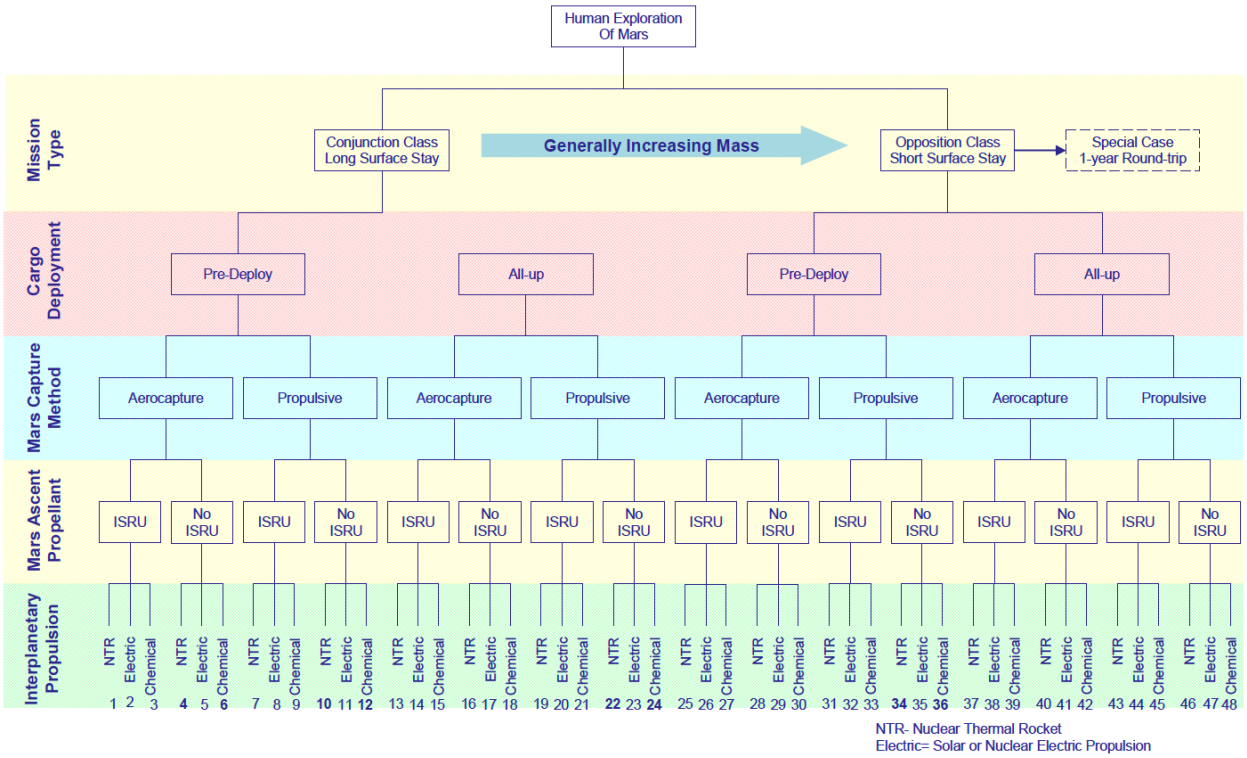

Figure 19: Systems trade tree in DRA 5.0 to determine the scope of the mission design space.

The use of ISRU to generate ascent propellant is a key trade of the architectures considered in DRA 5.0. It reduces the total mass needed to complete each mission and results in a significant reduction in lander size. However, DRA 5.0 takes a different approach from DRM 2.0 for its ISRU system. Rather than bringing hydrogen from Earth to produce methane via the Sabatier process, methane itself is brought from Earth. The oxidizer is designed to be produced on Mars via solid oxide electrolysis, consistent with former architectures. Carbon monoxide is also produced as a byproduct gas in the solid oxide electrolysis system but is vented. Also consistent with DRM 2.0, nitrogen and argon are captured to create buffer gases for life support systems. In addition, 400 kg of hydrogen are brought from Earth, but not for fuel production; the hydrogen is used to produce water to replace the water that is lost during EVA operations.

The ISRU system is divided into three primary subsystems: the atmospheric acquisition subsystem, the consumable generation subsystem, and the liquefaction subsystem. The atmospheric acquisition subsystem consists of a micro-channel adsorption pump that acquires CO_2 in a temperature-swing adsorption process. Thin beds of sorbent material are rapidly heated and cooled using micro-channel heat exchangers to adsorb and desorb CO_2 in a rapid manner. The consumable generation subsystem is primarily the solid oxide electrolysis stack. Finally, the liquefaction subsystem uses cryocoolers to liquefy both methane and oxygen.

A key finding of DRA 5.0 is that power is the limiting resource of the ISRU system. Therefore, it is possible to add redundancy to the system in the form of mass and volume, as these do not contribute to power usage. As a result, an entirely redundant ISRU unit was added to the architecture to buy down risk. The mass, power, and volume of the system was calculated with a model and is shown in Table 5.

Table 5: Power, mass, and volume estimates for an ISRU system in NASA's DRA 5.0

	Quantity	Unit Mass (kg)	Total Mass (kg)	Volume (m3)	Power (kWe)
Atmospheric Acquisition Subsystem	2	-	492.12	0.66	17.86
Filter/Frit	4	0.10	0.40	-	-
Microchannel CO2 Adsorption Pump	4	57.50	230.00	0.01	17.86
check Valve	8	0.10	0.80	-	-
Buffer gas pump	4	1.23	4.92	0.00	0.00
Isolation Valve	8	0.50	4.00	-	-
Buffer gas tank	1	250.00	250.00	0.60	-
Flow Controller	4	0.50	2.00	-	-
Oxygen Generation System	2	-	38.80	0.10	2.59
Solid Oxide Electrolysis Stack	2	17.00	34.00	0.05	2.59
Isolation Valve	8	0.50	4.00	-	-
Filter/Frit	4	0.10	0.40	-	-
check Valve	4	0.10	0.40	-	-
Liquefaction Subsystem	1	-	34.60	0.10	3.26
Hydrogen Cooler	2	10.60	21.20	0.01	0.34
Methane Cooler	2	1.20	2.40	0.01	0.02
Oxygen Crycooler	2	5.50	11.00	0.03	2.90
ISRU System (each)	**-**	**-**	**565.52**	**0.86**	**23.71**

Power estimates are based on a nuclear-powered system that enables continuous ISRU plant operation. The authors found that the ISRU plant was the overall highest consumer of power for the Mars reference mission, using 25 kWe continuously. This quantity of power is sufficient to supply the habitats, rovers, and miscellaneous power requirements of the human crew after their

arrival on Mars. Therefore, according to the authors, the power system for a human mission to Mars should be sized based on the ISRU requirements.

The DRA 5.0 team considered several ISRU technologies during their trade studies. These included producing oxygen on Mars while bringing methane from Earth, producing oxygen and methane on Mars while bringing hydrogen from Earth, and producing oxygen and methane on Mars using water from Martian soil (which varies between 3% and 8% by mass).

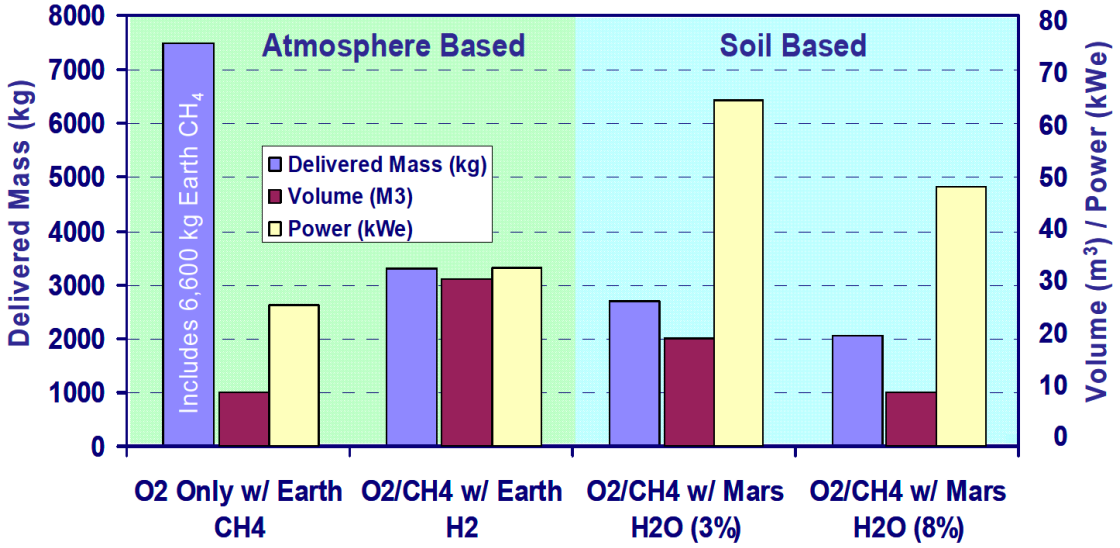

Figure 20: Comparison of ISRU strategies for Mars missions considered by DRA 5.0. All utilize oxygen produced from the carbon dioxide atmosphere on Mars and compare options to produce methane for Mars Ascent Vehicle fuel.

According to Figure 20, the oxygen-only architecture has the highest system mass but the lowest volume and power. The oxygen and methane atmosphere-based system has lower mass but the highest system volume. The oxygen and methane soil-based systems have the lowest mass but highest power requirements. Two options are listed because the water content in the Martian soil is assumed to range between 3% and 8%, depending on location. The authors recommend the first architecture, as it has the strongest combination of mass savings, low volume, and low power, and low system complexity. In all cases, the mass savings from ISRU are substantial when compared with bringing the oxygen from Earth.

2.2.3 Types of Martian ISRU

Thus far, several modes of ISRU operation on Mars have been proposed to produce the needed ascent vehicle propellant. These include the use of the carbon dioxide atmosphere to generate oxygen, the use of subsurface water to produce oxygen and hydrogen, the combination of the two to produce methane and oxygen, and the use of the atmosphere coupled with supplies brought from Earth to produce methane and oxygen. Another option that has only been briefly discussed in the analysis of DRA 5.0, but has been considered in many studies, is the processing of hydrated Martian regolith to extract water [35,45,46]. This represents an alternative approach to mining subsurface water ice, though it requires machinery that can process large quantities of regolith. In 2008, 2010, and 2012, NASA developed and tested technologies for processing of lunar ice and water, which included lunar regolith excavation [47]. While the environments on

the Moon and Mars differ significantly, there are still parallels between regolith processing technologies needed for ISRU on both bodies, such as the equipment that would be used to excavate and bake the regolith. Therefore, certain studies of ISRU on the Moon are beneficial for Mars ISRU technology development [48]. The proposed Resource Prospector mission, for example, led to the development of lunar polar ice prospecting technologies. While canceled, the design and development work completed for the mission informs future ground-based ISRU systems for Mars as well as ISRU systems that may be developed for commercial lunar landers [49].

Kleinhenz and Paz published a study in 2017 that outlines a plan to use atmospheric CO_2 in combination with water from the Martian regolith to produce oxygen and methane for ascent vehicle propellant [2]. They considered a range of water content in the soil from 1.3% – 8% and used an excel-based model to compute system mass and power. Three ISRU cases were considered and traded: i) oxygen production only, ii) oxygen and methane production for propellant, and iii) oxygen and methane production for propellant and life support. The system design for the propellant production system is shown in Figure 21 and the mass and power required for each case is shown in Figure 22.

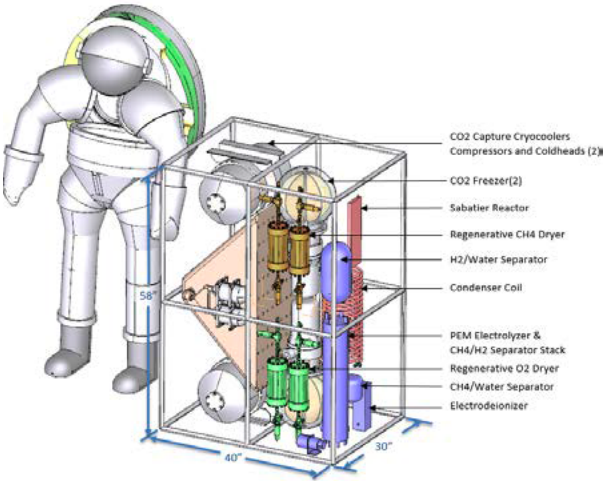

Figure 21: Propellant production system design from Kleinhenz and Paz (2017)

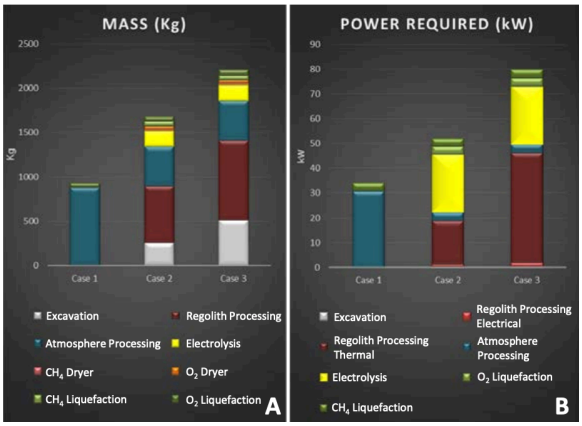

Figure 22: Mass and power requirements for three baseline ISRU cases, divided by subsystem

Case 1, the oxygen-only system, is the same type of system as MOXIE and was the simplest, weighing 0.9 mT and consuming 34 kW. Adding a regolith processing system and assuming 1.3% water content in the regolith for Case 2 increased mass to 1.7 mT and the power requirement to 52 kW. Adding life support system requirements in Case 3 increased the mass to 2.2 mT and power to 80 kW. To more fairly compare these cases, a "total landed mass" was calculated for each case, which included the mass of the ISRU systems as well as the mass of propellants supplied from Earth. The results are shown in Figure 23.

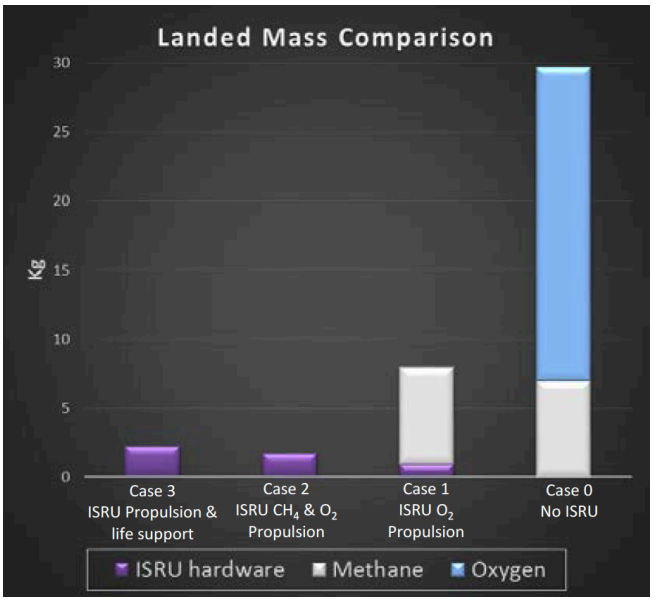

Figure 23: Landed mass required for each ISRU case, including the ISRU hardware mass and mass of propellants brought from Earth.

Producing oxygen in Case 1 results in a 75% mass reduction over Case 0. Adding an extra 0.8 mT of ISRU hardware to enable Case 2 results in a savings of 7 mT of methane that would have to be brought from Earth in Case 1. Therefore, the results from this study indicate that the use of water from Martian regolith should be considered in a full-scale ISRU system.

Sanders et al. published a study in 2015 that summarized past and present Mars ISRU options [25]. They reviewed findings from DRM 3.0, DRA 5.0, and several independent ISRU studies. They found that the primary criteria that should be used to evaluate ISRU options are impacts on mission mass, power, volume, and risk, mission and architecture flexibility, and failure recovery options. A design tree that lists different types and choices for Mars ISRU architectures is shown in Figure 24, most of which have been discussed in this chapter.

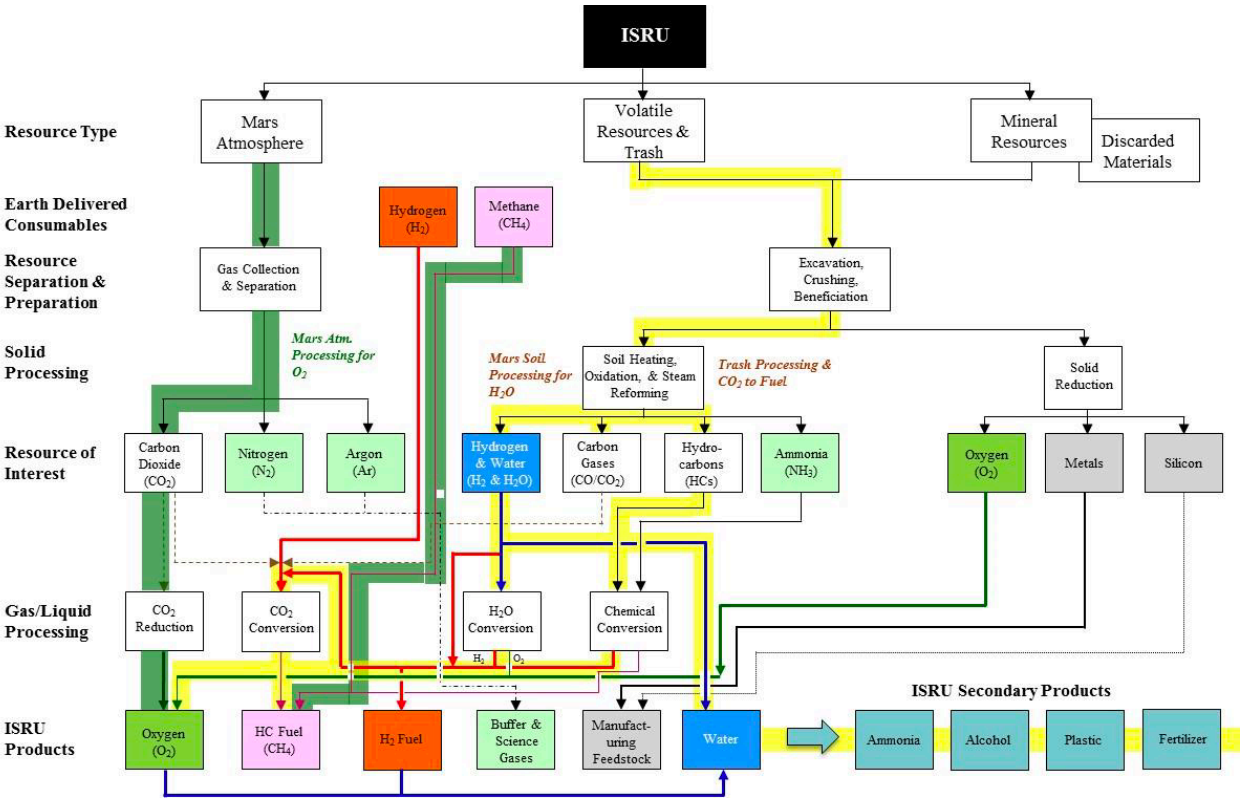

Figure 24: Mars ISRU design decision tree, depicting choices for Mars ISRU architectures, from Sanders et al. (2015)

Most of the study focused on comparing two architectures: atmosphere-only processing, and combined atmosphere/soil processing. Designs for the two systems are shown in Figure 25.

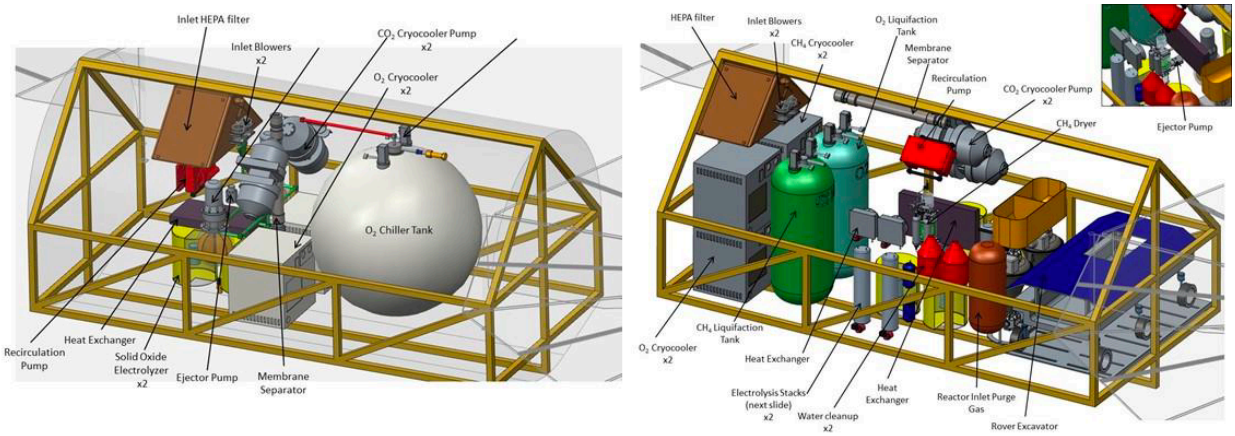

Figure 25: (left) Atmosphere-only ISRU plant design and (right) combined atmosphere/soil processing unit design from Sanders et al. (2015)

Based solely on minimization of mass and power, the authors found that processing only the atmosphere versus both the atmosphere and soil are comparable. Processing both the atmosphere and soil on Mars results in a larger number of benefits as well as a larger number of concerns compared to atmospheric processing alone. These are summarized in Table 6.

Table 6: Sanders et al. (2015) strengths and weaknesses comparing atmosphere-only ISRU processing on Mars with combined atmosphere and soil processing.

	Atmosphere Resource Processing	Atmosphere & Soil Resource Processing
Strengths	Atmosphere resources are known and are globally obtainabile (no landing site limitations)	Lessons-learned and hardware experience from lunar ice prospecting and regolith excavation and thermal processing technologies and systems are applicable to Mars
	Production of oxygen (O_2) makes >75% of the ascent propellant mass	Production of 100% O_2 and CH_4 possible; Allows for recovery of failures/leakage, refueling and reusing surface hoppers and landers, and O_2/CH_4 fuel cell power systems on rovers
	Significant research and testing has been performed on several methods of collecting and processing carbon dioxide (CO_2)	Even low concentrations of water in hydrated soils at the surface (3 to 8%) provide tremendous mass benefits compared to the mass of methane that must be brought from Earth
	Processing the atmosphere alone enables the least complex systems	Full backup to life support. Also, increased radiation shielding due to H_2O and soil
		A wide range of secondary products are possible: metals, ammonia, alcohols, plastics, fertilizers, etc.
Weaknesses	ISRU products limited to O_2 and nitrogen (N_2). Production of methane (CH4) or extra water (H_2O) requires delivery of liquid hydrogen (H_2)	Uncertainty still exists in the form and distribution (depth, concentration) of H_2O. Different technologies may be needed for hydrated soils vs icy subsurface soils
		Orbital data is at very low resolution for site selection. Makes landing site selection difficult
	Optimized ISRU processes are not synergistic with life uspport technologies	Concerns exist with respect to ISRU soil processing for water and planetary protection requirements
		Systems are more complex.
		Requires long term autonomous operation of excavation and soil processing equipment for pre-deployed systems

The majority of recent ISRU studies for producing Mars ascent vehicle propellant fall into one of two categories: i) use the atmospheric CO_2 to produce O_2, or ii) use the atmospheric CO_2 and H_2O from the surface to produce O_2 and CH_4. The former is a simpler system but results in less overall mass savings than the latter. A summary of these ISRU methods for O_2 production on Mars is shown in Table 7.

Table 7: ISRU methods to produce oxygen on Mars using feedstock CO_2. Required inputs are identified with red text, while primary outputs are identified with blue text.

ISRU Method	Reactions
Solid Oxide Electrolysis	$2CO_2 \rightarrow 2CO + O_2$
Reverse Water Gas Shift with Water Electrolysis	i. $2CO_2 + 2H_2 \rightarrow 2CO + 2H_2O$ ii. $2H_2O \rightarrow 2H_2 + O_2$
Sabatier with Water Electrolysis	i. $CO_2 + 4H_2 \rightarrow 2H_2O + CH_4$ ii. $2H_2O \rightarrow 2H_2 + O_2$

Two of the methods require two chemical reactions, as they use both CO_2 and H_2O as feedstocks. The other method, which uses solid oxide electrolysis to electrolyze CO_2, is discussed in the next section, followed by literature reviews of the other major components of a scaled-up atmospheric ISRU plant: dust mitigation, atmospheric compression, and oxygen liquefaction.

2.3 Solid Oxide Electrolysis

In 1899, Walther Nernst discovered that stabilized zirconia could conduct oxygen ions [50]. He found that pure zirconia had relatively low conductivity but, when doped with other oxides such as magnesium oxide, had significantly higher conductivity at high temperatures. Since then,

researchers have found that other doping and stabilizing agents such as yttria and scandia further improve the oxygen ionic conductivity [51]. The ability of zirconia to conduct oxygen ions has since been used to develop fuel cells, which combine gases to produce electricity, and electrolysis systems, which use electricity to produce gases. Fuel cells on Mars have been studied to provide power for human systems [52]. Electrolysis systems like MOXIE have also been studied to provide propellants on Mars. In solid oxide electrolysis (SOE), a gas flows over a porous cathode surface and is electrolyzed at the three-phase boundary between the electrolyte, the cathode, and the gas when a voltage is applied. In the case of MOXIE, CO_2 is electrolyzed into CO and O^{2-}. The oxygen ions migrate across the electrolyte and recombine on the anode side to form oxygen molecules that can be stored and used. While certain designers have proposed the use of proton exchange membrane (PEM) electrolyzers for Mars oxygen production, theoretical analysis has shown that the total energy requirements of the two are equivalent, and SOE minimum voltage is at least 20% lower than a PEM electrolyzer [53]. This leads to favorable system power scaling for the SOE as production rate is increased. As a result, SOE is considered the baseline technology for this dissertation.

2.3.1 SOE for Mars

Solid oxide electrolysis for Mars has been studied over the course of the past several decades to enable ISRU missions. Many of the ISRU design missions presented in the previous section utilized electrolysis of CO_2 as the primary means of producing oxygen for ascent vehicle propellant. These were a sampling of reference missions that incorporated the work of SOE researchers into their broader mission contexts. Here, a subset of the more specialized work on SOE for Mars ISRU is explored.

In 1982, Ash et al. designed a CO_2 SOE system that could enable a Mars sample return mission using a single Space Shuttle launch [54]. Their analysis was largely based on Richter's 1981 study on the theoretical and experimental aspects of YSZ membrane oxygen separation [55]. He developed a model of the thermodynamic electrochemical processes of a YSZ SOE system. Experimentally, Richter explored a range of operating conditions and their effect on performance. He found that oxygen production is limited by the flow resistance of the electrodes and the critical electrical potential of the electrolyte. Both Suitor and Tao continued the work, exploring the use of many different electrode materials and characterizing their performances with YSZ electrolytes [56,57,58].

Colvin, Schallhorn, and Ramohalli tested a tubular solid zirconia electrolyte cell for Mars applications in 1992 as part of a general study for an oxygen production plant [59]. They measured and characterized cell efficiencies by varying cell potential, operating temperature, and CO_2 flow rate. Cell potential was varied from 0.6 to 2.0 VDC, operating temperature was varied from 800 to 100 °C, and CO_2 flow rate was varied from 38 – 1475 sccm. Their findings included a second order dependence of oxygen production on the applied cell potential, a strong dependence of oxygen production on operating temperature, and a weak dependence of oxygen production on inlet carbon dioxide flowrate. These findings are significant for SOE system design as they yield insight into the design variables that have the largest effects on oxygen production.

The University of Arizona also conducted an extensive amount of testing on solid oxide electrolysis cells for Mars applications in the 1990s and 2000s. Sridhar and Vaniman demonstrated performance of planar solid oxide electrochemical cells in 1997 [60]. Later, they investigated the use of SOE as a combined electrolysis system for both water and carbon dioxide [61]. As discussed in Section 2.2, this uses a Sabatier reactor to produce methane and oxygen for use as rocket propellant. Sridhar also contributed to the oxygen production system onboard the Mars Surveyor Mission [41].

In more recent years, the companies Ceramatec and OxEon Energy near Salt Lake City, Utah, have developed and tested SOE technology for Mars applications [62,63]. These experiments have included testing conducted at Idaho National Laboratory to test improvements in long-term durability of SOE cells [64], high temperature co-electrolysis of carbon dioxide and water [65], and reversible solid electrolyzer cells [66]. Their findings have resulted in the development of SOE cells with improved resistance to degradation using novel material applications. Resistance degradation is important for Mars missions where an SOE system will be required to operate autonomously and continuously for many months. In addition, OxEon Energy's work on reversible cells could be used in a Mars ISRU system to both generate propellant and, when operated in reverse, combine propellant to generate electricity for emergency power [67]. Ceramatec and OxEon Energy have been key contributors to the development of the MOXIE system.

2.3.2 MOXIE and Other SOE Proposals

In 2013, NASA released an Announcement of Opportunity (AO) to develop an ISRU instrument for the next Mars rover that demonstrates that ISRU technology could work on Mars and that it could be scalable for a future human mission to Mars. More specifically, the instrument was tasked with filtering dust, capturing and compressing atmospheric CO_2, and producing and measuring small quantities of O_2 [68].

The joint proposal for MOXIE from MIT and the Jet Propulsion Laboratory was selected [69]. As discussed in Section 1.2, the MOXIE instrument includes a filter, scroll pump, two solid oxide electrolysis stacks of five electrolytic cells each, and a sensor array. The winning proposal also included the intent to model and test for the extensibility of MOXIE to study the scalability of the instrument. This dissertation addresses a portion of that extensibility research. In the following sections, the important principles of solid oxide electrolysis that have enabled MOXIE to accomplish its goals on Mars are explored.

2.3.3 SOE Electrolyte Materials

Zirconia, a ceramic, is a common material used for electrolytes in electrolysis applications. Another electrolyte that has been considered and tested is magnesium-doped lanthanum gallate (LSGM) [70], though it was found to be significantly more susceptible than zirconia to chromium poisoning from the interconnect, making it an inferior choice for long-duration applications. Doping zirconia with other materials, such as yttria or scandia, can improve its ionic conductivity properties [71,72]. MOXIE uses Scandia-Stabilized Zirconia (ScSZ) as its electrolyte for this reason. By embedding Sc^{3+} ions into the lattice of zirconia ions (Zr^{4+}), oxygen vacancies are created at Zr^{4+} sites. Without Scandia ions, the lattice is composed of ZrO_2. At the Scandia sites, Sc_2O_3 forms. Whereas two Zr atoms bond to four O atoms, two Sc atoms only

bond to three O atoms, creating an oxygen vacancy. Because of this, when an electric field is applied across a ScSZ electrolyte, oxygen ions can move through the electrolyte by transitioning from vacancy to vacancy until they arrive at the anode. This is depicted in the cross-sectional view of a ScSZ cell in Figure 26.

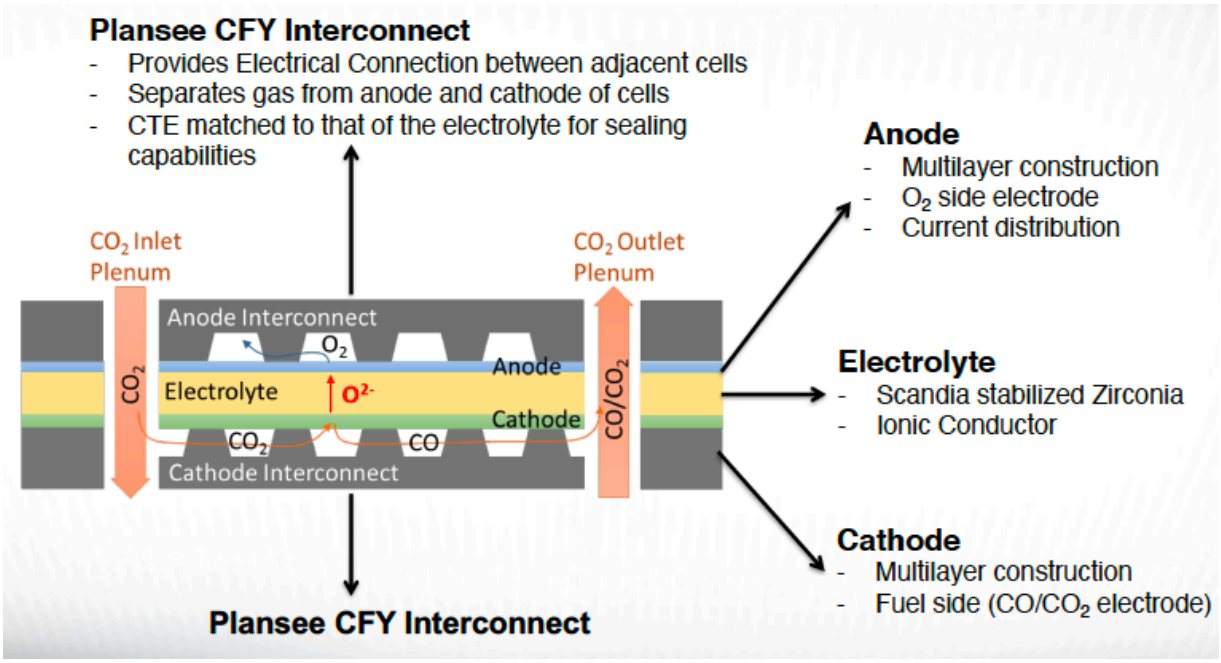

Figure 26: Cross-sectional view of a Scandia-Stabilized Zirconia electrolyte with its cathode and anode labeled and oxygen flow depicted. Credit: Ceramatec.

Importantly, the ScSZ electrolyte is a barrier to the flow of other molecules, such as CO and CO_2 that are present on the cathode. This acts as a filter, allowing pure oxygen to form on the anode side of the cell. The oxygen ions transfer through the electrolyte, carrying two electrons each with them. When the ions reach the anode, four electrons are returned to the cathode side via the anode and CFY interconnect. This completes the electric circuit and keeps the number of electrons in the system fixed.

2.3.4 The Nernst Potential

The Nernst potential is a value given by the Nernst equation, an electrochemical equation named after its formulator, Walther Nernst [50], that describes the voltage at which a given electrochemical reaction will take place. Each electrochemical reaction has its own Nernst potential, which also depends on the temperature and partial pressures of the system. For the reaction to proceed, the applied voltage must exceed the Nernst potential.

The Nernst potential can be derived from the Gibbs free energy of the electrochemical reaction. In thermodynamics, the free energy change (ΔG) is related to the standard state free energy change ($\Delta G°$) by the equation:

$$\Delta G = \Delta G° + RTlnQ \tag{7}$$

where R is the universal gas constant, T is the temperature, and Q is the reaction quotient, or the ratio of molar concentrations of the product species over the reactant species.

The change in free energy can be related to the electrochemical cell potential (E_N) by the relationships:

$$\Delta G = -nFE_N \tag{8}$$

and

$$\Delta G^\circ = -nFE_N{}^\circ \tag{9}$$

where F is Faraday's constant and n is the number of moles of electrons that are transferred in the reaction. Combining these equations and simplifying results in the Nernst equation:

$$\boldsymbol{E_N = E_N{}^\circ - \frac{RT}{nF} lnQ} \tag{10}$$

To formulate the Nernst potential equation for the electrochemical reaction that takes place in MOXIE, the following reaction is considered:

$$2CO_2 \rightarrow 2CO + O_2 \tag{11}$$

This can be applied to the Nernst equation by using the number of electrons transferred (4) and the molar concentrations of each product and reactant, as shown by Hartvigsen et al. [62]:

$$V_{Nernst} = E_N = E_N{}^\circ + \frac{RT}{4F} \ln\left(\frac{(P^0_{CO})^2 \left(P^0_{O_2}\right)}{\left(P^0_{CO_2}\right)^2}\right) \tag{12}$$

The standard state electrochemical potential term ($E_N{}^\circ$) can be calculated as $E_N{}^\circ = -\frac{\Delta G^\circ}{4F}$. ΔG° for the reaction can be found in thermodynamic tables.

Meyen [4] developed a model of the Nernst potential for the carbon dioxide electrochemical reaction given above as a function of molar ratio of carbon dioxide to carbon monoxide and temperature. Its results are shown in Figure 27.

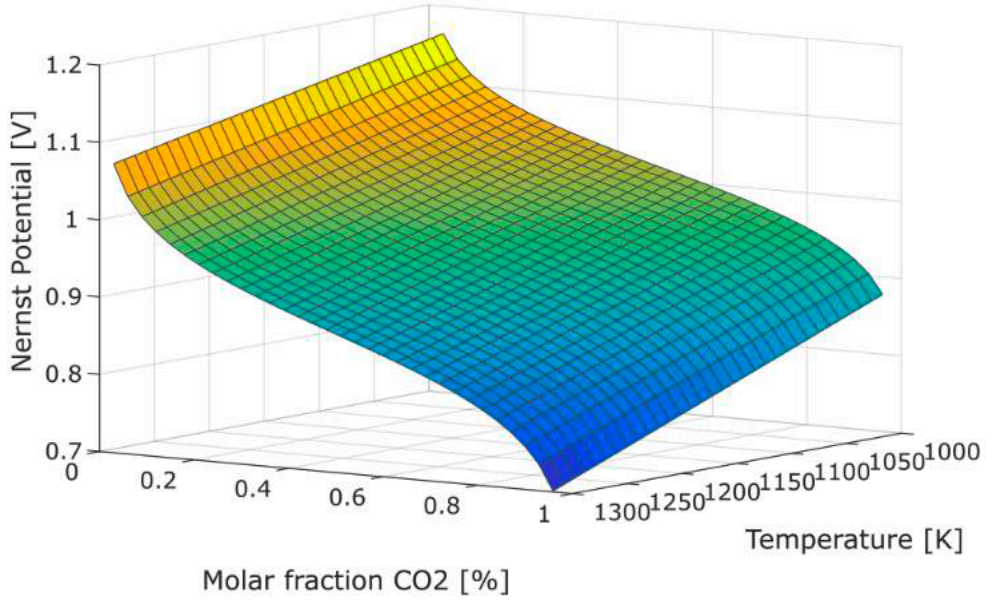

Figure 27: The Nernst potential for reduction of carbon dioxide as a function of mole fraction and temperature.

This plot demonstrates the fact that the Nernst potential for this reaction decreases with increasing temperature and increasing mole fraction of CO_2, both important implications for the operating conditions used to produce oxygen.

Meyen [4] also discussed the impact of cell geometry on the Nernst potential for oxygen production across an SOE cell on Mars. At the entrance of the cell, the composition of the gas is approximately equivalent to the composition of Mars' atmosphere: 95.3% carbon dioxide with trace amounts of carbon monoxide. To prevent oxidation of the nickel ceria cathode, MOXIE circulates excess carbon monoxide from the downstream flow to increase the concentration of CO, a reducing agent.

As the gas flows across the electrochemical cell and the electrochemical reaction takes place, the concentration of carbon dioxide decreases, and the concentration of carbon monoxide increases. This yields the following Nernst potential curve as a function of CO molar fraction, which is the equivalent to the Nernst potential as a function of longitudinal location on the SOE cell:

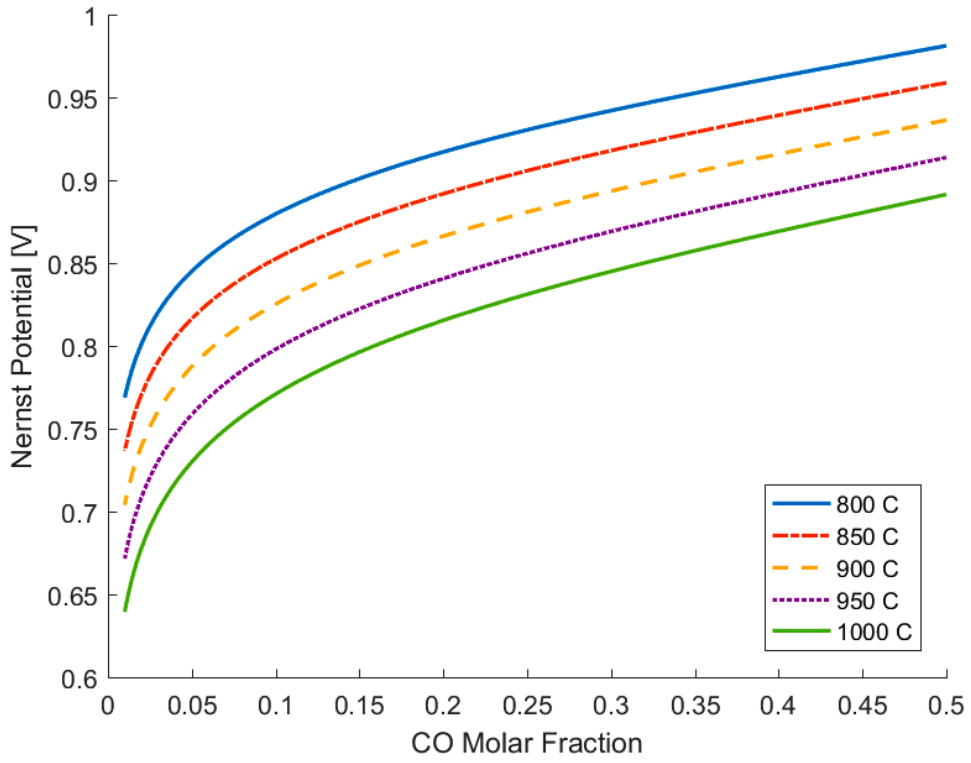

Figure 28: Nernst potential as a function of CO to CO_2 molar fraction, to represent the Nernst potential change as gas flows across an active SOE cell [4]

Clearly, as the gas flows across the cell and the CO fraction increases, the Nernst potential also increases. This means that, when choosing a voltage for the cell, the Nernst potential at the point on the cell with the highest concentration of CO should be chosen. If it is not, the Nernst potential may not be low enough across all areas of the cell and will inhibit oxygen production.

Meyen [4] furthermore translated this finding into a revised version of the Nernst potential, which assumes a uniform increase in molar CO fraction across the length of the electrochemical cell. This is referred to as the integral average Nernst potential.

$$V_{Nernst_{CO_2 \to CO}} = \frac{1}{x_{CO,out} - x_{CO,in}} \int_{x_{CO,in}}^{x_{CO,out}} \left(E_0 + \frac{RT}{4F} \ln \left[\frac{(P_c x_{CO})^2 P_{O_2}^0}{\left(P_c (1 - x_{CO})\right)^2} \right] \right) dx_{CO} \qquad (13)$$

where x is the local CO_2 utilization (fraction of CO in the gas stream), $x_{CO,in}$ represents the fraction of CO at the inlet of each SOE cell, $x_{CO,out}$ represents the fraction of CO at the outlet of each SOE cell, and P_c is the operating pressure of the cathode. This can be used to understand the Nernst potential changes across the cell.

For nominal operating conditions of MOXIE, which are taken to be 800 °C, 1 bar, and a composition of gas equivalent to Mars' atmosphere, the integral average Nernst potential is:

$$V_{Nernst_{CO_2 \to CO}} = 0.92\ Volts \qquad (14)$$

for each cell. Therefore, if the applied voltage for each cell exceeds 0.9208 V under these conditions, carbon dioxide will be reduced to carbon monoxide and oxygen ions. This is what MOXIE aims to do and what a scaled-up version of MOXIE must do in order to produce oxygen.

2.3.5 Boudouard Boundary

The Nernst potential for carbon dioxide reduction has been described. Importantly, there also exists a Nernst potential for an undesirable side reaction that can occur in a CO_2 electrolysis reaction: the breakdown of carbon monoxide into oxygen ions and solid carbon.

$$2CO\ (gas) \rightarrow 2C\ (solid) + O_2\ (gas) \tag{15}$$

If the voltage applied to the solid oxide cell exceeds the Nernst voltage for this reaction, the reaction will take place and solid carbon will be deposited onto the cell. This phenomenon is called "coking" and increases the resistance of the cell, ultimately leading to a drop in performance or even a failure of the system. The results of coking are shown in Figure 29, with a comparison between a non-coked cell and a coked cell.

Figure 29: A comparison of a non-coked SOE cell (left) to a cell that experienced coking (right).

For this reason, it is critical that the SOE be operated at a voltage *higher* than the Nernst potential for carbon dioxide reduction (to form oxygen) but *lower* than the Nernst potential for carbon monoxide reduction (which would form coke). The Nernst potential for carbon monoxide reduction is calculated as:

$$V_{Nernst_{\mathrm{CO}\rightarrow\mathrm{C}}} = E_N{}^\circ + \frac{RT}{2F}\ln\left(\frac{\left(P_{O_2}^0\right)^{\frac{1}{2}}}{P_{CO}^0}\right) \tag{16}$$

The Nernst potentials for both reactions are plotted in Figure 30.

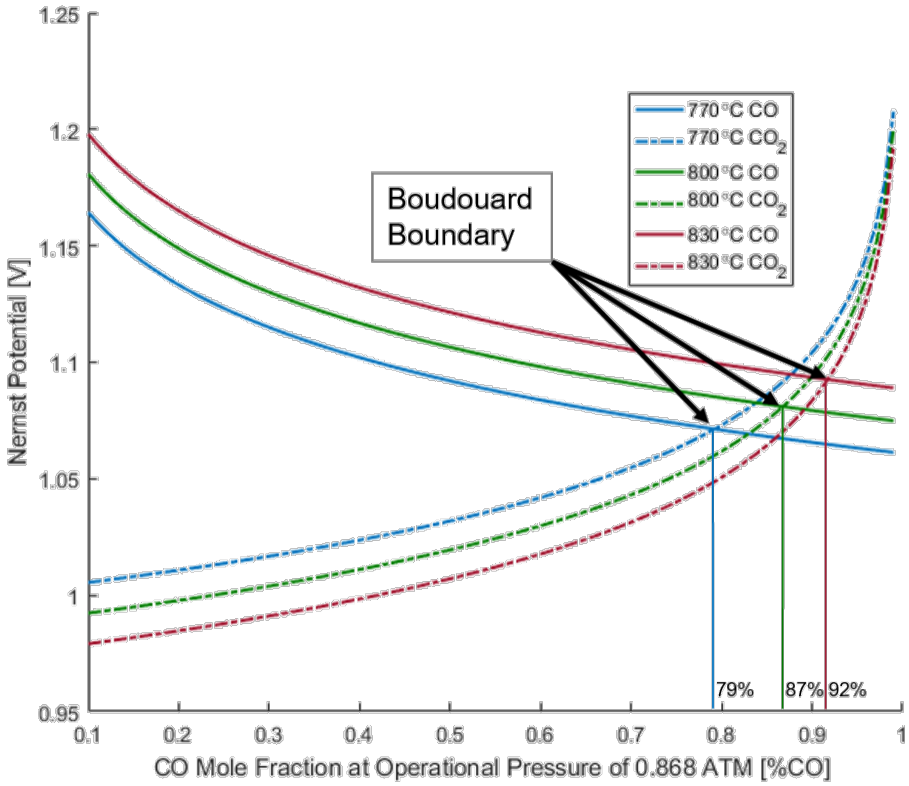

Figure 30: Nernst potentials as a function of CO mole fraction. The solid lines indicate the Nernst potential for carbon monoxide reduction into carbon and oxygen, while the dotted lines represent the reduction of carbon dioxide into carbon monoxide and oxygen. Image credit: OxEon Energy.

The dotted lines indicate the Nernst potential for the intended chemical reaction: carbon dioxide reduction into carbon monoxide and oxygen. The SOE must be operated above these lines to produce oxygen. The solid lines indicate the Nernst potential for the undesirable reaction: carbon monoxide reduction into oxygen and solid carbon. The SOE must be operated below these lines to prevent the deposition of carbon on the cell. This Nernst potential decreases as the concentration of CO increases; therefore, to avoid the formation of coke, the exit of the cathode is the most important Nernst voltage to consider, as the concentration of CO is the highest at the cathode exit. The three different lines for each Nernst potential represent different operating temperatures.

The Boudouard reaction is the reduction-oxidation reaction of a mixture of carbon monoxide and carbon dioxide given by the following:

$$2CO \leftrightarrow CO_2 + C(s) \tag{17}$$

The Boudouard boundary describes the chemical equilibrium mixture of these components at a given temperature [73]. The Boudouard boundary is labeled in Figure 30 and represents the composition ratio of CO to CO_2 that satisfies the chemical equilibrium expression. At CO to CO_2 ratios higher than that at the Boudouard boundary, solid carbon will be preferentially produced over oxygen and CO. Both the Boudouard reaction and the Nernst curves for CO_2 and CO reduction can be described by the Gibbs free energy of the reactions, and it can ultimately be

shown that the Boudouard boundary is equivalent to the point at which both reduction reactions' Nernst potentials are equal, as labeled in the figure. Beyond this point, for example, by increasing the CO mole fraction past 0.92 at 830 °C, it is more thermodynamically favorable at any voltage to form coke than to form oxygen. Operating beyond this point will not result in stable oxygen production and must be avoided.

2.3.6 Calculating Current

Oxygen production is directly proportional to the operating current in the SOE cells, as the current is formed by oxygen ions transporting electrons across the electrolyte. Therefore, predicting the current in the stack allows one to calculate the oxygen that should be produced under the given operating conditions. To calculate current, the following equation may be used:

$$V_{op} = V_{Nernst} + V_{Act} + I * \frac{iASR}{A} \tag{18}$$

where V_{op} is the operating voltage, V_{Nernst} is the Nernst potential for CO_2 reduction, V_{Act} is the activation voltage, I is the ionic current in the cell, $iASR$ is the intrinsic Area Specific Resistance of each cell, and A is the active area of each cell. This is analogous to Ohm's law:

$$I = \frac{V}{R} \tag{19}$$

The resistance of the cell is defined as the iASR divided by the area, which yields:

$$I = \frac{V}{\frac{A}{iASR}} \tag{20}$$

and, when voltage is broken down into its components as they relate to the electrolysis process, the original equation can be solved for current:

$$\boldsymbol{I = \frac{A\left(V_{cell,avg} - V_{act} - V_{Nernst,avg}\right)}{iASR}} \tag{21}$$

This does not take other resistances into account that may be present. The activation voltage is the difference in the open-circuit voltage and the extrapolation of the I-V curve at zero current. The value of the activation potential is dependent on temperature and flowrate. For typical MOXIE conditions, it is 0-0.08 V. The intrinsic ASR is described in more detail below.

Intrinsic ASR

Intrinsic ASR (iASR) is calculated as the slope of the I-V curve after the Nernst Potential has been subtracted from the operating voltage. iASR is constant across flow rates but dependent on temperature. The temperature dependence of MOXIE's iASR was characterized experimentally at 1073 K [4] and is corrected for temperature by the following equation:

$$iASR_T = \frac{iASR_{1073K}}{Ae^{-\frac{E_A}{RT}}} \tag{22}$$

where A is a pre-exponential term for the intercept of the linear fit of ln $(\frac{k}{k_0})$ vs. $-\frac{1}{T}$ and E_A is the activation energy of the reaction. k is the measured ionic conductivity per unit area in $\frac{S}{cm^2}$ while k_0 represents the reference conductivity at 800 °C.

Based on observed data, the activation energy of these SOXE cells is 82.6 $\frac{kJ}{mol}$ and the pre-exponential term has a value of 10,300. The baseline intrinsic ASR, measured at 1073 K for an experimental MOXIE stack, was 0.99 Ω-cm^2.

Thermoneutral Voltage

Another important value in a solid oxide electrolysis system is the thermoneutral voltage. This is the voltage at which all needed energy for the reaction is supplied electrically. In other words, it is the cross-over point between an endothermic and an exothermic reaction. In the case of MOXIE, if the voltage applied to the cell is above the thermoneutral voltage, an exothermic reaction takes place, meaning that the dissociation of CO_2 into CO and O^{2-} releases excess heat. If the voltage applied to the cell is below the thermoneutral voltage, the reaction is endothermic, meaning it consumes heat. MOXIE operates below the thermoneutral voltage and thus consumes heat during its reaction. The quantity of heat required can be calculated by taking the difference in the actual voltage at the stack and the thermoneutral voltage, and multiplying by current:

$$P_{heat} = I(V_{tn} - V_{actual}) \tag{23}$$

The thermoneutral voltage can be calculated as follows:

$$V_{tn} = \frac{\Delta H}{nF} \tag{24}$$

where n is the number of electrons transferred in the reaction $2CO_2 \rightarrow 2CO + O_2$, in this case, 4 electrons, F is Faraday's constant, and ΔH is the temperature-dependent enthalpy of the reaction. This is calculated as:

$$\Delta H = -0.00334T^2 - 0.57737T + 569263.5 \tag{25}$$

where T is the temperature of the cell in Kelvin. These constants are taken from a study of solid oxide electrolysis of CO_2 under similar conditions to those in this design [4]. For MOXIE at 800 °C, the thermoneutral voltage is 1.46 V.

2.3.7 SOE Degradation Mechanisms

One of the primary design considerations for an ISRU plant sent to Mars to generate ascent propellant is the degradation of its systems. Several degradation modes exist within the SOE subsystem itself, each of which could lead to a drop in performance and, ultimately, a mission failure if oxygen production fails to meet its requirement. Several of these degradation mechanisms for SOE are briefly described in the following sections.

Coking

As discussed in Section 2.3.5 and shown in Figure 30, coking can occur if the operating voltage surpasses the Nernst potential for carbon formation. Coking involves the physical deposition of solid carbon onto the electrolysis cells on the cathode side, resulting in a drop in performance. For cells operating in series, as is the case for MOXIE, the stack of cells is limited in performance by the "weakest cell" (the cell with the highest ASR). The voltage drop will be largest across the cell with the highest ASR, meaning that it will be the first cell to exceed the Nernst voltage for carbon formation if the applied voltage is too high. If this situation occurs, it will degrade even further, exacerbating the problem. Therefore, the applied voltage, and thus the oxygen-producing capability of the cells, is limited by the weakest cell in the stack.

Oxidation of Nickel Cathode

MOXIE uses a nickel coating on its cathode to enable CO_2 dissociation and electrical conductivity. A consideration in the operation of a nickel cathode is that it is prone to oxidation if it is exposed to an oxidizing environment, which leads to a loss of performance over the oxidized portion of the cell. Carbon dioxide, which makes up most of the inlet flow composition, is a mildly oxidizing gas, and thus can cause nickel oxidation via the following reaction:

$$Ni + CO_2 \leftrightarrow NiO + CO \tag{26}$$

This problem can be mitigated by introducing a small percentage of a reducing agent, such as carbon monoxide, into the stream. This will push the equilibrium of Equation (26) towards a non-oxidized nickel state and oxidation can be prevented [62]. MOXIE recycles a few percent of its cathode outlet stream, which is a mixture of CO_2 and CO, back into the compressor inlet such that the gas entering the electrolysis chamber contains enough CO to prevent significant oxidation during steady-state operation. Only the area of the cathode at the gas flow inlet to the cell is at risk of oxidation, since the electrode produces CO as gas flows across it. However, if not addressed, the area of oxidized nickel will grow and begin extending across the cell during operation. This necessitates the introduction of CO into the inlet stream; not only to prevent the oxidation from occurring at the inlet, but to prevent it from spreading across the cell. A full-scale system utilizing nickel will require these preventative measures to be implemented, as it operates over a long time period and thus would be susceptible to nickel oxidation. OxEon Energy is currently developing an oxidation-tolerant cathode material under a NASA SBIR grant that may eliminate the need to recycle tailgas back into the system.

Cracking of Electrolysis Cells

Thinner electrolysis cells have performance advantages. Namely, decreasing thickness of the cell incurs less ohmic voltage losses from transporting oxygen ions through the electrolyte, which in turn lowers the total cell voltage. The Nernst potential for carbon formation remains the same, so the lower cell voltage allows for a higher current density and thus more oxygen to be produced by the same area of cells.

A lower limit exists on the electrolyte thickness where it begins to become too susceptible to cracking. The cracking can occur from a variety of mechanisms, including thermal expansion and contraction, unequal pressure forces between the cathode and anode sides of the cell, and manufacturing imperfections that are magnified at lower thicknesses. MOXIE electrolytes are

250 μm thick. OxEon Energy is currently experimenting with thinner electrolyte cells to determine their performance and viability.

Damage to Electrolyte from Oxygen Disruption
A critical voltage exists where oxygen is driven from the lattice structure of the zirconia itself. Zirconia electrolytes are made of a combination of Zirconium (Zr) and Oxygen (O) and typically rely on oxygen vacancies in their lattice to allow the transport of oxygen ions from one side to the other. However, if the voltage drops below a critical value, the system becomes a fuel cell and oxygen from the electrolyte itself will be driven from the cell, causing permanent damage [74].

High Temperature Changes
The oxygen producing capability of SOE cells trends upwards as temperature is increased, as an increase in temperature results in a decrease in ASR, allowing for higher current densities according to Equation (22). An upper limit exists based on the materials involved. Using too high an operating temperature can result in permanent cell damage, as a phase change will occur in the zirconia electrolyte at 1150°C [59]. It is unlikely that the cell would be operated near that phase change temperature, however. As temperatures increase beyond approximately 830°C, ASR begins to increase with cycling more rapidly than at lower temperatures [75]. Operating at temperatures above 830°C therefore has the potential to quickly degrade the cell if it is cycled often. In a full-scale system such as BAM, the cycling will be minimized and so the high temperature degradation may be less impactful than on a system like MOXIE, which experiences many cycles.

2.3.8 SOE Extensibility
A brief review of key SOE extensibility parameters is discussed here.

Cell Size
The scale-up of SOE for a full-scale oxygen production system on Mars like BAM requires an increase in total active SOE cell area. This can be accomplished by adding more cells, increasing the size of each cell, or a combination of the two. OxEon Energy is currently developing and testing cells with an active area of 110 cm^2, which is approximately five times larger than the active area of each electrolysis cell in MOXIE. Additionally, they are creating 60-cell stacks, resulting in a factor of 30 increase over the active area in MOXIE per SOE stack. A comparison of the two is shown in Figure 31.

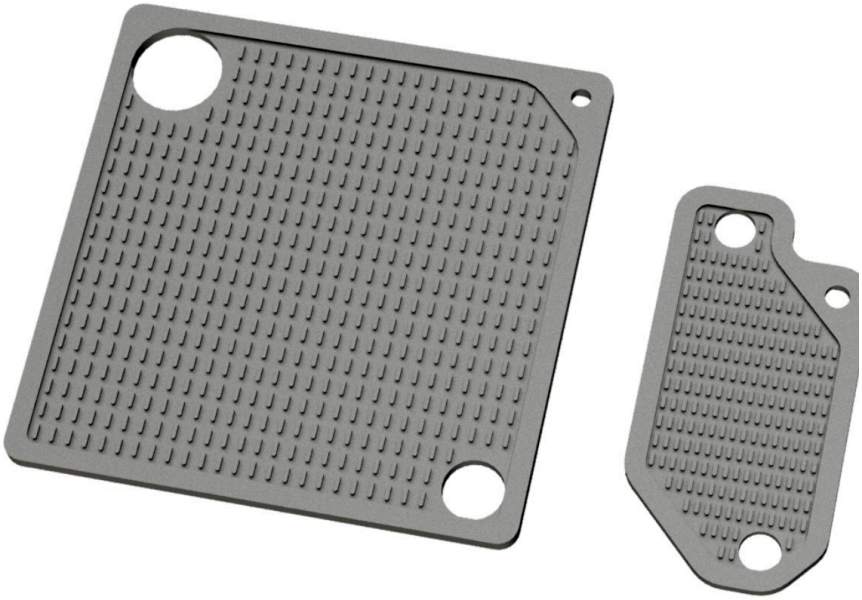

Figure 31: (Left) Scaled-up SOE cells being tested at OxEon Energy for extensibility of (right) MOXIE SOE cells. Image credit: OxEon Energy.

Larger cells have a higher active area to total area ratio, as the seals and other non-active sites surround the perimeter of the cell. However, moving to cells larger than those being tested by OxEon is problematic from a manufacturing point of view. This is primarily driven by the CFY interconnect manufacturing. The interconnects are 95% chromium, which starts as a powder and is pressed into a mold. No facility exists today to make CFY interconnects larger than those being tested by OxEon, and a significant capital investment would be required to enable it [76]. Additionally, mechanical failure modes such as cracking become more likely as the cell size is increased, assuming the thickness remains constant.

Operational Parameters

Colvin et al. (1991) conducted a series of tests to determine the effects on oxygen production rate of temperature, cell potential, and carbon dioxide flow rate [77]. Their study operated under long-duration conditions with realistic operating parameters. The authors drew several conclusions that have important implications for extensible ISRU systems. First, the oxygen production rate increased while CO_2 flow rate was increased up to a certain point, whereafter an increase in flow rate decreased the oxygen production rate. This was determined to be caused by thermal inertia effects, as the carbon dioxide did not receive sufficient time in the cell to achieve the required temperature at elevated flow rates. For operation at lower cathode pressures, as proposed by this dissertation, higher CO_2 flow velocities will need to be utilized to maintain equivalent mass flow rates through the system. Therefore, thermal inertia may create an obstacle for oxygen production. Second, the authors determined that the oxygen production rate increased with increasing cell potential. They tested this from values of 0 V – 2 V. Finally, the authors found that elevating temperature also increased the oxygen production rate across all measured cell potentials and a constant flow rate, as expected. The range of temperatures tested was 800 °C – 1100 °C and is ultimately limited by upper temperature limits of 1150 °C for the zirconia and its electrode.

2.4 Dust

Dust particles suspended in the Martian atmosphere can be problematic for mechanical systems on Mars if not properly filtered. Mars dust can cause physical damage to moving parts as it passes through a system, lock up gears or other rotating pieces of machinery, and poison SOE cathodes if the dust contains sulfates. To prevent dust from entering MOXIE, a HEPA filter with LydAll LydAir Micro Glass HEPA 3428 A/A media is used. A baffle is placed in front of the filter to prevent impact and abrasion damage to the filter. It is likely that a full-scale system would employ a similar dust removal strategy. While dust mitigation is not a focus of this dissertation, a brief overview of past dust research is included here.

Several studies have been conducted on the topic of Mars dust prevention. In 2016, Agui published results of a filtration study in which filter media was tested under Martian conditions to calculate its capturing efficiency [78]. Agui more recently tested a prototype filter system known as the Scroll Filter at NASA GRC for Mars applications [79]. Phillips et al. took a different approach, developing and testing an electrostatic precipitator to mitigate dust impact on ISRU systems [80]. McClean et al. undertook an experimental investigation into the effects of dust that could be experienced by MOXIE on the Mars 2020 rover [81]. They utilized a simulated Mars environment to establish a quantitative relationship between dust loading and pressure drop across the MOXIE filter. Their analysis was largely based on the theory developed by Pich in 1971 that theorized and experimentally validated the relationship between flow rate and pressure drop through filters [82].

In comparison to MOXIE, which will have a limited number of operational hours on Mars, an extensible system running continuously over many months is likely to encounter more severe dust environments from dust devils and global dust storms. One strategy to mitigate these instances of higher dust loading is to add margin to the dust rejection capabilities of the system to account for a worst-case dust storm scenario. The implications of dust loading are primarily its effect on the pressure drop across the filter. While dust rejection design is outside the scope of this dissertation, the expected pressure drop across the filter affects the ability of the system to operate at low pressures and therefore must be acknowledged.

2.5 Compressor

The acquisition and compression of the Mars atmosphere is one of the major steps in the operation of an atmospheric ISRU plant. The Mars atmospheric pressure is 5 to 10 mbar [83], whereas the solid oxide electrolysis system will likely be operated between 100 and 1000 mbar. Therefore, a collection and compression system is required that can achieve this compression ratio while managing dust loading, being tolerant of the seasonal and diurnal variations in pressure and being able to operate for long periods of time autonomously.

2.5.1 Compressor Options

At least three categories of compressors can be considered for an atmospheric ISRU system. These include mechanical compressors, cryogenic compressors, and sorption pumps. Certain studies have considered alternative architectures for capturing CO_2, including supported ionic liquid membranes, ionic liquid absorption, polymer membranes, chemical absorption, and molecular sieves [25,84,85]. However, these alternative technologies are at too low of a technology readiness level to be properly analyzed or considered. Instead, three primary options

are considered for atmospheric capture and compression in BAM: mechanical compression, cryogenic freezing, and sorption pumping.

Mechanical compressors use mechanical motion to move and compress a gas. Several commercial options exist for mechanical compression, including scroll pumps, axial compressors, lobe compressors, and centrifugal compressors. MOXIE utilizes a scroll pump [86], which works well at MOXIE's scale of production. A general challenge of mechanical compression is thermal management from frictional losses and heat of compression. Despite this, certain studies have identified mechanical compressors as the ideal choice for a scaled-up system [87].

Cryogenic compressors are a second option for CO_2 acquisition and compression on Mars. Cryopumps freeze a particular gas out of the air, causing a phase change from gas to solid. This system operates in a two-step process. First, there is an acquisition period where CO_2 is deposited onto a cold head in the cryogenic chamber. Second, there is a period where the CO_2 is released by warming it until it sublimates to generate pressure and feed the SOE system. At least two of these systems would operate in parallel in alternating phases to provide a constant supply of pressurized CO_2 to the system. The potential benefits of a cryogenic system are that it is relatively low mass and purifies the inlet gas stream. A cryogenic pump was originally considered for the MOXIE project. However, while it has a lower peak power than the scroll pump that was chosen, it uses more total power for each electrolysis cycle and is considered a more complex system [69]. It also requires a mechanical blower to remove inert gases that can form a diffusive barrier around the coldhead.

Sorption pumps are the third category of CO_2 acquisition and compression systems for Mars ISRU. Sorption pumps utilize a sorbent material, such as zeolites and activated carbon, to selectively adsorb carbon dioxide at low temperatures. Then, when isolated from the outside environment and warmed, CO_2 is desorbed and released at an increased pressure into the ISRU system. A mechanical blower is required for Mars sorption pumps as well to remove inert gas buildup. Sorption pumps have been utilized in many ISRU architecture designs over the past thirty years and are explored later in this section along with mechanical and cryogenic compressors.

It is useful to revisit the compressor options considered in previous design reference missions. In NASA's DRM 2.0, the authors outlined the need for a system that cleans the Martian atmosphere of dust and compresses it to a usable pressure [43]. However, they ultimately did not detail any compressors to accomplish that goal. The authors of NASA's DRA 5.0 considered the three primary categories of compressors and picked micro-channel adsorption pumping with cryogenic separation [28]. They determined that mechanical pumps would not be effective in compression of the Martian atmosphere to the desired levels, though no further details on that rationale were provided. More recently in 2011, Muscatello et al. published a general evaluation of various Mars CO_2 capture technologies that summarizes research in many types of compression for Mars applications [85].

It is not currently known which type of compressor is the optimal choice for a scaled-up ISRU plant. This is one of the primary design variables considered in the optimization put forth in this

dissertation. More detailed background on each type of compressor and their appearances in past literature will be discussed in the following sections.

2.5.2 Cryogenic Compressors

Cryogenic compression of CO_2 relies on the fact that CO_2 can be frozen out separately from all other major constituents of the Martian atmosphere. The composition of the Martian atmosphere, along with the phase diagram for CO_2, is given in Table 8 and Figure 32.

Table 8: Mars atmosphere constituents

Gas	Quantity (molar)
CO_2	95.32%
N_2	2.7%
Ar	1.6%
O_2	0.13%
CO	0.07%
H_2O	0.03%

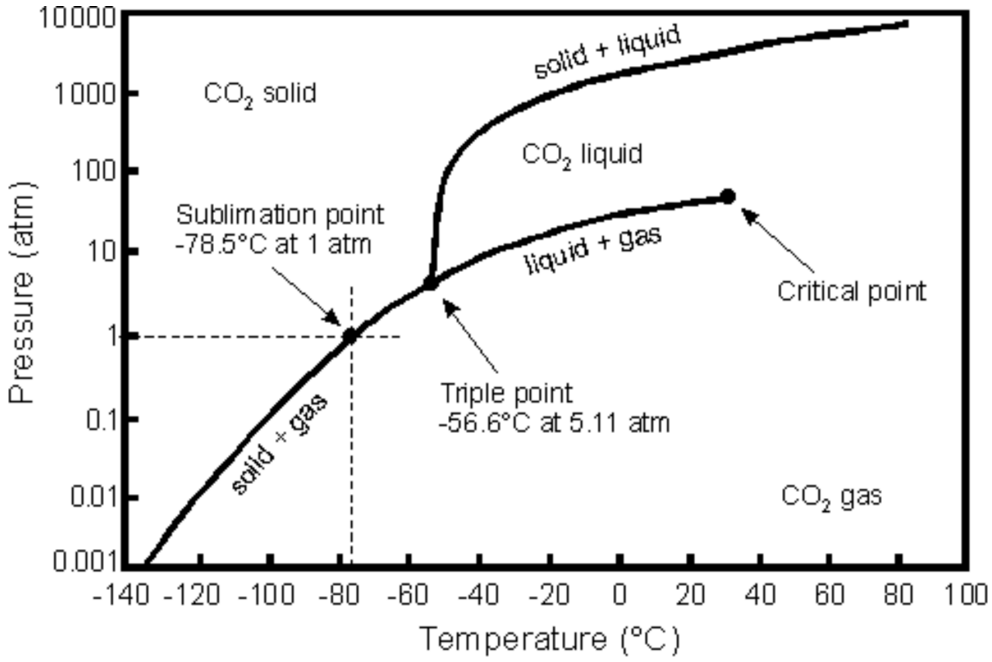

Figure 32: Phase diagram for carbon dioxide. The triple point, where all three phases are present, is labeled. Image credit: Earth Science Stack Exchange.

The freezing point of CO_2 is sufficiently different from the other gases to enable cryogenic separation from the Martian atmosphere.

Ash et al. (1978) proposed a cryogenic CO_2 collection system to produce methane and oxygen. Carbon dioxide solidifies from the Martian atmosphere at a temperature of 148 K and the Martian average ambient temperature is 200 K with temperatures near 148 K during winter

nights [88,89]. As a result, cryogenic collection using the atmosphere as a precooler to a cryocooler is feasible. The system proposed by Ash et al. is shown in Figure 33.

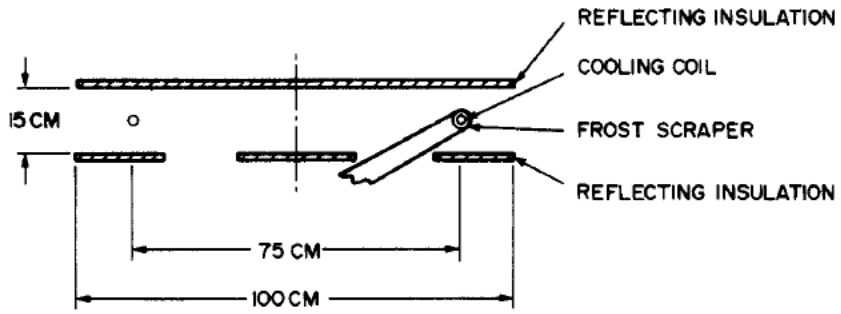

Figure 33: Cross-sectional view of cryogenic CO_2 collector as envisioned by Ash et al. (1978)

As the atmosphere flows between the plates and over the cooling coil, CO_2 deposits onto the coil. This frost is then collected by a scraper which scrapes the coil twice an hour. From there, the frost is fed into an extruder which compresses it to 68 bar and feeds it into a storage tank. The solid CO_2 is liquefied by heating it above 218 K during the extrusion process [90]. The authors expect the cryogenic collection system to have a total mass of 45 kg and require 348 W.

Sanders et al. [25] also used a cryogenic compression system in their ISRU design. For their design case that utilized only an atmospheric processing unit, CO_2 freezing was chosen because of its simplicity. For the design case that utilized combined atmospheric and soil processing units, the same CO_2 freezer was used. At a production rate of 0.48 kg/hr of oxygen, the CO_2 collection system was expected to have a mass of 43 kg and consume 574 W of power.

Clark et al. developed a proof of concept for cryogenic collection on Mars in 2001 [91]. They used a pulse-tube cryocooler to directly freeze carbon dioxide from the atmosphere, later thawing it in a closed pressure vessel to create liquid CO_2. Their design is shown in Figure 34.

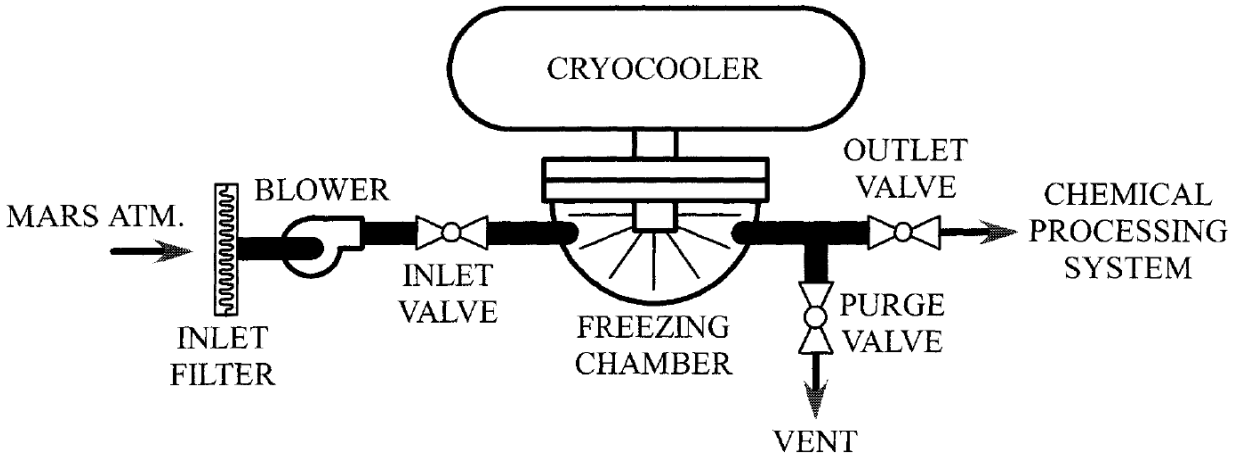

Figure 34: Cryocooler design from Clark et al. (2001) for CO_2 acquisition and compression [91]

The system works by pulling in the atmosphere with a blower and freezing the CO_2 out onto fins in the freezing chamber. The chamber is kept at 150 K by the cryocooler. To prevent the buildup of excess nitrogen and argon gas in the chamber, a purge valve is opened during CO_2 collection

that allows the excess gases, along with CO_2 that does not freeze in the chamber, to be vented. If capturing these gases is desirable, the blower can be replaced with a compressor, as the vapor pressure of CO_2 becomes a smaller fraction of the overall pressure at higher pressures, and therefore the resulting vented gas stream would contain a smaller fraction of CO_2. When enough CO_2 has been collected in the chamber, the cryocooler is switched off and the system is allowed to passively warm using the Martian surroundings. The conditions in the chamber will quickly reach the CO_2 triple point. The outlet valve can then be opened to move high purity CO_2 gas downstream. This will continue venting at a pressure equal to or above the triple point pressure of CO_2 (5.17 bar) until all the CO_2 ice and liquid has evaporated. The concept presented by the authors is scalable to larger sizes using a linear relationship between cooling power and acquisition rate.

Muscatello et al. designed and built a cryogenic acquisition device that uses dual cryocoolers to feed a Sabatier system [92]. They initially explored a design space for various types of acquisition technologies and determined that CO_2 freezing was the most promising option for several reasons [93]. It yields high collection rates, purifies the carbon dioxide, produces a high-pressure feed after warming of the collection tank, and requires less mass than adsorption pumping. Additionally, it takes advantage of the temperature swings between the Martian day and night. In their design, a Sunpower Cryotel GT cryocooler with 34 W of cooling capacity at 150 K was used, which provided the required level of cooling to freeze CO_2 and offset heat leaks to the environment. Three cryocooler cold head configurations were considered, as shown in Figure 35.

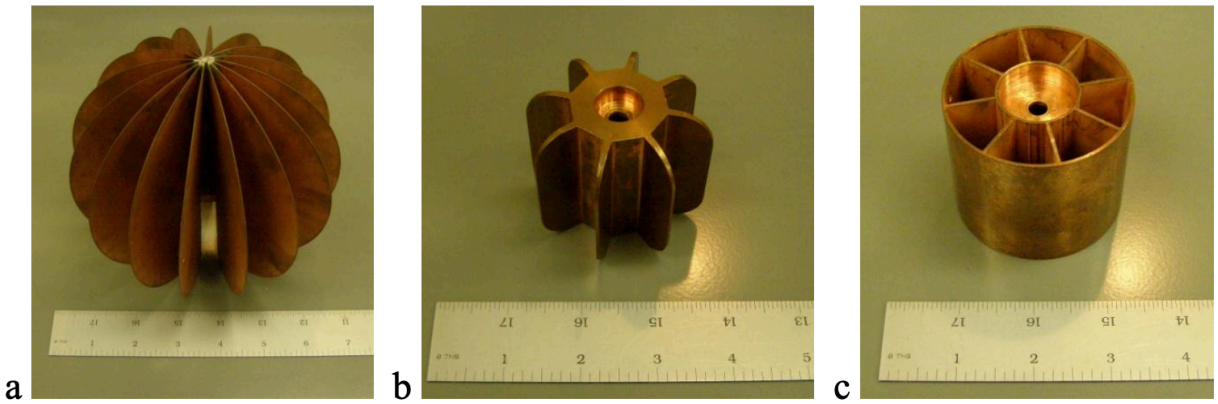

Figure 35: Cryocooler cold head configurations for testing: (a) orange slicer, (b) starburst, and (c) Ferris wheel

The Ferris wheel was the only cold head to meet the experimental requirements, capturing 94 g/hr of CO_2 from a simulated Mars environment.

Rapp et al. provided an overview and summary of prior work on cryogenic compressors for Mars [69]. They showed that parasitic heat transfer from the accumulation chamber to the cryocooler is a significant loss factor in these designs. For Muscatello et al.'s design, for example, they calculated that parasitics negated 100 g/hr of CO_2 collection, which equates to over half of the cooling power of the cryocooler. They also designed a cryogenic system that would work with MOXIE, which is shown in Figure 36.

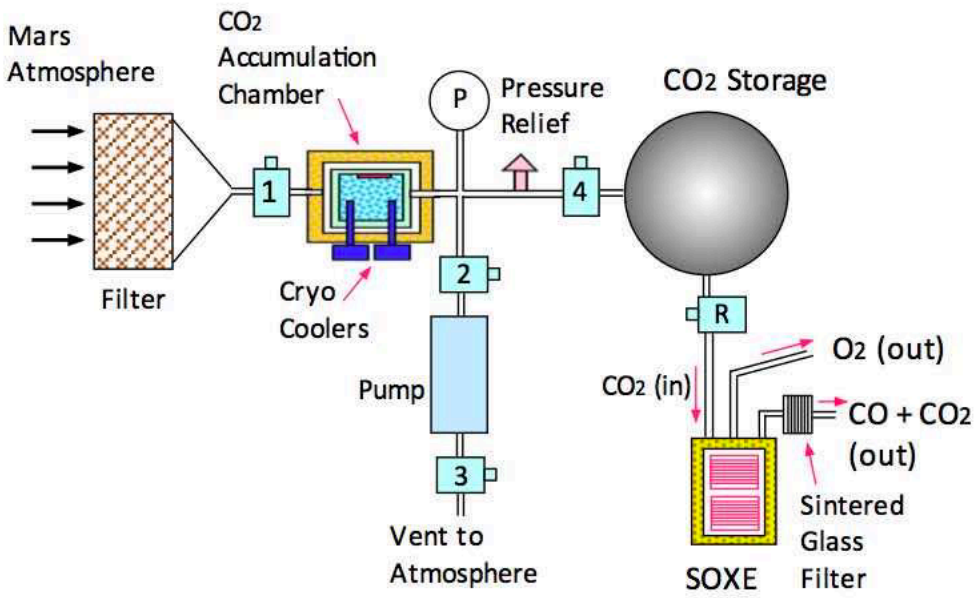

Figure 36: MOXIE hypothetical cryogenic compressor design as an alternate to its scroll compressor design

As discussed earlier, a mechanical pump is required to periodically vent the inert gases to the atmosphere. This is an additional complexity that must be added to a full-scale system, though it may lend itself to the beneficial capture and collection of inert gases for habitation pressure and airlocks.

2.5.3 Sorption Compressors

Sorption compressors function on the principle that an incoming gas can be adsorbed onto materials with high surface area to volume ratios, such as zeolites and activated carbons, at low temperature and pressure. In temperature-swing adsorption, the bed of material can be brought to a higher temperature, reducing the adsorption capacity of the bed, and causing the gas to desorb and exit the system. If it is released to a closed volume, as in the case of a sorption compressor, the gas will be pressurized.

In 1987, Frisbee et al. investigated the use of an adsorption pump using Zeolite 13 for atmospheric acquisition on Mars [74,94]. The researchers identified several benefits of the adsorption pump, including that it improved system reliability over mechanical pumps by eliminating rotating turbomachinery components. Another benefit was that sorption compressors could use thermal power to operate rather than electrical power, which could lead to a reduction in power requirements and mass. A key finding was that a large radiator would be required to cool the compressor, as efficient adsorption of CO_2 at the inlet pressure only occurs at low sorbent bed temperatures (220 K). The researchers also showed that an O_2 sorption compressor could be used downstream to pressurize and, in combination with a radiator, liquefy oxygen, eliminating the need for a cryocooler. For a 10 kg O_2/day system, the total CO_2 sorption compressor weighed 194.5 kg, including the radiator at 150 kg. The sorption compressor used 4.23 kWth of heat for desorption and 0.3 kWe for the pump motor.

In 1991, Colvin et al. [59] designed an oxygen production plant for Mars. Their choice of compressor was an adsorption compressor that compressed the ambient pressure to 1 bar. They

also used an oxygen adsorption compressor, like Frisbee, to pressurize the oxygen prior to refrigeration and storage.

Sridhar et al. designed a system to process the Martian atmosphere that utilized temperature-swing adsorption [95]. In addition to the benefits identified by other studies previously, the authors found that the energy requirements for the system could be met primarily through the diurnal temperature cycle on Mars. They studied several zeolite and carbon materials, finding that NaX zeolite was the superior adsorbent by quantity of pressurized gas produced per unit mass of sorbent. A simplified version of their system, which is representative of most adsorption systems for Mars applications, is shown in Figure 37.

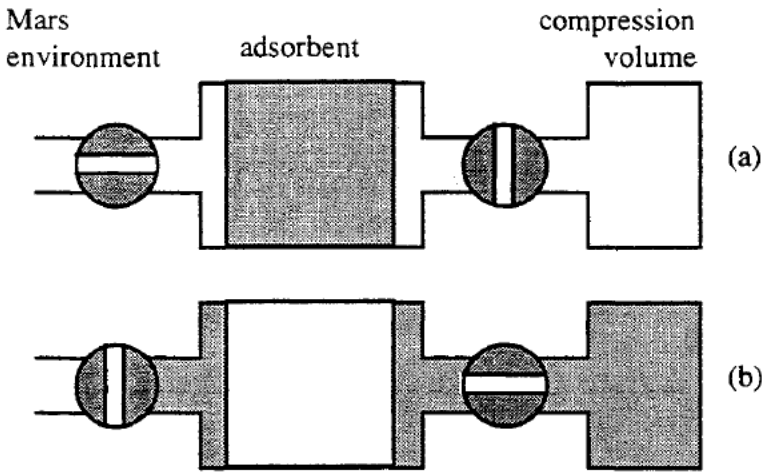

Figure 37: Temperature-swing adsorption compressor [95]. Shading indicates where CO_2 is present. In (a), gas from the environment is adsorbed into the sorbent material, and in (b), the bed is warmed, and the gas desorbs and is pressurized.

NASA's DRA 5.0 [28] utilized a microchannel CO_2 adsorption pump in its ISRU plant design. The use of microchannels facilitates rapid heat transfer to heat and cool the sorbent beds for temperature swing adsorption, which can result in a significant reduction in hardware volume and mass. Rapid thermal cycling also allows a given sorbent bed to capture and compress more CO_2 per day per kg of bed. This leads to a tradeoff between the productivity gained by a rapid-cycling system and the potential power savings of a long-cycle process that utilizes the Mars diurnal cycle for heating and cooling. The use of microchannel CO_2 adsorption pumps has been studied for use in methane production on Earth [96] as well as propellant production on Mars [97]. In the latter study, the authors designed an ISRU system to produce oxygen from CO_2 utilizing two CO_2 sorption pumps in series at the front end of the system. The pumps were expected to reduce N_2 and Ar levels to parts-per-million (PPM) levels and increase the pressure of the CO_2 by a factor of 167 between the two stages. For a Mars Sample Return case study, the authors projected that the required sorbent mass scaled with cycle time as shown in Figure 38.

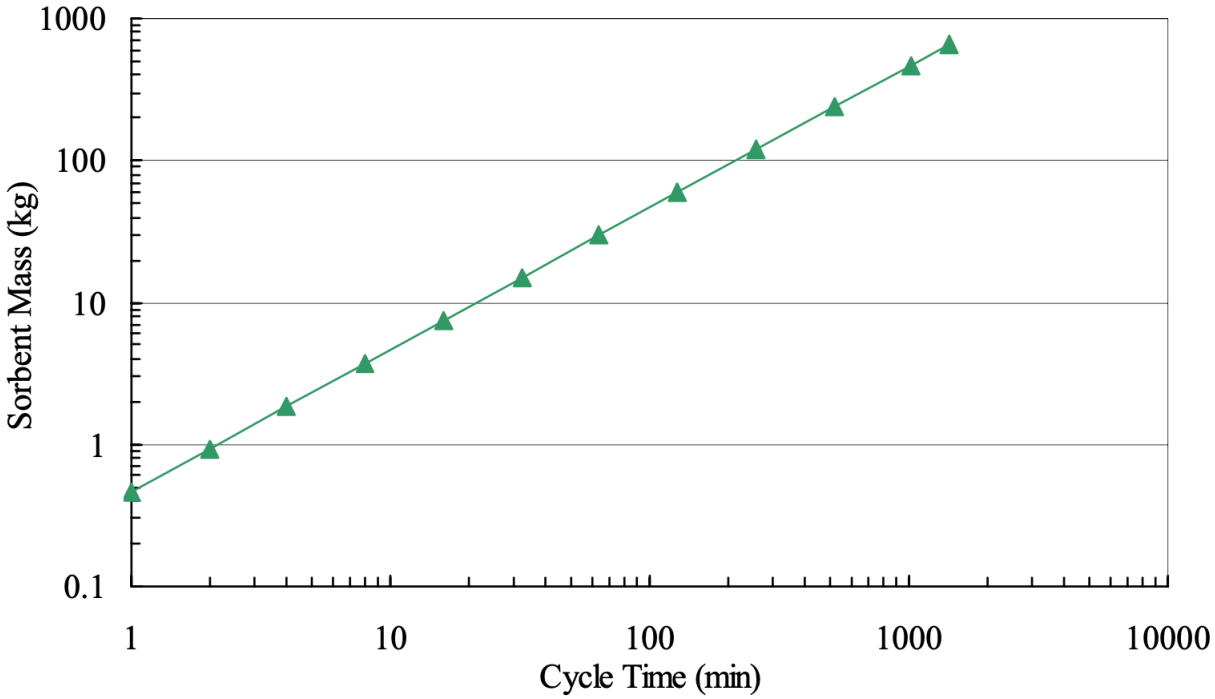

Figure 38: Required sorbent mass for a CO_2 adsorption pump compressing 1080 g/hr of CO_2 from 6 mbar to 1000 mbar as a function of adsorption/desorption cycle time [97]

To make this projection, the authors assumed a -25°C to 100°C temperature swing, a CO_2 compression from 6 mbar to 1000 mbar in two equally sized stages, a zeolite-13X adsorbent bed at 100% sorbent capacity utilization efficiency, and a total inlet mass flow rate of 1080 g/hr CO_2. As the figure indicates, a single-sol cycle (1480 minutes) requires more than 100 times the adsorbent mass than the 2-minute cycle time expected of their microchannel design. This has important implications for the design of a full-scale system, as a reduction in cycle time can lead to a significant reduction in mass.

The Mars In-situ-propellant-production Precursor (MIP) flight demonstration was built with an adsorption compressor [37,98]. It utilized 13X-Zeolite and was a small-scale demonstration, targeted to deliver 4.5 grams of compressed CO_2 during a 6-hour operation. Rapp et al. in 1997 also studied adsorption compression with the intent of determining how to prevent build-up of non-CO_2 gases and utilize daytime heating and nighttime cooling. They tested 13X and 5A zeolites and characterized their performances [99].

When comparing compression options, several authors noted potential downsides of sorption pumping. Chief among these were the view that the mass of the sorbent bed and its associated pressure vessel would be prohibitively high [91]. The large volumes of sorbent beds that are required to collect enough CO_2 may require heavy pressure vessels and large blowers to purge the bed. Therefore, in certain cases, sorption compressors may be heavier than mechanical or cryogenic systems. In addition, not only the gas but also the sorbent and pressure vessel mass must be heated and cooled during each cycle, adding to the power requirements.

However, because sorption pumps typically use less power than other compression options and can primarily be powered with waste heat from other parts of the ISRU system, the effective

mass of the entire sorption system may be comparable to or even less than its competitors. This interplay is explored in the optimization space for this dissertation. Sorption pumps also share a benefit with cryogenic compressors in that they purify the inlet gas stream. Another advantage is that the diurnal temperature swings on Mars can provide most of the energy requirements of adsorbent beds, albeit at the cost of mass. Finally, the Mars environment is especially conducive to adsorption compressors because CO_2, the predominant gas, is strongly and selectively adsorbed on common adsorbents.

2.5.4 Mechanical Compressors

Mechanical compressors have been reported less in literature than cryogenic compressors and sorption pumps for Mars ISRU architectures. A perceived problem with using mechanical compressors on Mars is the fact that the compressor mass may be too high and the efficiency too low to achieve the required compression ratio. Clark et al. (2001), for example, found that multi-stage mechanical compression would result in a prohibitively high system mass [91]. It may also be relevant to certain ISRU architectures that mechanical compressors provide no additional CO_2 purification. For a SOE-based system, this is not a disadvantage. Mechanical compressors may have rotating parts that could wear down and lubricants that could leak or outgas. While dry pumps exist, they are more susceptible to wear over extended periods of time. The advantages of mechanical compressors include a potentially lower power consumption than other compressor types, no requirements for cycling or storing gas at high pressures, and no requirements for purging inert gases.

MOXIE utilizes a mechanical compressor. Its scroll compressor was chosen because it was determined to be mechanically robust, at a relatively high TRL, and mass efficient for the scale of MOXIE [69]. It is, however, yet unknown how this would scale to a full-size system. Air Squared, the company that built the scroll compressor for MOXIE, has built and tested a larger scale version. Its output flowrate is approximately 20% of what would be needed on Mars for a full-scale system to support a crew of four to six astronauts. Therefore, either five units would need to be sent to Mars, or else a single unit on a significantly larger scale than has been built before.

Mechanical compressors for Mars also benefit from not needing to purge inert gases, not needing to thermally cycle, and being always available for startup and shutdown. They may become an even more viable option if the operating pressure of the SOE system is lowered. Most systems have been designed to operate at 1 bar or higher, but pressures below 100 mbar could potentially be used and produce comparable SOE results [55]. In this case, the compression ratio required of the compression system drops significantly. Ash et al. studied the use of a rotary lobe Roots compressor for a Mars ISRU system and found it to be a feasible option under the assumption of low-pressure SOE operation [100]. Roots compressors are dust tolerant and have similar reliability levels as centrifugal compressors.

2.6 Liquefaction

Liquefaction of oxygen is a necessary step in the design of a full-scale ISRU system. After oxygen is produced via solid oxide electrolysis, it must be compressed and liquefied to be stored in a propellant tank. Ultimately, the oxygen will be used as ascent propellant to lift astronauts off the surface after their mission has been completed. Liquefaction is a key subsystem that

influences the optimization of the ISRU system considered for this research. A brief literature review of liquefaction options for Mars is described in this section.

NASA's DRM 2.0 did not consider the details of liquefaction but did state that several gases would need to be liquefied and cryogenically stored, including oxygen, methane, and nitrogen. DRA 5.0, on the other hand, stated that cryogenic fluid management is a critical area for development. Current cryocoolers can be augmented with multilayer insulation (MLI) to liquefy and minimize boil-off of propellants. Colvin's architecture in 1992 [59] operated by passing the newly-produced oxygen through a radiator to cool it, then through an oxygen adsorption compressor to increase its pressure to 28 bar, then through a second radiator to cool it after its warming from compression, and finally through a molecular adsorption cryo-cooler refrigerator to liquefy and store it.

Mueller and Durrant also evaluated designs for liquefaction and storage of cryogenic propellants on Mars for human missions [101]. They designed a system with cryocooler cold-head heat exchangers in the MAV tanks that would liquefy and store oxygen and methane propellants. The cryocoolers use either split Stirling, split pulse tube, or turbo-Brayton heat engines and, in addition to liquefying propellants, mitigate heat leaks that enter through the insulation. Various insulation types were also considered and traded, including MLI in a rigid vacuum jacket, glass microspheres in a non-rigid vacuum jacket, aerogel blankets, and plastic foam. The authors performed heat transfer calculations and mass trade studies, finding that MLI and microsphere insulation systems were competitive, though microsphere insulation had a scalability advantage.

In 2016, Hauser et al. investigated different concepts of operation for liquefying and storing oxygen on Mars [102]. The concepts that were investigated including using an accumulator tank to store propellant and deliver it in batches to the MAV (option 1), liquefying oxygen in the flow stream on its way to the MAV tanks (option 2), and liquefying oxygen in the MAV tanks themselves (option 3). Ultimately, they found that liquefying within the propellant tank required the least mass and power for the mission. A comparison of the three options is summarized in Table 9 and the system design for option 3 is shown in Figure 39. These numbers assume a crew size of four.

Table 9: Comparison of three design options for liquefaction of oxygen in a full-scale ISRU plant from Hauser et al. (2016).

Component	Option 1 (kg)	Option 2 (kg)	Option 3 (kg)
Cryocooler	100	104	74
Radiator	110	112	80
Tank	450	-	-
Tank Insulation	19	-	-
Vacuum Jacket	115	-	-
Support Structure	225	-	-
Plumbing & Insulation	27	27	3
Condenser	-	3	-
Pump	12	12	-
Valves	10	10	10
Total Mass (kg)	**1068**	**268**	**167**
Cryocooler Lift (W)	410	375	310
Power Consumption (W)	**3600**	**3600**	**2600**

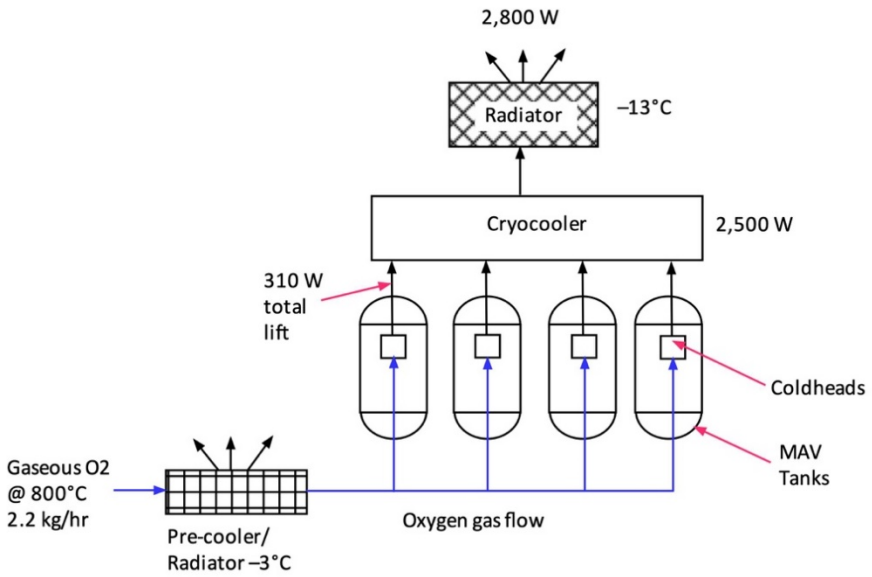

Figure 39: Oxygen liquefaction system from Hauser et al. [102], where the gaseous oxygen is first cooled in a pre-cooler, then liquefied directly in the MAV tanks via a cryocooler-radiator system.

Johnson et al. performed an extensive analysis of oxygen liquefaction methods for Mars ISRU systems in 2018 [103]. Five liquefaction options were reviewed and traded: tube on tank, tube in tank, Linde cycle, pulse tube cryocooler, and in-line liquefier. For each option, eight metrics were considered: mass, power, volume, cost, operability, manufacturability, reliability, and scalability. The tube-in-tank and tube-on-tank methods were found to score the highest overall and are shown in Figure 40.

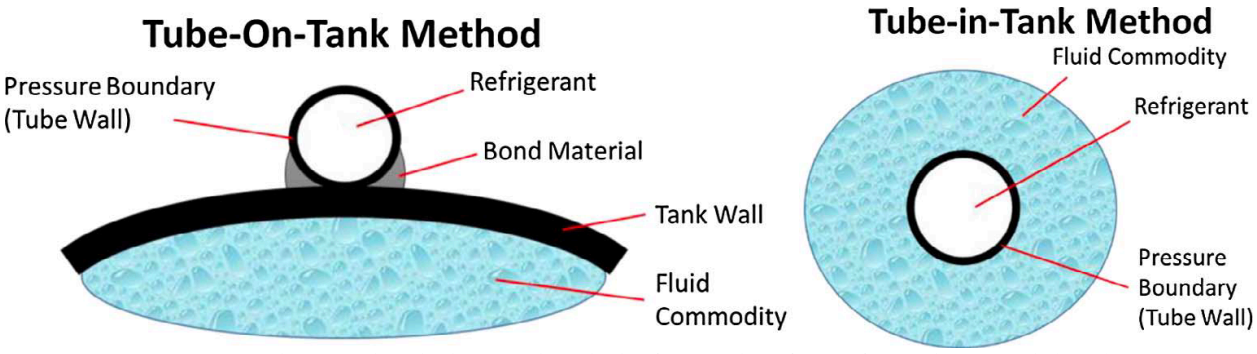

Figure 40: Tube-on-tank and tube-in-tank methods of oxygen liquefaction from Johnson et al. (2018).

They yielded similar results, because the limiting heat transfer step is the convection of heat out of the propellant, not conduction through the tank wall. Therefore, moving the tube into the tank rather than on top of the tank did not alter the performance significantly. The results of this study were expanded upon by Desai et al., where the tube-on-tank method was modeled with a reverse turbo Brayton cryocooler and validated against data taken from a nitrogen boil-off tank at Glenn Research Center [104]. Another study also found that a reverse Brayton single expander cycle was the most competitive, in terms of power, mass, and robustness, for liquefaction of oxygen on Mars [105].

A general consideration of safety with regards to compressing oxygen is also important in liquefaction systems. If the oxygen requires compression to raise the pressure, this can be done before or after the liquefaction step. It is recommended that this is done after liquefaction to avoid mechanical pumping of gaseous oxygen. Ash et al. [100] proposed a system to do this, raising the pressure of the oxygen to 28 bar after being liquefied.

2.7 Extensibility of MOXIE – Other Information

Extensibility in this dissertation refers to the ability to take a design or a product and implement it on a larger scale. Thus far, many design missions have already been discussed that laid out various plans for a full-scale atmospheric ISRU plant, essentially detailing options for the extensibility of MOXIE. The MOXIE Science Team has also put forth preliminary documentation on this. Rapp has written an extensibility document that outlines the major aspects of scaling MOXIE to a full-size system [106]. Additionally, Meyen [4] devoted a chapter of his dissertation to the extensibility of MOXIE. Specific aspects of extensibility are briefly covered in this section that, along with those previously discussed in this chapter, form the foundation for the optimization model of BAM, the full-scale system that has been developed for this dissertation.

2.7.1 Power for Full-Scale System

Power is a driving factor in extensible ISRU system designs. Power requirements for ISRU systems are high compared to other components of the mission and thus may drive the overall power budget of a human Mars mission, as discussed earlier in this chapter. An increase in power results in an increase in the mass of the power systems, ultimately increasing the cost of the mission in terms of launch vehicle cost. Minimization of power will therefore be one of the primary objectives of the design optimization in this dissertation, unless the ISRU power requirement falls below the power consumed by the crew upon their arrival. As such, it is

important to understand the power production options and the power requirements of the extensible system.

Power Production

Various studies have considered the use of solar power with non-continuous ISRU production, where the propellant-production plant is shut down at night and restarted in the day [107]. Issues with solar power on Mars include an increased risk of power loss during dust storms and an inability to operate at night which would incur unacceptable cycles on the SOE system. The latter can be mitigated by bringing a battery system to store energy during the day and discharge it at night. Other studies have considered the use of fission power to enable continuous ISRU operation [2,107], including both a single, large fission surface power unit [110] and several smaller Kilopower reactors [108,109]. Recent studies have baselined using several 10 kWe Kilopower reactors because of a subsequent mass and risk reduction [110,111]. As such, this appears to be the most favorable option.

Power Requirements

Surface power requirements for ISRU systems have been explored as a subcomponent of many of the studies previously discussed, including NASA's DRA 5.0 [28]. Others have specifically researched and evaluated the power requirements of a future human outpost. Rucker evaluated surface power needs for a 500-day crewed Mars mission [110]. She found that the ISRU propellant production system had a slightly higher power requirement than the crew systems. More specifically, the power requirements for a six crew, 500-day surface stay mission were 33.6 kWe during the crewed surface stay and 34 kWe during the uncrewed ISRU phase. Both numbers assumed 30% margin, an estimate of 23,500 kg of ascent propellant, and a production time of 480 days (16 months). A breakdown of these power requirements is shown in Table 10.

Table 10: Power requirements for a Mars reference mission including equipment needed for both the uncrewed (ISRU) and crewed phases of the mission [110].

Power Consuming Equipment	Power Used (W)			Duty Cycle	Mission Phase
	Min.	Max.	Avg.		
In-Situ Resource Utilization	17,640	32,760	25,200	100%	Cargo
Mars Ascent Vehicle	623	1,157	890	100%	Cargo + Crewed
Geological/Meteorological Science Stations	20	105	69	100%	Cargo + Crewed
Surface Habitat					
Crew Accommodations	2,599	4,827	3,713	100%	Crewed
Environmental Control and Life Support	4,287	7,961	6,124	100%	
Avionics	3,375	6,267	4,821	100%	
Other	882	1,638	1,260	25%	
Extravehicular Activity	1,120	2,080	1,600	25%	
Mars Sample Laboratory					Crewed
Express Rack #1	0	720	720	100%	
Materials Science Research Rack	0	5500	550	10%	
Science Glovebox	0	1500	105	7%	
Illumination	13	130	65	100%	
Heaters	0	500	500	100%	
Control and Data Acquisition System	16	29	22	100%	
Sample Handler (Robonaut)	100	600	150	25%	
Communications	45	65	50	100%	
Planetary Protection	0	500	50	10%	Crewed

Mueller et al. [111] provided similar numbers, estimating that an atmospheric ISRU plant would require between 25 and 40 kWe of power, depending on the time available to operate the system. The DRA 5.0 estimated 25 kWe of power would be required to run an atmospheric ISRU plant to support six astronauts in their launch vehicle [28]. Furthermore, Sanders et al. estimated a power requirement of approximately 7 kW for a 0.75 kg/hr O_2 production plant, which, when scaled to the oxygen production rate required for a full-scale system, also falls in the 25 kWe range [25].

For the extensibility of MOXIE, it is useful to compare the current power usage from MOXIE with that of a predicted, scaled-up system to identify areas that should be improved during scale-up [112].

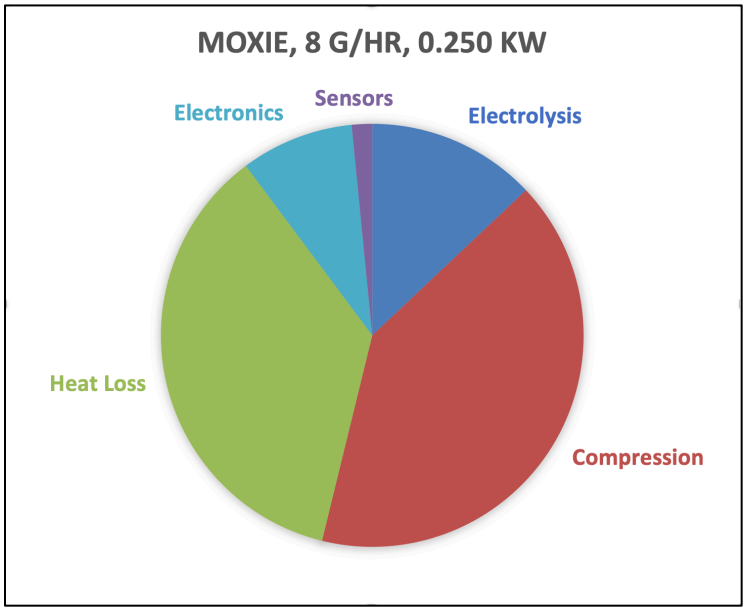

Figure 41: MOXIE power consumption by subsystem [112]

As Figure 41 indicates, heat loss and compression account for the majority of power consumption by MOXIE.

With power reduction improvements to the system from scaling, the addition of heat exchangers, and reduced operating pressure, it is expected that the power will scale beneficially with oxygen production output. The projected power usage of a scaled-up version of MOXIE is shown in Figure 42.

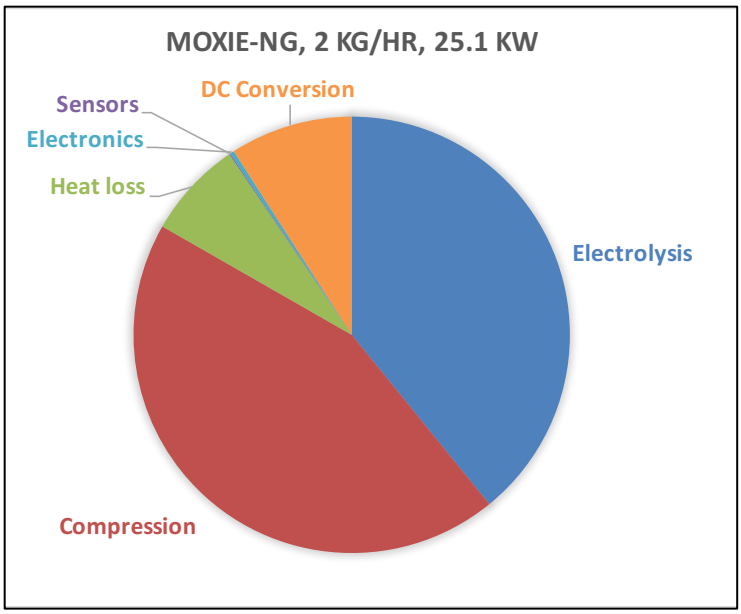

Figure 42: Projected power requirements of a scaled-up MOXIE [112]

As the figure indicates, the projected power demand increases from 0.25 kW with MOXIE to 25 kW in a full-scale system, which is consistent with the reference missions previously discussed. The total power and the associated portions of power consumed by each subsystem will vary based on the design of the full-scale system; however, this gives an estimate to compare to MOXIE. In addition, all scaled-up designs result in a more power-efficient system than MOXIE, indicated by the quantity of power dedicated to electrolysis compared to other subsystems. Note that these predictions were made during the MOXIE project; the actual power breakdown of BAM differs and is given in Chapter 6.

Rapp predicts a total power of 38.4 kW will be required to make the ascent vehicle oxygen for a crew of six, with an additional 6 kW to liquefy the oxygen [106]. This is shown in Table 11.

Table 11: Rapp [106] power requirement estimates for extensible MOXIE system.

Characteristic	Units	Crew size	
		4	**6**
Power for compressor	kW	13.6	20.4
Power for SOXE	kW	11.4	17.0
Power for O_2 Liquefaction	kW	4	6
Total Power for ISRU	kW	30.0	44.4

From this literature review, it is reasonable to assume that the power requirements for a full-scale system will fall in the range of 25 kWe – 45 kWe for a crew of up to six astronauts.

2.7.2 Mass for Full-Scale System

Sanders et al. [25] predicted a mass of 372 kg for a system that produces approximately 20% of the oxygen required for a crew of four and 13% for a crew of six, as shown in Table 12.

Table 12: Mars atmospheric ISRU plant mass and power to produce 0.45 kg/hr O_2 [25].

	Mass (kg)	Power (kW)
Filtration	1.23	0.00025
CO_2 Collection/Freezer	173	2.23
SOE Processor	5.6	3.7
SOE Recirculation System	34.6	0.187
O_2 Liquefaction and Storage	70	0.6
Secondary Structure (15%)	42.7	-
Solar Arrays (2)	45	-
Total:	**372.1**	**6.72**

Scaling the oxygen production to full-scale, without including the mass of the ancillary solar arrays, yields a system mass between 1400 kg and 2000 kg for the two crew sizes. This may be an over-estimate, as mass scales beneficially with oxygen production quantity. Mueller et al. predicted that an ISRU system weighing approximately 1000 kg could produce the liquid oxygen required to launch a MAV [111]. The DRA 5.0 refined these numbers, predicting a single ISRU system mass of 565 kg [28].

For the extensibility of MOXIE, it is useful to compare the current mass breakdown of MOXIE with that of a predicted, scaled-up system [112].

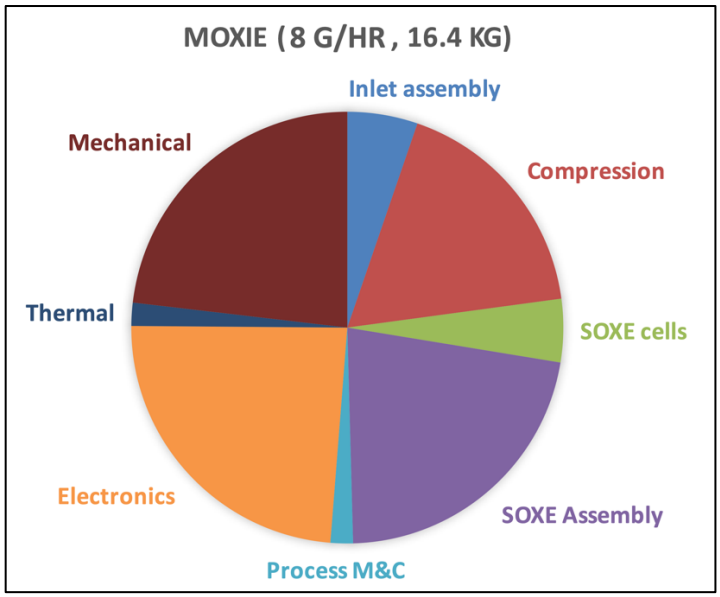

Figure 43: MOXIE mass by subcomponent [112]

As Figure 43 indicates, the electronics, SOXE assembly, mechanical components, and compressor occupy significant fractions of the mass budget. The projected mass usage of a scaled-up system is shown in Figure 44.

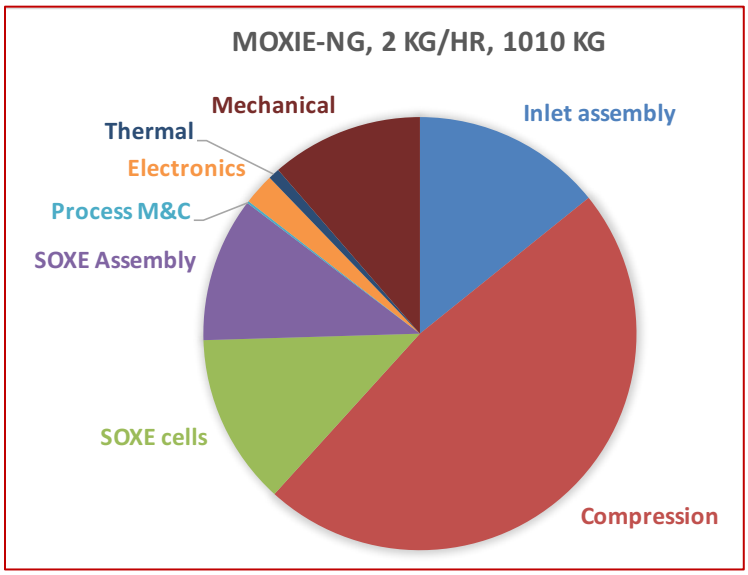

Figure 44: Projected mass breakdown of full-scale, extensible MOXIE system [112]

As expected, the relative fraction of mass occupied by the SOXE assembly, electronics, and mechanical systems decreases significantly. In a scaled-up system, less relative mass would be allocated to items such as the SOXE assembly housing, since the housing scales favorably as the volume of SOXE cells is increased. Figure 44 predicts that the full-scale MOXIE system mass to support a crew of four astronauts will be slightly greater than 1000 kg, which is consistent with Mueller et al. It is significantly higher than the prediction from DRA 5.0, primarily because the architecture proposed by DRA 5.0 predicts significantly less mass for the solid oxide electrolysis subsystem. The actual results from the optimization of BAM differ from this projection and are given in Chapter 6.

From this literature review, it is reasonable to assume that the mass of a full-scale system will be on the order of 1000 kg.

2.7.3 Cycling of a Full-Scale System

Cycling of MOXIE is one of the primary drivers of degradation. Cycling includes both electrical cycling of the equipment and thermal cycling of the SOE stack. Each has its own potential consequences that, if not properly controlled, could lead to a loss in system performance. MOXIE is cycled as a result of the nature of the Mars 2020 Rover mission. The power supply onboard the rover is limited, making it impossible to run MOXIE continuously. In addition, the rover carries several other science instruments, limiting MOXIE's runtime. These factors result in periodic, short-term MOXIE runs that require both electrical and thermal startups and shutdowns. Cycling of MOXIE's subsystems has been studied in laboratory settings, showing modest degradation of the SOE stack with each cycle [113].

Ideally, a full-scale system would experience minimal cycles. In contrast to MOXIE and the Mars 2020 rover, a full-scale system would be provided with enough power to produce oxygen on a continuous basis. If powered by a nuclear source, the ISRU plant would be able to run continuously, day and night. If powered by solar panels, a sufficient number of secondary batteries would have to be charged during the day to power the ISRU plant by night to allow for

continuous operation [107]. This is an important operational component of a full-scale ISRU system's architecture, as continuous running would theoretically eliminate electrical and thermal cycles while on the surface, minimizing the risk of cycle-induced degradation.

Practically speaking, a flight system would likely still undergo some cycles, both during its development and testing phase and its operational phase. NASA, for example, follows testing guidelines that require a flight system to undergo the minimum number of cycles required to demonstrate its functionality. This could result in several cycles before the full-scale system is launched. During the mission operation phase, it is probable that the flight system would encounter scenarios in which its control system would place it in a Safe Mode on Mars as a result of anomalous sensor readings or unsafe operational setpoints, further adding to its cycle count.

Therefore, it should be expected that a full-scale ISRU system will experience limited cycling from pre-mission tests and an approach of operational risk-aversion. This number of cycles should be kept at a minimum to minimize performance degradation from cycling.

2.7.4 Cycling-Induced Degradation of a Full-Scale System and Mitigation Strategies

As discussed, cycling of SOE cells can lead to degradation of the SOE system. One mitigation strategy is to reduce the number of cycles placed on the system, particularly once it leaves the Earth and can no longer be serviced. Operating in steady-state mode continuously for the duration of the ISRU mission will reduce the number of cycles. As a result, for a full-scale system, time-dependent degradation is likely to dominate cycle-dependent degradation.

In addition to SOE stacks, other components of the system will also degrade from thermal and electrical cycling. The insulation and heat exchange systems, for example, may experience a drop in performance from repeated thermal expansion and contraction due to thermal cycling. Repeated expansion and contraction, particularly between materials with different coefficients of thermal expansion, can lead to separation of interfaces and weakening of materials. These degradation modes will not be analyzed in detail in this research but are important points to consider for a more detailed system design.

In addition to reducing the number of cycles experienced by the system, a second strategy to mitigate degradation is to increase the robustness of the system by increasing the number of redundant units in the system. By adding redundancy, if one component experiences significant degradation, it may not cripple the ISRU plant as a whole. For example, rather than sending one large stack of SOE cells that produce the entirety of the oxygen, a large number of moderately sized stacks may be used to distribute the oxygen production capability. If one stack experienced significant degradation, a new stack could be activated to take its place. This methodology could be applied to other subsystems in BAM as well, for example, with the filtration or compression systems.

2.7.5 Challenges of Scaling MOXIE to a Full-Scale System

There are many challenges associated with creating a full-scale, continuously operating atmospheric ISRU plant. The learnings from the MOXIE project thus far provide valuable insight into a number of these challenges and associated mitigation strategies. As discussed in Section 2.3.7, SOE degradation from coking, oxidation, and mechanical failure are all scenarios

that have been experienced and improved upon during the research associated with MOXIE. Degradation of mechanical systems is a lifetime concern for a full-scale system that must operate for many months continuously. A scroll pump, for example, experiences tip seal wear from friction that could eventually cause leakages and reduce its pumping efficiency. Dust is another concern for mechanical systems on Mars and must be removed from the atmosphere before entering the ISRU system.

One challenge with scaling SOE that has not yet been addressed is cell-to-cell variability. MOXIE contains 10 SOE cells that each have minor differences due to manufacturing imperfections. Additionally, each cell is operated at a different temperature due to a thermal gradient and heat losses. Each cell may also experience a unique flow rate. As a result of these minor differences, variability in cell resistance can occur, causing a differential in the voltage drop across each cell. The cell that experiences the highest voltage is the most at-risk for carbon formation, and thus while the average voltage across all cells may be in a safe zone, specific cells may still experience degradation. This is both a physical and operational challenge for MOXIE that will also exist for a scaled-up system.

Another consideration that creates operational complications is the seasonal and diurnal variations in the atmospheric temperature, pressure, and density on Mars. Data are shown in Figure 45 for atmospheric conditions at Jezero Crater, the current location of MOXIE.

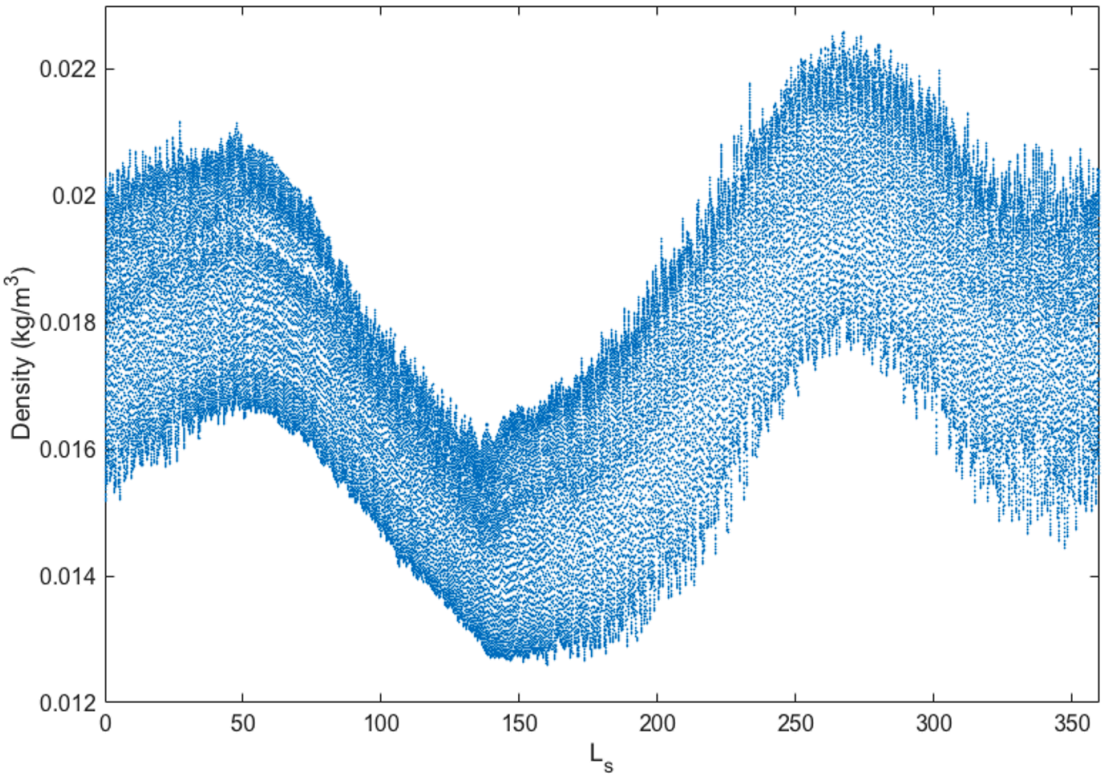

Figure 45: Atmospheric pressure, temperature, and density seasonal and diurnal fluctuations at Jezero Crater for selected Sols throughout the year. Values are shown for the morning, afternoon, evening, and night at each sol to demonstrate diurnal variations. Data acquired from the Mars Climate Database [114, 115].

A full-scale system must operate in all conditions, meaning that the changes in atmospheric conditions must be managed by either the compressor, a controls system, or both. The MOXIE project plans to operate MOXIE across all representative atmospheric conditions to better understand its performance at each in order to inform the operations of a full-scale system.

2.7.6 The Advantages and Disadvantages of MOXIE Compared to a Full-Scale System

It is useful to identify more explicitly the ways in which the design and operational choices made for MOXIE are advantageous, or disadvantageous, when compared to a full-scale system. This informs the aspects of MOXIE results that should and should not be extrapolated to BAM.

BAM has several advantages over MOXIE. Many of these advantages relate to the construction of the ISRU plant itself. A greater variety of options for the compression system are available at the larger scale of BAM, including cryogenic and sorption compressors. The scroll compressor on MOXIE was chosen in part for its compact size, not for its power efficiency; thermodynamic compression of gas only accounts for ~20% of the total MOXIE compressor power, with the rest being accounted for by scroll tip and bearing friction losses [116]. BAM can expect to see an improvement in this percentage because of better compressor choices and non-linear scaling of mass and power. Non-linear scaling laws will provide benefits not only to the compression system but also the SOE system; the SOE cells will have a larger active area to total area ratio. The percentage of mass and volume occupied by packaging will also drastically decrease with scaling. BAM will also have the capability for more robust and complex control systems, including more instrumentation and an improved sensor network. Similarly, it will have more advanced ground-based diagnostics and a higher level of autonomous controls. From a reliability standpoint, BAM has the option to add modularity and redundancy in its components to increase the robustness of the system; MOXIE did not have this option due to the strict mass and volume constraints of the rover.

Additional advantages of BAM are related to its operation. It should experience fewer on-off cycles, as it is intended to operate continuously once started. This is in contrast to MOXIE, which may only operate for 3-4 hours at a time due to power and energy constraints of the rover. On-off electrical and thermal cycles drive SOE degradation and possibly reduce the lifetime of other components as well. On MOXIE, the startup of each cycle also consumes approximately half of the energy budget of the entire oxygen production run; this will not be a concern for a full-scale system with minimal thermal startups. Operationally, BAM can operate at lower pressures to improve compressor and SOE performance. It may also have the ability for cell regeneration to counter the effects of oxidation or coking on the SOE cells. In addition, the SOE cells will be contained within an oven on BAM, providing more uniform heat distribution than the heated endcaps used in MOXIE.

Other advantages of BAM include the potential to separate, store, and use CO as a fuel, to recycle unused pressurized CO_2 from the cathode exhaust to improve performance, to employ a heat exchanger to capture waste heat, and to use co-electrolysis with water to improve performance and ultimately produce both fuel and oxidizer for the MAV. In addition, the landing site for the first crewed missions to Mars will likely have a substantially lower elevation than Jezero Crater, the landing site of MOXIE. This could increase gas density by 30% or more, thereby reducing power requirements of the compressor.

One final difference to acknowledge between BAM and MOXIE is that the former will be thermally coupled to the Mars environment, while the latter is thermally coupled to a rover chassis. This will impact power requirements and operations throughout the Martian year.

Many challenges will exist when developing, testing, and operating a full-scale ISRU system to support a human crew on Mars. Some have been studied with MOXIE, while others are yet to be explored in a testbed environment. This dissertation aims to develop a validated optimization framework to aid in the design of BAM, particularly in those areas unexplored by MOXIE. The approach and methods for the optimization model are described in the following chapter.

Chapter 3: Optimization Framework

Despite the multitude of ISRU missions investigated in the past, as well as research conducted on SOE, compressors, and liquefaction units for Mars, the field is lacking in a high-fidelity optimization model of an atmospheric ISRU plant for Mars. This dissertation fills that knowledge gap. It takes the lessons learned from the MOXIE project and the models that have been developed for it [117,118,119] and creates a new, high-fidelity model and optimization framework for BAM, the full-scale ISRU system.

3.1 System Design

A multi-objective design optimization model has been built in Simulink and validated with data from several laboratory sources to determine the optimal architecture for BAM, a full-scale Mars atmospheric ISRU plant to support a human mission. The primary objectives of the optimization are to minimize *power*, *mass*, *volume*, and *risk*. System and subsystem level constraints are implemented to constrain the design space to what is feasible. Similarly, a system boundary has been drawn to differentiate those components of BAM that are in-scope for this research and those which are considered to be out-of-scope. Those that are out-of-scope are considered system parameters and are assigned a set value based on literature. Collectively, those parameters make up a "reference mission" that informs all out-of-scope components of the design. Finally, the optimization model implements a design variable matrix that encompasses variables that are in-scope and can be altered to influence the objectives. Each of these aspects of the optimization architecture are described in more detail in the following sections.

Model Overview

An ISRU plant on Mars that creates oxygen from the atmosphere and stores it in liquid form must have, at a minimum, the following components: a pumping system to move the atmosphere into the plant, an electrolysis unit to electrolyze carbon dioxide, a liquefaction system to liquefy the gaseous oxygen, and a storage tank. A filter should be added to prevent dust from entering the system. The storage tank at the end can be assigned as part of the MAV. This barebones ISRU plant configuration is shown in Figure 46.

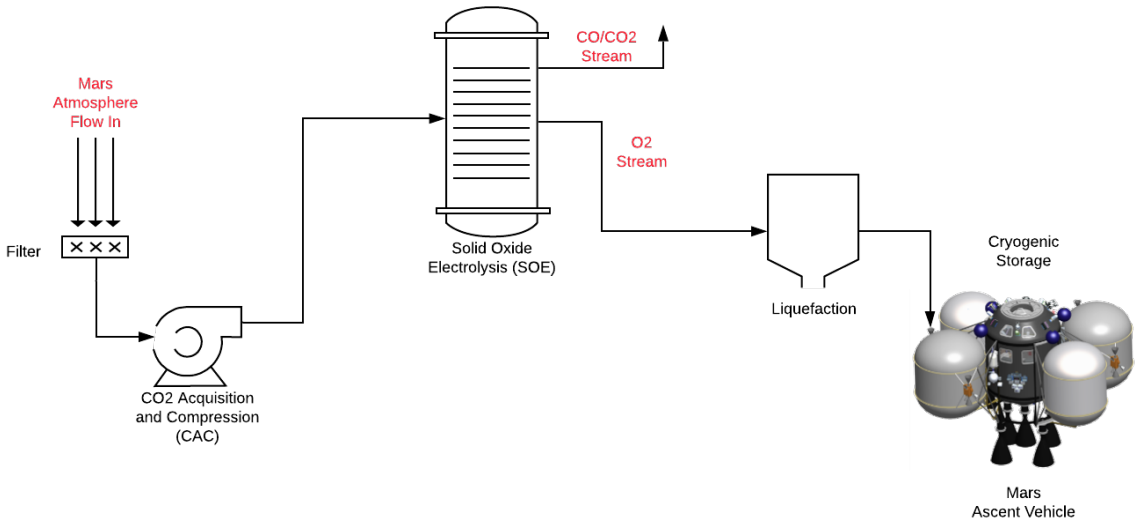

Figure 46: Barebones ISRU plant configuration

To improve the thermal efficiency of the design, a heat exchanger can be added to transfer heat from the hot SOE effluent to the CAC output. This addition is depicted in Figure 47, yielding the high-level design upon which all future calculations and modeling in this dissertation are based.

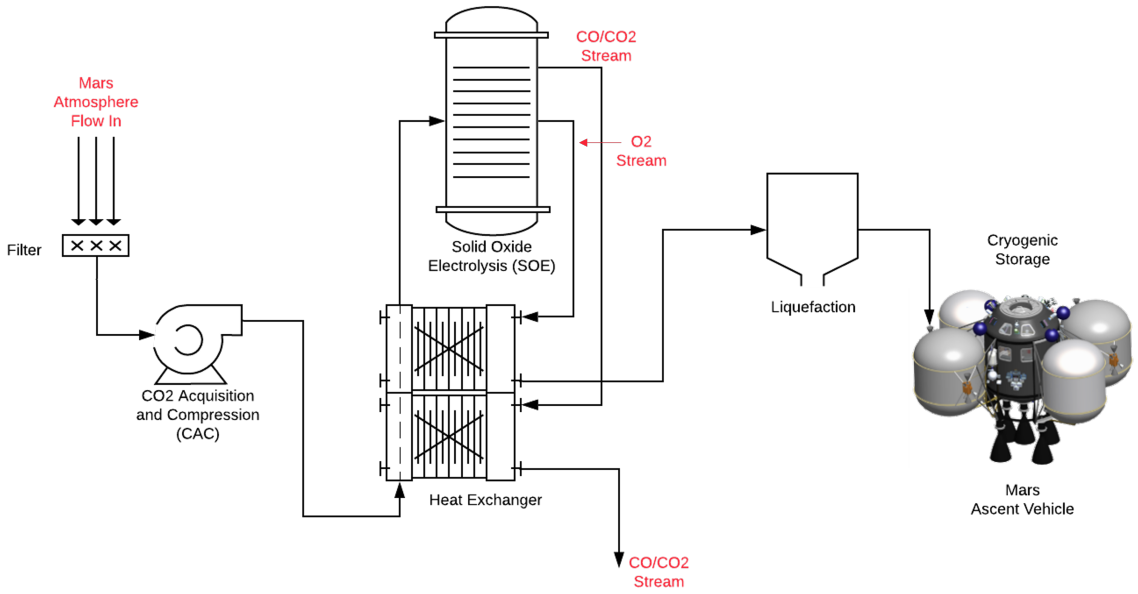

Figure 47: ISRU plant configuration with heat exchanger to improve thermal efficiency

The objective functions – volume, mass, power, and risk – associated with each of these components are calculated as functions of the design variables. The components themselves are modeled in detail as described in Chapter 4. The properties of the fluids flowing throughout this system are briefly described below, with additional detail provided in Chapter 4.

Gas Flows

It is necessary to calculate the characteristics of the gases and liquids throughout the system to accurately predict the performance of the ISRU plant. Each significant location within the ISRU plant has been assigned a number as an identification. For example, the Mars atmosphere is assigned location #1, the anode exhaust from the SOE is assigned location #6, and the liquefied oxygen output from the liquefaction unit is assigned location #10.

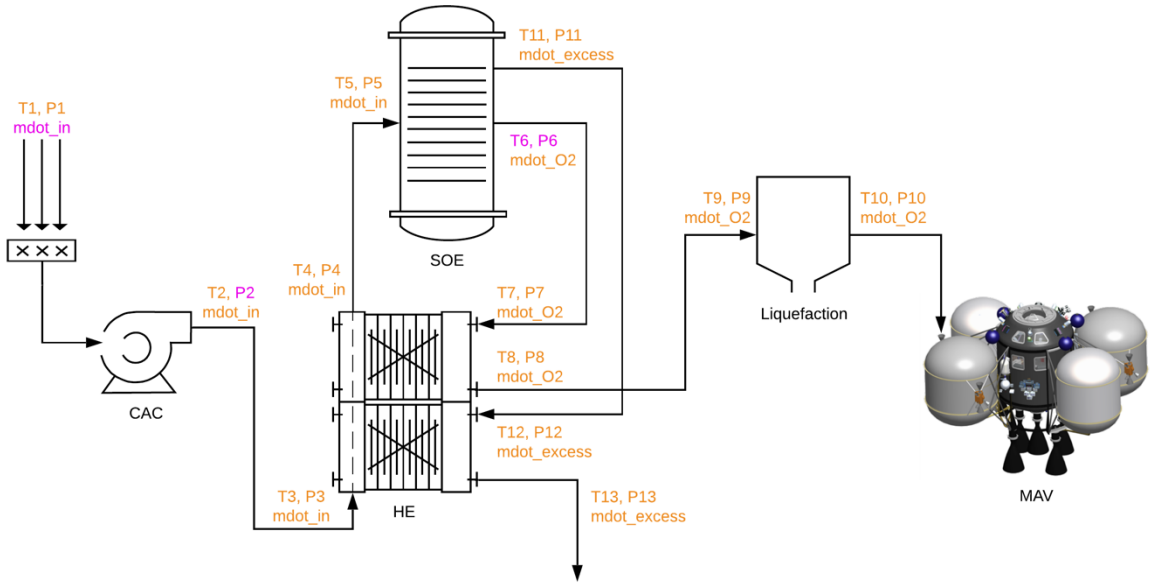

Figure 48: ISRU plant design with significant locations labeled. Gas characteristics are calculated at each assigned location. Blue text indicates that the gas characteristic at that location is a design variable that can be changed by the optimizer as an input.

Figure 48 shows the labels for temperature and pressure at each location. Several additional fluid characteristics are calculated for every assigned location, including mass flow rate, density, velocity, specific heat capacity, and Reynolds number. These characteristics become important when calculating values such as heat leaks, SOE electrochemistry, and the performance of all major subsystems.

Heat Flows Subsection

One of the more critical aspects of the model is the heat transfer throughout the system. Power is arguably the most important objective function to minimize, as additional power requirements incur significant mass and volume penalties. Much of the power consumption in the ISRU plant comes from heating and cooling both fluids and hardware components. As a result, accurately modeling the heat flows throughout the system is of high importance. Figure 49 identifies major heat fluxes throughout the system.

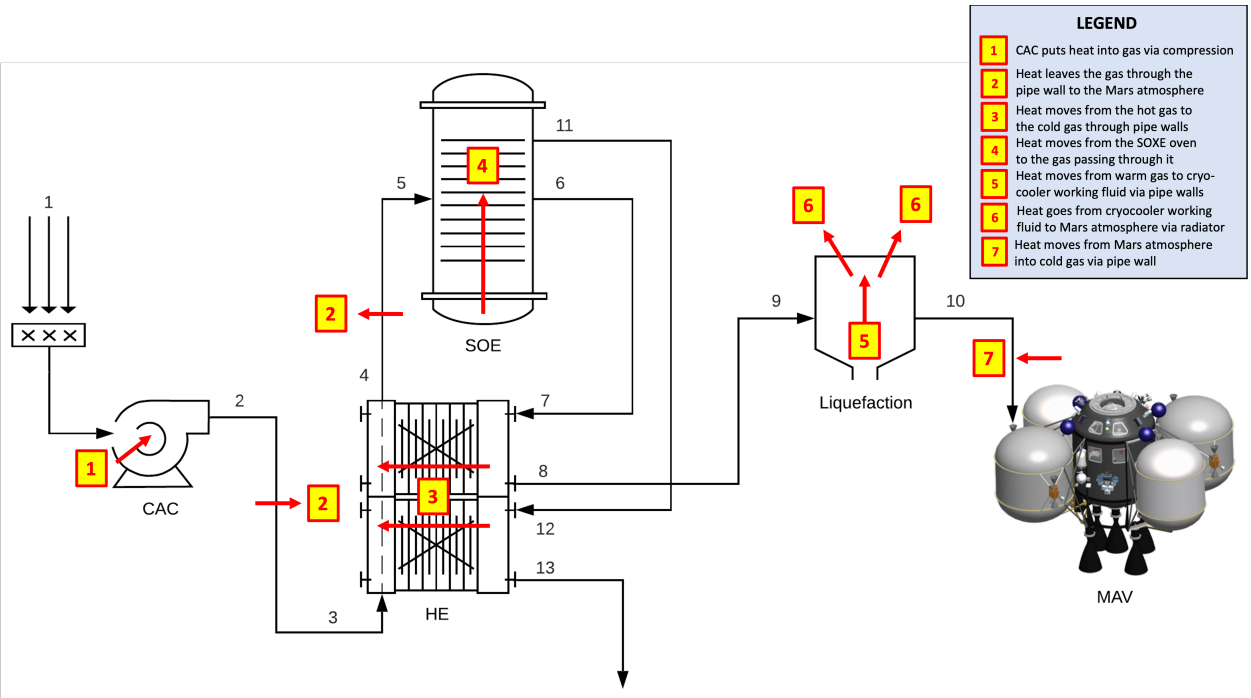

Figure 49: Heat fluxes throughout the ISRU system. Yellow squares indicate a heat flux, and red arrows indicate the direction of heat transfer.

As cold Martian gas enters the system, the mechanical CAC subsystem will heat the gas as it compresses it (yellow [1] in the diagram). Note that the heating and cooling requirements are different for cryopump and sorption CAC systems compared to a mechanical CAC system. The gas will then transfer a portion of its own heat through the piping and insulation [2] as it travels to the heat exchanger. This transfer of heat from the pipe to the environment takes place in all the exposed piping segments between subsystems. At the heat exchanger, the gas will acquire heat from the hot SOE exhaust [3]. Next, the gas is heated to the SOE's operating temperature via SOE cartridge heaters [4]. Downstream, the liquefaction unit will cool the gas [5] and radiate its heat to the Mars environment [6]. Depending on the configuration of the liquefaction unit, there may be a transfer step to move the liquefied oxygen into the MAV tank, in which case it will gain heat from the Mars environment through the transfer piping and insulation [7].

Pressure Drops Subsection

Pressure drops also play an important role in the performance of the system. Building on Figure 49, important pressure drop locations have been added and are shown in Figure 50 in blue squares.

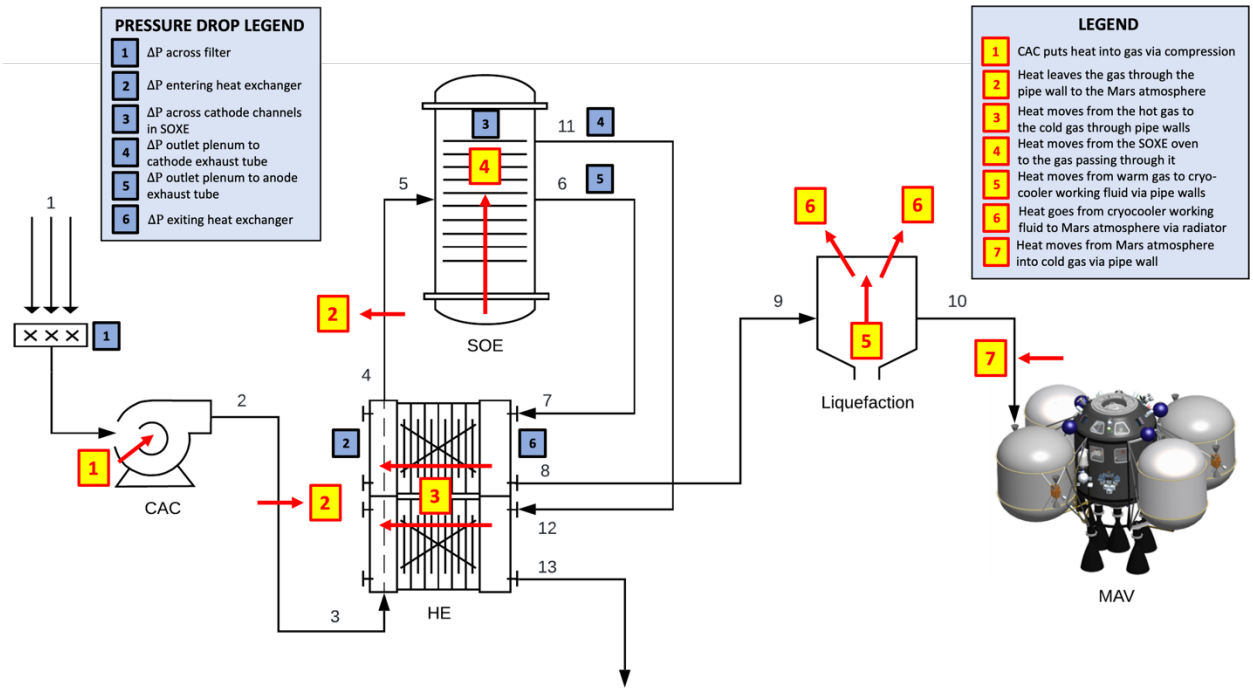

Figure 50: Heat fluxes and pressure drop locations throughout the Mars ISRU plant. Blue numbered squares indicate pressure drop locations, while yellow squares indicate heat fluxes.

The inlet filter, used to reject atmospheric dust, incurs the first pressure drop in the system (the blue [1] in the figure). The heat exchangers create pressure drops in both directions [2] and [6], as the piping is reduced from its nominal size to many small diameter channels in the heat exchanger that increase heat transfer efficiency. The SOE incurs a pressure drop [3] when the gas enters the small cathode channels of the SOE cells. Additionally, the gas in the cathode [4] and anode [5] experiences a pressure drop as the gas exits the SOE plenum and enters smaller diameter exit pipes. Pressure drops along the lengths of pipe that connect the subsystems are not labeled in the figure but are calculated in the model. All pressure drops are calculated in the model as a function of the physical characteristics of the components and the operating conditions of the system. Detailed pressure drop calculations can be found in Appendix B.2.

By modeling each individual component of the ISRU plant and all the necessary fluid characteristics, heat fluxes, and pressure drops throughout the system, the performance of the system can be predicted and optimized.

3.2 Optimization Problem Statement

As stated earlier in this chapter, a set of design variables, parameters, objectives, and constraints was created to frame this optimization problem. A summarized problem statement was also created to guide the optimization project:

> This optimization model **minimizes the power, mass, risk, and volume** of an atmospheric ISRU plant on Mars by changing **operating conditions and system components** while satisfying the given **oxygen production and operating time requirements** for the **selected reference mission to Mars.**

This problem statement encompasses all objective functions and makes note of the system design variables, constraints, and parameters that are embodied in the project. It is important to note that maximizing oxygen production is not an objective, as this would result in a BAM architecture designed to produce as much oxygen as possible rather than an architecture designed for the mission at hand. Instead, oxygen production is treated as a constraint, where the minimum amount of oxygen required to fill the MAV must be produced. This is described in more detail in Section 3.4.3.

3.3 System Boundary

It is necessary in system optimization problems to define system boundaries. These identify the components in the system that are in-scope versus those that are out-of-scope. The system boundary for this problem was drawn as follows: the components that are in-scope begin after the Martian atmosphere is filtered and end after the oxygen is liquefied and is ready to be transferred for storage. The liquefied oxygen is gravity-fed from the liquefaction unit into the MAV propellant tanks and can be disconnected by astronauts upon arrival at the MAV. The system bounds are shown in Figure 51. The technologies needed for dust filtration of the Mars atmosphere and long-term, cryogenic storage of liquid oxygen in the MAV tanks were placed outside the system bounds for this work to constrain it to a manageable scope. Also outside of the system bounds is the potential separation of the cathode exhaust, a mixture of CO and CO_2. It may be possible to use the cryogenic system from the liquefaction unit to separate these two gases, allowing the CO_2 to be recycled into the inlet stream and the CO stored for possible use as a fuel, but this study is beyond the scope of this work.

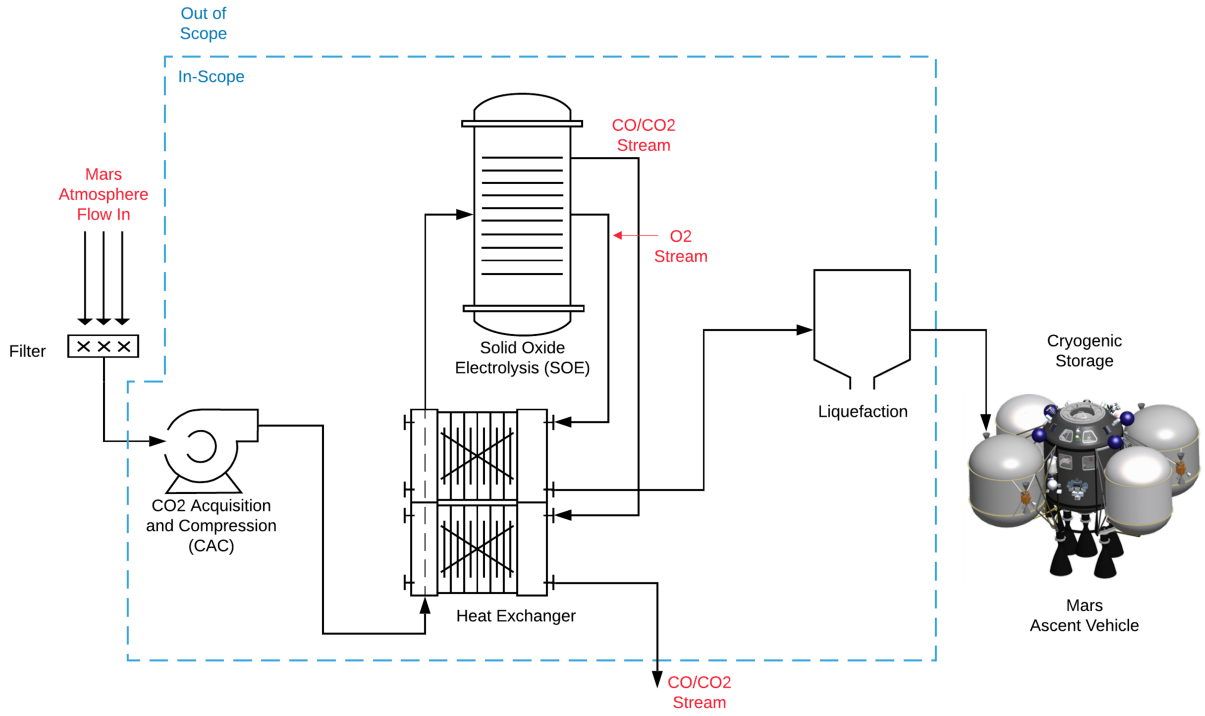

Figure 51: System boundary for the multi-objective optimization problem. The system begins when filtered, dust-free Mars gas enters the CAC system and ends when liquefied oxygen leaves the liquefaction system and is gravity-fed to the MAV tanks. The cathode exhaust is also out of scope.

As Figure 51 indicates, the primary components that are within the system boundaries are the CAC system, SOE system, liquefaction system, and heat exchanger. A recirculation loop to recycle a portion of the cathode exhaust into the inlet stream is also included in the design to prevent SOE oxidation. The modeling of each of these in-scope components is described in Chapter 4.

3.4 Objectives, Design Variables, Parameters, and Constraints

The combination of all objectives, constraints, design variables, and parameters helps formulate the important elements of the extensibility problem. The following sections will expand upon each of these aspects of the optimization problem setup.

3.4.1 Objectives

Due to the challenging, risky, and costly nature of sending objects to Mars, the *objective functions* selected for this optimization problem are the minimization of all the following quantities: *mass, volume, power,* and *risk.* Mass and volume are *form*-based objectives, as they represent the physical form of objects in the system. Power and risk, on the other hand, are *function*-based objectives, as they represent the functional outputs of the form. Mass should be minimized because mass is directly related to launch costs. Volume should be minimized to maximize payload storage capacity and ideally enable the system to be launched on a single rocket. Volume is also important since it will potentially drive aerobrake shield sizing, which has trickle-down effects on mass. Power consumption should be minimized to reduce the mass of the required power system, which is typically more massive than the entirety of the ISRU system itself. Finally, risk should be minimized to ensure high operational reliability. Note that risk and reliability are considered in the domain [0,1] and are taken to be opposites, such that:

$$Risk = 1 - Reliability \tag{27}$$

Mass and volume are typically directly related; a system with a lower volume is usually also less massive. Power may trade inversely with mass and volume. As an example, a heat exchanger can be added to reduce power requirements at the cost of adding the mass and volume of the heat exchanger unit. Risk typically trades inversely with all three of the other objectives. Risk may be reduced through the addition of redundant systems, which invokes a mass and volume penalty. Similarly, risk may be reduced by eliminating moving parts, which may invoke a power penalty. As an example, a mechanical pump can be replaced by a cryogenic pump, which may have fewer moving parts and thus less risk. However, the cryogenic pump replaces mechanical motion with heating and cooling cycles to move the gas, which results in a higher power consumption. In a system such as this, these tradeoffs between objectives are what drive the optimization towards a final solution.

A restatement of the optimization objective variables is given in Table 13.

Table 13: Objective variables that drive the optimization model for this dissertation

Objective Variable	Description	Units	Min/Max
Mass	Total system mass	kg	Min
Power	Total system power consumption	W	Min
Volume	Total stowed volume	m^3	Min
Risk	Quantified risk of failure	[0,1]	Min

3.4.2 Design Variables

With the system boundary defined, those variables that are considered in-scope and have an appreciable effect on the objective functions are defined as the design variables. The primary design variable values are varied by the optimization algorithm between their lower and upper bounds listed in Table 14.

Table 14: Primary design variables for the optimization algorithm. These variables impact the objective functions when varied. The optimization algorithm inputs these variables across their ranges to determine the optimal combination.

Design Variable	Variable Name	Description	Lower Bound	Upper Bound	Units
Inlet Flow Rate	$\dot{m}_{in}$	Flow rate of Mars atmosphere into the system	9	100	kg/hr
Compressor Pressure	P_2	Output pressure of the compressor	150	1000	mbar
CAC Type	CAC	Type of compressor. Options are (1) cryogenic, (2) mechanical - scroll, (3) mechanical - centrifugal, and (4) adsorption	N/A	N/A	-
Cell Area	A_{cell}	Active surface area of each electrolysis cell	22.5	111	cm^2
Number of cells per stack	N_{cps}	Number of SOE cells in each SOE stack	1	100	-
Number of stacks	N_{stacks}	Number of SOE stacks	1	20	-
Electrolysis Temperature	T_6	Operating temperature inside the SOE	1023	1123	K
Electrolysis Pressure	P_6	Output pressure of the SOE anode	50	2000	mbar
Voltage	V_{app}	Voltage applied to each SOE cell	0.9	1.05	V
Area of Heat Exchanger 1	A_{HE1}	Surface area of heat exchanger 1, which exchanges heat between SOE anode and inlet gas	0	10	m^2
Area of Heat Exchanger 2	A_{HE2}	Surface area of heat exchanger 2, which exchanges heat between SOE cathode and inlet gas	0	10	m^2
Number of CAC systems	N_{CAC}	Number of capture and compression (CAC) systems in parallel	1	10	-

A set of secondary design variables has also been defined in Table 15, which have their values varied by the optimization algorithm in the same manner as the primary design variables. These are denoted as "secondary" because they are expected to have less of an impact on the objective functions than the primary design variables.

Table 15: Secondary design variables for the optimization algorithm. These variables are expected to impact the objective functions when varied. The optimization algorithm will input these variables across their ranges to determine the optimal combination.

Design Variable	Variable Name	Description	Lower Bound	Upper Bound	Units
Liquefaction piping insulation	$t_{liq-pipe-ins}$	Thickness of aerogel insulation around the liquefaction piping	0	3	m
Liquefaction MAV insulation	$t_{liq-MAV-ins}$	Thickness of aerogel insulation around the MAV in the liquefaction subsystem	0	10	m
Inter-piping insulation	$t_{ins-pipe}$	Thickness of aerogel insulation around the piping between subsystems	0	3	m
SOE inner layer insulation	$t_{SOE-ins1}$	Thickness of Excelfrax insulation around the SOE quad and single stack modules	0	3	m
SOE outer layer insulation	$t_{SOE-ins2}$	Thickness of Excelfrax insulation between the SOE inner and outer hotbox shells	0	3	m
Spare blowers	$Blower_{numSpareUnits}$	Number of spare blowers in the cryogenic or sorption pumping systems	0	5	-
Spare cryocoolers	$Cryocooler_{numSpareUnits}$	Number of spare cryocoolers	0	3	-
Spare valves	$Valve_{numSpareUnits}$	Number of spare valves throughout the system	0	20	-
Spare mechanical pumps	$CACmechanical_{numSpareUnits}$	Number of spare mechanical compressors	0	5	-
Spare SOE cells	$SOECell_{numSpareUnits}$	Number of spare SOE cells	0	500	-
Spare SOE stacks	$SOEStack_{numSpareUnits}$	Number of spare SOE stacks	0	10	-
Spare Kilopower units	$Kilopower_{numSpareUnits}$	Number of spare 10 kWe Kilopower units	0	3	-
Spare heat exchanger plates	$Heatexchanger_{numSpareUnits}$	Number of spare plates in the Plate Heat Exchangers, to counter fouling	0	1000	-

The MAV tank insulation thickness design variable, $t_{liq-MAV-ins}$, has an upper bound of 10 meters. While this thickness is impractical, the upper bound was set this high for the sake of understanding how the optimizer would trade insulation mass with power savings.

Together, the primary and secondary design variables are perturbed with each iteration of the optimizer and result in new BAM architectures.

3.4.3 Reference Mission Parameters

One of the key aspects of the optimization problem is the mission design. A reference mission has been selected that includes the number of crew, duration of stay, launch constraints, launch windows, and Mars Ascent Vehicle design. Habitat and on-ground transportation requirements for the crew have also been taken from literature as mission parameters rather than traded and optimized. Additionally, the power source and landing site are determined from literature. Altogether, this reference mission enables calculations of oxygen production, mass, and power requirements that drive the design for the in-scope components. A subset of parameters that contribute to the reference mission are given in Table 16.

Table 16: Reference design mission parameters for this dissertation. These parameters are set as constants for the optimization framework rather than being considered as design variables.

Parameter	Description	Baseline
MAV Propellant	Oxidizer and fuel choice for the Mars Ascent Vehicle	LOX-CH_4
Number of Crew	Crew size for Mars mission	6 crew
MAV Propellant Quantity	Quantity of oxidizer needed to fill the Mars Ascent Vehicle.	30,804 kg
Power Source	Power source for the ISRU system	10 kWe Kilopower Units
Launch Timing	Timing between ISRU system and crew launches	26 months (1 synodic cycle)
Landing Site	Landing site for the ISRU system	Several – see Section 6.7.2
Electrolysis Type	Type of electrolysis used to produce oxygen	"Dry" Solid Oxide Electrolysis
Electrolyte Material	Type of electrolyte used in SOE	ScSZ
Electrolyte Thickness	Thickness of electrolyte	250 microns

These parameters can be changed if new data are acquired, technology is developed, or operational plans are altered. The parameters listed in Table 16 are described below.

Description of Reference Mission Parameters

The propellant combination chosen for the MAV is liquid oxygen (LOX) and liquid methane (CH_4). This is necessary to define as it informs the quantity of oxygen the ISRU system must produce. LOX-CH_4 is the standard propellant combination in most Mars reference missions, as CH_4 can be manufactured on Mars using a combination of atmospheric CO_2 and either Mars water or hydrogen brought from Earth. It is also a relatively efficient fuel.

The number of crew selected is six, following the recommendation of DRA 5.0. Most reference Mars missions are designed for either four or six astronauts. The number of crew influences the size of the MAV, quantity of propellant needed for the MAV, quantity of consumables for the crew, design of the EDL system, power required, and more.

The design of the MAV is also important as it contributes to the calculation of the quantity of oxygen required of the ISRU system. Polsgrove et al. published a comprehensive design in 2015 of a minimal mass MAV configuration with subsystem designs and mass summaries [120]. The system shares most critical assumptions about mission design with this dissertation, including the use of LOX-CH_4 propellant. One difference is that the MAV was designed for a crew of four, and its numbers have been scaled to account for a crew of six, from 22,717 kg to 30,804 kg. An alternate reference MAV design was put forth in DRA 5.0 and its subsequent addendums [121,122]. The authors of DRA 5.0 included a MAV configuration for both four and six crew members.

The power source to supply the ISRU system is a network of 10 kWe Kilopower reactors. Other options that were considered and rejected included solar panels that afford daytime-only operation, solar panels with batteries that afford round-the-clock operation, and a single, large fission power unit. The Kilopower reactors provide mission flexibility and reduce risk and are discussed in more detail in Section 2.7.1 and Section 4.7.

The baseline launch timing for the mission architecture is to launch the ISRU plant and its ancillary systems one launch opportunity ahead of a human mission. This would amount to a 26-month gap between launches and would allow the ISRU system to produce oxygen on Mars prior to, and possibly during, the crew's trip to Mars. By the time of the crew's arrival on Mars, the oxygen tanks on the MAV would be full. The crew would manually disconnect the ISRU system from the MAV tanks to prepare the vehicle for launch at the end of their surface mission.

The chosen landing site has important implications for an ISRU system on Mars [111]. The terrain must be sufficiently flat to permit ISRU systems as well as ancillary systems that will need to be moved into place, such as power units and propellant storage tanks. The site, if located near water reserves, could provide additional avenues for water-based ISRU. Additionally, lower altitude landing sites are preferable, as the increased atmospheric density would improve carbon dioxide acquisition from the atmosphere. Several landing sites were simulated, and the results are shown in Section 6.7.2.

In terms of electrolysis, CO_2-only electrolysis is defined as the baseline technology. This is the technology used on MOXIE. Scandia-Stabilized Zirconia (ScSZ), the technology used on MOXIE, is chosen as the electrolyte material to enable lessons learned from the MOXIE project to be applied to the optimization model. For the same reason, the electrolyte thickness is set at 250 microns, equivalent to the thickness of the MOXIE electrolytes and those of subsequent research studies at OxEon Energy.

Oxygen Production Rate Required

The oxygen production rate that is required of the ISRU system is a key driving factor in the ISRU system design. The rate is calculated in kg/hr from the total O_2 mass required to lift the MAV off Mars and the time available to make the O_2. As discussed earlier, this is treated as a constraint by the optimizer rather than trying to maximize oxygen production, such that at least the amount of oxygen required to fill the MAV must be produced by BAM. The hierarchy of factors influencing the oxygen production rate of the ISRU system is shown in Figure 52.

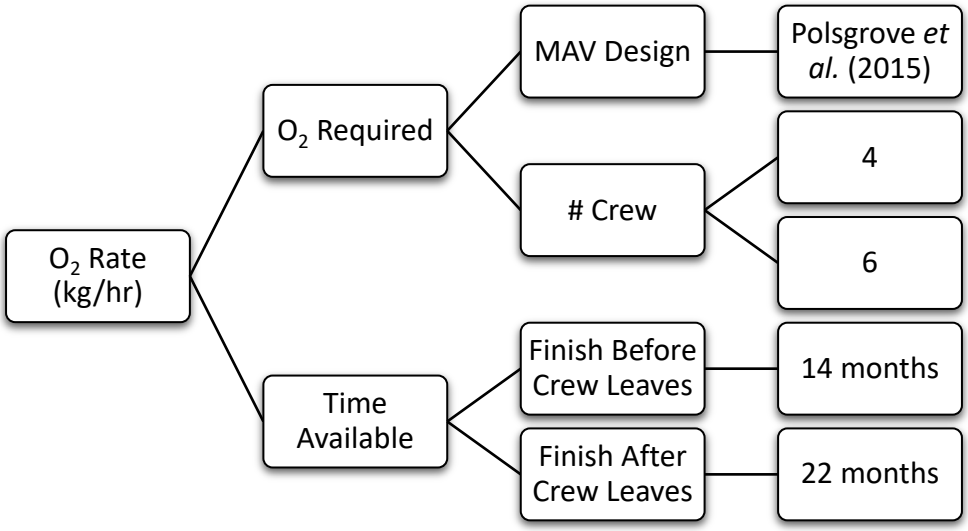

Figure 52: Hierarchy of factors influencing the oxygen production rate of the ISRU system.

The oxygen rate required of the ISRU plant is determined from the total oxygen required and the time available to produce it. The total oxygen required is determined from the selected MAV design and the number of crew on the mission. The time available is dependent on whether the ISRU plant will be active after the departure of the crew from Earth.

The quantity of oxidizer needed in the design put forth in this dissertation is based on the requirements of the MAV from Polsgrove et al. (2015), the most comprehensive MAV design found by the author [120]. The combined mass of LOX required in the design for both the first and second stage of the rocket is 22,717 kg. To increase from a crew of four to a crew size of six, the requirement is multiplied by a factor of 1.356, derived from the ratio of O_2 required between MAV designs for four-person and six-person crews in DRA 5.0. This derivation is shown in Table 17.

Table 17: MAV oxygen propellant requirements for a 4-person and 6-person crew using two different MAV architectures [120,122]

MAV Design and Crew #	MAV LO_2 Requirement (kg)
DRA 5.0 – 6 Crew	23,532
DRA 5.0 – 4 Crew	17,864
Ratio 6:4 Crew	1.356
Polsgrove – 4 Crew	22,717
Polsgrove – 6 Crew	**30,804**

Multiplying Polsgrove et al.'s (2015) number for a crew of four by the calculated ratio provides an estimate of the oxygen requirements for a crew of six using that MAV design: **30,804 kg**. This is the targeted oxygen mass for this dissertation for a crew of six

The second branch in Figure 52, time available, is dependent on if the ISRU oxygen production must be completed prior to the departure of the crew from Earth. The argument for oxygen production being completed prior to the crew departing Earth is that it reduces mission risk, as the crew will be certain that all the oxygen required is already produced on Mars before their launch. The argument against it is that a crewed mission to Mars may have the ability to abort and return to Earth (likely with a Mars swing-by) for a variety of reasons, including potential failure of MAV storage tanks. If this is the case, no risk reduction benefit would be realized by fully producing the oxygen prior the crew's departure, as the ability to abort already exists. It may actually pose additional risk, as the cryocooler system would have to maintain a full MAV tank in a zero boil-off state for a longer time. For this reason, the oxygen production window could be extended into the crew's travel time to Mars, thus reducing the production rate requirement. The oxygen should be fully produced before the crew begin their entry, descent, and landing sequence to the Mars surface, as the ability to abort would no longer be available once the crew lands on Mars. Both options for length of oxygen production time are summarized in Table 18.

Table 18: ISRU production time calculations for two mission scenarios: 1) the O_2 must be fully produced on Mars before the crew departs Earth, and 2) the O_2 may continue being produced while the crew is traveling to Mars

	Option 1: Complete O_2 Production Prior to Crew Departure	Option 2: Complete O_2 Production After Crew Departure
Time Between ISRU System Launch and Crew Launch (Earth-Mars Synodic Cycle)	26 months	26 months
Crew Transit Time to Mars	9 months	Irrelevant
ISRU Setup Time	1 month	1 month
Margin	2 months	3 months
Total ISRU Time Allowed:	**14 months**	**22 months**

The results from Table 17 and Table 18 are combined to calculate four different oxygen production rates that will drive the ISRU system design, shown in Table 19.

Table 19: Total oxygen production rate requirement for the ISRU system under four different mission scenarios

	Option 1: Complete O_2 Production Prior to Crew Departure	Option 2: Complete O_2 Production After Crew Departure
4 Crew	2.25 kg/hr	1.43 kg/hr
6 Crew	3.06 kg/hr	1.94 kg/hr

These results indicate that the ISRU system may need to produce oxygen at an average rate between 1.43 kg/hr and 3.06 kg/hr, depending on mission design and number of crew. A sensitivity analysis that determines how the crew size and oxygen production time affect the optimal BAM architecture is shown in Section 6.7.1. The nominal case in this dissertation is the most demanding: Option 1 with 6 crew. Thus, the required O_2 production rate is **3.06 kg/hr**.

3.4.4 Constraints

System level *constraints* were determined across the entire mission lifecycle. A violation of a constraint results in an infeasible mission. Therefore, any BAM architecture that violates a constraint is discarded by the optimizer. The primary constraint driving the system is the total quantity of oxygen that must be produced to lift a crew of six off the surface in the reference MAV design. All constraints are listed in Table 20.

Table 20: System level constraints for BAM optimization

Constraint	Equation	Description
Oxygen Production	$\dot{m}_{O_2} > O_{2_{prod-rate}}$	The oxygen production rate must be at least the oxygen production rate needed to fill the MAV in the allocated ISRU mission timeline. The MAV tank size and mission timeline are defined inputs to the simulation, which can vary based on crew size and ConOps assumptions.
SOE Inlet Pressure	$P_5 > P_{min}$	Inlet pressure to the SOE must be at least the pressure that defines the limit of SOE operability.
Voltage in Range	$V_{N,O} < V_{app} < V_{N,C}$	The voltage applied to each SOE cell must be at least the Nernst voltage for oxygen formation but no greater than the Nernst voltage for carbon formation. Only in this range will oxygen be produced without carbon deposition degrading the cells.
Boudouard Boundary	$V_{N,O} < V_{N,C}$	The utilization fraction must be controlled to ensure the Boudouard Boundary is not exceeded. Beyond this boundary, oxygen cannot be made without carbon deposition. The boundary is defined by the Nernst potentials for the two chemical reactions.
Utilization Fraction	$0 < U < 1$	The utilization fraction, or the fraction of inlet CO_2 that is converted to O_2, must lie between 0 and 1. It is physically impossible to have a U outside this range.

The lower limit of the SOE inlet pressure was determined experimentally. The remaining constraints are fully described by Table 20.

3.4.5 Multi-Objective Optimization Problem Formulation

With the objectives, design variables, reference parameters, and constraints in place, the optimization problem can be formalized. The objectives are defined in a vector $\boldsymbol{J}$:

$$\boldsymbol{J} = \begin{bmatrix} J_1 \\ J_2 \\ J_3 \\ J_4 \end{bmatrix} = \begin{bmatrix} \text{Power (W)} \\ \text{Mass (kg)} \\ \text{Risk} \\ \text{Volume (m}^3\text{)} \end{bmatrix} \tag{28}$$

The primary design variables, previously listed in Table 14, are defined in a vector $\boldsymbol{x}$:

$$\boldsymbol{x} = \begin{bmatrix} x_1 \\ x_2 \\ x_3 \\ x_4 \\ x_5 \\ x_6 \\ x_7 \\ x_8 \\ x_9 \\ x_{10} \\ x_{11} \\ x_{12} \end{bmatrix} = \begin{bmatrix} \dot{m}_{in} \\ P_2 \\ CAC \\ A_{cell} \\ N_{cps} \\ N_{stacks} \\ T_6 \\ P_6 \\ V_{app} \\ A_{HE1} \\ A_{HE2} \\ N_{CAC} \end{bmatrix} = \begin{bmatrix} \text{Mass flow rate (kg/hr)} \\ \text{Compressor output pressure (mbar)} \\ \text{Type of compressor} \\ \text{Active SOE cell area (cm}^2\text{)} \\ \text{Number of SOE cells per stack} \\ \text{Number of SOE stacks} \\ \text{SOE operating temperature (K)} \\ \text{SOE cathode pressure (mbar)} \\ \text{SOE applied voltage (V)} \\ \text{Surface area of heat exchanger 1 (m}^2\text{)} \\ \text{Surface area of heat exchanger 2 (m}^2\text{)} \\ \text{Number of CAC units in parallel} \end{bmatrix} \tag{29}$$

The constraints, previously described in Table 20, are defined in a vector $\boldsymbol{g}$:

$$\boldsymbol{g} = \begin{bmatrix} g_1 \\ g_2 \\ g_3 \\ g_4 \\ g_5 \\ g_6 \\ g_7 \end{bmatrix} = \begin{bmatrix} \dot{m}_{O_2} > O_{2_{prod-rate}} \\ P_5 > P_{min} \\ V_{app} > V_{N,O} \\ V_{app} < V_{N,C} \\ V_{N,O} < V_{N,C} \\ U > 0 \\ U < 1 \end{bmatrix} = \begin{bmatrix} \text{Oxygen production rate} > \text{Required rate} \\ \text{Cathode pressure} > \text{Minimum allowable pressure} \\ \text{Cell voltage} > \text{Nernst voltage for oxygen} \\ \text{Cell voltage} < \text{Nernst voltage for carbon} \\ \text{Oxygen Nernst voltage} < \text{Carbon Nernst voltage} \\ \text{Utilization fraction of } CO_2 > 0 \\ \text{Utilization fraction of } CO_2 < 0 \end{bmatrix}$$

Lastly, the parameters, previously listed in Table 16, are defined in a vector $\boldsymbol{p}$. Together, these four vectors allow the problem to be formulated in the following manner:

$$\text{Minimize } \boldsymbol{J}(\boldsymbol{x}, \boldsymbol{p}) \text{ such that } \boldsymbol{g}(\boldsymbol{x}, \boldsymbol{p}) = true$$

The objectives functions and constraints are a function of the design variables and parameters. All constraints must return a value of $true$ for the optimization to be successful, indicating no

constraint violations. This formalization of the problem statement provides the basic framework upon which the optimization algorithm will be built. Details of the optimization algorithm are given in the following section.

3.5 Optimization Algorithm – Simulated Annealing

Calculating the objective functions (power, mass, volume, and risk) for every combination of design variable inputs is not a computationally feasible method to determine the best BAM design. Instead, an optimization algorithm is employed to seek the optimal design with minimal computational time and power. A Simulated Annealing (SA) algorithm was chosen for this application. Heuristics-based techniques such as SA are well-suited to this problem, as the problem is nonlinear and has a combination of discrete and continuous variables. This makes it difficult or inaccurate to employ a more traditional, gradient-based optimization algorithm. Heuristics-based techniques, however, do not rely on gradient calculations and can solve nonlinear problems.

Heuristic algorithms often mimic nature. SA, for example, mathematically mirrors the behavior of a set of atoms cooling to a state of minimum energy in a hot metal. If the metal cools and anneals too quickly, its atoms will solidify into a sub-optimal configuration. Only by allowing the atoms to cool slowly will the metal solidify into its minimum energy state. This analogy is applied to other systems like BAM by attempting to minimize the notional energy of those systems: in the case of this design, SA attempts to minimize the power, mass, volume, and risk of BAM.

Another common heuristic optimization technique is the Genetic Algorithm (GA), which mimics Darwin's Theory of Evolution [123]. It has been used in the past to optimize an ISRU design for a lunar mission [124]. The same design was also optimized using a SA algorithm, and the SA yielded a slightly more optimal design. Both algorithms were considered for BAM, and SA was ultimately chosen due to its analogous energy minimization and the ability to easily adjust its cooling and exit criteria.

Temperature

Temperature is a key factor when employing SA for an optimization problem. In a physical system where many atoms are congregated, the distribution of atoms within a control space is dependent on temperature. A higher temperature system results in the atoms having a higher average kinetic energy, and thus a wider range of distributions within the space. As temperature is lowered, certain higher energy distributions are no longer possible. Instead, lower energy distributions of atoms are significantly more likely to be present. This begins to skew the possible configurations of atoms towards lower energy states. This same logic can be applied to the optimization problem. As the analogous "temperature" of the optimization, T, is lowered, the distribution of possible end states collapses into only the lowest energy states. The absolute lowest energy state corresponds to the global optimum of the problem, the desired solution. This collapse is shown in Figure 53 as the notional temperature is lowered from T = 10 to T = 1 and the average energy state of the solution decreases towards the global optimum.

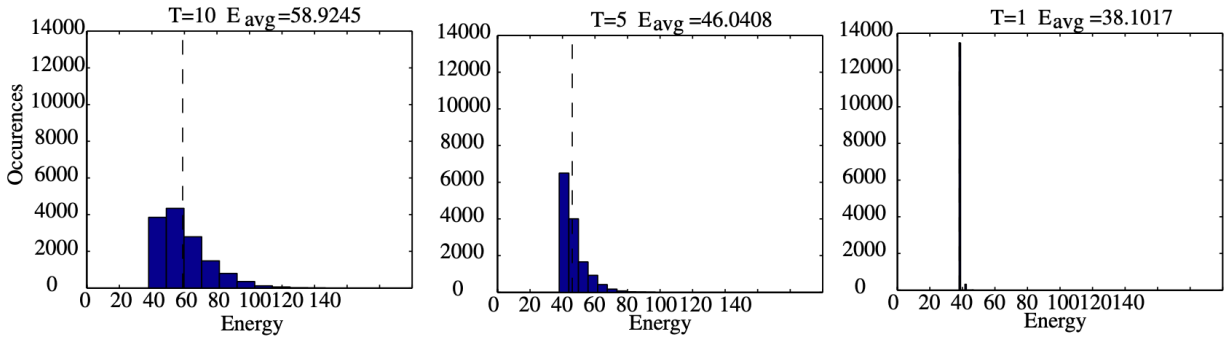

Figure 53: Simulated Annealing solution distribution collapse as temperature is lowered from T = 10 (left) to T = 5 (middle) to T = 1 (right) [125]

The occurrences of higher-energy states decrease as T is decreased across the three plots from left to right.

Freezing

As the specific heat, C, of the system (either a physical system or an optimization) begins to decline, the system is described as beginning to "freeze". In the physical world, this indicates a phase transition from a liquid to a solid. In the optimization world, this indicates that the algorithm is approaching the global optimum solution. When the system begins to freeze, it is important to control the speed at which the algorithm proceeds. Just as freezing a liquid too quickly may cause imperfections in the solid structure, freezing the optimization too quickly may result in a sub-optimal solution. The process of slow cooling to obtain defect-free solids is called *annealing*, from which Simulated Annealing draws its name. Cooling quickly is called *quenching* and, in an optimization problem, may find an end state more quickly but is prone to finding local optima rather than finding the true global optimum. For these reasons, it is important to cool the system slowly enough that the minimum energy state can be found.

Simulated Annealing Algorithm

The temperature of the system, the freezing conditions, and an important algorithm called the Metropolis algorithm are the key components of the simulated annealing optimization process. This process is shown as a block flow diagram in Figure 54.

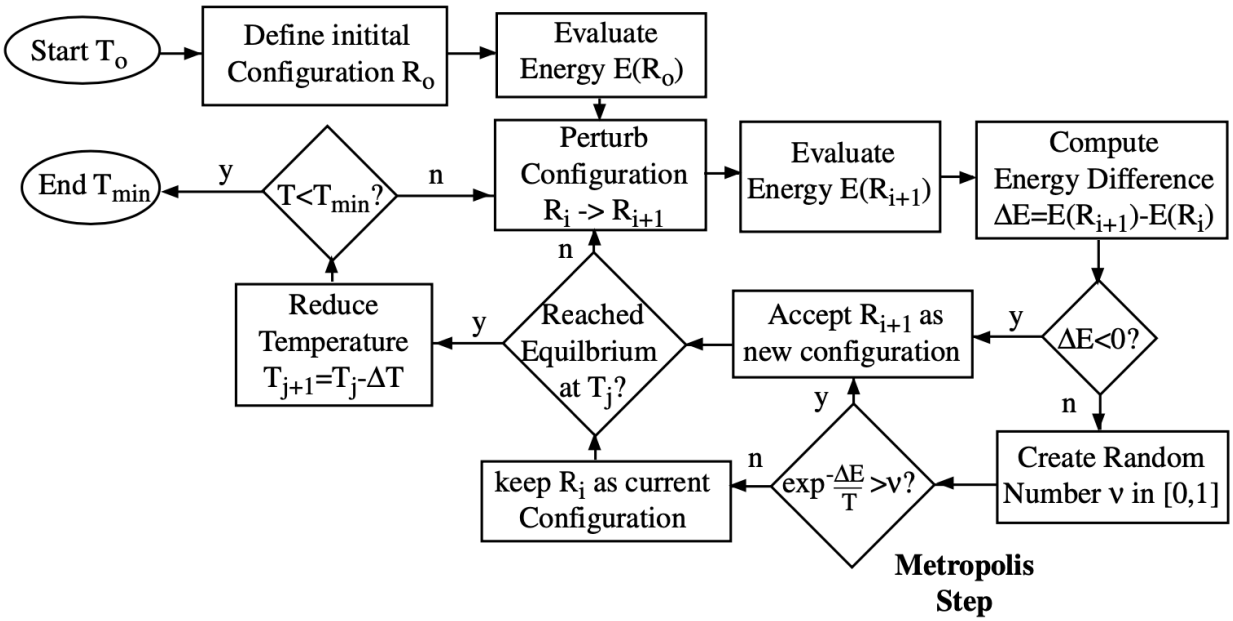

Figure 54: Block flow diagram that shows the Simulated Annealing algorithm [125]

The optimization begins with an initial configuration of design variables, R_o, and a starting temperature, T_o, which is analogous to the starting temperature of a hot metal prior to annealing. The breadth of the design space aligns with the atomic configuration of the metal; at a higher temperature, more energy states are available within the metal as the atoms have more thermal energy, and so at a higher temperature, more BAM designs are available to be considered by the SA algorithm. The energy of the system is calculated, which, in the case of BAM, is the combination of the power, mass, volume, and risk objective functions. The design variables are then perturbed to create a new configuration, R_{i+1}, which is evaluated. If its energy is less than the previous configuration, R_{i+1} is accepted as the new baseline. If its energy is not less than the previous configuration, a *quenching* algorithm would automatically reject it. Simulating *annealing*, however, may accept it as a new baseline despite it being in a higher energy state. This is a key step in the optimization process that helps avoid becoming stuck in local optima. This "Metropolis Step" calculates whether R_{i+1} is accepted or rejected with the following equation:

$$e^{-\frac{\Delta E}{T}} > \nu \tag{30}$$

where ΔE is the difference in energy states between R_i and R_{i+1}, T is the temperature of the system, and ν is a random number in the range [0,1]. As the temperature of the system cools, it becomes less likely that a higher-energy state will be accepted. Similarly, the likelihood of accepting a higher-energy state decreases as ΔE increases. If Equation (30) is true, R_{i+1} is accepted as the new baseline configuration; if not, R_i remains the baseline. Next, the algorithm determines whether an equilibrium condition, predefined by the user, has been met for the current temperature. If it has not, the cycle repeats until equilibrium has been achieved. Once equilibrium has been achieved, the temperature of the system is reduced by a predefined ΔT and the cycle repeats. The algorithm continues to run until the temperature falls below the predefined T_{min}, which indicates a "frozen" state and thus the final solution. This is analogous to a hot metal, at initial temperature T_o, cooling to its final temperature, T_{min}. Another possible exit

criteria occurs when the simulation has run through many iterations without a new configuration being accepted.

To summarize, Simulated Annealing is a strong algorithm for complex problems because it often finds a global optimum without becoming trapped in local optima like other, gradient-based methods would. It accomplishes this with the Metropolis Step, which forces Simulated Annealing to behave akin to a random search method when the temperature is high, but more like a gradient search method when the temperature is low. A description of how this algorithm was implemented in MATLAB to solve BAM's architecture follows.

3.6 MATLAB Functions

The code used to run the Simulated Annealing algorithm has three main components: the SA algorithm, the perturbation function, and the penalty function. The SA algorithm implements the process described in the previous section and is available in a standard MATLAB package. A starting vector of design variables, $\boldsymbol{x_o}$, is used as an input to the algorithm. The starting vector is an educated guess of the optimal design variable values and is generally selected from previous SA runs. The initial temperature, cooling schedule, equilibrium conditions, and termination criteria are also inputs to the MATLAB code. The selection of these tuning parameters is described in Section 3.8. The relationship between these inputs, MATLAB components, and outputs of the simulation are shown in Figure 55.

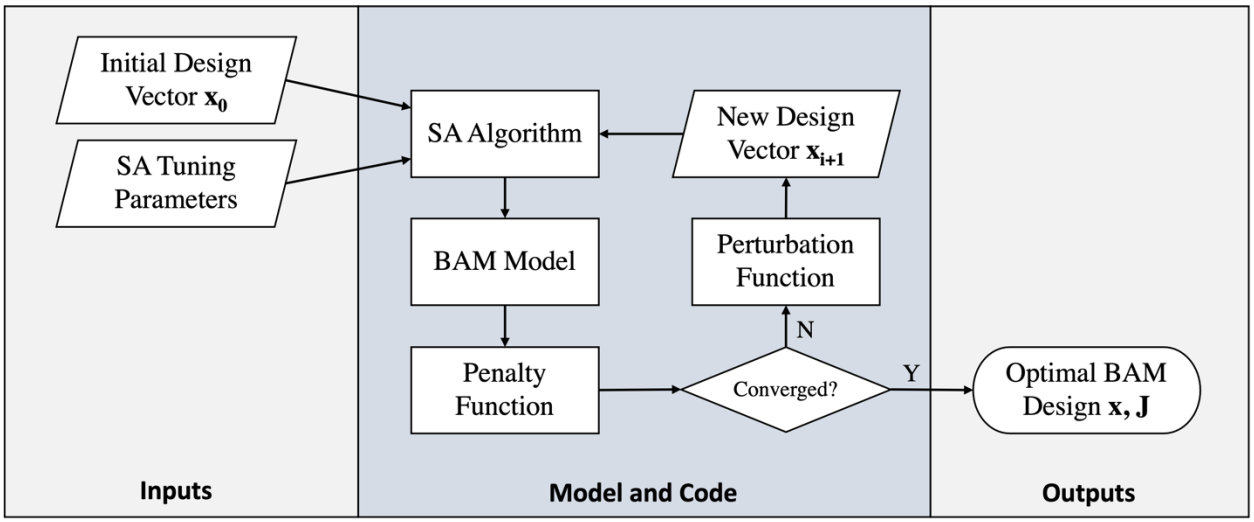

Figure 55: Block flow diagram of optimization process. The initial design vector and simulated annealing tuning parameters feed the model, which includes the simulated annealing algorithm, Simulink BAM model, penalty function, and perturbation function. The model iterates on the design variable vector until the algorithm converges on an optimal design.

The initial design vector and SA tuning parameters are fed as inputs to the SA algorithm. The SA algorithm calls the BAM model to evaluate the architecture and applies a penalty function, described in more detail below, if the resulting architecture violates a system constraint. The design variable vector is then perturbed, and the new vector is fed into the algorithm. This process repeats until the simulation converges on an optimal design.

In the perturbation function, each design variable is randomly perturbed within a certain percentage of its original value. The perturbed value must lie within the upper and lower bounds

of that design variable. If it does, it becomes the new value for that design variable that is used by the next simulation. For example, the variable that represents the outlet pressure of the compressor, P_2, may have an initial value of 150,000 Pa. After the SA algorithm runs one simulation with P_2 at that value, the perturbation function will perturb the value of P_2 using the following equation:

$$P_{2,new} = P_2(1 + cf) \tag{31}$$

where c is a random number in the range [-1,1] and f is a fraction multiplier. If f is set to 0.1, then the perturbation will adjust the value of P_2 by up to +/-10%. This means that the value of $P_{2,new}$ in this case could range from 135,000 Pa – 165,000 Pa. The full set of perturbation functions for all design variables can be found in Appendix D.

This perturbation process occurs for 3 randomly selected design variables every time a simulation is run. It would be possible to perturb all 25 design variables on every iteration during the optimization; however, this results in what is essentially a random search algorithm where the true effect of each design variable on the objective function is masked by the other 24 design variables that change at the same time. Perturbing all 25 design variables at the same time makes it unlikely that the optimizer will discover an optimum solution. On the other hand, perturbing only 1 design variable at a time results in exceptionally long computation times before the optimizer converges on a final solution. A balance between these two extremes was selected by perturbing 3 random design variables with each iteration. A side-by-side comparison of the optimization results from perturbing all 25 variables each iteration and perturbing just 3 variables each iteration is shown in Figure 56.

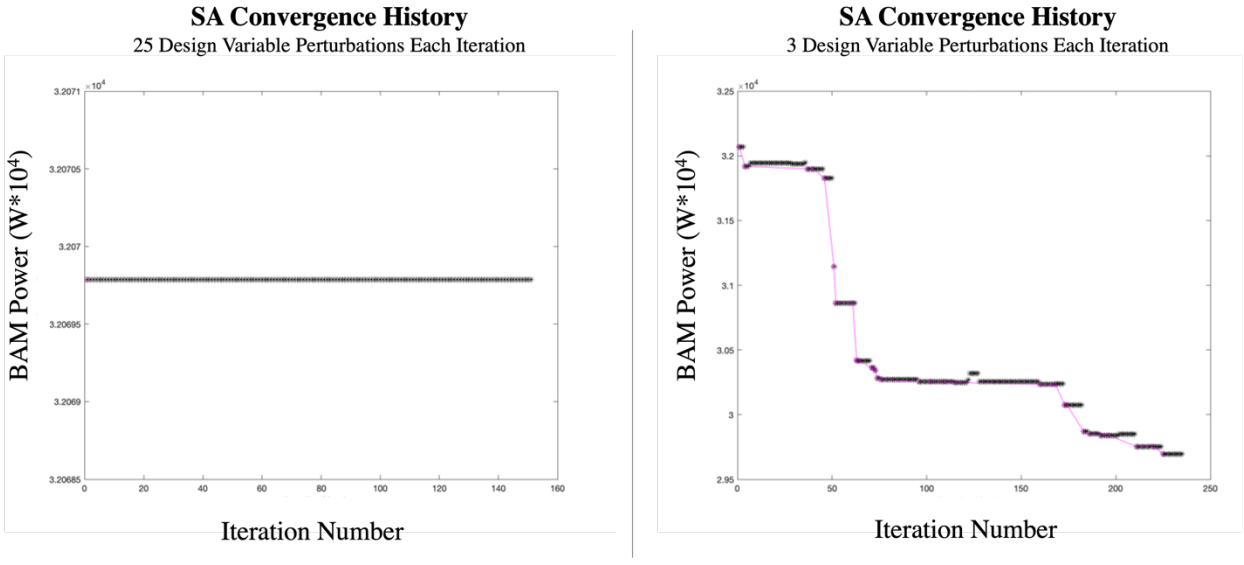

Figure 56: Comparison between two simulated annealing optimizations for BAM. On left, the optimizer perturbed all 25 design variables each iteration and did not find a single more optimal solution than the starting design, so power remains the same across 150 iterations. On right, only three design variables were perturbed each iteration, and the optimizer found greater than 10 solutions more optimal than the starting design, resulting in a lower system power.

In the case where 3 design variables are perturbed each iteration, the design variables are randomly selected to be perturbed, and change each iteration. This means that over the course of a full optimization, it is highly likely that all 25 design variables will have been perturbed

multiple times. As can be seen from Figure 56, the optimization where all 25 design variables were perturbed each iteration did not find any solutions more optimal than the starting design across 150 iterations. The optimization where only 3 design variables were perturbed each iteration, however, found greater than 10 solutions more optimal than the starting design, as is seen in the downward trend of BAM power across the optimization run. The resulting power in the latter case was approximately 10% less than the starting design.

The last component required for the SA optimizer to run is the penalty function. The penalty function exists to penalize solutions that violate a constraint so that they are rejected by the optimizer. The way that the function penalizes infeasible solutions is by multiplying the objective function by a large scalar so that it appears to be a poor solution that will be rejected by the optimizer. Thus, if a perturbed design variable results in a constraint violation, the final mass, power, volume, and risk of the system will be multiplied by the large scalar and that simulation will be rejected. The SA algorithm, perturbation function, and penalty function work together through the model to find an optimal design solution for BAM.

3.7 Scaling

Scaling of design variables and constraints is an important step in setting up an optimization solver. The purpose of scaling is to change the magnitude of each design variable and constraint such that they all have a similar magnitude. If, for example, pressure is a design variable and is operating at several thousands of Pascals, it may appear to the optimizer to have a larger effect on the objective function results than a design variable like cell area, which has a magnitude in the tens or hundreds of square centimeters. This can cause a heuristics-based algorithm like Simulated Annealing to not converge or to converge to a non-optimal solution. Scaling or nondimensionalizing the design variables to force equal magnitudes typically decreases the number of iterations required of the optimizer and improves the chances of converging on the optimal solution. The same is true of the constraints; scaling the constraints ensures they each have an equal weighting in the optimization.

In gradient-based optimization problems, a standard scaling methodology exists that involves determining the conditioning of the Hessian matrix [126]. An ill-conditioned Hessian indicates poor scaling, which means that the objective function may vary much more slowly with changes in some design variables than others. This essentially masks the true effects of those design variables on the objective functions. In a problem such as the one presented in this dissertation, which has discrete design variables and uses a heuristics-based solver, this Hessian-based process is difficult or impossible to fully implement. Instead, the upper and lower bounds of the design variables can be used to provide a linear transformation $\tilde{x} = Dx + b$, following the method from Papalambros and Wilde [127], given by:

$$D_i = \frac{2}{u_i - l_i}, \quad b_i = -\frac{u_i + l_i}{u_i - l_i} \tag{32}$$

where $\tilde{x}$ is the scaled design variable, u_i is the upper bound of that design variable, and l_i is its lower bound. This scaling results in all design variables having values between -1 and 1. This was implemented in the model by scaling the design variables in the MATLAB script controlled by the optimizer. However, in the Simulink model, where the design variables are used in

equations, the design variables are adjusted to reset them to their original values and units. In this way, the optimization algorithm controls unitless, scaled design variables, but the model uses design variables with proper values and units. This scaling process results in improved optimization speed and results.

3.8 Single Objective Optimization Setup

A variety of objective combinations were explored, including single objective optimizations of power, mass, and reliability. The motivation and optimization for single objective optimization of power is described in this section as an example. Section 3.9 describes the setup used for multi-objective optimization with power, mass, risk, and volume as driving factors. Together, these two sections describe the setup of the optimization problem, and the results of these optimizations are detailed in Chapter 6.

3.8.1 Motivation

Power appears to be the limiting factor in most Mars-based ISRU system designs, including MOXIE. This is primarily derived from the fact that several other objectives – mass, volume, and cost – flow down from power. As an example, consider a Mars atmospheric ISRU plant that requires 25 kWe power to run. The power is supplied by 3 independent, 10 kWe Kilopower fusion reactors. NASA's Design Reference Architecture [28] estimates that the mass of the ISRU system itself is on the order of 600 kg. Each Kilopower reactor, on the other hand, is 1500 kg, resulting in a total power system mass of 4500 kg. Therefore, the total system mass is primarily driven by the mass of the power subsystem. Volume follows a similar principle, as a significant portion of the volumetric space in the payload fairings will be occupied by the power systems. Launch costs are dependent on mass, which flows down from power. In summary, there is a strong argument for power acting as the primary objective in ISRU system design, as other objectives are heavily influenced by the size of the power subsystem.

3.8.2 Tuning Parameters DOE

A Design of Experiment (DOE) was conducted to determine the values of the SA tuning parameters that would yield the best model results in terms of objective function and computational time. A series of simulations were run to step through different values of the SA tuning parameters, and the resulting computational time and number of iterations required to reach the final BAM design were recorded, along with the final power of that BAM design. These data are recorded in a series of tables below.

Five SA tuning parameters were varied: initial system temperature, temperature increment, cooling schedule, equilibrium condition, and frozen condition. First, the initial system temperature was varied from 1 to 100. The results of the four optimization simulations are recorded in Table 21.

Table 21: DOE for various initial system temperatures, T_O, for Simulated Annealing algorithm

T_O	Power (W)	CPU Time (s)	Number Iterations
1	35171	1090	154
10	34459	1270	151
40	**34098**	**1152**	**151**
100	36381	1203	151

As described in Section 3.5, the temperature of the system determines how broad of a design space is considered by the optimizer. In theory, a higher starting temperature should result in a broader search. The power was minimized at a temperature of $T_O = 40$. While this may be in part due to the small sample size and randomness of the perturbations used in the SA algorithm, the baseline initial temperature was still set to a value of 40.

The temperature increment determines how quickly the system "cools" from its initial temperature, T_O, to its final, "frozen", condition. The results of five optimization runs across three temperature increments are shown in Table 22.

Table 22: DOE for temperature increments, ΔT, in the Simulated Annealing algorithm

ΔT	Power (W)	Avg Power (W)	CPU Time (s)	Number Iterations
0.5	36055	35493	992	151
0.5	34930		1036	151
0.75	**33952**	**33896**	**1040**	**151**
0.75	**33840**		**1162**	**151**
0.9	33395	34629	1029	151
0.9	35863		1078	151

In theory, a larger temperature increment should result in faster cooling, which may result in a sub-optimal solution but a faster computational time. In practice, this was not the case. The computation time and most optimal solution did not follow a clear trend with respect to the temperature increment. While the lowest power was found with a temperature increment of 0.9, the lowest average power across two optimizations at each increment was found at a temperature increment of 0.75, which was selected as the baseline.

The cooling schedule determines whether the cooling behavior of the algorithm behaves in a linear or an exponential fashion. Each was tested twice, and the results are shown in Table 23.

Table 23: DOE for cooling schedule in the Simulated Annealing algorithm

Cooling Schedule	Power (W)	Avg Power (W)	CPU Time (s)	Number Iterations
Exponential	**34189**	**34252**	**1152**	**151**
Exponential	**34314**		**1150**	**151**
Linear	33568	38345	1150	151
Linear	43121		1139	151

The exponential cooling schedule found, on average, the lowest system power. The computational time and number of iterations were consistent across both options. An exponential

cooling schedule allows the simulation to spend more time at lower system temperatures, which should theoretically allow it to obtain a closer result to the global optimum than a linear schedule. For these reasons, the exponential cooling schedule was selected as the baseline.

The equilibrium condition determines how frequently the temperature is decreased. The simulation will reduce the temperature according to its cooling schedule only after a specific number of configuration changes, N_{eq}, have been accepted at that temperature. An increase in N_{eq} is expected to increase the number of iterations and thus the computation time and should result in a more optimal solution. Three values of N_{eq} were tested, and the results are shown in Table 24.

Table 24: DOE for equilibrium condition, N_{eq}, in the Simulated Annealing algorithm

N_{eq}	Power (W)	CPU Time (s)	Number Iterations
1	44363	102	17
10	33840	1162	151
30	**33543**	**3722**	**451**

As expected, the larger the value of the equilibrium condition, the lower the BAM power and the higher the computation time. Despite the high computational cost of using a value of 30 for N_{eq}, this was selected as the baseline for final BAM architecture optimization cases to achieve the most optimal result for the design of BAM. For intermediate test cases, a value of 10 may be substituted to save computational time.

The final tuning parameter, the frozen condition, is the exit criterion for the optimization algorithm. The algorithm will terminate when N_{frozen} successive temperature increments have not yielded a new best design. When this occurs, the system is said to be "frozen" and may reflect its optimum design. Three values of N_{frozen} were tested, and the results are shown in Table 25.

Table 25: DOE for frozen condition, N_{frozen}, in the Simulated Annealing algorithm

N_{frozen}	Power (W)	CPU Time (s)	Number Iterations
1	37521	331	51
3	36364	1095	151
5	**33107**	**1765**	**251**

Like N_{eq}, a higher value of N_{frozen} resulted in a longer computational time but a more optimal result. For this reason, a value of 5 for N_{frozen} was selected as the baseline. Higher values result in prohibitively long computational times.

The optimal tuning parameters for single objective optimization, according to this DOE series, are summarized in Table 26.

Table 26: Optimal tuning parameters for single objective optimization using Simulated Annealing

Parameter	Description	Optimal Value
T_O	Starting temperature of the algorithm. Higher temperature equates to a broader search in the design space.	40
ΔT	Temperature increment used during cooling.	0.75
Cooling Schedule	Mathematical form of cooling equation.	Exponential
N_{eq}	Number of iterations that occur at a specific temperature before the temperature is decreased.	30
N_{frozen}	Number of successive temperatures that must	5

These tuning parameters form the baseline for the optimization simulations. It should also be noted that the values for system power found in this DOE do not necessarily reflect the optimum power of BAM, as finding the true global optimum is also dependent on the starting vector.

3.9 Multi-Objective Optimization Setup

While single objective optimization provides valuable insight into the architectures that minimize a single objective, BAM has multiple objectives that should all be minimized in its optimal configuration. These include power, mass, risk, and volume. In some cases, design variables have opposite effects on the objectives. As an example, an increase in heat exchanger area may decrease power but increase mass and volume. Therefore, to optimize the design of BAM with multiple objectives in consideration, single objective optimizations are conducted for power, mass, and risk individually, and the results are combined on a three-dimensional Pareto front, where all feasible, optimized solutions can be viewed and compared against one another. Volume is taken into consideration by observing the solutions on the Pareto front and down-selecting to only those solutions whose volume can fit in the fairing of a single launch vehicle. The Pareto front and discussion of the solution space can be found in Chapter 6.

Chapter 4: System Design and Modeling

With the optimization algorithm in place and its framework selected, a detailed model is required to enable the optimization algorithm to select designs for BAM. A multi-objective design optimization model has been built for BAM and will be described in this chapter.

4.1 Systems Engineering Tools

The problem is formulated as a system-of-systems engineering model based off the BAM design shown previously and again copied in Figure 57.

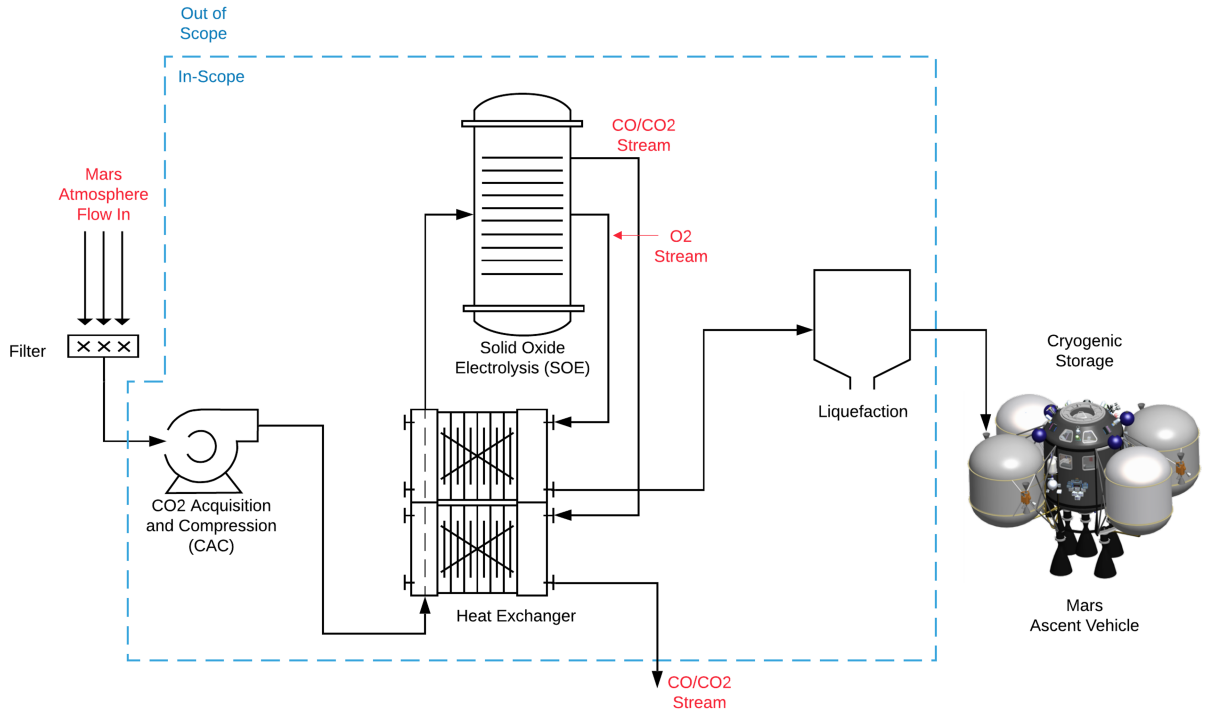

Figure 57: Block flow diagram design of BAM, indicating the in-scope design components for this dissertation

4.1.1 Block Flow Diagram

Four modules are apparent within the scope of BAM: the CAC system, the electrolysis system, the liquefaction system, and the heat exchanger. These modules flow into one another and are physical elements of a greater system. To further break the system into components, two additional modules have been defined: power and electronics.

A block diagram is shown in Figure 58 that details the six modules of the system, the design variables, the objectives, and the oxygen production constraint. Flows (physical, information, energy, and mass) are also shown.

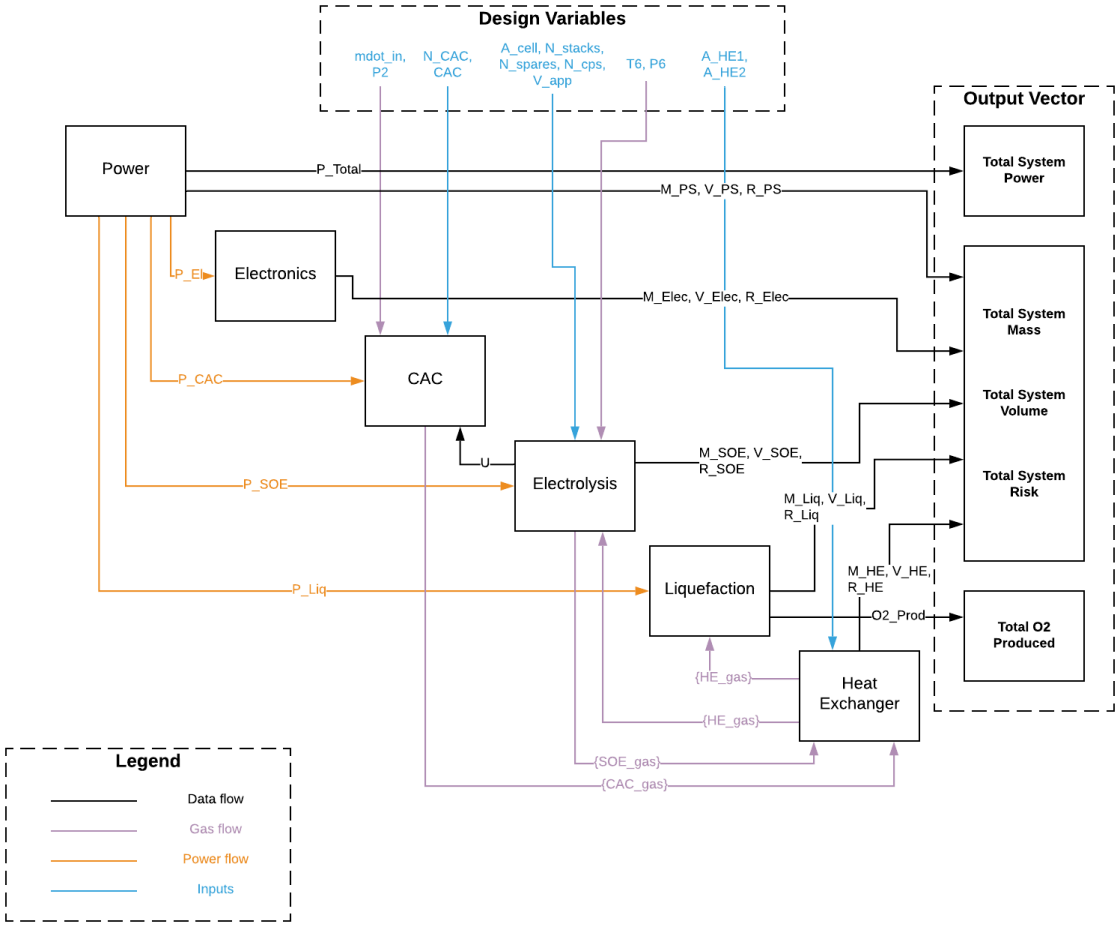

Figure 58: Block flow diagram for the top-level modules of the scaled-up ISRU system, including major design variables shown as inputs to the modules, and objectives shown as outputs

The diagram shows the design variables that feed into each subsystem. It indicates how the power system sends power to each of the other subsystems. Among other functionalities, it also allows one to trace the gas flow from the mdot_in design variable through to the liquefaction unit. Finally, it shows the four objective functions – power, mass, volume, and risk – and how they are each affected by the subsystems.

4.1.2 N-Squared Matrix

Another way to visualize a system's modules and their associated inputs and outputs is through an N^2 matrix. The matrix structure makes apparent the connections between the modules. The following color-coding highlights various elements of the matrix, which is shown in Table 27.

Design variable | Intermediate variable | Power | Mass, Volume | Risk

Table 27: N^2 matrix, visualizing the inputs and outputs of the major modules in the scaled-up ISRU system. Data and interfaces flow in a clockwise direction between subsystems. For example, CAC_cmd flows out of Electronics and into CAC, and CAC_sig flows out of CAC and into Electronics. Blank cells indicate no interface between the respective subsystems."sig" stands for "Signal", "cmd" stands for "Command", and "U" stands for Utilization Fraction of CO_2.

INPUTS		mdot_in, P2, N_CAC, CAC	A_cell, N_stacks, N_cps, N_spares, V_app, T6, P6		A_HE1, A_HE2		
	Electronics	CAC_cmd	SOE_cmd	Liq_cmd	HE_cmd	P_El	M_El, V_El, R_El
	CAC_sig	**CAC**			{CAC_ gas}	P_CAC	M_CAC, V_CAC, R_CAC
	SOE_sig	U	**Electrolysis**		{SOE_ gas}	P_SOE	M_SOE V_SOE, R_SOE, O2_Prod
	Liq_sig			**Liquefaction**		P_Liq	M_Liq, V_Liq, R_Liq,
	HE_sig		{HE_ gas}	{HE_ gas}	**Heat Exchanger**		M_HE, V_HE, R_HE
						Power	P_Total, M_PS, V_PS, R_PS
							OUTPUTS

The subsystems are listed along the diagonal. Every cell in the same row as a subsystem represents an output of that subsystem. Conversely, every cell in the same column as a subsystem represents an input to that subsystem. There are various outputs, labeled {XX_gas} that are shown in the block flow diagram. These represent the general gas outputs of each module, namely gas temperature, gas pressure, and gas composition. The input design variables are found in the top row and the major outputs of the design are found in the rightmost column.

The block flow diagram and N^2 matrix are two methods of describing the high-level functionalities of BAM.

4.2. BAM Design

The BAM system is designed in such a way as to minimize power, mass, volume, and risk. The block flow diagram version of BAM from Figure 57 has been converted into a 3-dimensional rendering shown in Figure 59.

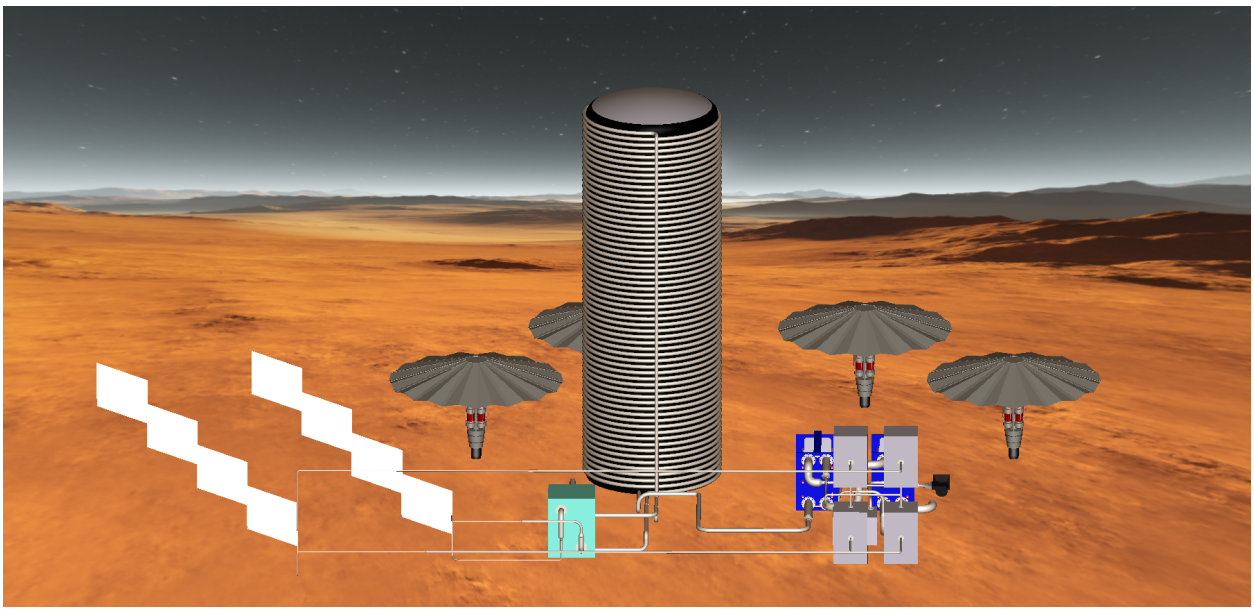

Figure 59: 3-dimensional rendering of BAM on Mars [128]

The filter, used to filter Mars dust ahead of the compressor, is placed flush against the opening of the compressor to eliminate any inlet warming or pressure drop as Martian gas flows into the compressor. Four compressors, shown as gray boxes, operate in parallel in BAM. After the gas is compressed, it flows into the blue heat exchanger where it is pre-heated by the hot SOE exhaust. From there, it flows into the SOE, which is hidden in this rendering, to be electrolyzed before traveling back into the heat exchanger to cool. It then flows into a liquefaction unit, the central green box, to be liquefied, and is finally deposited into the top of a tank. This tank will be situated inside the MAV but is shown here as a stand-alone tank to illustrate its piping network and size. Four 10 kWe Kilopower nuclear reactors are shown in the background, powering the system. These units would be placed farther away from the MAV than they appear to avoid the risk of radiation exposure once the crew arrives. The radiators are also shown on the on the left side of the figure, used to reject heat from the liquefaction subsystem.

These subsystems and components of BAM are described in more detail in the following sections.

4.3 CAC Subsystem

As discussed in Section 2.5, three categories of compressors can be considered for an atmospheric ISRU system on Mars. These are cryogenic pumps, mechanical pumps, and sorption pumps. All three categories have been designed and modeled as part of this dissertation to enable the optimization algorithm to compare how each contributes to the objective functions.

In all three cases, the design of the inlet system is an important feature. On MOXIE, a significant amount of gas density is lost in the inlet system due to warming of the gas in the inlet tube. With this finding in mind, BAM has been designed such that: i) the compressor is located as close to the filter as possible to minimize inlet tubing, ii) any tubing that does exist in the inlet system is exposed to the Martian atmosphere so that it will maintain a similar temperature as the atmosphere, and iii) any tubing that does exist in the inlet system is coated white to minimize heating. Air Squared has shown that a mechanical compression system placed in a Mars-like environment, even with an inlet tube, will experience significantly less heating than seen on MOXIE, which is enclosed in a warm rover body [129]. For the purposes of the BAM design and modeling, it will therefore be assumed that heating in the inlet system is minimal and the gas density that is taken into each of the three types of compressors is equal to that of the Mars atmosphere.

4.3.1 Cryopump

As described in Section 2.5.2, cryogenic compression and pumping of the Martian atmosphere has been studied for several decades. The freezing point of CO_2 is higher than the other major atmospheric constituents on Mars, making cryogenic pumping a feasible option. A cryopump uses a cryocooler to freeze CO_2 out of the air onto a cold head, where it can later be warmed and released as compressed, high-purity CO_2. An added benefit with cryopumping is that it can share cryocooler and radiator hardware with the oxygen liquefaction subsystem to simplify the overall BAM design.

Design

The cryopump subsystem was designed to provide many configuration options to the optimizer. In this way, the optimizer can iterate through different cryopump architectures to identify the combination that optimally minimizes power, mass, volume, and risk. A flow diagram of a cryopump is shown in Figure 60, followed by a 3-dimensional rendering of the BAM cryopump system shown in Figure 61.

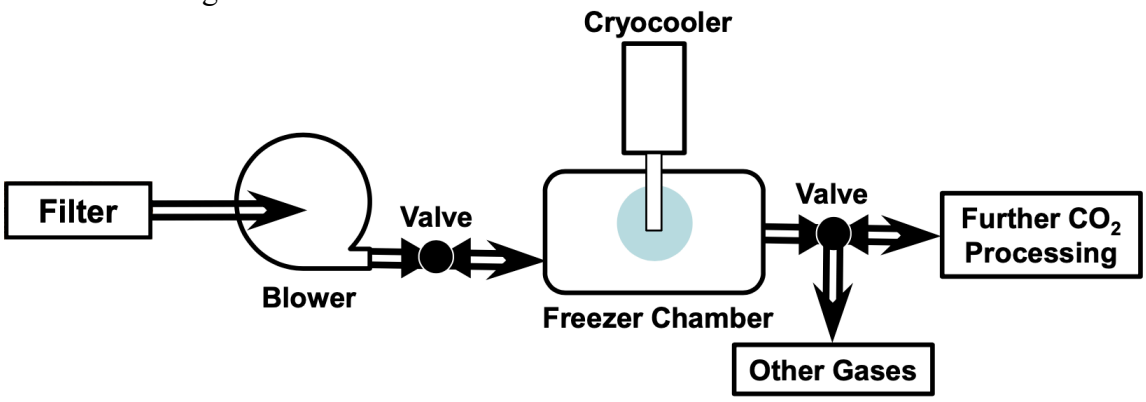

Figure 60: Block flow diagram of cryopump subsystem [131]

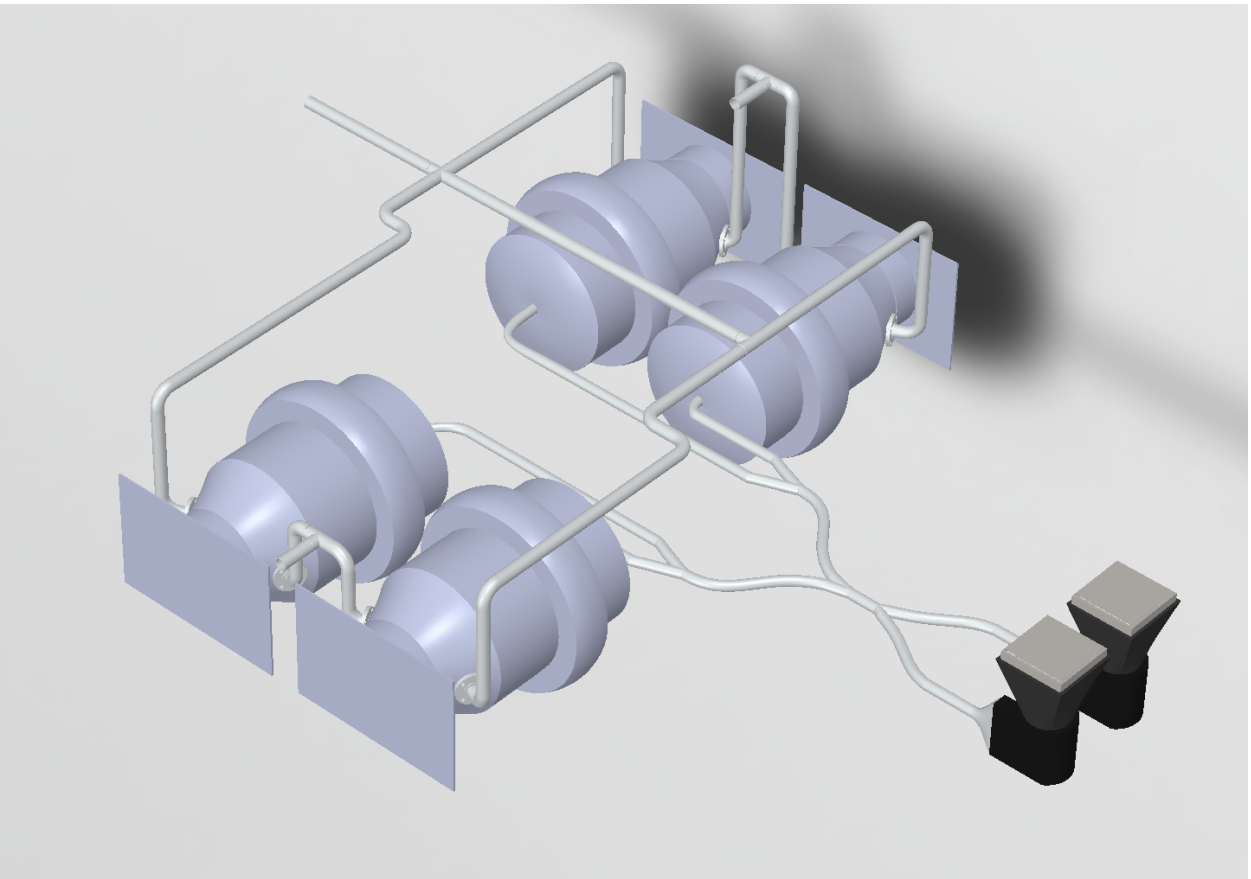

Figure 61: 3-dimensional rendering of the BAM cryopump assembly. Two filters are attached to two blower fans on the far right to reject dust. The piping routes the inlet gas to four separate cryopump assemblies, each of which contains a coldhead to acquire CO_2 [128].

Blower Fan

A blower fan is used to move Martian atmosphere through the piping and freezing chamber. A vacuum that pulls Mars atmosphere into the system is naturally created as CO_2 solidifies on the coldhead; however, the blower fan is still required for two reasons: i) to remove inert gases that might otherwise build up in the freezer chamber and inhibit CO_2 deposition, and ii) to overcome pressure drops in the system. Two blower fans are staged in parallel for redundancy, as only one will be used at a time. The blower is an axial fan, selected based on the results of two different types of blowers tested at NASA [130]. Test results have shown that nearly 100% of the CO_2 that passes through the chamber is solidified if designed properly [91]. The blower is cooled using a run-off line from the cryocooler. This is necessary to prevent motor burnout, as the rare Martian atmosphere does not provide adequate convective cooling for a motor of this type.

Freezer Chamber and Cold Head

The freezer chamber is an enclosed space where CO_2 is collected and later released. The cold head resides in the freezer chamber and is a metal fin-like structure where CO_2 frost can deposit. To freeze CO_2 at Mars ambient pressure, the cold head must operate at 150 K or lower. Because the cryopump shares a cryocooler with the oxygen liquefaction system that liquefies oxygen at 90 K, the cold head is also designed to operate at approximately 90 K. The other major

constituents of the Mars atmosphere, nitrogen and argon, do not freeze or liquefy at this temperature and pressure, resulting in minimal risk of CO_2 contamination.

Several researchers at NASA have studied the design of cold heads for Martian atmospheric ISRU. Most notably, Berg and Shah tested multiple configurations of cold heads and found that the "Tuning Fork" design had the highest sustained CO_2 collection rate over the first 100 minutes of its cycle [131]. The tuning fork design from this study was modified and adapted to the scale of the ISRU plant proposed in this dissertation and is shown in Figure 62.

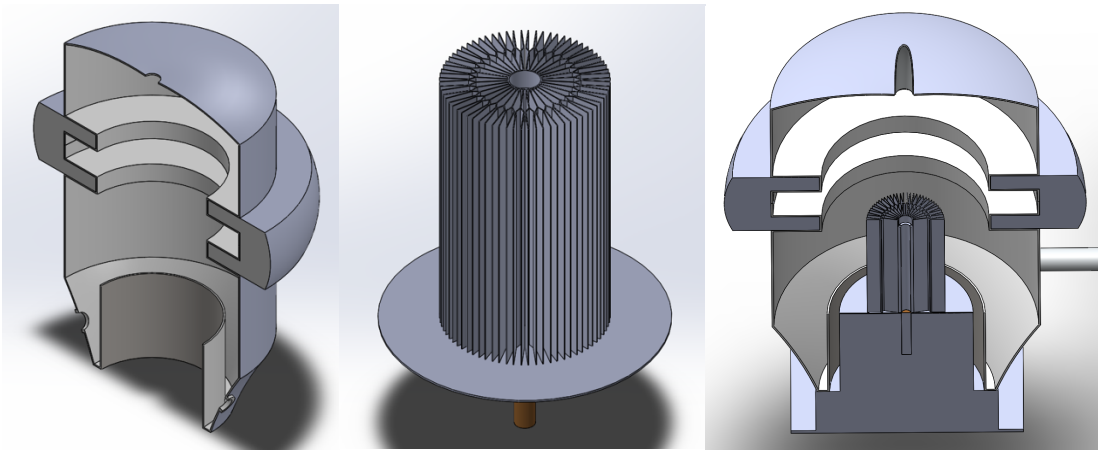

Figure 62: BAM cryocooler design. (a) Cryoshell housing cutaway, (b) tuning fork cold head design used to capture atmospheric CO_2 in the cryopump system, and (c) coldhead integrated into cryoshell [128].

The cold heads are built from a material with high thermal conductivity, either copper or silver. The size of the cold head is an important design consideration that is recomputed each time the optimizer is run. If the cold head and chamber are too small, a large number of cryopumps are required to provide the required flowrate, which results in a mass penalty. On the other hand, cold heads may have difficulty surviving launch loads if they are too large and fragile. The size of the cold head is determined with these factors in mind. The total cold head surface area that is required is determined by relating the surface area of the cold heads to the required CO_2 flow rate.

Cryocooler and Radiator

Two designs for the cryocooler were considered in this dissertation: i) self-contained Stirling cycle cryocoolers residing below the cold heads for each cryopump, and ii) the turbo-Brayton cycle cryocooler already in place for the oxygen liquefaction subsystem. Ultimately, the second option was chosen to minimize system complexity and mass and take advantage of synergies between subsystems. The same logic applies to the radiator used to reject heat to the Martian atmosphere; the cryopumps are tied into the existing oxygen liquefaction radiator. For this reason, the cryopumps are placed in close proximity to the cryocooler and radiator of the liquefaction subsystem when BAM is deployed. A neon gas working fluid provides the cooling lift required to maintain the cryopump cold heads at their required temperatures. More details on the turbo-Brayton cycle can be found in Section 4.5.

Heaters
Cartridge heaters are used to warm the cryochamber and release CO_2 after it is collected on the cold heads. Cartridge heaters are small, reliable electrical resistors used in many industries and are inserted into slots in the base of the cold head. When the CO_2 acquisition period is complete and the system is ready for CO_2 discharge, the cartridge heaters are electrically activated and used to sublimate the CO_2.

Heat Exchanger
Each cryopump has a partner cryopump with which it operates out-of-phase. As the first cryopump in the pair cools down and collects CO_2, the second warms up and sublimates CO_2. A heat exchanger plate is placed between each pair of cryocoolers to exchange heat and save power. Residual heat from the hot cold head and chamber in the first cryopump are shared with the frozen CO_2 in the second cryopump. Additional cooling is then provided to the cryopump that is in its collection phase by the cryocooler, and extra heating is provided to the cryopump that is in its discharge phase by cartridge heaters. By operating out-of-phase, each pair of cryopumps can essentially create a continuous discharge of CO_2 for the downstream systems.

Piping and Valving
Piping connects the various components of the cryopump. Large diameter pipes are used to connect the blower with the freezing chamber. This is necessary to minimize pressure drops across the pipe, as too small of a pipe will result in unmanageable pressure drops that cannot be overcome by the blower. Because of the relatively higher mass of the large diameter pipes, the blowers are placed close in proximity to the freezing chambers to minimize pipe length. Smaller diameter pipes can be used on the freezing chamber discharge port, as the discharged CO_2 has a significantly higher pressure after sublimation and thus can be pressure-driven down the pipe towards the SOE unit.

Valves are necessary to control the fluid flow in the system. Electrically activated solenoid valves are used to open and close pathways in the pipes leading to and from the chamber. Check valves are also used to prevent backflow from units operating in parallel. A dual plate check valve design provides a passive solution with significantly lower mass than other check valve options that are traditionally bulky.

Together, these components describe the cryopump system. The Concept of Operations (ConOps) for the cryopump is described in the following section.

ConOps
To produce a continuous flow of CO_2 to the downstream SOE unit, specific steps are followed by the cryopump subsystem. Several cryopump units operate in parallel, each with a partner cryopump with which it operates out of phase. Figure 63 depicts the ConOps for this system.

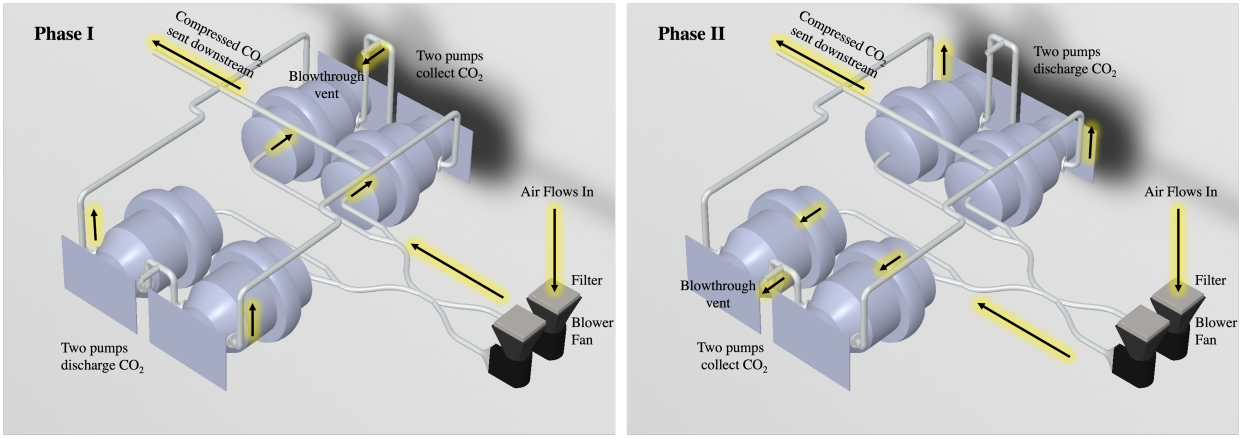

Figure 63: Concept of operations for the BAM cryopump. Martian atmospheric is pulled into the system through a filter and blower fan. In Phase I (left), the pair of cryopumps on the right side of the system collect CO_2 from the Martian atmosphere on their coldheads. Inert constituents of the Martian atmosphere pass through the pump and are vented. At the same time, the pair of cryopumps on the left side of the system discharge CO_2 downstream that was previously collected. In Phase II (right), the two pairs of cryopumps reverse their cycle [128].

Each cryopump has two distinct phases in its cycle: the cooling and freezing phase and the warming phase. The cycle for a cryopump begins with its cooling and freezing phase. First, the cryopump cools the cold head to sub-150 K. When this temperature range is achieved, a valve is opened on the freezer chamber inlet line and the blower is turned on. Martian atmosphere passes through the blower, travels down the inlet pipe and into the cryopump chamber, flows over the cold head, and freezes. Any non-CO_2 gases or CO_2 that did not freeze will pass by the cold head and out of the blow-through vent. This freezing process occurs for a set period of time, after which a sufficient quantity of CO_2 has deposited onto the cold head.

At this point, the cryopump begins its warming phase. Valves on the inlet and exhaust lines are closed to isolate the chamber. The cryopump cooling line is also redirected using valves to remove active cooling from the system during this phase. The cartridge heaters are then electrically activated and begin heating the cold head. As heating continues, the CO_2 sublimates and builds pressure inside the freezing chamber. When all the CO_2 has sublimated and the chamber has reached the desired pressure, a valve on the exit line is opened and a mass flow controller controls the exit flow rate of the CO_2 downstream. The CO_2 travels towards the heat exchanger and SOE system to be electrolyzed. When the CO_2 flow rate or pressure can no longer be sustained, the heaters are turned off, the exit line valve is closed, and the process repeats itself.

Cycle Time

At any given time, half of the cryopumps are discharging and the other half are charging. This simplifying assumption dictates that the combined cool-down time and freezing time must equal the discharge time. As a result, the cycles of the two cryopumps in each pair are out of phase but the same in duration, and thus when one cryopump is warming (discharging CO_2), the other is cooling down.

During the freezing phase, the highest collection rate of CO_2 on the coldhead occurs at the beginning of each collection period as demonstrated by Berg and Shah at NASA [131]. The observed CO_2 collection rates over time of three coldhead geometries are shown in Figure 64.

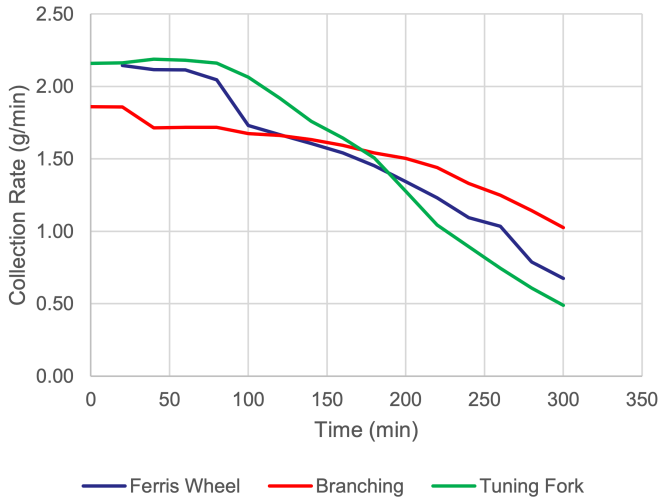

Figure 64: Collection rate of CO_2 in a cryopump over one collection period for three different coldhead designs [131]

These curves indicate that the collection rate peaks at the beginning of the collection cycle and decreases over time as accretion of solid CO_2 insulates the coldhead. This drives the ConOps towards a short cycle time to take advantage of the higher collection rates. A cooldown period is required to bring the coldhead to the proper temperature. During this period, no CO_2 is collected or discharged. This drives the ConOps towards a longer cycle time to minimize the percent of a cycle spent in this no-production period. As a result of these competing directions, there exists an optimal cycle time that balances the higher collection rates at the beginning of the cycle with the desire to minimize the impact of the cooldown period. This tradeoff is depicted in Figure 65.

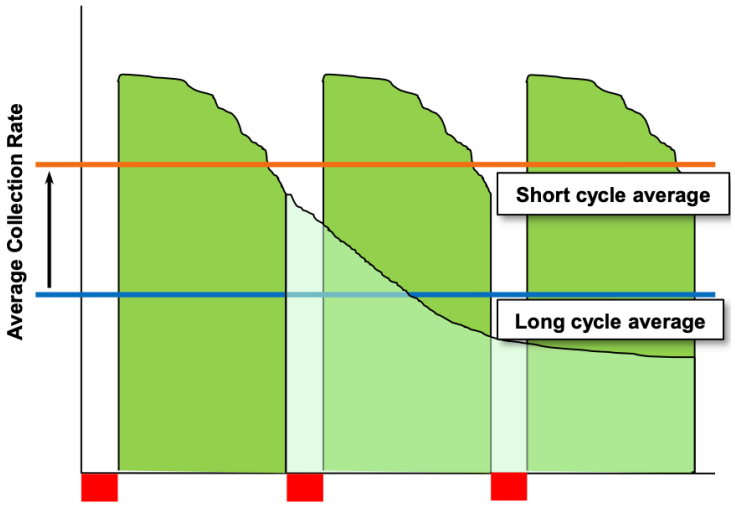

Figure 65: CO_2 collection rates on a coldhead as a function of time. Long cycle times result in a decreased average collection rate, while short cycle times increase the percentage of 'no-production' time required to cool the coldhead prior to each cycle [131].

The optimized cycle time is dependent on the number of parallel cryopumps, the inlet flow rate, the geometry of the coldhead, the relative geometry of the coldhead and cryochamber walls, and the flow path of gas through the cryochamber. A computational model could be developed to

predict an optimal cycle time if all these variables were known; however, laboratory testing would be needed to validate the model's design. For this dissertation, the experimental work conducted by Berg and Shah is instead used to set the optimized cycle time of the cryopumps. Their optimized cycle time for the Tuning Fork coldhead configuration is shown in Figure 66.

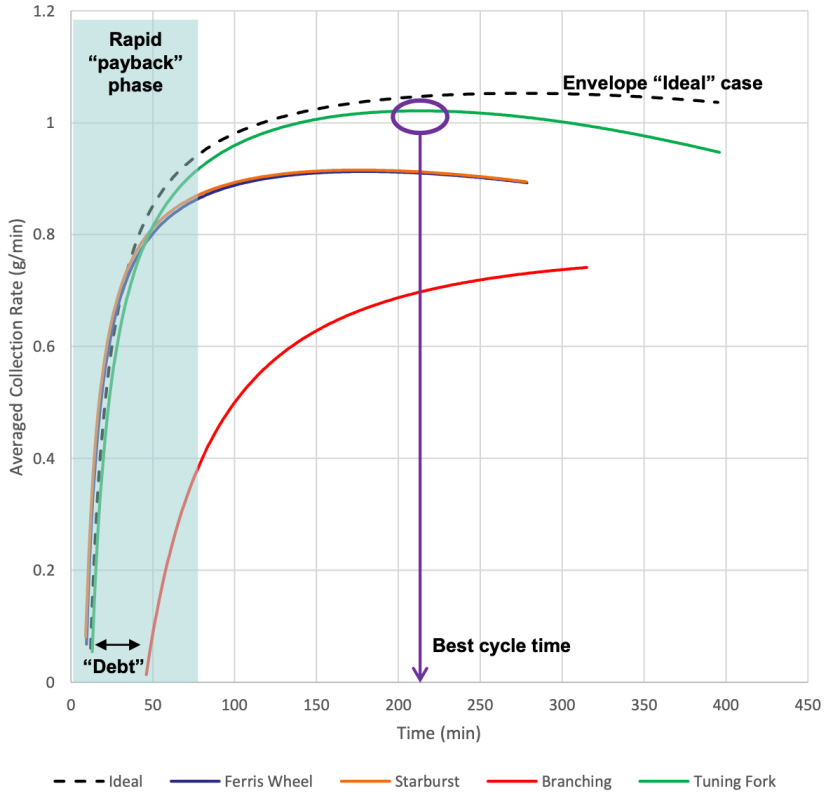

Figure 66: Optimized cycle time to maximize cycle-over-cycle collection rate of CO_2 coldhead in a cryopump. The Tuning Fork coldhead geometry represents the highest performing coldhead design tested [131].

This optimized cycle time results in a 17-minute cooldown period followed by a 100-minute CO_2 freezing period and ending with a 100-minute warming period to discharge the CO_2. The total optimized cycle time is 217 minutes, approximately 3.5 hours.

Sizing and Redundancy

The optimizer will change the number of cryopumps in the system to determine the optimal number that minimizes power, mass, volume, and risk. A lower number of cryopumps results in a lower total mass, as a few larger units are more mass-efficient than many smaller units. Less cryopumps also results in a lower total power as a result of minimizing heat leaks with increased volume to surface area ratios in the chambers, and higher risk from a lack of redundancy and an increase in cold head size. The cold head is fragile and is increasingly susceptible to mechanical failure during launch loads as its size increases.

A single radiator is shared between all parallel cryopumps and the liquefaction subsystem. This simplifies the design and reduces the mass and volume of BAM. The radiator is sized to achieve the cooling load required of all cryopumps that are capturing CO_2 at a given time as well as the O_2 cooling requirements. As an example, if the optimal design of BAM has four cryopumps, two

of which are capturing CO_2 at any given time while the other two are discharging CO_2, the radiator would be sized for the cooling load of two cryopumps.

The number of cryopumps is determined by the optimizer based on the required oxygen production rate and a tradeoff between mass and risk. Redundant cryopumps reduce risk; if one cryopump fails, a spare can be brought online as a replacement.

Modeling

With the design complete, the cryopump is modeled to calculate the objectives as functions of the design variables.

Power

The power required to cool the incoming Martian atmosphere and freeze the CO_2 onto the cold head is calculated as:

$$P_{cooling} = \frac{Q_{cool} + Q_{deposition}}{\eta_{cc}} \tag{33}$$

where Q_{cool} is the power required to cool the Martian atmosphere from its incoming temperature to the freezing point of CO_2, $Q_{deposition}$ is the power required to phase change the CO_2 from a gas to a solid at its freezing point, and η_{cc} is the efficiency of the cryocooler. Note that Q_{cool} and $Q_{deposition}$ are multiplied by the fraction of each cryocooler batch cycle that involves cooling. Approximately 50% of the total cycle time involves the cooling phase, and the power calculations are adjusted accordingly. The same is true for the heating calculations below.

When the cooling and freezing cycle has completed, the cryopump is warmed by cartridge heaters to sublimate and increase the temperature of the CO_2 before it is released downstream towards the SOE. The power required to sublimate and warm CO_2 is calculated as:

$$P_{warming} = \frac{Q_{sublimation} + Q_{heat}}{\eta_{heaters} * \eta_{heatloss}} \tag{34}$$

where $Q_{sublimation}$ is the power required to change the CO_2 from a solid to a gas, Q_{heat} is the heat required to warm the CO_2 gas to its exit temperature, $\eta_{heaters}$ is the electrical-to-thermal conversion efficiency of the cartridge heaters, and $\eta_{heatloss}$ is an efficiency factor to account for parasitic heat losses from the chamber. In practice, this power could be reduced in several ways, including using supplemental heat from the SOE exhaust, using the Martian atmosphere to warm the system, and running heat exchangers between parallel cryopumps. For this design, only the third option was implemented; each cryopump has a "partner" that it exchanges heat with. As one cools, the other warms, and thus a percentage of cooling and heating power is saved with the heat exchanger. 50% of heating and cooling is assumed to be recovered in this heat exchanger. Notably, this does not include the latent heat of sublimation, which accounts for the majority of cooling power consumption.

The overall power required to operate the cryopump subsystem is given by:

$$P_{cryopumps} = \eta_{HE}(P_{cooling} + P_{warming}) + P_{blower} + P_{wf} + P_v \quad (35)$$

Where η_{HE} is a factor between 0 and 1 that represents a percentage of heat savings from the heat exchanger placed between each pair of cryopumps, P_{blower} is the power consumed by the blower fan to move gas through the freezing chamber, P_{wf} is the power used by the pump that circulates the cryocooler's working fluid through the system, and P_v is the power consumed by the electrically-activated solenoid valves that control flow in the system.

Mass

The mass of the cryopump system is estimated by adding the mass of individual components and multiplying by the number of cryopumps. The major components that contribute to the mass of the cryopump are the blower, cold head, cryochamber shell, cartridge heaters, valves, and piping. Typically, the cryocooler and the radiator would also constitute major mass additions; however, in this case, those masses are calculated in the liquefaction subsystem as these components are shared between the two subsystems. The liquefaction subsystem's cryocooler and radiator are scaled by taking the cryopump power requirements into account.

The cold head, cryochamber shell, and heater masses are calculated using a scaling law to extrapolate the masses of these components in the system built by Meier et al. in 2018. The scaling law is written as follows for each component:

$$M_{comp} = M_{comp,Meier}\left(\frac{\dot{m}_{cp}}{\dot{m}_{Meier}}\right)^s \quad (36)$$

where $M_{comp,Meier}$ is the mass of that component in Meier et al.'s study, $\dot{m}_{Meier}$ is the flow rate of CO_2 produced by the cryopump in their study, $\dot{m}_{cp}$ is the flow rate of CO_2 produced by each cryopump in the current design, and s is an exponential term between 0 and 1 that represents a mass scaling factor.

The masses of the primary blower fan and its spare are calculated based on commercial blowers on Earth. The mass of the valves and piping are estimated based on the number of cryopumps. Each cryopump contains three solenoid valves: one on the inlet to the freezing chamber, one on the exhaust line, and one on the outlet to the freezing chamber. This ensures that the freezing chamber can be appropriately isolated during its heating phase. Latching solenoid valves are used to greatly reduce energy consumption compared to regular solenoid valves, which require a constant power source to remain open. A check valve is also used on the outlet lines for each cryopump to prevent backflow into the chamber from other cryopump outlet lines. Marotta Controls' space-qualified solenoid and check valves were referenced for mass and power numbers [132].

Future Work

Additional research could be conducted to refine and optimize the cryopump assumptions made in this section. Several questions remain unanswered:

1. What is the optimal thickness of frozen CO_2 on the cryopump's coldhead to maximize acquisition and power efficiency?
2. How does increasing the size of a coldhead affect its performance if the geometry is kept consistent?
3. What is the optimal way to capture inerts from the Martian atmosphere using a cryopump, and is it worthwhile?
4. Can a self-cleaning or self-scaping coldhead be designed to remove CO_2 frost into a secondary chamber, thus creating a more continuous and efficient system?

There are plans at NASA to continue studying these designs to improve coldhead performance, and those findings should be used to update this work in the future.

4.3.2 Mechanical Compressor

As described in Section 2.5.4, mechanical compressors are the second category of CO_2 acquisition and compression considered for Mars. Many types of mechanical compressors exist that could be applicable to a Mars mission, and these will be described below.

Comparison of Mechanical Compressor Types

Mechanical compressors are identifiable as either positive displacement or dynamic compressors. A hierarchy of these compressors is shown in Figure 67.

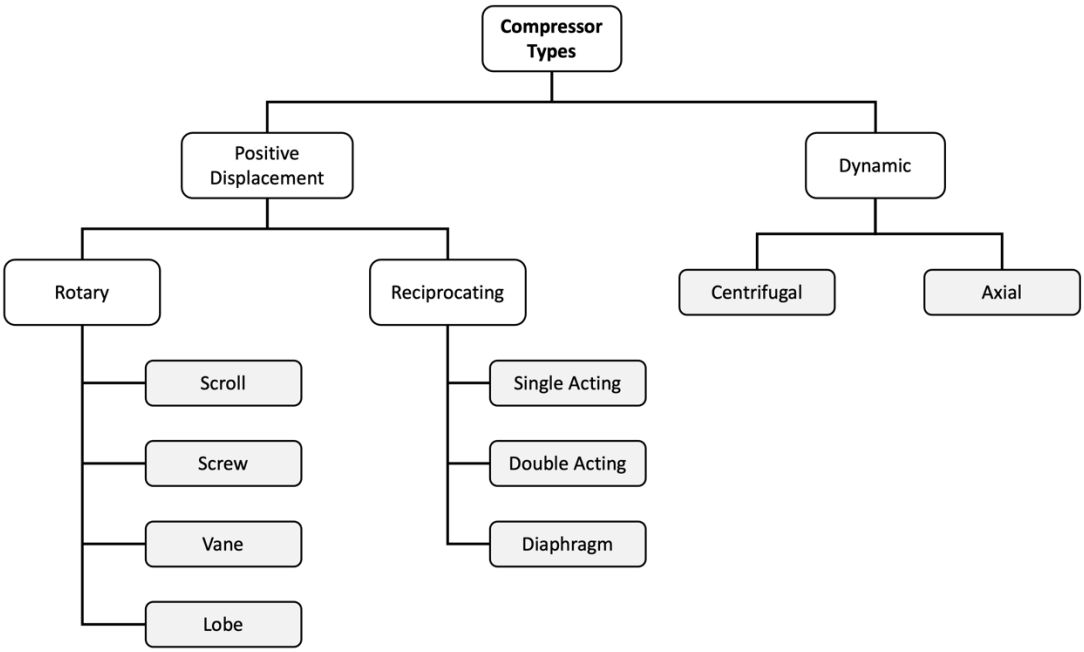

Figure 67: Hierarchy of mechanical compressor types. White boxes indicate a categorization, while gray boxes indicate a specific type of compressor.

Positive displacement (PD) compressors mechanically reduce the volume of a gas to increase its pressure. Dynamic compressors use rotating impellers to add energy to a gas, which is converted to pressure. In general, PD compressors are used for small volumes of gas and large pressure ratios, while dynamic compressors are used for large volumes of gas and small pressure ratios.

The BAM system lies in the middle of this design space, so both categories of compressors are considered viable options.

Positive Displacement (PD) Compressors

PD compressors can be split into two categories: rotary and reciprocating. Rotary compressors use a rotational motion to trap and compress gas, while reciprocating compressors rely on a piston. Seven types of PD compressors across both of these categories will be explored below and can be referenced in Figure 67.

Scroll Compressor

A scroll compressor uses two interlocked and extruded spirals to force gas from a larger volume at the outer radius to a smaller volume at the inner radius. MOXIE uses a scroll compressor, which was briefly described in Section 1.2.2. An image of a scroll compressor is shown in Figure 68.

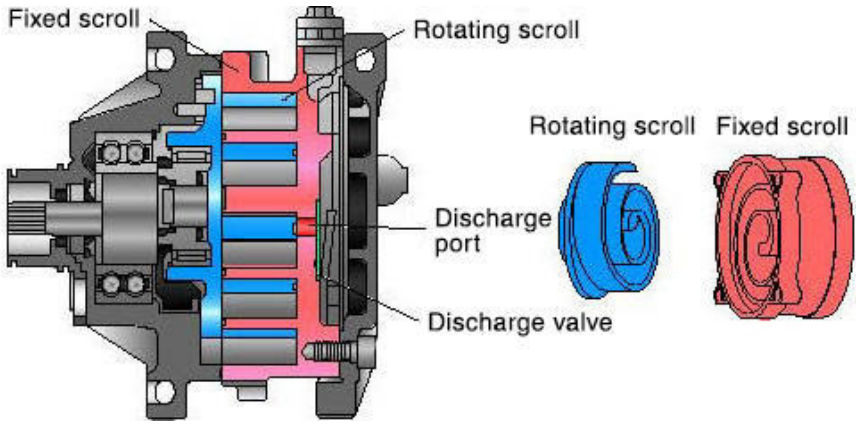

Figure 68: Scroll compressor cutaway showing the interlocking rotating and fixed scrolls (credit: Toyota Industries)

Scroll compressors offer a range of advantages and disadvantages with regards to compressing the Martian atmosphere for the BAM design. These are listed in Table 28.

Table 28: Advantages and disadvantages of scroll compressors

Advantages	Disadvantages
High adiabatic efficiency	Wear on seals could result in leak
Continuous flow	Poor volumetric efficiency at off-nominal pressures
Low vibration	Non-continuous flow
Simple design (few moving parts)	
Low mass	
Compact design	
Low maintenance requirements	
Demonstrated performance on Mars	

Scroll compressors typically have a relatively high adiabatic efficiency. Unlike reciprocating compressors, they provide continuous flow and have low vibration. They also have minimal moving parts, which may increase their reliability by decreasing the likelihood for component

failure. The compact nature of scroll compressors leads to a low mass and low volume system. Finally, as discussed, scroll compressors have Martian heritage on MOXIE, albeit at a smaller throughput than what will be required on a system the size of BAM.

An important disadvantage of scroll compressors is the potential for tip seal wear that could eventually lead to a leak. If a scroll pump were to experience significant tip seal wear, it could result in a mission-ending scenario by not being able to move the required quantity of gas into the system. Additionally, the MOXIE compressor experienced a poor overall efficiency owing to its design of compressing the gas primarily by forcing it into a plenum at the outlet of the scrolls. This can ultimately be negated by staging scroll compressors in series to achieve the desired compression ratio in the scrolls themselves. A final disadvantage common to many PD compressors is non-continuous flow, which is seen in scroll compressors from discrete packets of gas being discharged with each rotation of the scroll.

Screw Compressor

A screw compressor uses two interlocked, rotating, helical screws to force gas from a larger volume at the inlet to a smaller volume at the outlet. Screw compressors are common in industry and have a variety of designs. An image of a screw compressor is shown in Figure 69.

Figure 69: Screw compressor cutaway showing the interlocking screws used to compress fluid (credit: Ingersoll Rand)

Screw compressors typically rely on oil to prevent leakage and reduce wear between the screws. A lubricant-free compressor is an important design criterion, as lubricant can poison the SOE downstream. Continuous flow and large pressure ratios are possible with screw compressors, but with a lower efficiency than other compressor types in consideration.

Vane Compressor

A vane compressor uses an off-center rotating element with radial vanes designed to extend to the edge of the chamber during all points in its rotation. A fluid flows into the chamber and is forced through the pump by the rotating vanes. The available space for the fluid to occupy decreases as the fluid rotates around the chamber, compressing the fluid. An image depicting the operating principle of a vane compressor is shown in Figure 70.

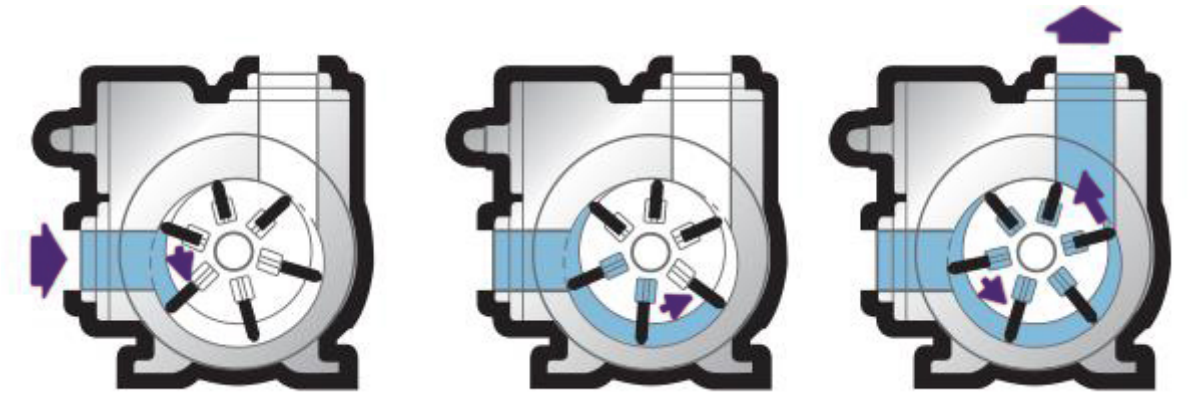

Figure 70: Vane compressor operation showing the progression of fluid through the pump. As the fluid moves around the chamber, it is forced into a smaller volume, which results in compression (credit: North Ridge Pumps)

Similar to a screw compressor, rotary vane compressors often use a pool of oil inside the compressor chamber to prevent leakage.

Lobe Pump

A lobe pump uses two counter-rotating lobes to drive fluid downstream. Unlike the other forms of rotary compressors that gradually reduce the volume of the fluid to compress it, the lobe pump continually forces fluid into the same, fixed volume, which results in an increase in pressure. An image depicting the operating principle of a lobe pump is shown in Figure 71.

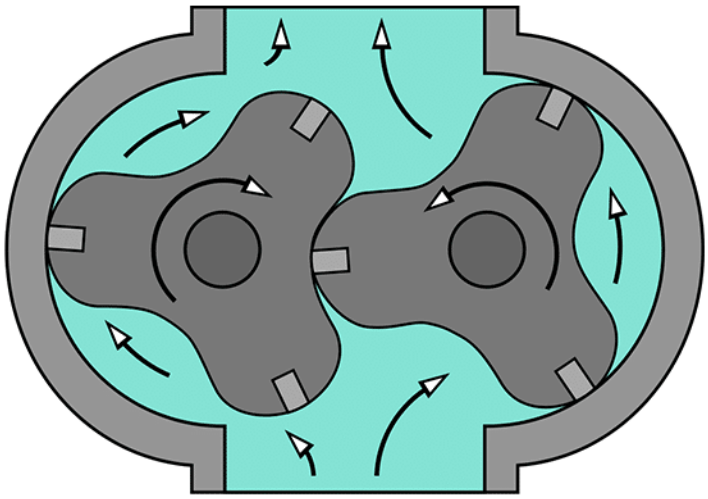

Figure 71: Lobe pump operation showing the counterrotation of two lobes that forces fluid downstream (credit: Air Compressor Works)

Lobe pumps have a simple design and are relatively efficient at low speeds but rely on seals with the casing and one another and generally require lubrication.

Screw compressors, vane compressors, and lobe pumps share many advantages and disadvantages. These shared characteristics are summarized in Table 29.

Table 29: Advantages and Disadvantages of screw, vane, and lobe compressors

Advantages	Disadvantages
Simple design (few moving parts)	Typically require lubricant to maintain seals
Lightweight	Not resistant to fouling
Continuous flow	Single stage designs have low efficiency

Reciprocating Compressor

A reciprocating compressor differs from the four rotary compressors previously described in that it uses a piston rather than a rotary motion to compress gas. Multiple pistons and cylinders are often used to increase the quantity of gas being compressed. These pistons can be driven by a single motor. An image of a reciprocating compressor is shown in Figure 72.

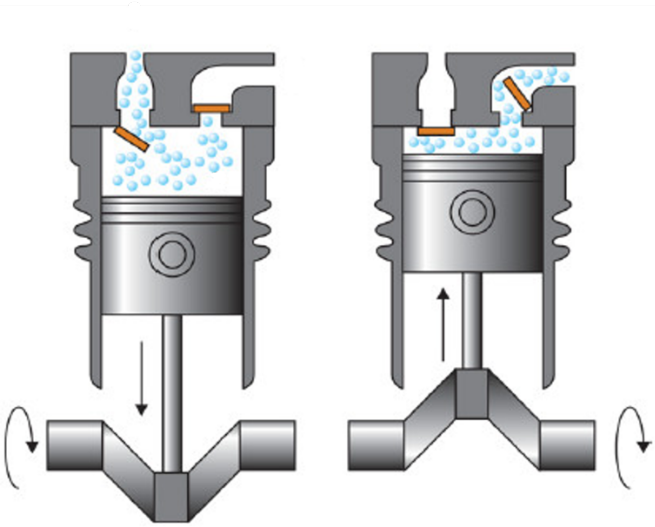

Figure 72: Single-acting reciprocating compressor working principle: a piston is pushed into a cylinder to compress a volume of gas (credit: Piping Engineering)

Reciprocating compressors can be single-acting or double-acting. A single-acting reciprocating compressor, like a simple syringe or the compressor shown in Figure 72, only engages the fluid being compressed on one side of the piston. A double-acting reciprocating compressor engages the fluid on both sides of the piston: one side always compresses the fluid with each stroke.

The advantages and disadvantages of reciprocating compressors with regards to compressing the Martian atmosphere are listed in Table 30.

Table 30: Advantages and disadvantages of reciprocating compressors

Advantages	Disadvantages
High adiabatic efficiency (70-90%)	Heavy
Sized to the mission flow rates	Seal wear if not using lubricant
Wide pressure ratios at low flow rates	Flow is not continuous
	Vibration

The primary advantage of reciprocating compressors is their relatively high adiabatic efficiency. It is also straightforward to size these compressors to the required flow rate and pressure ratio of the mission. This is particularly useful on systems like BAM, where a low flow rate but large pressure ratio is needed. This advantage becomes less impactful on a full-scale system where higher flow rates are required. Reciprocating compressors are heavy due to the mounting required to manage the vibrations from force imbalances associated with the piston motion. In addition, the piston seals may wear down over time if not lubricated. The pulsating nature of these compressors leads to a noncontinuous flow, which must be accounted for with a buffer plenum or flow controller downstream. Finally, the volumetric efficiency of reciprocating compressors is not as high as other compressor options, as a portion of the gas will remain in the piston after each discharge cycle owing to the impracticality of the piston head contacting the end of the cylinder.

Reciprocating compressors require cooling in multi-stage arrangements. Typically, these compressors can achieve a compression ratio of up to 3 per stage, which is limited by material temperature limits [133].

Diaphragm Compressor

A diaphragm compressor operates under the same principle as a reciprocating compressor, but the piston pushes against a flexible diaphragm rather than the end of the cylinder. These were not considered for the design of BAM owing to the difficulty in selecting a diaphragm material capable of withstanding the temperature and pressure ranges expected on Mars.

Dynamic Compressors

Dynamic compressors can be categorized as either centrifugal or axial. These will both be described below.

Centrifugal Compressor

A centrifugal compressor consists of a rotating impeller that imparts velocity to a gas and a diffuser that converts the kinetic energy of the gas to an increase in gas pressure. Larger pressure ratios can be achieved in centrifugal compressors by increasing the diameter of the impeller, increasing the speed of the impeller, or increasing the molecular weight of the fluid. The first two impart additional energy to the gas and are important design considerations. The third is a constant for BAM and thus is not considered as a design decision. Images of the impeller and a full centrifugal compressor system are shown in Figure 73.

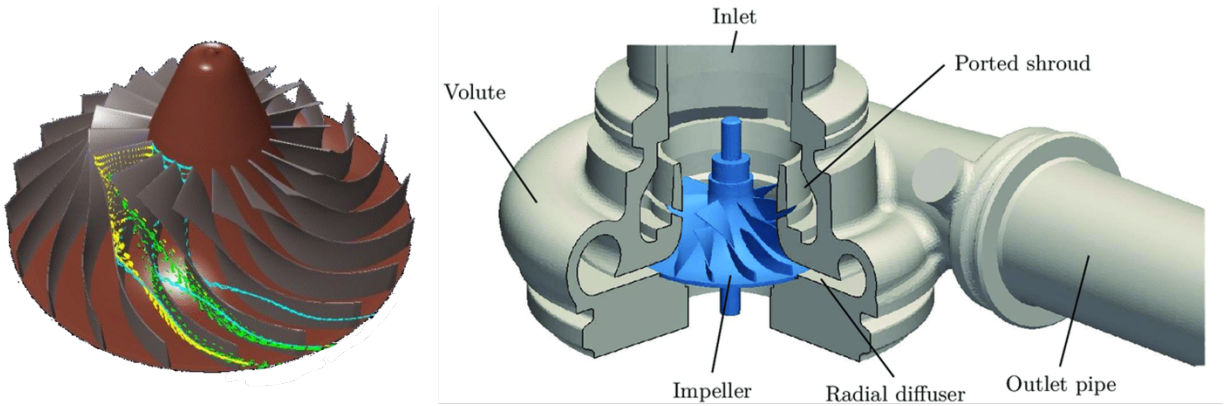

(a) Impeller (b) Centrifugal Compressor

Figure 73: (a) Impeller used to impart additional velocity to the fluid and (b) full centrifugal compressor cutaway view [134]

Centrifugal compressors are often staged to incorporate multiple impellers and thus achieve a greater pressure ratio. An example of a multistage centrifugal compressor is shown in Figure 74.

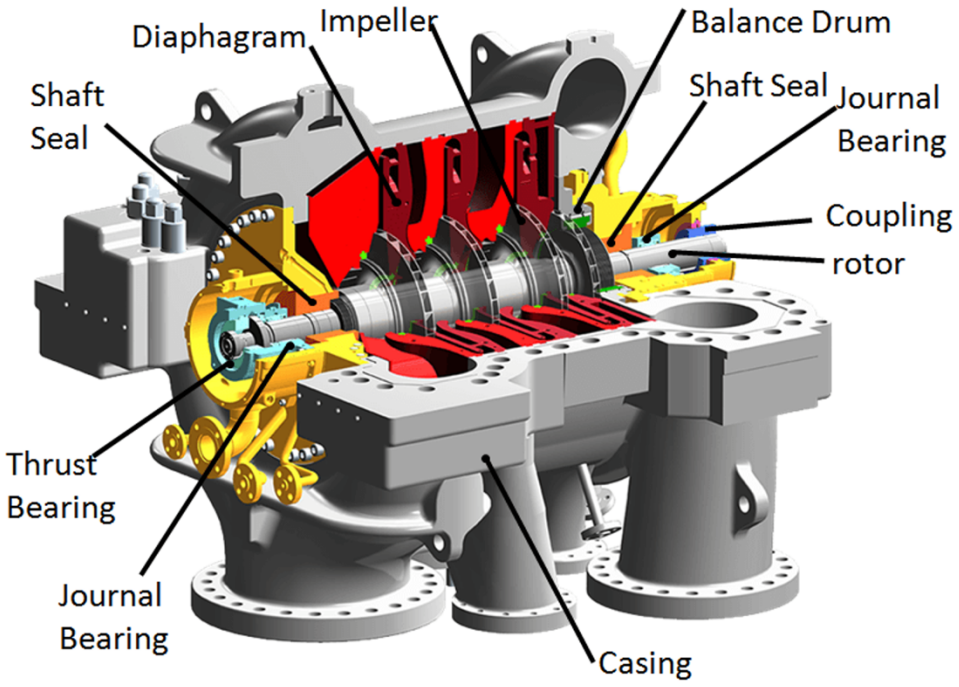

Figure 74: Multistage centrifugal compressor (credit:ThePipingTalk)

Centrifugal compressor blades must not come into contact with the outer casing of the housing. As a result, a certain amount of slippage is unavoidable, which leads to a decrease in volumetric efficiency. To minimize this efficiency loss, higher flow rates are typically employed in centrifugal compressors. BAM lies on the lowest end of practical centrifugal compressor use, though a system to support a larger human settlement on Mars would fall well within the typical centrifugal compressor operating range.

The advantages and disadvantages of a centrifugal compressor are listed in Table 31.

Table 31: Advantages and disadvantages of a centrifugal compressor

Advantages	Disadvantages
High adiabatic efficiency (85%) under certain conditions	Low efficiency at low flow rates
Lubrication-free operation	Complex
Very low maintenance; long lifetime	Limited pressure ratio without staging
Seal-free operation	

Centrifugal compressors typically experience high adiabatic efficiency; however, this efficiency decreases as flow rate decreases, which may be a concern for a system sized for BAM. These compressors operate without lubricant, have been demonstrated to have long lifetimes with low maintenance, and do not rely on seals. These are all important advantages for a remotely operated and non-serviceable system like BAM. Centrifugal compressors have complex components and a limited pressure ratio unless staged. These disadvantages are mitigated by the previous demonstrations of long lifetimes and the design decision to stage to achieve the proper pressure ratio, respectively. Therefore, the primary concern for a centrifugal compressor used in BAM is the efficiency at the relatively low flow rates of the BAM system.

Axial Compressor

An axial compressor consists of a series of rotor blades and stator blades. The rotor blades increase the energy level of the gas, and the stator blades convert that energy to pressure. Axial compressors are used in jet engines, ship engines, and many industrial applications. They are not considered a viable option for BAM, however, because they require too high a flow rate to operate efficiently. The flow rate range for BAM and the compressors considered for it will be described in the following section.

Operating Envelope

Each type of compressor previously discussed is designed to function within a certain operating envelope. This envelope is defined by the pressure ratio and flow rate that the compressor is designed to manage. Figure 75 depicts the typical operating envelopes for different types of compressors.

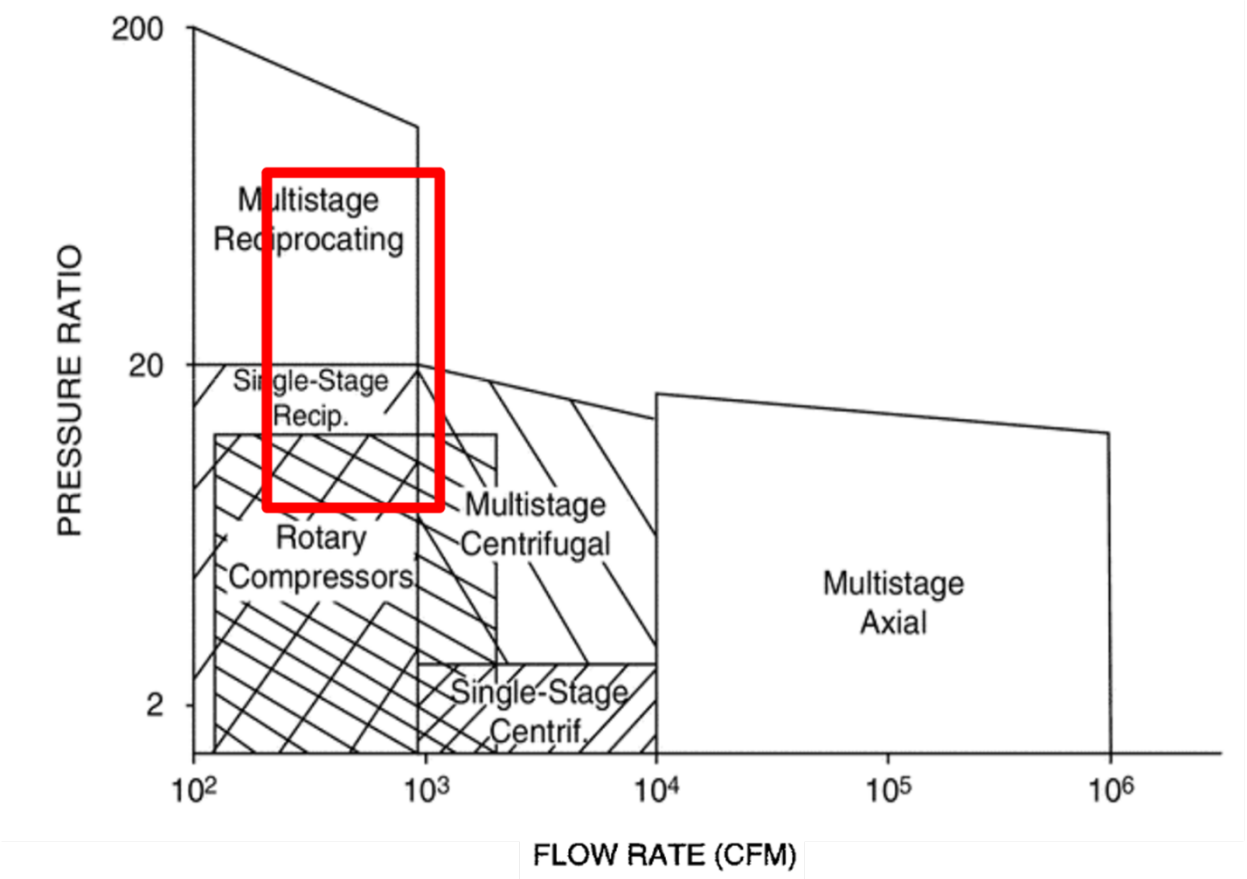

Figure 75: Typical operating envelopes of several types of mechanical compressors, with respect to pressure ratio and flow rate [135]. The expected operating envelope for BAM is highlighted in red [136].

The operating envelope that is expected for BAM is highlighted in red. This represents a pressure ratio in the range of approximately 5 to 50 and a flow rate in the range of 250 CFM to 1100 CFM, which corresponds to approximately 8 kg/hr to 35 kg/hr. Both pressure ratio and flow rate are given as ranges because they are design variables that are controlled and adjusted by the optimizer.

According to the figure, multistage axial compressors and single-stage centrifugal compressors do not overlap the possible operating envelope of BAM, which is why they are not considered as viable compressor options. Those that do overlap the possible operating envelope include reciprocating compressors, multistage centrifugal compressors, and rotary compressors (scroll, screw, vane, and lobe).

With the operating envelope and advantages and disadvantages of each type of compressor known, it is possible to select the best compressor options and design and model them. This will be discussed in the following sections.

Design

To further down-select from the available compressor types, a multi-attribute utility analysis (MAUA) was conducted on the four most relevant compressor options to rank them against a set of criteria relevant to BAM. The MAUA is shown in Table 32.

Table 32: Multi-attribute utility analysis (MAUA) for the four compressor options most likely to fit the BAM architecture [136]

Criteria	Scroll		Dry Screw		Reciprocating		Direct Drive Centrifugal		Weight
Risk	4	Tip seal concern, but minimal moving parts	2.5	More prone to failures without lubrication	2	Seals degrade, force imbalance, high vibrations	4.5	Robust, long lifetime, no seals	4
Power	4	Moderate to high efficiency	2.5	Low adiabatic efficiency, prone to slippage without lubrication	4	High efficiency, small volumetric losses	3	Typically, high efficiency, but low at low flow rates	4
Mass/ Volume	4	Compact, lightweight	3	Relatively compact	1.5	Heavy, large frame	4	Very lightweight, modest volume	2
TRL	3	Martian heritage, never built at scale	4	Significant use in industry	5	Well understood technology	3	Significant use, but minimal at this small a scale	1
Mars/ BAM Fit	4	Tolerant of varying inlet conditions, sensitive to dust	4	Tolerant of varying inlet conditions, sensitive to dust	4	Tolerant of varying inlet conditions	4.5	Tolerant of varying inlet conditions, less sensitive to dust	4
Total	**59**		**46**		**48**		**59**		

The criteria against which the compressors were compared include risk (as a function of reliability), power (as a function of efficiency), mass/volume, TRL, and Mars/BAM fit (ability to manage Mars atmospheric conditions and suitability to the pressure ratio and flow rate expected of BAM). The best score a compressor could receive was a 5 for each criterion, and the worst score a 1. The final column of Table 32 is a weighting factor, with 4 being the highest weighting and 1 being the lowest. Power, Risk, and Mars/BAM Fit are all weighted the highest because each of those three criteria is mission critical. Mass and volume are less of a concern, as the compressor is not expected to constitute a significant percentage of the overall BAM mass. TRL is given the lowest weighting, as no mechanical compressor has a high TRL for this particular application, and significant research and development work would need to be conducted regardless of the selected compressor type.

The MAUA resulted in a tie for the best compressor between a scroll compressor and centrifugal compressor with 59 points. The reciprocating compressor, which suffers from high risk and high mass, was third place with 48 points. The dry rotary screw placed last with 46 points, owing to its high risk and low efficiency in the absence of lubricant.

Based on the results of the MAUA, two types of mechanical compressors were modeled for use in the BAM system: scroll and centrifugal. The scroll compressor is compact, reliable, and broadly representative of all rotary compressors. The centrifugal compressor is a dynamic compressor type with high efficiency.

Scroll Compressor

The design of the scroll compressor follows the scaled-up compressor work conducted by Air Squared of Broomfield, Colorado, the company that built the scroll compressor for MOXIE and has been conducting follow-on tests of larger scale units [137]. Two cutaway renderings of a scroll compressor sized for BAM and designed independently of Air Squared are shown in Figure 76.

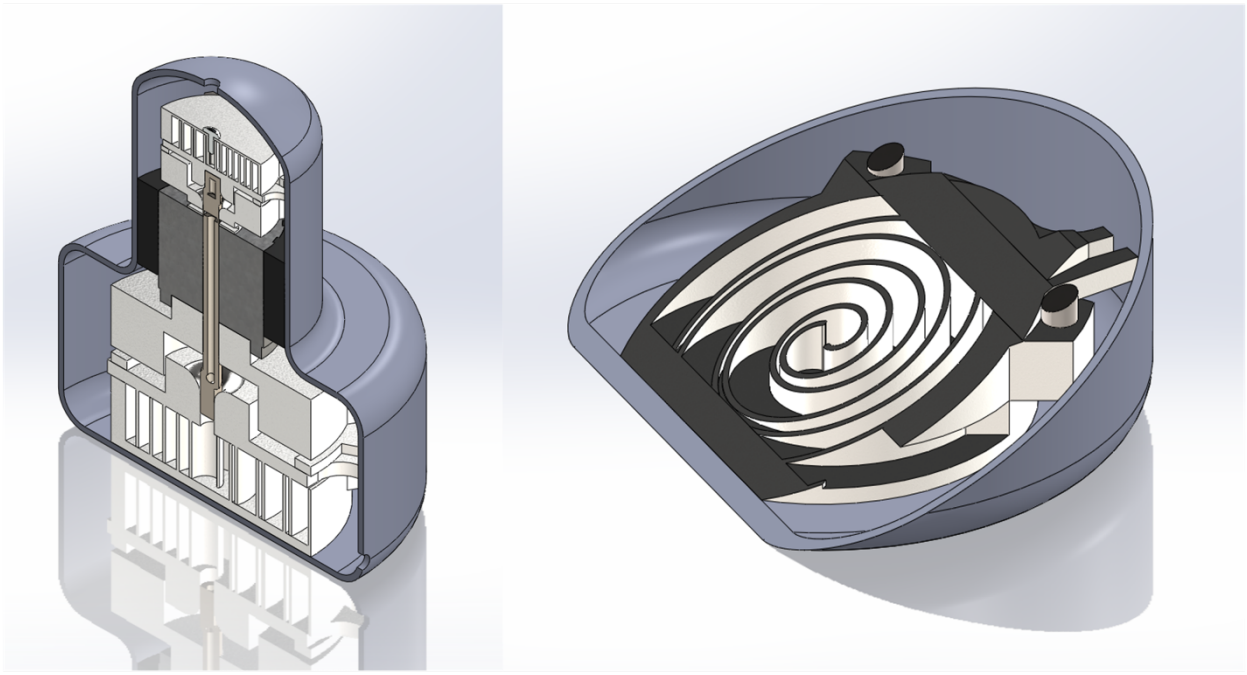

Figure 76: Cutaways of scroll pump designed for BAM [128]

Several scroll compressors would likely be arranged in a parallel configuration to provide redundancy. An assumption is that the scroll compressor will be designed to provide the full compression ratio required. Depending on the value of the output pressure of the compressor, which is a design variable in this optimization problem, two compressors may be required in series to achieve the full compression ratio. An example arrangement of four scroll compressors in parallel is shown in Figure 77.

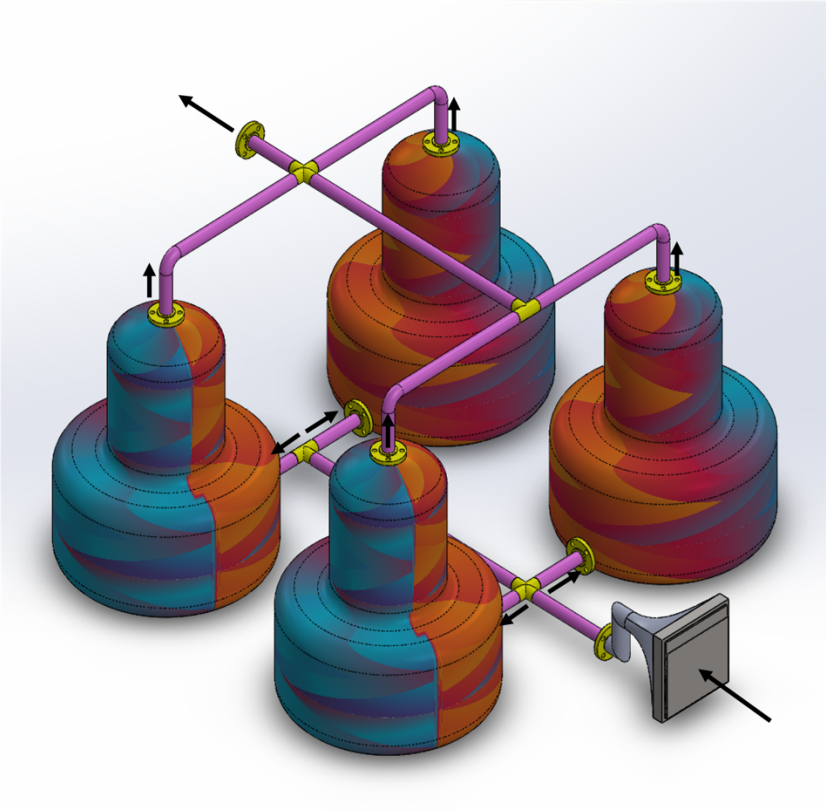

Figure 77: Example arrangement of four scroll compressors operating in parallel with a filter to prevent dust from entering the system. Gas flow direction is indicated with arrows [128].

A filter is placed at the inlet to prevent dust from entering the system. The outlet line directs compressed gas downstream towards the heat exchanger.

Centrifugal Compressor

The centrifugal compressor will be a scaled-down version of existing multistage centrifugal compressors, as it will operate at the low end of the compressor's range. A variable speed drive is required to counteract the effects of Martian atmospheric variations and provide a continuous flow rate to the downstream systems. Magnetic bearings are used to remove frictional contact and improve longevity. Additionally, cooling between stages may be necessary to avoid material failures at high temperatures. This is dependent on the design variables, which change with each simulation.

Ingersoll Rand Nash, an industry expert in centrifugal compression, ran a series of simulations to better understand how a compressor for BAM might perform under Mars conditions [139]. They recommended a five-stage centrifugal compressor for the operating conditions expected in BAM: a compression ratio of approximately 30 and flow rates between 10 and 20 kg/hr. To increase the compression ratio to a factor of 100, the team recommended a seven-stage compressor. Each stage is driven with an independent high speed variable drive. High temperature was a notable concern in the design, as terrestrial centrifugal compressors are not generally designed to exceed 500 K, which is a possibility in the BAM design. As a result, the compressor is designed to be made of a high temperature composite, which will also decrease its mass compared to a terrestrial steel compressor. As an additional countermeasure, heat can be removed between each

stage, though this is less desirable as the gas will have to be heated to SOE temperatures farther downstream anyway.

A notable takeaway from the Nash analysis was that there is not a centrifugal compressor available commercially that has been built to operate at the low flow rates expected in BAM. The resulting compressor would be small and suffer from inefficiencies associated with low flow rates. As the scale of Martian operations increases over time and larger flow rates are needed, centrifugal compressors become more and more efficient. This is explored in more detail in the following section.

Next Generation

A final consideration on the design and selection of the compressor for BAM is the future of Mars exploration. If a settlement of people larger than a single-mission crew were to eventually exist on Mars, a significantly higher CAC flow rate may be required to provide an increased flow rate of oxygen. If the flow rate requirement increases significantly beyond that of the first-generation BAM, a centrifugal compressor becomes the clear choice for a mechanical compressor, as it offers a significantly higher efficiency at higher flow rates. For this future-case scenario, Table 32 has been updated to include higher flow rates. TRL was also removed as a criterion under the assumption that TRL 9 will have been achieved by any compressor that has been used on multiple missions prior to a larger human settlement on Mars. The MAUA for compressors for a long-term Mars settlement scenario is shown in Table 33.

Table 33: Multi-attribute utility analysis (MAUA) for the four compressor options most likely to fit a future Mars scenario with a larger number of people visiting and living on Mars

Criteria	Scroll		Dry Screw		Reciprocating		Direct Drive Centrifugal		Weight
Risk	4	Tip seal concern, but minimal moving parts	2.5	More prone to failures without lubrication	2	Seals degrade, force imbalance, high vibrations	4.5	Robust, long lifetime, no seals	3
Power	4	Moderate to high efficiency	2.5	Low adiabatic efficiency, prone to slippage without lubrication	4	High efficiency, small volumetric losses	5	High efficiency	4
Mass/ Volume	4	Compact, lightweight	3	Relatively compact	1.5	Heavy, large frame	4	Very lightweight, modest volume	2
Mars/ BAM Fit	4	Tolerant of varying inlet conditions, sensitive to dust	4	Tolerant of varying inlet conditions, sensitive to dust	4	Tolerant of varying inlet conditions	4.5	Tolerant of varying inlet conditions, less sensitive to dust	4
Total	**52**		**46**		**48**		**59.5**		

The modifications made to this table for a Mars settlement scenario include the assumption of a higher flow rate, which improved the efficiency score of the centrifugal compression, and a decrease in the weighting of risk as a criterion, as there will be people present to conduct maintenance on the compression system if needed. These modifications result in the centrifugal compressor as the clear winner.

Despite this forward-looking table, for the purposes of this dissertation, the original MAUA presented in Table 32 for a crew of four to six astronauts will be used.

Modeling

With the designs selected, the two types of mechanical compressors are modeled to calculate the objectives as functions of the design variables.

Power

The total power is calculated by calculating the adiabatic power of compression and dividing it by the adiabatic efficiency:

$$P = \frac{\frac{T_1 \dot{m}_{in} R}{MW}\left(\frac{\gamma}{\gamma - 1}\right)\left(\left(\frac{P_2}{P_1}\right)^{\frac{\gamma-1}{\gamma}} - 1\right)}{\eta_{ad}} \tag{37}$$

where T_1 is the inlet temperature, $\dot{m}_{in}$ is the inlet mass flow rate, R is the universal gas constant, MW is the molecular weight of the gas, γ is the ratio of specific heats, equal to $\frac{C_p}{C_v}$, P_2 is the outlet pressure of the compressor, P_1 is the inlet pressure to the compressor, and η_{ad} is the adiabatic efficiency of the compressor.

The adiabatic efficiency of a compressor is a function of inefficiencies of its components, including motor losses, seal friction, and bearing friction. The adiabatic efficiency is therefore dependent on the compressor type as well as the compression ratio and flow rate. A scroll compressor is expected to have an adiabatic efficiency of approximately 70% at the BAM conditions [138]. For a centrifugal compressor, adiabatic efficiencies near 90% are possible at higher flow rates. However, for the relatively low flow rates expected in BAM, industry experts expect an adiabatic efficiency between 50% and 60% [139]. This decrease in efficiency due to low flow rate is derived from the viscous effects of low Reynolds number flow and relatively large clearance gaps over the blades.

Temperature

The outlet temperature of the compressor is calculated, as it has important power implications for the SOE preheater as well as materials implications for the compressor. The outlet temperature, T_2, is calculated using an isentropic compression assumption as:

$$T_2 = T_1\left(\frac{P_2}{P_1}\right)^{\frac{\gamma-1}{\gamma}} \tag{38}$$

Mass and Volume – Scroll Compressor

The mass and volume of the scroll compressor are calculated using scaling laws applied to specifications of the scroll compressor built by Air Squared, Inc. [140]. The compressor they built and tested in recent years is sized to produce a mass flow rate of 2.7 kg/hr of CO_2. It has a mass of 28.2 kg and measures 0.343 m x 0.349 m x 0.350 m. Two equations were derived from these numbers to calculate mass and volume of larger systems, with an exponential scaling factor, k, included to account for the non-linear scaling of mass and volume. The scaling factors for all systems can be found embedded in Appendix D. The mass is calculated as:

$$M = M_{AS} * \left(\frac{\dot{m}}{\dot{m}_{AS}}\right)^k \tag{39}$$

where M_{AS} is the mass of the Air Squared compressor with a flow rate capacity of $\dot{m}_{AS}$, and $\dot{m}$ is the mass flow rate produced by each compressor in the BAM system. The volume was calculated in a similar manner, using the following equation:

$$V = V_{AS} * \left(\frac{\dot{m}}{V_{AS}}\right)^k \tag{40}$$

One of the design variables is the number of CAC units, which allows the optimizer to select how many compressor units operate in parallel. If fewer units are used, the units must be larger to provide the necessary flow rate into the system. A second design variable is the number of spare compressors, to be used if a primary compressor fails. The total mass and volume of the CAC system is therefore the mass and volume of each individual compressor multiplied by the total number of active and spare units.

Mass and Volume – Centrifugal Compressor

The mass and volume of the centrifugal compressor are estimated from the modeling work conducted by Ingersoll Rand Nash for this application [139]. The Nash team determined that a five-stage compressor would enable compression to 200 mbar from Mars ambient pressure. The diameter of the first stage impeller is 10 cm, and each stage is progressively smaller. Using this diameter and accounting for other components of the multistage compressor as shown in Figure 74, the dimensions of the compressor are extrapolated to be 42 cm in length, 20 cm in depth, and 34 cm in height. This results in a volume of approximately 0.030 m^3. The volume is modified so that it is pressure-dependent, as larger pressure ratios will require more stages and thus more volume:

$$V = 0.03\left(\frac{\left(\frac{P_2}{P_1}\right)}{\left(\frac{P_{2,o}}{P_{1,o}}\right)}\right)^k \tag{41}$$

where $P_{i,o}$ is the baseline case considered by Ingersoll Rand Nash with an inlet pressure of 7 mbar and an outlet pressure of 200 mbar, and k is an exponential scaling factor equal to 0.28, determined from the modeling results of the same company.

Assuming most of the structure is built from a carbon composite, the mass of the system is calculated as:

$$M = f\rho_{cc}V \tag{42}$$

where ρ_{cc} is the density of carbon composite, V is the volume of the compressor, and f is the factor of that volume that is occupied by carbon composite mass. This mass calculation also includes a pressure ratio dependency, as it is a function of volume.

The reliability of the mechanical pump was also modeled and is described in more detail in Section 4.9.

4.3.3 Sorption Pump

As described in Section 2.5.3, sorption pumps are the third category of CO_2 acquisition and compression considered for Mars ISRU. Sorption pumps utilize a sorbent material to selectively adsorb carbon dioxide. The rate of adsorption and desorption can be controlled by controlling the pressure and temperature of the sorbent bed area; CO_2 adsorbs more effectively at low temperatures and high pressures. Sorption pumps have been utilized in many ISRU architecture designs over the past thirty years and remain an ongoing area of study for NASA.

Two primary architectures exist for sorption pumping on Mars: long-cycle and short-cycle. A long-cycle sorption architecture takes advantage of the day-night thermal swing on Mars to minimize power consumption. The sorption bed can be passively cooled by the atmosphere overnight to adsorb CO_2 at the night-time temperature. Then, as the atmosphere warms up during the day and with the aid of supplemental heating, the CO_2 can be desorbed. A short-cycle architecture, on the other hand, uses an active cooling and heating cycle to control temperature independently of the atmospheric conditions. This allows more control of the system and a shorter cycle time but may result in higher power consumption.

Design

As discussed in Section 2.5.3, sorption bed mass is a strong function of cycle time. Figure 78 shows that for the long-cycle architecture that takes advantage of Mars' diurnal temperature swings and thus has a cycle time of 1 day (~1440 hours), the sorbent mass may exceed 1000 kg. BAM will likely require 10 – 20 of these sorbent beds to produce the required inlet flowrate of CO_2, driving the sorbent mass to 10,000 kg – 20,000 kg. Alternatively, a short-cycle architecture with a cycle time of 2 minutes would only require a sorbent mass on the order of ~1 kg. A system like this has been designed and brought to TRL 4 by Battelle Memorial Institute under a NASA grant [141] and is show in Figure 79.

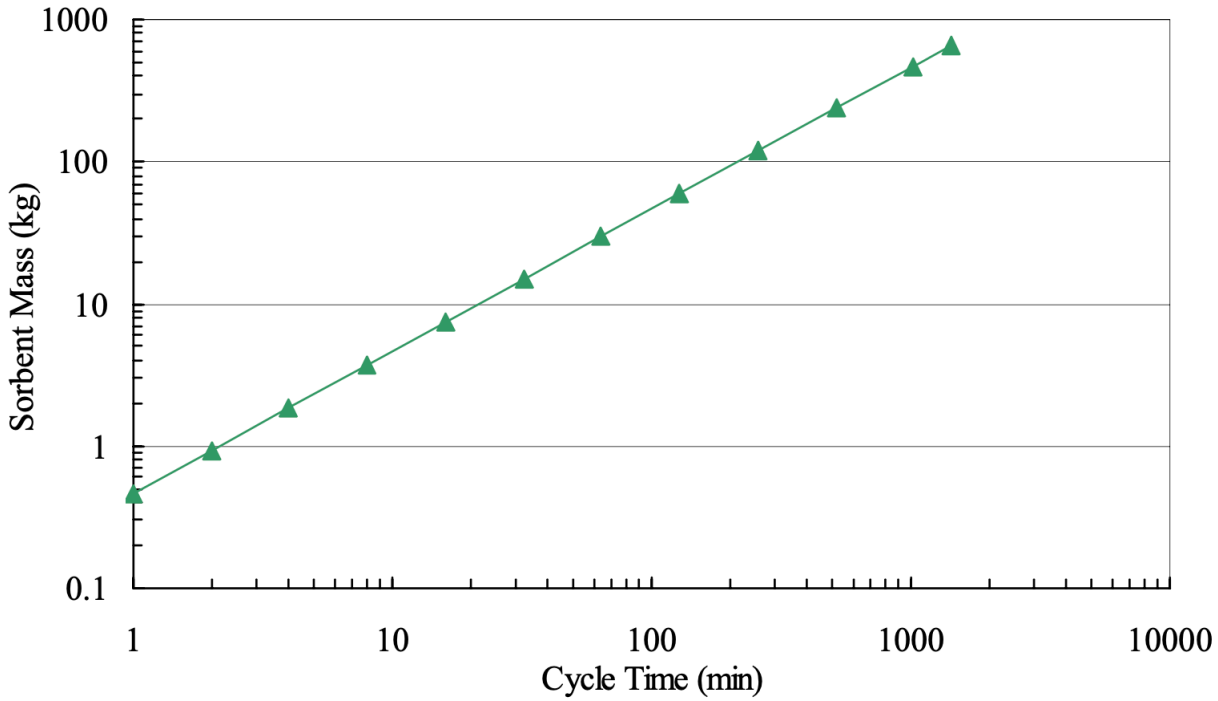

Figure 78: Required sorbent mass for a CO_2 adsorption pump compressing 1.08 kg/hr of CO_2 from 6 mbar to 1000 mbar as a function of adsorption/desorption cycle time [97]

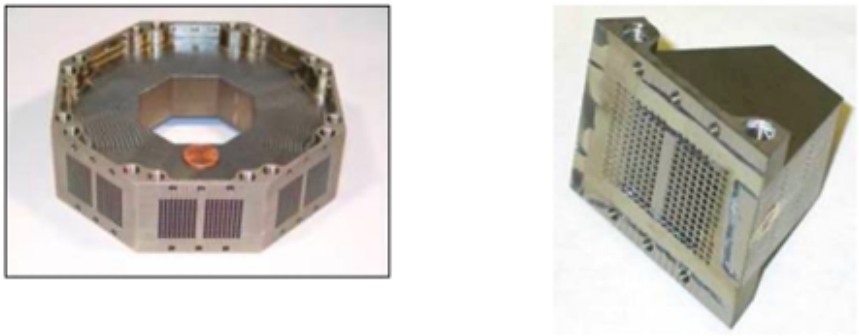

Figure 79: Titanium 8-cell CO_2 sorption pump at TRL-4 from Battelle [142]

The mass of a long-cycle sorption pump is prohibitive and cannot compete against mechanical or cryogenic pumps regardless of potential power savings. It is apparent that significantly less mass is needed if the cycle time is shortened. For this reason, a short-cycle sorption system was selected for this dissertation's modeling effort rather than a large, day-night cycle sorption system. The sorbent material that is modeled is zeolite, as the 13X and 5A varieties of zeolite have been shown to be effective for Mars applications. They adsorb ~15% of their weight in CO_2 [143].

Staging

Staging is an effective tool for optimizing the design of a short-cycle sorption pump. Multiple stages in series reduce the power requirements by dividing the required compression ratio between the stages. Analyses have shown that 2-3 stages are optimal for a Mars scenario for output pressures of 1 bar to 5 bar [146]. However, if operating lower than 1 bar, a single stage design may be optimal. The SOE in BAM will be operated at a pressure lower than 1 bar, indicating a single stage may be sufficient. Each sorption pumping stage can accomplish a compression ratio of approximately 10, which has been demonstrated in a laboratory environment [146].

Pressure and Temperature Ranges

Pressure is a function of the difference in temperature between the adsorption and desorption phases. The larger the temperature differential, the larger the compression ratio that can be achieved by the sorption pump. The Pacific Northwest National Laboratory (PNNL) team achieved a compression ratio of 10 using a temperature range of 12 °C to 77 °C. The temperature range is expanded significantly for the BAM design to achieve higher values of outlet pressure. The PNNL team extrapolated their data to predict that a single stage sorption pump could achieve a compression ratio of 125 at an adsorption-desorption temperature range of -50 °C to 100 °C [146]. Using this range as a baseline, the BAM sorption pump can theoretically compress the Martian atmosphere to 1 bar in a single stage.

ConOps

A sorption pump operates in a four-step cycle, shown in Figure 80.

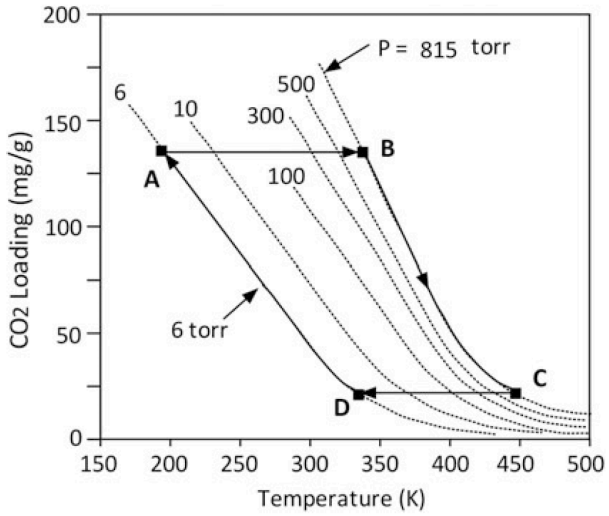

Figure 80: Sorption pump cycle showing temperature and associated CO_2 loading at each step in the cycle [144]

Beginning at point D in the diagram, the system is cooled, and the Mars atmosphere is pulled through the sorption bed via a blower fan to begin the adsorption process. An outlet valve allows non-adsorbed CO_2 and the other constituents of the Mars atmosphere to pass through the bed and back to the Mars atmosphere. At point A, the sorption chamber is isolated from the Mars environment at both its inlet and outlet. The sorption bed is heated to temperature B, desorbing most of the adsorbed CO_2 and increasing the pressure within the system. At point B, a valve is opened that allows the pressurized CO_2 gas to leave the sorption chamber and flow downstream towards the SOE subsystem. As the gas leaves the system, the temperature continues to increase via the heating system to drive off the majority of the CO_2 at a constant pressure. At point C, the downstream valve is closed to isolate the chamber. The chamber is cooled to prepare for the next adsorption cycle, which begins at point D when the inlet and exhaust valves are opened.

To maintain a constant outlet pressure, the heater power must be increased over the course of the desorption period to continually increase the temperature of the sorbent bed. The desorption rate is proportional to temperature *and* sorbent loading. In effect, it becomes more difficult to desorb CO_2 as less CO_2 is in the adsorbed state. This is illustrated in Figure 81.

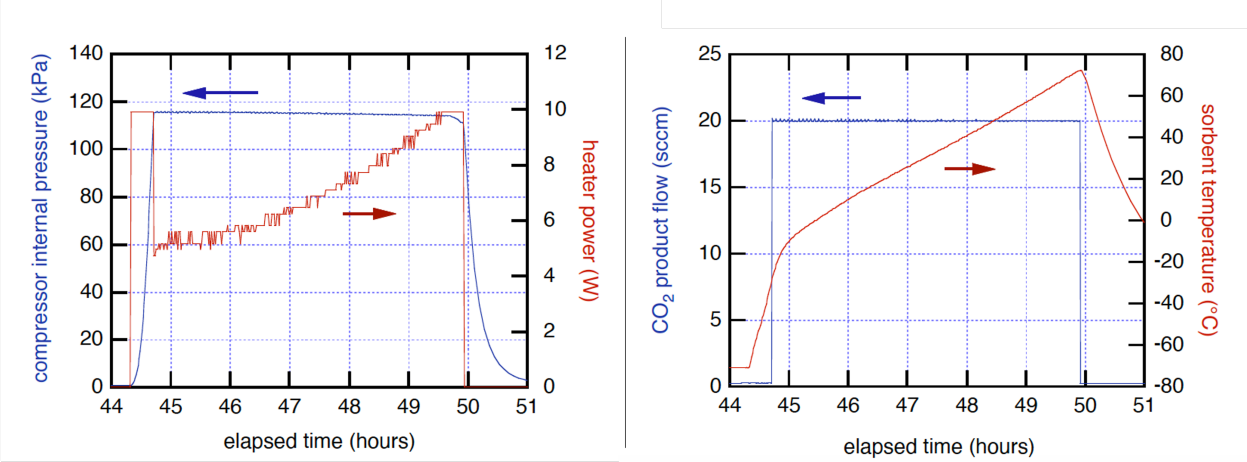

Figure 81: Performance curves for a sorption pump [145]. (Left) Pressure vs. time and heater power vs. time, (Right) CO_2 flow rate vs. time and temperature vs. time

As the figure shows, to maintain a constant pressure (left, blue), the heater power (left, red) and sorbent temperature (right, red) must be continuously increased over the course of a desorption period.

A design decision was made with BAM to run the blower fan continuously rather than cycling it on and off every sorption cycle. The fan is needed only during the adsorption phase, which constitutes approximately half of the cycle. Turning the fan off during every desorption phase would cut its power consumption in half but also subject it to thousands of on-off cycles over the course of the mission. The power consumed by running it continuously is a worthwhile trade for the significant increase in blower fan reliability achieved by avoiding on/off cycling, as found during the optimization analysis described in Chapter 6. To enable this architecture, a valve is activated when each adsorption/desorption phase starts that will either direct the blower fan's exhaust into the sorption chamber or back out to Mars through an exhaust port. This is a notable operational difference when compared to the cryopump, where the blower fan is turned on and off each cycle. The cryopump has a cycle time two orders of magnitude higher than the sorption pump, making the power savings worth the smaller number of cycles it will have to endure.

Pacific Northwest National Laboratory (PNNL) Battelle System

The PNNL Battelle short-cycle system that has been previously described is the most developed system that has been built and thus stands as a useful case study for the operation of this technology. Brooks, Rassat, and TeGrotenhuis published a detailed report for NASA in 2005 regarding their development and testing efforts [146]. The sorption pump design and modeling in this dissertation is based on the work done by this team with minor design modifications.

PNNL designed a multi-cell, eight-stack sorption pump and validated it with experimental work performed on a single channel adsorber. They used water as the heating and cooling fluid, achieving a temperature cycle between 12 °C and 77 °C in less than 2 minutes. Water may not be the correct choice for a Mars system, as the water would freeze under ambient conditions. Regardless, the PNNL team found that with a prototype microchannel sorbent cell using 1.2 grams of Zeolite 13X and a pure CO_2 stream fed at 50 mL/min, the bed reached its desired temperature of 77 °C within 60 seconds. Then, when cooled to 12 °C, 90% of the gas desorbed in ~20 seconds. The adsorption and desorption cycles are shown in Figure 82.

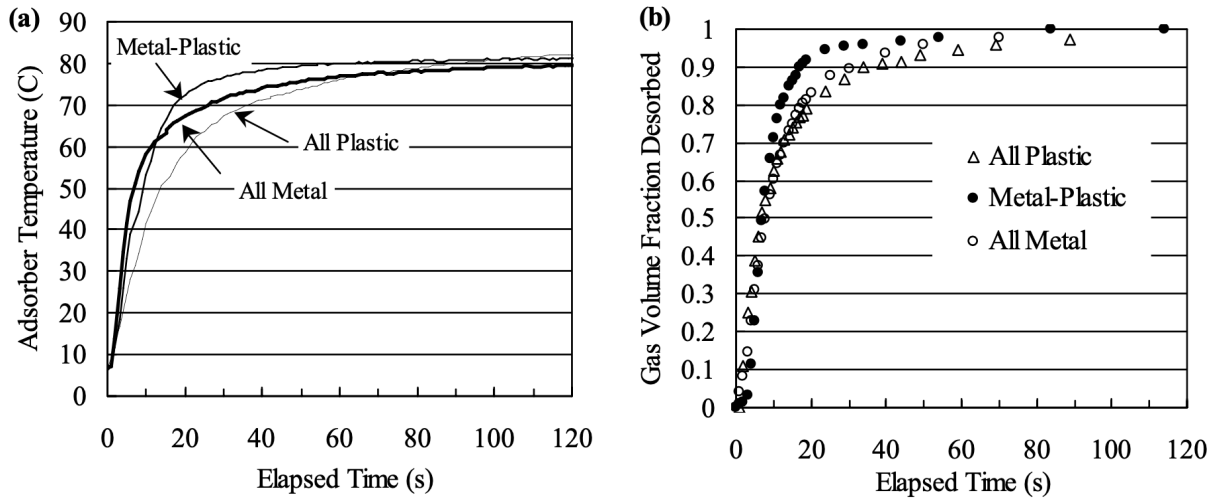

Figure 82: Results from the rapid-cycle sorption pump developed by PNNL and Battelle. (a) Temperature of sorbent bed during warm-up phase, and (b) fraction of gas desorbed during desorption phase [146]

To provide a flow rate of 15 kg/hr of CO_2, over 4000 of these cells would need to be stacked. Alternatively, the cells could be increased in size so that a smaller number would be required, if the 2-minute heating and cooling cycle could still be achieved.

The PNNL team created an 8-stack configuration of cells shown in Figure 79 capable of recuperating 80% of heat. Heat exchange to heat and cool adjacent sorption cells is critical in reducing the power requirements of the sorption pump. The simplest way to visualize how the 8-stack configuration functions is to imagine the stacks rotating clockwise, as depicted in Figure 83. The stacks are heated on the left side of the cycle to desorb CO_2. As they finish desorbing and approach the right side of the circle, they are cooled. The heating and cooling fluids move in the opposite direction. As the system only recuperates 80% of its heat, make-up heat is added at the top of the circle and make-up cooling is provided at the bottom.

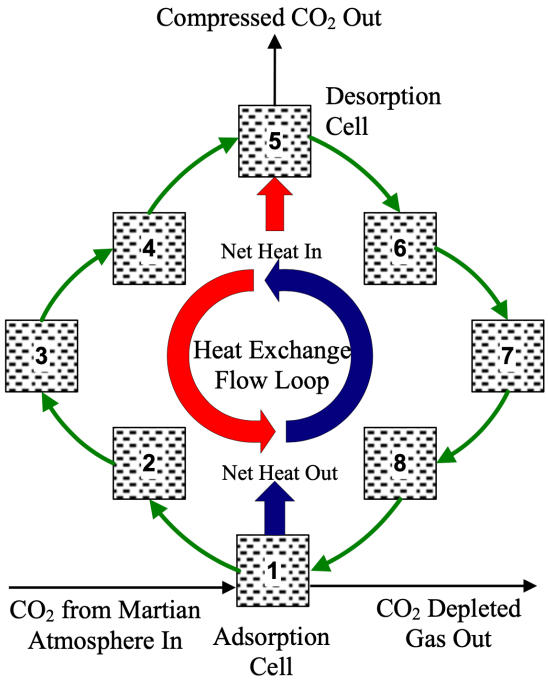

Figure 83: Eight-cell CO_2 sorption pump showing heat recuperation via a heat exchange flow loop [146]

If designed for a flight mission, the cycling of beds and fluids would be accomplished with a series of valves that direct gas flow in one direction and heating and cooling fluids in the other. As discussed earlier, this design sacrifices simplicity and reliability for significant mass and power savings when compared to a long-cycle variant.

Potential Issues on Mars

CO_2 sorption pumps face difficulties with respect to their practicality on a Mars mission as primary ISRU equipment. For one, water poisoning of the beds is a potential issue. Water is strongly adsorbed on these zeolites, which reduces their working capacity over time. The atmospheric water content on Mars is minimal but could still result in the need for periodic water bakeouts over the course of a long mission. Nitrogen and argon, both present in the Mars atmosphere, may also form a diffusive barrier around the zeolite, preventing CO_2 from making its way to the zeolite surface. This can be mitigated with the use of a blower fan that prevents the inert barrier from forming.

The nature of the short-cycle pump architecture may also lead to operational challenges. The sorbent bed design consists of many layers of thin zeolite wafers, each with their own heating and cooling mechanisms. This results in a highly complex design with potentially fragile components that may be damaged during launch and landing. Additionally, each of these sorbent beds will undergo over 300,000 thermal cycles in a 14-month production period, which may reduce performance or cause more serious issues such as leaks and cracks.

These potential risks may be reduced to acceptable levels with significant testing, design iteration, and redundancy. As a result, before this technology can be seriously considered for a Mars mission, its TRL will need to be raised to an acceptable level.

Modeling

The sorption pump system that has been designed for BAM is based on the PNNL system and is shown in its full assembly with four parallel pumps in Figure 84 and as a single pump in Figure 85.

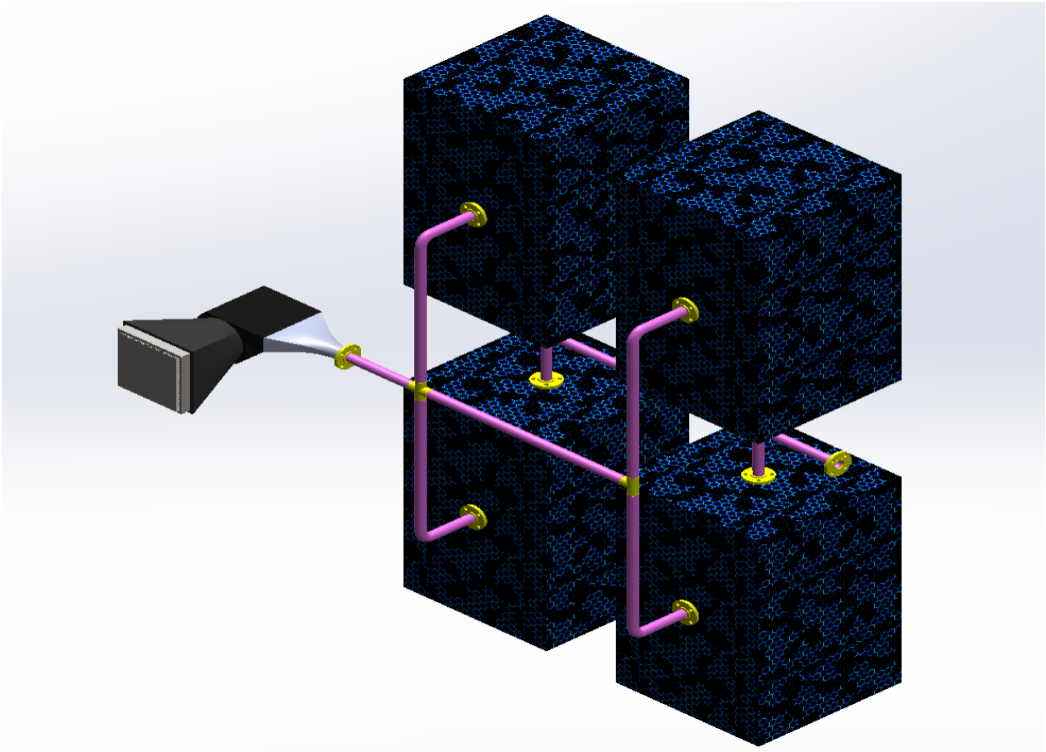

Figure 84: BAM sorption pump assembly rendering with four parallel pumps in their housings, supplied by a blower fan [128]

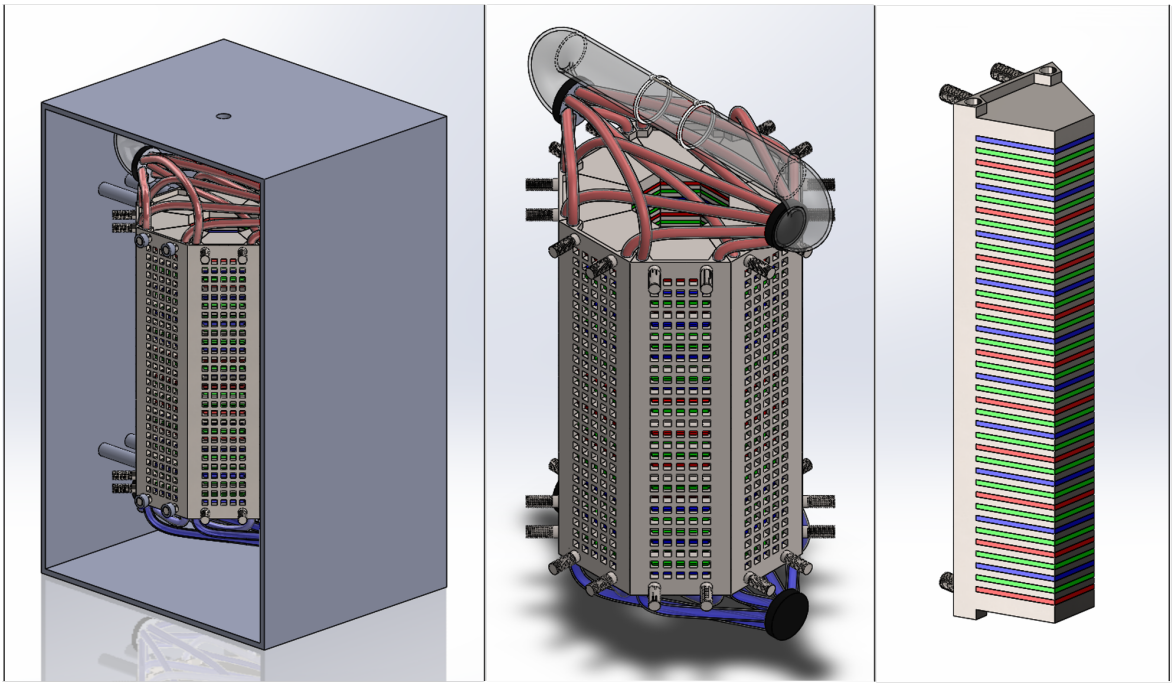

Figure 85: BAM sorption pump rendering of octagonal sorption pump inside its protective casing (left), sorption pump outside its protective casing with heating assembly on top and cooling assembly on bottom (middle), and one of eight identical wedges with zeolite layers shown in green, heating layers shown in red, and cooling layers shown in blue that form the octagonal sorption pump (right) [128].

Layers of zeolite cells are stacked, separated by heating and cooling layers to manage the thermal cycling of the pump. The octagon shape is employed to enable a continuous flow of CO_2 out of the pump; one of the eight wedges begins desorbing CO_2 every 15 seconds in a two-minute cycle. Heat is recuperated by taking the heat from a desorbing stack at its highest temperature and using it to warm the stack next to it. This process repeats for every stack around the octagon until the original stack begins its next desorption cycle. Heating is accomplished using a heating fluid that is distributed to the cells within each stack from a heating assembly mounted to the top of the pump. Cooling is accomplished with a cooling fluid that is distributed to the cells within each and is connected to the liquefaction subsystem's cryocooler and radiator heat rejection system.

A blower fan is used to prevent argon and nitrogen from accumulating and forming a diffusive barrier around the sorbent bed. The blower is cooled, if needed, using a run-off line from the liquefaction subsystem's cryocooler. This may be necessary to prevent motor burnout, as the Martian atmosphere does not provide adequate convective cooling.

Power

The power of the sorption pump is calculated as a combination of three power requirement inputs: cooling, heating, and pumping.

To calculate the power required for cooling and heating, the output temperature must be calculated. Assuming isentropic compression of the gas from its initial, pre-sorption state to its desorbed state enables the outlet temperature, T_2, to be calculated based on the outlet pressure, P_2, which is a design variable.

$$T_2 = T_1 \left(\frac{P_2}{P_1}\right)^{1-\frac{c_v}{c_p}} \tag{43}$$

where T_1 and P_1 are the ambient temperature and pressure, and $\frac{c_v}{c_p}$ is the inverse of the specific heat ratio of carbon dioxide.

The total cooling required is calculated as a summation of the cooling required of the gas, the sorbent bed, and a portion of the frame surrounding it:

$$Q_{cooling} = \frac{(Q_{gas} + Q_{bed} + Q_{frame}) * (1 - \eta)}{2} \tag{44}$$

where η is the fraction of heat that is recovered in each heating-cooling cycle. This fraction is assumed to be equal to 0.8, per modeling and test results from the PNNL apparatus [146]. The entire cooling load is divided by two because cooling only takes place during half of the sorption pumping cycle.

The three cooling terms from Equation (44) are calculated as follows:

$$Q_{gas} = \dot{m}_{in} c_{p,CO_2} (T_1 - T_{cold}) \tag{45}$$

$$Q_{bed} = \frac{m_{bed} c_{p,z} (T_1 - T_{cold})}{\frac{t_c}{2}} \tag{46}$$

$$Q_{frame} = \frac{f * m_{frame} c_{p,ti} (T_1 - T_{cold})}{\frac{t_c}{2}} \tag{47}$$

where T_{cold} is the specified cold-side temperature to which the sorbent bed is cooled during the adsorption phase, c_p is the specific heat capacity of the relevant material, t_c is the sorption pump cycling time (divided by two as only half of the cycle involves cooling), and f is the fraction of the framing material that is heated, representing a heat loss term. The cold-side temperature is set to -40 °C, whereas the hot temperature is above 100 °C and dependent on the pressure setpoint. This range falls in line with previous studies conducted on sorption pumps [147]. The total cooling load is later converted to a power requirement by dividing by the cryocooler efficiency.

The total heating requirement is calculated in the same manner, as the gas, bed, and frame are both cooled and heated each pumping cycle. The only difference in the calculations is that the temperature differential becomes $T_2 - T_{cold}$, where T_2 is the output temperature of the sorption pump, adjusted to achieve the desired P_2. The calculation for the power of the blower fan is shown in Appendix B.3. The total power of the sorption pump is the sum of the heating, cooling, and blower power.

Mass

The typical capacity of a sorbent bed for CO_2 acquisition is on the order of 0.15 g CO_2 per g sorbent [148]. Specific isotherms can be calculated for given operating conditions to predict this number more accurately, but an estimate of 0.15g/g is sufficient for the scope of this model. As such, the mass of the sorbent bed can be calculated as:

$$M_{bed} = \left(\frac{1\ g\ sorb}{0.15\ g\ CO_2}\right) * \frac{\dot{m}_{in,CO_2} * t_{cycle}}{\eta} \tag{48}$$

where $\dot{m}_{in,CO_2}$ is the inlet flowrate of Mars atmosphere, t_{cycle} is the cycle time of the adsorption – desorption process, and η is an efficiency term used to correct for observed drops in performance from inert gas buildup [143]. Values can be substituted as a case study to determine a typical bed mass: 2 minutes for the cycle time, 3 kg/hr for the oxygen production rate, and 50% for the utilization fraction. This yields:

$$M_{bed} = \left(\frac{1\ kg\ Sorb}{0.15\ kg\ CO_2}\right) * \left(3\frac{kg\ O_2}{hr}\right) * \frac{1\ kmol\ O_2}{32\ kg\ O_2} * \frac{44\ kg\ CO_2}{1\ kmol\ CO_2} * \frac{2\ kmol\ CO_2}{1\ kmol\ O_2} * \frac{1}{0.5} * (2\ mins) * \frac{1\ hr}{60\ mins} / 0.7 \ = \mathbf{5.23\ kg} \tag{49}$$

This is a low mass system compared to other pumping options, and these results are in line with Figure 78.

The sorbent bed mass is only a fraction of the mass of the pumping system, however. In a small channel sorption pump, most of the mass lies in the structure surrounding and supporting the sorbent material. For a similar system operating in the same temperature regime, it was found that the combined structural and sorbent mass was a factor of 15 higher than the sorbent alone [146]. This factor is included in the mass calculation for BAM to give a sorbent pump mass as follows:

$$M_{pump} = 15 * M_{bed} \tag{50}$$

The multiplication factor assumes a titanium structure surrounding the sorbent bed layers and includes the heat exchange channels, header and end plates, valves, and piping. The total mass of the sorption pump subsystem is then the mass of the pump added to the mass of the blower fan that is used to remove inert gases from the sorption chambers:

$$M_{sorption} = M_{pump} + M_{blower} \tag{51}$$

The heating and cooling power required to operate the sorption pump result in an equivalent radiator and cryocooler mass penalty. This mass is calculated as part of the liquefaction subsystem.

4.4 SOE Subsystem

The CAC subsystem captures and compresses carbon dioxide from the Martian atmosphere to feed the solid oxide electrolysis (SOE) subsystem. The SOE is the core technology of the ISRU

plant, converting carbon dioxide into oxygen. The design and modeling of this subsystem are described in this section.

4.4.1 Design

The design of the SOE subsystem is built on lessons learned from the MOXIE project, continuing work on scalability of SOE systems between OxEon and NASA, and general heat transfer and mass optimization design principles. The subsystem consists of electrolysis cells placed in pressurized stacks, which are packaged inside a hotbox enclosure. CO_2 flows into the hotbox from the upstream CAC system, and O_2 and CO/CO_2 exhaust streams flow out of the hotbox towards the downstream subsystems. All electrochemistry equations that are modeled and used are catalogued in Section 2.3.6.

SOE Hotbox

The SOE system is designed to consist of a series of stacks of cells arranged inside a "hotbox". The hotbox is an insulated container with an inner and outer shell that minimizes heat leaks to the Martian environment from the hot SOE stacks inside. It also includes inlet and outlet tubes for gases and electrical interfaces. A cutaway of the hotbox for the SOE system in BAM is shown in Figure 86.

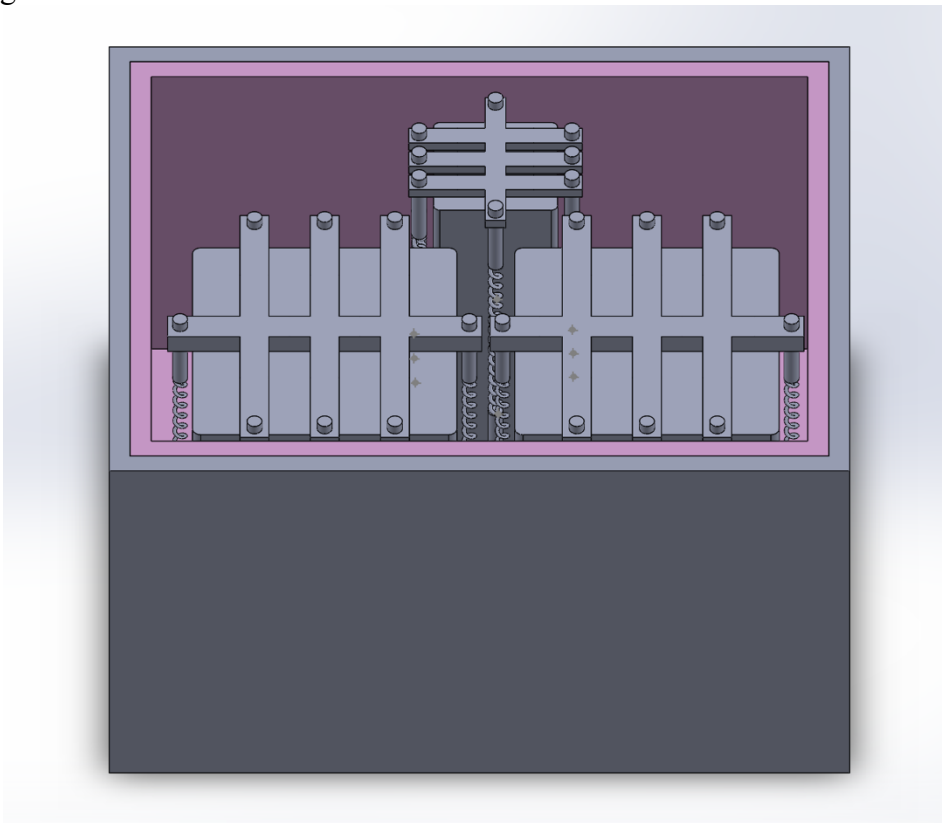

Figure 86: 3-dimensional model of the SOE hotbox for BAM with its lid removed, showing enclosures of SOE cells inside. Two insulation layers minimize heat leak out of the hotbox to the environment [128].

The cells are maintained at their temperature setpoint by cartridge heaters placed vertically along the stacks inside the hotbox. Insulation minimizes parasitic heat losses to the environment. Excelfrax 1800 insulation, similar to aerogel, is used in multiple layers. Excelfrax 1800 has a thermal conductivity of 0.03 W/m-K at atmospheric pressure, a density of 230 kg/m^3, and can be

cut to fill in areas with complex geometries around the stacks [149]. Materials such as Excelfrax 1800 have a thermal conductivity that varies with pressure; at Mars pressure, the thermal conductivity could be expected to vary between 0.005 and 0.01 W/m-K [150]. The thicknesses of insulation between the SOE stacks and the inner shell and between the inner shell and outer shell are design variables that are controlled by the optimizer. An increase in insulation thickness results in a decrease in parasitic heat losses but an increase in system mass and volume.

The SOE hotbox unit will consist of a combination of quad-stack modules, which contain four stacks of SOE cells in a 2x2 configuration, and single-stack modules, which contain a single stack of SOE cells. Schematics of a quad-stack module and single-stack module are shown in Figure 87 and a cutaway of the single stack module, showing the SOE cells stacked inside, is depicted in Figure 88.

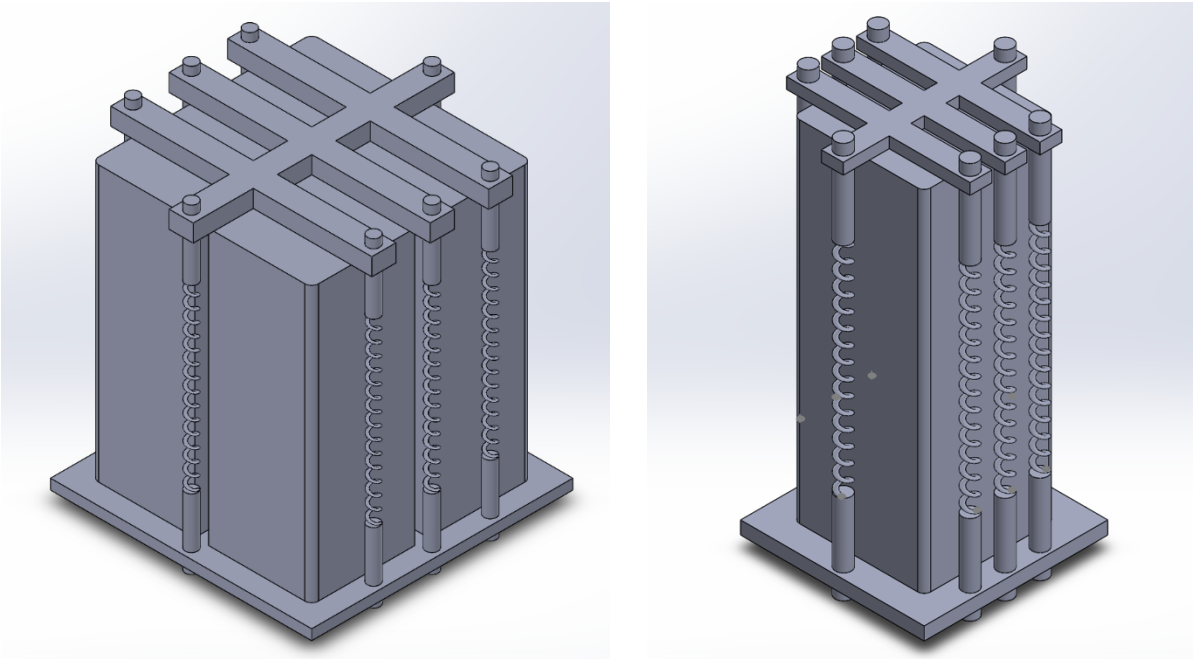

Figure 87: Quad stack module (left) and single stack module (right) for the SOE system in BAM [128]

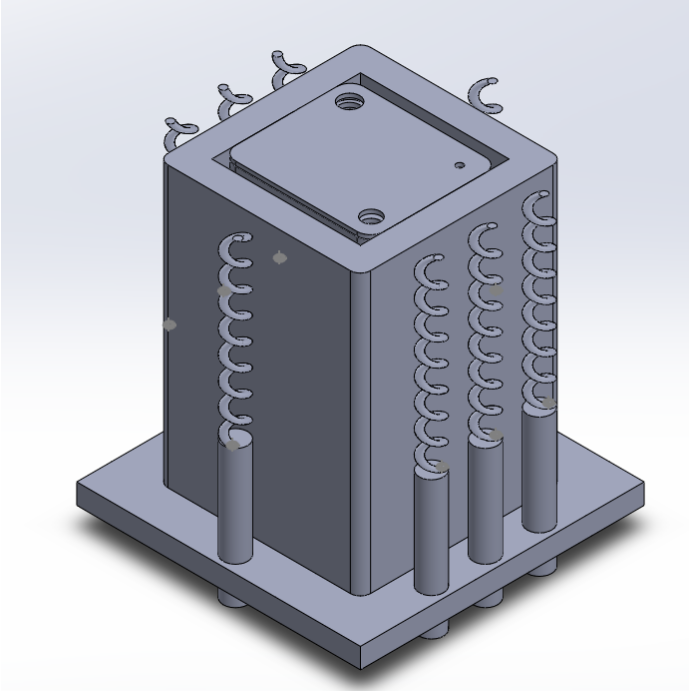

Figure 88: Cutaway of a single stack module in the SOE system for BAM, showing a stack of SOE cells inside [128]

Quad-stack modules provide favorable mass, volume, and power compared to single-stack modules. Single-stack modules may be required if the optimized number of stacks is not a multiple of four. Mechanical compression is applied with crossbars and steel compression springs on all sides of the modules. This is necessary, as it was in the MOXIE design, to counter the pressure imbalance caused by having gas inside the SOE at a higher pressure than the external Mars atmosphere. In addition, to buy down risk, the four stacks in a quad-cell module are electrically interconnected every fifth cell. In this way, if one cell fails, only that grouping of five cells is lost and the rest of the stack can continue operating. Furthermore, redundant cells within each stack and redundant stacks can be added to minimize risk.

An algorithm was developed to calculate the dimensions of the SOE hotbox unit as a function of the number of stacks chosen by the optimizer. The algorithm first maximizes the number of quad-stack modules available and then fills in the remaining stacks as single-stack modules. It attempts to organize the modules in such a way that the surface area of the hotbox is minimized. Example configurations are shown in Figure 89.

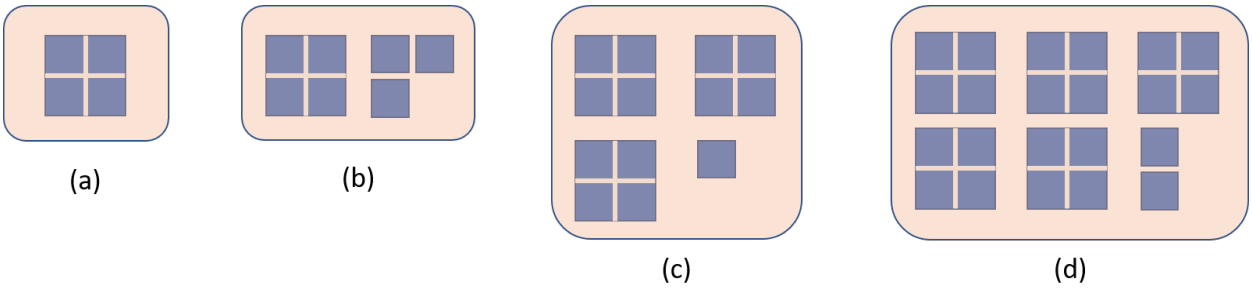

Figure 89: Birds-eye view of hotbox configurations. (a) a single quad-stack module is placed inside the hotbox. (b) seven total stacks are required, and the algorithm determines that one quad-stack module and three single-stack modules should be placed in the orientation shown. (c) thirteen total stacks are required, and the algorithm determines that three quad-stack modules

should be arranged in a 2x2 configuration, with the lone single-stack module placed in the empty corner. (d) twenty-two stacks are required, and the algorithm determines that five quad-stack modules should be arranged in a 2x3 configuration with the remaining two single-stack modules placed in the empty corner.

The number of cells per SOE stack is limited to a maximum of 100 due to potential mechanical stability issues for larger stacks. OxEon Energy has demonstrated successful tests of 60-cell stacks [162].

Pre-Heater

An in-line tubular heater was chosen for the SOE inlet gas pre-heating element. The purpose of this element is to increase the temperature of the incoming gas from T5, its post-heat-exchanger temperature, to T6, the setpoint temperature of the SOE system. The preheater is placed upstream of the SOE system to ensure the gas is warmed to the appropriate temperature before entering the solid oxide stacks. In-line heaters are compact, lightweight, and easily integrated into the piping architecture. An example is shown Figure 90.

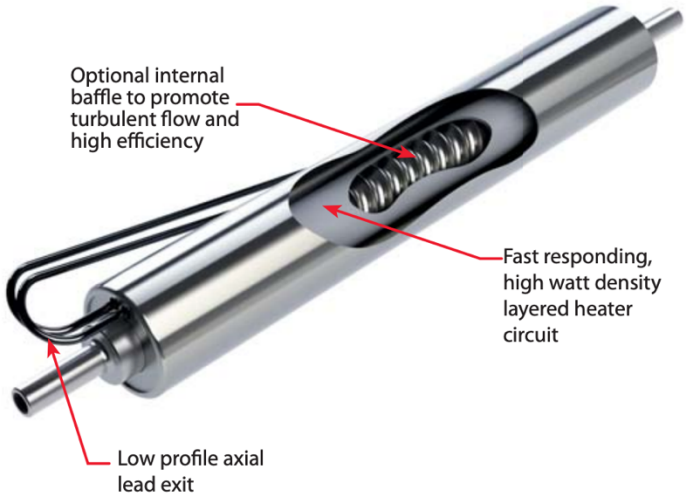

Figure 90: In-line electrical preheater to increase gas temperature to SOE setpoint (Watlow FLUENT Heater).

Typical electrical to thermal conversion efficiencies approach 100%. A 10% loss of heat to the environment is assumed, making this solution 90% energy efficient in BAM.

4.4.2 Modeling

With the design complete, the SOE system is modeled to calculate the objectives as functions of the design variables.

Power

There are several contributors to the total power requirements of the SOE subsystem, including the pre-heater, parasitic heat loss, electrolysis, and electrochemical compression.

Pre-heater

The power consumption of the pre-heater is modeled as follows:

$$P_{preheat} = \frac{\dot{m}_{in} Cp_{Mars} (T6 - T5)}{\eta} \tag{52}$$

where $\dot{m}_{in}$ is the inlet gas mass flow rate, Cp_{Mars} is the specific heat capacity of a typical Mars atmospheric composition, $T6$ is the temperature of the SOE unit, $T5$ is the temperature of the inlet gas after leaving the heat exchanger, and η is the combined thermal-to-electrical conversion efficiency and preheater-to-gas-stream efficiency (assuming a 10% loss to the environment).

Cartridge Heaters

The heating requirement of the cartridge heaters is defined by the heat lost to the surrounding Mars environment from the hotbox. Total heat loss is determined by calculating conduction through both layers of Excelfrax insulation and convection and radiation to the Mars environment. The heat loss is broadly defined as:

$$Q_{heatloss} = \frac{T_i - T_o}{R_t} \tag{53}$$

where T_i and T_o are the inner and outer temperatures of the SOE hotbox and R_t is the total thermal resistance of the heat path, including conduction, convection, and radiation:

$$R_t = R_{cd} + R_{cv} + R_{rd} \tag{54}$$

The total thermal resistance from conduction through multiple layers is calculated as:

$$R_{cd} = \frac{A}{\frac{A_1}{R_1} + \frac{A_2}{R_2}} \tag{55}$$

where A_1 and A_2 are the cross-sectional areas of conduction through the inner and outer insulation layers, and $A = A_1 + A_2$. The thermal resistances through each layer, R_i, are calculated as:

$$R_i = \frac{t}{k * A_i} \tag{56}$$

where t is the thickness of the insulative layer and k is the thermal conductivity of the insulation. Similarly, the thermal resistance of convection from the surface of the hotbox to the Martian environment is calculated as:

$$R_{cv} = \frac{1}{h * A_2} \tag{57}$$

where h is the convective coefficient of the Mars atmosphere.

Radiation often plays an equal or larger role in heat dissipation than convection on Mars. In this case, however, the outer shell of the hotbox is coated with a material that has a low emissivity (< 0.1), making heat loss from radiation negligible. Dust loading may be problematic, as it could

increase the emissivity over time. This system should therefore be tested during development to minimize dust coating.

A margin is applied to the heat loss to account for losses through the tubing and electrical interfaces with the hotbox. In addition, conduction through the inner and outer shells was assumed to be negligible, as the shells have a significantly higher thermal conductivity and are thinner relative to the insulative layers for which conduction was calculated.

Electrolysis

Electrical power is required to drive the electrolysis process, where CO_2 is reduced to CO and oxygen ions. The electrical power of electrolysis is calculated as:

$$P_{electrolysis} = IV_{tn}N_{cells} \tag{58}$$

where I is the current generated by each cell, V_{tn} is the thermoneutral voltage, and N_{cells} is the number of active SOE cells in the system. The thermoneutral voltage refers to the crossover point between endothermic and exothermic reactions in electrochemistry and its calculation is described in more detail in Section 2.3.6. If the cell is running at a higher voltage than its thermoneutral voltage, it will create an exothermic reaction, and if it is running at a lower voltage than its thermoneutral voltage, it will create an endothermic reaction. The SOE cells must operate at a voltage below the thermoneutral point to avoid producing carbon, meaning that an endothermic reaction will take place. Therefore, $P_{electrolysis}$ includes both the power for electrolysis *and* the additional heater power required to compensate for the endothermic reaction. The typical power found in BAM designs for this electrolysis was ~16 kW.

Electrochemical Compression

When the anode pressure (P_a) is greater than the cathode pressure (P_c), additional power is used by the stack for electrochemical compression. This is calculated as an additional voltage:

$$\Delta V_c = \frac{RT}{2F}\ln\left(\frac{P_a}{P_c}\right) \tag{59}$$

which is converted to a thermodynamic power of compression term:

$$P_c = I\Delta V_c \tag{60}$$

This additional power term was predicted for MOXIE operations [151] and may be impactful for BAM operations as well, depending on the pressure ratio between anode and cathode.

Mass and Volume

The calculations for mass and volume of the SOE subsystem can be found in Appendix B.5 SOE Calculations.

SOE Stack Operation

A fraction of the SOE cathode exhaust is recycled to the inlet of the SOE to maintain a required minimum level of CO in the inlet stream. This follows a similar design to the tubing in MOXIE,

and the fraction of SOE cathode exhaust that is recycled is defined by the variable *rec_frac*. A minimum level of CO is required in the inlet to prevent oxidation of the nickel cathode by CO_2, which is a degradation mechanism that would decrease performance of the cells.

A maximum allowable pressure differential exists across the electrolytic cell before mechanical failure becomes a concern. A previous study on similarly sized SOE cells found that the maximum allowable pressure differential was approximately 2000 mbar [152]. While this number could decrease if thinner electrolytes are used, it would remain a significantly larger differential than will ever be realized in BAM's design, making this failure mechanism irrelevant.

Electrochemical compression was considered in an effort to increase the pressure of the anode gas. This would, in turn, reduce the amount of cooling needed to liquefy the oxygen downstream. A previous study found that the increase in power needed to electrochemically compress the anode gas did not result in any significant reduction in total system power or mass [152]. Regardless, the model accounts for the possibility of electrochemical compression, the extent of which is controlled by the optimization algorithm.

4.5 Liquefaction Subsystem

The purpose of the liquefaction subsystem is to take gaseous oxygen from the output of the SOE subsystem and phase change it to a liquid for long-term storage. Oxygen is stored as a liquid to take advantage of the higher density afforded by the liquid phase; if stored as a gas, the storage system becomes too heavy and voluminous. The liquid oxygen is stored in the tank of the MAV, and as a result, the gas is liquefied directly in the storage tank to minimize system mass. Heat is rejected via an external cryocooler and radiator, which is disconnected by the astronaut crew prior to MAV liftoff. A zero-boiloff (ZBO) state has been shown to be feasible in the propellent tank by a recent study using a similar cryocooler architecture to what is proposed in this section [153]. As an added precaution, a vent is included on the tank to regulate pressure, as past studies have found it necessary when attempting to achieve a ZBO state [154].

This section provides a detailed analysis of the design and modeling of the liquefaction subsystem.

4.5.1 Design

The liquefaction subsystem was designed through a combination of research, calculations, and trade studies. One of the primary design decisions that was made was to liquefy the oxygen in the MAV tank itself rather than liquefying it externally and pumping it into the tank. As a result, the mass and volume of the MAV tanks are not considered in this optimization scheme: the MAV tanks are a required component in a human mission regardless of the chosen ISRU design. An extensive trade study was conducted by Johnson et al. in 2018 [103], and, as discussed in Section 2.6, the tube on tank method was found to be the most desirable for oxygen liquefaction on Mars. In this configuration, a coolant tube is coiled around the MAV oxygen tank and removes heat from the gas and liquid within, as shown in Figure 91. Another study by Hauser and Johnson in 2016 had similar findings, showing that liquefying propellant directly in the MAV tank resulted in the lowest liquefaction subsystem mass of the various designs considered [102]. Notably, this study found that if returning to the same Mars landing site several (~5)

times, a separate liquefaction tank and cryocooler may become a competitive architecture. BAM, however, is designed for the pioneering missions to Mars and thus does not assume a permanent settlement scenario.

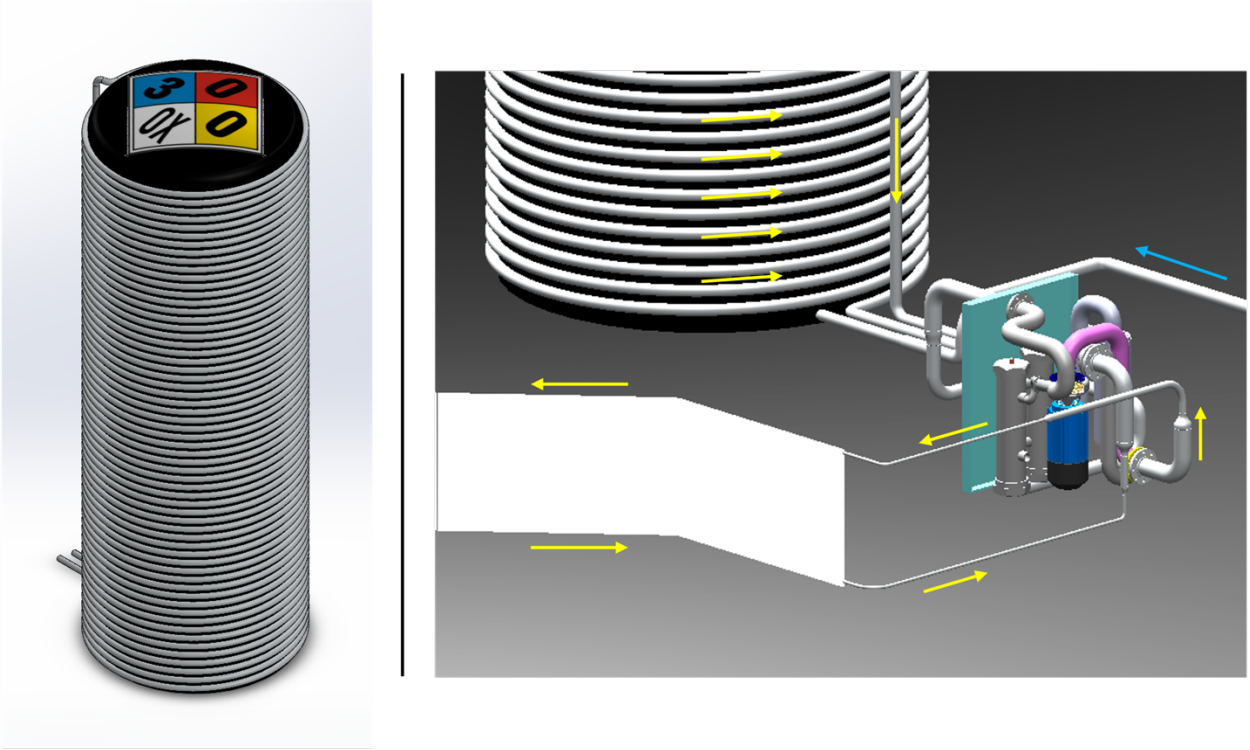

(a) MAV Tank wrapped with cooling piping

(b) Liquefaction system isometric view

Figure 91: Liquefaction system. (a) MAV tank with cooling piping, demonstrating the tube-on-tank liquefaction method; (b) isometric view of the liquefaction system, showing radiator in white, cryocooler on right, and MAV tank lower section in back. Arrows indicate gas flow direction. Blue arrow on right-hand side of image is gaseous oxygen, which flows directly into the tank. Yellow arrows indicate the flow path of the coolant, which spirals up the tank, comes down from the top of the tank in a vertical pipe, is fed into the cryocooler for compression, flows into the radiator for heat rejection, and returns to the cryocooler for expansion cooling [128].

In addition to the MAV tank, Figure 91 shows an isometric view of the liquefaction system. The components associated with both views will be discussed in further detail in the following sections.

Cooling Cycle

A cryocooler is used to cool and liquefy the gaseous oxygen in the tank. Two cooling cycles were considered for this system based on past designs that have flown in space: the Stirling cycle and the turbo Brayton cycle. Whereas a Stirling cycle employs a piston to expand and compress a gas to reject heat, a turbo Brayton cycle uses a rotary turbine and compressor, as shown in Figure 92.

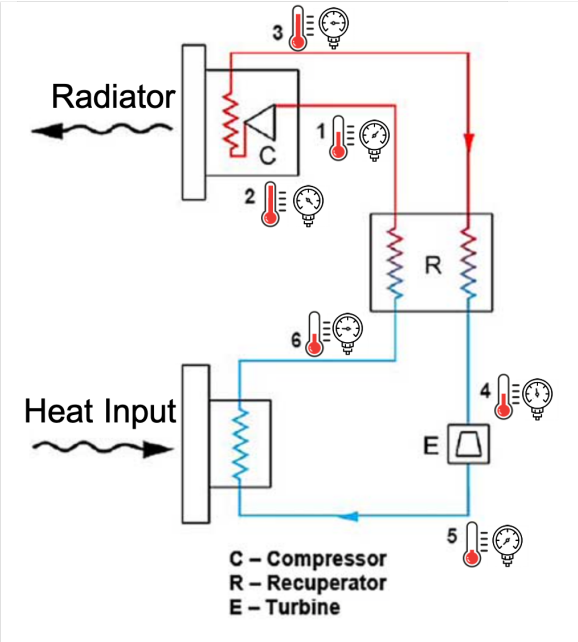

Figure 92: Turbo-Brayton refrigeration cycle. Beginning at location (1), the working fluid is compressed, cooled via an external radiator, cooled further through a recuperator, and expanded to low pressure with a turbine before wrapping around the MAV oxygen tank to liquefy the gaseous oxygen. The working fluid passes once again through the recuperator before beginning the cycle again. Thermometer and pressure gauge icons indicate the relative temperature and pressure of the working fluid at each stage in the process.

Figure 92 depicts the path followed by the working fluid, which is used to draw heat out of the MAV tank and reject it to the Mars environment. The turbo-Brayton cycle has several main components, and its operation is described below.

1. **Compressor:** Beginning at location (1) in Figure 92, the working fluid, a gas, passes through one or more centrifugal compressors. The compressor motors are driven electrically. As the gas is compressed, its temperature and pressure increase.
2. **Radiator:** The gas then enters a radiator, which passively radiates heat from the gas to the Martian atmosphere, cooling the gas.
3. **Recuperator:** The gas passes through a recuperator, which further cools it and is used to transfer heat and improve cycle efficiency. The recuperator also pre-warms the gas stream exiting the Heat Input step.
4. **Turbine:** The gas enters a turbine, where it is expanded to a lower pressure. The expansion process causes a decrease in gas temperature to occur. Energy is captured from this expansion process that can be used to drive the compressor by coupling the turbine and compressor shafts.
5. **Heat Input:** The cold gas then passes in a spiral around the MAV oxygen tank, drawing heat from the gaseous oxygen and liquefying the oxygen in the tank. This is represented by the “Heat Input” label in Figure 92.

The turbo Brayton cycle was selected because its components are highly reliable with long lifetimes and can be scaled to the level required of this ISRU plant or larger [155]. The only moving parts in the turbo Brayton cryocooler are the turbomachine rotors, which, when designed with non-contact gas bearings, have an extremely long lifetime. One such system has been demonstrated in a variety of longevity tests, including a 14-year test with no maintenance or

performance degradation, a 10,000 start-stop cycle test that required no maintenance and experienced no performance degradation, and over 6.5 years of in-space operation [156]. Another in-space application of this technology is in the cooling system for the near infrared camera and multi-object spectrometer (NICMOS) onboard the Hubble Space Telescope [157]. A third example is the Minus Eighty-Degree Laboratory Freezer for ISS (MELFI), a freezer onboard the ISS built by the European Space Agency (ESA) that uses a turbo Brayton cycle to cool and store biological science samples [158]. Turbo Brayton cycles are relatively lightweight, compact, and efficient at high cooling loads, which is why they have been selected for multiple space missions. These findings agree with a study that found that a Brayton cycle was the most competitive cryocooler option in terms of power, mass, and robustness for liquefaction of oxygen on Mars [105]. At the scale required in the BAM design, the turbo Brayton cycle is expected to operate at 10% – 20% thermal efficiency, meaning that the system will consume 5 – 10 times as much energy as the heat energy that is removed from the hot O_2 stream.

Radiator

The cryocooler rejects heat via a radiator that is thermally coupled to the Mars environment. The radiator is oriented vertically, perpendicular to the Mars surface, with radiating sides facing the horizons on Mars. It is positioned to minimize its exposure to the sun across a Martian sol. On Earth, the majority of heat rejected by a radiator typically occurs through convection. On Mars, radiation has a larger effect than convection, accounting for at least 70% of heat removal across a range of radiator temperatures as shown in Figure 93.

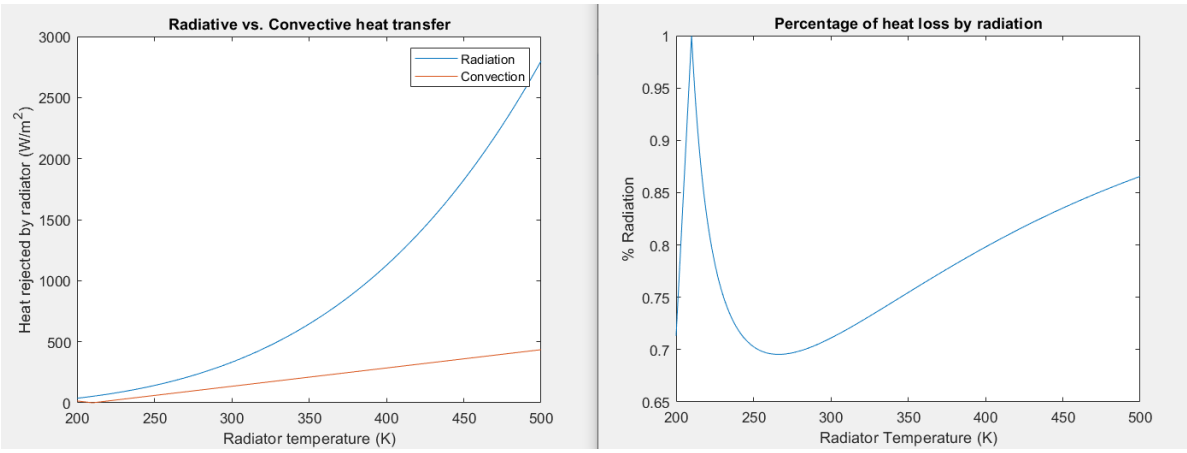

Figure 93: Radiator heat rejection mechanism at standard Mars atmospheric conditions and a variety of radiator temperatures. Radiation has an increasingly larger heat rejection rate than convection as radiator temperature increases [159].

The calculations used to generate Figure 93 assume an atmospheric temperature of 270 K and an effective Martian sky temperature of 170 K, a worst-case scenario for radiation [160]. This does not take wind into account for the convection term. An increase in convective heat transfer on the BAM radiator could be achieved through forced convection by mounting a blower fan to move air across the surface of the radiator, however, this design was not pursued due to the added mass and complexity that it would require [161]. Figure 93 illustrates that both radiation and convection must be considered when designing and modeling a Mars radiator.

The BAM radiator consists of an aluminum pipe that circulate the working fluid and carbon-carbon (C-C) composite fins that radiate and convect heat to the atmosphere. C-C fins were

selected because of their low weight and high thermal conductivity. The fins are coated in a magnesium-oxide white paint, similar to the paint used on the Mars 2020 rover radiator [162], with an absorptivity of 0.09 and emissivity of 0.92. This enhances the fins' radiation capabilities while reflecting 91% of the incoming solar radiation to minimize external heating. The radiator is external to the MAV, reducing MAV complexity and allowing future missions to use the radiator and cryocooler liquefaction system if returning to the same landing site.

An additional consideration for radiator design is the impact of dust on radiator performance. Deposition of dust on the radiator surface from dust storms can result in abrasion from dust particle impact and reduced emissivity. Dust-carrying winds at speeds greater than 90 m/s have been shown to contribute to significant degradation of radiator surfaces over time [163], however, dust storms on Mars rarely exceed 25 m/s.

Working Fluid

A single-phase gas is used as the primary working fluid for the cryocooler loop. Typical gases for cryocooler applications are nitrogen for temperatures above 100 K, neon for temperatures between 30 K and 100 K, and helium for temperatures below 30 K [164]. Oxygen is liquefied at 90 K, making neon gas the appropriate working fluid choice for this application. The neon gas transfers heat between the oxygen, the MAV tank, and the cryocooler. It then exchanges its heat with a liquid anhydrous ammonia working fluid that runs between the cryocooler and the radiator to reject the heat to the Martian atmosphere through convection and radiation. The liquid state of the ammonia allows it to carry more heat per volume to the radiator than a gas. It is pressurized to several atmospheres to maintain a liquid phase throughout its cycle.

Insulation

The choice of insulation is another important radiator design decision, as it impacts the energy requirement of the cryocooler to maintain a zero-boiloff (ZBO) state. Multi-layer insulation (MLI) is a standard insulation for in-space applications, where it has a thermal conductivity of ~0.1 mW/m-K [165]. This requires a hard vacuum environment, which is not available on Mars. The soft vacuum pressure on Mars reduces the thermal performance of MLI by an order of magnitude and, as a result, MLI is not recommended for Mars surface applications. A second insulation option is layered composite insulation, which is composed of various materials including aerogel. Aerogel is used as the primary insulator in MOXIE and has been shown to have superior thermal insulation when compared to MLI in a soft vacuum [166]. For this reason, BAM uses aerogel as its low-temperature insulator.

Summary

Table 34 provides a summary of the critical design decisions that were made on the liquefaction subsystem and the rationale for those decisions. A cross-section of the tank wall showing the tube-on-tank architecture and aerogel insulation is shown in Figure 94.

Table 34: Primary design decisions for liquefaction subsystem design

Component	Design Decision	Rationale
Liquefaction Method	Tube on Tank	Most effective, low mass
Cryocooler Cycle	Turbo-Brayton	Upward scaling advantage over primary competitor (Stirling cycle)
Radiator Placement	External to MAV	Mounting to MAV would increase MAV mass, increasing LO_2 requirement
Radiator Material	Carbon-Carbon Composite	Low mass, high thermal conductivity, high resistance to dust abrasion
Insulation	Multi-layer Aerogel	Proven to work well in Mars-like environments, superior performance at Mars atmospheric pressure to traditional MLI
Working Fluid	Neon Gas	Single-phase gas is ideal (no phase transitions), and neon provides the best thermal properties at the expected oxygen liquefaction temperature.

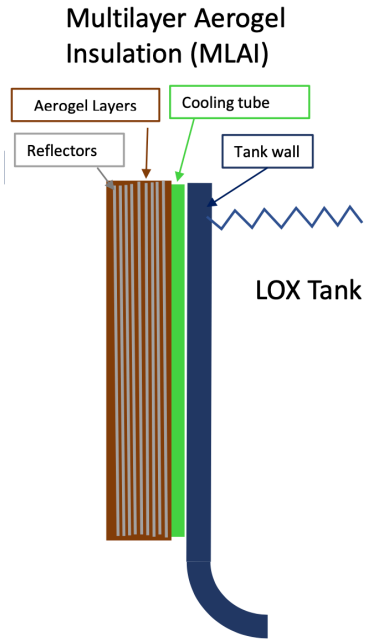

Figure 94: Cut-away of LOX tank wall demonstrating tube-on-tank architecture and aerogel insulation. (Credit: NASA) [167]

4.5.2 Modeling

With the design complete, the liquefaction subsystem is modeled to calculate its contributions to the objective functions.

Heat Rejection Requirements

The heat that must be removed from the system by the cryocooler is calculated as the cooling required to lower the temperature of the gaseous oxygen to its boiling point and liquefy it. The power required to cool gaseous oxygen to its boiling point is calculated as:

$$Q_{cool_{O_2}} = \dot{m}_{O_2} C_{p_{O_2}} \left(T_{O_2} - T_{bp}\right) \tag{61}$$

where $\dot{m}_{O_2}$ is the mass flow rate of the oxygen gas, $C_{p_{O_2}}$ is the specific heat capacity of the oxygen stream calculated as a function of temperature, T_{O_2} is the temperature of the gaseous oxygen as it enters the liquefaction subsystem from the heat exchanger, and T_{bp} is the boiling point of oxygen. The boiling point of oxygen is calculated as a function of inlet pressure using the Antoine Equation and constants from the National Institute of Standards and Technology (NIST) [168] as:

$$T_{bp} = \frac{B}{A - \log_{10} P} - C \tag{62}$$

The power required to phase change the oxygen from a gas to a liquid at its boiling point is given by:

$$Q_{liq} = \dot{m}_{O_2} H_{latent} \tag{63}$$

where H_{latent} is the latent heat of condensation of oxygen. The total heat that must be removed from the oxygen by the cryocooler is then calculated as:

$$Q_{O_2} = \dot{m}_{O_2} C_{p_{O_2}} \left(T_{O_2} - T_{bp}\right) + \dot{m}_{O_2} H_{latent} \tag{64}$$

Heat from the external environment that enters the liquid oxygen tank adds a third quantity of heat that must be removed. This yields the final calculation for the heat that must be removed by the cryocooler:

$$Q_{cc} = \dot{m}_{O_2} C_{p_{O_2}} \left(T_{O_2} - T_{bp}\right) + \dot{m}_{O_2} H_{latent} + Q_{leak,tank} \tag{65}$$

Downstream of the cryocooler, the radiator must reject the heat removed from the cryocooler given by Equation (65), the input power to the cryocooler (Equation (65) divided by the efficiency of the cryocooler), and any heat leaks from the environment through the piping insulation.

$$Q_{sys} = Q_{cc} + \frac{Q_{cc}}{\eta_{cc}} + Q_{leak,pipe} \tag{66}$$

The overall efficiency of the cryocooler is set at 10% based on literature values, including a study of oxygen liquefaction on Mars conducted by NASA [103]. As a result, 500 W of cooling power requires an electrical input power of 5000 W. Both $Q_{leak,tank}$ and $Q_{leak,pipe}$ are calculated as a function of the insulation thickness around the MAV tank and transfer piping, respectively. An increase in insulation thickness will therefore result in a decrease in system power by minimizing heat leaks but an increase in insulation system mass. In this way, the optimizer trades system mass with system power to find an optimal design solution.

Radiator Heat Transfer

The radiator for the liquefaction subsystem rejects heat through radiation and convection, with radiation having a larger effect. A heat balance is used to calculate the required radiator area size.

Heat sources include the heat from the fluid passing through the radiator, Q_{sys}, and incoming solar radiation, Q_{solar}. Emitted infrared radiation from the Martian surface is negligible. The quantity of heat rejected by the radiator through radiation, Q_{rad}, is defined by the Stefan-Boltzmann Law:

$$Q_{rad} = \sigma \epsilon A (T_r^4 - T_{sky}^4) \tag{67}$$

where σ is the Stefan-Boltzmann constant, ϵ is the infrared emissivity of the radiator surface (assumed to be 0.9), A is the surface area of the radiator, T_r is the surface temperature of the radiator, and T_{sky} is the sky temperature. Algebraically manipulating this equation and substituting the heat sources for Q allows one to solve for an estimated required area of the radiator:

$$A = \frac{Q_{sys} + Q_{solar}}{\sigma \epsilon \left(T_r^4 - T_{sky}^4\right)} \tag{68}$$

A simplifying assumption with this calculation is that the radiator has a constant temperature across its surface. To calculate the temperature gradient that exists across the radiator surface, the radiator was modeled as a two-component system consisting of a pipe and a fin. Temperature gradients may exist in two orthogonal directions: i) across the radiator fin and ii) along the length of the pipe. The Biot number, which is a dimensionless quantity that compares heat transfer inside a body to heat transfer at the surface of the body, can be used to determine if temperature varies across the radiator fin or if it is relatively constant:

$$Bi = \frac{h}{k} L = 0.0001 \tag{69}$$

where h is the convective heat transfer coefficient, k is the thermal conductivity of the fin, and L is the characteristic length of the fin. If $Bi \ll 1$, as it is in this case, the temperature across the fin, perpendicular to the flow of fluid, can be considered uniform.

The temperature gradient in the second direction, the path along the direction of the fluid pipe, is also calculated. Figure 95 depicts the assumption of constant temperature across the surface of the radiator in the direction of the fins as well as the non-uniform temperature along the direction of fluid flow.

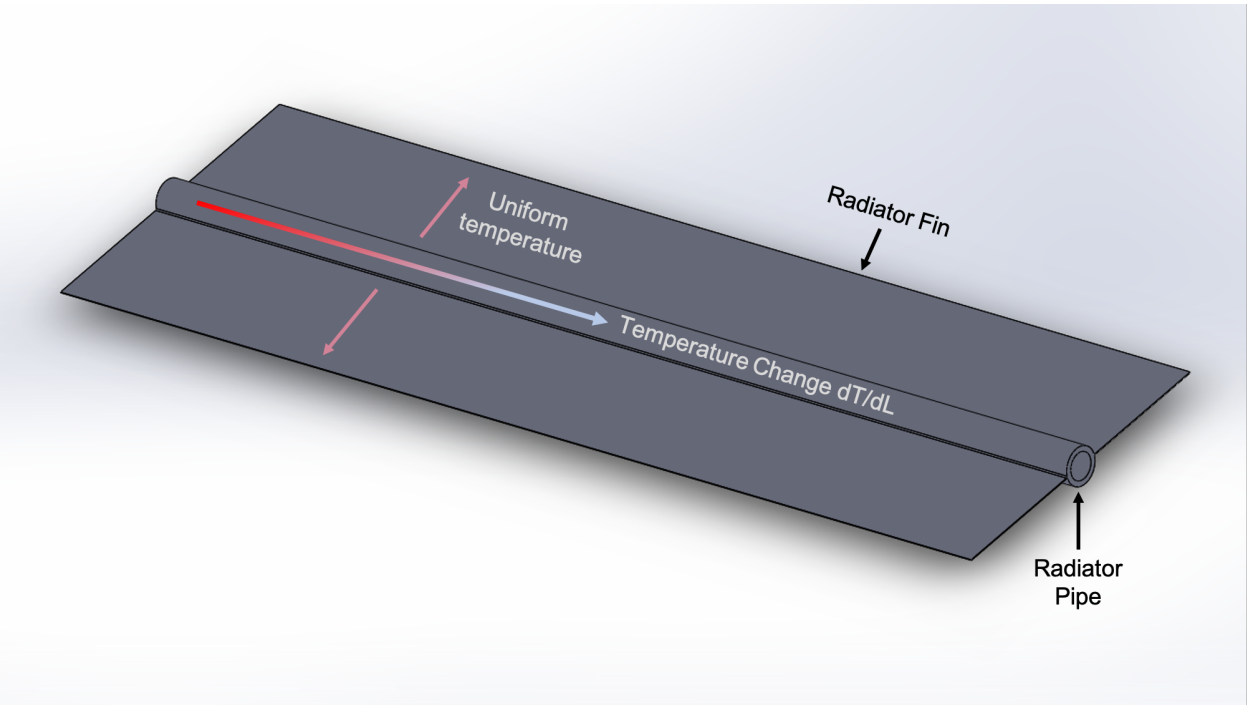

Figure 95: A section of radiator with fluid flowing along a pipe and releasing heat from grid fins to the environment via radiation and convection. The temperature is assumed to be uniform in the direction of the fins, as justified by the Biot number [159].

The heat balance for the change in temperature along the direction of the fluid pipe, $\frac{dT}{dL}$, is as follows:

$$Q_{radiation} + Q_{convection} = Q_{fluid} + Q_{solar} \tag{70}$$

The heat lost from the radiator via radiation and convection is equal to the heat lost by the fluid along the length of the radiator, represented as a temperature drop in the radiator fluid, added to the extra heat input to the radiator from solar radiation. Each of these terms can be expanded to yield the following intermediary equation:

$$\sigma\epsilon A\left(T_r^4 - T_{sky}^4\right) + hA(T_r - T_a) = -c_p\dot{m}_{\mathrm{NH_3}}\Delta T + Q_{solar} \tag{71}$$

The mass flow rate of the radiator working fluid, liquid anhydrous ammonia, was calculated using the following equation:

$$\dot{m}_{NH_3} = \rho_{NH_3} vA \tag{72}$$

where A is the cross-sectional area of the fluid pipe and v is the flow velocity, set to 2 m/s to compromise between efficiency and reliability based on Earth-based water pipe testing [169].

Equation (71) can be modified to represent heat radiated from an infinitesimal area of the radiator:

$$\sigma\epsilon\left(T_r^4 - T_{sky}^4\right)dA + h(T_r - T_a)dA = -c_p\dot{m}_{\mathrm{NH_3}}dT + Q_{solar} \tag{73}$$

To further refine the equation, the infinitesimal area of the radiator can be defined as the exposed area of the pipe and radiator fin along an infinitesimal length:

$$\sigma\epsilon\left(T_r^4 - T_{sky}^4\right)(2\pi r + 2w)dL + h(T_r - T_a)(2\pi r + 2w)dL = -c_p\dot{m}_{\mathrm{NH_3}}dT + Q_{solar} \tag{74}$$

where r is the radius of the fluid pipe in the radiator, w is the width of the radiator fin in both directions away from the central pipe, and L is the length along the radiator. w is multiplied by a factor of two to represent both sides of the radiator. $2\pi r$ represents the circumference of the radiator pipe, which is assumed to also be exposed to the ambient Mars atmosphere. Equation (74) can be rearranged to solve for the final form of the equation:

$$\frac{dT}{dL} = \frac{Q_{solar} - (2\pi r + 2w)\left[\sigma\epsilon\left(T_r^4 - T_{sky}^4\right) + h(T_r - T_a)\right]}{\dot{m}_{\mathrm{NH_3}}c_p} \tag{75}$$

This equation describes the change in temperature of the radiator surface area along the length of the fluid pipe in the radiator. This differential equation was solved using a MATLAB script, which generated the results shown in Figure 96.

Table 35: Radiator values used for temperature analysis use case. The values that were not design variables were chosen based on terrestrial radiator data.

Parameter	Value
Pipe length (m)	2
Pipe diameter (m)	0.05
Fin width (m)	0.25
Working fluid	Anhydrous liquid ammonia
Fluid density (kg/m³)	0.73
Mass flow rate (kg/s)	0.003
Flow velocity (m/s)	2.093
Coolant heat capacity (J/kg-K)	4744
Convective coefficient	1.5

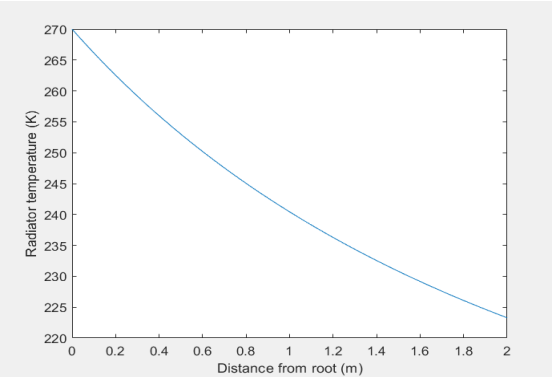

Figure 96: Radiator surface temperature along its length

In this example, the temperature drop between the inlet of the pipe and the end is approximately 50 K. This results in a 41% decrease in heat rejection compared to an idealized radiator in which the temperature of the radiator surface is constant along the length of the radiator. Clearly, it is valuable to model the change in temperature experienced by the radiator along its length as it provides a significantly more accurate estimate of the required radiator surface area and mass to satisfy the heat rejection requirement.

A MATLAB function [159] determines the dimensions of the pipe and fins needed to reject the required amount of heat from the radiator. A binary search algorithm returns the proper radiator fin dimensions.

Mass and Volume

The major components of the liquefaction subsystem that contribute to mass and volume are the cryocooler, radiator, piping, and insulation. The mass and volume of the MAV tank are not included, as the MAV tank is required for a human mission to Mars regardless of the ISRU plant design. Additional margin is added to account for other in-line components that add to mass, including valves, sensors, and the working fluid recirculation pump.

The mass of the cryocooler is calculated as a function of cooling lift, where an increase in cooling lift requires a larger and more capable cryocooler. A power regression fit on data taken from Zagarola and McCormick [164] and Meier et al. [157] is employed to calculate the BAM design cryocooler mass listed in Table 36.

Table 36: Cryocooler lift capabilities and mass from three relevant laboratory experiments (columns 2-4), with mass per unit cooling calculated as a figure of merit. The predicted mass of BAM is calculated (column 5) by extrapolating these data using a power regression fit.

Parameter	Zagarola Moderate Design	Zagarola Scaled Design	Meier Design	BAM Design
Cryocooler lift required (W)	6.3	40	400	~500
Cryocooler Mass (kg)	11.9	37	154	160
Mass per unit cooling	**1.9 kg/W**	**0.9 kg/W**	**0.39 kg/W**	**0.32 kg/W**

Using these numbers and fitting a power law to the mass per unit cooling as a function of cryocooler lift, an estimate for the mass per unit cooling of BAM is obtained. For a lift of approximately 500 W, the system specific mass is 0.32 kg/W, resulting in a cryocooler mass of 160 kg. These numbers serve as an example; the mass of the BAM cryocooler is calculated with each simulation as a function of the power regression law and cryocooler lift required. The cryocooler volume is calculated in the same way. It is notable that the cryocooler used by Meier et al. in 2018 was a commercial off the shelf (COTS) unit. This, therefore, represents a conservative estimate of mass per unit cooling, as COTS components typically experience a significant reduction in mass when optimized for space applications.

The mass of the radiator is calculated by multiplying the volume of material used in the radiator design by the density of the materials. As discussed in the previous section, the fluid pipes are made of aluminum, while the radiator fins are made of a carbon-carbon composite. The length of pipe and dimensions of the fins are adjusted by the optimizer with each simulation to minimize objective functions. The radiator size varied across simulations, but typically had a surface area of ~4 m^2 and a mass of ~65 kg.

The volume and mass of the piping are calculated with the known lengths, diameters, and thicknesses of the piping. The pipe is made of aluminum, which offers adequate heat transfer capabilities, lower mass than other piping materials, and matches the thermal expansion and contraction of the MAV tank to which it is affixed, if the MAV tank is made of aluminum. The insulation on the piping is calculated in a similar manner to the piping, though the thickness of the insulation is a design variable that is adjusted by the optimizer with each simulation.

4.6 Heat Exchanger Subsystem

The heat exchanger is another central component to the BAM design, as it has the ability to significantly reduce power requirements by recuperating heat. A heat exchanger can be used to transfer heat between the cold CAC outlet stream and the hot SOE outlets streams. This provides benefits for both streams; the CAC stream must be heated to the SOE operating temperature and thus benefits from increasing in temperature in the heat exchanger, and the hot SOE oxygen stream must be cooled for liquefaction and thus benefits from a decrease in temperature. The hot cathode exhaust from the SOE is also used to increase the temperature of the CAC outlet stream in the same heat exchanger. Counterflow heat exchangers are efficient devices that can be used to transfer heat between gas streams. In doing so, the power required to pre-heat the CAC outlet stream and the power required to cool and liquefy the oxygen stream are reduced. An increase in heat exchanger area therefore presents a tradeoff between an increase in system mass and a decrease in system power.

Several types of heat exchangers were considered in the design of BAM. The shell and tube heat exchanger, which consists of a series of pipes contained within an outer shell, is the most common form used in the chemical industry. However, Plate Heat Exchangers (PHEs) have increased in use in recent years. PHEs have several advantages over other heat exchangers, including a more compact design and lower mass. The primary advantage of a PHE is its inherently high efficiency, owing to a high thermal contact area that results from the plates being pressed together, as well as corrugations on the plate surface that induce turbulent flow, which further increases heat transfer. For these reasons, the BAM heat exchanger follows a PHE architecture.

4.6.1 Design

PHEs consist of a stack of plates, each of which has channels to allow a fluid to flow through it. The two fluids that are exchanging heat occupy every-other plate such that one fluid is sharing heat with the other fluid via both adjacent plates. The BAM heat exchanger is shown in Figure 97, with a deconstructed view of two plates and the frame shown in Figure 98.

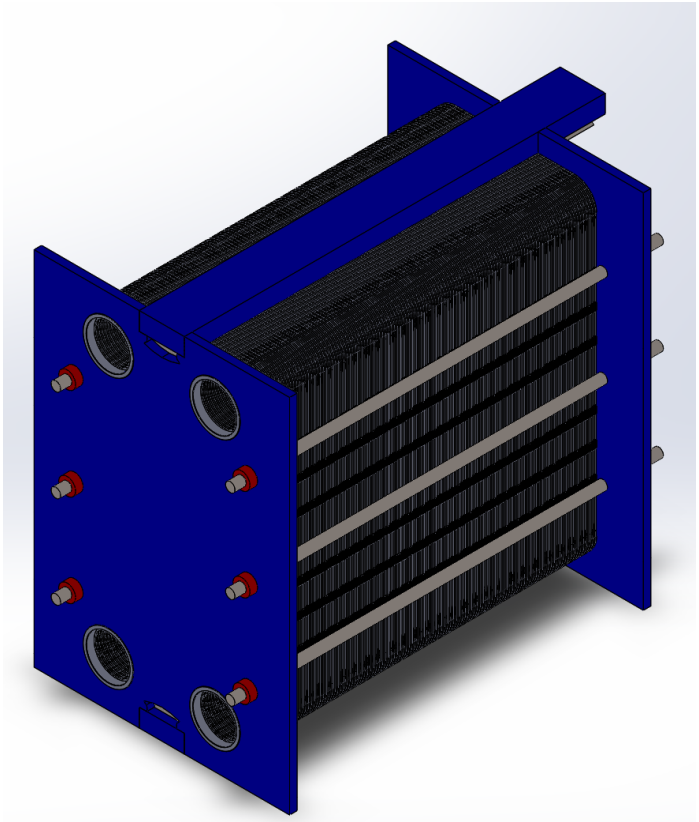

Figure 97: Plate heat exchanger on BAM, used to recover waste heat to minimize system power consumption [128]

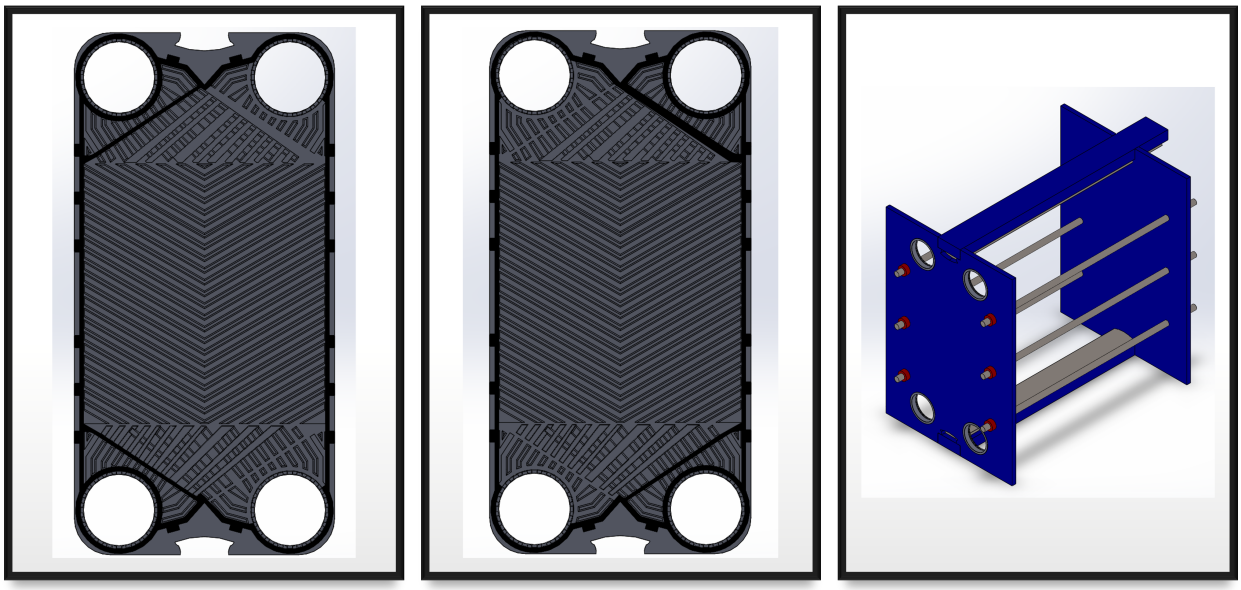

Figure 98: (Left, middle) BAM plate heat exchanger plates with gaskets in opposing directions to allow two different fluids to flow, one per plate; (right) heat exchanger frame [128]

The hot fluid – which, in the case of BAM, is either hot cathode exhaust or hot anode exhaust, depending on the heat exchanger – flows through every second plate in the stack. The cold fluid – which, in the case of BAM, is the compressor exhaust before it enters the SOE – flows through

the remaining plates. Directional gaskets ensure that the two fluids do not mix, and heat is exchanged between every sandwiched pair of plates as both fluids flow across the heat exchanger. The paths of the hot and cold fluids are depicted in Figure 99.

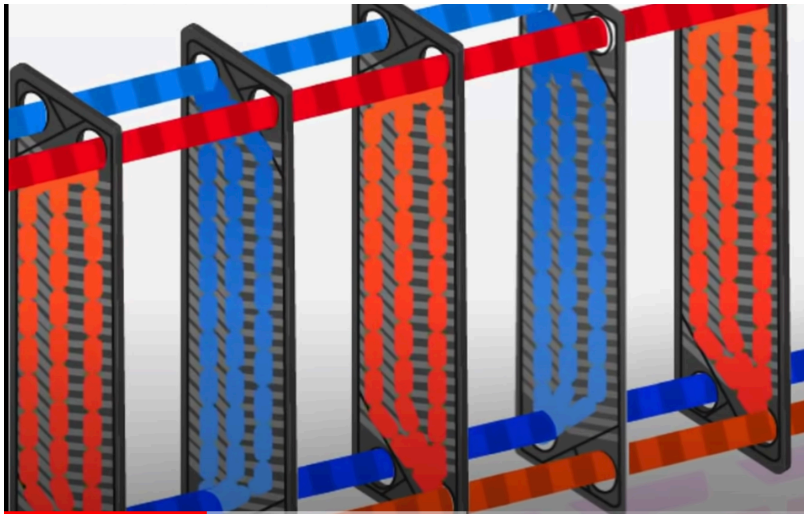

Figure 99: Exploded view of a PHE, showing the hot and cold fluids flowing across every other plate in the stack

The BAM heat exchanger is a counter flow heat exchanger, which is the most effective at heat transfer in a compact space. Other design options that were discarded included parallel flow and cross flow geometries.

The cooling capacity of the BAM PHE can be changed by adding or removing plates and adjusting the flow rate.

Potential Issues

Typical PHEs would not be operational at the temperature extremes experienced by the PHE used in BAM. The rubber gaskets that are typically used on each plate would have the potential to fail at both the high temperatures (800 °C) and low temperatures (Mars ambient) experienced in the heat exchanger. Rather than use rubber gaskets, BAM uses a welded PHE design, which allows for higher temperatures and pressures [170]. Inconel is used as the primary material of construction owing to its high melting point, strength, and chemical resistance. It has a low thermal conductivity compared to copper, but a similar thermal conductivity compared to stainless steel and titanium. Unfortunately, copper cannot be used due to potential of the temperatures involved in BAM's operation to approach the melting point of copper.

Another initial cause for concern that had to be addressed was the pressure drop experienced in gas-gas PHEs. Typical PHEs have small channels in the plates, causing gases with high velocities to experience significant pressure drops and thus limit the usability of the heat exchanger. To prevent this, a modified PHE with expanded channel sizes is used on BAM to minimize the pressure drop while maintaining the compact form that makes PHEs desirable for this application.

PHEs are also more expensive than other heat exchanger options. For a space application, particularly one that would likely be part of a flagship mission, this is an acceptable trade for the benefits provided by a PHE.

Lastly, if high temperature O_2 from the anode and CO from the cathode were to accidentally mix in the heat exchanger from a leak, the metal plates could act as a catalyst for the CO to combust, causing a fire or explosion. This is naturally mitigated by using two separate heat exchangers to keep the anode and cathode exhaust streams separate. One heat exchanger will exchange heat between O_2 and the Mars atmosphere, which is primarily CO_2. The second heat exchanger will exchange heat between a CO/CO_2 mix from the cathode and the Mars atmosphere.

4.6.2 Modeling

To model the heat exchanger, the *effectiveness-NTU (Number of Transfer Units)* method was employed. This is an iterative approach to solving the outlet temperatures of the heat exchanger and the heat exchanged between gas streams when only the inlet temperatures, mass flow rates, and gas compositions are known [171]. The *effectiveness* of a heat exchanger is defined as the ratio of the actual heat transfer rate to the maximum possible heat transfer rate:

$$\epsilon = \frac{q}{q_{max}} \tag{76}$$

q_{max} is the heat transfer rate that would occur in an infinitely long counterflow heat exchanger where the fluid with the lower specific heat capacity rate (defined as $C_j = \dot{m}_j c_{p,j}$) achieves the maximum possible temperature difference, $T_{h,i} - T_{c,i}$. Therefore, q_{max} is:

$$q_{max} = C_{min}\left(T_{h,i} - T_{c,i}\right) \tag{77}$$

where $C_{\min}$ is the lower heat capacity rate between the two streams, h is the hot stream, c is the cold stream, and i specifies an inlet stream. The actual heat transfer rate is solved by rearranging and combining Equations (76) and (77) to yield:

$$\boldsymbol{q = \epsilon C_{min}\left(T_{h,i} - T_{c,i}\right)} \tag{78}$$

The only unknown is ϵ, which can be solved for as a function of the heat capacity rate ratio, $C_r \stackrel{\text{def}}{=} \frac{C_{min}}{C_{max}}$, and a dimensionless parameter common in heat exchanger analysis, the NTU. The NTU is defined as:

$$NTU \stackrel{\text{def}}{=} \frac{UA_{HE}}{C_{min}} \tag{79}$$

Where U is the overall heat transfer coefficient, and A_{HE} is the area of the heat exchanger. ϵ is a function of NTU and C_r for all types of heat exchangers. For a counter-flow heat exchanger, ϵ is calculated as [171]:

$$\epsilon = \frac{1 - \mathrm{e}^{-\mathrm{NTU}(1-\mathrm{C_r})}}{1 - C_r \mathrm{e}^{-NTU(1-C_r)}} \qquad (C_r < 1) \tag{80}$$

$$\epsilon = \frac{NTU}{1 + NTU} \qquad (C_r = 1) \tag{81}$$

For a counter-flow heat exchanger, the effectiveness approaches its maximum value of 1 with approximately 5-10 NTUs, depending on the specific heat capacity ratio. Equation (80) can be used to solve Equation (78) for the actual heat transfer rate of the two fluids in the heat exchanger.

q represents the heating and cooling heat load saved with the heat exchanger. Multiplying this value by two to capture both the heating and cooling savings results in the net heat load saved by the heat exchanger:

$$P_{HE} = 2 * q \tag{82}$$

This quantity represents the reduction in power *requirement* achieved by the heat exchanger. In practice, a power savings several times the value of P_{HE} will be realized due to inefficiencies in the heating and liquefaction units.

Finally, the outlet temperatures of both the hot and cold streams can be calculated by rearranging the following equation:

$$q = \dot{m}_j c_{p,j} (T_{j,i} - T_{j,o}) \tag{83}$$

for each case of the hot (h) and cold (c) streams to yield:

$$T_{h,o} = T_{h,i} - \frac{q}{\dot{m}_h c_{p,h}} \tag{84}$$

$$T_{c,o} = T_{c,i} + \frac{q}{\dot{m}_c c_{p,c}} \tag{85}$$

The objective function equations are summarized in Table 37. These are key modeling outputs that drive the optimization algorithm. The details for the mass and volume calculations can be found in Appendix B.

Table 37: Summarized equations of key objectives for the heat exchanger subsystem.

Objective	Equation	Units
Power (Saved)	$P_{HE} = 2 * \left(\frac{1 - \mathrm{e}^{-\frac{UA_{HE}}{C_{min}}(1-\mathrm{C_r})}}{1 - C_r \mathrm{e}^{-\frac{UA_{HE}}{C_{min}}(1-C_r)}} \right) C_{min}(T_{h,i} - T_{c,i}) * A_{HE}$	W
Mass	$M_{HE} = \rho w l * (N_p t_p + h)$	kg
Volume	$V_{HE} = w l * (N_p t_p + h)$	m^3

4.7 Power Subsystem

The power system consists of several 10 kWe Kilopower systems arranged in an array at an acceptable distance from the habitat to mitigate radiation concerns for the crew. An example of how this might look is shown in Figure 100.

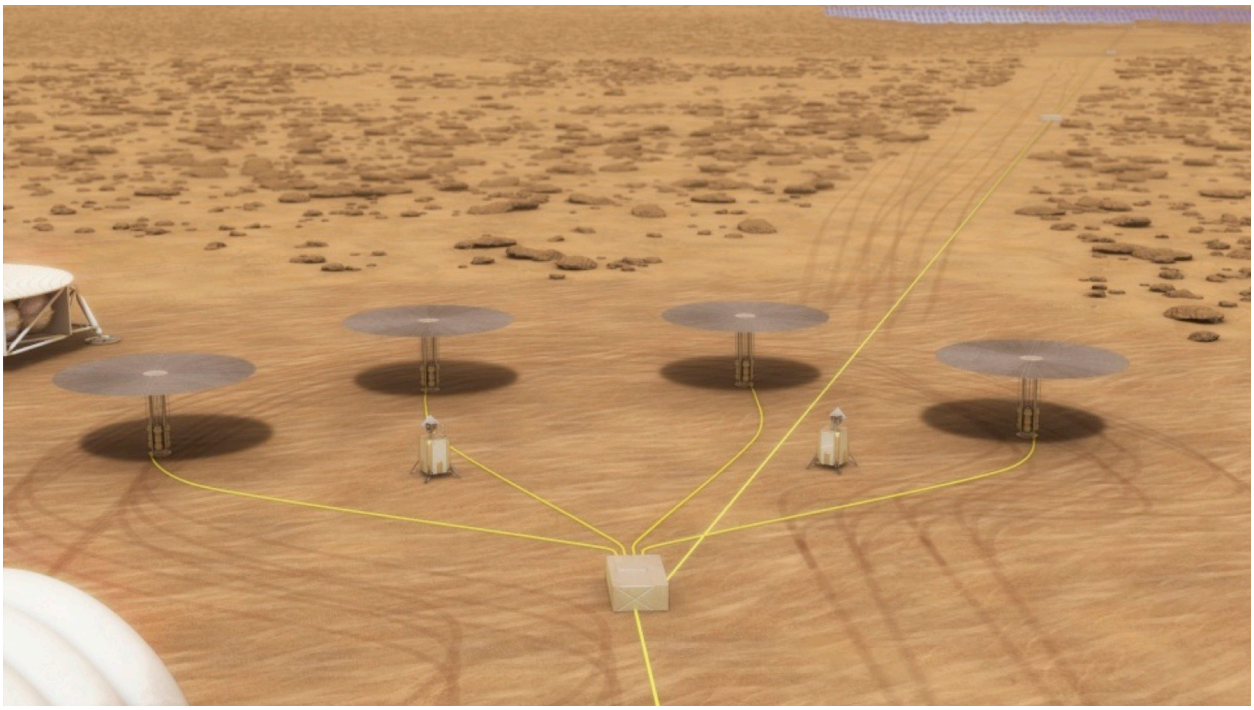

Figure 100: Four Kilopower units in an array to provide nuclear power to the ISRU system (Credit: NASA). Power lines connect each Kilopower unit to a power processing unit, which distributes power to systems in two directions.

The Kilopower project between NASA and several collaborators is an experimental study aimed at developing nuclear fission power systems for planetary missions. Uranium is used as a fuel that generates heat, which is converted to electricity using Stirling cycle converters. Kilopower reactors are expected to be developed in multiple sizes, ranging from 1 kWe to 10 kWe. The 10 kWe unit is expected to have a mass of approximately 1500 kg, a diameter of 1.5 m and a height of 3.3 m [108]. The volume was calculated from these dimensions for use in the BAM model. A substantial amount of heat is rejected from the radiators on top of each Kilopower unit. While it is not considered in this design due to the complexity of laying long heat pipes, this heat could be captured and used to improve the efficiency of future iterations of this ISRU system.

4.8 Gas Flow Modeling

Several gas streams are present in the BAM system: the inlet gas stream from Mars, the oxygen stream from the anode outlet of the SOE system, and the mixed gas stream from the cathode outlet of the SOE system. To track the characteristics of these gas streams throughout the system, numeric labels were given to each significant location in the system. These are shown in Figure 101.

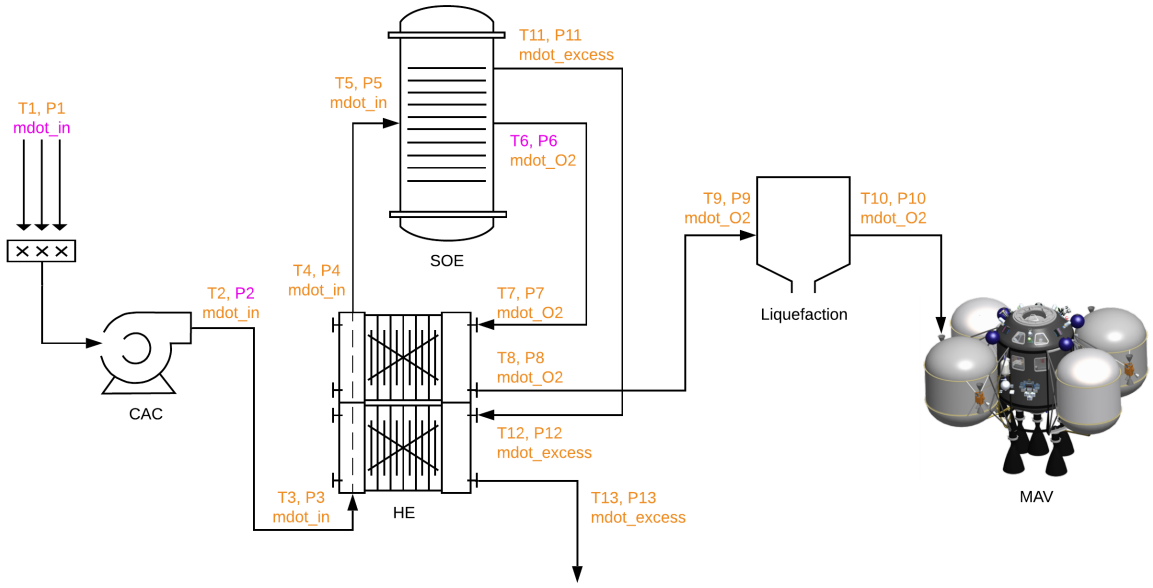

Figure 101: ISRU system overview with subsystem entrance and exit points labeled numerically.

The locations, marked as numbers 1 – 13, are placed in positions at the entrance and exit of every major subsystem. For example, position 2 (represented by "T2" and "P2" in the figure) is placed at the exit of the CAC subsystem. The gas at this location has a Mars atmosphere composition, a pressure and temperature defined by the CAC system, and a mass flow rate determined by the optimizer.

Several important gas characteristics were calculated at each of these positions: pressure, temperature, density, velocity, and specific heat capacity. The calculations for these variables, including changes for each in piping segments, are described in Appendix B.1.

4.9 Risk Modeling

One of the objective functions that the optimizer attempts to minimize is risk. In space missions such as this, two categories of risk emerge: operational risk and programmatic risk. Operational risk refers to the actual operation of hardware and software during the mission, from failure rates of individual components to those of integrated systems. Programmatic risk, on the other hand, encompasses risks of budget overruns, schedule slippage, and personnel movement, among others. For this dissertation, it is only appropriate to consider operational risk, as programmatic risk is difficult to predict and model accurately. Operational risks can be predicted and modeled using typical component lifetimes, known degradation rates, and other experimental data.

A qualitative or quantitative approach can be taken when modeling risk. Qualitative methods include Failure Mode and Effect Analysis (FMEA) and Risk Matrices. Risk matrices typically combine a likelihood of failure with a severity of failure to prioritize risk reduction efforts. The risk matrix is useful for identifying individual risk contributors. One of the limitations of qualitative methods like risk matrices is that they may fail to characterize the robustness of the system as whole. They do not calculate cumulative risk, nor do they calculate the relative cumulative risk of individual contributors [172]. Quantitative risk analysis methods provide an

avenue by which risks can be explored and characterized, from individual components to complex interactions within the system.

Quantitative Risk Analysis (QRA), also called Probabilistic Risk Assessment (PRA), was first conducted on a large-scale, complex system approximately 50 years ago in the nuclear power industry [173]. Since that time, PRA has become more widely adopted in other industries, including space systems. NASA began to implement PRA after the Challenger accident. Prior to the accident, NASA primarily assessed risks qualitatively via hazard analysis and failure mode and effects analysis (FMEA). However, in the aftermath of the Challenger event, NASA committed itself to a more robust safety program, establishing the Office of Safety, Reliability, Maintainability and Quality Assurance (now called SMQ) and defining requirements for a quantitative risk analysis approach for its major programs [174,175].

To determine if a PRA could be used to identify high-risk areas that a traditional, qualitative approach could not, NASA conducted a pilot study on the auxiliary power units (APUs) of the Shuttle [176]. The PRA enabled NASA to discover several important failure scenarios that had not been identified in previous analyses and determine that only a small number of items contributed to most of the shuttle failure risk. This created new critical path items while also allowing NASA to focus on a fraction of the total risk items that had been identified by previous qualitative analyses. A PRA framework is used in this study to identify and quantify risks. This, in turn, is modeled and enables risk to be used by the Simulated Annealing optimization algorithm as an objective function to minimize.

PRA is a top-down approach that is used to answer three questions: (1) what can go wrong? (2) how likely is it that it goes wrong? (3) what are the consequences? According to Apostolakis [177], a PRA proceeds as follows:

1. A set of *end states* is defined that represent consequences of a failure (e.g., loss of crew, loss of mission, etc.)
2. For each end state, a set of *initiating events* (IEs) is developed that could lead to the end state.
3. *Fault trees* are employed to identify sequences of events that begin with an IE and end with an end state. Each path on the fault tree is considered an *accident scenario*.
4. The probabilities for each accident scenario are evaluated using available data and expert judgment.
5. The accident scenarios are ranked by their expected frequency to inform a risk mitigation strategy.

A common critique of all methods of quantifying risk is that it requires too many assumptions. Step #4 can be subjective and difficult to justify. One mitigation strategy is to have independent experts conduct a peer review on the probabilities listed in step #4. The first PRAs in the nuclear industry held such reviews [178, 179], as did NASA's QRA for the International Space Station [180]. In addition, where available, quantitative engineering analyses, relevant test data, and near miss events can be used when assigning probabilities in PRA.

A key finding from many institutions employing PRAs is that estimates should not be made conservatively when assigning values to probabilities and consequences. If they are, the end

results of the PRA will be meaningless. This is what happened in the Apollo program; overly-conservative quantitative analysis assumptions led to unacceptably high predictions of failure. In response, NASA discarded the results of the quantitative analyses and instead moved towards more qualitative methods [181].

With this information, the following ground rules and assumptions are established for this PRA:

1. The scope of this risk assessment includes only operational risk; programmatic risk is ignored.
2. The scope of this risk assessment is confined to the boundary of this extensibility design, considering all components post-filtration of the Mars atmosphere through the oxygen liquefaction step. It also includes the Kilopower nuclear reactor units that power the ISRU system. It does not include filtration or long-term storage of liquid oxygen in the MAV tank.
3. Probabilities of failure are assigned based on known data and expert judgment.

Piyush Khopkar, member of the MOXIE Science Team, contributed significantly to the risk analysis for this dissertation.

4.9.1 Identification of Risks

The first step in conducting a PRA is the identification of end states and initiating events (IEs) that create risk scenarios. A *scenario* is a sequence of events that begins with an IE and leads to an undesirable end state. The initiating event could be a hardware, software, or process malfunction or failure. The end state could include loss of ISRU system, partial loss of oxygen production, and loss of liquefaction ability, among others. All end states can be combined into a single, over-arching end state in this case: loss of mission, resulting from any failure or series of failures that render the ISRU plant incapable of producing the minimum quantity of oxygen required to fuel the MAV in the allocated length of time.

IEs were considered for all components in the design. Table 38 lists all IEs that could result in a loss of mission.

Table 38: Initiating Events (IEs) that could lead to a loss of mission

Initiating Event	Subsystem	Description
Cryopump blower fan malfunctions	CAC	A blower fan on the cryopump moves Martian atmospheric gas into the cryopump chamber. If the fan fails, CO_2 will not be collected at a sufficient rate to enable the required oxygen production.
Sorption pump blower fan malfunctions	CAC	A blower fan on the sorption pump moves Martian atmospheric gas into the sorption chamber. If the fan fails, CO_2 will not be collected at a sufficient rate to enable the required oxygen production.
Sorption cooling/heating/feed lines fail	CAC	The microchannel sorption pump consists of hundreds of individual sorbent beds, each with their own heating, cooling, gas inlet, and gas outlet systems. This level of complexity, combined with the thousands of thermal

		cycles the system will experience, could lead to several failure states.
Cryocooler fails	CAC	The cryocooler could fail for several reasons, including failure of the turbo Brayton cycle components (compressor, expander, shaft, working fluid pump), a loss of working fluid, or failed cartridge heaters. If the cryocooler fails, there will be no ability to liquefy and store the oxygen. This is relevant to the cryopump, sorption pump, and liquefaction subsystem.
Mechanical pump failure	CAC	The exact mechanism of mechanical pump failure is dependent on the type of pump chosen but will likely be related to moving parts within the pump degrading or failing.
Nernst voltage exceeded, causing coking of electrolytes	SOE	If the operating voltage of an individual solid oxide electrolysis cell exceeds the Nernst potential of that cell in the given operating environment, carbon may deposit on the cell. This increases the cell's iASR, resulting in a decrease in performance. If enough cells experience this coking, the system may be unable to produce the required quantity of oxygen.
Mechanical failure of electrolyte cells	SOE	Electrolyte cells and their seals could fail mechanically. Cracking of cells could result from over-compression from the SOE stack housing, launch and landing vibrations, or a large pressure differential between the cathode and anode of the cells. Cracked cells will either be unable to produce oxygen or will produce oxygen at a decreased rate, depending on the nature of the mechanical failure.
Mechanical failure of SOE stack	SOE	The SOE housing is under compression and undergoes thermal cycling. It also must survive launch and landing. As the number of cells per stack is increased, the risk of mechanical failure of the SOE stack increases.
Heater Failure	SOE	If the pre-heaters or cartridge heaters used to warm and maintain the temperature of the gas as it passes through the SOE system fail, the gas may not achieve a sufficient minimum temperature to enable oxygen production.
MAV Tank Over-pressurizes	Liquefaction	If the pressure of the tank exceeds a maximum threshold, a catastrophic failure of the system could occur. The tank pressure may increase for several reasons, including a loss of cooling capability or a failed vent.
Kilopower Unit Failure	Power	If a Kilopower unit fails to produce the expected amount of power, the ISRU system may not receive sufficient power to produce the required oxygen.
Valve Failure	All	Most subsystems utilize solenoid valves that control the flow of fluid. If a valve fails open or fails closed, the system could experience a critical failure.

Similarly, the Fault Tree Diagram in Figure 102 shows these IEs as part of accident scenarios leading to a loss of mission end state.

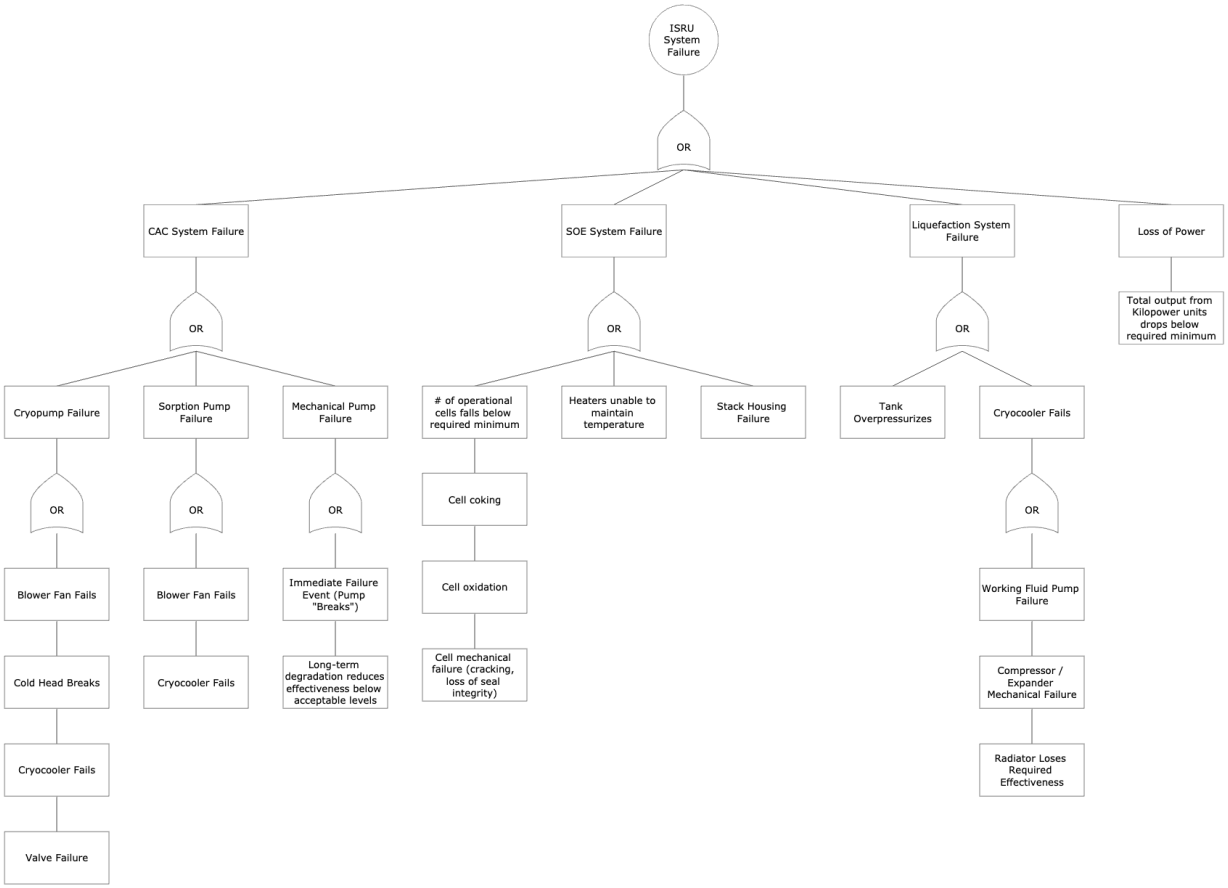

Figure 102: Fault Tree Diagram showing initiating events and their path to causing a loss of mission end state. "Or" blocks indicate that any of the failures that feed that block will result in a failure of the next level up.

In terrestrial systems, several safeguards typically exist to prevent the end state from occurring if one component of the process fails. This is also true for BAM. Table 39 describes safeguards employed to mitigate the risk of each of the IEs above.

Table 39: Mitigation measures employed in ISRU plant design to minimize risk of initiating events resulting in a loss of mission end state.

Initiating Event	Subsystem	Mitigation Measures
Cryopump blower fan malfunctions	CAC	Lower inlet flow rate, redundancy
Sorption pump blower fan malfunctions	CAC	Lower inlet flow rate, redundancy
Cryocooler fails	CAC	Lower cooling load required, redundancy
Mechanical pump failure	CAC	Lower inlet flow rate, redundancy
Nernst voltage exceeded, causing coking of electrolytes	SOE	Redundant cells, redundant stacks, smart control system to detect rising iASR, voltage limits, electrically isolate every five cells so entire stack is not affected by one failed cell
Mechanical failure of electrolyte cells	SOE	Increase electrolyte thickness, decrease pressure differential across the cells
Mechanical failure of SOE stack	SOE	Redundancy, decrease number of cells per stack
Heater Failure	SOE	Redundancy
MAV Tank Over-pressurizes	Liquefaction	Pressure control, relief valve
Kilopower Unit Failure	Power	Redundancy
Valve Failure	All	Redundancy

These safeguards are modeled and factor into the calculations of failure rates for each subsystem, which are described in more detail in the following section.

4.9.2 Quantification of Risks

After identifying initiating events and organizing them in a fault tree, the next step in a PRA is to assign probabilities to each event. The probability of failure of the entire system can be determined if probabilities for each IE are known. Another important step in the optimization process is to consider the effect of spares when calculating probabilities of failure. The baseline assumption is that a system with redundancy has a lower probability of failure than the same system without redundancy, at the cost of an increased mass and volume.

A Poisson distribution was used to calculate the probability of failures and the effects of redundancy on each subsystem responsible for an IE. This is a discrete probability distribution that describes the probability of a sequence of events happening over an interval of time. The event frequency and length of time must be specified. In the case of risk quantification, the event frequency, λ, is the number of failures of a component that take place, which is equal to one divided by the mean time between failures (MTBF) of that component:

$$\lambda = \frac{1}{MTBF} \tag{86}$$

A Poisson distribution is a relevant modeling tool if the occurrence of one event does not impact the probability that a second event will occur. This is largely true throughout the system; for

example, if a primary pump and a backup pump are sent to Mars, the failure of the primary pump from excessive wear should not impact the likelihood that the second pump, once brought online to replace the primary, will fail. An exception to this assumption is if a component fails due to a design flaw that could affect the primary and backup units.

Another criterion when using the Poisson distribution is that the system must use "dry spares", or standby redundancy, as opposed to "wet spares" or active redundancy. In the standby redundancy case, a backup unit is kept offline until the primary fails, at which point it is brought online to replace the primary. In the active redundancy case, both units operate simultaneously from the start of the mission, with one contributing useful work to the system and the backup running in place until a need arises for it to be connected to the system as a replacement. The use of active redundancy would, in many cases, result in an unacceptable consumption of power. For example, if two pumps are sent to Mars but only one is needed, it would use twice the necessary power to have both running in an active redundancy configuration. Therefore, all spares in this system are assumed to be dry spares, turned off until they are needed.

The cumulative distribution function (CDF) of the Poisson distribution can be used to calculate the reliability of a component and its backups. The CDF calculates the probability of sequential failures of a system with standby redundancy. Using the CDF, the reliability for a system where *m* of *n* units must be functioning at the end of the mission is calculated as follows [182]:

$$R_{m-of-n} = e^{-m\lambda t} \sum_{k=0}^{n-m} \frac{(m\lambda t)^k}{k!} \tag{87}$$

where λ is the failure frequency and t is the length of the mission. Reliability, in this case, is defined as unity minus the probability of failure of the system. It follows that the probability of failure of the component, i, and its backups is:

$$P_{f,i} = 1 - R_i \tag{88}$$

Example

As an example, consider a blower fan sent to Mars to push CO_2 through a cryopump over a 14-month (10,080-hour) mission. Experience on the ISS has demonstrated that the MTBF for a space-rated blower fan is 129,700 hours [183]. Using Equations (86) and (87), the CDF can be calculated as:

$$R_{m-of-n} = e^{-m\left(\frac{1}{129{,}700}\right)(10{,}080)} \sum_{k=0}^{n-m} \frac{\left(m\left(\frac{1}{129{,}700}\right)(10{,}080)\right)^k}{k!} \tag{89}$$

For an *m* of one, meaning that one blower must always be operational, this yields the following CDF as a function of *n* units:

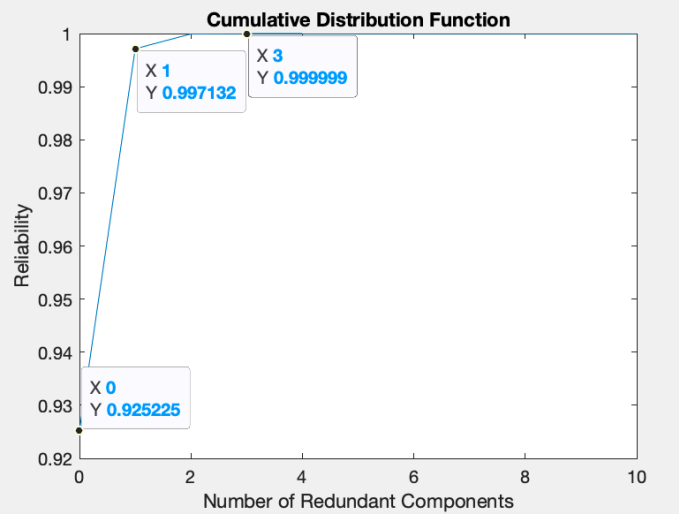

Figure 103: Cumulative Distribution Function results for a blower fan. Number of redundant blower fans is on the x-axis, while the reliability of the blower fan system, including any spare units, is on the y-axis.

Figure 103 indicates that with a single blower fan (zero redundant units), the system has a 92.5% reliability, or a 7.5% chance of failure. That reliability increases to 99.7% when one stand-by redundant unit is added, and 99.9999% when three stand-by units are added. This can be shown mathematically by considering a 1-of-2 case of Equation (89), where one blower must always be functional and two are sent to Mars:

$$R_{1-of-2} = e^{-1\left(\frac{1}{129{,}700}\right)(10{,}080)} \sum_{k=0}^{2-1} \frac{\left(1\left(\frac{1}{129{,}700}\right)(10{,}080)\right)^{k}}{k!} = 0.997 \tag{90}$$

Limitations

Limitations exist when using these methods to calculate the reliability of a component. First, the MTBF is reliant on data from similar, but not identical, systems. This leaves margin for error, as it is likely that the true MTBF is unknown for almost every component in the system. Second, the Poisson distribution is an exponential distribution model that assumes a constant failure rate over a given amount of time, which may not represent reality. In general, the probability of failure of a component calculated with this method increases over time, yielding a probability of failure curve with the following shape:

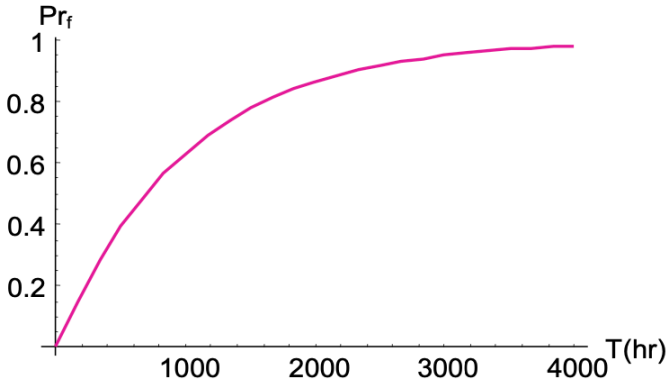

Figure 104: Generic shape of probability of failure of a component or subsystem versus time

This precludes the possibility that there may be an increased probability of failure at the start of the mission from bringing the equipment online. Along the same lines, the equipment may change over time and thus have a variable failure rate throughout its lifetime. A scroll pump, for example, is known to gradually wear down its tip seals over time, eventually resulting in a tip seal leak. Thirdly, the generic CDF formula used to calculate reliability does not consider any design variables used in this simulation. This latter point is addressed by modifying the CDF to incorporate design variables such as mass flow rate of gas, temperature of the SOE unit, pressure output of the CAC, and more. These modifications allow the Simulated Annealing algorithm to optimize reliability in the system as a function of the BAM design variables and are described in the following section.

4.9.3 Modeling of Risk

Using the methodology described above and a set of input data from past space missions and terrestrial analogues, the reliability of each component can be calculated. From there, the reliability of each subsystem can be calculated, and, ultimately, the reliability of the entire atmospheric ISRU plant. It is important to note that data from past space missions and terrestrial analogues are not necessarily relevant to Mars, as the Mars operating environment is different. These data are, however, the best available and therefore are used as discussed below.

Inputs

Two primary inputs are required to form the desired reliability calculations: mission length and MTBF for each component. The mission length is a parameter in this design, set to 14 months. This translates to 10,080 hours and is kept as a constant equal to this value for all reliability calculations. Table 40 lists the MTBF for each relevant component in the system, together with their sources.

Table 40: Mean Time Between Failures (MTBF) for each relevant component in the ISRU plant design

Subsystem	Component	MTBF (h)	Source
CAC	Blower Fan	129,700	[183]
CAC	Mechanical Pump	46,800	[184]
Many	Valve	300,000	[183]
SOE	Cell	15,000	[185]
Heat Exchanger	Heat Exchanger	219,000	[186]
Liquefaction	Cryocooler	129,700	[183]
Power	Kilopower Reactor	175,200	[109]

Modification of CDF with Design Variables

Certain component reliabilities are dependent on the design variables in this optimization. For example, the reliability of a pump may be dependent on how fast the pump is spun; higher spin rates will increase the wear on the system over a long period. These dependencies are factored into the BAM risk assessment model by modifying the Poisson CDF equations to incorporate design variables. In this way, reliability is more accurately calculated and, importantly, the optimizer can trade reliability against other objective functions (power, mass, and volume) by adjusting these design variables. An example of a risk equation modified with a design variable

is shown and described below, followed by a table summarizing the remainder of the modified equations and their design variable dependencies.

The reliability of the blower fan used in both the cryopump and the sorption pump is calculated as a function of inlet flow rate. A higher inlet flow rate will result in higher speed requirements from the blower fan, which will decrease its longevity. The original reliability calculation for the blower fan was provided earlier in Equation (89), which included an implicit assumption about the flow rate. Assuming that the baseline flowrate for which that equation was true was $\dot{m}_{in,o}$, the equation can be modified to include any value of flowrate, $\dot{m}_{in}$. This results in a pair of equations based on the relationship between $\dot{m}_{in}$ and $\dot{m}_{in,o}$, which has the following logic:

If $\dot{m}_{in} \leq \dot{m}_{in,o}$,

$$R_{blower} = R_{blower,o} + \left(1 - R_{blower,o}\right)\left(\frac{\dot{m}_{in,o} - \dot{m}_{in}}{\dot{m}_{in,o}}\right)^{\frac{1}{b}} \tag{91}$$

Otherwise, if $\dot{m}_{in} > \dot{m}_{in,o}$,

$$R_{blower} = R_{blower,o} - R_{blower,o}\left(\frac{\dot{m}_{in}}{\dot{m}_{in} + \dot{m}_{in,o}}\right)^{\frac{1}{c}} \tag{92}$$

where $R_{blower,o}$ is the original Poisson-based reliability calculated in Equation (89) and b and c are exponential constants that tune the effect of the design variable on the component's reliability. The values for b, c, and the baseline design variable $R_{i,o}$ were determined by the author and are tunable parameters that can be adjusted if new data become available. Equation (91) takes the original reliability and adds to it, as the reliability of the blower fan will be higher than the baseline when the inlet flowrate is lowered, and thus less damaging to the blower fan. Equation (92), on the other hand, takes the original reliability and subtracts from it, as the reliability will be lower given that the blower fan is operating at higher speeds than its baseline. In this way, the new reliability of the blower fan will be calculated to be either higher or lower than the original reliability calculation, depending on the speed of the fan, and will always be a value between 0 and 1. The generic form of this pair of equations, which is applied to every relevant component R_i to modify its reliability based on a design variable, x, is:

If $x \leq x_o$,

$$R_i = R_{i,o} + \left(1 - R_{i,o}\right)\left(\frac{x_o - x}{x_o}\right)^{\frac{1}{b}} \tag{93}$$

Otherwise, if $x > x_o$,

$$R_i = R_{i,o} - R_{i,o}\left(\frac{x}{x + x_o}\right)^{\frac{1}{c}} \tag{94}$$

Table 41 lists the details of all reliability calculations that are dependent on a design variable, including values of the baselines and exponential terms. The form for each component follows the format in Equations (93) and (94).

Table 41: Modification of component reliability calculations with design variables

Component	Design Variable Dependence	Baseline Value	b	c	Description
Blower Fan	$\dot{m}_{in}$	15 kg/hr	1	0.1	Inlet flow rate affects the blower fan speed
Cryocooler	Q_{load}	2000 W	1	0.08	Cooling load of the cryocooler affects cryocooler longevity
Mechanical Compressor	$\dot{m}_{in}$	15 kg/hr	1	0.1	Inlet flow rate affects the mechanical compressor speed
Mechanical Compressor	$P2$	20 kPa	1	0.06	The outlet pressure affects the compression ratio of the pump
SOE Stack	N_{CPS}	65	1	0.13	The number of SOE cells in a stack affects its mechanical stability
SOE Cell	ΔP	10 kPa	0.55	0.08	The pressure differential across the SOE cells affects their mechanical stability
SOE Cell	ΔV	0.1 V	0.15	0.48	The gap in voltage between the operating voltage and the Nernst potential affects the risk of coking

The set of equations for each of these design variables can be found in Appendix B.8. With these modified equations, the model more accurately calculates and optimizes the design of BAM with reliability as a primary objective.

Component Reliability to System Reliability

With component reliabilities calculated, simple Boolean logic was employed to calculate subsystem and system reliabilities. The individual component reliabilities were multiplied together to calculate subsystem reliabilities using the following general form:

$$R_{subsystem} = R_a * R_b * R_c * \dots * R_n \tag{95}$$

where a, b, c, and n represent individual components in the subsystem. The total system reliability was then calculated using the following form:

$$R_{system} = R_{subsystem1} * R_{subsystem2} * \dots * R_{subsystemN} \tag{96}$$

Specifically, the reliability of the entire BAM system was calculated as:

$$R_{BAM} = R_{CAC} * R_{SOE} * R_{Liq} * R_{HE} * R_{Power} \tag{97}$$

to incorporate reliabilities from the CAC, SOE, liquefaction, heat exchanger, and power subsystems, respectively.

4.10 Synergies Between Subsystems

The optimization algorithm may be able to take advantage of synergies that exist between certain subsystems. These synergies are briefly described here, as they may not be apparent from the results of the optimization alone.

A primary synergy exists between the cryopump and the liquefaction unit. If a cryopump is chosen as the compressor of choice for the CAC system, it may share the cryocooler and radiator infrastructure already in place for the liquefaction system. This allows the system to take advantage of non-linear scaling laws; rather than building a separate cryocooler and radiator for the cryopump, the existing infrastructure can be scaled up to take on the additional cooling load required of the cryopump. This synergy is modeled and is reflected in a net mass and volume savings when combining the cryopump and liquefaction hardware.

A second synergy that exists in BAM is the use of hot SOE exhaust gases to warm the cold SOE inlet gas. The benefits of sharing heat between these gas streams are twofold: the cold inlet gas stream requires less heat when it is prewarmed, and the hot exhaust gas requires less cooling for liquefaction when precooled. This synergy is enabled through the inclusion of a pair of heat exchangers. While the heat exchangers add mass and volume to the system, they significantly lower the power required to operate BAM.

A third potential synergy that is not included in the BAM design but could be in future iterations is the capture of waste heat from the Kilopower reactors. Each 10 kWe unit outputs several times its production of electrical energy in the form of waste heat. Currently, this heat is not captured, as the Kilopower units are located >1 km from the rest of the ISRU plant for radiation safety reasons. In future iterations of the design, however, the heat could be transported to BAM using heat pipes and be used to preheat the inlet gas to further reduce heating requirements.

Similarly, any excess heat from the hot SOE exhaust gases that is not used up in the heat exchangers could be routed through the cryopump or sorption pump to aid in their heating. Cryopump operation involves heating with power requirements on the order of 1 kW to sublimate the frozen CO_2 from the coldhead. In the case of the sorption pump, heating has power requirements on the order of 4 kW to desorb the CO_2 from the sorbent beds. Excess heat from the hot SOE exhaust could replace some or all of the cartridge heaters used as heat sources for these applications, resulting in significant power savings. This was not modeled as it is not clear whether the routing of these hot gases into the coldhead and microchannel sorbent beds is feasible. It should, however, be considered during the construction of BAM.

4.11 Designing for Atmospheric Variations

BAM must be designed to function across all variations in atmospheric pressure and temperature at its location on Mars. Figure 105 shows the variations in atmospheric density across each day-night cycle of the year at Jezero Crater, the Perseverance landing site.

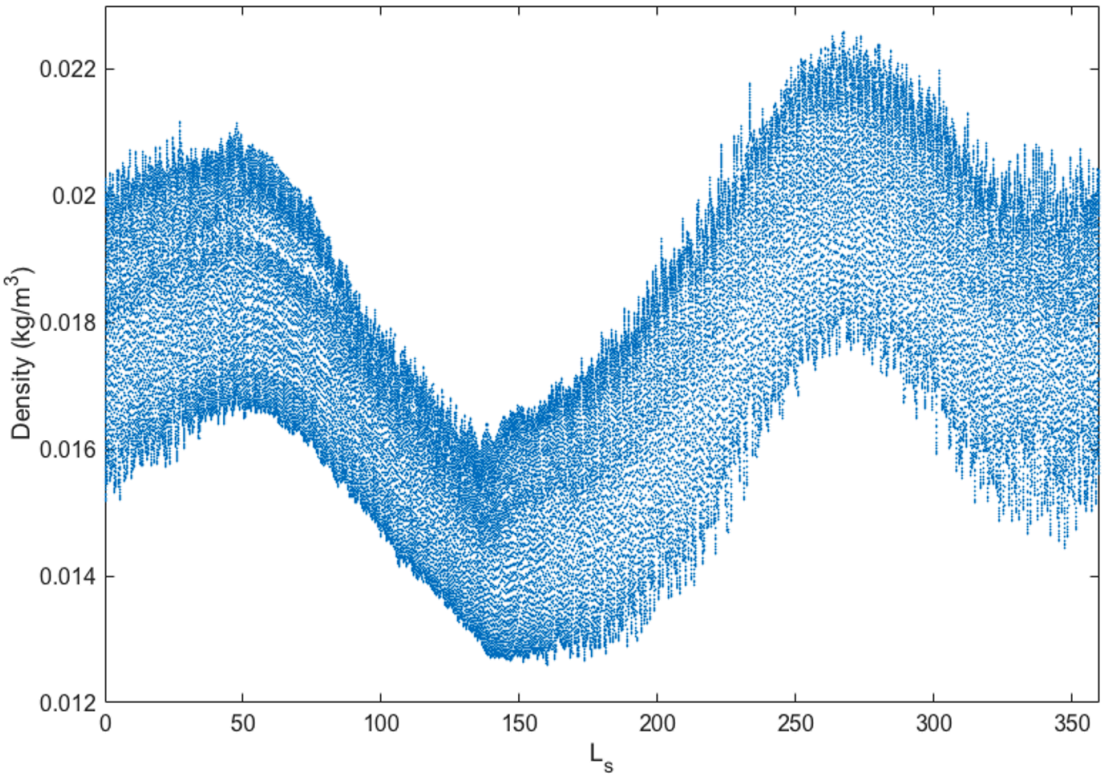

Figure 105: Atmospheric pressure, temperature, and density across days and seasons at Jezero Crater. Data acquired from the Mars Climate Database [114,115].

Two methods of handling these variations in density were considered for BAM operations. The first, "Method 1", involves adjusting the CAC to ensure a constant output mass flow rate. For mechanical compression, this means adjusting the rotational speed of the compressor, while for cryogenic and sorption pumping, this means adjusting the cycle time. The second method considered, "Method 2", involves running the CAC at its maximum capacity and instead adjusting the voltage applied to the SOE stack to target a constant utilization fraction of CO_2. To determine which method to recommend for BAM operations, the impact on the objective functions – mass, volume, risk, and power – were considered for each.

Mass and Volume

In the example given in Figure 105 from Jezero Crater, density varies by a factor of ~2 throughout the year. In Method 1, the CAC system must be sized to produce its targeted output mass flow rate at the lowest density in the year. Therefore, during times with the highest density, it will only run at ~half capacity. This means that to output a constant mass flow rate, the CAC system will be oversized for most of the year. The CAC system in Method 2, on the other hand, will always run at full capacity and will therefore be smaller. As a result, the CAC system in Method 1 will be up to ~twice as massive and voluminous as it will be in Method 2.

On the other hand, all downstream subsystems, including the heat exchanger, SOE, and liquefaction unit, will receive a constant flow rate in Method 1 throughout the year and can therefore be sized for that flow rate. Those subsystems in Method 2 will experience flow rates that vary with the atmospheric density and must therefore be sized to manage the highest flow rates. The heat exchanger design is driven by pressure drops, which are proportional to flow rate,

so the heat exchanger channels must be larger in Method 2 to minimize pressure drops at the peak flow rates and thus will be oversized for the majority of the year. Similarly, the cryocooler and radiator in the liquefaction unit must be sized to manage the heat loads from the peak oxygen flow rates and will be oversized for the majority of the year. At times of low atmospheric density, a portion of the radiator surface area will be unused, the cryocooler will run at ~half capacity, and pipe insulation will be oversized. In summary, for downstream units including the heat exchanger and liquefaction unit, Method 2 will have a higher mass and volume than Method 1. The differences in mass and volume for the SOE unit between Method 1 and Method 2 are minimal, as the differing flowrates are mostly managed by adjusting voltage.

Method 1 results in a larger CAC system than Method 2, while Method 2 results in a larger heat exchanger and liquefaction system than Method 1. In general, the CAC system in BAM accounts for ~3% of the total mass, while the heat exchanger and liquefaction unit together account for ~15%. The total effect on mass and volume is difficult to state with certainty, as it depends on the values of many design variables, but it appears that Method 2 may result in a more massive overall system than Method 1.

Risk

In Method 1, the CAC system varies its speed or cycle time to account for atmospheric variations. This could increase risk by increasing wear, in the case of a mechanical compressor, or by increasing the likelihood of a leak or other mechanical failure from varying thermal expansions and contractions, in the case of a cryogenic or sorption pump. In Method 2, the CAC system always runs at the same capacity or speed, making it less likely to suffer a cycling-induced failure. Downstream subsystems in Method 1 will always experience the same flow rate during the year, minimizing cycling-induced degradation. In Method 2, however, the heat exchanger, SOE, and liquefaction subsystems will experience varying flow conditions, potentially increasing risk from cycling-induced degradation.

Method 2 also requires a more sophisticated control system to account for varying flow conditions in downstream subsystems. In particular, the SOE system will be constantly adjusting its voltage to ensure oxygen is produced without exceeding the Nernst potential for carbon formation. Higher complexity generally implies more failure points, so the increase in complexity of the controls system for Method 2 in BAM could increase system risk.

Power

The average power between the two methods will be approximately the same, as both systems will produce the same total quantity of oxygen over the course of the mission, and average power is primarily driven by oxygen production quantity. There may be slight variations in average power between the two methods, as CAC efficiencies and heat transfer effectiveness in the heat exchanger and liquefaction unit vary with size. However, the main power difference between the two methods is that Method 2 will have a higher *peak* power than Method 1, as it will produce higher flow rates of oxygen during times of peak atmospheric density. The Kilopower system must be sized to accommodate peak power loads, or else batteries must be sent to be charged during low power draws and discharged during peak power draws. In either scenario, the higher peak power of Method 2 will require additional power system mass.

Summary

Table 42 summarizes the differences between Method 1 and Method 2 in terms of the objective functions, with a green shaded cell indicating the better method for that objective.

Table 42: Comparison summary between two methods of handling atmospheric variations on Mars. A green shaded cell indicates the superior method for that objective function.

Objective	Method 1: Vary CAC speed	Method 2: Vary SOE Voltage	Explanation
Mass/Volume			The CAC system is larger in Method 1, but the heat exchanger and liquefaction systems are larger in Method 2. The CAC system accounts for ~3% of the total BAM mass, while the heat exchanger and liquefaction units account for ~15%. Therefore, Method 1 is expected to be less massive overall.
Power			The two methods have similar average powers, but the peak power will be higher for Method 2, driving up power system mass in the form of extra Kilopower capacity or batteries.
Risk			The CAC system has higher risk in Method 1, but the SOE and liquefaction units have higher risk in Method 2, owing to the varying flow conditions and more sophisticated controls systems that will be required.

While both methods have merit, and this analysis was largely qualitative, it appears that Method 1 is the superior operational choice for handling atmospheric variations on Mars. Varying the CAC system's speed or cycle time to provide a constant downstream flowrate at all times during the mission will be the baseline operational assumption for BAM.

This chapter has described the design and modeling of the BAM system. The following chapter will explain and analyze key data that were taken to validate this model.

Chapter 5: Data to Inform Optimization Model

The systems in BAM that have been modeled are validated, where possible, with experimental data. OxEon Energy, as discussed in Section 2.3, is currently developing and testing scaled-up SOE cells with active areas a factor of five higher than the cells used on MOXIE, the largest cells manufacturable with current technology. Ingersoll Rand Nash conducted modeling work to design a Mars centrifugal pump for BAM, which is described in Section 5.1. MOXIE data have also been used to inform the BAM model, including the effect of cycling on iASR, operational challenges of the SOE, and the onboard controls system, all of which are described in Section 5.2. Finally, the majority of this chapter is concerned with the low-pressure operation of SOE cells, which has been experimentally tested for this dissertation to determine SOE performance as a function of pressure. This constitutes a significant new data set and is described and analyzed in Section 5.3.

Collectively, these past and ongoing research studies have been used to validate the models of each subsystem in BAM. This creates a robust model to better inform an optimized ISRU plant design.

5.1 Centrifugal Compressor Simulation

Ingersoll Rand Nash is a leading global provider of vacuum pumps and compression systems. An engineering team at Nash, led by Gary Lada, aided in the design and modeling of a centrifugal compressor for BAM [139]. A summary of their results is discussed in Section 4.3.2. More detailed data regarding the design and simulation of the BAM compressor is described in this section.

The inlet conditions assumed by Nash in their simulation were a 95% CO_2, 5% N_2 gas stream at 200 K, 7 mbar, and 18 kg/hr. The primary outlet pressure was 200 mbar, though a case for 700 mbar was briefly considered as well. After modeling, the Nash team recommended a five-stage centrifugal compressor to achieve the desired compression ratio of approximately 30. Table 43 summarizes the results of the Nash modeling effort.

Table 43: Centrifugal compressor design results from Ingersoll Rand Nash modeling [139]

Stage # (Impeller #)	Impeller Diameter (cm)	P Ratio	P_{in} (mbar)	P_{out} (mbar)	T_{in} (K)	T_{out} (K)	ΔT (K)	Tip Speed (ft/s)	Wc (kW)
1	10.2	2.4	7.0	16.8	200	267	67	298	0.126
2	9.7	2.09	15.1	31.4	219	279	60	283	0.061
3	6.4	2.23	31.2	66.3	219	286	67	296	0.031
4	4.9	1.65	64.5	106.2	219	259	40	229	0.014
5	4.1	1.93	104.5	202.0	219	273	54	265	0.009

The table provides information about the sizing, pressure, temperature, tip speed, and work done by each stage in the compressor. Each stage is sized to provide a compression ratio of approximately 2. Water cooling was assumed between each stage to avoid high temperature concerns with the materials used to construct the compressor; however, for BAM, materials will

be selected specifically to withstand higher temperatures than terrestrial designs to enable the compression to preheat the gas for the SOE downstream.

The Nash team predicts an adiabatic efficiency in the range of 55% - 60%. This is significantly lower than is typically seen in centrifugal compressors, owing to the lower flow rates of BAM. It is recommended to build and test a direct drive multistage centrifugal compressor at the size for BAM, as this sizing has possibly never been built before. Laboratory testing will be critical in proving the design and better understanding the efficiency at these low flow rates. Despite the lack of a commercial unit in this size, the modeling effort conducted by Nash provides valuable insight into the design of a centrifugal compressor, which is one of two primary mechanical compressor options for BAM.

5.2 Data from MOXIE

The MOXIE experiment on the Mars 2020 rover is a precursor to the eventual scaled-up design of BAM and has been tested many times on Earth and Mars. The results from the MOXIE experiments lend valuable insight into the design of BAM. Notably, the subsystem most similar between the two is the SOE subsystem.

5.2.1 iASR

One of the most important findings from MOXIE has been the characterization of the iASR, a property of the SOE subsystem. With each oxygen production cycle, the iASR has increased, within specifications, in the Flight Model (FM) on Mars, as shown in Figure 106.

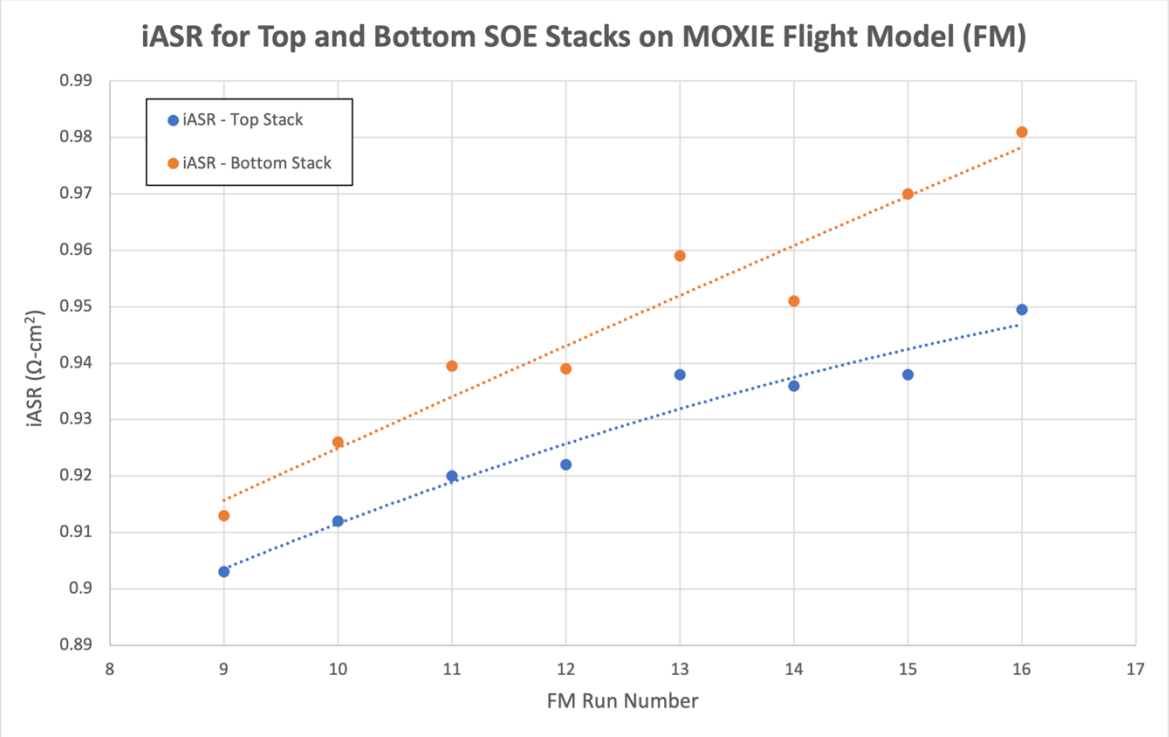

Figure 106: Intrinsic Area Specific Resistance (iASR) trends for the MOXIE Flight Model (FM) top SOE stack and bottom SOE stack across the eight most recent operational cycles on Mars. Image credit: MOXIE Science Team.

This trend indicates degradation of the electrolyte cell, resulting in a higher cell resistance. A higher resistance in turn means that a higher voltage must be applied for each subsequent cycle to achieve the same current. Eventually, an increasing voltage may begin to encroach upon the Nernst potential for carbon formation, which could rapidly degrade the SOE cells. Understanding the degradation of the SOE and how it may impact oxygen production in a full-scale system is important, reinforcing the idea that the number of cycles placed on the SOE system of BAM should be minimized.

5.2.2 Oxygen Purity

A minor leak between the cathode and anode in SOE cells was discovered in the laboratory model of MOXIE during the Mars 2020 mission. The leak is believed to be pressure-driven. When oxygen leaks from the anode to the cathode, it oxidizes CO back into CO_2. The oxygen purity from the anode outlet stream remains at approximately 100%. However, when CO or CO_2 leak from the cathode to the anode, the oxygen purity is reduced. A full-scale system like BAM requires high purity oxygen. If the SOE cells on BAM experience a leak like those on MOXIE, high purity oxygen can still be produced by operating with anode pressure sufficiently higher than cathode pressure. This is an operational consideration that will be implemented in BAM if necessary.

5.2.3 Controls System

Testing and validating the control loops onboard MOXIE has informed, to a certain degree, the design of the controls for BAM. MOXIE has three internal control loops. The first controls the electrical current in the SOE by modifying the voltage. The second controls the temperature of the SOE by modifying the heater power. The third controls the pressure on the cathode side of the SOE by modifying the speed of the compressor. The MOXIE team has tested the gains of each control loop to understand the optimal configuration for a given scenario. The pressure control loop is of particular importance for BAM, as the atmospheric pressure and temperature of Mars vary seasonally and diurnally, as shown previously in Figure 105.

MOXIE only runs intermittently, and there is time before every run to estimate the density at the time of the run and command a compressor speed to input the desired amount of Mars atmosphere. BAM will operate continuously and will therefore require a more sophisticated controls system than MOXIE's in order to constantly tune the compressor output to provide a constant pressure to the downstream SOE. For sorption and cryogenic compression, this involves adjusting the cooling and warming cycle times to accommodate atmospheric variations. In a mechanical compressor, the rotational speed of the compressor will be adjusted as it is in MOXIE. The BAM model takes this into account by sizing the CAC for the worst-case atmospheric conditions, when the density is the lowest. The CAC power is calculated using the average atmospheric density throughout the year. A sensitivity study showing the effect of different landing sites on the BAM design is discussed in Section 6.7.2.

5.3 SOE Operation at Low Pressure

The operation of SOE at a range of pressures lower than the pressure used on MOXIE has been tested with experiments carried out by the author at OxEon and is described in this section.

5.3.1 Benefits of Low-Pressure Operation

Operating the SOE at a relatively low cathode pressure provides two primary benefits for the BAM system: it lowers the compressor power requirements and allows for a higher CO_2 utilization fraction to be safely achieved. The power in most mechanical compressors is a function of the compression ratio, or the ratio of the outlet pressure to the inlet pressure. A higher compression ratio requires a higher power. By operating the SOE at a lower inlet pressure, the outlet pressure of the compressor is correspondingly reduced, with a consequent reduction in power. For cryogenic and sorption pumps, the outlet pressure is a function of the heat applied to the cold head or sorbent bed. Therefore, a lower inlet pressure for the SOE system also reduces the power required of cryogenic and sorption pumps by lowering the required heat input.

The second advantage afforded by operation at a low cathode pressure is that a higher CO_2 utilization fraction may be safely achieved. This means that more oxygen can be produced per CO_2 molecule flowing through the system, reducing the requirements for dust rejection, CAC throughput, heating of the gas, and SOE cell area. A higher utilization fraction can be achieved at a lower pressure because the Nernst potential for CO_2 reduction is independent of cathode pressure while the Nernst potential for CO reduction increases as cathode pressure decreases. This increases the gap between the two Nernst potentials as pressure decreases.

To prove this, the Nernst potentials for CO_2 reduction and CO reduction are:

$$V_N(2CO_2 \rightarrow 2CO + O_2) = -\frac{\Delta G^\circ}{4F} + \frac{RT}{4F}\ln\left(\frac{(P_{CO}^0)^2\left(P_{O_2}^0\right)}{\left(P_{CO_2}^0\right)^2}\right) \tag{98}$$

$$V_N(2CO \rightarrow 2C + O_2) = -\frac{\Delta G^\circ}{4F} + \frac{RT}{4F}\ln\left(\frac{(P_C^0)^2\left(P_{O_2}^0\right)}{(P_{CO}^0)^2}\right) \tag{99}$$

The effective partial pressure of pure solids and liquids, known as the thermodynamic activity, are equal to unity. Therefore, the partial pressure of solid carbon, $(P_C^0)^2$, is equal to unity. The partial pressures of the cathode gases, CO_2 and CO, can be written in terms of cathode pressure, P_{Ca}, and mole fractions, x_i, as follows:

$$V_N(2CO_2 \rightarrow 2CO + O_2) = -\frac{\Delta G^\circ}{4F} + \frac{RT}{4F}\ln\left(\frac{(P_{Ca}x_{CO}^0)^2\left(P_{O_2}^0\right)}{\left(P_{Ca}x_{CO_2}^0\right)^2}\right) \tag{100}$$

$$V_N(2CO \rightarrow 2C + O_2) = -\frac{\Delta G^\circ}{4F} + \frac{RT}{4F}\ln\left(\frac{\left(P_{O_2}^0\right)}{(P_{Ca}x_{CO}^0)^2}\right) \tag{101}$$

These can be simplified to:

$$V_N(2CO_2 \rightarrow 2CO + O_2) = -\frac{\Delta G^\circ}{4F} + \frac{RT}{4F}\ln\left(\frac{(x_{CO}^0)^2\left(P_{O_2}^0\right)}{\left(x_{CO_2}^0\right)^2}\right) \tag{102}$$

$$V_N(2CO \rightarrow 2C + O_2) = -\frac{\Delta G^\circ}{4F} + \frac{RT}{4F}\ln\left(\frac{\left(P_{O_2}^0\right)}{(P_{ca})^2(x_{CO}^0)^2}\right) \quad (103)$$

Equation (102) demonstrates that the Nernst potential for CO_2 reduction is independent of cathode pressure while equation (103) demonstrates that the Nernst potential for CO reduction is inversely proportional to cathode pressure. Taking these results and applying them to Figure 107, it becomes evident that by decreasing cathode pressure, the Nernst potential for CO reduction will increase while the Nernst potential for CO_2 reduction will stay constant. This shifts the Boudouard Boundary along the x-axis towards a higher utilization fraction, creating a larger safe operating range.

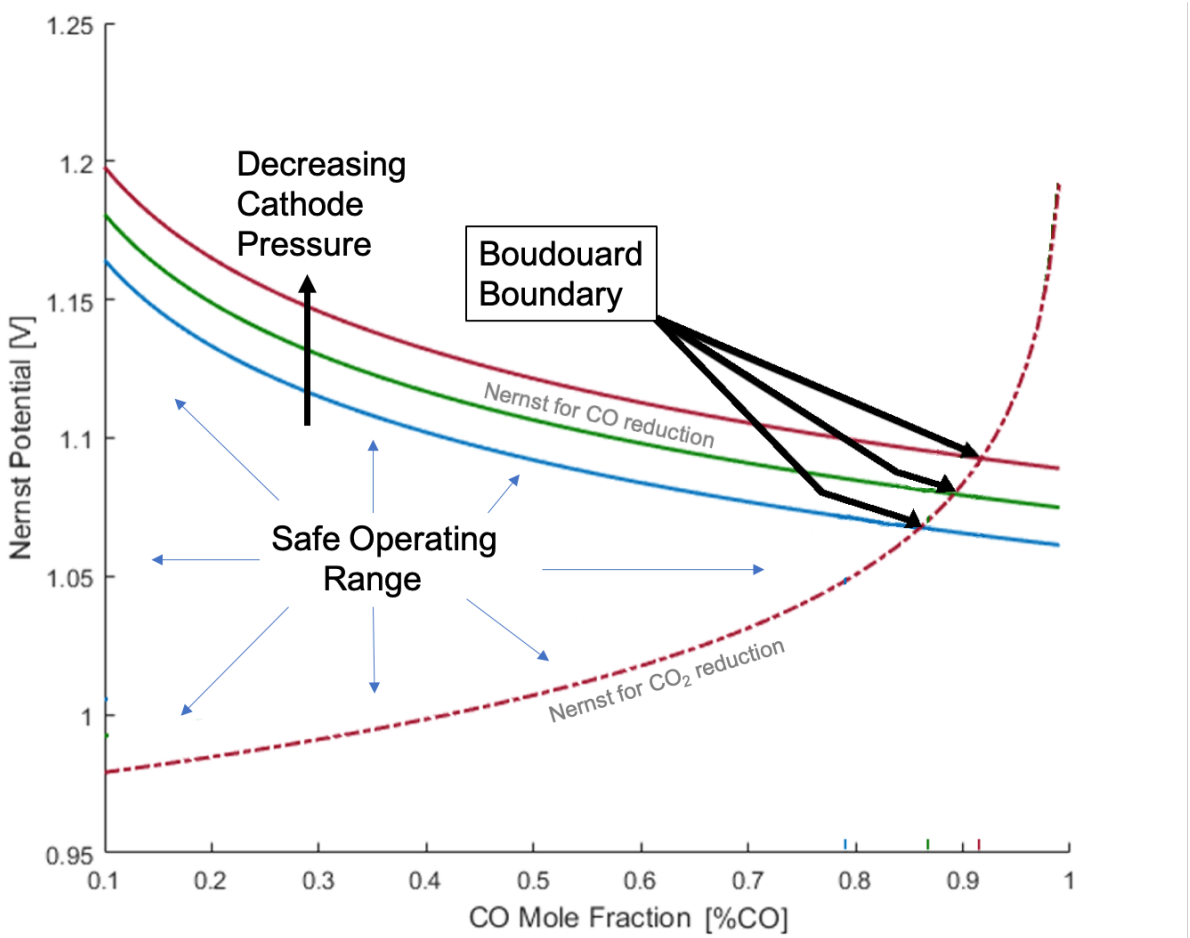

Figure 107: Nernst potential for CO reduction as a function of pressure (top three lines) plotted against Nernst potential for CO_2 reduction (bottom line). This assumes a constant partial pressure of O_2. As cathode pressure is decreased, the Nernst potential for CO reduction increases, creating a wider safe operating range for voltage (y-axis) and utilization fraction (x-axis). Original image credit: OxEon Energy.

Therefore, operating at a lower cathode pressure enables the SOE system to produce oxygen at a higher CO_2 utilization fraction without creating an undesirable side product, carbon.

As mentioned, there are several benefits to operating at a higher CO_2 utilization fraction. First, less CO_2 must pass through the system. This reduces dust rejection requirements, CAC system throughput, and the quantity of gas that must be preheated prior to entering the SOE system, resulting in power and mass savings. In addition, by enabling higher operating voltages and thus higher current densities, less total cell area is required to meet the same O_2 production rate. This reduces SOE system mass and volume. Meyen [4] conducted a trade study on the relationship between inlet pressure and SOE cell mass for an extensible system producing 2 kg/hr of O_2 using cells with an active area of 100 cm^2. The results are summarized in Table 44.

Table 44: Effect of lowering cathode pressure on total number of SOE cells required and their subsequent mass. Numbers assume SOE cells with an active area of 100 cm^2 [4].

Cathode Pressure	# SOE Cells	Total Cell Mass (kg)
1 bar	674	221
0.5 bar	548	180
0.1 bar	382	125

These results indicate a substantial reduction in SOE cell mass as pressure is lowered. Lowering the pressure from 1 bar to 0.1 bar reduces the number of SOE cells required by 43%. This may also enable increased redundancy by enabling extra SOE cells to be included in the design.

The preceding section shows that many benefits can be realized by lowering the inlet pressure of the SOE system. The limitations of low-pressure SOE operation are discussed in the following section.

5.3.2 Literature Review

Little research has been published on operating CO_2 solid oxide electrolysis cells at reduced pressures. Bernadet et al. [187] conducted modeling and experimental analysis of water-based SOE performance under a range of pressures in 2015. They studied two commercial SOE cells at a range of 1 bar to 10 bar. Two main findings resulted from the study. First, the open circuit voltage increased with pressure, as shown in Figure 108. Second, the performance of the cell in terms of current density increased with pressure. The performance increased because the concentration overpotential of the cathode decreased with pressure. As discussed below, the concentration overpotential represents a resistance to diffusion. By decreasing the resistance, diffusion through the electrolyte improved and additional SOE products were produced. However, the authors found that an optimum pressure existed where any further increase in pressure decreased SOE performance because of an increase in open circuit voltage. The study was limited by only taking data at two pressures, 1 bar and 10 bar, although the authors developed a theoretical model for additional pressures that was validated with their data. While this study did not consider sub-atmospheric pressures and focused on water electrolysis rather than CO_2 electrolysis, the results may still be used to predict the effects of low-pressure operation of CO_2 SOE.

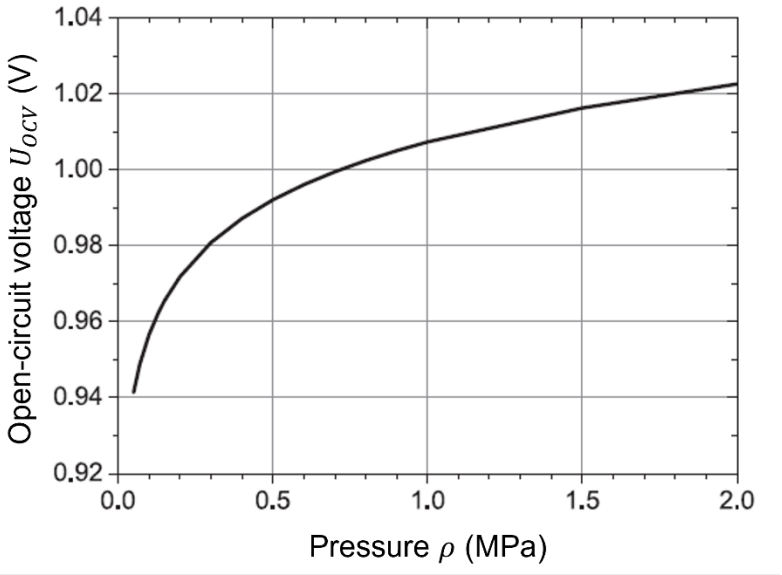

Figure 108: Pressure effects of SOE operation on open circuit voltage (OCV). Values are based on water electrolysis [188].

A second paper published by Henke et al. in 2014 [188] investigated a range of pressures between 0.5 bar and 20 bar. The low end of this pressure spectrum is relevant to this dissertation. The study was purely theoretical and was also based on water electrolysis as opposed to carbon dioxide electrolysis. The authors found that a decrease in pressure positively influenced thermodynamics but negatively influenced kinetics and gas transport. As a result, net pressure effects on the performance of the cell were small. In fact, at low current densities, the SOE cell showed better performance at low pressures whereas at high current densities, the SOE cell showed better performance at high pressures.

Jensen et al. [189] formed a similar conclusion after testing SOE cells from 0.4 bar to 1 bar, noting that an increase in pressure decreased the ASR but increased the Nernst voltage and thus the open circuit voltage, leading to a small overall benefit to performance.

5.3.3 Limitations of Low-Pressure Operation

Cell performance as a function of pressure is influenced and limited by overpotentials. Three types of overpotentials are relevant to SOE performance: ohmic, activation, and concentration. The effect of all three overpotentials is shown in Figure 109 for the cathode ("hyd") and anode ("oxy") of a water electrolysis study.

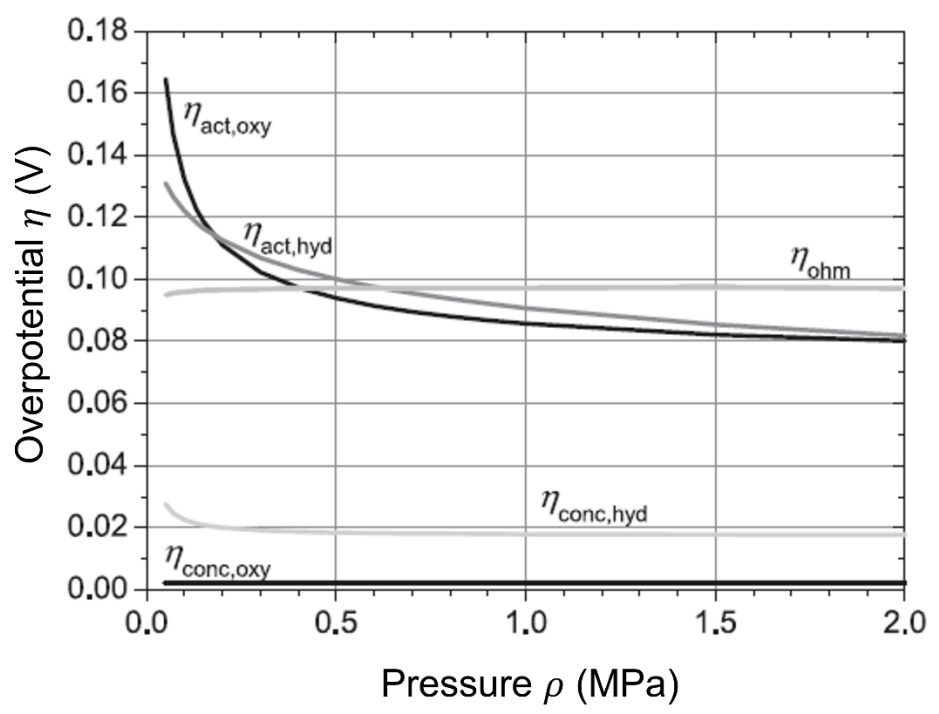

Figure 109: Influence of pressure on three types of overpotentials (ohmic, activation, and concentration) for the hydrogen cathode (hyd) and oxygen anode (oxy) of a water SOE system [188].

Ohmic overpotentials are a result of electrical resistance of the electrode and electrolyte and are not affected by pressure. *Activation overpotentials* are a result of chemical resistance of the electrochemical reaction and increase as pressure decreases. Pressure has a strong effect on the adsorption rate of reactants at the electrode interface; at higher pressure, a larger percentage of the electrode surface is covered in reactants, facilitating the surface reaction, and thereby reducing activation overpotentials. This effect has a strong influence at lower pressures but has a minimal effect at higher pressures as the cathode surface becomes saturated with reactants.

Concentration overpotentials are a result of the physical resistance of molecules diffusing through the electrode and electrolyte and become the limiting factor in SOE performance at low pressures. Figure 110 shows the molecular fluxes involved in a SOE reaction.

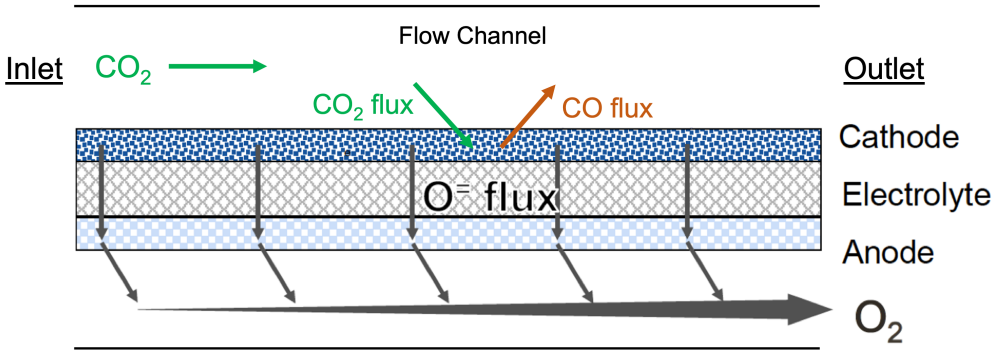

Figure 110: Fluxes of CO_2, CO, and O during an electrochemical reaction on the SOE cell. Original image credit: OxEon Energy.

The magnitude of the flux of CO_2 to the boundary between the cathode and the electrolyte surface is dependent on a partial pressure differential:

$$N_{CO_2} = F_x(P_{CO_2,fc} - P_{CO_2,b}) \tag{104}$$

Where F_x is the mass transfer coefficient, $P_{CO_2,fc}$ is the partial pressure of CO_2 in the flow channel of the SOE cell and $P_{CO_2,b}$ is the partial pressure of CO_2 at the boundary between the cathode and the electrolyte.

The mass transfer coefficient, which is analogous to the convective heat transfer coefficient, is calculated as:

$$F_x = \left(\frac{D_{AB}}{RTz}\right)\left(\frac{V_P}{T_u}\right) \tag{105}$$

where D_{AB} is the diffusivity coefficient of A in a solution of B, R is the universal gas constant, T is the temperature, z is the distance of diffusion in the z direction, V_p is the porosity of the electrode, and T_u is the tortuosity, which accounts for the length of path actually traveled by the diffusing molecules.

The diffusivity coefficient is dependent on the molecular species involved, the temperature, and the total pressure. A value from literature for CO_2 and CO taken at standard temperature and pressure was modified according to the temperature and pressure dependence specified in that literature [190]:

$$D_{CO_2-CO} = 1.39 * 10^{-5}\left(\frac{T}{273K}\right)^{\frac{3}{2}}\left(\frac{1atm}{P_{Ca}}\right) \tag{106}$$

The partial pressures of the gases specified in Equation (104) are defined as the mole fraction of that gas multiplied by the total pressure of the cathode, which is equal in the flow channel and at the boundary, such that:

$$\left(P_{CO_2,fc} - P_{CO_2,b}\right) = P_{Ca}\left(X_{CO_2,fc} - X_{CO_2,b}\right) \tag{107}$$

Combining Equations (104), (105), (106), and (107) yields:

$$N_{CO_2} = \frac{1.39 * 10^{-5}\left(\frac{T}{273K}\right)^{\frac{3}{2}}\left(\frac{1atm}{P_{Ca}}\right)}{RTz} P_{Ca}\left(X_{CO_2,fc} - X_{CO_2,b}\right) \tag{108}$$

The P_{Ca} terms cancel in the above equation, leading to the unexpected conclusion that molar flux from the flow channel to the boundary of the electrolyte is independent of cathode pressure. This implies that decreasing the cathode pressure should not impact molar flux and thus cannot be a limiting factor. Intuitively, this logic must fail when P_c approaches a value of zero, as there would no longer be any CO_2 to diffuse to the boundary. It is likely, per conversations with SOE

experts [191], that the theoretical equations used in this section do not remain true at near-vacuum conditions likely owing to a transition to a molecular flow regime for gas diffusion.

In an SOE reaction, CO_2 and CO undergo equimolar diffusion; for every molecule of CO_2 that diffuses to the boundary between the cathode and the electrode and is electrolyzed, one molecule of CO must diffuse out of the same space. Therefore, N_{CO} must be equal in magnitude to N_{CO_2}. The flux of oxygen ions, $N_{O^=} = \frac{j_i}{2F}$, is also equal in magnitude, as one oxygen ion is produced for every CO_2 molecule that is reduced. Therefore, the oxygen production rate is dependent on N_{CO_2}.

At most pressures, concentration overpotentials are relatively constant. At low pressures, however, the effect of the overpotential becomes more pronounced. This is a result of the diffusion mechanism changing; at high pressures, molecular diffusion is governed by ordinary diffusion mechanisms that are independent of pressure. On the other hand, at low pressures, molecular diffusion is governed by Knudsen diffusion, which is proportional to pressure. Ni et al. discuss the vulnerability of the cathode to high concentration overpotentials in more detail [192].

The previous research studies explored in Section 5.3.2 and the theory behind them have demonstrated that the performance of steam-based SOE decreases as inlet cathode pressure is decreased, owing to an increase in ASR that is not entirely compensated by a decrease in Nernst voltage. As pressure continues to be decreased, diffusion of gases between the flow channel and the electrode-electrolyte boundary becomes the rate-limiting step, causing an exponential rise in the concentration overpotential and thus the ASR of the cell. This defines the lower pressure limit at which an SOE cell can be productively operated, as an exponentially increasing ASR results in a cell incapable of producing oxygen. These findings from previous research studies conflict with the theory described in this section, which demonstrated that molar flux is independent of total pressure. This dissertation has extended the findings of previous research to CO_2 SOE at a lower pressure range (down to 0.15 bar) to experimentally characterize the performance curves against pressure. The experimental setup and results will be explored in the following sections.

5.3.4 Design of Experiment

Equipment Setup

Tests were conducted at OxEon Energy in North Salt Lake, Utah in January 2022 with the goal of characterizing the effect of cathode pressure on SOE performance. A stack of 10 SOE cells, each with an active area approximately five times larger than the cells in MOXIE, was used. The stack had been previously built at OxEon and had been tested at JPL. The stack was placed inside an oven to control the temperature. OxEon mass flow controllers and gas sources were used to flow gases into the stack. A pneumatics system was designed and built to control the cathode pressure by restricting the upstream flow through an orifice to induce choked flow conditions and installing a vacuum pump downstream to adjust pressure. The pneumatics system is shown as a block flow diagram in Figure 111 with an image of the actual equipment used shown in Figure 112.

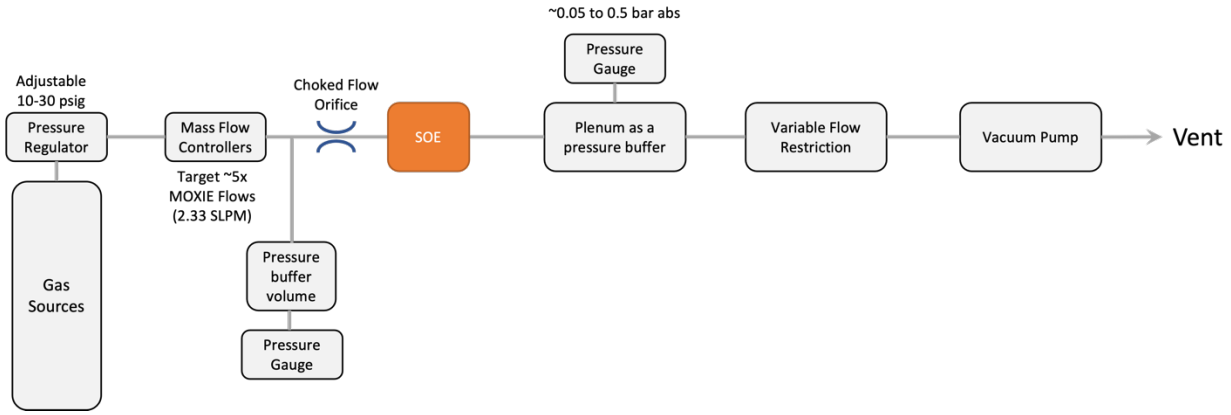

Figure 111: Block flow diagram of the pneumatics system used to control flow composition (via mass flow controllers) and pressure for the SOE low-pressure experiment

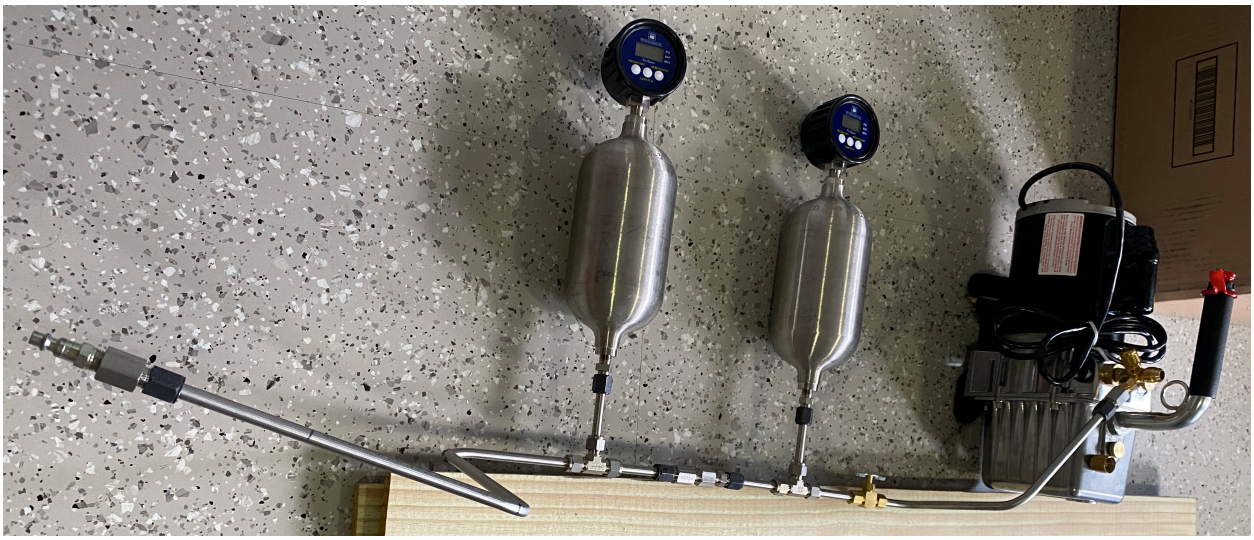

Figure 112: Pneumatics system equipment used in low-pressure SOE tests at OxEon Energy

Mass flow controllers were used to input the correct composition of gases. A plenum was used to ensure adequate mixing of the gases. The flow then passed through a restrictive orifice, which induced sonic (choked) flow. This was necessary to ensure that, even with changes in downstream pressure, the mass flow rate through the SOE stack would remain constant. At the outlet of the SOE stack, a vacuum pump and variable control valve were used to control cathode pressure. By opening the variable control valve to different degrees, the downstream pressure could be adjusted. If the valve was opened more, for example, the pump would evacuate more gas and the pressure would decrease. The cathode pressure was displayed on a commercial vacuum gauge attached to the downstream plenum.

Test Plan

To determine the effect of pressure on the performance of the SOE stack, a pressure sweep was designed for the stack. The stack was operated at a range of cathode pressures, from atmospheric pressure to 150 mbar. A current-voltage (I-V) sweep was conducted at each pressure range to better characterize the performance of the SOE stack at each pressure. Hydrogen was used as a reducing gas to prevent oxidation of the cathode. The anode was kept at atmospheric pressure,

equal to approximately 860 mbar in North Salt Lake. The cathode pressure was stepped down with each experiment until reaching a final pressure of 150 mbar. The initial test plan called for two additional tests at 100 mbar and 50 mbar, but the vacuum pump was unable to achieve those pressures. This indicated a leak in the SOE stack, which was later confirmed. The leak was determined to be an atmospheric leak, resulting from a failed seal between the cathode and the ambient atmosphere inside the SOE oven. As a result, ambient air was pulled into the cathode under the vacuum conditions studied in these tests, yielding a mixture of CO_2, H_2, N_2, O_2, and trace gases entering the cathode.

The leak resulted in the production of water from the mixing of hydrogen and oxygen in the SOE stack. This created co-electrolysis conditions, where both water and carbon dioxide were electrolyzed together. Co-electrolysis has a different expected performance than "dry" (CO_2-only) electrolysis and was therefore considered a confounding variable in the data from the first day of testing.

To eliminate the formation of water leading to co-electrolysis, a dry electrolysis pressure sweep was conducted on the next day of testing using CO_2 mixed with a reducing agent, CO, to prevent oxidation of the cathode. It followed the test plan shown in Table 45.

Table 45: Day 2 pressure sweep conducted at OxEon Energy to determine effects of low-pressure operation on SOE performance

Cathode Pressure (mbar)	Test Conducted	Gases Used
860	I-V Sweep	CO_2, CO
700	I-V Sweep	CO_2, CO
500	I-V Sweep	CO_2, CO
300	I-V Sweep	CO_2, CO
200	I-V Sweep	CO_2, CO
150	I-V Sweep	CO_2, CO

The lowest pressure possible was once again limited by the leak rate in the stack.

Despite the effects of the leak, the data that were acquired provided valuable insights into the performance of SOE under varying cathode pressures. The results are shown in the next section.

5.3.5 Results

The pressure was recorded along with the commanded current and measured voltage from 0 to ~12.5 Amps for each I-V sweep. The data from the first pressure sweep are omitted from this dissertation, as the formation of water confounded the results. A portion of the data taken from the second pressure sweep are shown in Table 46.

Table 46: I-V sweep data for dry electrolysis at 493 mbar cathode pressure. Data taken at OxEon Energy facilities.

Cathode Pressure (mbar)	CO_2 Flow (SLPM)	CO Flow (SLPM)	Measured Amps	Measured Volts	Measured Volts / Cell
493	3.74	0.077	0.000	7.989	0.799
493	3.74	0.077	1.050	8.426	0.843
493	3.74	0.077	2.541	8.958	0.896
493	3.74	0.077	5.070	9.515	0.952
493	3.74	0.077	7.515	9.948	0.995
493	3.74	0.077	10.000	10.360	1.036
493	3.74	0.077	12.530	10.740	1.074

The data in this table show the current and voltage recorded for the stack of 10 SOE cells operated at a pressure of 493 mbar. I-V sweeps at five other pressures were recorded as well, and the full data from each can be found in Appendix C. The CO flow rate shown in this table has been corrected to account for the leak. The process by which the flow rate was corrected is described in the following section.

Correction for Leak

To extract the most information possible from the data, the leak was characterized, and its effects were removed from the data. This was accomplished by first determining the difference between the actual inlet CO flow rate and the theoretical CO flow rate needed to achieve the appropriate open-circuit voltage (OCV). The actual CO flow rate was chosen for each I-V sweep by adjusting the CO concentration until an OCV of approximately 8.0 V was achieved on the SOE stack. This OCV corresponds, in theory, to an inlet flow rate ratio of 2% CO and 98% CO_2 by volume. O_2 from the leak reacted with CO on the cathode to form CO_2, effectively removing a portion of the CO from the cathode stream:

$$2CO + O_2(from\ leak) \rightarrow 2CO_2 \tag{109}$$

The difference in theoretical and actual CO in the feed stream was used to calculate the quantity of oxygen present on the cathode, according to Equation (109). The total leak could then be calculated using the quantity of oxygen present on the cathode and assuming an atmospheric composition of 21% O_2 and 79% N_2. Table 47 shows the resulting information from the leak calculation process.

Table 47: Targeted inlet flow conditions for the SOE pressure sweeps conducted at OxEon Energy (left) and calculated values to account for the leak in the stack (right)

Targeted Values for Pressure Sweeps					Calculated Values to Account for Leak				
P (mbar)	CO_2 Flow (SLPM)	CO Flow (SLPM)	Total Targeted Flow (SLPM)	%CO	%CO Unreacted	CO Flow Baseline (SLPM)	CO Excess Flow (SLPM)	O_2 Leak (SLPM)	Total Leak (SLPM)
860	2.4	0.2	2.6	5%	2%	0.056	0.12	0.06	0.29
694	2.4	0.7	3.1	23%	2%	0.085	0.62	0.31	1.46
493	2.4	1.3	3.7	36%	2%	0.121	1.22	0.61	2.90
297	1.1	1.7	2.8	60%	2%	0.115	1.57	0.78	3.73
194	1.1	1.9	3.0	63%	2%	0.124	1.73	0.86	4.11
150	1.1	1.9	3.0	63%	2%	0.127	1.77	0.89	4.22

The first column, pressure, was set by pulling a partial vacuum on the cathode exit line. The second and third columns were set using mass flow controllers upstream of the cathode. The first two columns on the right half of the table represent the percentage and flowrate in SLPM of CO in the inlet stream that would result in an OCV of 8.0 V. The CO Flow Baseline was iteratively calculated against the total flow rate until it converged to 2% of the total flow rate, including the leak flow. The CO Excess Flow column is the difference between the CO flow in the third column and the seventh column. The O_2 leak is a stoichiometric calculation using the CO excess flow column, which represents the quantity of CO that reacted with oxygen on the cathode. Lastly, the total leak is calculated by assuming the O_2 leak represents 21% of the total leak. Figure 113 shows the targeted flow rate, leak flow rate, and total flow rate as a function of pressure.

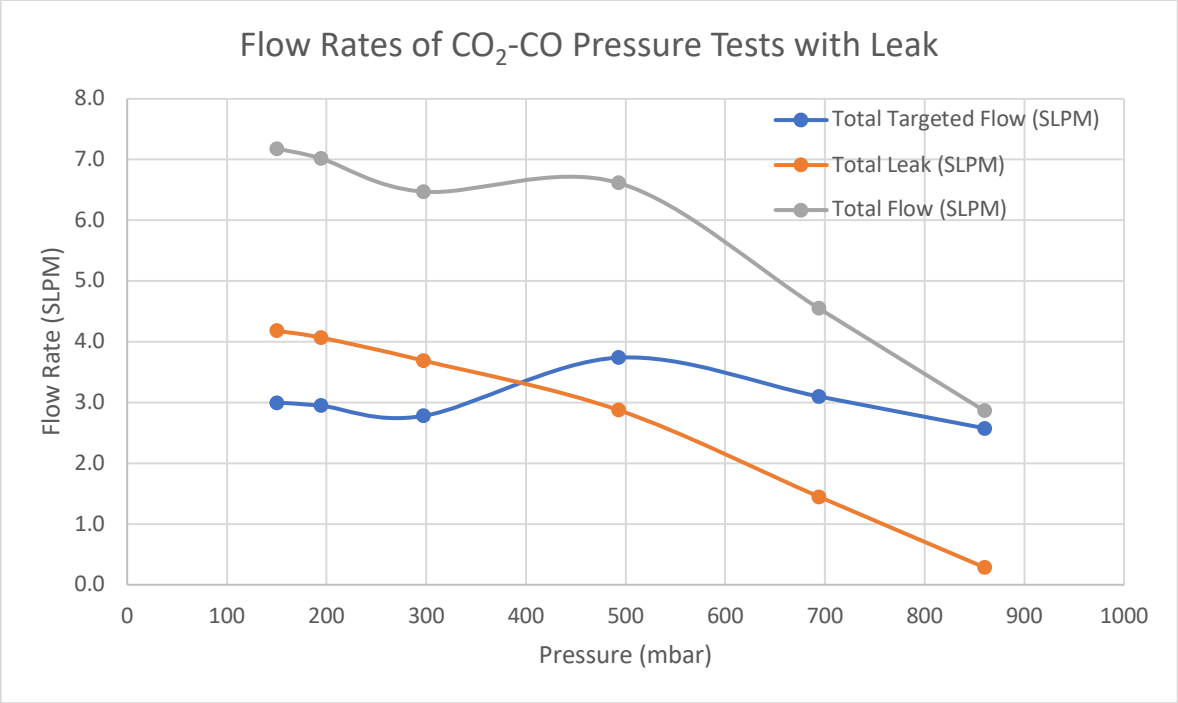

Figure 113: Total targeted flow rate, leak flow rate, and total actual flow rate of the CO_2-CO mixtures used in the OxEon SOE stack pressure sweep

As the figure demonstrates, the leak increased as the cathode pressure decreased. This is expected behavior, as a greater pressure differential would drive a higher leak rate. Correspondingly, the gap between the targeted flow and the actual total flow increased as pressure decreased.

The process and charts shown above provide an approximate characterization of the true inlet flow composition. To gain a higher level of detail, the data were further refined by adjusting the composition of the inlet flow such that the calculated OCV exactly matched the observed OCV, rather than using 8.0 V as a generic benchmark. This involved small adjustments to the inlet CO composition.

Characterization of Stack Performance

With the leak characterized and the data adjusted to account for it, it was possible to characterize stack performance as a function of pressure. This was done by calculating the iASR of the stack at each pressure using the I-V data. The iASR is an indicator of performance because under low pressure conditions it is expected to rise, as discussed in Section 5.3.3. An increase in iASR indicates a decrease in oxygen flux, which is caused by a decrease in CO_2 flux to the electrode-electrolyte interface. This last step is expected to be a function of cathode pressure.

The iASR was calculated by minimizing the sum of squared errors (SSE) from the difference between the observed current and the modeled current. The modeled current was calculated as follows:

$$I = \frac{A_{cell}(V_{cell} - V_{act} - V_{Nernst})}{iASR} \tag{110}$$

By minimizing the difference between the observed current and the current calculated in Equation (110) across the I-V sweep, it was possible to solve for the iASR of the stack. This process was repeated for each I-V sweep conducted at a different cathode pressure, resulting in the relationship between pressure and iASR shown in Figure 114.

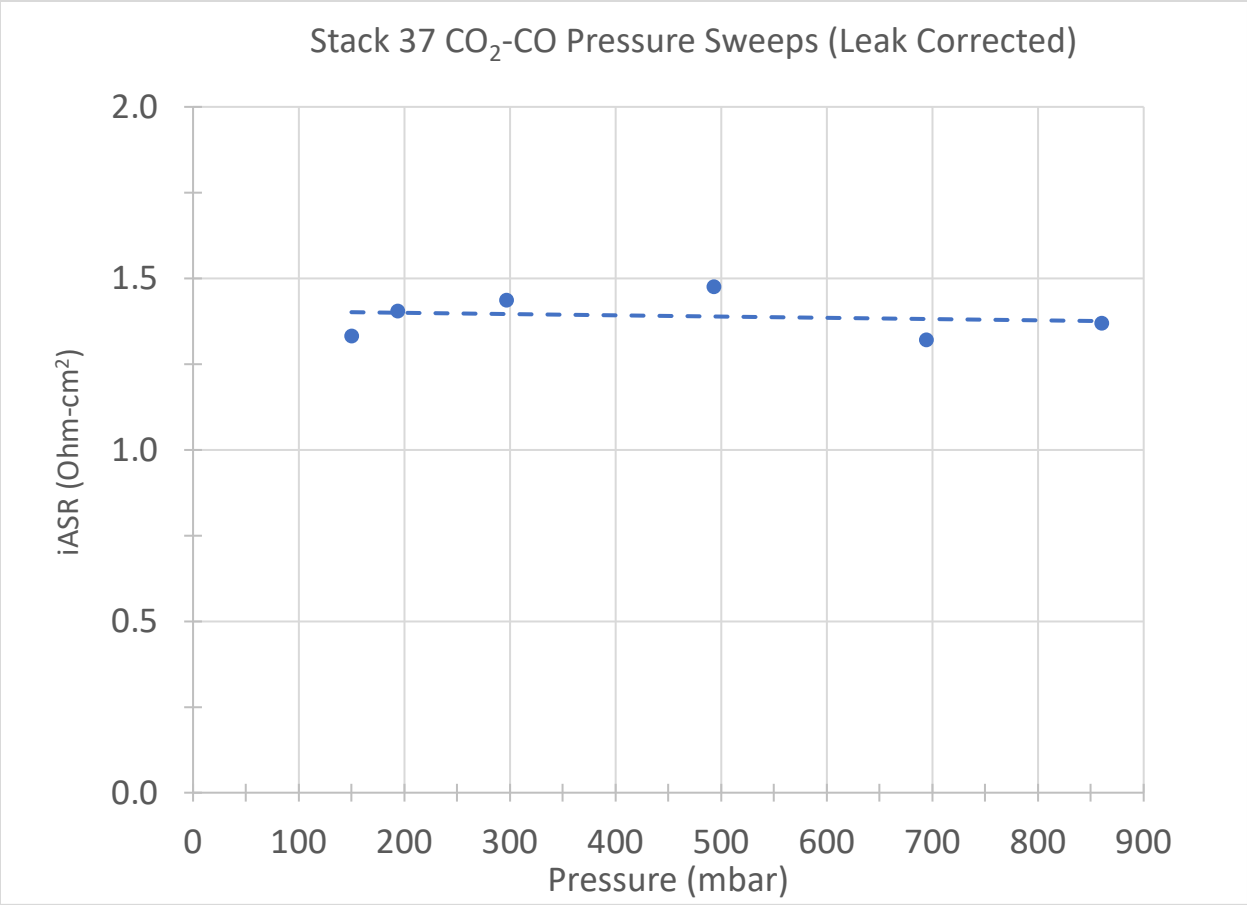

Figure 114: iASR as a function of cathode pressure for a range of I-V sweeps conducted on an SOE stack at OxEon Energy

A full copy of the I-V sweep data at each pressure, with the associated iASR calculations, are included in Appendix C.

5.3.6 Discussion

The results from Figure 114 show a relatively constant iASR across the pressure range of 150 mbar to 860 mbar. This means that the lower limit of pressure, as defined by an expected sharp increase in iASR, was not exceeded. 150 mbar was the lowest pressure the vacuum pump could produce with the leak. In the absence of a leak, the pump would have been capable of lowering the cathode pressure to 10 mbar or lower, and this should be done in future work to confirm a lower pressure limit for SOE performance.

A minimum pressure at which BAM can be operated exists. This minimum pressure is defined either by the lowest pressure at which the SOE can be operated, as discussed earlier, or by the cumulative effect of pressure drops throughout the BAM system. Pressure drops across the filter,

heat exchanger, SOE flow channels, and SOE outlet are the most significant, and are shown as blue squares in Figure 115.

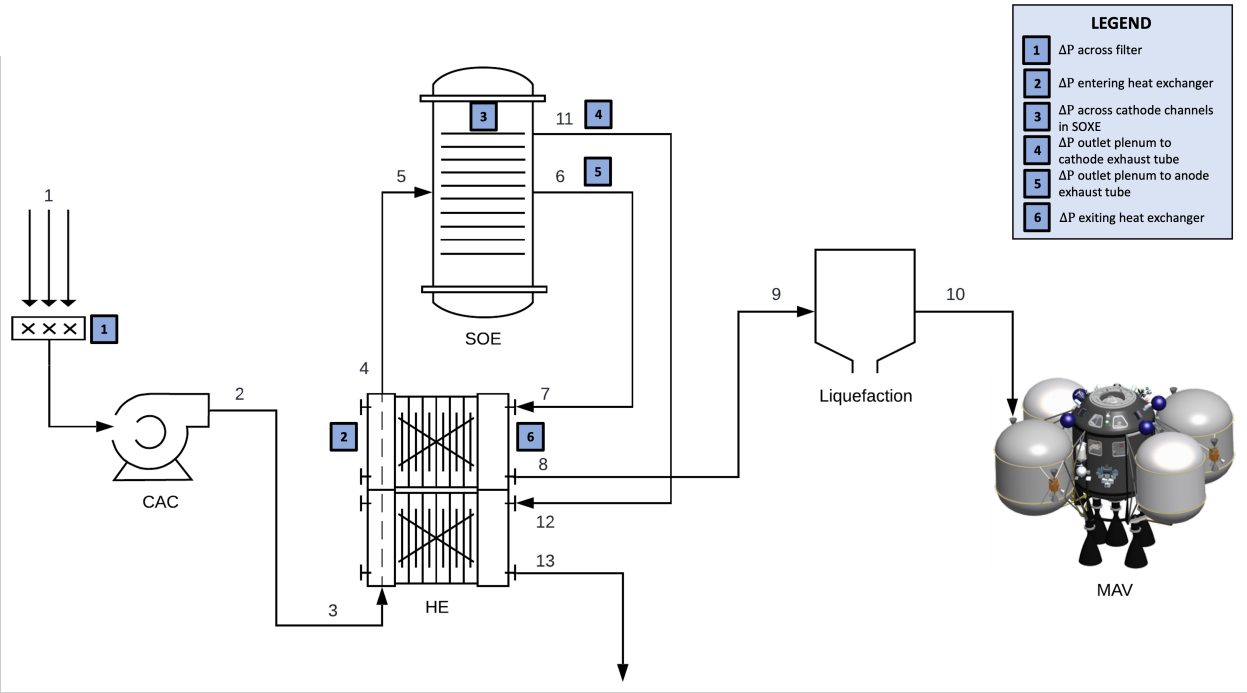

Figure 115: Block flow diagram of the end-to-end BAM system, with major pressure drops located in blue boxes

As operating pressure decreases, the velocity of the gas must increase to maintain a constant mass flow rate in the system. Pressure drops are proportional to gas velocity, resulting in larger pressure drops as operating pressure is lowered.

Eventually, a pressure will be reached where the pressure drops identified in Figure 115 become crippling for this system. A series of test cases were simulated with the model to determine the minimum pressure possible. The results are shown in Table 48.

Table 48: Pressure data from a series of simulated test cases run on the model to determine minimum viable pressure. All pressures are in Pascals.

P2 (Pa)	P3	P4	P5	P6	P7	P8	P9	P11	P12
100000	99990	99430	99370	17170	17170	17140	17140	99310	99250
90000	89990	89370	89300	17170	17170	17140	17140	89240	89170
80000	79990	79290	79210	17170	17170	17140	17140	79140	79070
70000	69990	69180	69100	17170	17170	17140	17140	69020	68930
60000	59990	59050	58950	17170	17170	17140	17140	58850	58750
50000	49980	48860	48740	17170	17170	17140	17140	48620	48500
40000	39980	38570	38420	17170	17170	17140	17140	38270	38120
30000	29970	28100	27890	17170	17170	17140	17140	27680	27470
20000	19960	17140	16800	17170	17170	17140	17140	16460	16110
15000	14940	11180	10660	17170	17170	17140	17140	10120	9552
13300	**13240**	**8989**	**8346**	**17170**	**17170**	**17140**	**17140**	**7645**	**6899**
10000	9914	4244	2884	17170	17170	17140	17140	854.9	0
7500	7385	0	0	17170	17170	17140	17140	0	0

Each row in the table represents a CAC outlet pressure setpoint (P2) and the resulting pressure calculations at each stage in the BAM process. Locations are identifiable on Figure 115, with the final location, P12, being the pressure of the cathode exhaust after running it through a secondary heat exchanger, which is not shown in the figure. The first simulation was run with a P2 setpoint of 100,000 Pa, or 1 bar, and each subsequent simulation stepped down the pressure. The bolded (blue) row in the table represents the lowest pressure at which P2 could be set before the pressure drops became crippling. The last two rows, highlighted with green text, resulted in pressure drops too high for the system to function, as indicated by a pressure value of 0 Pa at a location in the BAM system.

According to these test cases with the model, the lowest pressure at which the SOE cathode (P5) can operate before the pressure drops cripple the system occurs at 8346 Pa, or 83.5 mbar. According to the empirical data presented in Figure 114, the SOE appears to be operable down to a cathode pressure of at least 150 mbar. In the absence of empirical data down to 83.5 mbar, the minimum pressure that the SOE can be operated at must be treated as 150 mbar, defined by the SOE mass diffusion limits. However, it is likely that the SOE diffusion limits would occur below 83.5 mbar, meaning that the true limiting factor in the operating pressure of BAM is the pressure drops in the system, and not the SOE diffusion limits.

Chapter 6 will show the results of the optimization and provide recommended architectures for the BAM system.

Chapter 6: Optimization Model Results and Discussion

This chapter shows and analyzes the results of the various optimizations that have been conducted on BAM. Sections 6.1 and 6.2 review the results of single-objective optimizations for power and mass, respectively. Sections 6.3 and 6.4 review the results of multi-objective optimizations for power and mass, and power, mass, and reliability, respectively. The results of reliability optimization are explored in more detail in Section 6.5, followed by a sensitivity analysis to demonstrate the impact of each design variable on the objective functions in Section 6.6. Section 6.7 continues the sensitivity study, analyzing the impact of parameters such as mission duration and landing site location on the optimized BAM design. Section 6.8 synthesizes the multi-objective optimization findings by discussing tradeoffs between objective functions throughout the BAM design. A final, recommended design for BAM is selected and discussed in Section 6.9, and Section 6.10 summarizes the findings of this chapter.

6.1 Single-Objective Optimization Results – Power

Optimization Result

Twenty-one SA optimizations were conducted with power as the objective, resulting in over 2300 valid designs of BAM. The most optimal design for power minimization yielded a total BAM power of 25.3 kW, a mass of 13,420 kg, a volume of 40 m^3, and a reliability of 0.99. The convergence history of the optimization that resulted in this design is shown in Figure 116.

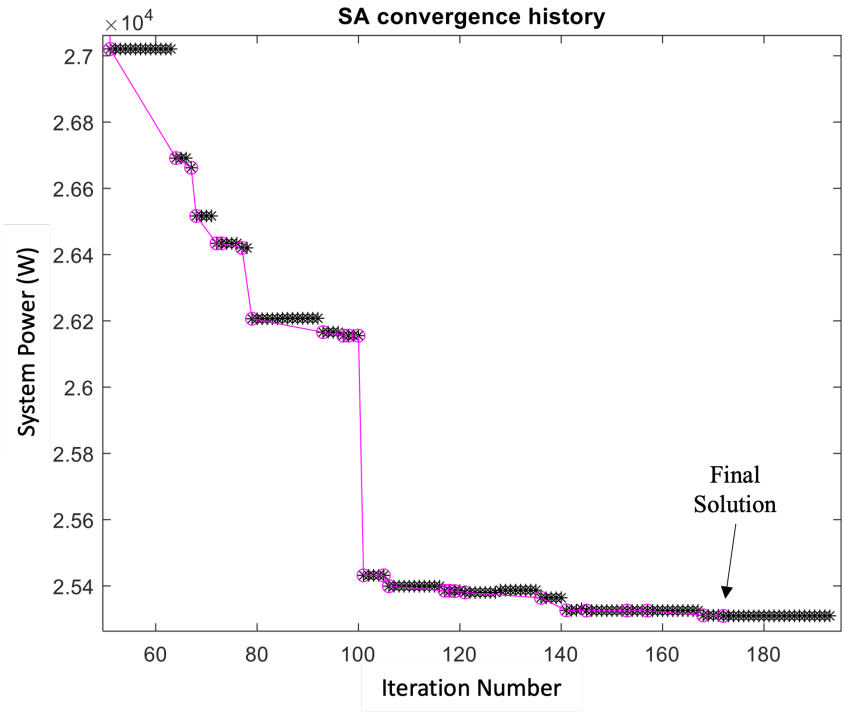

Figure 116: Simulated Annealing (SA) convergence history for power optimization of BAM, resulting in a final system power of 25.3 kW after 193 iterations.

The figure shows the final ~150 iterations of the optimization; the first ~50 iterations of the optimization resulted in solutions with significantly higher power and are omitted from the figure for clarity of the final convergence. The y-axis displays the total BAM power in Watts, as calculated by the model for the inputs dictated by the optimizer. Each blue circle represents a new best design that was found at that iteration.

Objectives

A breakdown of power, mass, and volume by subsystem for the final solution are given in Figure 117:

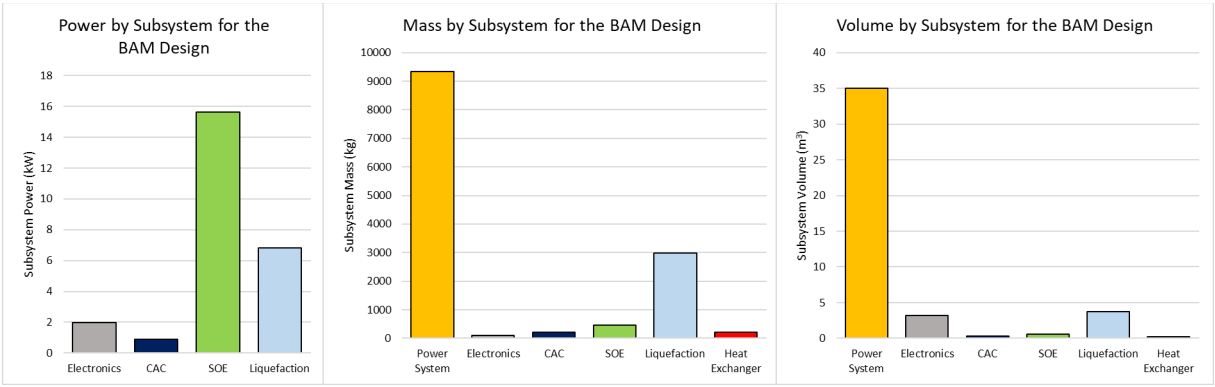

Figure 117: Breakdowns of power, mass, and volume for each subsystem in BAM for the power-optimized design

Power is dominated by the SOE, accounting for over 60% of the total power draw of the system. The vast majority of this power is from the electrolysis itself, with only a small percentage accounting for power dedicated to gas preheating, heat loss, and electrochemical compression. The mass and volume are dominated by the Kilopower subsystem, owing to the three active and three spare units selected by the optimizer. Even without spare units, the Kilopower subsystem would dominate the total mass and volume.

Rucker et al. [107] conducted a study that compared the expected mass of Kilopower units with the expected mass of solar panels for Mars ISRU power generation. They found that to provide 23 kW of power to an ISRU plant, which is similar to the power in this BAM design, it would require 9,154 kg of Kilopower units or 11,713 kg of solar panels and batteries. They assumed that the ISRU plant would operate continuously, so solar panels would power the system and charge batteries by day, and batteries would power the system by night. The panels were sized to manage a dust storm scenario. They also assumed an equatorial landing position, and noted that as latitude increased, the disparity between Kilopower and solar power mass increased. At Jezero Crater, they predicted the solar power system would weigh 17,815 kg, nearly double that of the Kilopower system. Therefore, despite the overwhelming dominance of Kilopower in terms of BAM mass, a solar power system would contribute an even larger mass.

The total volume available in the fairing of a SpaceX Falcon Heavy rocket is approximately 145 m^3 [193]. The optimized design presented here has a total volume of 40 m^3, allowing it to be transported to Mars in a single rocket fairing.

Design Variables

The final solution from this optimization is described by the final values of the design variables, shown in the bolded column of Table 49:

Table 49: Initial and final design variable values for the most successful single objective optimization run for power minimization

Design Variable	Variable Name	Initial Value	Final Value	Units
Inlet Flow Rate	$\dot{m}_{in}$	12	**11.1**	kg/hr
Compressor Pressure	P_2	20370	**16478**	Pa
CAC Type	CAC	Scroll	**Scroll**	-
Cell Area	A_{cell}	100	**89.3**	cm^2
Number of cells per stack	N_{cps}	53	**44**	-
Number of stacks	N_{stacks}	5	**4**	-
Electrolysis Temperature	T_6	1086	**1086**	K
Electrolysis Pressure	P_6	17090	**17090**	Pa
Voltage	V_{app}	0.936	**0.936**	V
Area of Heat Exchanger 1	A_{HE1}	5.6	**4.7**	m^2
Area of Heat Exchanger 2	A_{HE2}	4.1	**6.9**	m^2
Number of CAC systems	N_{CAC}	4	**5**	-
Liquefaction piping insulation	$t_{liq-pipe-ins}$	0.25	**0.37**	m
Liquefaction MAV insulation	$t_{liq-MAV-ins}$	3.2	**4.6**	m
Inter-piping insulation	$t_{ins-pipe}$	0.03	**0.06**	m
SOE inner layer insulation	$t_{SOE-ins1}$	0.06	**0.07**	m
SOE outer layer insulation	$t_{SOE-ins2}$	0.18	**0.14**	m
Spare blowers	$Blower_{\#SU}$	3	**4**	-
Spare cryocoolers	$Cryocooler_{\#SU}$	1	**2**	-
Spare valves	$Valve_{\#SU}$	7	**10**	-
Spare mechanical pumps	$CACmechanical_{\#SU}$	5	**4**	-
Spare SOE cells	$SOECell_{\#SU}$	202	**204**	-
Spare SOE stacks	$SOEStack_{\#SU}$	2	**1**	-
Spare Kilopower units	$Kilopower_{\#SU}$	1	**3**	-
Spare heat exchanger plates	$Heatexchanger_{\#SU}$	7	**10**	-

All design variable values appear reasonable and within their bounds, with the exception of the MAV insulation thickness. A thickness of 4.6 meters is likely impractical and should be minimized in future optimizations. Several notable trends include the movement of inlet flow rate and compressor pressure towards their lower bounds to minimize power consumption of the CAC system, relatively large heat exchanger areas to recuperate heat, and insulation layers to minimize heat leaks.

Constraints

The optimal solution was bounded by the first two constraints listed in Table 20 in Section 3.4.4: oxygen production rate and SOE inlet pressure. The oxygen production rate converged to the minimum needed to fill the MAV. This makes sense, as producing extra oxygen would require

additional power. The SOE inlet pressure converged to the minimum allowable pressure, which also makes sense, given that a higher pressure would require additional compression power. The other constraints, including the applied voltage and utilization fraction of CO_2, did not converge on a boundary, indicating that these constraints do not dictate the design of BAM for this objective function.

The most optimal power-based solution for BAM among the 2300 valid solutions resulted in a system with low inlet flow rate, low inlet SOE pressure, large heat exchangers, and moderately thick insulation layers. The heat exchanger and insulation, in combination with spare Kilopower units, however, resulted in a relatively high system mass. The following section explores the results of the single objective optimizations conducted with mass as the primary objective to determine how low of a mass can be achieved within the system bounds and constraints.

6.2 Single-Objective Optimization Results – Mass

Optimization Result

Twenty-one SA optimizations were conducted with mass as the objective, resulting in approximately 2000 valid designs of BAM. The most optimal design for mass minimization yielded a total BAM mass of 7002 kg, a power of 28.6 kW, a volume of 26 m^3, and a reliability of 0.86. The convergence history of the optimization that resulted in this design is shown in Figure 118.

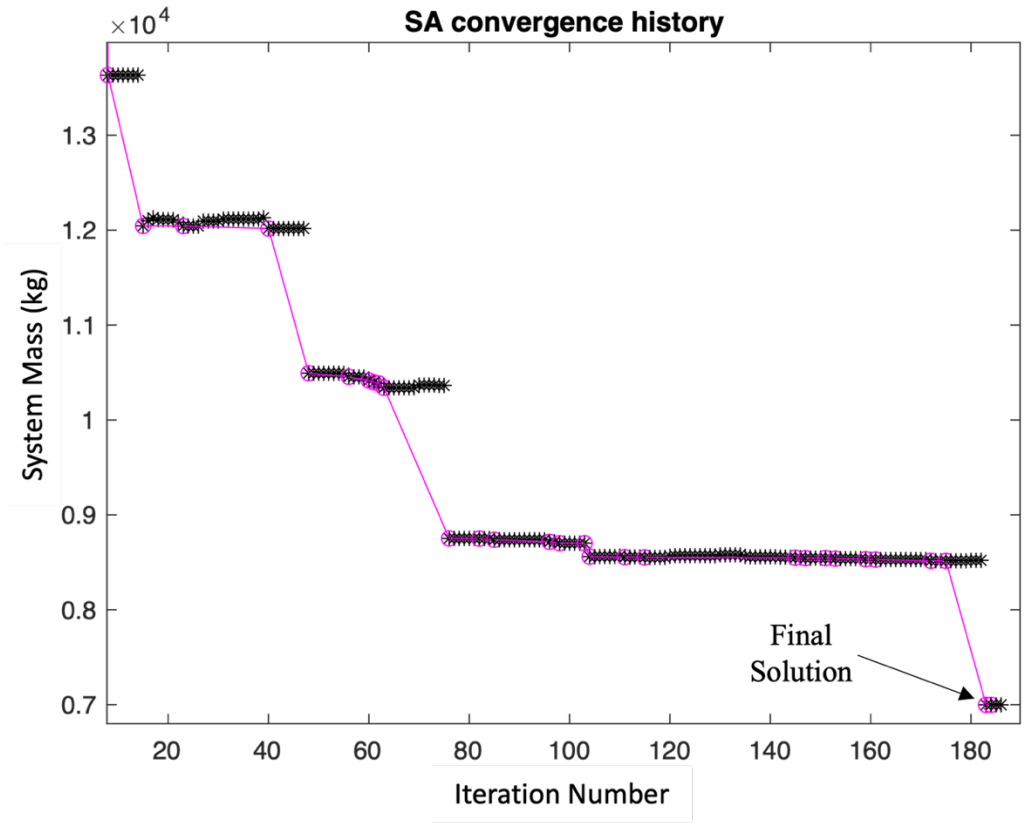

Figure 118: Simulated Annealing (SA) convergence history for mass optimization of BAM, resulting in a final system mass of 7002 kg after 186 iterations.

The y-axis displays the total BAM mass in kg, as calculated by the model for the inputs dictated by the optimizer. As before, each blue circle represents a new best design that was found at that iteration.

Objectives

A breakdown of power, mass, and volume by subsystem for the final solution are given in Figure 119:

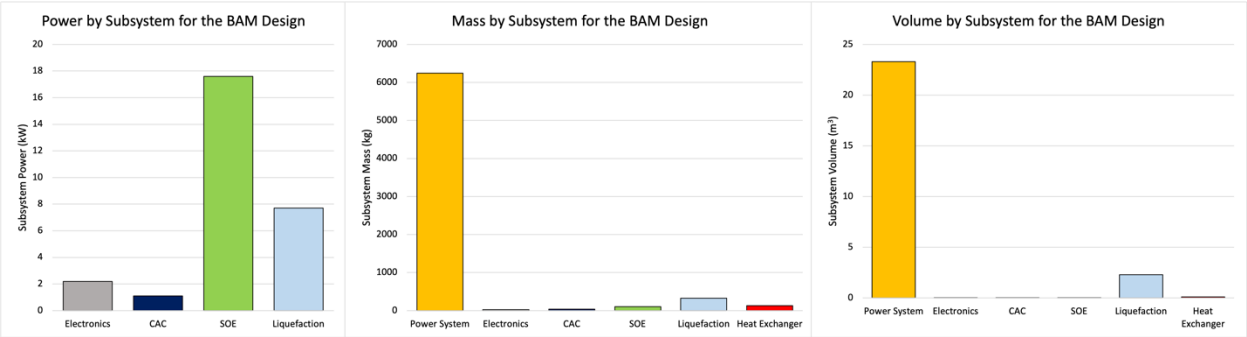

Figure 119: Breakdowns of power, mass, and volume for each subsystem in BAM for the mass-optimized design

The relationship between subsystems in terms of the objective functions is similar to those in the power-optimized design from the previous section. Power is dominated by the SOE, accounting for over 60% of the total power draw of the system. The mass and volume are dominated by the Kilopower subsystem to an even greater degree than before, accounting for nearly 90% of the total mass and volume of BAM. The liquefaction unit is the second highest contributor to each.

The volume is substantially reduced when compared to the power-optimized design from the previous section, shrinking from 43 m^3 to 26 m^3. As before, this will easily fit inside a single standard rocket fairing.

Design Variables

The optimal design from this optimization is described by the final values of the design variables, shown in the bolded column of Table 50:

Table 50: Initial and final design variable values for the most successful single objective optimization run for mass minimization

Design Variable	Variable Name	Initial Value	Final Value	Units
Inlet Flow Rate	$\dot{m}_{in}$	18.3	**10.8**	kg/hr
Compressor Pressure	P_2	27291	**17942**	Pa
CAC Type	CAC	Scroll	**Centrifugal**	-
Cell Area	A_{cell}	93.8	**70.8**	cm^2
Number of cells per stack	N_{cps}	89	**89**	-
Number of stacks	N_{stacks}	3	**1**	-
Electrolysis Temperature	T_6	1099	**1123**	K
Electrolysis Pressure	P_6	20854	**32449**	Pa
Voltage	V_{app}	0.954	**0.954**	V
Area of Heat Exchanger 1	A_{HE1}	0.77	**2.1**	m^2
Area of Heat Exchanger 2	A_{HE2}	3.3	**3.1**	m^2
Number of CAC systems	N_{CAC}	3	**2**	-
Liquefaction piping insulation	$t_{liq-pipe-ins}$	0.02	**0.04**	m
Liquefaction MAV insulation	$t_{liq-MAV-ins}$	0.5	**3.5**	m
Inter-piping insulation	$t_{ins-pipe}$	0.05	**0.02**	m
SOE inner layer insulation	$t_{SOE-ins1}$	0.03	**0**	m
SOE outer layer insulation	$t_{SOE-ins2}$	0.04	**0**	m
Spare blowers	$Blower_{\#SU}$	2	**1**	-
Spare cryocoolers	$Cryocooler_{\#SU}$	0	**0**	-
Spare valves	$Valve_{\#SU}$	0	**5**	-
Spare mechanical pumps	$CACmechanical_{\#SU}$	3	**1**	-
Spare SOE cells	$SOECell_{\#SU}$	161	**176**	-
Spare SOE stacks	$SOEStack_{\#SU}$	1	**0**	-
Spare Kilopower units	$Kilopower_{\#SU}$	2	**1**	-
Spare heat exchanger plates	$Heatexchanger_{\#SU}$	16	**12**	-

There are notable results with these design variables that indicate trends when optimizing for mass. The number of SOE stacks ended with a single stack, which is non-optimal for reliability as it lacks redundancy but is the most mass-efficient method of designing the SOE subsystem. The electrolysis temperature ended at its upper bound of 1123 K, likely because this results in more efficient electrolysis which allows the system to have less cell area and thus less mass.

More predictable trends that were observed included a general reduction in number of spare units, insulation thickness, and heat exchanger size when compared to the power optimized solution. All these trends result in the system having less physical material present, which reduces its mass. Notably, the heat exchanger area and insulation thickness did *not* converge to values of zero, indicating that a certain amount of heat recuperation and heat loss prevention is

beneficial to the mass of the system. This is likely because heat savings reduces the size of the heating and cooling systems, reducing total system mass. The largest mass reduction, when compared to the power-optimized solution, comes from the use of only one spare Kilopower unit. It was not possible to remove all spare Kilopower units, as this would result in a reliability below 0.8, which would be rejected by the optimizer.

Constraints
The optimal solution was bounded only by the minimum oxygen production constraint. The oxygen production rate converged to the minimum oxygen production rate required, as extra oxygen production would require additional mass in nearly every subsystem.

Mass of ISRU vs. Mass of Oxygen
The mass of the oxygen required to launch one MAV for a crew of six is expected to be approximately 30,800 kg. The total mass of the ISRU system found in this mass optimization is 7,002 kg. This immediately demonstrates a savings of over 23,000 kg in launched mass by sending an ISRU plant to Mars to produce oxygen rather than sending the oxygen itself. The savings are actually significantly more substantial, owing to two additional considerations.

The first is that the majority of the ISRU system mass is from the Kilopower units. When a crew arrives on Mars, they will require an estimated 21 – 25 kW to operate their systems, including their habitats and life support equipment [107], meaning that they will require multiple Kilopower units. For this reason, it is more accurate to compare the mass of the oxygen to the mass of the ISRU system without the mass of the power systems that must be there for the crew anyway.

The second consideration is that the ISRU system, including the Kilopower units, can be used for multiple missions, if the crew returns to the same location. In contrast, in the case of sending oxygen to Mars rather than producing it with ISRU, the same 30,800 kg of oxygen would have to be sent for every Mars mission.

Table 51 shows the mass of the system with both of these considerations taken into account. It assumes only one additional 10 kWe Kilopower unit is needed to supplement the ISRU system beyond the requirements of the crew's systems. It also assumes that the ISRU system can be reused for two missions before needing to be replaced based on its MTBF [109]. These are both conservative estimates.

Table 51: Comparison of equivalent mass between sending oxygen to Mars and producing it with ISRU. Results shown for a single Mars mission and for two Mars missions to the same location. The ISRU system mass should be considered with one Kilopower unit only, as the crew will require several Kilopower units upon arrival to run their habitat and equipment.

	One Mars Mission	Two Mars Missions
O_2 Mass if sent from Earth (kg)	30,800	61,600
ISRU system mass (kg)	7,000	7,000
ISRU system mass, 1 Kilopower only (kg)	2,320	2,320
Mass Savings (kg)	**28,480**	**59,280**

The equivalent mass savings of the ISRU system ends up being nearly 60,000 kg over two missions. This could save billions of dollars in launch costs and demonstrates the potential of ISRU for Mars propellant production.

Summary
The most optimal mass-based solution for BAM among the 2000 valid designs resulted in a system with low inlet flow rate, a centrifugal compressor, a single SOE stack, a low number of redundant units, and a small amount of insulation. The total system power was significantly higher than in the power optimized solution, indicating tradeoffs between mass and power that are discussed in more detail in Section 6.8. The following section discusses and analyzes a combined Pareto front of power and mass optimizations with the intent to find the optimal balance between the two objectives.

6.3 Multi-Objective Optimization Results – Power and Mass

Methodology
To transition from single objective optimization to multi-objective optimization, power and mass were considered together. It is possible to identify optimal solutions in this multi-objective optimization in a variety of ways. One method involves running optimizations with an objective function that is a weighted sum of the power and mass of the system. Another option, which was used in this dissertation, is to combine the results of single objective optimizations for each individual objective function into a large design space and form a Pareto front. This gives a broader view of the design space than a weighted sum method, which is why it was selected.

A Pareto front represents the set of nondominated solutions to a multi-objective optimization problem. A solution is considered nondominated when no objective function can be improved by another solution without worsening another objective function. In the case of this two-objective optimization of BAM, this means that a BAM design is nondominated when it is not possible to decrease either the power or mass without increasing the other.

Pareto Front
18,453 valid designs of BAM were recorded over the course of many single objective optimizations. The power and mass for each of these designs were passed through a MATLAB

code [194] that identified 17 nondominated solutions from this set. These nondominated solutions form the Pareto front shown in Figure 120.

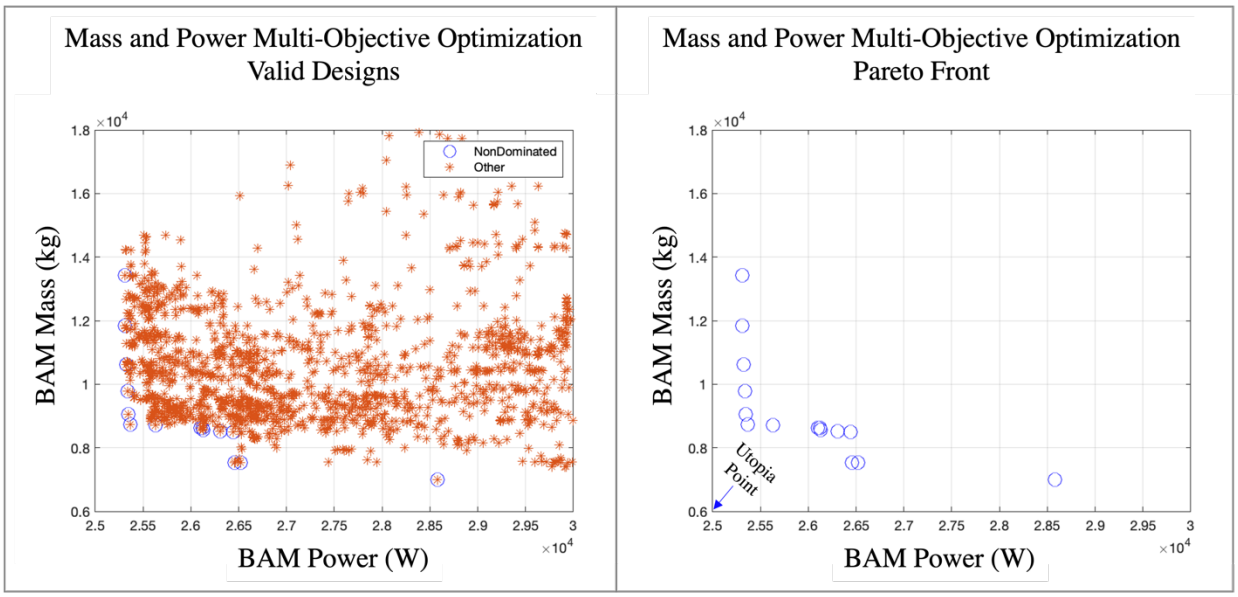

Figure 120: Multi-objective optimization results for power vs. mass. (Left) Design space showing dominated solutions (stars) and nondominated solutions (circles). (Right) Filtered results showing only nondominated solutions, which form the Pareto front. The ideal point, called the Utopia point, indicates the direction that minimizes both objectives and is indicated on the plot.

The left side of the figure shows many of the dominated solutions of BAM, indicated by stars, and the nondominated solutions, indicated by circles. The right side of the figure filters out the dominated solutions to leave only the nondominated solutions visible, which form the Pareto front. Each of these 17 nondominated solutions represents an optimized BAM design. The optimal combination of objective functions is indicated by the utopia point, which in this case is the minimization of both power and mass. It represents an idealistic solution and is used to indicate the direction of optimality for both objectives.

Discussion

It is useful to analyze the spread of values for each design variable across the 17 nondominated solutions. If a design variable converged to its lower bound for most of the 17 nondominated solutions, for example, that design variable may be optimized at its lower bound. The spread of values for each primary design variable in these nondominated solutions are shown in the parallel coordinates plot in Figure 121.

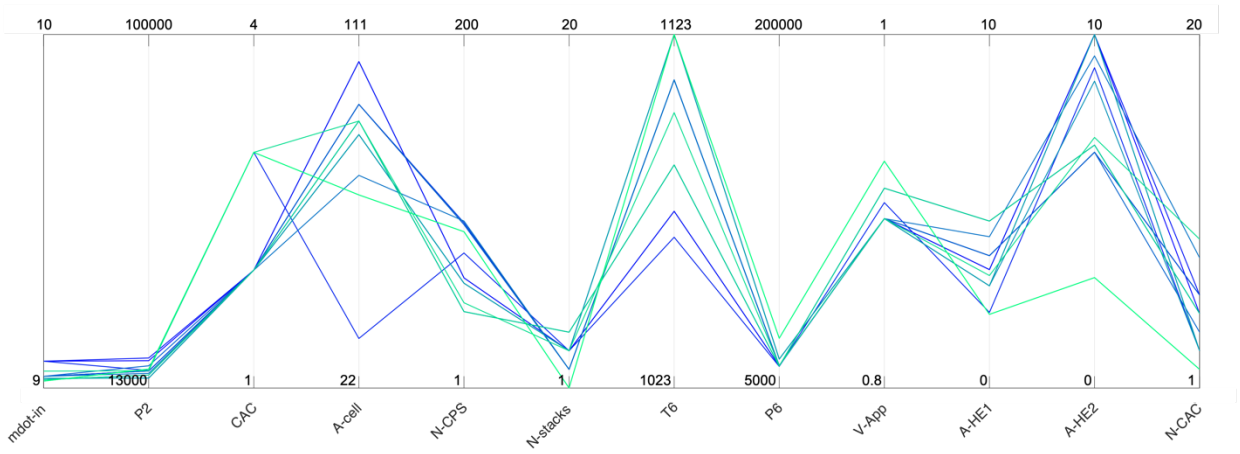

Figure 121: Parallel coordinates plot of primary design variable values across 17 nondominated solutions in the two-objective optimization of BAM. The variables are bounded vertically by their upper and lower bounds.

The y-axis changes for each design variable and has maximum and minimum values equal to the upper and lower bounds of that design variable. Each vertical axis, representing a single design variable, will be described below.

$\dot{m}_{in}$, the inlet mass flow rate to the system, shown on the far left of the parallel coordinates plot, converged towards its lower bound for all 17 designs, indicating that the lower bound is the optimal value for this design variable. P2 had a similar trend. The type of CAC converged to a value of 2 for 14 of the designs, indicating a scroll compressor, and a value of 3 for the remaining 3 designs, indicating a centrifugal compressor. Clearly, for mass and power optimization, either type of mechanical compressor is dominant compared to a cryogenic or sorption compressor. The SOE cell area was spread across its allowable range, with a preference towards the upper half of its range. Intuitively, SOE cell area should converge to its upper bound, as larger cells are more mass efficient and would experience less overall heat leaks. The failure of it to converge to its upper bound may therefore indicate that cell area has only a marginal effect on the two objective functions.

The number of cells per stack, N_{CPS}, weakly converged to the middle of its range, with all nondominated solutions having an N_{CPS} between 44 and 93. The number of stacks, N_{stacks}, converged near its lower bound of 1 for all nondominated solutions. T6, the SOE temperature, was spread across the upper half of its range. Higher temperature electrolysis leads to a lower mass, as each SOE cell can produce more oxygen and thus less total cell area is required. It does require additional preheating and increases heat losses in the system, however, which leads to a conflict between power and mass. This may be why T6 failed to converge to a standard value in this optimization. The anode pressure, P6, converged near its lower bound, likely owing to the reduced power of compression required.

The voltage of each cell weakly converged to the middle of its range, which strikes a balance between the mass efficiency benefits of operating at a higher voltage and thus requiring less cell area to produce the same quantity of oxygen, and the reliability benefits of operating at a lower voltage to reduce the risk of coking. Reliability was not one of the two objectives that were optimized in this particular analysis, but was rather treated as a constraint, where a minimum

system reliability had to be met. It is possible this constraint drove the voltage down to the middle of its range. The area of the heat exchanger 1, which exchanges heat between the anode exhaust and the incoming Mars gas, converged towards the middle of its range. The addition of heat exchanger area causes a significant reduction in power at the cost of only a marginal increase in mass. Therefore, it is expected that both heat exchangers would converge towards their upper bounds. The reason heat exchanger 1 does not is because a heat exchange area approximately halfway between its bounds is sufficient to transfer nearly 100% of the heat from the anode exhaust to the incoming SOE gas. Any increase in area beyond that does not result in a power reduction but increases the mass, which is nonoptimal. Lastly, the number of CAC units weakly converges towards the lower half of its range. This variable does not impact power, so it was expected that it would converge to its lower bound to minimize mass. The lack of a strong convergence indicates that mass is only marginally influenced by this variable, which makes sense given that the CAC system mass is only a small fraction of the total BAM mass.

The same analysis was conducted for the 13 secondary design variables and is shown in Figure 122.

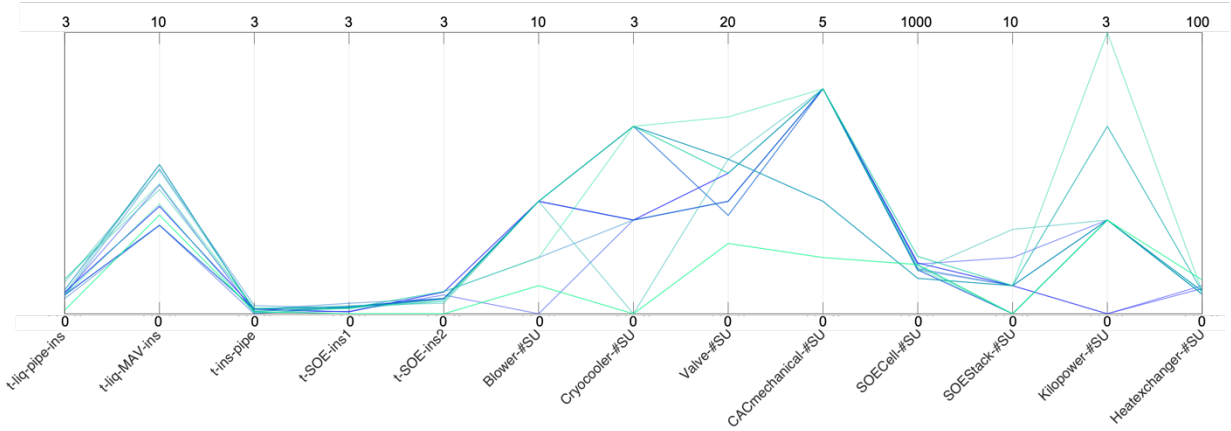

Figure 122: Parallel coordinates plot of secondary design variable values across 17 nondominated solutions in the two-objective optimization of BAM. The variables are bounded vertically by their upper and lower bounds.

For the sake of conciseness, the convergence of these variables will be analyzed in less detail than the primary variables. Broadly, the insulation thickness of the liquefaction piping ($t_{liq-pipe-ins}$) the piping between subsystems ($t_{ins-pipe}$) and the SOE hotbox ($t_{SOE-ins1}$ and $t_{SOE-ins2}$) all converged near the lower ends of their bounds. This indicates that any additional insulation would result in minimal power savings but increase the mass, which is nonoptimal. The insulation of the MAV converged to a higher value owing to the increased heat leaks from the larger MAV tank. The last eight design variables in the parallel coordinates plot all describe the number of spare units of a certain part of BAM. A decrease in spare units generally has no meaningful effect on power but decreases mass. It was therefore expected that these would converge towards their lower bounds, as only mass and power are optimized in this scenario. The fact that they did not show strong convergence towards their lower bounds indicates that either these design variables had minimal effects on mass, or else the minimum reliability constraint had to be satisfied by increasing spare units in certain instances.

Takeaways
Mass and power are clearly competing objectives in the design of BAM, as indicated by the Pareto front in Figure 120. The combined optimization of these two objective functions resulted in 17 nondominated solutions, each of which is a valid optimal design for BAM. Many trends in the design variable values were observed across these solutions, including the minimization of inlet flow rate, compressor outlet pressure, and number of SOE stacks, and the maximization of heat exchanger area.

The following section adds reliability as a third objective in the optimization of BAM, which alters its optimal design and the convergence of its design variables.

6.4 Multi-Objective Optimization Results – Power, Mass, Risk, and Volume

Methodology
A similar methodology was used to generate the optimization results for this multi-objective optimization as the one presented in Section 6.3. The results of single objective optimizations for mass, power, and reliability were combined to form a Pareto front of nondominated solutions. In this case, a BAM design is considered nondominated when it is not possible to decrease the power or mass, or increase the reliability, without negatively affecting one of the other objectives.

Pareto Front
The same 18,453 valid designs of BAM mentioned in Section 6.3 that were recorded over the course of many single objective optimizations were used for this three-objective optimization. The power, mass, and reliability for each of these designs were passed through a MATLAB code [194] that identified 153 nondominated solutions from this set. This is a substantially higher number of nondominated solutions compared to the 17 found in Section 6.3, owing to the addition of a third objective function. These nondominated solutions form the three-dimensional Pareto front shown in Figure 123.

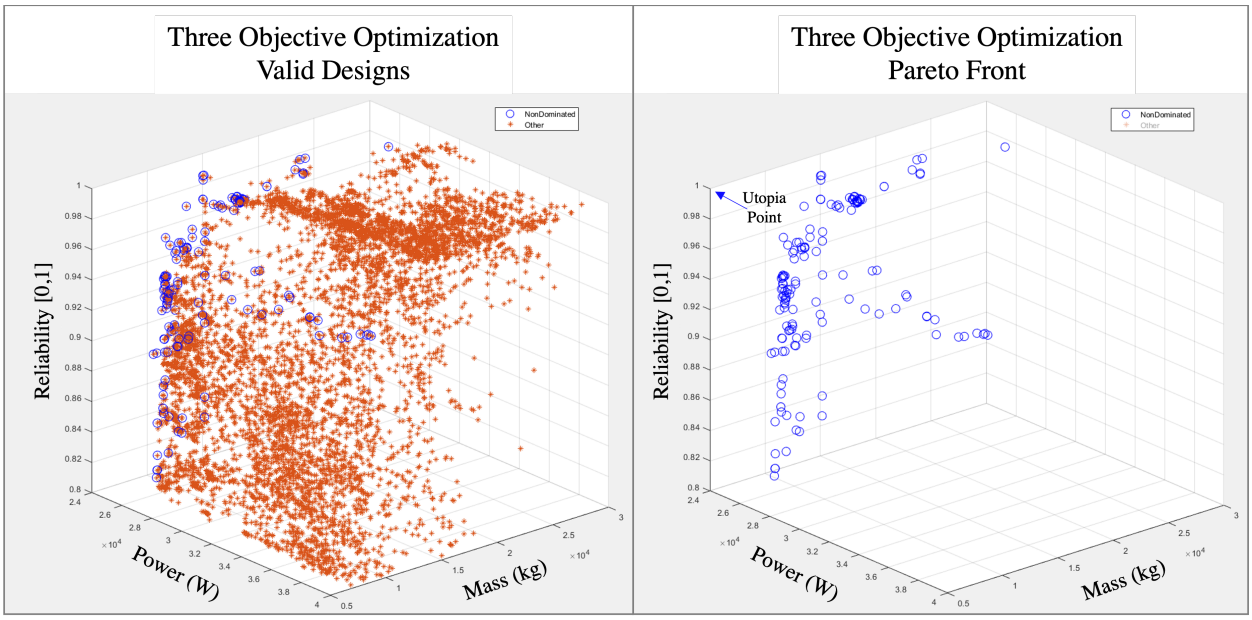

Figure 123: Multi-objective optimization results for combined power, mass, and reliability optimization. (Left) Design space showing dominated solutions (stars) and nondominated solutions (circles). (Right) Filtered results showing only nondominated solutions, which form the Pareto front. The ideal point, called the Utopia point, indicates the direction that optimizes all three objectives and is indicated on the plot.

The left half of the figure shows most of the dominated solutions of BAM, indicated by stars, and the nondominated solutions, indicated by circles. The right side of the figure only shows the nondominated solutions. The direction that indicates the optimal values of all three objectives is indicated on the right half of the figure by the utopia point arrow. In this case, it represents a design that minimizes mass and power while maximizing reliability.

Discussion

Once again, it is useful to analyze the spread of values for each design variable across the 153 nondominated solutions. These are shown in Figure 124 and Figure 125, where each design variable has its own y-axis with a range covering the lower bound to the upper bound for that design variable.

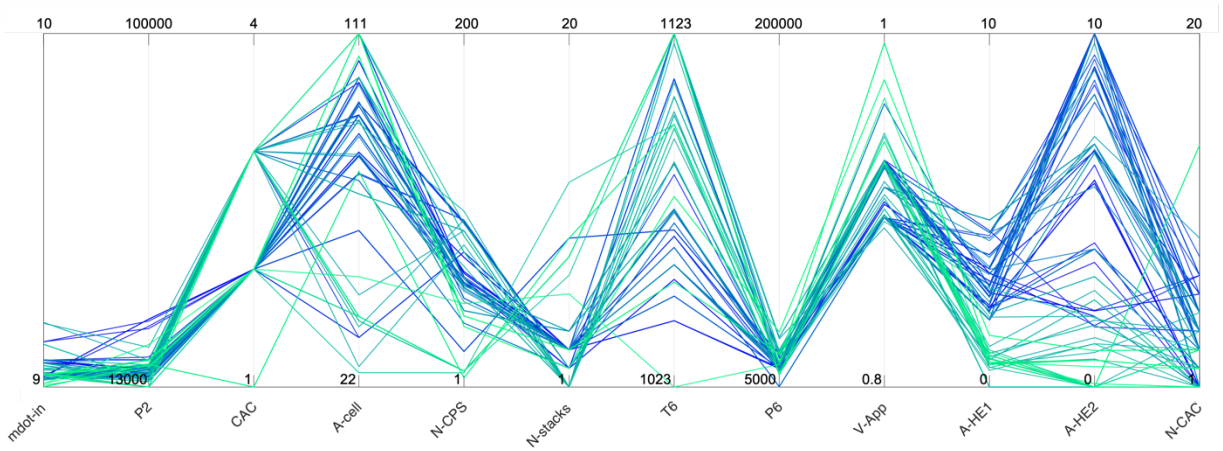

Figure 124: Parallel coordinates plot of primary design variable values across 153 nondominated solutions in the three-objective optimization of BAM. The variables are bounded vertically by their upper and lower bounds.

As in Section 6.3, each of the primary design variables shown in Figure 124 will be analyzed here. The inlet mass flow rate to the system, $\dot{m}_{in}$, converged towards its lower bound for all 153 designs, indicating that the lower bound is the optimal value for this design variable. This was the same trend as seen with two-objective optimization. Similarly, P2 kept its trend of converging towards its lower bound. The type of CAC differed slightly when compared to the two-objective optimization, as it was more evenly split between scroll and centrifugal compressors and had three nondominated solutions with a value of 1, representative of a cryogenic compressor. No solutions had a value of 4, representing a sorption compressor, indicating that sorption compressors are always dominated by another compressor type according to this model. The SOE cell area was once again spread across its range, indicating that it either has opposite effects on two or more objective functions, or else it has minimal effects on all of them. This will be explored in more detail in Section 6.6 with a sensitivity analysis on each design variable.

The number of cells per stack, N_{CPS}, weakly converged to the lower half of its range. There is a shift towards the lower bound when compared with the two-objective optimization results, implying that the addition of reliability as an objective makes a lower N_{CPS} more favorable. This makes sense, as a lower number of cells per stack would require an increase in the number of SOE stacks to maintain the same number of cells, which also increases stack redundancy and thus reliability. Indeed, the number of SOE stacks, N_{stacks}, experienced a shift towards its upper bound with several of the nondominated solutions in Figure 124 when compared to the results in the two-objective optimization in Figure 121. T6, the SOE temperature, was once again spread across its range owing to its opposing influences on mass and power. The anode pressure, P6, again strongly converged to its lower bound. It has weak influences on mass and reliability but a strong influence on power, which explains its convergence to a lower value which would reduce the compression power requirements.

The applied voltage to the SOE cells remained in the center of its range for most nondominated solutions, but interestingly had several solutions with a voltage near its upper bound that were not present in the two-objective optimization from Section 6.3. This is unexpected, as the addition here of reliability as a third objective intuitively would have driven the voltage lower, given that a high voltage increases the risk of cell coking. This is better explored in the Sensitivity Analysis in Section 6.6. The areas of the heat exchangers have a significantly wider spread across their range when compared to the nondominated solutions in the two-objective optimization. This can be explained by the fact that the heat exchanger area does not impact reliability, and thus a wide range of values for heat exchanger area would be accepted by reliability-driven optimizations. Lastly, the number of CAC units remained near the lower half of its range but included more solutions near the middle of its range owing to the favorable increase in reliability that results from an increase in the number of CAC units.

The same analysis was conducted for the 13 secondary design variables and is shown in Figure 125.

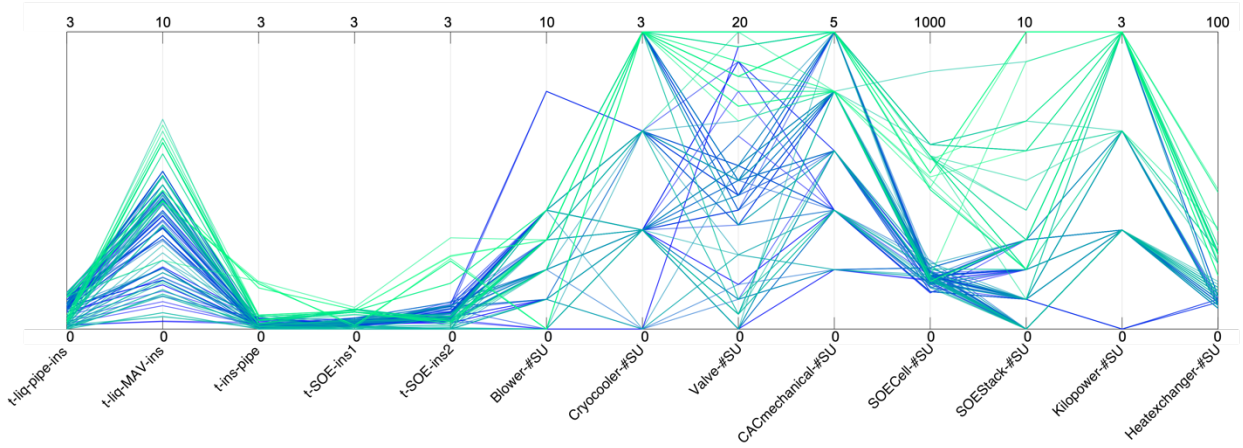

Figure 125: Parallel coordinates plot of secondary design variable values across 153 nondominated solutions in the three-objective optimization of BAM. The variables are bounded vertically by their upper and lower bounds.

A broad analysis indicates the same trends of the five insulation thickness design variables as in the two-objective optimization: most solutions favor designs with a non-zero amount of insulation near the lower bound. This allows BAM to prevent most heat leaks without adding significant mass to the system. Reliability is unaffected by insulation thickness at any location in the BAM design. The remaining eight design variables, all of which describe the number of spare units of a certain part of BAM, show a significantly wider spread in this analysis than in the two-objective optimization. The reason for this is clear: an increase in spare units increases the reliability, and thus the addition of reliability as a third objective here shifts the nondominated results for these design variables towards their upper bounds. A wide range is observed for all of these spare unit design variables, since reliability optimization accepts solutions with large numbers of spare units, mass optimization accepts solutions only with a low number of spare units to keep mass down, and power optimization accepts solutions across the entire range, as power is mostly unaffected by spares.

Takeaways

The addition of a third objective resulted in a significant increase in the number of nondominated solutions that form the 3-dimensional Pareto front. It is important to note that volume was not considered as a fourth objective because all valid BAM solutions found over the course of these optimization runs had a volume that would fit in a single Falcon Heavy rocket fairing. This makes the minimization of volume insignificant, as a single launch will be required regardless of any further decreases in system volume.

Many trends in the design variable values were observed within the 153 solutions. These included the minimization of inlet flow rate, compressor outlet pressure, number of SOE stacks, and insulation thickness, and the maximization of cell area and applied voltage. In general, design variables had a wider spread of values in the three-objective Pareto front than in the two-objective Pareto front, owing to more complex relationships between design variables and the three competing objectives. The tradeoffs between objectives throughout the BAM system is described in more detail, with examples, in Section 6.8.

The following section analyzes the results of the reliability analysis in more detail.

6.5 Discussion of PRA Results

It is useful to investigate the results of the reliability analysis, first described in Section 4.9, to determine how reliability changes over the course of the mission. Plots of the system reliability and subsystem reliabilities will be given for the optimal designs previously shown in Section 6.1 and Section 6.2, respectively.

The optimal design based on power optimization, as described in Section 6.1, had a final power of 25.3 kW, a mass of 13,420 kg, and a reliability of 0.95. This assumed a 14-month ISRU production time. A change in the length of the mission would impact the reliability. To illustrate this, the reliability of this BAM design over the course of the mission is shown in Figure 126.

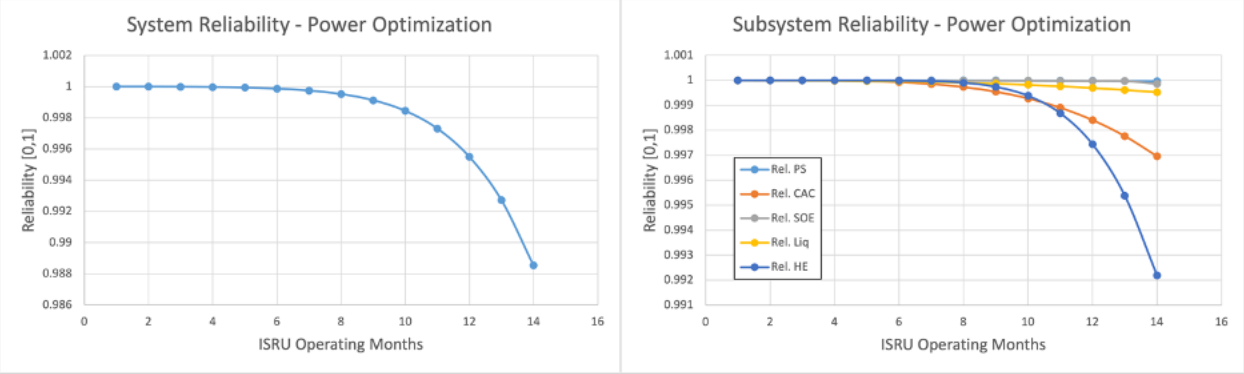

Figure 126: Reliability for the power-optimized design as a function of ISRU operating months. Results shown for the BAM system as a whole (left) and its individual subsystems (right), including the power system (PS), CAC, SOE, liquefaction (Liq), and heat exchanger (HE).

The reliability decreases over time as expected for all subsystems and the system as a whole. The least reliable subsystem in this design is the heat exchanger owing to the minimal amount of spare heat exchanger plates. The power system, on the other hand, is the most reliable system owing to the three backup Kilopower units used to support the three active Kilopower units. In reality, this is likely too many spares that contribute little to improving reliability but incur a heavy mass penalty.

The optimal design based on mass optimization, as described in Section 6.2 and whose design is listed in Table 50 of that section, had a final mass of 7002 kg, a power of 28.6 kW, and a reliability of 0.86. The reliability of this design over the length of the mission is shown in Figure 127.

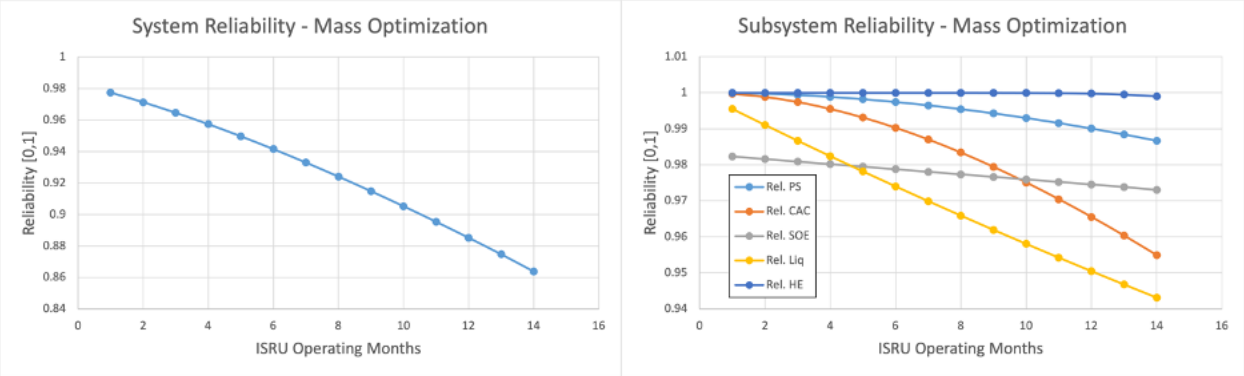

Figure 127: Reliability for the mass-optimized design as a function of ISRU operating months. Results shown for the BAM system as a whole (left) and its individual subsystems (right), including the power system (PS), CAC, SOE, liquefaction (Liq), and heat exchanger (HE).

This design had a significantly lower reliability than the power-optimized design that would likely be rejected for a human mission to Mars. The liquefaction has a relatively low reliability due to the lack of cryocooler spares in this design. The CAC system also has a lower reliability than in the power-optimized design owing to a decrease from four spare compressors to a single spare compressor. The heat exchanger, on the other hand, has improved reliability from the power-optimized design due to its increase in spare units.

The reliability, as it changes over the course of the mission, has been shown here in two examples. The individual impact of each design variable on reliability, power, and mass is described in significantly more detail in the following section.

6.6 Sensitivity Analysis – Design Variables

A two-part sensitivity analysis was conducted to determine the effect that each design variable has on each objective function. The first part of the sensitivity analysis included running an optimization with the design variable in question at its upper and lower bound in the starting design vector. In this way, the direction of the optimization was influenced by the design variable, and it was, in certain cases, possible to draw conclusions about the optimal value of that design variable based on where each optimization converged. For example, if two SA optimizations were run to study P_2 with starting values for P_2 of 10,000 Pa (lower bound) and 100,000 Pa (upper bound), and both optimizations converged to a final P_2 value of 10,000 Pa, it would be reasonable to conclude that a value of P_2 near its lower bound is optimal. Changing the value in the starting vector and allowing a full optimization to run, rather than simply adjusting the value and running a stand-alone calculation, was important to avoid becoming trapped in local optima. The full optimization allows interactions between the design variable in question and other design variables to take place. This study was conducted for most design variables across each of the three major objectives – power, mass, and reliability – resulting in a total of over 60 SA optimizations. A standard starting vector for each objective, based on prior optimization runs, was used to keep all other design variables constant in the starting vector.

The second part of the sensitivity analysis involved running the model across an array of values for each design variable and recording the corresponding values of the objective functions. This is often referred to as one-at-a-time (OAT) analysis, where one input variable is changed while all others are held constant. The OAT did not involve any SA optimization runs, but rather stand-

alone simulations. The results of this sensitivity analysis were normalized to determine the relative effects of each design variable using the following calculation:

$$\frac{dJ}{dx} = \frac{\frac{\Delta J}{J_o}}{\frac{\Delta \mathrm{x}}{\mathrm{x_o}}} \tag{111}$$

where J_o is initial value of the objective function in question, x_o is the initial value of the design variable in question, ΔJ is equal to $J_i - J_o$, the difference in the objective's value during the sensitivity analysis and its initial value, and Δx is equal to $x_i - x_o$, the difference in the design variable's value during the sensitivity analysis and its initial value. This normalization process allows one to quantify the effect that a change in a design variable will have on the objective function.

A limitation of OAT analysis is that it does not detect interactions between input variables. This is the reason the first part of the sensitivity analysis was conducted, to ensure interactions were considered. The results of both sensitivity analysis components will be analyzed and discussed in the following sections, which are organized by design variable.

6.6.1 Inlet Mass Flow Rate

The magnitude of the inlet mass flow rate, $\dot{m}_{in}$, has direct effects on many subsystems in BAM. A higher inlet mass flow rate means a higher dust loading on the filter, a higher throughput requirement of the CAC, more gas to pre-heat in the heat exchanger, and a lower utilization fraction in the SOE. The lower end of the inlet mass flow rate range is bounded by the minimum needed to produce the required oxygen flow rate, approximately 10 kg/hr CO_2. The upper end is unlimited, though it was bounded at 35 kg/hr to prevent excessive oversizing of the CAC system.

Effect of Changing $\dot{m}_{in}$ in the Optimization Design Vector

The value of $\dot{m}_{in}$ was adjusted in the initial design vector, x_0, to determine its effects on the SA optimization. Six SA optimizations were run to cover all combinations of $\dot{m}_{in}$ extremes and objective functions. These combinations are listed in Table 52.

Table 52: SA optimizations run to determine effect of inlet mass flow rate on objective functions

Objective Function to be Optimized	$\dot{m}_{in}$ Value in x_0
Mass	12 kg/hr
Mass	30 kg/hr
Power	12 kg/hr
Power	30 kg/hr
Reliability	12 kg/hr
Reliability	30 kg/hr

The final values of $\dot{m}_{in}$ converged to 12 kg/hr for power optimization and 11 kg/hr for reliability optimization, both near the lower bound of $\dot{m}_{in}$. This indicates that a lower value of $\dot{m}_{in}$ is more optimal for power and reliability. $\dot{m}_{in}$ did not appear to have a significant impact on mass.

Effect of $\dot{m}_{in}$ Array Sweep in Model

$\dot{m}_{in}$ was then varied between its bounds in an OAT study. The resulting scaled sensitivities are shown in Table 53 and can be used to analyze the impact of $\dot{m}_{in}$ on each objective function. The results for reliability as an objective function are excluded for most design variables in this section, as it was found that each of these design variables had a negligible impact on reliability. The design variables that had the largest impact on reliability were the secondary design variables involving spare units, which are summarized in the Conclusions portion of this section.

Table 53: Scaled sensitivity values for OAT analysis of $\dot{m}_{in}$ across its range for power and mass objective functions

Design Variable	Value	Units	Power - Scaled Sensitivity	Mass - Scaled Sensitivity
$\dot{m}_{in}$	9	kg/hr	0.90	1.10
	10		0.89	0.02
	15		0.87	0.47
	20		0.86	0.43
	30		0.83	0.31
	50		0.77	0.25
	100		0.67	0.20

The scaled sensitivity numbers in the table indicate the percent change in the objective function when a 1% change in the design variable occurs. For example, when considering $\dot{m}_{in}$ at its lower bound of 9 kg/hr and power optimization, the scaled sensitivity is 0.9. This means that a 1% increase in $\dot{m}_{in}$ would result in a 0.9% increase in BAM system power at that point. The fact that the values of the scaled sensitivity change as $\dot{m}_{in}$ changes indicates a nonlinear relationship. Indeed, nearly all design variables demonstrated a nonlinear relationship with each objective function.

Analyzing the scaled sensitivity values for power, it is clear that an increase in $\dot{m}_{in}$ results in an increase in BAM power. This effect is nonlinear, as the magnitude of the effect of $\dot{m}_{in}$ on power diminishes as $\dot{m}_{in}$ increases, resulting in only a 0.67% increase in power when $\dot{m}_{in}$ is at its upper bound of 100 kg/hr. The reason for this is that CAC power scales sublinearly with $\dot{m}_{in}$; as the flow rate that must be achieved by the CAC system increases, the power requirement of the CAC system increases sublinearly because CAC efficiency increases with scale. The scaled sensitivity values for mass follow a similar trend for the same reason; mass efficiency of the CAC system also improves with size of the CAC system, which is driven in part by the inlet flow rate.

6.6.2 Compressor Output Pressure

The magnitude of the compressor output pressure, P_2, impacts the compression ratio required of the CAC system, the pressure drops across the heat exchangers, and the performance of the SOE

unit as a function of cathode pressure. The lower end of the P_2 range is bounded by the minimum pressure to overcome pressure drops in the system and the minimum SOE cathode pressure. This is set to a value of 15 kPa. The upper end of the range is theoretically unlimited, though it was bounded at 100 kPa.

Effect of Changing P_2 in the Optimization Design Vector

The value of P_2 was adjusted in the initial design vector, x_0, to determine its effects on the SA optimization. Six SA optimizations were run to cover all combinations of P_2 and objective functions. These combinations are listed in Table 54.

Table 54: SA optimizations run to determine effect of compressor output pressure on objective functions

Objective Function to be Optimized	P_2 Value in x_0
Mass	18 kPa
Mass	100 kPa
Power	18 kPa
Power	100 kPa
Reliability	18 kPa
Reliability	100 kPa

The values of P_2 converged to 20 kPa for power optimization, 15 kPa for mass optimization, and 21 kPa for reliability optimization. This indicates that a value of P_2 near its lower bound is optimal for all three objectives. Intuitively, this makes sense when considering the CAC system alone, as a lower output pressure would require a lower compression ratio, which results in less compression power, a less massive system, and a potentially lower level of risk when dealing with smaller pressure ranges.

Effect of P_2 Array Sweep in Model

P_2 was varied across its range in an OAT study to reveal any additional dependencies of the objective functions on this design variable. Table 55 shows the scaled sensitivity values for P_2 on power and mass.

Table 55: Scaled sensitivity values for OAT analysis of P_2 across its range for power and mass objective functions

Design Variable	Value	Units	Power - Scaled Sensitivity	Mass - Scaled Sensitivity
P_2	10000	Pa	N/A	0.007
	20000		0.060	0.005
	40000		0.045	0.184
	70000		0.035	0.079
	100000		0.029	0.051

P_2 appears to have a small impact on power, given by the small magnitude of the scaled sensitivities. The nonlinearity for power, given by the changing scaled sensitivity values across

the range of P_2, is explained by the nonlinear power of compression equation. While it may seem that the compressor output pressure, P_2, should have a larger impact on overall BAM power since it drives compression power, the small magnitude of its impact results from the fact that the CAC power only accounts for a small fraction of the total BAM system power, which is dominated by the SOE power of electrolysis. The mass is negligibly impacted by the value of P_2. It appears that a value of 40 kPa may have an important effect on mass, as the scaled sensitivity spikes to a value of 0.184. This, however, is the result of the system power crossing a threshold that necessitates the addition of another Kilopower unit. Each Kilopower unit has a mass of 1545 kg, so the addition of one unit increases the overall system mass substantially. Therefore, the apparent dependency of mass on a specific value of P_2 is an artifact of the system power being near the threshold of requiring an additional Kilopower unit and is not specific to P_2.

Because the scaled sensitivity is masked by the dominance of SOE power, two additional, full optimizations were run to identify the actual power savings of operating at lower pressure. This is a critical design decision that was experimentally investigated, the results of which were described in Chapter 5. The first optimization held P_2 at a constant value of 16.5 kPa, or 0.165 bar, near its lower bound, while the second optimization held P_2 at a constant value of 100 kPa, or 1 bar.

The optimization at low pressure resulted in a total system power of 25.3 kW, while the optimization at high pressure resulted in a total system power of 32.6 kW. This means that by operating at a lower pressure, over 7 kW of power can be saved. This is a significant portion of the power, and results in a significant mass savings as well by allowing one less Kilopower unit to be sent to provide that power. The main power savings come from the CAC system, where the compression power is reduced from 4.5 kW to 0.9 kW, and the liquefaction unit, where the power is reduced from 9.5 kW to 6.8 kW. The reduction in compression power results from the fact that the Martian atmosphere must be compressed to a significantly lower final pressure, thus using less power. The reduction in liquefaction power is the result of the Martian atmosphere being heated less during compression, and thus being more useful in the heat exchanger to cool the outlet oxygen stream from the SOE. This increase in cooling capacity results in a significant savings of cooling power required from the liquefaction unit. Overall, there are clear power and mass benefits of operating at a lower pressure.

6.6.3 SOE Active Cell Area

The size of the SOE cell area, A_{cell}, impacts the number of cells and number of SOE stacks needed to produce the required amount of oxygen. Larger cell areas should, in theory, result in a higher fraction of active cell area in the total SOE subsystem. Smaller cells require a higher volume and mass percentage of ancillary components, such as packaging, insulation, and piping, thus increasing the overall volume and mass of the SOE subsystem. The lower end of the A_{cell} range is bounded by the cell size in MOXIE, 22.7 cm^2. The upper end of the range is bounded by the largest cells OxEon Energy has produced, 110 cm^2.

Effect of Changing A_{cell} in the Optimization Design Vector

The value of A_{cell} was adjusted in the initial design vector, x_0, to determine its effects on the SA optimization. Six SA optimizations were run to cover all combinations of A_{cell} extremes and objective functions. These combinations are listed in Table 56.

Table 56: SA optimizations run to determine effect of SOE cell area on objective functions

Objective Function to be Optimized	A_{cell} Value in x_0
Mass	30 cm^2
Mass	110 cm^2
Power	30 cm^2
Power	110 cm^2
Reliability	30 cm^2
Reliability	110 cm^2

The values of A_{cell} did not appear to converge on any particular value or range of values for power or reliability calculations. An argument could be made that lower cell area should result in more power, as more cells would be required and thus the total heat leak in the system may be higher. This would be a weak correlation, however, as the majority of power used in the SOE subsystem is for electrolysis, which does not depend on cell area. Reliability could be affected by cell area in both directions, as a smaller cell area resulting in more cells means additional failure points, but higher redundancy.

As discussed, a lower cell area should have resulted in a higher mass. However, the optimization displayed the opposite trend, showing that mass was more favorable at lower cell areas. While this may be true due to unforeseen relationships between subsystems, this could also be the result of two other design variables, N_{cps} and N_{stacks}, not changing enough in the optimization. By increasing the cell area but keeping the total number of cells constant, the optimizer recognizes an excess of oxygen produced beyond the requirement. There are several design variables that could be changed to lower the oxygen production, including N_{cps}, N_{stacks}, and A_{cell}. It is possible that the optimizer randomly selected A_{cell} to be lowered first, thus giving a false impression that a lower value of A_{cell} is optimal, when in reality, it could have lowered the other design variables to find a more optimal solution.

Effect of A_{cell} Array Sweep in Model

In an attempt to counter the confounding effect previously described, the total SOE cell area was held constant by varying the values of A_{cell}, N_{cps}, and N_{stacks} together. The product of these three design variables is equal to the total SOE cell area that is available for oxygen production. By varying the design variable values but keeping their product relatively constant, it was possible to determine the effect of total cell area on each of the three objective functions. The results of this analysis are shown in Table 57.

Table 57: Scaled sensitivity values for OAT analysis of total cell area (the product of A_{cell}, N_{cps}, & N_{stacks}), varying each of the three design variables across their ranges while keeping total cell area relatively constant.

Design Variable Product	A_{cell} Value (cm^2)	N_{cps} Value	N_{stacks} Value	Total Cell Area (cm^2)	Power - Scaled Sensitivity	Mass - Scaled Sensitivity	Reliability - Scaled Sensitivity
A_{cell} $* N_{cps}$ $* N_{stacks}$	60	20	10	12000	0.092	-0.008	-0.018
	60	40	5	12000	0.100	0.022	-0.010
	60	50	4	12000	0.105	0.044	-0.006
	60	67	3	12060	0.095	0.011	0.016
	60	100	2	12000	0.101	0.027	0.059
	22.5	89	6	12015	-0.104	-0.015	0.041
	40	60	5	12000	-0.003	0.006	-0.001
	79	38	4	12008	0.191	0.052	-0.011
	111	27	4	11988	0.319	0.057	-0.016
	40	100	3	12000	-0.008	-0.011	0.059
	80	75	2	12000	0.193	0.039	0.023
	111	108	1	11988	0.318	0.051	0.074
				AVERAGE:	**0.117**	**0.023**	**0.018**

The scaled sensitivity values vary across each row in the table due to the fact that three different design variables are changing. The average of each, across a range of values for A_{cell}, N_{cps}, and N_{stacks}, is given in the last row of the table. This average indicates a slight positive relationship between cell area and each of the three objective functions. For power, an increase in cell area would result in a slight increase in power owing to an increase in SOE size that results in more heat loss. This increase in SOE size is also the reason that mass shows a positive relationship, as a larger SOE is more massive. Reliability has a slight positive relationship with SOE cell area as well, likely owing to the average increase in number of SOE cells and stacks compared to the baseline, which increases the effectiveness of redundancy in the system.

Overall, it is difficult to draw conclusions from an OAT sensitivity analysis of A_{cell}, N_{cps}, and N_{stacks}, as these three variables are directly tied together in many calculations in the BAM model. The impact of the latter two variables in the optimization starting vector will be explored in the section below, but the OAT analysis will be omitted as it was covered here in combination with A_{cell}.

6.6.4 Number of SOE Cells

The number of SOE cells per SOE stack, N_{cps}, and the number of SOE stacks, N_{stacks}, together determine the total number of SOE cells in BAM that are used to produce oxygen. These two design variables impact the size of the SOE subsystem.

Effect of Changing N_{cps} and N_{stacks} in the Optimization Design Vector

Different combinations of N_{cps} and N_{stacks} were used in the initial design vector, x_0, to determine its effects on the SA optimization. Six SA optimizations were run to cover different

combinations of these design variables and the objective functions. These combinations are listed in Table 58.

Table 58: SA optimizations run to determine effect of number of cells per SOE stack and number of SOE stacks on objective functions

Objective Function to be Optimized	N_{cps} Value in x_0	N_{stacks} Value in x_0
Mass	100	2
Mass	20	10
Power	100	2
Power	20	10
Reliability	100	2
Reliability	20	10

The values of N_{cps} and N_{stacks} did not converge for power optimization. They trended towards fewer stacks with more cells for mass optimization, which makes sense as mass would be minimized with a smaller number of stacks, owing to the framework, piping, and insulation that must surround each individual stack. Lastly, they trended in the opposite direction for reliability, giving more optimal solutions with high numbers of stacks and low numbers of cells per stack. This is explained by the fact that if one cell were to malfunction, having more stacks would allow for greater redundancy. These results indicate that mass and reliability are conflicting objectives with regards to N_{cps} and N_{stacks}.

6.6.5 SOE Temperature

The temperature of the SOE, T_6, impacts the amount of gas preheating that is required to raise the CO_2 up to temperature, the heat losses through the SOE stack, the performance of the SOE with respect to iASR, and the cooling that is required to bring the O_2 down to liquefaction temperature.

Effect of Changing T_6 in the Optimization Design Vector

The value of T_6 was adjusted in the initial design vector, x_0, to determine its effects on the SA optimization. Six SA optimizations were run to cover all combinations of T_6 extremes and objective functions. These combinations are listed in Table 59.

Table 59: SA optimizations run to determine effect of SOE temperature on objective functions

Objective Function to be Optimized	T_6 Value in x_0
Mass	1023 K
Mass	1123 K
Power	1023 K
Power	1123 K
Reliability	1023 K
Reliability	1123 K

The values of T_6 did not converge for mass nor reliability, indicating either a weak or absent correlation between the two. The values of T_6 trended towards the lower bound for power, indicating that the increase in heating power needed to preheat the gas to higher temperatures, and the increased heat leak from higher temperatures in the SOE hotbox, were more impactful than any power savings from increased SOE efficiency at higher temperatures.

Effect of T_6 Array Sweep in Model

The OAT array sweep for T_6 yielded the scaled sensitivity results shown in Table 60.

Table 60: Scaled sensitivity values for OAT analysis of T_6 across its range for power and mass objective functions

Design Variable	Value	Units	Power - Scaled Sensitivity	Mass - Scaled Sensitivity
T_6	1023	K	5.9	2.63
	1048		6.1	3.46
	1073		6.3	0.15
	1098		6.4	0.15
	1123		N/A	N/A

The upper bound at 1123 K does not have scaled sensitivity values because it was used as the baseline against which the others were calculated. The scaled sensitivity of power is significant, indicating a strong relationship between power and T_6. As was discovered in the first part of the sensitivity analysis for T_6, a higher T_6 results in a higher power. The power increases superlinearly with T_6 because of the increasing inlet heating and heat leaks that occur at higher temperatures.

The mass shows a strong sensitivity with T_6 in this OAT analysis. This is explained, once again, by the addition of a Kilopower unit. As temperature rises, additional power is required, which eventually causes the total BAM power to cross a threshold and require an additional Kilopower unit. This adds significantly to the system mass. In the case of this sensitivity study, the additional Kilopower was added as temperature was increased from 1048 K to 1073 K. The baseline temperature against which these sensitivities were calculated was 1123 K, so the additional Kilopower unit was already included in the baseline. This is why the mass appears to be affected only minimally by temperatures of 1073 K and 1098 K, but appears to be affected significantly at 1023 K and 1048 K.

6.6.6 Anode Pressure

The magnitude of the SOE anode pressure, P_6, impacts the magnitude of electrochemical compression required of the cell as well as pressure differential across the SOE electrolyte. The pressure of the oxygen stream also influences the heat exchanger performance and the oxygen liquefaction temperature. A wide range of values is feasible for P_6, which was bounded in the simulation from 5 kPa to 200 kPa.

Effect of Changing P_6 in the Optimization Design Vector

The value of P_6 was adjusted in the initial design vector, x_0, to determine its effects on the SA optimization. Six SA optimizations were run to cover all combinations of P_6 bounds and objective functions. These combinations are listed in Table 61.

Table 61: SA optimizations run to determine effect of anode (oxygen) pressure on objective functions

Objective Function to be Optimized	P_6 Value in x_0
Mass	5 kPa
Mass	200 kPa
Power	5 kPa
Power	200 kPa
Reliability	5 kPa
Reliability	200 kPa

The value of P_6 did not converge for power optimization, indicating a weak or absent correlation between the two. Two optimizations, one with a starting value of P_6 of 5 kPa and the other with a starting value of 200 kPa, resulted in nearly identical total system powers. P_6 also did not appear to have a significant impact on mass nor reliability. Intuitively, a higher P_6 should result in an increase in electrochemical compression power but a decrease in liquefaction power owing to a higher boiling point (and thus less cooling required to reach it). It is possible that these effects cancel one another, which is why no significant correlations are seen.

Effect of P_6 Array Sweep in Model

To further investigate whether P_6 impacts the objective functions in a meaningful way, an OAT analysis was conducted across the range of P_6. The results for this analysis are shown in Table 62.

Table 62: Scaled sensitivity values for OAT analysis of P_6 across its range for power and mass objective functions

Design Variable	Value	Units	Power - Scaled Sensitivity	Mass - Scaled Sensitivity
P_6	5000	Pa	-0.398	-0.2695
	30000		-0.193	-0.0045
	60000		-0.128	-0.0034
	100000		-0.091	-0.0026
	200000		-0.055	-0.0017

According to this analysis, P_6 appears to have a negative impact on power that decreases in magnitude as the pressure increases. As discussed before, this is likely because of the tradeoff between electrochemical compression power and liquefaction power that are dependent in opposite ways on P_6. The trend of scaled sensitivity for power indicates that the decrease in liquefaction power from the change in oxygen boiling point is more impactful at lower values of P_6, but the increase in power from electrochemical compression begins to have a larger impact as

the pressure rises towards its upper bound. At a high enough pressure, this effect would dominate and the relationship between P_6 and power would become positive.

Mass appears to be negatively influenced by P_6 at its lower bound. This is an artifact of the slight power savings from operating at low pressure crossing a threshold that allows for the removal of a Kilopower unit. It is fair to say that P_6 has a slight negative impact on mass, but not that it alone is responsible for the magnitude of the scaled sensitivity seen at the lower bound in the table. Lastly, the impact of P_6 on reliability was confirmed to be negligible.

6.6.7 Cell Voltage

The cell voltage, V_{app}, determines the quantity of oxygen produced by each SOE cell. A higher value of V_{app} results in more oxygen production per cell, but too high a V_{app} will exceed the Nernst potential for carbon formation and lead to coking of the cell.

Effect of Changing V_{app} in the Optimization Design Vector

The value of V_{app} was adjusted in the initial design vector, x_0, to determine its effects on the SA optimization. Six SA optimizations were run to cover all combinations of V_{app} bounds and objective functions. These combinations are listed in Table 63.

Table 63: SA optimizations run to determine effect of applied SOE cell voltage on objective functions

Objective Function to be Optimized	V_{app} Value in x_0
Mass	1.04 V
Mass	0.91 V
Power	1.04 V
Power	0.91 V
Reliability	1.04 V
Reliability	0.91 V

The value of V_{app} did not converge for any of the three objective functions. Power optimization was not expected to converge to a specific value of V_{app}, as a higher voltage would produce more oxygen per cell but require fewer cells, resulting in the same total electrolysis power. For that same reason, it was expected that V_{app} would converge to its upper limit for mass optimization, as fewer cells would require less mass. For reliability optimization, it was expected that V_{app} would converge to its lower limit, as a higher cell voltage decreases the gap between that voltage and the Nernst potential for carbon formation, which is considered a risk. It is possible that interactions between multiple design variables or subsystems resulted in V_{app} not influencing power or reliability as strongly as expected. It is also possible that the optimization did not perturb V_{app} enough to demonstrate its influence on those objectives.

Effect of V_{app} Array Sweep in Model

The results of the OAT array sweep for V_{app} indicate strong, but misleading, relationships between the design variable and power and mass. The results are shown in Table 64.

Table 64: Scaled sensitivity values for OAT analysis of V_{app} across its range for power and mass objective functions

Design Variable	Value	Units	Power - Scaled Sensitivity	Mass - Scaled Sensitivity
V_{app}	0.9	V	8.6	4.07
	0.93		8.5	0.17
	0.96		7.1	0.17
	0.99		10.3	6.00

The magnitude of the scaled sensitivity for power and mass are the highest among any design variable, indicating at first glance that V_{app} is the most impactful variable on these BAM objectives. The reason this appears to be the case is that an increase in V_{app} results in an increase in the quantity of oxygen produced. As shown in Section 6.1 and Section 6.2, BAM system power is dominated by the SOE power, and, more specifically, by the power used to electrolyze CO_2 into O_2 in the SOE. Therefore, an increase in the quantity of O_2 produced will result in a significant increase in system power. If taken at face value, the scaled sensitivities are deceptive because there is no benefit in producing excess O_2. Increasing V_{app} by itself is wasted power, which also results in the addition of another Kilopower unit that increases system mass needlessly.

In reality, V_{app} could be increased to produce more O_2 per SOE cell, but the number of SOE cells would be decreased accordingly to keep the total O_2 production at its required value. This relationship between design variables is not explored in an OAT analysis. Therefore, the relationship between V_{app} and the objective functions from the first part of the sensitivity analysis, not the OAT analysis, should be considered.

6.6.8 Heat Exchanger Area

The area of the two main heat exchangers in BAM, A_{HE1} and A_{HE2}, impact the size of the heat exchanger subsystem and the amount of power saved by recuperating heat. A secondary impact of the heat exchanger sizing is determining the magnitude of the pressure drops of the gases flowing through the heat exchangers, which affects the performance of the other subsystems in BAM. The heat exchanger sizes were bounded from 0 m^2 (no heat exchanger) to 10 m^2 each. Theoretically, the upper bound of the heat exchangers could have been removed to allow the heat exchangers to have an unlimited size, but 10 m^2 was determined, through several optimization runs, to be a sufficient upper bound, as it resulted in nearly all possible heat being transferred between the gases.

Effect of Changing A_{HE1} and A_{HE2} in the Optimization Design Vector

The value of A_{HE1} and A_{HE2} was adjusted in the initial design vector, x_0, to determine its effects on the SA optimization. Six SA optimizations were run to cover all combinations of A_{HE} bounds and objective functions. Though the upper bound was constrained to 10 m^2 for each heat exchanger, a value of 5 m^2 was used in these experiments to allow the optimizer to demonstrate the impact of increasing or decreasing the heat exchanger area at a middle value. These combinations are listed in Table 65.

Table 65: SA optimizations run to determine effect of heat exchanger area on objective functions

Objective Function to be Optimized	A_{HE1} Value in x_0	A_{HE2} Value in x_0
Mass	5 m^2	5 m^2
Mass	0 m^2	0 m^2
Power	5 m^2	5 m^2
Power	0 m^2	0 m^2
Reliability	5 m^2	5 m^2
Reliability	0 m^2	0 m^2

The heat exchanger areas displayed weak correlations with all three objective functions. As expected, larger heat exchanger areas resulted in lower BAM power, as more heat was recuperated. Also as expected, larger heat exchanger areas resulted in higher BAM mass, as larger heat exchangers contribute more mass. A weak correlation existed between heat exchanger area and reliability as well, where lower heat exchanger area resulted in higher reliability. This either results from complex interactions between subsystems and design variables or was a false correlation. It will be explored in the second part of the sensitivity study in the following paragraphs.

Effect of A_{HE1} and A_{HE2} Array Sweep in Model

The results of the second component of the sensitivity study, the OAT analysis, agreed with the previous results for power and mass. There was no significant sensitivity with reliability, however. The results of the analysis for both heat exchangers are shown in Table 66.

Table 66: Scaled sensitivity values for OAT analysis of A_{HE1} and A_{HE2} across their ranges for power and mass objective functions

Design Variable	Value	Units	HE1 Power - Scaled Sensitivity	HE2 Power - Scaled Sensitivity	HE1 Mass - Scaled Sensitivity	HE2 Mass - Scaled Sensitivity
A_{HE1} & A_{HE2}	0	m^2	-0.2854	-0.062	N/A	0.0105
	1.5		-0.0133	-0.025	0.0021	0.0055
	3		-0.0021	-0.015	0.0033	0.0055
	4.5		-0.0005	-0.011	0.0035	0.0055
	6		-0.0002	-0.008	0.0036	0.0055

The negative values of the power sensitivities indicate that increases in the area of either heat exchanger resulted in a decrease in system power, as expected. The magnitudes of the scaled sensitivities decrease as the heat exchangers grow in size, which reflects the diminishing returns that occur with the continued addition of heat exchanger area.

The positive values of the mass sensitivities indicate that increases in the area of either heat exchanger resulted in an increase in system mass, due to the addition of heat exchanger mass. These numbers are fairly constant, indicating a linear relationship. This is expected, as the addition of heat exchanger mass directly adds to the total BAM system mass.

6.6.9 Number of Parallel CAC Systems

N_{CAC} defines the number of CAC systems – whether mechanical, cryogenic, or sorption – that operate in parallel. A larger number of CAC systems should result in higher system mass, owing to non-linear mass scaling, and higher system reliability, owing to an increased ability for redundancy. The number of CAC systems should also impact the efficiency of the compression, as efficiency typically scales beneficially with CAC size.

Effect of Changing N_{CAC} in the Optimization Design Vector

The value of N_{CAC} was adjusted in the initial design vector, x_0, to determine its effects on the SA optimization. Six SA optimizations were run to cover a range of starting values of N_{CAC} with each objective function. These combinations are listed in Table 67.

Table 67: SA optimizations run to determine effect of number of parallel CAC systems on objective functions

Objective Function to be Optimized	N_{CAC} Value in x_0
Mass	1
Mass	10
Power	1
Power	10
Reliability	1
Reliability	10

The value of N_{CAC} did not converge for power optimization, indicating a weak or absent correlation between the two. Since the only impact of N_{CAC} on BAM system power is a slight modification of the efficiency of the pump, only small changes in power would result. The value of N_{CAC} had a weak correlation with mass, which decreased as N_{CAC} decreased, as expected. The most optimal mass values resulted from a single CAC unit. Lastly, the value of N_{CAC} had a strong inverse correlation with reliability, with the highest reliabilities resulting from 21-23 CAC systems operating in parallel. The same trends were observed in the OAT analysis across all three objectives.

6.6.10 Insulation Thickness

Five instances of insulation in the BAM system are modeled and controlled with the design variables listed in Table 15 in Section 3.4.2, ranging from MAV insulation to the insulation covering pipes between subsystems. The insulation thicknesses should primarily impact power and mass, as an increase in insulation thickness increases the mass of the system but generally results in less heat leak and thus a lower power requirement.

Effect of Changing Insulation Thickness in the Optimization Design Vector

The values of all five insulation thickness design variables were varied between 0 m and 3 m. Like the heat exchanger area, the upper bound of insulation thickness could be unlimited, but a value of 3 m was determined to virtually eliminate heat leaks at all points throughout BAM and thus was considered a sufficient upper starting point for the sensitivity analysis.

The sensitivity analysis revealed that the insulation thickness has an inverse correlation with power, as expected, but no observable correlation with mass and reliability. The absence of a correlation with mass is illogical, and most likely arises from the fact that insulation thickness is a minimal fraction of the total mass of BAM. The full effects of insulation thickness on mass are studied in more detail in the second half of the sensitivity analysis, which is described in the following paragraphs.

Effect of Insulation Thickness Array Sweep in Model

An OAT analysis was conducted for each of the five insulation thickness design variables in the BAM system. The results of the analysis are shown in Table 68.

Table 68: Scaled sensitivity values for OAT analysis of five insulation thickness design variables for power and mass objective functions

Design Variable	Value	Units	Power - Scaled Sensitivity	Mass - Scaled Sensitivity
$t_{liq-pipe-ins}$	0	m	-0.2482	-0.07
	0.2		-0.0102	0.20
	0.5		-0.0050	0.34
	1		-0.0028	0.56
	3		-0.0011	1.46
	10		-0.0004	4.62
$t_{liq-MAV-ins}$	0	m	-10.604	-5.089
	0.2		-0.207	-0.191
	0.5		-0.083	-0.002
	1		-0.041	-0.001
	3		N/A	N/A
	10		-0.002	-4.8E-05
$t_{ins-pipe}$	0	m	0.0000248	0.001
	0.2		0.0000002	0.003
	0.5		0.0000003	0.006
	1		0.0000002	0.010
	3		0.0000001	0.030
	10		0.0000000	0.097
$t_{SOE-ins1}$	0	m	-0.406	-0.15
	0.2		0.002	0.03
	0.5		0.004	0.06
	1		0.005	0.11
	3		0.009	0.59
	10		0.025	5.23
$t_{SOE-ins2}$	0	m	-0.2496	-0.14
	0.2		-0.0024	0.06
	0.5		-0.0003	0.11
	1		0.0005	0.23
	3		0.0012	1.24
	10		0.0015	11.22

Across all five of these design variables, the relationship with power is two orders of magnitude higher at 0 m insulation thickness than it is at just 0.2 m of insulation thickness. This is because only a small amount of insulation is required to prevent most of the heat leaks throughout the BAM system. The diminishing returns of adding more insulation thickness are clearly seen by the decreasing magnitude of scaled sensitivity as insulation thickness is increased across these design variables. It is important to note that the insulation thickness has an inverse relationship

with power, indicated by a negative scaled sensitivity, since power decreases as insulation thickness increases. The exceptions to this in the table are values that are close to 0 and thus considered negligible.

The effect of insulation thickness on mass is fairly complex. Several negative values are seen in the table at insulation thicknesses of 0 m. The reason for this is that the addition of insulation thickness at this point saves a significant amount of power, which results in a step change in the number of Kilopower units required in the system. Thus, the addition of insulation mass actually decreases the total system mass, because the mass savings from the reduced number of Kilopower units outweigh the mass cost of the insulation material. After that change, the relationship between insulation thickness and mass becomes positive, as the addition of more insulation results in a slight increase in system mass from the additional insulation material. This number grows nonlinearly, achieving large positive sensitivity values at insulation thicknesses of 10 m, because insulation mass increases as the square of insulation thickness, creating a superlinear relationship.

The results from this sensitivity analysis indicate that a small amount of insulation is important for reducing both system power and mass, but additional insulation beyond that only serves to increase system mass with minimal additional power savings.

6.6.11 CAC

The design variable that controls the type of CAC system was analyzed in a different method than the design variables previously discussed in this section. Four distinct CAC systems are considered as options – the cryopump, the scroll compressor, the centrifugal compressor, and the sorption pump – and each may influence other subsystems, resulting in a different BAM design throughout the system. For this reason, a stand-alone optimization was conducted for each of the four CAC options for a power optimization objective function and for a mass optimization objective function, to better understand the impact of the CAC choice on the objectives. The CAC type was held constant in each optimization, while all other design variables were allowed to change. The results of these eight optimizations are shown and discussed here.

Power

The total BAM power of the final designs for the cryopump, scroll compressor, centrifugal compressor, and sorption compressor optimizations were 32.2 kW, 25.4 kW, 25.6 kW, and 30.1 kW, respectively. The breakdown of power by subsystem for each of these four architectures is given in Figure 128.

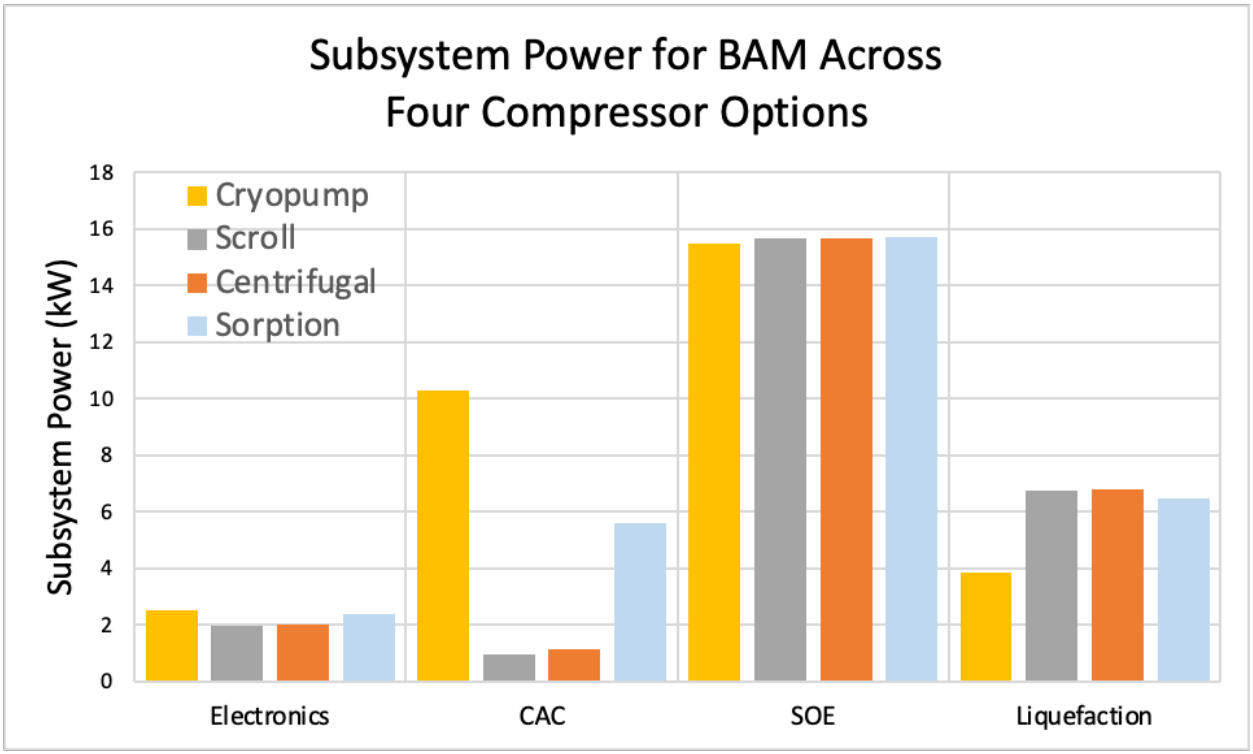

Figure 128: Subsystem power breakdown for four power-optimized BAM designs, each with a unique CAC system: (1) cryopump, (2) scroll compressor, (3) centrifugal compressor, and (4) sorption compressor.

The cryopump architecture had the highest total power. This is primarily driven by the increased power of the cryopump CAC system due to the high cooling requirements of freezing out CO_2 gas, which results in the cryopump system having an order of magnitude higher power when compared to mechanical compressors. Both types of mechanical compressors – scroll and centrifugal – had the lowest total system BAM power.

Mass

The total BAM mass for the cryopump, scroll compressor, centrifugal compressor, and sorption compressor were 9257 kg, 7298 kg, 7262 kg, and 8631 kg, respectively. The breakdown of mass by subsystem for each of these architectures is shown in Figure 129.

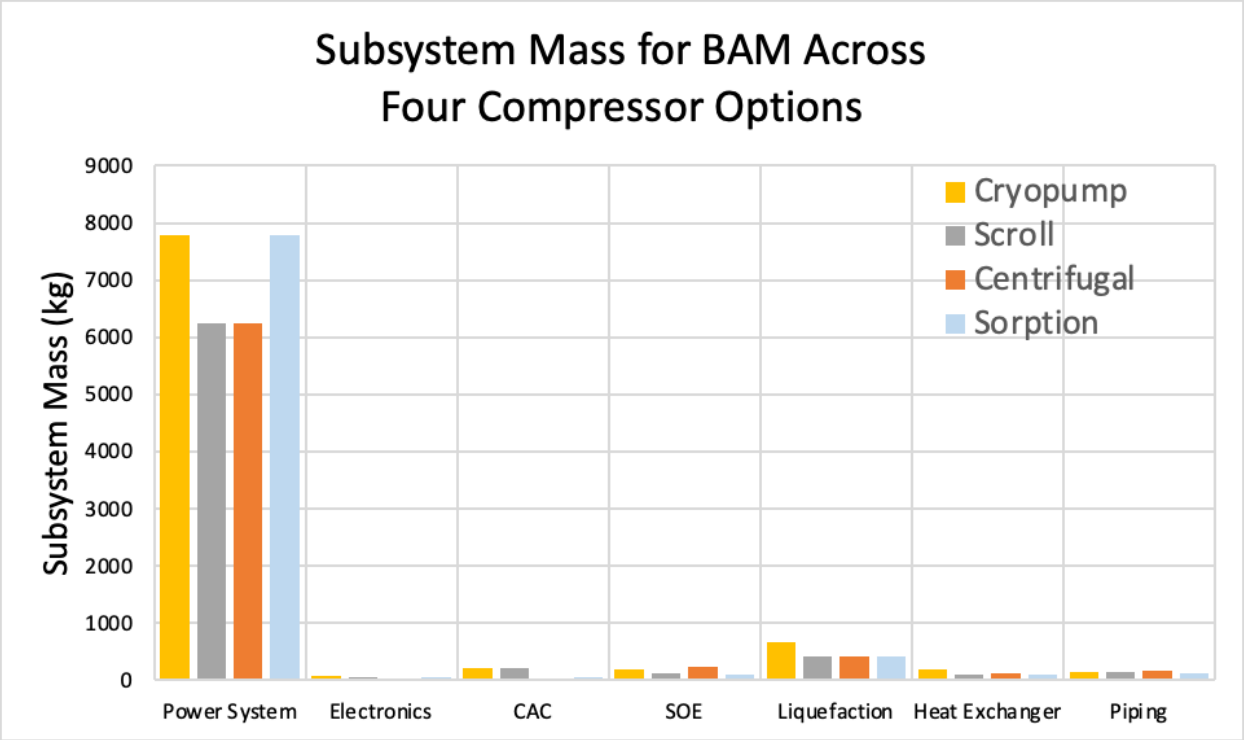

Figure 129: Subsystem mass breakdown for four mass-optimized BAM designs, each with a unique CAC system: (1) cryopump, (2) scroll compressor, (3) centrifugal compressor, and (4) sorption compressor.

As previously discussed, the power system in all four architectures is dominated by the mass of the Kilopower units. Each Kilopower unit weighs 1545 kg, which can be seen in the figure by realizing that the scroll compressor and centrifugal compressor use four Kilopower units while the cryopump and sorption compressor use five owing to their larger power demands. To better understand the mass comparisons of the other subsystems, Figure 130 shows the same data but with the mass of the power system omitted.

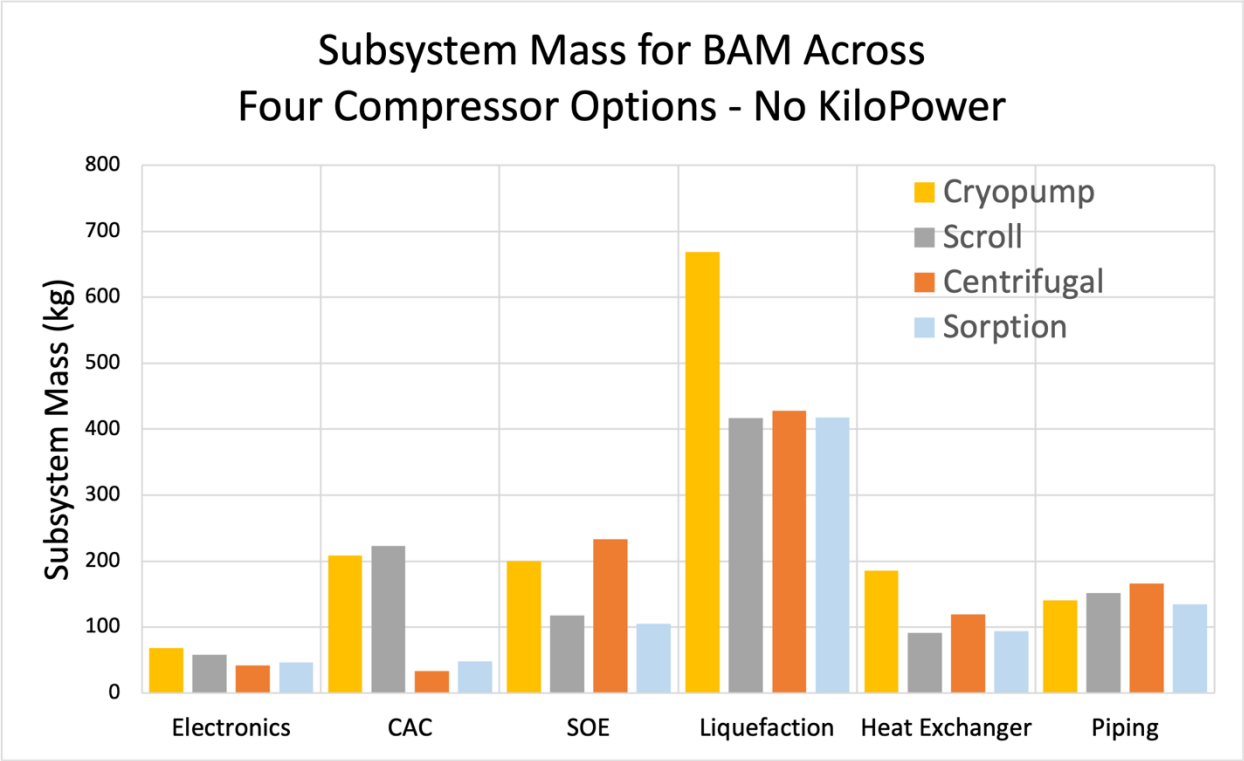

Figure 130: Subsystem mass breakdown for four mass-optimized BAM designs, with the mass of the Kilopower subsystem removed to give better clarity to the mass distribution amongst other subsystems.

From this figure, it is clear that the liquefaction unit is the second highest contributor to mass after the Kilopower units. The cryopump architecture has the most massive liquefaction unit because it relies on the liquefaction unit to manage the cooling load from its CAC in addition to the oxygen liquefaction that takes place across all architectures in the liquefaction unit. Another notable difference in architectures is the small mass of the centrifugal compressor and sorption compressor compared to the cryopump and scroll compressor.

Design Variables

The nuances of the power and mass optimization shown in the previous figures can be better understood by comparing the designs of the four architectures. This is accomplished by comparing the optimized results of the 25 design variables across the four architectures. These are shown in Table 69.

Table 69: Design variable values for each of eight optimizations run to analyze the impact of each compressor option. Each pair of columns represents the optimized design based on power (left) and mass (right). Four pairs of columns represent the four CAC options.

	Cryopump		Scroll Compressor		Centrifugal Compressor		Sorption Compressor	
Design Variable	Power	Mass	Power	Mass	Power	Mass	Power	Mass
$\dot{m}_{in}$ (kg/hr)	12.0	12.0	12.0	12.1	12.0	11.0	12.0	10.1
P_2 (kPa)	20.7	16.7	15.7	13.3	15.7	14.9	14.3	17.3
A_{cell} (cm^2)	95	34	94	86	97	84	101	65
N_{cps}	63	49	63	49	51	69	62	40
N_{stacks}	3	4	3	2	3	2	3	2
T_6 (K)	1073	1082	1073	1084	1074	1123	1073	1119
P_6 (kPa)	18.1	19.4	18.1	15.5	15.8	22.7	18.3	15.8
V_{app} (V)	0.94	0.95	0.94	0.95	0.94	0.93	0.94	0.96
A_{HE1} (m^2)	3.5	3.4	3.5	1.0	3.5	1.6	2.7	1.6
A_{HE2} (m^2)	6.7	6.5	7.0	0.8	7.0	2.8	5.2	0.6
N_{CAC}	3	1	4	10	5	5	6	8
$t_{liq-pipe-ins}$ (m)	0.23	0.11	0.28	0.08	0.28	0.08	0.33	0.01
$t_{liq-MAV-ins}$ (m)	5.24	1.87	5.71	3.77	4.64	2.01	3.89	2.06
$t_{ins-pipe}$ (m)	0.00	0.03	0.05	0.06	0.12	0.08	0.00	0.00
$t_{SOE-ins1}$ (m)	0.15	0.02	0.06	0.00	0.04	0.01	0.08	0.00
$t_{SOE-ins2}$ (m)	0.16	0.04	0.20	0.00	0.29	0.10	0.22	0.01
$Blower_{\#SU}$	2	1	2	1	1	1	4	3
$Cryocooler_{\#SU}$	1	1	0	0	2	0	2	1
$Valve_{\#SU}$	12	8	9	14	14	4	14	12
$CACmechanical_{\#SU}$	2	5	5	5	5	3	4	0
$SOECell_{\#SU}$	220	167	123	139	233	132	151	123
$SOEStack_{\#SU}$	6	6	0	0	1	0	5	0
$Kilopower_{\#SU}$	3	1	1	1	2	1	3	1
$Heatexchanger_{\#SU}$	7	11	8	12	8	9	9	11

The four CAC architectures occupy each pair of columns, and each pair of columns is comprised of a power-based optimization architecture and a mass-based optimization architecture. Therefore, eight optimized BAM designs are shown in the eight columns of this table. The effects of certain design variables, and their changes across each type of CAC design, will be discussed below.

The inlet flowrate, $\dot{m}_{in}$, and the compressor outlet pressure, P_2, converged near their lower limits across all eight optimizations. This indicates, as expected, that a lower flow rate and compression ratio is optimal for all types of compressors. The heat exchanger areas, A_{HE1} and A_{HE2}, converged to similar large values across all power-based optimization runs, indicating that larger heat exchangers help reduce power regardless of the type of CAC. The same heat exchanger areas all converged to similar small values across all mass-based optimizations, as expected, with

the notable exception of the cryopump architecture, where the heat exchanger area stayed high. A possible explanation for this is that the additional heat exchanged by the larger heat exchangers helped reduce the total power usage enough that a Kilopower unit was able to be removed from the architecture, thus minimizing the mass. In other CAC designs, this threshold was not crossed by increasing heat exchanger area, so the minimum mass possible was achieved by minimizing the heat exchanger size. The number of spare Kilopower units followed the same trend across most designs, with 1 spare unit being used in all mass-optimization cases and between 1 and 3 units being used in all power-optimization cases.

While analyzing the design variables is useful, the most important takeaways from the CAC sensitivity analysis is how the change in compression type affects the total optimized power and mass of BAM. The cryopump has the highest power and mass, followed by the sorption compressor. The two mechanical compressor designs have the lowest power and mass.

6.6.12 Conclusions

The two-part sensitivity analysis conducted for each design variable revealed important impacts of the design variables on the objective functions that are summarized in this section.

OAT Results

The results of the OAT analysis for each design variable are summarized in a conglomerate of plots for each objective function, which make it possible to scan for general trends across each objective function. The impact of nine design variables on power is shown in Figure 131, their impact on mass is shown in Figure 132, and their impact on reliability is shown in Figure 133.

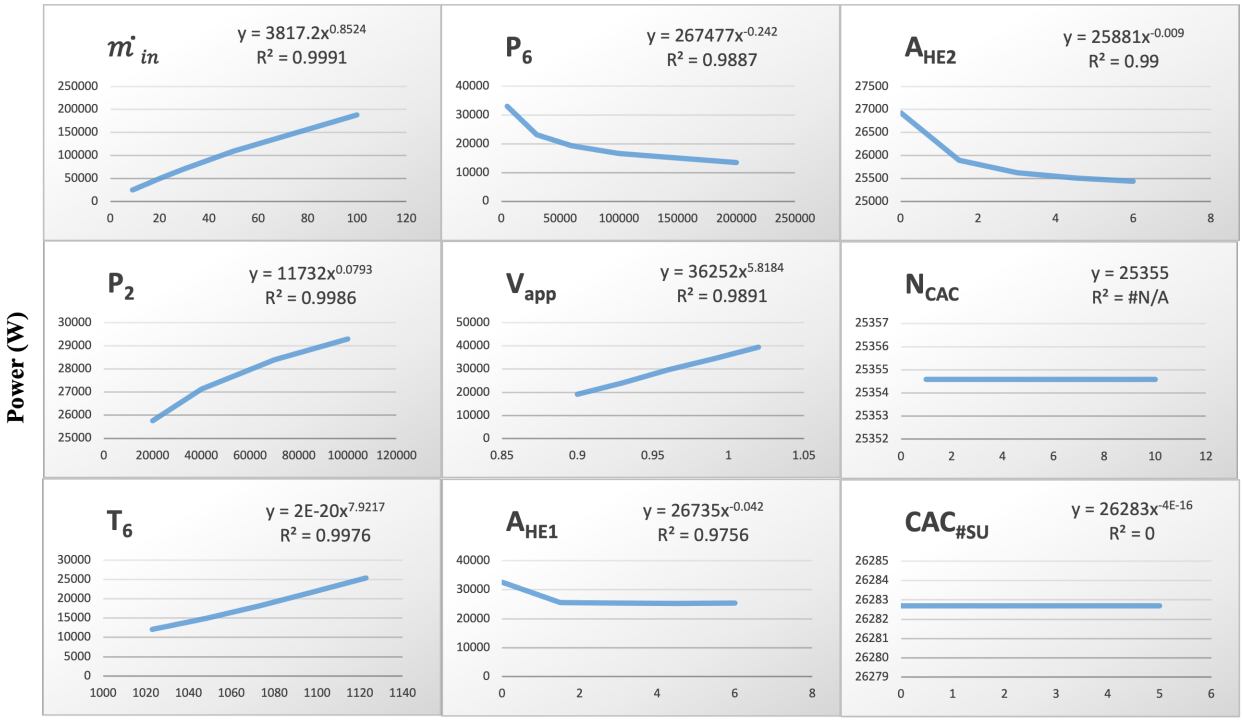

Figure 131: Results of the one-at-a-time (OAT) analysis for nine design variables, showing their impact on power. Each design variable is labeled in the upper left quadrant of its plot. The value for the design variable is displayed without units on the x-axes, while BAM power in Watts is displayed on the y-axis for all plots. Best fit lines following a power law are displayed on each plot, along with the coefficient of determination, R^2, which represents the proportion of the variance in the data.

The results of these plots should be interpreted by following the trendlines and observing the power law exponents for the best fit lines. An exponent of one indicates a linear relationship between the design variable and the objective, while an exponent less than one indicates a sublinear relationship and an exponent greater than one indicates a superlinear relationship. For example, there is a sub-linear, but nearly linear, relationship between $\dot{m}_{in}$ and BAM power, shown in the top-left plot in Figure 131 and confirmed by the best-fit line exponent of 0.8524. On the other hand, there is no significant relationship between power and N_{CAC} or $CAC_{\#SU}$, shown by their flat lines and best-fit exponents of ~0.

The trends between these same nine design variables and BAM system mass are shown in Figure 132.

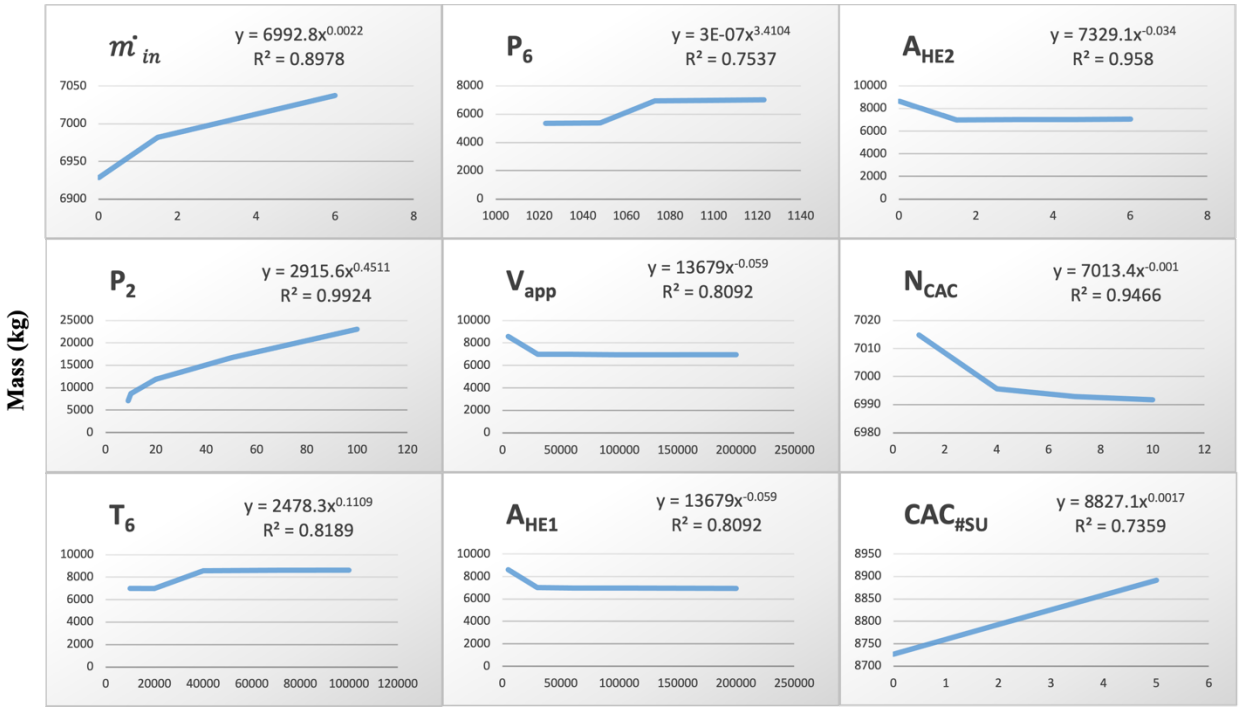

Figure 132: Results of the one-at-a-time (OAT) analysis for nine design variables, showing their impact on mass. Each design variable is labeled in the upper left quadrant of its plot. The value for the design variable is displayed without units on the x-axes, while BAM mass in kg is displayed on the y-axis for all plots. Best fit lines following a power law are displayed on each plot, along with the coefficient of determination, R^2, which represents the proportion of the variance in the data.

A step-change in mass is observed in the plots of nearly all these design variables, most noticeably in P_6 and T_6. This is the result of the addition of an extra Kilopower nuclear reactor, which adds significantly to the system mass. These step changes make the power law exponents unreliable for analysis, but general trends are still observable in the plots.

The trends for these design variables and the third objective function, BAM reliability, are shown in Figure 133.

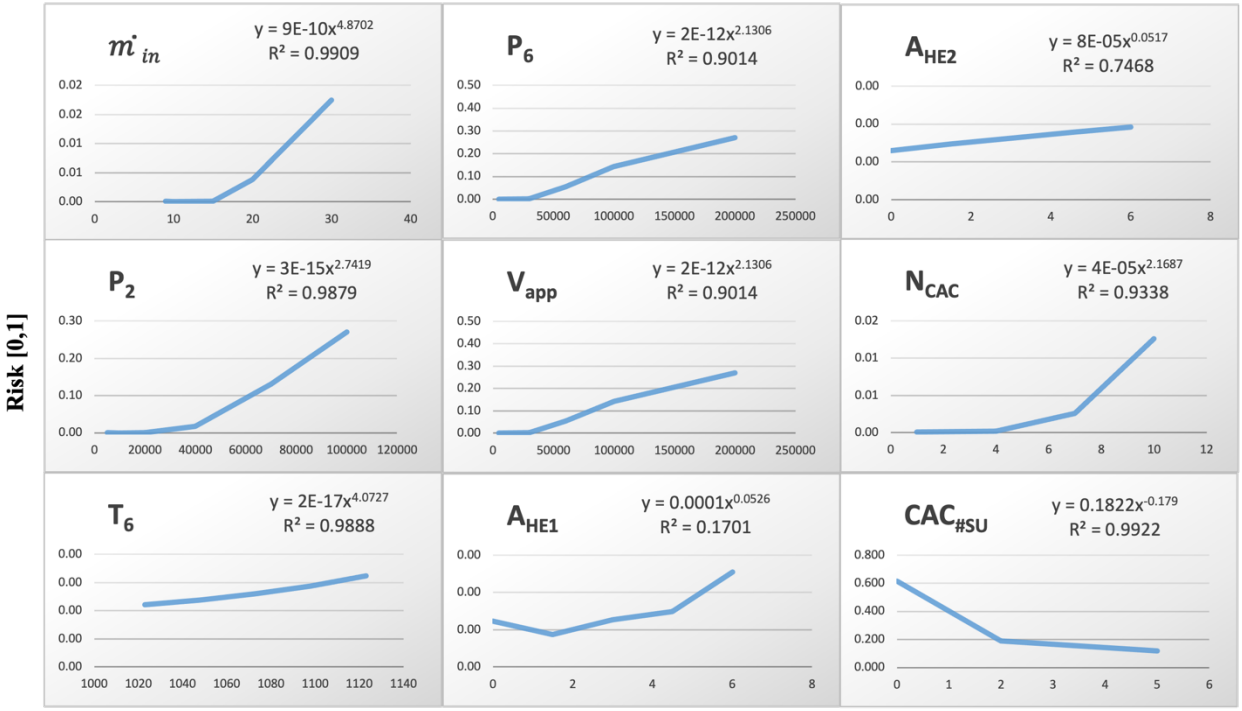

Figure 133: Results of the one-at-a-time (OAT) analysis for nine design variables, showing their impact on risk. Each design variable is labeled in the upper left quadrant of its plot. The value for the design variable is displayed without units on the x-axes, while risk is shown on the y-axis for all plots in the range [0,1]. Best fit lines following a power law are displayed on each plot, along with the coefficient of determination, R^2, which represents the proportion of the variance in the data.

The y-axis was plotted as risk, which is defined as one minus reliability, for the sake of fitting power laws. Therefore, an upward trend indicates that an increase in that design variable's value results in an increase in system risk and thus a decrease in system reliability. An increase in nearly all of the values of these design variables resulted in an increase in risk. For inlet flow rate, this is because a higher inlet flow rate results in the blower fan or mechanical compressor having to spin faster and thus lowering its lifetime. For V_{app}, an increase in value results in a closer approach to the Nernst potential for carbon formation, which decreases SOE reliability. The only negative trend viewed here is in the last plot, where an increase in the number of spare CAC units results in a decrease in risk, which is the expected relationship between redundancy and risk.

The results of the scaled sensitivity calculations that were derived from the raw values presented in these three plot groupings will be discussed in further detail in the following section. Scaling the values of the relationship between these design variables and the objective functions is an important step in analyzing their relative impacts.

Scaled Sensitivity Values

The scaled sensitivity values that were calculated and shown throughout Section 6.6 for each combination of design variable and objective function are summarized for a selected number of design variables at their upper bounds (UB) and lower bounds (LB) in Table 70.

Table 70: Scaled sensitivity values for design variables across each objective function. The results are analyzed for each lower bound (LB) and upper bound (UB) of the design variables. The value indicates the percent change in the objective function when a 1% change in the design variable occurs.

Design Variable	Sensitivity for Power		Sensitivity for Mass		Sensitivity for Reliability		Analysis
	LB	UB	LB	UB	LB	UB	
$\dot{m}_{in}$	0.9	0.67	1.10	0.20	0.00	-0.01	Positive impact on power and mass, which decreases in magnitude as flow rate increases.
P_2	0.06	0.03	0.01	0.05	0.00	-0.04	Marginal positive impact on power and mass.
T_6	5.90	6.40	2.63	0.15	0.00	0.00	Strong positive impact on power and mass.
P_6	-0.40	-0.06	-0.27	-0.00	0.00	-0.02	Slight negative impact on power and mass.
V_{app}	8.60	10.30	4.07	3.34	0.00	0.00	Strong positive impact on power and mass.
A_{HE1}	-0.29	0.00	0.00	0.00	0.00	0.00	Slight negative impact on power, which decreases in magnitude as heat exchanger area increases.
A_{HE2}	-0.06	-0.01	0.01	0.01	0.00	0.00	Marginal negative impact on power, which decreases in magnitude as heat exchanger area increases.
$A_{cell,T}$ $(A_{cell} * N_{cps} * N_{stacks})$	0.117		0.023		0.018		Total cell area has a slight positive impact on power, marginal positive impact on mass and reliability.
$t_{liq-MAV-ins}$	-0.21	0.00	-0.19	0.00	0.00	0.00	Slight negative impact on power and mass, decreasing in magnitude as insulation thickness increases.
$CAC_{\#SU}$	0.00	0.00	0.01	0.01	0.56	0.01	Positive impact on reliability, decreasing in magnitude as number of spares increases.

The scaled sensitivities at the lower bound (LB) and upper bound (UB) of each design variable's range are reported in the table. For example, the first design variable, $\dot{m}_{in}$, had a lower bound of 9 kg/hr and an upper bound of 100 kg/hr. The scaled sensitivity was calculated for the power, mass, and reliability of the BAM system that resulted at each of these bounds. The numbers in the table indicate the percent change in the objective function when a 1% change in the design variable occurs. For example, a value of 0.9 for $\dot{m}_{in}$ in the power column indicates that a 1% increase in $\dot{m}_{in}$ results in a 0.9% increase in BAM system power.

The first significant conclusion that can be drawn from the results presented in the table is that reliability is relatively insensitive to all the design variables presented here, shown by the scaled sensitivity values of ~0, except the last. This is not surprising, as the majority of reliability calculations center around the number of spare units. The impact of spare units can be seen in the last row of the table, where the addition of spare mechanical compressors increases the system reliability.

The strongest sensitivities for power and mass existed with T_6 and V_{app}. A higher SOE temperature requires additional power for gas preheating but also increases the rate of heat leak from the SOE hotbox. This is why the scaled sensitivity grows in magnitude as T6 increases from its lower bound to its upper bound, as the power requirement grows superlinearly with T_6. This increase in power results, at some point, in a step function change in the number of Kilopower units required to supply that power. Each Kilopower unit represents a significant contribution to the mass of BAM, which explains the strong sensitivity between mass and T_6. The strong relationship between V_{app} and power is deceiving, as previously described, since an increase in V_{app} results in excess oxygen being produced that is not needed for the six-person MAV. Producing extra oxygen clearly requires extra power, which results in the strong relationship seen. This extra power eventually necessitates the addition of an extra Kilopower unit, which increases the system mass as well.

These examples lead to another key takeaway from this analysis: the Kilopower units drive system mass. All strong relationships that were seen between design variables and mass were the result of the addition or subtraction of a Kilopower unit. This is an indirect result of changes in power, since an increase or decrease in power can change the number of Kilopower units needed to supply that power. Therefore, the power of the system, in the form of Kilopower units, is the main driver of the system mass.

Tornado Charts

A final way to visualize the impact of each design variable on the objective functions is with tornado charts, which show the scaled sensitivities in decreasing order of magnitude. Figure 134 is the tornado chart for power, Figure 135 is the tornado chart for mass, and Figure 136 is the tornado chart for reliability.

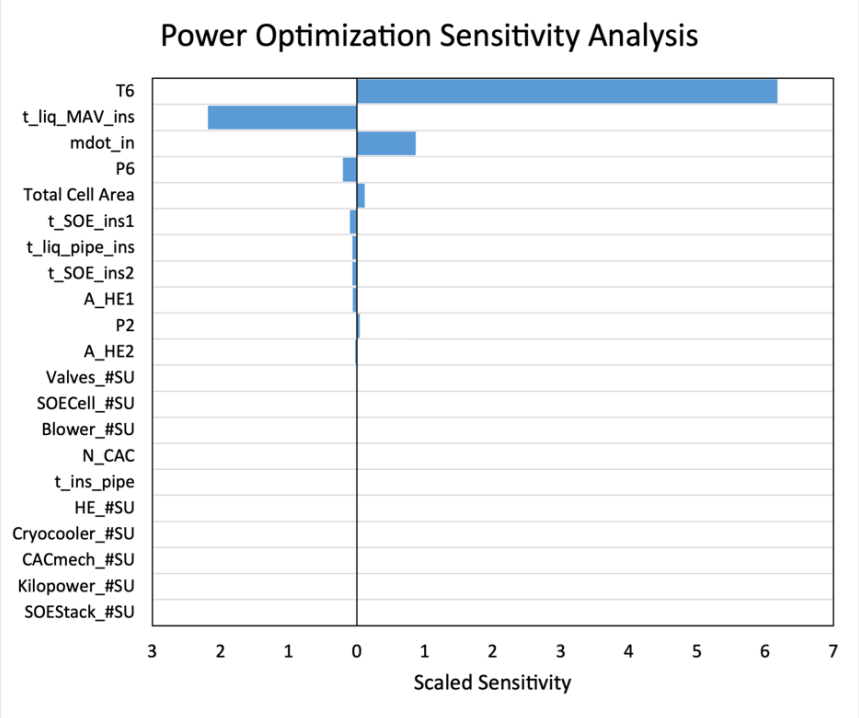

Figure 134: Tornado chart for power optimization. The design variables are ranked in decreasing order based on their scaled sensitivity with power.

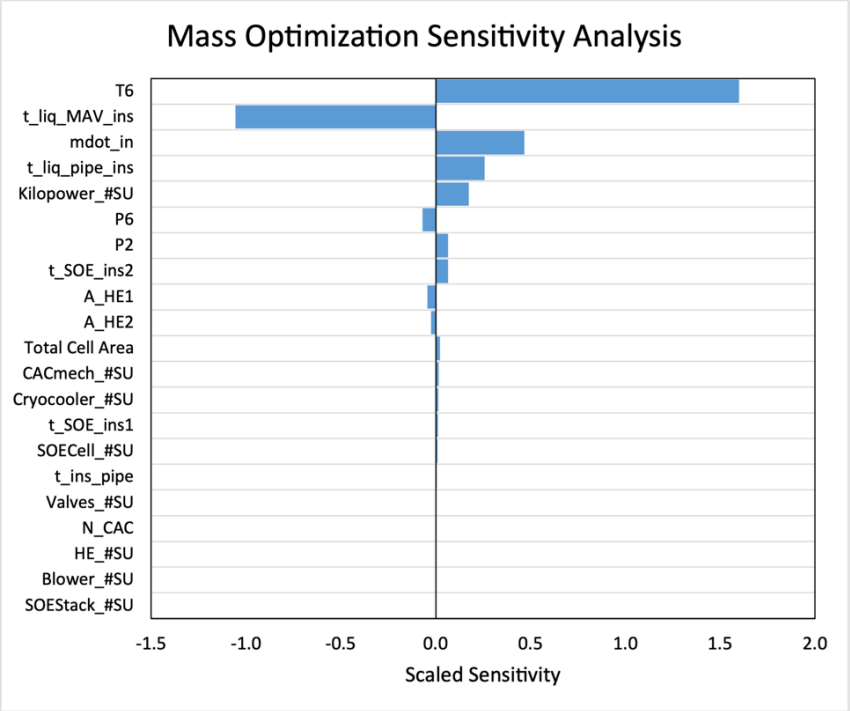

Figure 135: Tornado chart for mass optimization. The design variables are ranked in decreasing order based on their scaled sensitivity with mass.

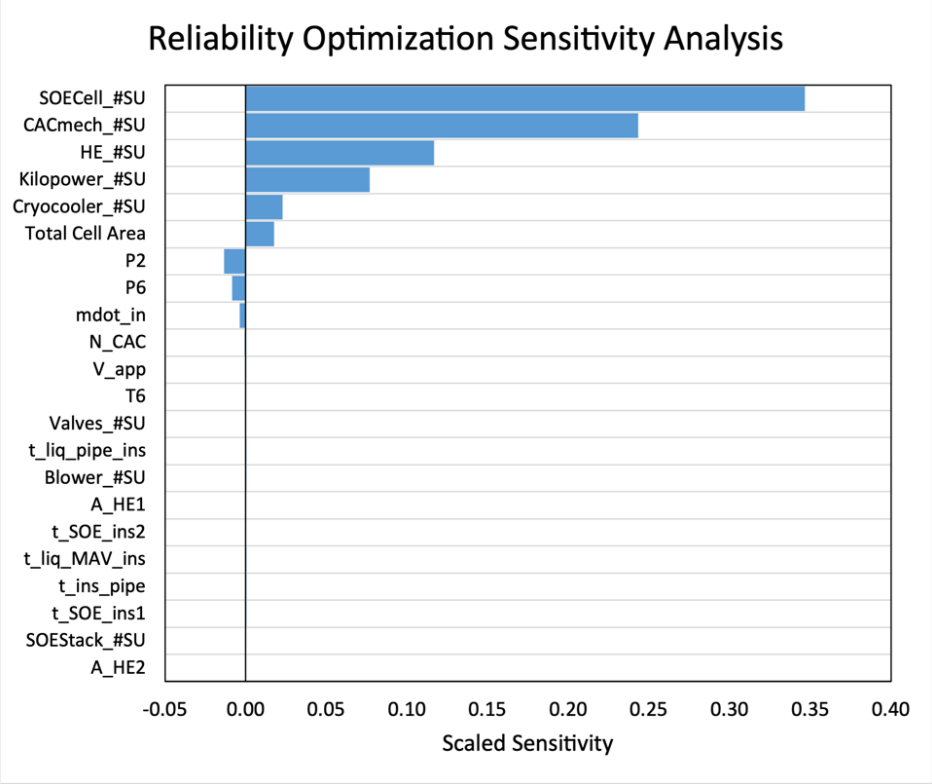

Figure 136: Tornado chart for reliability optimization. The design variables are ranked in decreasing order based on their scaled sensitivity with reliability.

V_{app} was removed from the power and mass charts for reasons previously described. These tornado charts give a concise overview of the relative impacts of each design variable on each objective function. A positive scaled sensitivity indicates that as the design variable value increases, the objective function value increases. A negative scaled sensitivity, such as that seen with P_6 in all three plots, indicates that as the design variable increases in value, the objective function value decreases. The temperature of electrolysis, T_6, insulation thickness on the MAV, $t_{liq,MAV,ins}$, and inlet flow rate, $\dot{m}_{in}$ are the three variables that impact BAM power and mass the most. On the other hand, the design variables based on number of spare units (#SU) dominate reliability optimization as expected. These tornado charts show the tradeoff between objective functions, as the order of variables differs between the three charts.

The three objectives were given equal weighting and combined into one tornado chart to show the variables that have the largest impact across all three objectives. This is shown in Figure 137.

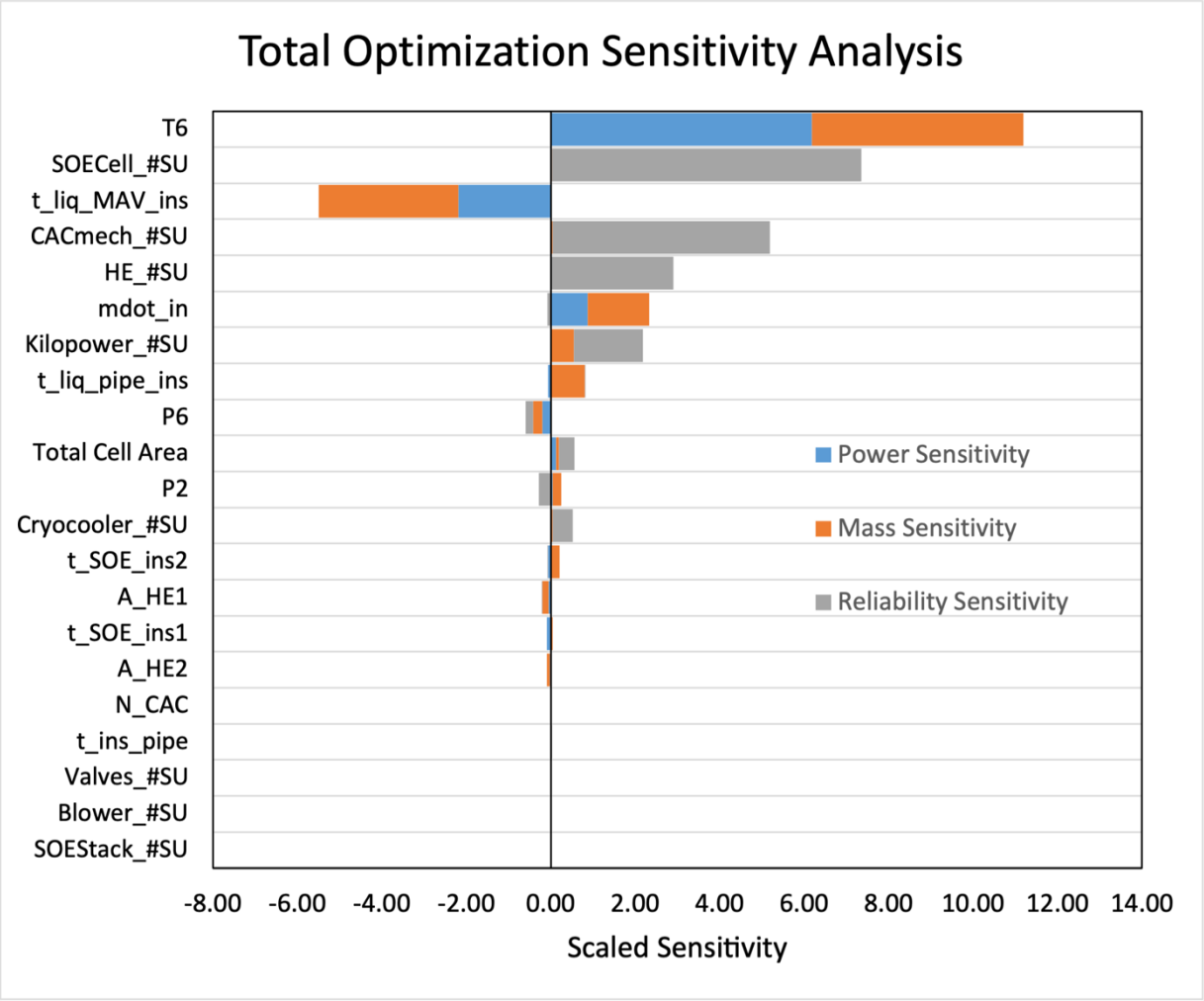

Figure 137: Tornado chart showing the equally weighted, combined impact of design variables on all three objective functions.

T_6, the temperature of the SOE electrolysis, is the most impactful design variable across all three objectives in this analysis scenario. This is not surprising, as it had the largest impact on power and mass. The design variable with the second-highest impact is the number of spare SOE cells, which has minimal effects on power and mass but a significant impact on reliability. The variables that have the least impact on all three objectives are of interest as well. This analysis indicates that the number of spare units of the SOE stack, the blower, and the valves, and the piping insulation, $t_{ins,pipe}$, have minimal impact on overall BAM optimization. It would be possible in future optimizations to set these values as parameters and allow the optimizer to focus on adjusting those variables with larger impacts in order to achieve a more ideal solution.

6.7 Sensitivity Analysis – Mission Parameters

The previous section explored how changing each design variable affects the objective functions – power, mass, and reliability – of BAM. This section will explore how changing key system parameters, which were previously held constant, affects the design and performance of BAM. The parameters that are investigated in this section are the mission duration, crew size, and landing site.

A Simulated Annealing optimization was run for each parameter change below. Some amount of randomness exists in the convergence of the algorithm, but the results are consistent enough to safely compare and analyze the optimization outputs at different parameter values. It is not appropriate to conduct an OAT sensitivity analysis, as was done on the design variables, since changing each of these parameters has many effects on the rest of the design variables.

6.7.1 Mission Duration Effects and Crew Size

The mission duration and crew size are considered together because they are collectively responsible for identifying the oxygen production rate that BAM must achieve. The crew size dictates the size of the MAV, which in turn dictates the total quantity of oxygen that must be produced to propel it, M_{O_2}. The length of the mission, t_m, determines the time available for BAM to fill the MAV tank. Therefore, the rate of oxygen production required of BAM is:

$$\dot{m}_{O_2} = \frac{M_{O_2}}{t_m} \tag{112}$$

which is directly proportional to oxygen quantity and inversely proportional to mission length.

Sensitivity Analysis Setup

The combinations of crew size and mission length that were each passed through a SA optimization are listed in Table 71.

Table 71: Combinations of crew size and mission length for each optimization that was conducted to investigate the sensitivity of the objective functions on these parameters.

Sim ID	Crew Size	Mission Length (months)	O_2 Production Rate
SIM1	4	14	2.25 kg/hr
SIM2	4	22	1.43 kg/hr
SIM3	4	40	0.79 kg/hr
SIM4	6	14	3.06 kg/hr
SIM5	6	22	1.94 kg/hr
SIM6	6	40	1.07 kg/hr

The oxygen production rate is calculated based on the quantity of propellant required in the 4-crew and 6-crew MAV designs, previously described in Section 3.4.3. The two selected crew sizes, 4 and 6, are the most prevalent in Mars mission literature. Three mission lengths were studied and are detailed in Table 72.

Table 72: ISRU production time for three mission scenarios: 1) the O_2 must be fully produced on Mars before the crew departs Earth, 2) the O_2 may continue being produced while the crew is traveling to Mars, and 3) The crew is launched to Mars two synodic cycles after the ISRU system.

	Option 1: Complete O_2 Production Prior to Crew Departure	Option 2: Complete O_2 Production After Crew Departure	Option 3: Launch Crew Two Synodic Cycles After ISRU
Time Between ISRU System Launch and Crew Launch (Earth-Mars Synodic Cycle)	26 months	26 months	52 months
Crew Transit Time to Mars	9 months	Irrelevant	9 months
ISRU Setup Time	1 month	1 month	1 month
Margin	2 months	3 months	2 months
Total ISRU Time Allowed:	**14 months**	**22 months**	**40 months**

The first option, 14 months, is the reference mission previously justified in Section 3.4.3, which assumes the oxygen production must be completed prior to the crew's launch one Earth-Mars synodic cycle after the ISRU plant launched. It also includes one month of setup time and two months of margin. The second, 22 months, is a similar scenario but assumes that the oxygen production can continue after crew launch up until the crew lands on Mars, and with an extra month of margin. The third option, 40 months, is a case where the ISRU system is launched two full synodic cycles ahead of the crew. This was an interesting case to determine if the reduced oxygen production rate could significantly improve the power, mass, and reliability of the system.

Sensitivity Analysis Results

The final power values of the six optimizations are shown in Table 73, ordered from smallest oxygen production rate to largest.

Table 73: Resulting BAM power values for the six optimizations conducted to study the impact of crew size and mission length on BAM design

Sim ID	Crew Size	Mission Length (months)	O_2 Rate (kg/hr)	BAM Power (kW)
SIM3	4	40	0.79	**8.1**
SIM6	6	40	1.07	**11.0**
SIM2	4	22	1.43	**13.1**
SIM5	6	22	1.94	**17.6**
SIM1	4	14	2.25	**18.9**
SIM4	6	14	3.06	**25.1**

The bolded column in the table details the power of each design and is shown graphically in Figure 138.

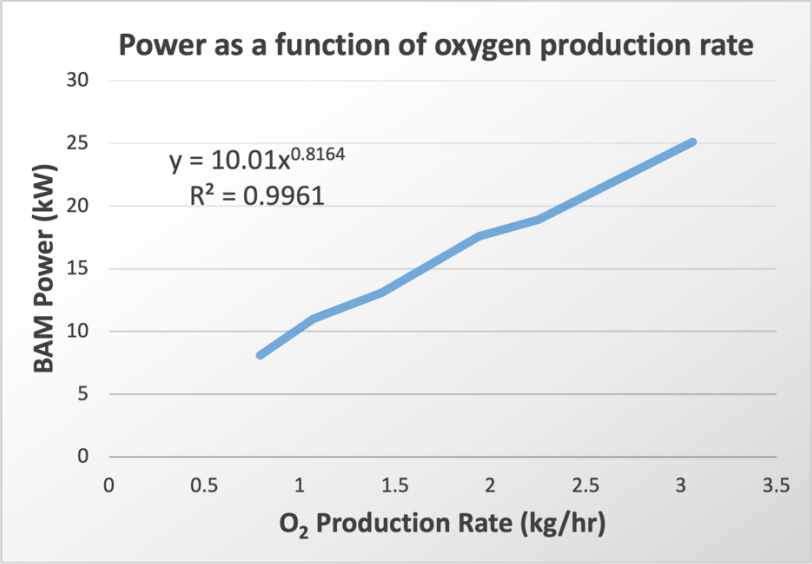

Figure 138: Relationship between oxygen production rate and total system power. The relationship is slightly sublinear.

This relationship, with an exponent of 0.82, indicates a sublinear but near-linear relationship between oxygen production rate and total BAM power. It is a near-linear relationship because SOE electrolysis power scales linearly with oxygen production rate, and SOE power dominates the total BAM power. Other components, such as the CAC and liquefaction, scale favorably (sublinearly) with oxygen production rate.

The ways in which the design of BAM changed with changes in crew size and mission duration were also analyzed by mapping the design variable values for each architecture. The six architectures are shown with parallel coordinates plots in Figure 139 and Figure 140.

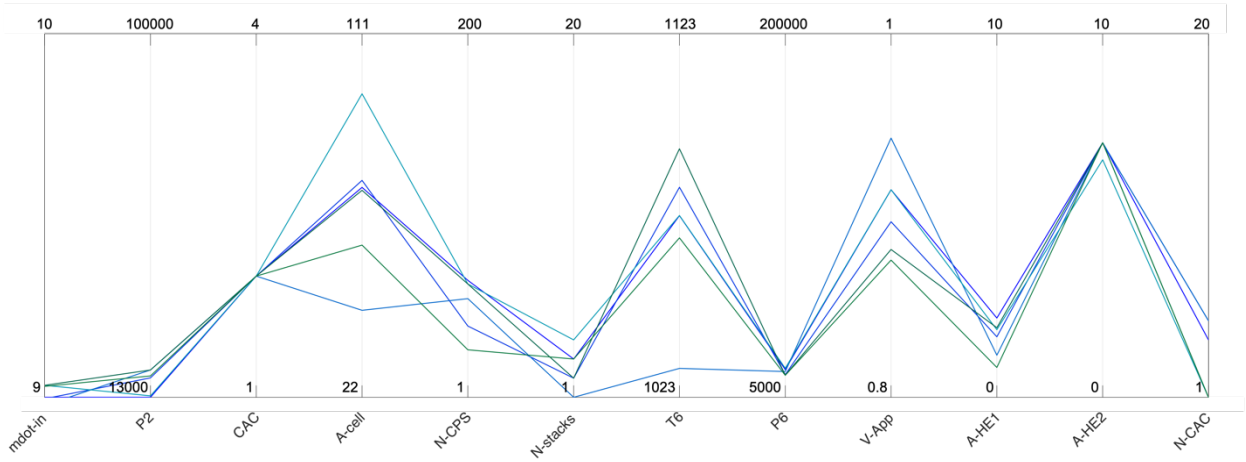

Figure 139: Parallel coordinates plot for the primary design variables across six BAM architectures from differing crew sizes and mission lengths

The six BAM designs were similar across the primary design variables shown in Figure 139, converging to similar values on each as shown by the convergence of the parallel coordinates plot at each vertical axis. All six designs had values for m_{in} and P_2 at their lower bounds, for example, and all converged to the same CAC option. The only two exceptions were a spread of

values across the range of A_{cell} and one design that had a T_6 near its lower bound. There are many reasons these divergences could have occurred, but they likely have more to do with the random perturbations of the optimization algorithm than with a physical mechanism that minimizes power. The secondary variables are shown for the same six designs in Figure 140.

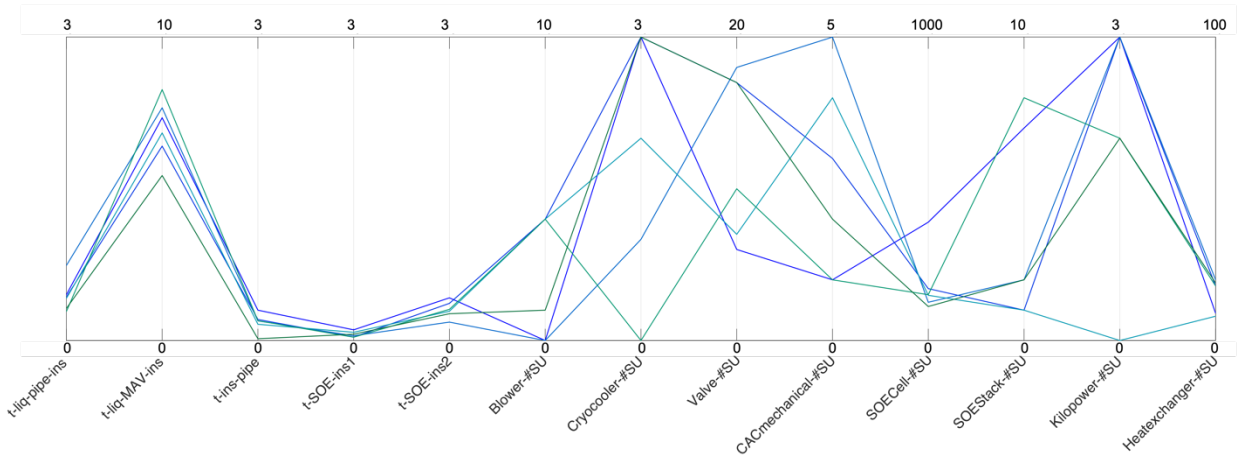

Figure 140: Parallel coordinates plot for the secondary design variables across six BAM architectures from differing crew sizes and mission lengths

The designs have similar insulation thickness values, the first five design variables in the figure. They diverge, however, for the last seven design variables, all of which deal with number of spare units. This is unsurprising, as the number of spare units throughout BAM does not impact power, which was the objective for which these designs were optimized. Therefore, any value for the number of spare units would result in a similar power and thus they should appear randomized, as they do. If the optimizations were to be run for mass or reliability, the values of these design variables would be expected to converge, since both of these objectives are impacted by spare units.

Overall, the results of this sensitivity analysis reveal that power increases sub-linearly as crew size is increased or mission length is decreased. The design of BAM stays relatively constant across the range of crew sizes and mission length considered, with the design variables generally converging to the same ranges across all architectures. The BAM subsystems are simply scaled up or down to accommodate the increase or decrease in required oxygen production resulting from the change in crew size or mission length.

6.7.2 Landing Site Effects

The landing site that is chosen for future Mars missions has a strong influence on the operation and performance of the ISRU system. At sites with lower elevation, the air density is higher, leading to a reduction in required compression. Certain areas of the globe have relatively wide ranges of atmospheric temperatures and pressures throughout the year that must be accounted for by the ISRU controls system and could impact system reliability. Yet another factor to consider is the availability of water and sunlight, both important resources for future human settlements.

NASA's Evolvable Mars Campaign (EMC) has investigated many potential landing sites for human missions to Mars. Landing sites are described by Exploration Zones (EZs) and Regions of

Interests (ROIs); an EZ contains a set of ROIs and spans a region of approximately 100 km in radius. A NASA workshop was held in October 2015 [195], at which 47 EZs were presented, shown in Figure 141. Justification for each included scientific merit and ISRU capabilities. The selections were made with the assumption that a single site would be picked as a home base, and subsequent crewed missions would return to that site. Additionally, all proposed EZs were constrained between +/- 50 degrees latitude and less than 2 km altitude. The reasoning for this was that higher latitudes put additional propulsive requirements on the ascent vehicle for each mission and higher altitudes make it more difficult to land payloads on the surface. By definition, these constraints rule out the North Pole, which some scientists believe may be a preferential landing site largely owing to the large deposits of H_2O and CO_2 ice. The North Pole will be considered in this sensitivity analysis even though it is not represented as an EZ in the figure.

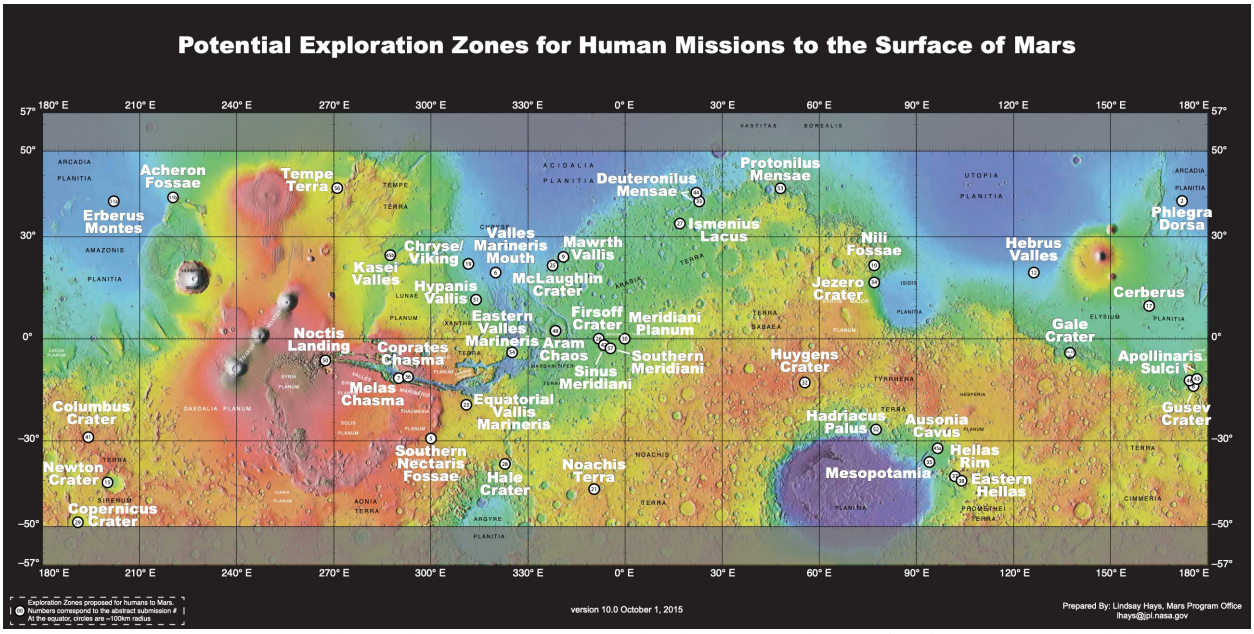

Figure 141: Forty-seven candidate exploration zones proposed at the First Landing Site/Exploration Zone Workshop [195]

To determine the effects of landing site on the optimal atmospheric ISRU plant design, five sites were chosen to be simulated: the Tempe Terra site in the northern hemisphere at a relatively high elevation, the Noctis Landing site near the equator and also at a relatively high elevation, the Planum Boreum site near the North Pole, the Gale Crater site near the equator and at a low elevation, and the Phlegra Dorsa site in the northern hemisphere at a low elevation. Between these five sites, a wide range of latitudes and elevations are covered, both of which contribute to the atmospheric temperature and pressure present at those sites. The atmospheric data for each, across a typical Mars year, was obtained using the Mars Climate Database [115] and run through the BAM model as an annual average.

The modeling results for these five sites are labeled in Figure 142 and listed in Table 74.

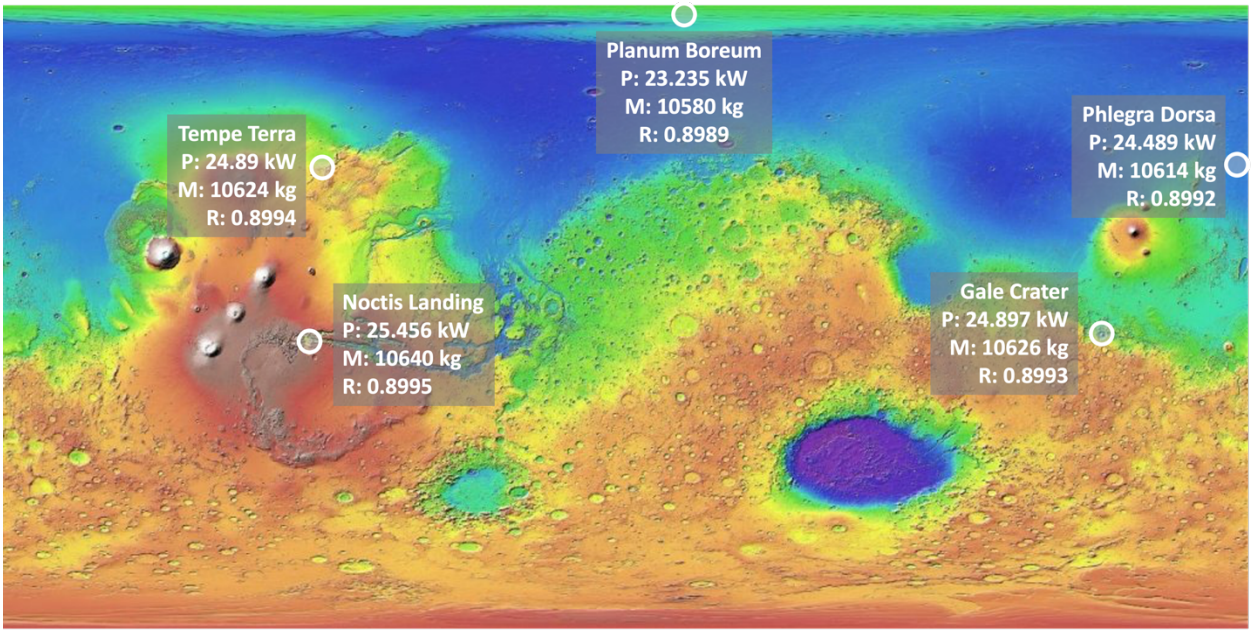

Figure 142: Selected landing sites and the resulting power, mass, and reliability of their BAM designs

Table 74: Selected landing sites for sensitivity study, including atmospheric properties and BAM modeling results

Name	Location	Elevation (m)	Avg. T (K)	Avg. P (Pa)	Avg ρ (kg/m³)	O_2 Rate (kg/hr)	BAM Power (kW)	BAM Mass (kg)	BAM Reliability [0,1]
Tempe Terra	42°N, 272°E	1000	216	540	0.015	3.06	**24.890**	**10624**	**0.89935**
Noctis Landing	-6.49°N 267.6°E	0	234	570	0.0145	3.06	**25.456**	**10640**	**0.89949**
Planum Boreum (North Pole)	88°N 15°E	-2500	177	640	0.021	3.06	**23.235**	**10580**	**0.89891**
Gale Crater	-5.4°N 137.8°E	-4400	236	820	0.019	3.06	**24.897**	**10626**	**0.89932**
Phlegra Dorsa	39°N 172°E	-4000	225	840	0.022	3.06	**24.489**	**10614**	**0.89921**

The results indicate that the mass and reliability of the system are only minimally affected by the selected landing site, as all values are within 1% of each other across the five sites. The power, on the other hand, is influenced more substantially by the changes in atmospheric density. In general, as atmospheric density increases, the total power demand of BAM decreases. This is the result of several factors, mostly driven by a decrease in the compression ratio required of the CAC system at higher pressures.

The lowest power design occurred at the North Pole, which had the second highest atmospheric density after the Phlegra Dorsa design. The lower temperature of the North Pole resulted in a

lower overall power requirement owing to over 1 kW of savings in the liquefaction subsystem. The lower inlet temperature at the North Pole resulted in a greater quantity of heat exchange between the hot SOE oxygen exhaust and the cold incoming Martian atmosphere. As a result, the temperature of the oxygen entering the liquefaction unit was lower in the North Pole design than in the Phlegra Dorsa design. This decreased the cooling load required of the liquefaction unit, ultimately saving over 1 kW of power. This net power savings occurs despite the fact that the colder gas at the North Pole had to receive extra heating to achieve proper SOE temperature because heating is more efficient than cooling; with heating, nearly 100% electrical to thermal energy conversion can be achieved, while with cooling, cryocoolers can only achieve ~10% thermal efficiency. As a result, a lower inlet temperature provides a favorable system power.

Many other considerations apart from BAM power must be factored into the selection of a human landing site. The presence of subsurface water is a requirement for long-term human settlement of Mars but may not be as important for scouting expeditions. The latitude and elevation of the landing site impact the delta-V requirements of the landing system and departing MAV. The diurnal and seasonal temperature swings also must be taken into account, as thermal cycles may result in degradation of equipment. The North Pole, while an extreme location in terms of landing and launch, may offer the least amount of thermal cycling of any location on Mars, as it stays at a relatively similar temperature throughout the day and night. These considerations should all be taken into consideration when selecting a landing site, along with the landing site's impact on BAM power, mass, and reliability.

6.8 Tradeoffs Between Objectives

In this section, various examples of tradeoffs between objectives are examined. In many scenarios, a change in a design variable will result in one objective becoming more favorable and one becoming less favorable. It is useful to understand and document these relationships to better inform future BAM designs if the priority of objectives changes. The tradeoffs will be organized by the subsystem in which they originate. All the tradeoffs described below are modeled and taken into account by the optimization algorithm during its selection of optimal BAM designs.

6.8.1 CAC System Tradeoffs

A key tradeoff between power and mass exists in the sorption compressor. The architecture for temperature swing adsorption systems for Mars can be divided into two primary categories, as discussed in Section 4.3.3: short-cycle and long-cycle. Short-cycle systems used rapid temperature swings and many thin sorption beds to adsorb and desorb CO_2 from the Martian atmosphere in two-minute cycles. Long-cycle systems take advantage of the diurnal thermal swings on Mars to passively heat and cool one large sorption bed. The long-cycle option has lower power, as it supplements its active heating and cooling with the Martian atmosphere, but significantly higher mass owing to the need for significantly more sorption bed area to achieve the same CO_2 flow rate. While the power requirement could nearly be eliminated for the long-cycle option, its mass ends up being a factor of ~500 more than the short-cycle requirement, as shown in Figure 78, and makes it infeasible for a Mars mission. This is summarized as a tradeoff between mass and power with cycle time. Notably, this same tradeoff exists for the cryopump, as a shorter cycle time in the cryopump would result in less mass but higher power.

A second tradeoff in the sorption compressor system exists between reliability and mass. Considering the same two architectures as before, the short-cycle option has significantly lower mass owing to its rapid cycling but may have significantly lower reliability as a result. Over the course of a 14-month ISRU production mission, the short-cycle system will undergo approximately 300,000 thermal cycles. This high quantity of cycling, combined with the fragility of the thin sorption beds and their microchannel temperature control systems, leads to a lower reliability than the long-cycle option.

6.8.2 SOE System Tradeoffs

The SOE system has several examples of objective tradeoffs. First, the SOE cell area trades between mass and reliability. Larger cells will result in a less massive system, as a larger fraction of the SOE stack will be devoted to active cell area versus the total cell area that includes framing, gaskets, piping, and insulation. Table 75 illustrates this, showing the increase in active cell area percentage as a function of total cell area between the MOXIE cells and the larger SOE cells developed at OxEon Energy.

Table 75: Comparison of active area to total area of two sizes of SOE cells

	MOXIE SOE Cells	OxEon Energy Large SOE Cells
Active Cell Area (cm^2)	22.74	110.8
Total Cell Area (cm^2)	50	169
% Active Area	**46%**	**66%**

Though the larger cells are individually more mass-efficient than smaller cells, they require a higher mass for redundancy than the smaller cells. Every spare cell of the larger variety has more mass than three spare cells of the smaller variety. This means that it could be difficult to achieve the same number of spares, and thus the same reliability, when using larger cells as compared to smaller cells.

A second tradeoff in the SOE system is also between mass and reliability, but as a function of the number of SOE stacks. A higher number of stacks with a smaller quantity of SOE cells in each would result in a more massive but more reliable system. Similar to the cell area mass efficiency previously described, smaller stacks of SOE cells have a lower mass efficiency owing to the packaging, piping, and insulation required on each stack. Therefore, to achieve the same total cell area with a higher number of stacks, more mass will be required. This is a more reliable system, however, as the failure of one stack will have less of an impact on the system the more stacks that exist.

A third tradeoff in the SOE between mass and reliability originates with the voltage applied to each cell, V_{app}. A higher voltage per cell will result in more oxygen production per cell, and thus less total cell area required to achieve the same total oxygen production. This improvement in mass comes at the expense of a decrease in reliability, as increasing the cell voltage moves it closer to the Nernst potential for carbon formation, a degradation mechanism for the cell. As described in Section 6.6, the optimizer generally opted to keep the applied voltage low to improve reliability, as the subsequent increase in mass was less impactful to the system as a whole.

6.8.3 Heat Exchanger Tradeoffs

The heat exchanger as a stand-alone system is a straightforward tradeoff between mass and power. A larger heat exchanger area will result in more heat recuperated from the hot SOE exhaust stream, which decreases pre-heating power requirements for the SOE. It also decreases the cooling power required of the liquefaction unit, as the oxygen from the anode is cooled in the heat exchanger. The power savings in the liquefaction unit are actually an order of magnitude higher than the heat exchanged in the heat exchanger, as the cryocooler operates at approximately 10% thermal efficiency, meaning that for every Watt of cooling accomplished in the heat exchanger, 10 Watts of cooling power are saved.

A full sensitivity analysis of heat exchanger mass was explored in Section 6.6. An illustrative example is shown in Table 76 to show the impact of adding a heat exchanger to BAM:

Table 76: Illustrative example of the impact of adding a heat exchanger to BAM on power and mass. The addition of a 10 m^2 heat exchanger saves nearly 10 kW of power and over 1,500 kg of system mass. Increasing the heat exchanger beyond this size results in additional system mass and minimal power savings.

	Heat Exchanger Mass (kg)	BAM System Mass (kg)	BAM System Power (kW)
No Heat Exchanger	0	10,592	34.7
Heat Exchanger (10 m^2)	183	9,010	25.4
Heat Exchanger (100 m^2)	650	9,488	25.3

The addition of a 10 m^2 heat exchanger saves nearly 10 kW in this example, a critical power savings that significantly changes the requirements of BAM. Another key finding from this study is that, while the addition of this heat exchanger adds 183 kg in heat exchanger mass, it actually results in a net savings in total system mass. In this case, it saves over 1,500 kg. This is primarily the result of a decrease in the number of Kilopower reactors that must be sent, but a small decrease in liquefaction system mass is also observed owing to a reduction in radiator area needed for heat rejection.

A heat exchanger area of 10 m^2 is sufficient to recuperate nearly 100% of the heat from the SOE exhaust streams in most Pareto-optimal architectures of BAM. Increases beyond 10 m^2 increase the system mass but result in negligible power savings, as shown when comparing the last two rows of Table 76.

6.8.4 Other Tradeoffs

Other tradeoffs that are not specific to a particular subsystem exist. The first is related to the diameter of the fluid pipes that connect each subsystem. A larger diameter pipe contributes more mass but decreases the pressure drop of the fluid flowing through it. The compressor must compress the fluid to a pressure sufficient to counter the pressure drops throughout the system, meaning lower pressure drops require less initial compression. Therefore, a larger diameter pipe represents a trade between pipe mass and compressor power.

Another tradeoff that exists throughout the system is between power and mass as it relates to the thickness of insulation. Insulation is modeled on all pipes in the system as well as on the MAV

tank and in the SOE oven and is controlled by five separate design variables. Thicker insulation results in smaller heat leaks and thus less heating and cooling power, but more insulation mass. In most cases, the optimizer drives insulation towards zero thickness for mass optimization but towards up to several meters thick for power optimization. In reality, a balance between the two is likely optimal and is reflected in many Pareto-optimal designs.

6.8.5 Redundant Units

A general note must be made about redundant units. In general, redundancy offers a tradeoff between mass and reliability; an increase in redundant units within a subsystem increases the mass and increases the reliability of that subsystem, up to a point. If the reliability of the subsystem is satisfactory, adding additional redundant units does not positively influence the design, it only adds additional mass. Redundancy is considered by the optimizer in every subsystem in BAM through eight design variables dedicated to redundancy. The general trend in most Pareto-optimal designs of BAM is that redundancy increases when optimizing for reliability, redundancy decreases when optimizing for mass, and redundancy stays constant when optimizing for power.

6.9 Final Design Selection

Many possible designs for BAM have been shown and discussed in this chapter, including the 153 unique, nondominated designs presented in Section 6.4. Any one of these designs has merit and could reasonably be defended as the best option to build and send to Mars, depending on the weight placed on each objective function by mission planners. As a result, it is impossible to identify a single solution as the "most optimal". With that in mind, one solution will be recommended here for the sake of discussion. To put this into context, a generic rendered design of BAM is shown on a Mars background in Figure 143, which includes all major components that have been discussed in this dissertation.

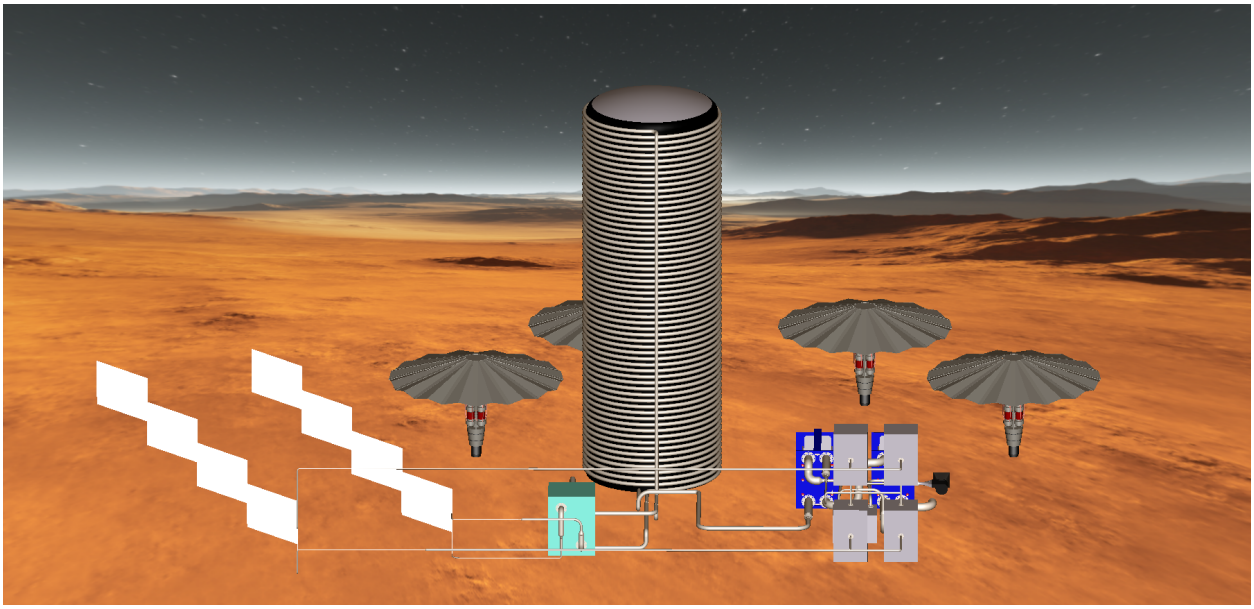

Figure 143: BAM design rendered on Mars background [128]. The MAV tank with cooling piping surrounding it is centered in the frame, with four Kilopower units surrounding it to provide power. On the right in the front are four cryopumps operating in parallel. Behind them, in blue, is the plate heat exchanger. On the far left is the radiator in white and located next to it in the front is the cryocooler.

Several factors determined which of the 153 nondominated solutions presented in Section 6.4 was selected as the recommended final design. First, the BAM power was considered. As discussed throughout this chapter, power is the primary driver of system mass, as an increase in power can result in the addition of a Kilopower unit, which dominates system mass. It would not, however, be beneficial to minimize the power below the level that will be required to run the habitats, laboratories, and other equipment for the crew once they arrive on Mars, since that amount of power must be supplied regardless. This assumes the ISRU plant will be shut down upon crew arrival and all power rerouted to support the crew's mission. This should be the case regardless of power concerns, as the MAV should be fully fueled upon crew arrival to minimize mission risk.

The power used by either a crew of four or six astronauts on the first missions to Mars for their habitat and laboratories is expected be in the range of 21 – 25 kW [107]. An additional ~1.5 kW will be required by the cryocooler to maintain the liquid oxygen in a zero boiloff state during the mission, bringing the expected power demand of the crew to 22.5 – 26.5 kW. Minimizing power below this range is not beneficial, so any BAM designs with a lower power than this are discarded. Moreover, the assumed power source for this mission is a series of 10 kWe Kilopower nuclear units. A power demand of 21 kWe and a power demand of 30 kWe would both require three 10 kWe Kilopower units. With this in mind, any power minimization below 30 kWe would not provide significant benefits. For margin, in the event that the primary Kilopower units lose up to 10% power efficiency over time, the threshold where power minimization no longer becomes helpful was set to 27 kWe instead of 30 kWe. This drove the design of the recommended BAM design; all designs above 27 kWe were discarded, as they would require an additional Kilopower unit. Note that if a different power source were used on Mars that could provide power in more discrete quantities, the power threshold would have been set to 22.5 – 26.5 kWe.

With the power threshold set, the recommended BAM design was then selected from the remaining nondominated designs based on reliability and mass. It was determined that a minimum reliability of 0.95 should be achieved. After filtering all nondominated solutions such that only those with a power of 27 kW or lower and a reliability of 0.95 or higher remained, 23 solutions were left. Of these, the solution with the lowest mass was selected as the recommended design. It is shown as a highlighted point in the 3-dimensional Pareto front shown in Figure 144.

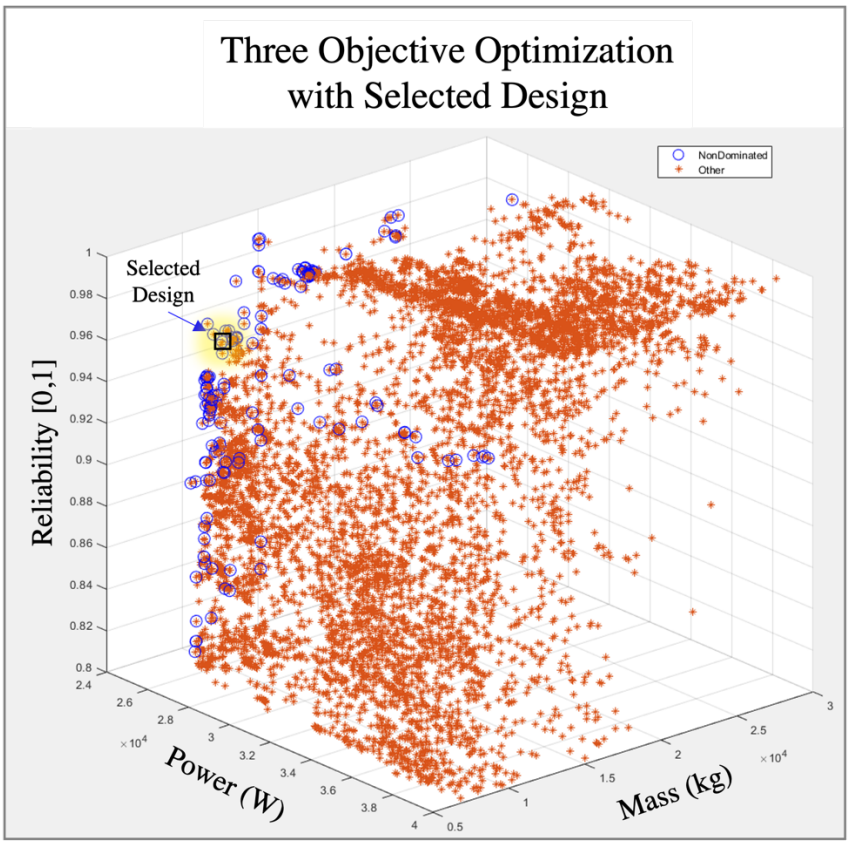

Figure 144: All valid BAM designs in a 3-dimensional space. Valid designs are indicated by a star (*), nondominated designs are indicated by a circle and form the Pareto front, and the selected design is highlighted and identified with a black box.

This design has a power of 26.7 kW, a mass of 9142 kg, and a reliability of 0.97. A breakdown of the power and mass by subsystem is shown in Figure 145.

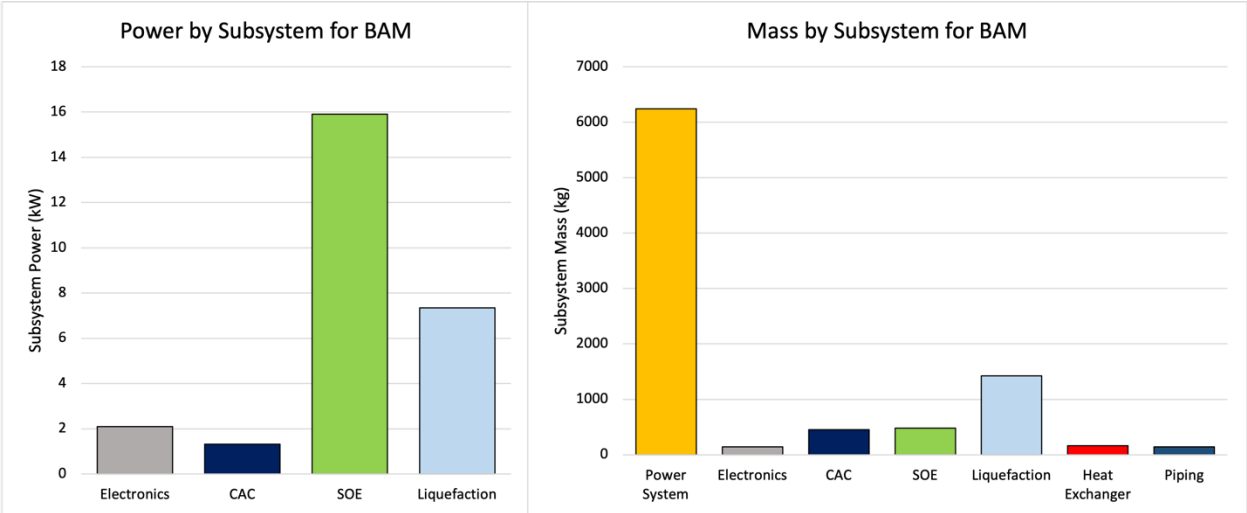

Figure 145: Breakdown of power and mass by subsystem for the selected BAM design.

As expected, the system power is dominated by SOE, and followed by the liquefaction unit. The mass is dominated by the Kilopower units, which themselves are a function of power. The

liquefaction unit, which includes the cryocooler, radiator, insulation, and piping around the MAV, has the second highest subsystem mass.

This design is described as a function of its design variables in Table 77 with the design variables and their values overlaid onto a block flow diagram of BAM in Figure 146 for a visual representation of the final architecture.

Table 77: Recommended BAM design, showing values for all 25 design variables that define the architecture of BAM

Design Variable	Variable Name	Value	Units
Inlet Flow Rate	$\dot{m}_{in}$	**15.3**	kg/hr
Compressor Pressure	P_2	**18**	kPa
CAC Type	CAC	**Scroll**	-
Cell Area	A_{cell}	**111**	cm^2
Number of cells per stack	N_{cps}	**60**	-
Number of stacks	N_{stacks}	**3**	-
Electrolysis Temperature	T_6	**1073**	K
Electrolysis Pressure	P_6	**15.3**	kPa
Voltage	V_{app}	**0.915**	V
Area of Heat Exchanger 1	A_{HE1}	**2.3**	m^2
Area of Heat Exchanger 2	A_{HE2}	**5.9**	m^2
Number of CAC systems	N_{CAC}	**1**	-
Liquefaction piping insulation	$t_{liq-pipe-ins}$	**0.23**	m
Liquefaction MAV insulation	$t_{liq-MAV-ins}$	**1.64**	m
Inter-piping insulation	$t_{ins-pipe}$	**0.04**	m
SOE inner layer insulation	$t_{SOE-ins1}$	**0.05**	m
SOE outer layer insulation	$t_{SOE-ins2}$	**0.15**	m
Spare cryocoolers	$Cryocooler_{\#SU}$	**2**	-
Spare valves	$Valve_{\#SU}$	**18**	-
Spare mechanical pumps	$CACmechanical_{\#SU}$	**3**	-
Spare SOE cells	$SOECell_{\#SU}$	**150**	-
Spare SOE stacks	$SOEStack_{\#SU}$	**3**	-
Spare Kilopower units	$Kilopower_{\#SU}$	**1**	-
Spare heat exchanger plates	$Heatexchanger_{\#SU}$	**9**	-

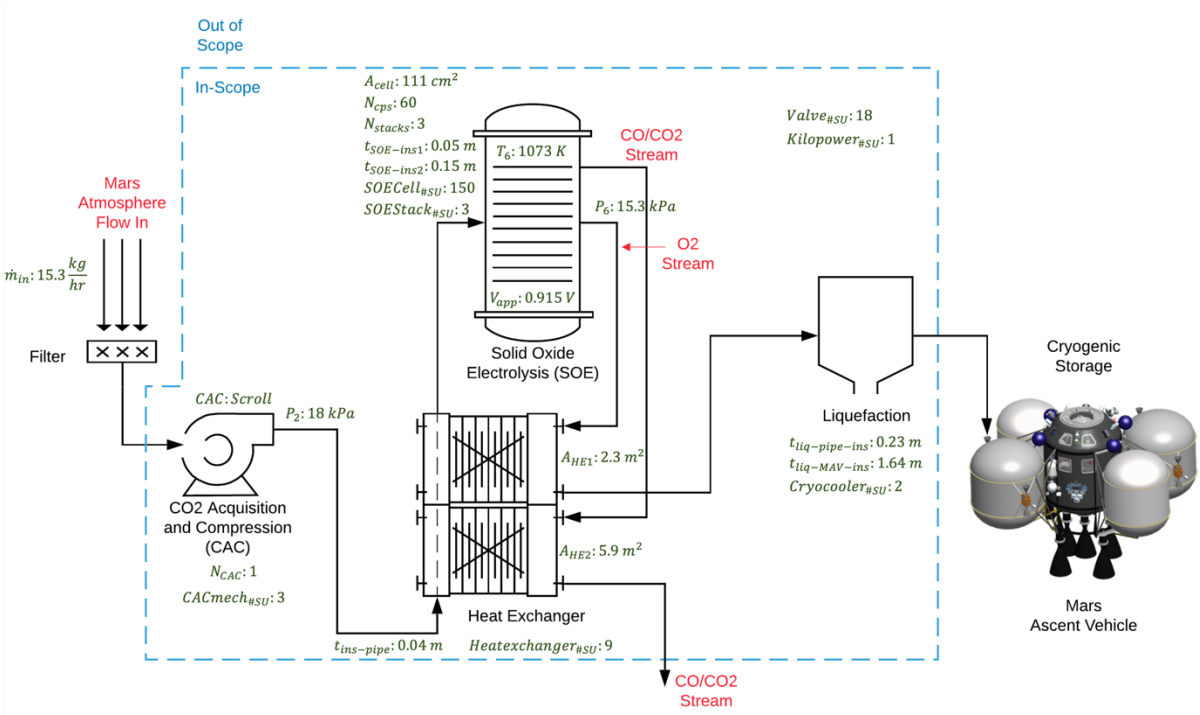

Figure 146: BAM block flow diagram with all design variables labeled in green with their values for the selected BAM design

The design of the system followed many of the trends identified in the Section 6.6 sensitivity analysis: the inlet flow rate, compressor pressure, and electrolysis pressure were near their lower bounds, the area of the second heat exchanger was relatively high, and the insulation thickness was minimal on all areas except the MAV tank. The spare number of SOE cells is nearly as large as the number of active SOE cells, owing to the increase in reliability that results from this redundancy with only a minimal increase in mass as a penalty. Lastly, one spare Kilopower unit is sent, increasing the system mass by 1545 kg but greatly increasing system reliability.

6.10 Conclusions

This chapter has covered the results and analysis of a series of optimizations and sensitivity analyses for the BAM system. Sections 6.1 and 6.2 explored the results of a single-objective analysis for power and mass, respectively. They both showed that system power is dominated by the electrolysis power in the SOE subsystem, and system mass is dominated by the Kilopower units. Section 6.3 explored a multi-objective optimization of both power and mass, which resulted in a Pareto front of 17 nondominated solutions. The clear presence of a Pareto front indicated that mass and power are competing objectives in the design of BAM. Nearly all the design variables for these solutions converged to similar values with the exception of the eight design variables for spare units, which did not impact power and minimally impacted system mass. Section 6.4 added reliability as a third objective to the multi-objective optimization, and across over 18,000 valid designs of BAM that were generated, 153 were nondominated and formed the 3-dimensional Pareto front. The addition of the third objective significantly increased the number of nondominated solutions. The design variables were analyzed across these 153 solutions and found to converge to similar values on approximately 50% of the design variables.

Section 6.5 showed the results of the PRA for reliability analysis using two case studies. Section 6.6 explored the sensitivity of each objective function with the primary design variables, finding that nearly all combinations of objective functions and design variables displayed nonlinear behavior. The temperature of the SOE electrolysis, the number of spare SOE cells, and the thickness of the insulation covering the MAV tank were the three design variables with the largest combined impact on the three objective functions. Section 6.7 explored the sensitivity of mission length, crew size, and landing site, finding that power scales sublinearly with mission length and crew size, and that landing site has a marginal influence on power, but not on mass or reliability.

Section 6.8 summarized where and how tradeoffs between objective functions occur within the BAM system. These tradeoffs identify where design changes might take place if one objective were to be weighted higher than another by mission planners. Lastly, Section 6.9 recommended a final, optimized solution for BAM, noting that any of the 153 nondominated solutions presented in Section 6.4 would be viable solutions.

Chapter 7: Contributions and Future Work

This chapter summarizes the major contributions of this dissertation work and provides guidance to the future work that should be conducted to best prepare oxygen-based ISRU systems to support humans on Mars.

7.1 Contributions

The primary contributions of this dissertation are listed in Table 78.

Table 78: Primary dissertation contributions

ID	Contribution	Location
C1	Designed and developed a detailed and flexible model of a full-scale ISRU system based on MOXIE, called BAM.	Chapter 4
C2	Created a multi-objective optimization framework to optimize the design of BAM in the context of selected mission parameters.	Chapter 3
C3	Provided optimized designs of BAM on the basis of power, mass, and reliability.	Chapter 6
C4	Quantitatively and qualitatively analyzed the impact of changing design variables and mission parameters on the power, mass, and reliability of BAM.	Section 6.6 Section 6.7
C5	Analyzed and modeled three categories of compressors for Mars atmospheric acquisition – cryogenic, sorption, and mechanical – and determined that mechanical compressors offer the lowest mass and lowest power systems.	Section 2.5 Section 4.3 Section 5.1 Section 6.6
C6	Tested and characterized SOE cells under low-pressure operation, finding that SOE performance is unaffected down to cathode pressures of 150 mbar.	Chapter 5
C7	Developed a new method for quantifying operational risk, based on a Probabilistic Risk Assessment, and successfully implemented it into the BAM model.	Section 4.9

Each of the primary contributions will be explained in more detail below.

C1: Design and modeling of BAM
The design and modeling of BAM resulted in the development of models to calculate the expected performance, power consumption, mass, volume, and reliability of every component in BAM. This includes several types of compressors, a scaled-up SOE system, an oxygen liquefaction system, a heat exchanger, and plumbing throughout the system. These subsystem models were integrated into a model-of-models to simulate the performance of a scaled-up ISRU system. The model is scalable and modular to enable it to be applied to a wide range of ISRU systems.

C2: Optimization framework
A heuristics-based algorithm, Simulated Annealing, was modified and integrated with the BAM model to enable the optimization of the BAM design. This involved a DOE conducted on the

tuning parameters of the algorithm itself, custom code developed to integrate it with the BAM model, and unique perturbation functions created for each of the 25 design variables controlled by the optimizer.

C3: Optimized BAM designs
A critical contribution of this dissertation is the set of nondominated BAM designs presented in Section 6.4 and the recommended design presented in Section 6.9. This provides a blueprint to enable the development of a physical ISRU system to support the first human missions to Mars.

C4: Sensitivity analyses
Sections 6.6 and 6.7 provided an in-depth analysis of the impact of design variables and mission parameters (operating time, crew size, and landing site) on the BAM design. The analysis revealed which design variables had significant impacts on the objective functions and which were negligible. It also provided insight as to how BAM power, mass, and reliability scale with the design variables. Some variables had a sublinear scaling relationship with the BAM objectives, while others were superlinear. This information is valuable when designing a BAM system under changing objective weightings or changing BAM sizing.

C5: Compressor analysis
The literature review presented in Chapter 2 found that no clear consensus had been reached in the scientific community on the correct type of compressor that should be used for Mars atmospheric acquisition. Cryogenic pumps, mechanical compressors, and sorption compressors all have advocates, but a thorough and quantitative comparison between the options was lacking in the field. This dissertation provides that quantitative comparison and finds that mechanical compressors are the clear optimal choice for Mars ISRU in terms of system power and system mass minimization. Cryogenic compressors remain competitive for reliability as an objective but have the highest mass and a power that is an order of magnitude higher than mechanical compressors. Sorption compressors fall in-between the other options in terms of mass and power but are inherently riskier due to their complexity and large amount of thermal cycling.

C6: Low pressure operation of SOE
Another unknown in the field before this dissertation was completed was how SOE cells perform at low pressure. Significant benefits in terms of power reduction, mass reduction, and risk reduction can all be realized by operating the SOE cathode at a lower pressure. This was studied from a theoretical point of view, which revealed that operation at low pressure should be possible. Then, an apparatus to allow low pressure testing of SOE cells was designed, built, and used at OxEon Energy in North Salt Lake, Utah on a stack of full-size SOE cells, which experimentally validated the theoretical hypothesis. It is now known that SOE cells will not lose any significant performance down to at least 150 mbar of cathode pressure, which results in significantly more optimal BAM designs than those resulting from higher pressure operation.

C7: Risk Quantification
Quantification of risk is difficult to implement in complex mechanical systems by traditional means. As a result, a new method was developed for this dissertation, using Probabilistic Risk Assessment (PRA) as a baseline and supplementing it with a modified Poisson distribution

analysis. This allowed the reliability of each component, subsystem, and the system as a whole to be calculated and optimized by the simulated annealing algorithm.

7.2 Scalability of Results

BAM was designed to support a crew of six astronauts. However, it was designed to be scalable to larger crews, primarily through the use of modularity. The scalability of each subsystem will be briefly discussed in this section.

The filtration system is scalable by using a larger filter or by adding several smaller filters in parallel. In the latter case, pipes exiting the filter can be joined at a manifold to bring several parallel flow-paths together. The CAC system can be scaled in a similar manner. In the case of sorption pumping, additional sorbent beds can be added in parallel to the existing infrastructure to meet the flowrate requirement. This same principle can be applied to cryogenic pumps and mechanical pumps. In addition to the ease of scaling provided by this modularity, another benefit is redundancy; extra units can be integrated with the system to minimize risk.

The SOE system can be scaled using a similar modularized approach. The number of SOE stacks can be increased to bring the total oxygen production rate to the required level. The oven can be increased in size to accommodate the additional stacks. Similarly, the number of Kilopower units can be increased to match new power demands.

Lastly, the cryopump and radiator in the liquefaction system need to be scaled up to accommodate an increased oxygen flowrate and maintain zero boil-off conditions in a larger MAV tank. This is not expected to be a roadblock for the scaleup of a Mars ISRU plant, as cryogenic systems are implemented on Earth at a wide range of scales. The same is true of the heat exchanger system.

To summarize, this ISRU plant was designed in such a way that, for the majority of subsystems, additional units can be added in parallel to the existing infrastructure until the needs of the mission are met. For those subsystems that are not modularized, scaling is not expected to be an issue as it has been demonstrated on Earth. Therefore, this design is flexible and can be adapted to a wide variety of crewed Mars missions.

7.3 Generalizability of the Model

A brief discussion on the generalizability of this model to other ISRU-based systems will be included here. BAM is designed to produce oxygen on Mars from the carbon dioxide atmosphere. As discussed in the previous section, the design of BAM can be easily scaled to increase or decrease the quantity of oxygen produced, depending on the requirements of the mission. In a similar vein, the design of BAM can be extended to other ISRU-based systems or applications.

The most relevant extension of the BAM design is to a system that includes water, either through co-electrolysis with CO_2 or as stand-alone water electrolysis. In either case, the majority of the BAM model can be used without significant modification, including the compressor (only required for co-electrolysis), heat exchanger, power system, oxygen liquefaction system, and piping. The SOE model would require adjustment in the form of the extension of the

electrochemical reactions to include steam as an input. If the system used a different form of electrolysis than solid oxide, such as a proton exchange membrane (PEM), a new electrolysis model would need to be built. This model could then be inserted into the greater BAM model, replacing the SOE module.

Another extension of the BAM design is to the electrolysis of water on Earth's moon or an asteroid. In these instances, a new module would need to be built to model the mining, purification, and vaporization of water ice. Assuming solid oxide electrolysis as the baseline electrolysis technology, once the modeled water was in a purified gas form, it could be input into the BAM model with the electrolysis module and take advantage of the liquefaction module as well. In the case of alternate water electrolysis technologies where the water remains in liquid form during electrolysis, the compression system would not be required.

In general, the BAM model can be extended to other planetary ISRU applications with modification. Its intentional design as a model-of-models allows individual subsystem models to be switched out with new or modified subsystem models to adapt the design of the ISRU plant.

7.4 Other Considerations

Additional considerations should be considered that may affect the design of BAM. While they were not explicitly studied for this dissertation, the impact of the controls system, mission concept of operations, and SOE exhaust recirculation are briefly explored in this section.

7.4.1 Control System

Controls are an integral part of the design and operation of any future atmospheric ISRU plant like BAM. As a system that must operate autonomously and without the ability to be repaired, a robust sensors and controls network is necessary to make BAM feasible. This includes the detection and flagging of faults, automated shutdowns and restarts in the event of unsafe operating conditions, and dynamic adjustments made to counter changing environmental conditions and subsystem performance. The design of the controls system for BAM was not considered in detail in this dissertation. Instead, initial guidelines will be put forth in this section and more detailed analysis is recommended for future work.

One of the primary functions of the control system will be to adjust system performance based on atmospheric variations. As discussed in Section 4.11, the atmospheric density on Mars varies by up to a factor of two throughout the year, which has significant implications for the way in which the subsystems in BAM are operated. With the controls system described in Section 4.11, the controls will primarily be responsible for sensing atmospheric density at the inlet of the CAC system and adjusting the CAC speed or cycle time to output a constant mass flow rate throughout the Martian year. This should consist of a PID feedback controller that senses atmospheric temperature and pressure, calculates the density, and then sets the compressor speed or cycle time accordingly.

The SOE system will be outfitted with a variety of controls systems as well. First, the inlet gas temperature must be measured and increased to the operating temperature of the SOE, T_6. This requires a PID controller that senses gas temperature and adjusts the inline preheater's power to compensate. Similarly, the temperature inside the SOE hotbox must be measured and the heater

power controlled to ensure a constant operating temperature despite varying heat leaks throughout the Martian day and seasons.

The voltage must also be strictly controlled such that it does not exceed the Nernst potential for carbon formation, which could lead to coking of the SOE cell. This could most feasibly be accomplished by maintaining a minimum offset voltage from the Nernst potential. This implies a voltage controller, where the voltage of each cell, or the stack as a whole, is measured and controlled. Because the resulting electrical current is dependent on both the voltage and the iASR of the cells, the current must be measured either electrically or by measuring the flow rate of oxygen being produced at the anode. The Nernst potential would be calculated using an onboard computer connected to sensors that measure the temperature of the SOE and the partial pressures of the cathode and anode. In the event that the cell experiences a drop in performance and less oxygen is produced than expected, operators on Earth can bring spare SOE cells online to ensure the total oxygen production rate is sufficient.

The liquefaction system will also use a network of sensors and controllers to ensure safe operation. The speed of the compressor in the cryopump will be dynamically controlled based on the inlet temperature of the oxygen. This oxygen temperature will vary slightly over the course of a Martian day and year due to varying heat leaks, and the compressor must compensate for this to ensure all oxygen is liquefied in the cryopump. The MAV tank, where the liquid oxygen is stored, will have a zero boil-off (ZBO) system in place that uses a network of sensors to measure pressure, temperature, and fluid level in the tank. In the event that the tank begins building too high a pressure from boiloff gases, the level of cooling can be increased by a controller that adjusts the cryocooler's compressor speed and working fluid pump speed.

The properties of the gases and liquids will be measured throughout the BAM system with a wide array of sensors. The majority of control systems will exist within, and be designed for, each subsystem. The sensor and control network does not dictate the optimal architecture of BAM but is nevertheless an integral part of its design that must be designed, developed, tested, and characterized before BAM can be flown to Mars.

7.4.2 Mars Mission ConOps

It is useful to frame the mission as part of a concept of operations (ConOps) to better understand how BAM will be deployed and what ancillary systems may be needed. The ConOps is outside the scope of this dissertation but plays a role in framing the design of BAM. The ConOps is divided into five phases:

Phase 1: ISRU plant travels to Mars
Phase 2: ISRU plant is deployed on Mars and begins operations
Phase 3: Crew launch and travel to Mars
Phase 4: Crew land and conduct mission operations
Phase 5: Crew departs Mars

Each of these phases will be described in more detail below.

Phase 1: ISRU Plant Travels to Mars
This phase of the ConOps involves the launch of the ISRU system to Mars. The entire system, as discussed in Chapter 6, is capable of fitting in a single standard rocket fairing and therefore can be launched as a single unit. All components of the ISRU system will have undergone pre-launch tests to ensure they can survive the harsh conditions of the launch environment. The ISRU system will travel to Mars on a standard trajectory, which lasts between six and nine months. Upon arrival to Mars, the system must undergo a successful entry, descent, and landing (EDL) sequence at the targeted landing site. The capability to land multiple metric tons on the surface of Mars does not currently exist and is a significant challenge that must be overcome to enable large-scale ISRU and human missions to Mars.

Phase 2: ISRU Plant is Deployed and Begins Operations
After successfully landing, the system must be deployed on Mars to begin operating. Possibly the largest challenge that must be addressed in this phase is the decision of how to locate the Kilopower nuclear power systems a safe distance away from the rest of the ISRU plant, assuming the crew will eventually land and deploy their habitat near the ISRU plant. This assumption dictates that the Kilopower units and the rest of the ISRU plant be separated by approximately 1 km prior to crew arrival [107]. To limit risk to the crew, it may make the most sense to perform this separation immediately after the ISRU system lands, as opposed to waiting to separate the units until after the crew lands.

The ISRU system mass presented in Section 6.2 is dominated by the Kilopower units, which account for up to 90% of the total mass of the system. This leads to the preliminary conclusion that it may be easier to move the ISRU plant 1 km and leave the Kilopower units where they landed. However, the MAV must be located adjacent to the ISRU plant to enable liquefied oxygen to be stored in its tank. The mass of the MAV was not considered in this dissertation and would add considerably to the ISRU mass. Polsgrove et al. (2015) estimate that the dry mass of a 4-crew MAV would be approximately 9,400 kg [120]. Applying the scaling law developed for oxygen production rate between crews of 4 and 6, as presented in Section 3.4.3, the estimated dry MAV mass for a crew of 6 would be approximately 12,800 kg. Table 79 shows the mass of the two systems that must be separated by 1 km upon landing:

Table 79: Mass comparison between the two units that must be separated after landing on Mars to avoid nuclear radiation concerns: 1) The ISRU system and the empty MAV, and 2) the Kilopower nuclear reactors. The mass numbers are shown from the mass-optimal design

	ISRU + MAV Mass (kg)		Kilopower Mass (kg)
ISRU Mass	842	**Kilopower Mass**	6160
MAV Mass	12800		
Total	**13642**	**Total**	**6160**

The total mass of the ISRU system and the MAV is significantly higher than the mass of the four Kilopower units that supply the power for the ISRU. For this reason, the ISRU system and MAV should be deployed at the landing site and the Kilopower units should be moved a safe distance away by an autonomous transport vehicle. Another option to consider for separating the two systems would be to deploy them separately. If the EDL technologies at the time of the mission

have the capability to guide multiple payloads to targeted landing sites with high precision, the Kilopower units and the combined ISRU-MAV system could be deployed separately while in the atmosphere of Mars. In this way, they would be guided to separate landing sites by the EDL systems and would not require ground transportation to achieve that separation.

Regardless of the method used to separate the systems, the ISRU system will need to be powered to begin its operation. This means that the Kilopower units must be connected via cable to the ISRU power distribution network. A small rover can be deployed to traverse the 1 km distance separating the systems with a cable, as depicted in Figure 147.

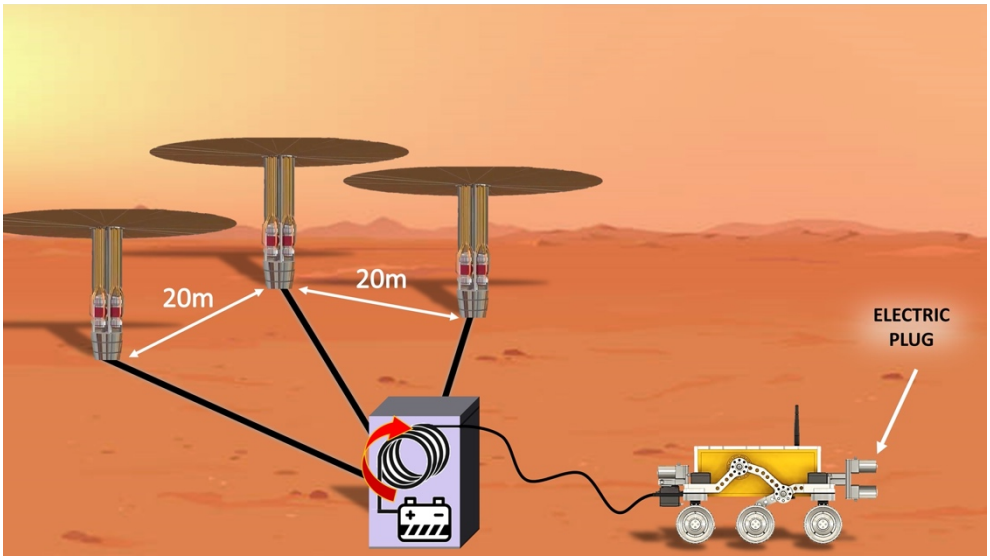

Figure 147: Depiction of a small rover carrying a power cable from the Kilopower units to the ISRU system [196].

A second option is to begin with the Kilopower unit and ISRU system connected and have the power cable unspool as the Kilopower units are transported 1 km away from the ISRU system.

The Kilopower units require deployment of their own, as the large radiators will need to be extended as shown in the figure. This will require either a cache of batteries to power the initial deployment of the Kilopower radiators, or else a separate solar-based power system. Once the Kilopower unit is functional and the cable is connected to the ISRU system, the ISRU system will initiate system checkouts, warm up its SOE oven, deploy its own radiators on the liquefaction unit, and eventually move into oxygen production. The system is expected to run continuously, only shutting down due to unforeseen errors that cause a fault in the system.

Phase 3: Crew Launches and Travels to Mars

The crew will launch to Mars at the next launch opportunity, approximately 26 months after the ISRU system was launched to Mars. The ISRU system will have produced all the required oxygen prior to the crew launch. There is an alternate option where the oxygen continues to be produced during the crew's flight, which is explored in Section 3.4.3. The crew will spend six to nine months in deep space before arriving at Mars at the same landing site as the MAV.

Phase 4: Crew Lands and Conducts Mission Operations
Upon crew arrival to the surface, the ISRU system will have fulfilled its oxygen production requirement and will be turned off by the crew. The power cables will be rerouted to the crew habitat, mobility systems, life support systems, and any other powered systems that they need to carry out their mission. The cooling system on the MAV tank will remain powered, as the liquid oxygen inside must be kept in a zero boiloff state.

Phase 5: Crew Departs Mars
The final phase involves the end of the surface mission and the departure back to Earth. The power cables will be fully disconnected from the MAV by the crew prior to liftoff. Additionally, the ISRU system will be manually disconnected, which primarily involves disconnecting the piping from the liquefaction unit to the MAV propellant tank. The ISRU system, crew habitat, and Kilopower units will be left behind on Mars, capable of supporting another mission if needed.

Several ancillary systems need to be developed or addressed prior to the first human mission to Mars. These include substantially increasing Mars EDL capabilities to accommodate payloads of several metric tons, development of a transport or EDL system to separate the ISRU plant from the Kilopower units, and a transport system to connect the power cable between the Kilopower units and the ISRU plant. These all represent significant challenges that will require extensive research and development before becoming operational.

7.4.3 Recirculating SOE Exhaust

Another consideration for a full-scale system is the utilization fraction of the CO_2. Operating at a higher utilization fraction improves system performance in multiple ways. By converting a larger fraction of the incoming CO_2 to O_2, less mass flow is required to produce the same quantity of oxygen. This reduces the throughput of the filter, requiring less filter area, and reduces the throughput of the CAC system, reducing its size and power consumption. Additionally, less gas must be heated in the SOE, reducing the power requirement of that subsystem. The cost to operating at a higher utilization fraction is an increased chance of coking the SOE cells, as a higher utilization fraction pushes the SOE operating conditions towards the Boudouard boundary as shown in Figure 30.

Several architectures exist to improve the utilization fraction of CO_2. Two of these architectures include staging SOE units in series or recycling the unused cathode exhaust back into the SOE stack. Both of these options attempt to pass the cathode exhaust, a mixture of CO_2, CO, and inert gases, back into an SOE to convert additional CO_2 to O_2. The same effect can be achieved by simply operating a single SOE unit at a higher utilization fraction, which is achievable at low cathode pressures.

An alternative design that improves the utilization fraction of CO_2 involves separating the CO and CO_2 in the cathode exhaust. Many separation technologies exist, including cryogenic sorbent separations. By separating the two gases, the CO_2 can be recycled back into the SOE or passed to a second SOE unit downstream to produce additional oxygen. This may result in a net power savings, as the recycled CO_2 would not require filtration or compression like CO_2 from the Martian atmosphere. The separation process may be power intensive, however. Therefore, a

systems analysis should be conducted to determine if the power and mass benefits of separating and recycling filtered and compressed CO_2 from CO in the cathode exhaust stream outweigh the costs of that separation process.

7.5 Future Work

The work put forth by this dissertation outlines a detailed model, optimization scheme, design, and analysis of an ISRU system that could be sent to Mars to produce oxygen to support a human mission. During the course of this process, several key topics that should be developed in the future were identified and will be discussed here.

Solid Oxide Electrolysis

The SOE represents the core technology behind oxygen production in BAM. As such, continued development of more resilient and higher performing SOE cells is encouraged. OxEon Energy is currently developing a new cathode that is fully oxidized, which would eliminate concerns about nickel oxidation during operations. Similarly, a cathode that uses novel materials or manufacturing processes to be more resistant to coking would reduce mission risk. OxEon Energy is also testing thinner electrolyte cells, which would reduce the iASR and thus improve performance. A primary concern with thinner cells is the risk of mechanical failure, which creates a tradeoff between failure risk and improved performance.

A different approach to SOE from that used on MOXIE and proposed for BAM is the integration of water, either through co-electrolysis or pure steam electrolysis. In the former, steam and carbon dioxide are fed into the SOE, and a mixture of oxygen, carbon monoxide, and hydrogen are produced:

$$H_2O(steam) + CO_2 \rightarrow O_2 + CO + H_2 \tag{113}$$

The addition of steam into the electrolysis process enables the SOE to run at a higher utilization fraction than CO_2-only electrolysis. This is because co-electrolysis raises the Boudouard threshold, enabling higher utilization fractions before coking occurs [113]. In addition, the product stream of H_2 and CO, together referred to as "synthesis gas", can be used to manufacture a wide range of hydrocarbon fuels.

The Sabatier process can also be employed on Mars, which converts carbon dioxide and hydrogen into methane and water. This is especially relevant to Mars missions because it uses carbon dioxide, a resource abundant on Mars, to produce methane, which can be combined with oxygen to satisfy all propellant requirements of a MAV. Since the Sabatier process requires a feedstock of hydrogen, it can only be used if hydrogen is brought from Earth or if water is electrolyzed on Mars to form hydrogen. The Sabatier process uses the following reaction:

$$CO_2 + 4H_2 \rightarrow CH_4 + 2H_2O \tag{114}$$

Transitioning from CO_2-only electrolysis to co-electrolysis with steam will be a key turning point in human missions to Mars that should take place once the capability to extract water from Mars is established. The addition of water to electrolysis improves performance and produces a fuel by-product, both of which would be beneficial to the crew. A summary of these different types of ISRU technologies and how they can be used alongside one another is given by Sanders

et al. [197]. Primarily, the combination of SOE, Sabatier, and water electrolysis may be the most promising way to fuel a MAV. The pioneering missions to Mars, however, should use CO_2-only electrolysis, as it is a simpler and more reliable system for oxygen production than one that relies on water harvesting technologies.

One additional aspect of SOE that should be further tested is the ability to operate the cathode at pressures lower than 150 mbar, the threshold tested for this dissertation. As described in Section 5.3, a leak was encountered during SOE testing that prevented pressures below 150 mbar from being tested. While it was valuable to characterize SOE performance from atmospheric pressure down to 150 mbar, it would be advantageous to know the true lower limit where molar diffusion causes a sharp increase in iASR.

CAC System

As described in Section 5.1, mechanical compressors do not currently exist that are built for the compression ratio and flow rates required of the BAM system. The modeling work done for this dissertation was based on industry simulations and extrapolated data. However, prior to sending a full-scale system to Mars, a scroll compressor and a centrifugal compressor should be developed and tested at scale in Mars-like conditions to better understand their performance.

Use of CO

A more detailed investigation into the potential use of compressed CO from the exhaust stream of the SOE cathode should be made. CO has the potential to be used as a propellant directly, to be manufactured into a hydrocarbon, and to generate electricity in a fuel cell. For the compressed CO to be useful, it would likely have to be separated from the residual CO_2, N_2, and Ar in the cathode exhaust stream. The complexity of this separation unit is the reason it was excluded from the baseline BAM design; however, in future iterations, or possibly once human presence on Mars has become more established, it may make sense to use the CO. A significant amount of energy is put into the CO by the time it leaves the SOE exhaust, as it has been filtered, compressed, and raised to a high temperature. For these reasons, it may improve the overall efficiency of the system if energy, in some form, were to be extracted from the CO.

Model Improvements

While every effort has been made to create a model of BAM that is fully functional and validated with data, the model created for this dissertation is a steady-state model that assumes an average atmospheric inlet condition for the entirety of the mission. This provides a good estimate of average performance over the course of a Martian year and drives the optimization successfully in that regard. However, the model could be expanded to include a varying atmospheric state and model the BAM system's response to those variations. This is not expected to generate a significantly different optimal BAM design but would provide a more detailed understanding of power fluctuations, gas flow variations, and thermal cycles throughout BAM. This additional information would be of particular importance when designing the controls system for BAM, which must account for variations like these in the system.

Appendix A: Variables

This appendix contains a glossary of the variable names used in the BAM model. It can be used to look up variable descriptions and values.

A.1 Input Values

Table 80 lists all variables that are assigned a constant value as inputs to the model. Design variables are excluded, as the values of design variables change with the optimizer. The variable name is given as it is coded into the model along with a description, its value, its units, and a justification for the selected value. Variables are grouped into several logical sections, each of which has a header within the table.

Table 80: All constant values used by the model. Any input or assumed value can be found here.

Variable	Descriptor	Value	Units	Justification
MARS CONSTANTS				
xCO_a	Mole fraction of ambient CO in Mars atmosphere	0.0007	-	Average Martian atmospheric composition
xN2_a	Mole fraction of ambient N_2 in Mars atmosphere	0.0197	-	Average Martian atmospheric composition
xAr_a	Mole fraction of ambient Ar in Mars atmosphere	0.0231	-	Average Martian atmospheric composition
xCO2_a	Mole fraction of ambient CO_2 in Mars atmosphere	0.9565	-	Average Martian atmospheric composition
PO2_a	Ambient partial pressure of oxygen on Mars	1.5e-4	bar	Average Mars atmospheric composition
T_MA	Average Mars temperature	251.4	K	Average Mars surface temperature at Jezero Crater, using the Mars Climate Database (MCD)
T_ML	Low Mars temperature	179.2	K	Lowest Mars temperature across 7 M2020 candidate landing sites (MCD)
T_MH	High Mars temperature	291.7	K	Highest Mars temperature across 7 M2020 candidate landing sites (MCD)

P_MA	Average Mars surface pressure	850	Pa	Expected average atmospheric pressure at a human landing site on Mars
MissionLength	Length of time available for ISRU plant to make oxygen	10,080	hrs	Assumes 14 months available to produce O_2 before crew arrives
POWER				
P_kilopower	Electric power output of one 10 kWe Kilopower unit	10,000	W	NASA Kilopower specs
M_kpcable	Mass of Kilopower cable	60	kg	Assumes 1 km cable, 60 kg/km density. Source: Rucker 2017.
h_kilo	Height of 10 kWe Kilopower unit	3.3	m	NASA Kilopower spec sheet
r_kilo	Radius of 10 kWe Kilopower unit	0.75	m	NASA Kilopower spec sheet
m_kilopower	Mass of 10 kWe Kilopower unit	1,545	kg	NASA Kilopower specs
ELECTRONICS				
El_P	Fraction of total BAM power allocated to onboard computing	0.085	-	Confirmed with MOXIE PEL, Linne at NASA, and SMAD (Wertz, 1999)
El_M	Fraction of total BAM mass allocated to onboard computing	0.05	-	SMAD (Wertz, 1999)
rho_El	Density of electronics	300	kg/m^3	Based on satellite electronics
CO_2 ACQUISITION AND COMPRESSION (CAC)				
deltaP_f	Pressure drop across the inlet filter	30	Pa	Based on D. Rapp's "Extensibility of MOXIE"
cryo_Volume	Volume of cryopump that produces 1.1 kg/hr CO_2	1.1	m^3	Meier et al. (2018)

cryo_blower	Energy required to move 1 kg of Mars air through a cryopump	16,800	J/kg	Calculated from standard blower charts, assumes Mars density of 0.02 kg/ m^3. Engineering Toolbox.
cryo_blower_eff	Efficiency of blower fan	0.60	-	Engineering Toolbox
cycle_time_cryo	Cycle time of cryocooler	217	mins	Berg and Shah (2018)
cool_time_cryo	Cooling time during one cycle	100	mins	Berg and Shah (2018)
warm_time_cryo	Warming time during one cycle	100	mins	Berg and Shah (2018)
blower_spec_mass	Specific mass of blower	0.4	kg blower / kg/hr CO_2	COTS blowers
blower_spec_vol	Specific volume of blower	0.003	m^3 blower / kg/hr CO_2	COTS blowers
cryo_efficiency	Thermodynamic cryocooler efficiency	0.1	-	W. Johnson (NASA)
heater_efficiency	Cartridge heater efficiency	1	-	100% thermal to electrical conversion is common
heatloss_efficiency	Heat loss efficiency	0.85	-	Assumes 15% parasitic heat loss
cryo_HE_factor	Power consumption reduction factor	0.5	-	Heat exchanger between cryopump pairs recuperates 75% of heat
H_latent_CO2	Latent heat of CO_2 sublimation	591,000	J/kg	Engineering Toolbox
rho_frost	Frost density of CO_2	800	kg/m^3	Ash et al. (1978)
k_CO2	Frost thermal conductivity of CO_2	0.15	W/m-K	Ash et al. (1978)
T_freeze_CO2	Freezing point of CO_2	148	K	Taken at Mars pressure
sol_valve_m	Mass of single solenoid valve	1.4	kg	Marotta space-qualified solenoid valve. Part#MV172
sol_valve_p	Power for single solenoid valve	1	W	COTS
check_valve_m	Mass of single check valve	0.3	kg	Marotta space-qualified check valve
cycle_time	Sorption cycle time	0.033	hr	NASA design
loading	Sorbent bed loading capacity	0.15	g/g	Clark [148]

sorp_eff	Sorbent efficiency term for inert barrier	0.8	-	NASA
sorp_mass_factor	Sorption pump mass multiplier	15	-	Brooks et al. (2015)
T_hot	Sorbent bed desorption temperature	373	K	Hasseeb & Iannetti (2017)
T_cold	Sorbent bed adsorption temperature	233	K	Hasseeb & Iannetti (2017)
Cp_zeolite	Specific heat of Zeolite 13x	1100	J/kg-K	Lu et al. (2020)
Cp_ti	Specific heat of titanium	544	J/kg-K	Engineering Toolbox
CpCv_C_{o2}	Specific heat ratio of CO_2 (Cp/Cv)	1.28	-	Engineering Toolbox
SOLID OXIDE ELECTROLYSIS				
iASR	Intrinsic ASR	2.26	Ω-cm^2	OxEon Energy
rec_frac	SOE recycle fraction	0.05	-	MOXIE
MW_O2	Molecular weight of O_2	0.032	kg/mol	Engineering Toolbox
MW_CO2	Molecular weight of CO_2	0.044	kg/mol	Engineering Toolbox
MW_CO	Molecular weight of CO	0.028	kg/mol	Engineering Toolbox
MW_Ar	Molecular weight of Ar	0.04	kg/mol	Engineering Toolbox
MW_N2	Molecular weight of N_2	0.028	kg/mol	Engineering Toolbox
VNernstA	Term for Nernst potential	-4.4924e-4	V/K	Meyen (2017)
VNernstB	Term for Nernst potential	1.4629	V	Meyen (2017)
VN_CO_A	Term to calculate Gibb's Energy	110.177	V	OxEon Energy
VN_CO_B	Term to calculate Gibb's Energy	0.0902247	V/K	OxEon Energy
VN_CO_C	Term to calculate Gibb's Energy	1.42044e-6	V/K^2	OxEon Energy
VN_CO_D	Term to calculate Gibb's Energy	-1.55108e-9	V/K^3	OxEon Energy
heater_eff	Efficiency of gas preheater	0.9	-	COTS

rhoZ	Density of ScSz electrolyte with coatings	5440	kg/m^3	MOXIE
rhoIC	Density of CFY interconnect material	7200	kg/m^3	JPL (2017)
rhoEP	Density of MOXIE endplate	7200	kg/m^3	JPL (2017)
rho_efrax	Density of Excelfrax 1800	230	kg/m^3	OxEon Energy
rho_ti	Density of titanium	4500	kg/m^3	Engineering Toolbox
t8	Thickness of SOE hotbox inner shell	0.00635	m	¼" titanium
t10	Thickness of SOE hotbox outer shell	0.00635	m	¼" titanium
tZ	Thickness of ScSz cell with coatings	0.00032	m	OxEon Energy
tIC	Thickness of CFY interconnect	0.0025	m	OxEon Energy
tEP	Thickness of endplate	0.003	m	OxEon Energy
f_SOE	Factor to include nickel felt and glass seals	1.3	-	OxEon Energy
fIC	Factor to account for flow channels in interconnects	0.77	-	OxEon Energy
fEP	Factor to account for flow channels in endplates	0.927	-	OxEon Energy
w_quad	Width of SOE quad stack	0.35	m	OxEon Energy
w_single	Width of SOE single stack	0.21	m	OxEon Energy
l_quad	Length of SOE quad stack	0.37	m	OxEon Energy
l_single	Length of SOE single stack	0.23	m	OxEon Energy
k_efrax	Excelfrax 1800 thermal conductivity	0.03	W/m-K	OxEon Energy
k_efrax_Mars	Excelfrax 1800 thermal conductivity at Mars pressure	0.008	W/m-K	OxEon Energy
ff_SOE	Friction factor of SOE flow channels	0.5	-	Darcy's Law charts
h_SOE	Height of SOE flow channels	0.0004	m	OxEon Energy

d_SOE	Equivalent diameter for SOE flow channels	0.0008	m	OxEon Energy
VactA	Activation voltage term	-4.255e-5	V/K	Meyen (2017)
VactB	Activation voltage term	0.06739	V	Meyen (2017)
Ea	Activation energy	82,557	kJ/mol	Meyen (2017)
A	Pre-exponential factor	10,300	-	Meyen (2017)
PIPING				
Lpipe	Length of pipe between each BAM subsystem	6	m	BAM design decision
Di	Inner pipe diameter	0.05	m	Standard chemical piping
t_pipe	Pipe thickness	0.003	m	Double standard pipe thickness for safety
k_ins	Fiberglass thermal conductivity	0.04	W/m-K	Engineering Toolbox
k_copper	Copper thermal conductivity	385	W/m-K	Engineering Toolbox
k_alum	Aluminum thermal conductivity	205	W/m-K	Engineering Toolbox
k_inc	Inconel thermal conductivity	20.5	W/m-K	Engineering Toolbox
h_c	Mars atmosphere convective coefficient	1	W/m^2-K	Phoenix Lander
density_copper	Density of copper	8960	kg/m^3	Engineering Toolbox
density_ins	Density of insulation	30	kg/m^3	Engineering Toolbox
density_inc	Density of Inconel 625	8400	kg/m^3	MOXIE
HEAT EXCHANGER				
U_HE	Heat transfer coefficient for PHE	3	W/m^2-K	Engineering Toolbox
t_PHE	Thickness of PHE plate	0.003	m	2-7x standard thickness to increase channel size
l_PHE	Length of PHE plate	1.1	m	BAM design decision
w_PHE	Width of PHE plate	0.55	m	BAM design decision
h_end	Height of endplates	0.02	m	BAM design decision

A_eff_PHE	Area efficiency of PHE plate	0.7	-	30% of area is occupied with framing
ff_HE	Moody friction factor for PHEs	0.04	-	Moody diagram for turbulent flow
LIQUEFACTION				
r_MAV	Radius of MAV oxygen tank	1.3	m	BAM design decision
h_MAV	Height of MAV oxygen tank	7.7	m	BAM design decision
rho_piping_MAV	Density of MAV aluminum piping	2700	kg/m^3	BAM design decision
H_latent_O2	Latent heat of oxygen vaporization	214,000	J/kg	Engineering Toolbox
T10	Oxygen condensation temperature	90	K	Engineering Toolbox
P10	Liquid oxygen pressure	100,000	Pa	BAM design decision
Cp10	Specific isobar heat capacity of oxygen at T10 and P10	1062	J/kg-K	Peace Software Calculator
rho_LO2	Density of liquid oxygen	196.21	kg/m^3	Engineering Toolbox
od_liq_piping	Outer diameter of MAV pipe	0.025	m	W. Johnson (NASA)
t_liq_piping	Thickness of MAV pipe	0.002	m	W. Johnson (NASA)
T_root	Radiator working fluid inlet temperature	315	K	BAM design decision
skytemp	Mars sky temperature	170	K	Worst-case value, NASA
emissivity_r	Emissivity of white paint on radiator surface	0.92	-	Engineering Toolbox
absorptivity_r	Absorptivity of white paint on radiator surface	0.09	-	Engineering Toolbox
sb	Stefan-Boltzmann Constant	5.67e-8	$W/m^2\text{-}K^4$	Engineering Toolbox
Cp_NH3	Specific heat capacity of LNH_3	4744	J/kg-K	Engineering Toolbox
rho_NH3_liq	Density of LNH_3	696	kg/m^3	Engineering Toolbox
vel_NH3	Velocity of LNH_3	2	m/s	Safe flow rate to avoid pipe damage

kvisc_NH3	Kinematic viscosity of LNH_3	0.3e-6	m^2/s	Engineering Toolbox
Q_solar	Heat flux arriving on Mars	400	W/m^2	Calculated
d_hp_r	Diameter of radiator heat pipe	0.05	m	BAM design decision
n_heat_pipes	Number of heat pipes in radiator	5	-	BAM design decision
rho_piping	Density of copper heat pipes	8960	kg/m^3	Engineering Toolbox
CONSTANTS				
R_CO2	Carbon dioxide gas constant	188.92	J/kg-K	Engineering Toolbox
R_O2	Oxygen gas constant	259.84	J/kg-K	Engineering Toolbox
R_excess	Gas constant of a 50/50 CO/CO_2 mixed stream	242.88	J/kg-K	Engineering Toolbox
R	Universal gas constant	8.3145	J/mol-K	Engineering Toolbox
c	Faraday's constant	96,485.332	C/mol	Engineering Toolbox
SYSTEM PARAMETERS				
Num_Crew	Number of crew sent to Mars	6	people	BAM design decision
Op_months	Number of months the ISRU plant will produce oxygen	14	months	BAM design decision
O2_prod_req	Kg of oxygen required to fuel a 4-crew MAV	22,717	kg	Polsgrove et al. (2015)
CrewLaw	Ratio of propellant required in MAV for a crew of 6 to a crew of 4	1.356	-	NASA DRA 5.0 (2009)

A.2 Glossary of Variable Names

All variables that are not input variables, but are rather used in calculations or as outputs, are recorded in Table 81 as a reference guide. These are grouped by their location in the Simulink model.

Table 81: Glossary of variables used in the Simulink model

Variable	Units	Description
KILOPOWER		
$P_{non_{el}}$	W	Total power used by BAM except the power used by the electronics system
P_{Total}	W	Total power used by BAM, including the electronics system
M_{PS}	kg	Mass of the Kilopower system
V_{PS}	m^3	Volume of the Kilopower system
ELECTRONICS		
P_{El}	W	Power of BAM electronics
M_{El}	kg	Mass of BAM electronics
V_{El}	m^3	Volume of BAM electronics
CAC - CRYOPUMP		
$cryo_{blower_{power}}$	W	Power of the blower fan used in the cryopump
$cryo_{blower_{mass}}$	kg	Mass of the blower fan used in the cryopump
$cryo_{blower_{vol}}$	m^3	Volume of the blower fan used in the cryopump
M_{Blower}	kg	Total mass of the blower fans, including spares
V_{Blower}	m^3	Total volume of the blower fans, including spares
$P_{cryo_{CO2_{cooling}}}$	W	Cooling power needed to cool the CO_2 in the cryopump to the CO_2 freezing point
$P_{cryo_{CO2_{deposition}}}$	W	Cooling power needed to phase change the CO_2 in the cryopump between gas and solid
$P_{CAC_{cryo_{cooling}}}$	W	Total cooling needed to cool the CO_2 and freeze it in the cryopump
$P_{CAC_{cryo_{warming}}}$	W	Total power needed to sublimate and warm the CO_2 in the cryopump
M_{CH}	kg	Mass of the coldhead in the cryopump
$M_{CC_{shell}}$	kg	Mass of the cryocooler shell in the cryopump
$M_{heaters}$	kg	Mass of the cartridge heaters in the cryopump
$M_{CAC_{cryo}}$	kg	Combined mass of the coldhead, cryocooler shell, and cartridge heaters in the cryopump
$V_{CAC_{cryo}}$	m^3	Volume of the coldhead, cryocooler shell, and cartridge heaters in the cryopump

$cryo_{v_{power}}$	W	Power of the valves and piping in the cryopump
$cryo_{v_{mass}}$	kg	Mass of the valves and piping in the cryopump
$P_{CAC_{cryo}}$	W	Total power of the cryopump
$M_{CAC_{cryo}}$	kg	Total mass of the cryopump
$V_{CAC_{cryo}}$	m^3	Total volume of the cryopump
CAC – MECHANICAL COMPRESSOR		
$M_{CAC_{scroll_{single}}}$	kg	Mass of a single scroll compressor
$V_{CAC_{scroll_{single}}}$	m^3	Volume of a single scroll compressor
$P_{CAC_{scroll}}$	W	Total power of the scroll compressors
$M_{CAC_{scroll}}$	kg	Total mass of the scroll compressors
$V_{CAC_{scroll}}$	m^3	Total volume of the scroll compressors
$P_{CAC_{centr}}$	W	Centrifugal compressor power
$M_{CAC_{centr}}$	kg	Centrifugal compressor mass
$V_{CAC_{centr}}$	m^3	Centrifugal compressor volume
$P_{CAC_{mech}}$	W	Power of the selected mechanical compressor (either scroll or centrifugal)
$M_{CAC_{mech}}$	kg	Mass of the selected mechanical compressor (either scroll or centrifugal)
$V_{CAC_{mech}}$	m^3	Volume of the selected mechanical compressor (either scroll or centrifugal)
CAC – SORPTION PUMP		
$sorp_{blower_{power}}$	W	Power of the blower fan used in the sorption pump
$sorp_{blower_{mass}}$	kg	Mass of the blower fan used in the sorption pump
$sorp_{blower_{vol}}$	m^3	Volume of the blower fan used in the sorption pump
M_{Blower}	kg	Total mass of the blower fans, including spares
V_{Blower}	m^3	Total volume of the blower fans, including spares
$sorb_{mass}$	kg	Mass of sorbent material in the sorption pump
$pump_{mass}$	kg	Mass of the sorbent material and all framework and supporting materials in the sorption pump
$Q_{sorp_{cooling}}$	W	Heat that must be removed during the cooling process in the sorption pump
P_{cool}	W	Power to remove the heat from the cooling process
P_{heat}	W	Heat to desorb the CO_2 from the sorbent bed
P_{sorp}	W	Total power for the sorption pump across one adsorption-desorption cycle
$M_{CAC_{sorption}}$	kg	Total mass of the sorption pump
$P_{CAC_{sorption}}$	W	Total power of the sorption pump
$V_{CAC_{sorption}}$	m^3	Total volume of the sorption pump

P_{CAC}	W	Total power of the CAC system (cryo, mechanical, or sorption)
M_{CAC}	kg	Total mass of the CAC system (cryo, mechanical, or sorption)
V_{CAC}	m^3	Total volume of the CAC system (cryo, mechanical, or sorption)
P_{1f}	Pa	Pressure of gas after filter pressure drop
SOE		
$iASR_{temp}$	$\Omega-cm^2$	Temperature-corrected intrinsic area specific resistance of the SOE cell
Res_{cell}	Ω	Resistance per SOE cell
V_{act}	V	Activation voltage for each SOE cell
V_{Nernst}	V	Nernst potential for CO_2 reduction into CO and O
V_{Nernst_C}	V	Nernst potential for CO reduction into C and O
I	A	Total electrical current in the SOE system
$P_{Electrolysis}$	W	SOE power for electrolyzing CO_2
V_{tn}	V	Thermoneutral voltage
$P_{Heat_{Gas}}$	W	Power to preheat the gas coming into the SOE system
$P_{Heat_{Loss}}$	W	Heat lost through the SOE oven
$P_{Compression}$	W	Power of electrochemical compression
$N_{quadSOE}$		Number of quad stack SOE modules (four SOE stacks packaged together)
$N_{singleSOE}$		Number of single stack SOE modules
N_{EP}		Number of endplates in the SOE subsystem
A_{cell}	cm^2	Electrochemically active area of each SOE cell
A_{cellT}	cm^2	Total area (active + framing) of each SOE cell
f_{SOE}		Multiplication factor to account for nickel felt and glass seal mass and volume in the SOE cell calculations
f_{IC}		Multiplication factor to account for flow channel gaps in interconnects of SOE subsystem
f_{EP}		Multiplication factor to account for flow channel gaps in endplates of SOE subsystem
$f_{modules}$		Margin factor to account for spacing between SOE stack modules
λ		Pipe friction coefficient
$N_{stacks_{actual}}$		Number of total stacks in the SOE subsystem, including spares
$M4$	kg	Mass of one SOE stack. Includes ScSz, InterConnects, EndPlates every 10 cells, Nickel Felt, and Glass Seals
$M5$	kg	Mass of inlet and outlet tubes for SOE
$M6$	kg	Mass of compression rig surrounding each stack
$M7$	kg	Mass of insulation between stacks and inner shell of hotbox
$M8$	kg	Mass of inner hotbox shell, assumed to be made of titanium
$M9$	kg	Mass of insulation between inner and outer shell of hotbox
$M10$	kg	Mass of outer hotbox shell, assumed to be made of titanium
t_8	m	Thickness of SOE hotbox inner shell

t_{10}	m	Thickness of SOE hotbox outer shell
$w_{num_{quad}}$		Number of quad stack modules in the width (x) direction
w_{quad}	m	Width of a quad-stack module in the SOE subsystem
$w_{num_{single}}$		Number of single stack modules in the width (x) direction
w_{single}	m	Width of a single-stack module in the SOE subsystem
$l_{num_{quad}}$		Number of quad stack modules in the length (y) direction
l_{quad}	m	Length of a quad-stack module in the SOE subsystem
$l_{num_{single}}$		Number of single stack modules in the length (y) direction
l_{single}	m	Length of a single-stack module in the SOE subsystem
N_{cells}		Number of active SOE cells in the system at any given time
M_{pipe}	kg	Mass of piping system, including pipes, insulation, and valves
CSA	m^2	Cross-Sectional Area
$\mathbf{M_{SOE}}$	kg	Mass of SOE subsystem
V_{SOE}	m^3	Volume of SOE subsystem
$MW_{mix_{in}}$	g/mol	Average molecular weight of the gas coming into the SOE system
U		Utilization fraction of CO_2
$x_{CO_{in}}$		Fraction of inlet SOE gas that is CO
$deltaP_{SOE_{channels}}$	Pa	Pressure drop across the SOE flow channels
$deltaP_{SOE_{outlet}}$	Pa	Pressure drop from the SOE exit into the outlet plenums
$deltaP_{SOE}$	Pa	Total pressure drop across the SOE subsystem
LIQUEFACTION		
Q_{pipe}	W	Total heat leak through piping and MAV tank in the liquefaction subsystem
M_{pipe}	kg	Total mass of pipes, valves, and insulation in the liquefaction subsystem
V_{pipe}	m^3	Total volume of pipes, valves, and insulation in the liquefaction subsystem
$P_{liquefy_{O2}}$	W	Heat removal needed to liquefy oxygen
P_{cc}	W	Power needed to liquefy oxygen, including cryocooler efficiency
V_{cc}	m^3	Volume of the cryocooler in the liquefaction system, consisting of a cryocooler chamber, coldhead, and mount.
M_{cc}	kg	Mass of the cryocooler in the liquefaction system, consisting of a cryocooler chamber, coldhead, and mount.
w_{fin_r}	m	Width of one radiator fin
l_{pipe_r}	m	Length of main radiator pipe
$Q_{radiator_{req}}$	W	Heat rejection requirement for the radiator
$M_{radiator}$	kg	Mass of t ehar diator
$A_{radiator}$	m^2	Surface area of the radiator
$V_{radiator}$	m^3	Volume of the radiator

P_{Liq}	W	Total power of the liquefaction unit
M_{Liq}	kg	Total mass of the liquefaction unit
V_{Liq}	m^3	Total volume of the liquefaction unit
FULL SYSTEM		
P_{Total}	W	Total BAM system power
M_{Total}	kg	Total BAM system mass
V_{Total}	m^3	Total BAM system volume
R_{Total}		Total BAM system reliability
$mdot_{O_2}$	kg/hr	Oxygen production rate
$mdot_{excess}$	kg/hr	Cathode exhaust flow rate

Appendix B: Equations

Appendix B contains a repository of equations used in the BAM model. Any equations not previously described earlier in this dissertation are recorded here.

B.1 Gas Characteristics Modeling

This section describes the calculations that take place at every major location in the diagram shown in Figure 148, to accurately model the gas characteristics throughout the system.

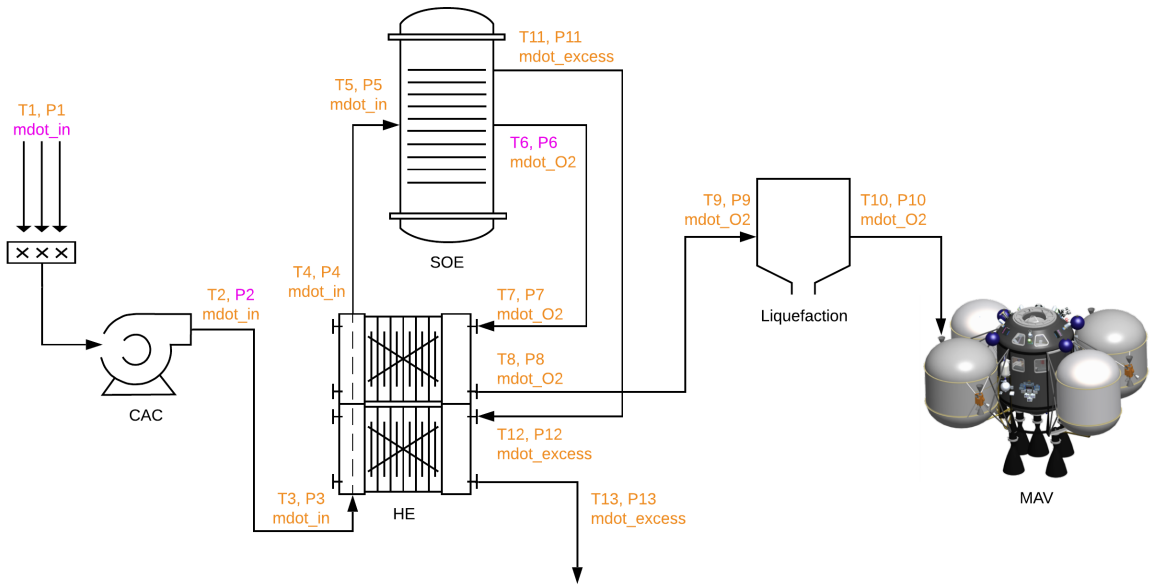

Figure 148: ISRU system overview with subsystem entrance and exit points labeled numerically.

Gas Pressure

The outlet pressure of the CAC system, P2, and the outlet pressure of the SOE anode stream, P6, are design variables that are defined by the optimizer. All other pressures throughout the system are calculated from these numbers using pressure drops and rises. The calculations for pressure drops and gains *within* each subsystem are shown in the next section. The pressure drops *between* subsystems are described here.

The pressure drop from a fluid traveling down a length of straight pipe is calculated in the model as:

$$\Delta P = \lambda \left(\frac{L}{D_i}\right) * \left(\frac{1}{2}\rho v^2\right) \tag{115}$$

where L is the length of the pipe, D_i is the inner diameter of the pipe, ρ is the fluid's mass density, v is the velocity of the fluid in the pipe, and λ is the friction coefficient of the pipe. The friction coefficient is calculated as a function of the Reynold's number of the fluid.

Gas Temperature
The outlet temperature of the SOE system, T6, is a design variable that is defined by the optimizer. The inlet temperature, T1, is a parameter set to be equal to the average temperature of Mars for the selected landing site. All other temperatures are calculated from these starting points, using heat transfer equations and component heat input modeling.

The temperature drops along piping lengths between subsystems are described here. The temperature drop from a fluid traveling down a length of straight pipe is calculated in the model via an iterative process using the following equations:

$$\mathrm{Q} = \frac{2\pi \mathrm{L}(\mathrm{T} - \mathrm{T_{Mars}})}{\frac{\ln\left(\frac{r_1}{r_i}\right)}{k_{pipe}} + \frac{\ln\left(\frac{r_2}{r_1}\right)}{k_{ins}} + \frac{1}{r_2 h_c}} \tag{116}$$

and

$$\Delta T = \frac{Q}{\dot{m} C_p} \tag{117}$$

where Q is the heat transferred from the fluid to the Mars environment, ΔT is the temperature drop from one end of the pipe to the other, T is the exit temperature of the pipe, T_{Mars} is the temperature of the Mars atmosphere, r_i is the inner radius of the pipe, r_1 is the outer radius of the pipe, r_2 is the outer radius of the pipe including insulation, k is the thermal conductivity, h_c is the convective coefficient for the Mars atmosphere, $\dot{m}$ is the mass flow rate of the fluid, and C_p is the specific heat capacity of the fluid.

Gas Density
The gas density is calculated at each major location in the system using the following equation:

$$\rho = \frac{P}{RT} \tag{118}$$

This is derived from the ideal gas law and uses the values of pressure (P) and temperature (T) at each location in the system to calculate the associated gas density. R is a mass-based universal gas constant. A different value is used for each type of gas present in the system, as it depends on the molecular weight of the gas.

Gas Velocity
The flow velocity is calculated using the mass flow rate, $\dot{m}$, and density at each location. Three mass flow rates are present in the system: (1) the CO_2 inlet flow rate, which is a design variable and is constant from the CAC inlet to the SOE inlet, (2) the SOE cathode exhaust, which is calculated based on the SOE system's inputs, and (3) the SOE anode exhaust, which is also calculated based on the SOE system's inputs and is constant from the SOE anode outlet to the final MAV storage inlet stream. The flow velocity is calculated as:

$$\mathrm{v} = \frac{\dot{m}}{\rho A} \tag{119}$$

where A is the cross-sectional area of the pipe.

Reynolds Number

The Reynolds number is an indicator of laminar versus turbulent flow and is calculated at each location throughout the system using the following equation:

$$Re = \frac{\mathrm{v} * D_i}{v} \tag{120}$$

where D_i is the inner diameter of the pipe and v is the kinematic viscosity of the fluid. The kinematic viscosity is calculated as a function of the pressure of the gas at that location in the system.

Specific Heat Capacity

The specific heat capacity of a gas stream is primarily dependent on the temperature and composition of that stream. Data have been tabulated for the measured specific heat capacity of the major constituents present in this system: CO_2 [198], O_2 [199], N_2 [200], and CO [201]. These were plotted and a polynomial fit was applied across the relevant temperature range (175 K – 1500 K) to create the temperature-dependent equations for each gas shown in Table 82.

Table 82: Specific heat capacity equations derived from measured data for CO_2, O_2, N_2, and CO.

Gas	Equation	Units
CO_2	$C_p = 2.5 * 10^{-7} * T^3 - 1.0 * 10^{-3} * T^2 + 1.5 * T + 470$	$\frac{J}{kg - K}$
O_2	$C_p = 3.3 * 10^{-10} * T^4 - 1.2 * 10^{-6} * T^3 + 1.4 * 10^{-3} * T^2 - 0.37 * T + 940$	$\frac{J}{kg - K}$
N_2	$C_p = -1.9 * 10^{-7} * T^3 + 5.0 * 10^{-4} * T^2 - 0.2 * T + 1100$	$\frac{J}{kg - K}$
CO	$C_p = 1.8 * 10^{-10} * T^4 - 8.0 * 10^{-7} * T^3 + 1.2 * 10^{-3} * T^2 - 0.45 * T + 1100$	$\frac{J}{kg - K}$

An example of the data used to formulate these polynomial fits is shown in Figure 149.

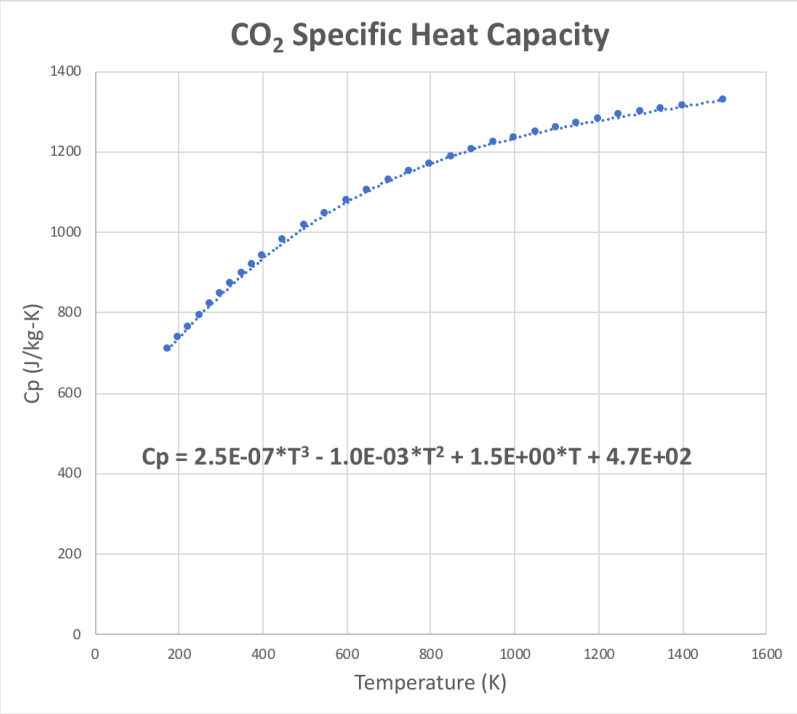

Figure 149: Specific heat capacity of carbon dioxide as a function of temperature, with a polynomial fit.

The specific heat capacity of argon was assumed to be half that of nitrogen [202], as temperature-dependent data were lacking for argon. To calculate the specific heat capacity of a mixed gas stream, such as the cathode exhaust of the SOE system, the specific heat capacity of each gas constituent was calculated individually at the given temperature. They were then combined into a total specific heat capacity by multiplying each by the mass fraction of the gas and summing:

$$C_{p,cathode} = x_{CO_2} C_{p,CO_2} + x_{CO} C_{p,CO} + x_{N_2} C_{p,N_2} + x_{Ar} C_{p,Ar} \quad (121)$$

where x is the mass fraction of the gas in the mixed stream.

Having the specific heat capacity of the various gas streams at all major points in the system is valuable for calculating heating and cooling requirements.

Recycle Stream Flowrate

A portion of the cathode exhaust gas is recycled back to the inlet of the SOE system to prevent oxidation of the nickel cathode. The composition of this stream is the same as that of the cathode exhaust. The flowrate of this stream is calculated as that of the cathode exhaust multiplied by the recycle fraction (F_{RC}) for each gas present. An example for the CO molar flowrate is given below:

$$\dot{n}_{CO_r} = \dot{n}_{CO} * F_{RC} \quad (122)$$

Utilization Fraction
The utilization fraction of CO_2 (i.e., the fraction of CO_2 that is converted into O_2) is calculated as:

$$U = \frac{x_{\mathrm{CO}} - x_{CO_{in}}}{x_{CO_2,in}} \tag{123}$$

where x_{CO} is the molar fraction of CO at the exit of the SOE cathode, $x_{CO_{in}}$ is the molar fraction of CO at the entry of the SOE cathode, and $x_{CO_2,in}$ is the molar fraction of CO_2 at the entry of the SOE cathode.

B.2 Pressure Drops and Gains Across Subsystems

Pressure drops in the BAM system are important to quantify, particularly when operating at relatively low SOE cathode pressures. The pressure drops across piping segments were described in the previous section, and the pressure drops across the subsystems themselves will be described here.

SOE Subsystem
Two distinct pressure drops occur as gas traverses the SOE subsystem. The first occurs as the gas passes through the channels within the SOE cells. The second occurs when the gas exits the flow channels and recombines in the exit tubes of the cathode and anode.

The first is modeled similarly to pressure drops across a length of pipe. A modified version of Equation (115) is employed:

$$\Delta P_{SOE} = \lambda \left(\frac{LP}{4A}\right) * \left(\frac{1}{2}\rho v^2\right) \tag{124}$$

where the D_i term is substituted with $\frac{P}{4A}$. P is the perimeter and A is the cross-sectional area of the flow channel. Under expected operating conditions for this ISRU plant, the pressure drop across the flow channels is negligible (less than 1 mbar).

The second pressure drop in the SOE subsystem, the drop that occurs when the gas exits the flow channels and enters the exit tubes, is modeled as a pipe contraction. Equation (124) is used but with an effective length term, L_{eff}, substituted for L:

$$L_{eff} = \frac{K * \left(d_{SOE} * N_{cps}\right)}{\lambda} \tag{125}$$

where d_{SOE} is the equivalent diameter of the flow channels in the SOE cells, N_{cps} is the number of SOE cells per stack, and K is the factor used to calculate equivalent pressure drop for a piping contraction, given by:

$$K = \frac{1}{2}\left(1 - \frac{D_i^2}{\left(d_{SOE} * N_{cps}\right)^2}\right) \tag{126}$$

where D_i is the inner diameter of the outlet pipes. The pressure drop into the outlet pipes dominates the pressure drop across the SOE flow channels in most BAM designs.

Heat Exchanger Subsystem

A Plate Heat Exchanger (PHE) is used in BAM, which consists of a stack of plates across which two fluids flow to exchange heat. There are two heat exchangers in the system: one to exchange heat between the anode exhaust and the incoming CO_2, and the other to exchange heat between the cathode exhaust and the incoming CO_2. The calculations are the same for both, so a generic representation of the equations used to calculate pressure drops across either heat exchanger is shown here.

The equation is similar to other pressure drop equations used in the model:

$$\Delta P_{HE} = f\left(\frac{L}{D}\right) * \left(\frac{1}{2}\rho v^2\right) \tag{127}$$

where f is the Moody friction factor, taken to be 0.04 for turbulent flow with minimal roughness in the Reynold's number range of 10^3 - 10^4 [203], L is the effective length of the heat exchanger, D is the flow path height between plates, ρ is the average gas density, and v is the gas velocity.

The effective length, L, is calculated as:

$$L = \frac{N_{plates}}{2} * l_{PHE} \tag{128}$$

where N_{plates} is the number of PHE plates stacked together and is calculated from the design variable for heat exchanger area, l_{PHE} is the length of one heat exchanger plate, and the product is divided by a factor of two because each fluid only travels along every-other PHE plate.

The gas velocity, v, from Equation (128) is calculated using Equation (119), where A is the cross-sectional area of each plate where fluid flows in the PHE, calculated as the average flow field height multiplied by the width of a plate.

The outlet pressures from the heat exchangers can then be calculated from the inlet pressures and the pressure drops as:

$$P_o = P_i - \Delta P_{i-o} \tag{129}$$

The pressure drops are heavily dependent on the flow-field height, D. If a lower pressure drop is desired, D can be increased at the expense of a higher PHE mass and volume.

B.3 CAC Calculations

The equations used to calculate mass, volume, and power of the CAC subsystem are shown in Figure 150.

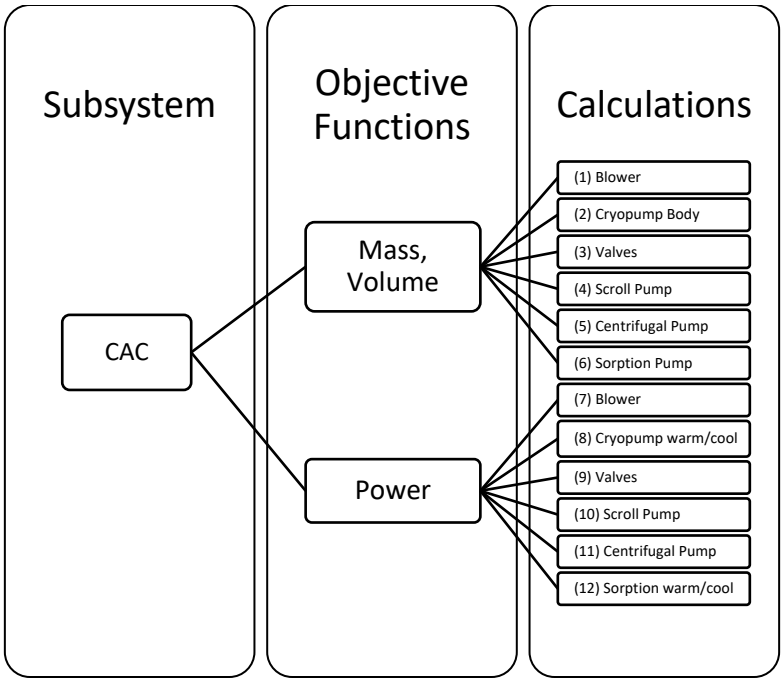

Figure 150: CAC subsystem calculations flowchart

The majority of the calculations in Figure 150 are shown in Section 4.3. Those that have not been previously described will be shown below.

Blower Power: The power of the blower fan used in the cryopump and sorption pump is calculated as:

$$P_{blower} = \frac{E_{blower}\dot{m}_{in}}{\eta_{blower}}\left(\frac{t_{on}}{t_{cycle}}\right) \tag{130}$$

where E_{blower} is the energy required to move 1 kg of Mars air through the system, taken from standard blower charts [204], η_{blower} is the efficiency of the blower, taken to be 60%, and $\frac{t_{cool}}{t_{cycle}}$ is the fraction of time that the blower is turned on during each cryogenic or sorption pumping cycle. The mass and volume of the blower are calculated based on commercial off the shelf blower systems and scaled according to flow rate capacity.

Cryopump Mass

The cryopump mass is calculated as the sum of the masses of the coldhead, cryochamber shell, and cartridge heaters:

$$M_{CP} = M_{CH} + M_{CCshell} + M_{heaters} \tag{131}$$

The mass of the coldhead is calculated from a reference coldhead mass, M_{ref}, which is constructed of copper and capable of producing 1.5 grams of CO_2 per minute [131]. A scaling law is applied based on the flow rate to calculate the mass of the coldhead in the BAM cryopump:

$$M_{CH} = M_{ref}\left(\frac{\dot{m}_{in}}{\dot{m}_{ref}}\right)^{x} \tag{132}$$

where x is a scaling exponential. The cryochamber shell and cartridge heater masses are calculated in the same way using reference masses and scaling by flow rate capacity.

Cryopump Volume

The volume of the cryopump is also calculated in the same way:

$$V_{CP} = V_{ref}\left(\frac{\dot{m}_{in}}{\dot{m}_{ref}}\right)^{x} \tag{133}$$

where the reference design used was for a cryopump capable of producing 1.1 kg/hr of CO_2 whose dimensions were taken from a NASA study [157].

Sorption Pump Volume

The volume of the sorption pump was calculated based on scaling laws from a prior sorption pump study for Mars applications [74]:

$$V_{SP} = 0.0022\,\dot{m}_{O_2} f \tag{134}$$

where f is a scalar multiplier to account for framing, piping, and heating and cooling infrastructure that surrounds the sorbent bed.

B.4 Heat Exchanger Calculations

The calculations for heat transfer and inlet/outlet temperatures of the heat exchanger are shown in Section 4.6. The calculations for the volume and mass of the heat exchanger are shown here.

First, the surface area of one plate in the plate heat exchanger is calculated by multiplying the length by the width of the plate:

$$\mathrm{A_{plate}} = l_{PHE} w_{PHE} \tag{135}$$

This product is used to calculate the number of plates needed to achieve the required heat exchanger surface area, A_{HE}, which is an input design variable.

$$\mathrm{N_{plates}} = \frac{A_{HE}}{A_{plate}} * \frac{1}{A_{eff,PHE}} \tag{136}$$

where $A_{eff,PHE}$ is the area efficiency of a PHE plate. This is assumed to be equal to 70%, since 30% of the plate's area cannot be used for exchanging heat as it is occupied by mounting equipment and gaskets.

The volume of the entire plate heat exchanger can then be calculated as follows:

$$\mathrm{V_{HE}} = 2.25 A_{plate}\left(N_{plates} t_{PHE} + h_{end}\right) \tag{137}$$

where t_{PHE} is the thickness of a single PHE plate, h_{end} is the combined height of the top and bottom end plates on the PHE stack, and the entire product is multiplied by a factor of 2.25 to account for the volume occupied by rails and bolts around the perimeter that hold the stack together.

The mass of the entire plate heat exchanger is calculated as follows:

$$\mathrm{M_{HE}} = 0.3\rho_{inc}A_{plate}\left(N_{plates}t_{PHE} + h_{end}\right) \tag{138}$$

where ρ_{inc} is the density of the primary plate material, Inconel, and the entire product is multiplied by a factor of 0.3 to account for 70% of the volume of the heat exchanger being carved out as flow channels.

B.5 SOE Calculations

The SOE equations used to calculate mass, volume, and power of the SOE subsystem are captured here. They follow the format of Figure 151.

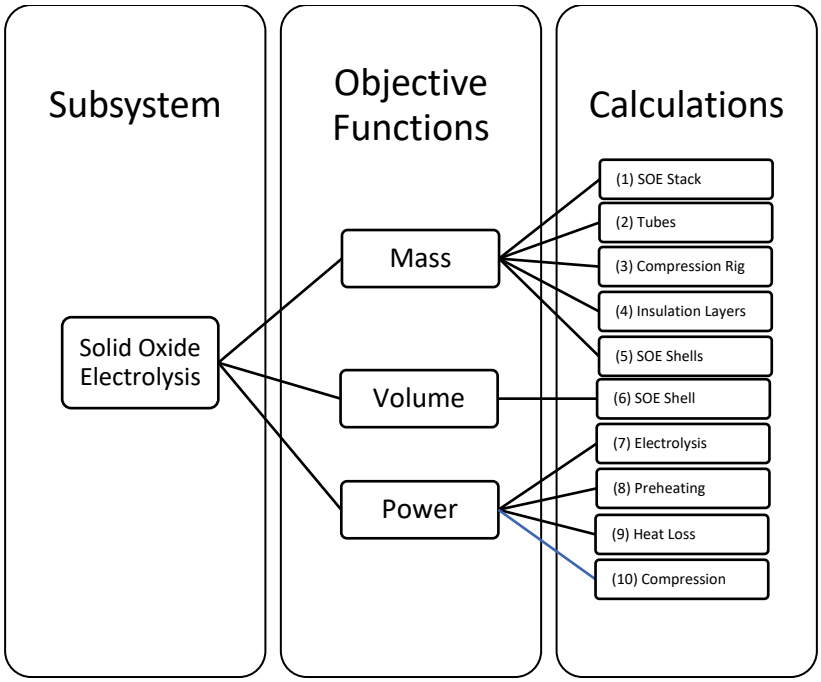

Figure 151: SOE subsystem calculations flowchart

For reference, the SOE hotbox is depicted below in Figure 152 with labels on all components that are modeled.

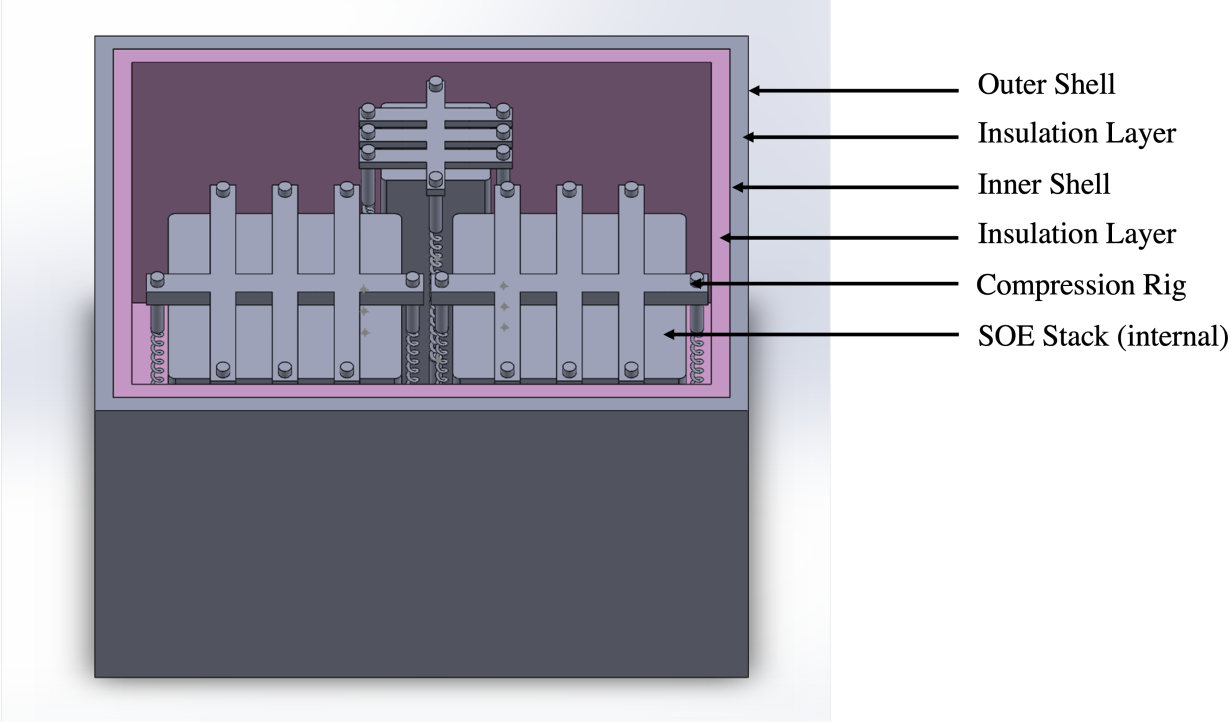

Figure 152: SOE hotbox with major components labeled

Mass

The mass of the SOE system is calculated as:

$$\mathrm{M_{SOE}} = N_{stacks_{actual}}(M4 + M5 + M6) + M7 + M8 + M9 + M10 \tag{139}$$

(1) SOE Stack: The mass of the SOE stack is calculated as:

$$M4 = N_{cps} * \frac{A_{cellT}}{100^2} * (f_{SOE}\rho_Z t_Z + f_{IC}\rho_{IC}t_{IC}) + N_{EP} * \frac{A_{cellT}}{100^2} * \rho_{EP}t_{EP} \tag{140}$$

where Z represents ScSz electrolyte cells, IC represents an interconnect, and EP represents an endplate every 100 cells.

The total cell area is derived from the active cell area using a logarithmic function based on MOXIE's dimensions ($A_{cell} = 22.74, A_{cellT} = 50$) and larger SOE cells developed at OxEon ($A_{cell} = 110.8, A_{cellT} = 169$), resulting in:

$$A_{cellT} = \frac{A_{cell}}{0.0357 + 0.133 * \ln(A_{cell})} \tag{141}$$

The number of endplates and midplates is calculated under the assumption, from conversations with OxEon, that a midplate is required every 100 SOE cells and one is needed on either end of each stack.

$$N_{EP} = ceil\left(\frac{N_{cps}}{100}\right) + 1 \tag{142}$$

(2) Tubes: M5 represents the mass of the inlet and outlet tubes for the SOE, which are assumed to have a negligible mass.

(3) Compression Rig: The mass of the compression rig is calculated as a fraction of the mass of each stack.

$$\mathrm{M6} = 0.2 * \mathrm{M4} \tag{143}$$

(4) Insulation Layers: The mass of the insulation between the SOE stacks and the inner shell (M7) and between the inner and outer shells (M9) are calculated as:

$$\mathrm{M7} = \mathrm{t}_{\mathrm{SOE}_{\mathrm{ins1}}} A_{inner_{shell}} \rho_{efrax} \tag{144}$$

and

$$\mathrm{M9} = \mathrm{t}_{\mathrm{SOE}_{\mathrm{ins2}}} A_{outer_{shell}} \rho_{efrax} \tag{145}$$

The selected insulation is Excelfrax 1800 Microporous board, similar to aerogel.

(5) SOE Shells: The mass of the inner shell (M8) and outer shell (M10) are calculated as:

$$\mathrm{M8} = \mathrm{t}_8 A_{inner_{shell}} \rho_{ti} \tag{146}$$

and

$$\mathrm{M10} = \mathrm{t}_{10} A_{outer_{shell}} \rho_{ti} \tag{147}$$

The shells are made of titanium for its low mass, high melting point, and low thermal conductivity.

Volume

(6) SOE Shell: The volume of the SOE subsystem is calculated using the dimensions of the outer shell of the SOE hotbox:

$$\mathrm{V}_{\mathrm{SOE}} = h_o w_{base_o} l_{base_o} \tag{148}$$

The height of the box is calculated as:

$$h_o = f_{modules}(0.004 N_{cps} + 0.05) + 2t_{SOE_{ins1}} + 2t_{SOE_{ins2}} \tag{149}$$

which represents the height of the modules (based on OxEon's model and number of cells per stack, with 0.05 m added for endplates) and the thickness of both insulation layers on the top and bottom of the stack.

The width of the box is calculated as:

$$w_{base_o} = f_{modules}(w_{num_{quad}} w_{quad} + w_{num_{single}} w_{single}) + 2t_{SOE_{ins1}} + 2t_{SOE_{ins2}} \quad (150)$$

The length of the box is calculated as:

$$l_{base_o} = f_{modules}(l_{num_{quad}} l_{quad} + l_{num_{single}} l_{single}) + 2t_{SOE_{ins1}} + 2t_{SOE_{ins2}} \quad (151)$$

The variables $l_{num_{quad}}, l_{quad}, l_{num_{single}}, l_{single}, w_{num_{quad}}, w_{quad}, w_{num_{single}}$, and w_{single} are calculated using an algorithm that determines the number of single-stack and quad-stack SOE stacks that are needed to accommodate the required number of cells while minimizing total volume. The algorithm is copied below.

```
% Calculate number of quad and single stack modules
N_quadSOE = floor(N_stacks/4);        % ( ) Round down to the nearest integer. Example: if we
have 7 stacks, N_quadSOE = floor(7/4) = 1, so we will have 1 quad stack.
N_singleSOE = N_stacks-N_quadSOE*4    % ( ) The remaining stacks will be single stack modules.

% Calculate configuration of quad and single stack modules
w_num_quad = ceil(sqrt(N_quadSOE));         % ( ) number of quad stack modules in the width
direction, assuming they are flush against one another. If there are 4 quads, we want a 2x2
arrangement. If there are 5 quads, we want a 3x2 arrangement. This formula helps us calculate the
appropriate width for this.

%If we have no quad-stack modules:
if w_num_quad == 0                % If there are no quad-stack modules...
    l_num_quad = 0;               % ( ) there are zero quad-stack modules in the length direction
    if N_singleSOE == 3           % If number of single stack moduels is 3 (i.e. total stacks =
                                    exactly 3)
        w_num_single = 2;         % ( ) we have a 2x2 configuration (with one empty slot)
        l_num_single = 2;
    elseif N_singleSOE == 2       % If number of single stack modules is 2 (i.e. total stacks =
                                    exactly 2)
        w_num_single = 2;         % ( ) Do a 2x1 arrangement of modules
        l_num_single = 1;
    elseif N_singleSOE == 1       % If number of single stack moduels is 1 (i.e. total stacks =
                                    exactly 1)
        w_num_single = 1;         % ( ) Do a 1x1 arrangement of modules
        l_num_single = 1;
    elseif N_singleSOE == 0       % If number of single stack moduels is 0 (i.e. total stacks =
                                    exactly 0)
        w_num_single = 0;
        l_num_single = 0;
    else
        error('Something is wrong with the Electrolysis -> Power Heat Loss inputs, causing an
                                    error in the number of single and quad-stack SOE modules.');
    end

%If we do have quad-stack modules:
else                                        % If there ARE quad-stack modules
    l_num_quad = ceil(N_quadSOE/w_num_quad);    % ( ) number of quad stack modules in the length
                                                  direction, assuming they are flush against one
                                                  another.
    l_num_single = 0;                           % ( ) we will never have to extend the lengthwise
                                                  direction for single stack modules if we have
                                                  at least one quad-stack module; increasing the
                                                  width is enough to accomodate up to 3 single
                                                  stack modules, which is the max we'd ever have
    if w_num_quad*l_num_quad > N_quadSOE        % if we have a blank slot in our arrangement
                                                  (i.e. 3x2 arrangement but we only have 5 quad
                                                  modules, so sixth slot is open)
        w_num_single = 0;                       % ( ) no extra space is needed for single stack
                                                  modules
    else
        if N_quadSOE >= 3
```

```
            if N_singleSOE == 0                 % If we have no single stacks...
                w_num_single = 0;               % ( ) then we obviously do not need to extend the
                                                   volume for the single stacks!
            else                                % but if we do have single stacks...
                w_num_single = 1;                  % ( ) we will extend the width of the space
                                                   by the total width of one single stack module.
                                                   Reasoning: if we have at least 3 quad modules,
                                                   we have at least a 2x2 configuration. That
                                                   means that by adding one slot in the width
                                                   direction, we can then stack 3 single modules
                                                   deep. There will be enough space.
            end
        else
            if N_singleSOE == 3                 % If we have 3 single stacks in addition to our
                                                   one or two quad-stacks...
                w_num_single = 2;               % ( ) If we have only 1 or 2 quad SOE stacks,
                                                   that means we have a 1x1 or 2x1 configuration
                                                   for the quads. For 1 or 2 single stacks, we
                                                   can get away with only extending the width of
                                                   the hotbox by one single stack width length.
                                                   But if we have 3 single stacks, we have to
                                                   extend it by 2 (essentially making a mini 2x2
                                                   single stack area)
            elseif N_singleSOE == 0             % If we have zero single stacks in addition to
                                                   our one or two quad-stacks (i.e. we have
                                                   exactly 4 or 8 total stacks)
                w_num_single = 0;
            elseif N_singleSOE < 3              % If we have either 1 or 2 single stacks in
                                                   addition to our 1 or 2 quad-stacks...
                w_num_single = 1;
            else
                error('Something is wrong with the Electrolysis -> Power Heat Loss inputs, causing
                                                   an error in the number of single and quad-
                                                   stack SOE modules.');
            end
        end
    end
end
```

Power

The power calculations were described in Section 4.4. Some elaboration will be provided here on the power terms.

(7) Electrolysis: Electrical power is required to drive the electrolysis process, where CO_2 is reduced to CO and oxygen ions. The electrical power of electrolysis is calculated as:

$$P_{electrolysis} = IV_{tn}N_{cells} \tag{152}$$

where I is the current generated by each cell, V_{tn} is the thermoneutral voltage, and N_{cells} is the number of active SOE cells in the system. The thermoneutral voltage refers to the crossover point between endothermic and exothermic reactions in electrochemistry and its calculation is described in more detail in Section 2.3.6. $P_{electrolysis}$ includes the power of electrolysis *and* the additional heater power required to compensate for the endothermic reaction.

(8) Preheating: The gas flowing into the SOE subsystem must be preheated to increase it to electrolysis temperature. The power consumption of the pre-heater was modeled as follows:

$$P_{preheat} = \frac{\dot{m}_{in}Cp_{Mars}(T6 - T5)}{\eta} \tag{153}$$

where $\dot{m}_{in}$ is the inlet gas mass flow rate, Cp_{Mars} is the specific heat capacity of a typical Mars atmospheric composition at a temperature equal to the average of $T6$ and $T5$, $T6$ is the temperature of the SOE unit, $T5$ is the temperature of the inlet gas after leaving the heat exchanger, and η is the combined thermal-to-electrical conversion efficiency and preheater-to-gas-stream efficiency (assuming a 10% loss to the environment).

(9) Heat Loss: Total heat loss from the SOE subsystem is determined by calculating conduction through both layers of Excelfrax insulation and convection and radiation to the Mars environment. The heat loss is broadly defined as:

$$Q_{heatloss} = \left(\frac{T_i - T_o}{R_t}\right) * \text{margin} \tag{154}$$

where T_i and T_o are the inner and outer temperatures of the SOE hotbox, R_t is the total thermal resistance of the heat path, including conduction, convection, and radiation, and $margin$ is a margin factor of 1.5 to account for unexpected heat loss pathways. This calculation is derived in more detail in Section 4.4.

Miscellaneous

Flow Rates out of SOE

The flow rates of each gas out of the SOE stack are calculated. The molar flow rate of oxygen is calculated using the electrical current:

$$\dot{n}_{O_2} = \left(\frac{I}{4F}\right)\left(N_{cps} * N_{stacks}\right) \tag{155}$$

which can be converted to mass flow rate with the molecular weight:

$$\dot{m}_{O_2} = \dot{n}_{O_2} * MW_{O_2} \tag{156}$$

The flow rate of carbon monoxide out of the stack is calculated as:

$$\dot{m}_{CO} = 2 * \dot{n}_{O_2} * MW_{CO} \tag{157}$$

The flow rate of carbon dioxide out of the stack is calculated as:

$$\dot{m}_{CO_2} = (\dot{n}_{CO_2,in} - \dot{n}_{CO}) * MW_{CO_2} \tag{158}$$

where $\dot{n}_{CO_2,in}$ is the inlet molar flow rate of CO_2 from the Mars atmosphere.

B.6 Liquefaction Calculations

The equations used to calculate mass, volume, and power of the liquefaction subsystem are captured here. They will follow the format of Figure 153.

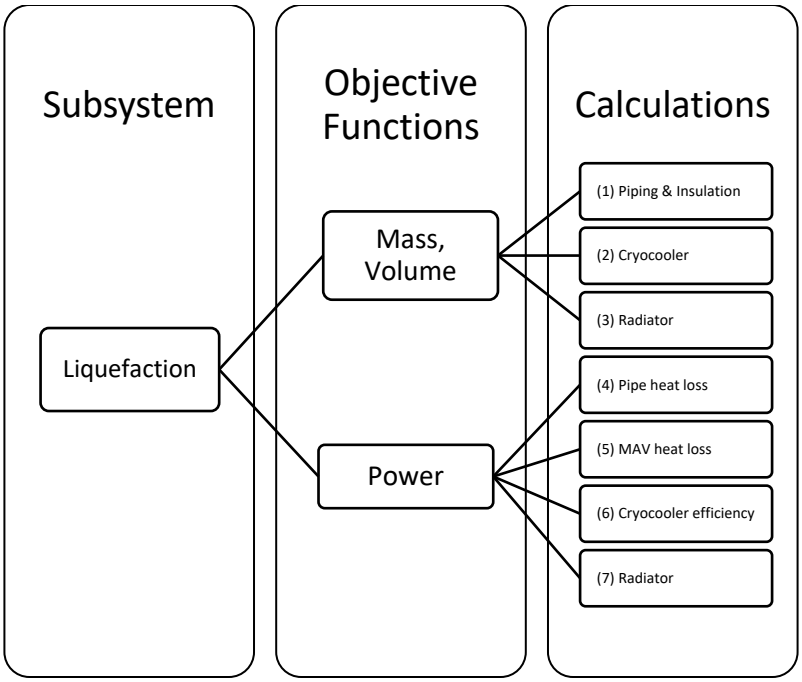

Figure 153: Liquefaction subsystem calculations flowchart

Mass and Volume

The mass and volume of the liquefaction system are calculated as the sum of the contributions of the piping network, the cryocooler, and the radiator:

$$M_{Liq} = M_{pipe} + M_{cc} + M_{rad} \tag{159}$$

and

$$V_{Liq} = V_{pipe} + V_{cc} + V_{rad} \tag{160}$$

The mass and volume of the MAV are not considered, as the MAV is a required part of any Mars mission and thus is not specific to the BAM design.

(1) Piping: The mass of the piping network throughout the liquefaction subsystem includes the mass of the pipe, insulation, and valves, and is calculated as follows:

$$M_{pipe} = M_{valves} + M_{piping} + M_{ins} \tag{161}$$

M_{valves} is set to an estimated value of 5 kg. M_{piping} is the mass of the physical pipes and is calculated as:

$$M_{piping} = \rho_{piping} * l_{liq_{piping}} * CSA_{piping} \tag{162}$$

where CSA_{piping} is the cross-sectional area of the pipes:

$$CSA_{piping} = \pi\left(\left(\frac{od_{liq_{piping}}}{2}\right)^2 - \left(\frac{od_{liq_{piping}} - 2t_{liq_{piping}}}{2}\right)^2\right) \tag{163}$$

The mass of the piping insulation, M_{ins}, is calculated in a similar way:

$$M_{ins} = \rho_{efrax} * l_{liq_{piping}} * CSA_{ins} \tag{164}$$

where CSA_{ins} is the cross-sectional area of the insulation surrounding the pipes:

$$CSA_{ins} = \pi\left(\left(\frac{od_{liq_{piping}} + 2t_{liq_{pipe_{ins}}}}{2}\right)^2 - \left(\frac{od_{liq_{piping}}}{2}\right)^2\right) \tag{165}$$

The volume of the piping network is set to 0, as all piping will exist within the envelope of the larger units in the liquefaction subsystem.

(2) Cryocooler: The mass of the cryocooler is calculated as a function of cooling lift, using extrapolated data from [164] and calculated using a power regression fit.

$$M_{cc} = 3.9985 * \left(P_{liquefy_{O_2}}\right)^{0.596} \tag{166}$$

The results of this fit are documented in Table 36.

The volume of the cryocooler is calculated in a similar manner:

$$V_{cc} = 0.052 * \left(P_{liquefy_{O_2}}\right)^{-0.404} \tag{167}$$

(3) Radiator: The mass of the radiator is calculated as follows:

$$M_{rad} = 2w_{fin_r}t_{radiator}l_{pipe_r}\rho_{cc_{fins}} + \pi d_{hp_r}t_{liq_{piping}}l_{pipe_r}\rho_{piping} \tag{168}$$

Similarly, the volume of the radiator is calculated as follows:

$$V_{rad} = 2w_{fin_r}t_{radiator}l_{pipe_r} + \pi\left(\frac{d_{hp_r}}{2}\right)^2 l_{pipe_r} \tag{169}$$

Power

(4) Pipe Heat Loss: Heat is lost or gained from the oxygen in the liquefaction system to the Mars atmosphere through the piping and piping insulation. This is calculated as follows, using Equation 10.2.30 from Middleman [205]:

$$Q_{liq_{pipes}} = \frac{2\pi l_{liq_{piping}}(T_{10} - T_{MA})}{\frac{\ln\left(\frac{r_1}{r_i}\right)}{k_{pipe}} + \frac{\ln\left(\frac{r_2}{r_1}\right)}{k_{efrax_{Mars}}} + \frac{1}{r_2 h_c}} \tag{170}$$

This term includes conduction through the pipe and insulation as well as convective losses to the environment. Radiation to the environment is minimal at these temperatures.

(5) MAV Heat Loss: Heat is also lost (or gained) from the oxygen in the liquefaction system through the MAV tank using the same equation:

$$Q_{liq_{MAV}} = \left(\frac{2\pi h_{MAV}(T_{10} - T_{MA})}{\frac{\ln\left(\frac{r_{MAV_2}}{r_{MAV}}\right)}{k_{efrax_{Mars}}} + \frac{1}{r_{MAV_2} h_c}} \right) \left(1 + \frac{2\pi r_{MAV_2}^2}{2\pi r_{MAV_2} h_{MAV}} \right) \tag{171}$$

This equation takes the form of $Q_{liq_{MAV}} = (Heat\ lost\ through\ sides\ of\ tank) * (Factor)$, where $Factor$ is a modification to include the top and bottom of the MAV tank. It accomplishes this by multiplying the primary expression by a factor equal to $\frac{A_{side}+A_{top+bottom}}{A_{side}}$.

(6) Cryocooler Efficiency: The cryocooler must remove the heat from the gaseous oxygen as well as any heat leaks in the MAV tank. This corresponds to the combination of Equations (64), (170), and (171). The efficiency of the cryocooler is considered when calculating cryocooler power as follows:

$$P_{cc} = \frac{Q_{O_2} + Q_{liq_{pipes}} + Q_{liq_{MAV}}}{\eta_{cc}} \tag{172}$$

(7) Radiator: The radiator must reject the heat already mentioned from the system in addition to an additional heat load it acquires from solar absorption. This additional heat flux is calculated as:

$$Q_{solar} = \alpha_r * Q_{Mars} * A_r \tag{173}$$

Where α_r is the absorptivity of the radiator and A_r is the surface area of the radiator that is exposed to the Sun during the day. This area is optimized by the simulation as one of the design variables in the system.

B.7 Baseline Reliability Calculation

As described in Section 4.9.2, the cumulative distribution function (CDF) of the Poisson distribution can be used to calculate the reliability of a component and its spares. The CDF calculates the probability of sequential failures of a system with standby redundancy. Using the CDF, the reliability for a system where *m* of *n* units must be functioning at the end of the mission is calculated as follows [182].

$$R_{m-of-n} = e^{-m\lambda t} \sum_{k=0}^{n-m} \frac{(m\lambda t)^k}{k!} \tag{174}$$

where λ is the failure frequency and t is the length of the mission. Reliability, in this case, is defined as unity minus the probability of failure of the system. It follows that the probability of failure of the component, i, and its backups is:

$$P_{f,i} = 1 - R_i \tag{175}$$

This was used to calculate the reliability of every relevant component in the BAM system.

B.8 Modified Reliability Calculation

As described in Section 4.9.3, certain components have reliabilities that are dependent on design variables. Therefore, the reliability calculations in the previous section are modified to include a dependence on these variables using the following format, where $R_{i,o}$ is the initial reliability calculation for that component, x is a generic design variable, and x_o is its baseline value.

If $x \leq x_o$,

$$R_i = R_{i,o} + \left(1 - R_{i,o}\right)\left(\frac{x_o - x}{x_o}\right)^{\frac{1}{b}} \tag{176}$$

Otherwise, if $x > x_o$,

$$R_i = R_{i,o} - R_{i,o}\left(\frac{x}{x + x_o}\right)^{\frac{1}{c}} \tag{177}$$

All modified reliability equations follow this format and are written below. Values for their baseline and exponential values – x_o, b, and c – can be found in

Table 41.

Blower Fan for Cryopump and Sorption Pump

If $\dot{m}_{in} \leq \dot{m}_{in,o}$,

$$R_{blower} = R_{blower,o} + \left(1 - R_{blower,o}\right)\left(\frac{\dot{m}_{in,o} - \dot{m}_{in}}{\dot{m}_{in,o}}\right)^{\frac{1}{b}} \tag{178}$$

Otherwise, if $\dot{m}_{in} > \dot{m}_{in,o}$,

$$R_{blower} = R_{blower,o} - R_{blower,o}\left(\frac{\dot{m}_{in}}{\dot{m}_{in} + \dot{m}_{in,o}}\right)^{\frac{1}{c}} \tag{179}$$

Cryocooler

If $P_{cool} \leq P_{cool,o}$,

$$R_{cc} = R_{cc,o} + \left(1 - R_{cc,o}\right)\left(\frac{P_{cool,o} - P_{cool}}{P_{cool,o}}\right)^{\frac{1}{b}} \tag{180}$$

Otherwise, if $P_{cool} > P_{cool,o}$,

$$R_{cc} = R_{cc,o} - R_{cc,o}\left(\frac{P_{cool}}{P_{cool} + P_{cool,o}}\right)^{\frac{1}{c}} \tag{181}$$

Mechanical Compressor

If $\dot{m}_{in} \leq \dot{m}_{in,o}$,

$$R_{mech} = R_{mech,o} + \left(1 - R_{mech,o}\right)\left(\frac{\dot{m}_{in,o} - \dot{m}_{in}}{\dot{m}_{in,o}}\right)^{\frac{1}{b}} \tag{182}$$

Otherwise, if $\dot{m}_{in} > \dot{m}_{in,o}$,

$$R_{mech} = R_{mech,o} - R_{mech,o}\left(\frac{\dot{m}_{in}}{\dot{m}_{in} + \dot{m}_{in,o}}\right)^{\frac{1}{c}} \tag{183}$$

Mechanical Compressor

If $P_2 \leq P_{2,o}$,

$$R_{mech} = R_{mech,o} + \left(1 - R_{mech,o}\right)\left(\frac{P_{2,o} - P_2}{\dot{m}_{in,o}}\right)^{\frac{1}{b}} \tag{184}$$

Otherwise, if $P_2 > P_{2,o}$,

$$R_{mech} = R_{mech,o} - R_{mech,o}\left(\frac{P_2}{P_2 + P_{2,o}}\right)^{\frac{1}{c}} \tag{185}$$

Solid Oxide Electrolysis Stack

If $N_{CPS} \leq N_{CPS,o}$,

$$R_{SOEstack} = R_{SOEstack,o} + \left(1 - R_{SOEstack,o}\right)\left(\frac{N_{CPS,o} - N_{CPS}}{N_{CPS,o}}\right)^{\frac{1}{b}} \tag{186}$$

Otherwise, if $N_{CPS} > N_{CPS,o}$,

$$R_{SOEstack} = R_{SOEstack,o} - R_{SOEstack,o}\left(\frac{N_{CPS}}{N_{CPS} + N_{CPS,o}}\right)^{\frac{1}{c}} \tag{187}$$

Solid Oxide Electrolysis Cell

If $\Delta P \leq \Delta P_o$,

$$R_{SOEcell} = R_{SOEcell,o} + \left(1 - R_{SOEcell,o}\right)\left(\frac{\Delta P_o - \Delta P}{\Delta P_o}\right)^{\frac{1}{b}} \tag{188}$$

Otherwise, if $\Delta P > \Delta P_o$,

$$R_{SOEcell} = R_{SOEcell,o} - R_{SOEcell,o}\left(\frac{\Delta P}{\Delta P + \Delta P_o}\right)^{\frac{1}{c}} \tag{189}$$

Solid Oxide Electrolysis Cell

If $\Delta V \geq \Delta V_o$,

$$R_{SOEcell} = R_{SOEcell,o} + \left(1 - R_{SOEcell,o}\right)\left(\frac{\Delta V - \Delta \mathrm{V_o}}{\Delta V}\right)^{\frac{1}{b}} \tag{190}$$

Otherwise, if $\Delta V < \Delta V_o$,

$$R_{SOEcell} = R_{SOEcell,o} - R_{SOEcell,o}\left(\frac{\Delta V_o}{\Delta \mathrm{V} + \Delta V_o}\right)^{\frac{1}{c}} \tag{191}$$

B.9 Miscellaneous Calculations

Kilopower System

The mass and volume of the Kilopower system are calculated using specifications from NASA [206] for 10 kWe units:

$$M_{power} = ceil\left(\frac{P}{P_{kp}}\right) * m_{kp} + m_{kp_{cable}} \tag{192}$$

$$V_{power} = ceil\left(\frac{P}{P_{kp}}\right) * V_{kp} \tag{193}$$

where P is the total power required of the ISRU system, P_{kp} is the electric power provided by a single Kilopower unit, m is mass, and V is volume. A ceiling function is used because partial Kilopower units cannot be sent; therefore, only integer values are acceptable for the number of Kilopower units required.

Electronics

The power, mass, and volume of the miscellaneous electronics used throughout BAM are calculated as linear functions of the power consumption and mass of the rest of BAM.

$$P_{el} = P_{non_{el}} * f_{el,P} \tag{194}$$

$$M_{el} = M_{non_{el}} * f_{el,M} \tag{195}$$

$$V_{el} = M_{non_{el}} * f_{el,V} \tag{196}$$

where non_{el} stands for "non-electronics", or the power/mass of all the other components in BAM. The factors, f_i, are non-dimensional fractions of electronics for power and mass based on the composition of a typical spacecraft.

Mass of Connecting Piping

The mass of the piping that connects each subsystem is calculated in the model as:

$$M_{pipe} = \pi \left(\left(\frac{D_o}{2} \right)^2 - \left(\frac{D_i}{2} \right)^2 \right) L \rho_{pipe} \tag{197}$$

where D_o is the outer diameter of the pipe, D_i is the inner diameter of the pipe, L is the length of the pipe, and ρ_{pipe} is the density of the pipe. The pipe is assumed to be made of copper.

The mass of the insulation that covers this pipe is calculated in a similar manner as:

$$M_{ins} = \pi \left(\left(\frac{D_{ins}}{2} \right)^2 - \left(\frac{D_o}{2} \right)^2 \right) L \rho_{ins} \tag{198}$$

where D_{ins} is the outer diameter of the insulation and ρ_{ins} is the density of the polyurethane foam insulation.

This appendix has shown all equations used in the BAM model that were not previously shown in this dissertation. The full contents of the equations, including the values used for each, can be found in the raw code in Appendix D.

Appendix C: SOE Data Taken at OxEon Energy

SOE data were taken at OxEon Energy in North Salt Lake, Utah in January 2022. The purpose of the tests was to characterize the performance of the SOE stack as a function of cathode pressure. A current-voltage (I-V) sweep was taken at a series of cathode pressures ranging from 860 mbar to 150 mbar.

In the data below, the observed current and voltage at each pressure are displayed. In addition, the component compositions (X) of the gas stream and the relevant Nernst voltages (V) are shown. The modeled current is calculated using Equation (110) and the squared error is calculated as the square of the difference between the measured and modeled current, as follows:

$$Squared\ Error = (I_{meas} - I_{mod})^2 \tag{199}$$

The iASR was calculated by minimizing the sum of squared errors using the Solver function in Microsoft Excel. For the purposes of calculation, the activation voltage was set to a constant value of 0.03 mV, per experts at OxEon Energy, and the cell area was set to its known value of 110.8 cm^2. The data will be displayed for each pressure in descending order below.

Table 83: Cathode Pressure: 860 mbar. Flow Conditions: 2.52 SLPM CO_2, 0.056 SLPM CO, 0.23 SLPM N_2 (2% CO:CO_2+CO). Utilization Fraction: 41.6%

Measured, Amps	Avg Cell Voltage	Model Current	Squared Error	
0.000	0.801			
0.541	0.835			
1.055	0.857	-1.18	4.98	
2.512	0.901	0.06	6.01	
5.054	0.956	5.14	0.01	
7.515	1.002	7.58	0.00	
10.040	1.044	9.96	0.01	
12.540	1.084	12.33	0.04	**iASR**
		SSE:	**11.05**	**1.370**

X CO_2	X CO	X N_2	V CO-CO_2	V ave CO-CO_2	Avg Cell V CO-Cs	Stack V CO-Cs	Margin Vc-Vop
0.898	0.020	0.081	0.802	0.802	1.249	6.243	0.448
0.885	0.033	0.081	0.826	0.826	1.225	6.124	0.390
0.872	0.046	0.081	0.842	0.842	1.210	6.050	0.353
0.836	0.082	0.081	0.870	0.870	1.183	5.916	0.282
0.773	0.146	0.081	0.900	0.863	1.157	5.784	0.201
0.712	0.207	0.081	0.920	0.878	1.141	5.703	0.139
0.649	0.269	0.081	0.937	0.891	1.128	5.642	0.084
0.587	0.332	0.081	0.951	0.902	1.119	5.594	0.035

Table 84: Cathode Pressure: 694 mbar. Flow Conditions: 3.10 SLPM CO_2, 0.056 SLPM CO, 1.19 SLPM N_2 (1.3% CO; 1.8% $CO:CO_2+CO$). Utilization Fraction: 29.5%

Measured, Amps	Avg Cell Voltage	Model Current	Squared Error	
0.000	0.792			
1.032	0.845			
2.565	0.890	2.48	0.01	
5.028	0.943	5.11	0.01	
7.494	0.988	7.57	0.01	
9.993	1.029	10.03	0.00	
12.520	1.068	12.43	0.01	**iASR**
		SSE:	**0.03**	**1.322**

X CO_2	X CO	X N_2	V CO-CO_2	V ave CO-CO_2	Avg Cell V CO-Cs	Stack V CO-Cs	Margin Vc-Vop
0.714	0.013	0.274	0.792	0.792	1.269	6.345	0.477
0.697	0.029	0.274	0.831	0.831	1.231	6.154	0.386
0.672	0.054	0.274	0.861	0.831	1.203	6.013	0.312
0.633	0.094	0.274	0.889	0.852	1.177	5.887	0.234
0.593	0.133	0.274	0.908	0.867	1.161	5.805	0.174
0.553	0.173	0.274	0.924	0.879	1.149	5.744	0.120
0.513	0.214	0.274	0.937	0.890	1.139	5.696	0.071

Table 85: Cathode Pressure: 493 mbar. Flow Conditions: 3.74 SLPM CO_2, 0.077 SLPM CO, 2.37 SLPM N_2 (1.2% CO; 2% CO:CO_2+CO). Utilization Fraction: 23.2%

Measured, Amps	Avg Cell Voltage	Model Current	Squared Error	
0.000	0.799			
1.050	0.843			
2.541	0.896	2.79	0.06	
5.070	0.952	5.51	0.19	
7.515	0.995	7.74	0.05	
10.000	1.036	10.00	0.00	
12.530	1.074	12.13	0.16	**iASR**
		SSE:	**0.46**	**1.476**

X CO_2	X CO	X N_2	V CO-CO_2	V ave CO-CO_2	Avg Cell V CO-Cs	Stack V CO-Cs	Margin Vc-Vop
0.605	0.012	0.383	0.798	0.798	1.270	6.352	0.472
0.593	0.024	0.383	0.830	0.830	1.240	6.198	0.397
0.576	0.041	0.383	0.856	0.829	1.215	6.077	0.320
0.547	0.070	0.383	0.882	0.848	1.191	5.955	0.239
0.520	0.097	0.383	0.900	0.862	1.176	5.878	0.181
0.492	0.125	0.383	0.914	0.873	1.164	5.819	0.128
0.463	0.154	0.383	0.927	0.882	1.154	5.772	0.080

Table 86: Cathode Pressure: 297 mbar. Flow Conditions: 2.79 SLPM CO_2, 0.064 SLPM CO, 3.08 SLPM N_2 (1.1% CO; 2.2% CO:CO_2+CO). Utilization Fraction: 29.1%

Measured, Amps	Avg Cell Voltage	Model Current	Squared Error	
0.000	0.802			
1.085	0.847			
2.554	0.895	2.05	0.26	
5.028	0.960	5.43	0.16	
7.517	1.009	8.07	0.31	
10.050	1.030	8.75	1.70	
12.480	1.094	12.91	0.19	**iASR**
		SSE:	**2.61**	**1.437**

X CO_2	X CO	X N_2	V CO-CO_2	V ave CO-CO_2	Avg Cell V CO-Cs	Stack V CO-Cs	Margin Vc-Vop
0.470	0.011	0.519	0.803	0.803	1.278	6.388	0.476
0.457	0.023	0.519	0.840	0.840	1.241	6.207	0.395
0.440	0.041	0.519	0.867	0.838	1.216	6.079	0.321
0.411	0.070	0.519	0.896	0.859	1.191	5.955	0.231
0.382	0.099	0.519	0.915	0.874	1.175	5.874	0.166
0.352	0.129	0.519	0.931	0.887	1.163	5.813	0.133
0.323	0.157	0.519	0.944	0.897	1.153	5.767	0.059

Table 87: Cathode Pressure: 194 mbar. Flow Conditions: 2.98 SLPM CO_2, 0.064 SLPM CO, 3.43 SLPM N_2 (1.0% CO; 2.1% CO:CO_2+CO). Utilization Fraction: 28.7%

Measured, Amps	Avg Cell Voltage	Model Current	Squared Error	
0.000	0.800			
1.075	0.841			
2.523	0.887	1.70	0.68	
5.010	0.948	4.87	0.02	
7.545	1.000	7.78	0.06	
10.020	1.042	10.17	0.02	
12.550	1.081	12.44	0.01	**iASR**
		SSE:	**0.79**	**1.405**

X CO_2	X CO	X N_2	V CO-CO_2	V ave CO-CO_2	Avg Cell V CO-Cs	Stack V CO-Cs	Margin Vc-Vop
0.460	0.010	0.530	0.800	0.800	1.281	6.406	0.481
0.449	0.021	0.530	0.837	0.837	1.245	6.227	0.404
0.433	0.037	0.530	0.864	0.835	1.220	6.101	0.333
0.406	0.064	0.530	0.892	0.856	1.195	5.975	0.247
0.379	0.091	0.530	0.912	0.871	1.179	5.893	0.179
0.352	0.118	0.530	0.927	0.883	1.167	5.833	0.125
0.325	0.145	0.530	0.940	0.893	1.157	5.785	0.076

Table 88: Cathode Pressure: 150 mbar. Flow Conditions: 3.02 SLPM CO_2, 0.065 SLPM CO, 3.52 SLPM N_2 (1.0% CO; 2.1% CO:CO_2+CO). Utilization Fraction: 29.6%

Measured, Amps	Avg Cell Voltage	Model Current	Squared Error	
0.000	0.800			
1.028	0.839			
2.563	0.883	1.51	1.12	
5.039	0.943	4.79	0.06	
7.523	0.991	7.51	0.00	
9.992	1.033	10.04	0.00	
12.500	1.075	12.69	0.04	**iASR**
		SSE:	**1.22**	**1.333**

X CO_2	X CO	X N_2	V CO-CO_2	V ave CO-CO_2	Avg Cell V CO-Cs	Stack V CO-Cs	Margin Vc-Vop
0.458	0.010	0.532	0.800	0.800	1.281	6.407	0.481
0.447	0.021	0.532	0.836	0.836	1.247	6.235	0.408
0.431	0.037	0.532	0.864	0.835	1.220	6.102	0.337
0.404	0.063	0.532	0.892	0.856	1.196	5.978	0.252
0.378	0.089	0.532	0.911	0.871	1.179	5.897	0.189
0.352	0.115	0.532	0.926	0.882	1.168	5.838	0.135
0.326	0.142	0.532	0.939	0.892	1.158	5.790	0.083

These data were used to form the plots and conclusions discussed in Section 5.3.

Appendix D: Code

This Appendix records all code used in the MATLAB-Simulink model of BAM. It can be used to view equations, understand values used for different variables, and explain the reasoning for those equations and values. The commenting on the code is included as well. This section is lengthy and therefore is best used with the search function to find keywords of interest rather than reading through the code line by line.

D.1 MATLAB Master Code

The MATLAB master code contains the inputs used for the Simulink model of BAM. It is organized by subsystem of BAM.

```
% Mars ISRU Oxygen Plant Production
% Eric Hinterman
% Loads variables in Matlab to connect with Simulink
% Version: 44
% Version Created: Feb 17, 2022
clear all; close all; clc; warning off;

record_on = 0;          % 1 to record values in excel, 0 to not record
Label = "Mass Reliability Analysis";
%------------------ Primary Input Variables --------------------------------
inputvector = 2;    %1 for power, 2 for mass, 3 for reliability, 4 for misc.

if inputvector == 1
    xo = [11.5 15726 2 85.9 60 3 1123 20939 0.915 2.89 10 3,...
        0.25 5.3 0.03 0.065 0.16 4 2 11 2 126 1 2 8];              % Best
            power ending vector
elseif inputvector == 2
    xo = [10.78 17942 3 70.85 89 1 1123 32449 0.954 2.08 3.12 2,...
        0.04 3.51 0.02 0 0 1 0 5 1 176 0 1 12];                    % Best
            mass ending vector
elseif inputvector == 3
    xo = [12.40 13300 2 40.16 10 8 1123 11690 0.952 0.705 0 1,...
        0.07 5.16 0.095 0.195 0.08 3 3 19 5 583 4 3 22];           % Best
            reliability ending vector
elseif inputvector == 4
    xo = [11.1 16478 2 89.3 44 4 1086 17090 0.936 4.7 6.9 5,...
        0.37 4.6 0.06 0.07 0.14 4 2 10 4 204 1 3 10];
else
    error('Select a valid starting vector');
end



mdot_in         = xo(1);         % (kg/hr) flow rate of Mars atmosphere into
            the system
P2              = xo(2);      % (Pa)    operating pressure inside the system
            (output pressure of the CAC). 100 Pa = 1 mbar.
CAC             = xo(3);          % ( )     1 = Cryo, 2 = Mechanical
            (Scroll), 3 = Mechanical (Centrifugal), 4 = Sorption
A_cell          = xo(4);        % (cm^2)  active surface area of each
            electrolysis cell. Assume min is 22.74 cm^2 (MOXIE) and max is
            110.8 cm^2 (per Joe - manufacturing limit with the interconnect
            sintering press)
```

```
N_cps           = xo(5);         % ( )     number of SOE cells per stack.
            Oxeon is building 65-cell stacks for NASA SBIR. 6 stacks would
            provide the desired flowrate.
N_stacks        = xo(6);          % ( )     number of stacks of SOE cells
            producing oxygen in the system (does NOT include spare SOE cells)
T6              = xo(7);       % (K)     operating temperature of the
            electrolysis stack
P6              = xo(8);      % (Pa)    output pressure at SOE anode. This is
            dictated by the ideal gas law (P = nRT/V). n, R, and T are known,
            but V is determined by a mass flow controller at the anode that
            changes its volume to set the pressure. P6 affects the Nernst
            potential and thus is a valuable design variable. The optimizer
            will control P6 across a range of values (0.1 bar - 100 bar,
            maybe).
V_app           = xo(9);      % (V)     voltage applied to each SOE cell to
            produce oxygen. Total applied voltage is V_app*N_cps*N_stacks
A_HE1           = xo(10);          % (m2)    surface of area of first heat
            exchanger, which exchanges heat between the hot anode exhaust gas
            and the incoming Mars gas pre-SOE (increasing it decreases total
            system power but increases total system mass)
A_HE2           = xo(11);          % (m2)    surface of area of second heat
            exchanger, which exchanges heat between the hot cathode exhaust
            gas and the incoming Mars gas pre-SOE (increasing it decreases
            total system power but increases total system mass)
N_CAC           = xo(12);          % ( )     number of capture-and-
            compression (pumping) devices

%------------------ Secondary Input Variables -----------------------------

t_liq_pipe_ins  = xo(13);      % (m)    Thickness of aerogel insulation
            around the liquefaction piping
t_liq_MAV_ins   = xo(14);      % (m)    Thickness of aerogel insulation
            around the MAV tank
t_ins_pipe      = xo(15);      % (m)    Thickness of aerogel insulation
            around the piping that connects the rest of the subsystems
t_SOE_ins1      = xo(16);      % (m)    Thickness of aerogel (Excelfrax 1800)
            insulation around SOE quad and single stack modules inside the
            inner SOE hotbox shell
t_SOE_ins2      = xo(17);      % (m)    Thickness of aerogel (Excelfrax 1800)
            insulation between SOE inner shell and outer shell in hotbox

Blower_numSpareUnits        = xo(18);      % Spare # of each of the following
            components. Higher # of spares = higher reliability but higher
            mass
Cryocooler_numSpareUnits    = xo(19);
Valve_numSpareUnits         = xo(20);
CACmechanical_numSpareUnits = xo(21);
SOECell_numSpareUnits       = xo(22);
SOEStack_numSpareUnits      = xo(23);      % Spare # of STACKS of SOE cells
Kilopower_numSpareUnits     = xo(24);
Heatexchanger_numSpareUnits = xo(25);

% t_PHE = XX;   This could be a design variable too if I want. Increasing it
            decreases pressure drop across HE but increases HE mass and
            volume.

%------------------ Constants -----------------------------
```

```
%SYSTEM PARAMETERS
Num_Crew        = 6;                        % CHOOSE 4 or 6 crew
Op_months       = 14;                       % (months)  number of months the
            ISRU system has to produce oxygen
Op_time         = Op_months*30*24;          % (hr)      operating time in
            hours the ISRU system has to produce oxygen
CrewLaw         = 1.356;                    % For 6 crew, multiply the
            propellant requirements of a 4-crew MAV by CrewLaw (based on DRA
            5.0, Eric has a calculation sheet to show the number)
O2_prod_req     = 22717;                    % (kg)      kg of LOX required to
            fuel a 4-crew MAV (Polsgrove et al, 2015). DRA 5.0 says 23,532 kg
            for a crew of 6.
if Num_Crew     == 6
    O2_prod_req = O2_prod_req * CrewLaw;    % If 6 crew, scale up the O2
            ratio accordingly. If 4 crew, it stays as-is.
end
O2_prod_rate    = O2_prod_req/Op_time;      % (kg/hr)   rate of oxygen
            production required to fill the MAV tank. Final mdot_O2 must be
            >= to this variable.

%MARS CONSTANTS
xCO_a           = 0.0007;                   % mole fraction ambient CO on
            Mars
xN2_a           = 0.0197;                   % mole fraction ambient Nitrogen
            on Mars
xAr_a           = 0.0231;                   % mole fraction ambient Argon on
            Mars
xCO2_a          = 1-xCO_a-xN2_a-xAr_a;      % mole fraction ambient CO2 on
            Mars (assume it is the remaining fraction after N2, Ar, and CO
            are taken out. A slight overestimation given other trace gases
            that are present.)
PO2_a           = 0.00001479;               % (bar)     Ambient partial
            pressure of Oxygen on Mars
T_MA            = 251.4;                    % (K)       Average Mars
            Temperature @ Jezero (MCD)
T_ML            = 179.2;                    % (K)       Low Mars Temperature
            across 7 M2020 potential landing sites (MCD)
T_MH            = 291.7;                    % (K)       High Mars Temperature
            across 7 M2020 potential landing sites (MCD)
P_MA            = 850;                      % (Pa)      M Hecht expects
            between 700-1000 Pa surface pressure for a human mission. Can
            look up NASA past human Mars mission landing sites candidates for
            more info. 677.2 Pa is the average Mars Pressure across 7 M2020
            potential landing sites (MCD)

%RISK / RELIABILITY
MissionLength   = Op_months*30*24;          % (hrs)     Length of mission
            (length of time available for ISRU plant to make oxygen)

%POWER
P_kilopower     = 10000;                    % (W)       Watts electric for
            one Kilopower nuclear reactor
P_power_regulation = 0;                     % (-)       TBD: We assume the
            power needed to regulate and distribute electricity for this
            system is taken into account with their 10 kWe numbers (i.e. the
```

```
            system produces 10.3 kWe, for example, but uses 0.3 kWe for power
            regulation and distribution). Have not confirmed.
M_kpcable       = 60;                       % (kg)      60 kg/km. 1 km
            separation from humans. Unclear if it changes based on # of
            kilopower units. Reference: Rucker et al. (2017)
h_kilo          = 3.3;                      % (m)       Height of 10 kWe unit
            (confirmed). Source:
            https://ntrs.nasa.gov/api/citations/20160012354/downloads/2016001
            2354.pdf?attachment=true
r_kilo          = 0.75;                     % (m)       Radius of 10 kWe unit
            (confirmed). Source:
            https://ntrs.nasa.gov/api/citations/20160012354/downloads/2016001
            2354.pdf?attachment=true
V_kilopower     = pi()*r_kilo^2*h_kilo;     % (m^3)     10kWe unit is 3.3 m
            tall and appears ~0.75 m radius when packaged. Treating as a
            cylinder (confirmed)
m_kilopower     = 1545;                     % (kg)      Mass per 10 kWe unit
            of Kilopower nuclear reactor (confirmed)

%ELECTRONICS
El_P            = 0.085;                    % ( )       non-dimensional
            fraction of % total power by subsystem for onboard computing
            (SMAD Table 14-20). SMAD says 11%, MOXIE uses 8.5% during O2
            production run for sensors and OBC (according to MEL-PEL). Linne
            also has two ISRU studies that show ~8.5% for electronics, C&DH,
            and comms.
El_M            = 0.045;                    % (%)       non-dimensional
            fraction of % total mass by subsystem for Cubesat (SMAD Table 14-
            18). Cubesat is 5%, BAM is assumed to be 4% with nonlinear
            scaling.
rho_El          = 940;                     % (kg/m^3)  Density of plastic =
            940 kg/m3, density of copper wire = 9000 kg/m3, density of rubber
            insulation = 1000 kg/m3

%CAC
    deltaP_f            = 30;               % (Pa)      Pressure drop across
            the inlet filter. Source: Extensibility of MOXIE (Rapp). Normally
            this would be calculated as a function of inlet velocity, but as
            the design of this filter is outside the scope of this thesis, it
            is fair to set this as a constant.
% Mechanical
    gamma               = 1.30;             % ( )       Ratio of specific
            heat capacities of CO2 (Cp/Cv). It does change slightly with
            temperature and pressure but for simplicity, will consider it a
            constant
    eff_ad_scroll       = 0.70;             % ( )       Adiabatic efficiency
            of a scroll compressor at the expected operating conditions
    eff_ad_centr        = 0.60;             % ( )       Adiabatic efficiency
            of a centrifugal compressor at the expected operating conditions
    P1_IR               = 700;              % (Pa)      Inlet pressure
            considered by IR Nash in their compressor study for BAM
    P2_IR               = 20000;            % (Pa)      Outlet pressure
            considered by IR Nash in their compressor study for BAM
    k_IR                = 0.28;             % ( )       Exponential factor
            for volume and mass scaling, calculated from IR Nash data
    f_centr             = 0.4;              % ( )       Factor of centrifugal
            box that defines its volume that is actually occupied by material
% Cryopump
```

```
cryo_Volume         = 1.1;              % (m^3)     Volume for a system
        that produces 1.1 kg/hr CO2 based on length of 100 cm, width of
        50 cm, and height of 221 cm (calculated from images of source)
        Source: Meier et al. 2018
cryo_blower         = 16800;            % (J/kg)    Energy required to
        move 1 kg of Mars air through the system. Calculated from
        standard blower charts, assuming a Mars atmospheric density of
        0.02 kg/m^3. Source: https://www.engineeringtoolbox.com/fans-
        efficiency-power-consumption-d_197.html
cryo_blower_eff     = 0.60;             % ( )       Efficiency of blower
        fan. Source: https://www.engineeringtoolbox.com/fans-efficiency-
        power-consumption-d_197.html
cycle_time_cryo     = 217;              % (min)     Cycle time of
        cryocooler for one batch. Includes cooldown time (17 min),
        collection period (100 min), and sublimation period (100 min)
cool_time_cryo      = 100;              % (min)     100 minutes per 217
        minute cycle are used for cooling
warm_time_cryo      = 100;              % (min)     100 minutes per 217
        minute cycle are used for warming
blower_spec_mass    = 0.4;              % (kg blower / kg/hr CO2 moved) A
        specific mass number for blower mass to size it based on flow
        rate it moves. Sized based on the 115V/0.75A version that is 6
        lbs at source at end of comment. This is roughly the same power
        we need to move 15 kg/hr, according to my blower power
        calculations. So 6lbs/15 kg/hr =~ 0.3 kg blower / 1 kg/hr CO2.
        0.4 for margin and to account for scaling law. Source:
        https://www.amazon.com/Durable-Lightweight-Carpet-Janitorial-
        Cleaner/dp/B00AEUYCFA
blower_spec_vol     = 0.003;            % (m3 blower / kg/hr CO2 moved) A
        specific volume number for blower volume to size it based on flow
        rate it moves. Sized based on the 115V/0.75A version that is
        0.025 m^3 at source at end of comment. Source:
        https://www.amazon.com/Durable-Lightweight-Carpet-Janitorial-
        Cleaner/dp/B00AEUYCFA
cryo_efficiency     = 0.1;              % (-)       Efficiency of
        cryocooler. Pulse-tube cryocoolers have 20% according to Clark
        (2001). Johnson et al. show Linde cycle for O2 liquefaction has
        an efficiency of 20%. Brian Hoh recommended 15% thermal
        efficiency. Wes Johnson at NASA recommended 10%. So I'm going
        with 10% (Wes is my SME on this).
heater_efficiency   = 1;                % ( )       Cartridge heaters
        convert electrical energy to thermal energy with 100% efficiency
heatloss_efficiency = 0.85;             % ( )       Assume 15% losses
        from parasitic heat leaks
cryo_HE_factor      = 0.5;              % ( )       Power reduction
        factor (between 0 and 1) to represent the heat exchanger that is
        placed between each pair of cryopumps. This will exchange heat
        from the residual heat of the hot cold head / chamber in one
        cryopump with the cold gas trapped in the second cryopump.
H_latent_CO2        = 591e3;            % (J/kg)    Latent heat of
        sublimation of CO2 at 180 K.     Source: engineeringtoolbox.com
rho_frost           = 800;              % (kg/m^3)  Frost density of CO2,
        assuming some porosity. Upper limit is 1500 kg/m^3. Source: Ash
        et al. 1978
k_CO2               = 0.15;             % (W/m-K)   Frost thermal
        conductivity of CO2, assuming some porosity. Upper limit is 0.25.
        Source: Ash et al. 1978
```

```
    T_freeze_CO2        = 148;              % (K)       Freezing point of CO2
            at Mars pressure
    sol_valve_m         = 1.4;              % (kg)      Mass of a single
            solenoid valve used in cryopump system. Source: Marotta space-
            qualified solenoid valves. Part MV172 (1" diameter). General
            Site: https://marotta.com/markets/space/
    sol_valve_p         = 1;                % (W)       Power used by a
            single latching solenoid valve in the cryopump system. Latching
            solenoid valves only require ~0.2 seconds of power draw to
            operate, so they are very low energy. 1 W is likely an
            overestimate by a factor of 4-10. Source: http://www.connexion-
            developments.com/12-volt-solenoid-valve.html
    check_valve_m       = 0.3;              % (kg)      Mass of a single
            check valve used in the cryopump system. Source: Marotta space-
            qualified check valves. 1" line.
            https://marotta.com/products/flow-controls/pressure-
            controls/check-valves/
% Sorption
    cycle_time          = 0.033;            % (hr)      Cycle time for the
            rapid swing sorption units. 2 minutes as designed by NASA.
    loading             = 0.15;             % (g/g)     Grams of CO2 the
            sorption bed can hold per gram of sorption bed material. Source:
            Clark "Mars Atmospheric Acquisition and Compression Systems -
            Initial Results"
    sorp_eff            = 0.8;              % ( )       Efficiency term to
            account for the fraction of heat that is exchanged between
            adjacent sorption bed cells.
    sorp_eff2           = 0.8;              % ( )       Efficiency term to
            account for part of the sorbent material being blocked by a
            diffusive barrier of nitrogen and argon. Even with a blower fan,
            NASA's preliminary tests found that the N2 and Ar created a drop
            in performance.
    sorp_mass_factor    = 15;               % ( )       Multiplication
            factor. Gives total mass of sorption pump when multiplied by the
            mass of sorbent required. Most of the mass of the system comes
            from the structural mass to support it. Assumes titanium. Source:
    T_hot               = 373;              % (K)       Typical desorption
            temperature of sorbent bed. Source: Hasseeb & Iannetti (2017).
    T_cold              = 233;              % (K)       Cold end adsorption
            temperature. Selected based on literature review for microchannel
            sorption pumps.
    Cp_zeolite          = 1100;             % (J/kg-K)  Specific heat of
            zeolite 13x, the adsorbent material. Source: Lu et al. (2020).
            "Evolution of Specific Heat Capacity with Temperature for Typical
            Supports Used for Heterogeneous Catalysts."
    Cp_ti               = 544;              % (J/kg-K)  Specific heat of
            titanium, the frame material. Source:
            engineersedge.com/materials/specific_heat_capacity_of_metals_1325
            9.htm
    CpCv_CO2            = 1.28;             % ( )       Specific heat ratio
            of CO2, equal to Cp/Cv. Source:
            https://www.engineeringtoolbox.com/specific-heat-ratio-d_608.html

    %------------------ Solid Oxide Electrolysis ----------------------------
            --
%ELECTROLYSIS - GENERAL
iASR            = 2.26;                     % (ohm-cm^2)  0.99 for SOE cells
            per Meyen thesis, 2.26 for large OxEon cells. Some at OxEon, w/
```

```
            thinner electrolyte, were 3.0. Going with worst-case for now, but
            should get better way to predict this.
rec_frac        = 0.05;                     % (-)       fraction of cathode
            molar flow that is recycled back into the SOE inlet
MW_O2           = 0.032;                    % (kg/mol)  Molecular weight of
            O2
MW_CO2          = 0.044;                    % (kg/mol)  Molecular weight of
            CO2
MW_CO           = 0.028;                    % (kg/mol)  Molecular weight of
            CO
MW_Ar           = 0.040;                    % (kg/mol)  Molecular weight of
            Ar
MW_N2           = 0.028;                    % (kg/mol)  Molecular weight of
            N2
MW_Mars         = 0.0436;                   % (kg/mol)  Molecular weight of a
            Mars mix of 96% CO2, 2% Ar, and 2% N2
VNernstA        = -4.4924e-4;               % (V/K)     (Static Physics)   A
            term for Vrev of the form A*T+B where T is in K. (White Model)
            Ref. Meyen 2017 Ph.D. Thesis Chapter 3
VNernstB        = 1.4629;                   % (V)       (Static Physics)   B
            term for Vrev of the form A*T+B where T is in K. (White Model)
            Ref. Meyen 2017 Ph.D. Thesis Chapter 3
VN_CO_A         = 110.177;                  % (V)       First term in
            calculating Gibb's Energy @ standard state. Source: Hartvigsen
            testing sheet macro. His source: Ihsan Barin.
VN_CO_B         = 0.0902247;                % (V/K)     First term in
            calculating Gibb's Energy @ standard state. Source: Hartvigsen
            testing sheet macro. His source: Ihsan Barin.
VN_CO_C         = 1.42044e-6;               % (V/K^2)   First term in
            calculating Gibb's Energy @ standard state. Source: Hartvigsen
            testing sheet macro. His source: Ihsan Barin.
VN_CO_D         = -1.55108e-9;              % (V/K^3)   First term in
            calculating Gibb's Energy @ standard state. Source: Hartvigsen
            testing sheet macro. His source: Ihsan Barin.
heater_eff      = 0.9;                      % ( )       Efficiency of inlet
            gas heater. Two parts: electric to thermal conversion efficiency,
            and then heat exchanger efficiency to transfer that heat to the
            gas. Former is 1, latter is assumed to be 0.9 (10% heat goes to
            environment, 90% stays in pre-heater structure and gas. Assume an
            inline heater such as this one:
            https://www.thermaldevices.com/wp-content/uploads/2018/04/Watlow-
            Fluent-Heater-Catalog-Pages.pdf. Electric to thermal energy
            conversion is typically 100% efficient.

%ELECTROLYSIS - MASS & VOLUME
rhoZ            = 5440;                     % (kg/m3)   density of ScSz
            electrolyte with coatings, calculated from MOXIE values and
            confirmed to be close to zirconia density (5680 kg/m3).
rhoIC           = 7200;                     % (kg/m3)   density of CFY
            interconnect material (Nohtal, Aug 2017)
rhoEP           = 7200;                     % (kg/m3)   density of endplates.
            On MOXIE, made of CFY (Nohtal, Aug 2017).
rho_efrax       = 230;                      % (kg/m3)   density of Excelfrax
            1800 Microporous board, the "soft" insulation that is similar to
            aerogel and is recommended by OxEon for the scaled SOE
rho_ti          = 4500;                     % (kg/m3)   density of Titanium
```

```
t8              = 0.00635;                  % (m)       thickness of SOE
            hotbox inner shell. 1/4" titanium.
t10             = 0.00635;                  % (m)       thickness of SOE
            hotbox outer shell. 1/4" titanium.
tZ              = 0.000320;                 % (m)       thickness of ScSz
            cell, including cathode and anode coating. Measured to be 320
            microns.
tIC             = 0.0025;                   % (m)       thickness of
            interconnect. MOXIE = 0.00215, OxEon (according to Koorosh) =
            0.00263. I chose inbetween. This is a major influencer on stack
            mass.
tEP             = 0.003;                    % (m)       thickness of MOXIE
            endplates. Confirmed with Koorosh's model of OxEon scaled cells
            as well.

f_SOE           = 1.3;                      % ( )       multiplication factor
            to account for nickel felt and glass seal mass and volume (1.2
            means we assume Ni + glass = 20% of mass and volume of each
            cell). 30% confirmed with Koorosh's model.
fIC             = 0.77;                     % ( )       reduction factor to
            account for flow channels in interconnects. While they take up a
            certain volume, they have flow channels cut out of them, reducing
            the mass. 0.77 is the value for MOXIE per Nohtal, will confirm
            with Joe H. for scaled cells.
fEP             = 0.927;                    % ( )       reduction factor to
            account for flow channels in endplates. While they take up a
            certain volume, they have flow channels cut out of them, reducing
            the mass. 0.927 is the value for MOXIE per Nohtal.

w_quad          = 0.35;                     % (m)       width of a quad stack
            SOE module, courtesy of OxEon
w_single        = 0.21;                     % (m)       width of a single
            stack SOE module, courtesy of OxEon
l_quad          = 0.37;                     % (m)       length of a quad
            stack SOE module.  Includes current tabs.
l_single        = 0.23;                     % (m)       length of a single
            stack SOE module. Includes current tabs.

k_efrax         = 0.03;                     % (W/m-K)   thermal conductivity
            of excelfrax 1800 microporous board, according to OxEon. This is
            the recommended "soft" insulation for the scaled SOE unit.
k_efrax_Mars    = 0.008;                    % (W/m-K)   thermal conductivity
            of excelfrax 1800 microporous board at 10 mbar. Source:
            https://link.springer.com/content/pdf/10.1007%2F978-0-387-88953-
            5_46.pdf

%ELECTROLYSIS - DELTA-P

ff_SOE          = 0.5;                      % ( )       friction factor of
            the SOE channels. Value of 0.0025 taken from OxEon, though this
            seems way too low. Technically varies with channel size, but only
            by a marginal amount. When I calculate Reynold's number in the
            channels (which I do in Simulink), I get ~150. According to the
            following source, that means my friction factor is ~0.5 because
            we are well into the laminar regime.
            https://en.wikipedia.org/wiki/Darcy%E2%80%93Weisbach_equation#/me
```

```
            dia/File:Darcy_Friction_factor_for_Re_between_10_and_10E8_for_val
            ues_of_relative_roughness.svg
h_SOE           = 0.0004;                   % (m)       height of SOE
            channels. May vary with SOE cell size. The MOXIE cell channel
            heights are 0.4 mm
d_SOE           = 0.0008;                   % (m)       equivalent diameter
            for flow channels in SOE. According to JJH at OxEon, they are 0.4
            mm high and 1.2 mm wide. Average diameter is therefore 0.8 mm,
            used in flow calculations.

VactA           = -4.255e-5;                % (V/K)     (Static Grey)  A term
            for Vact of the form A*T+B where T is in K. (Grey CSA5 Model)
            Ref. Meyen 2017 Ph.D. Thesis Chapter 5
VactB           = 0.06739;                  % (V)       (Static Grey)  B term
            for Vact of the form A*T+B where T is in K. (Grey CSA5 Model)
            Ref. Meyen 2017 Ph.D. Thesis Chapter 5
Ea              = 82557;                    % (kJ/mol)  (Static Grey)
            Activation Energy, derived from CSA 005 ASR @ 100g/hr. Ref. Meyen
            2017 Ph.D. Thesis Chapter 5
A               = 10300;                    % ( )       (Static Grey)  Pre-
            exponential factor, derived from CSA 005 ASR @ 100g/hr. Ref.
            Meyen 2017 Ph.D. Thesis Chapter 5

%HEAT LOSS (CONNECTING FLOW)
Lpipe           = 6;                        % (m)       length of pipe
            between each subsystem (one section only, not all lengths
            combined)
Di              = 0.05;                     % (m)       inner diameter of
            pipe
t_pipe          = 0.003;                    % (m)       thickness of pipe.
            Standard 2" copper pipe thickness is 0.0015 meter. Doubled for
            safety.
Do              = Di+2*t_pipe;              % (m)       outer diameter of
            pipe
Dins            = Do+2*t_ins_pipe;          % (m)       outer diameter of
            pipe plus insulation
k_ins           = 0.04;                     % (W/m-K)   insulation thermal
            conductivity. Set to 0.04 for fiberglass thermal conductivity:
            http://hyperphysics.phy-astr.gsu.edu/hbase/Tables/thrcn.html
k_copper        = 385.0;                    % (W/m-K)   copper thermal
            conductivity: http://hyperphysics.phy-
            astr.gsu.edu/hbase/Tables/thrcn.html
k_alum          = 205;                      % (W/m-K)   aluminum thermal
            conductivity
k_inc           = 20.5;                     % (W/m-K)   inconel600 thermal
            conductivity (per J. Hua, JPL)
h_c             = 2;                        % (W/m2-K)  convective
            coefficient for Mars atmosphere from Phoenix lander:
            https://www.reddit.com/r/Colonizemars/comments/732jgq/heat_transf
            er_on_mars/. "2" is a conservative estimate that uses wind speeds
            of only 1 m/s (higher wind speeds are typical and result in a
            higher h and thus better convection). Source:
            https://www.researchgate.net/publication/299600459_Convective_Hea
            t_Transfer_Measurements_at_the_Martian_Surface
density_copper  = 8960;                     % (kg/m3)   Density of copper
density_ins     = 30;                       % (kg/m3)   Density of insulating
            material, source: http://www.fao.org/3/y5013e/y5013e08.htm
```

```
density_inc     = 8400;                     % (kg/m3)   Density of Inconel
            625 (Nohtal, Aug 2017)

%Specific Heat Capacity #s based on my own trendline fits to
%EngineeringToolbox data. See "Specific Heat Calculator.xls" for details.
CO2_coef        = [0.00000025 -0.00101 1.5 472.3];                      % ( )
            Coefficients for Cp = AT^3 + BT^2 + CT + D, derived from
            EngineeringToolbox data as a function of temperature
O2_coef         = [0.00000000033 -0.00000119 0.0014 -0.368 935.3];      % ( )
            Coefficients for Cp = AT^3 + BT^2 + CT + D, derived from
            EngineeringToolbox data as a function of temperature
CO_coef         = [0.00000000018 -0.000000797 0.00116 -0.453 1089.9];   % ( )
            Coefficients for Cp = AT^4 + BT^3 + CT^2 + DT + E, derived from
            EngineeringToolbox data as a function of temperature
N2_coef         = [-0.00000019 0.000498 -0.205 1060.4];                 % ( )
            Coefficients for Cp = AT^4 + BT^3 + CT^2 + DT + E, derived from
            EngineeringToolbox data as a function of temperature
MarsMix_coef    = [0.00000024 -0.000960 1.46 493.1];                    % ( )
            Coefficients for Cp = AT^3 + BT^2 + CT + D, derived from
            EngineeringToolbox data as a function of temperature

%HEAT EXCHANGER
U_HE            = 3;                        % (W/m2-K)  heat transfer
            coefficient for specific heat exchanger. Going on lower end of
            gas-gas tubular HE, since we are at lower than atmospheric
            pressure. Source: https://engineeringtoolbox.com/heat-transfer-
            coefficients-exchangers-d_450.html. Update: this is confirmed
            with a Mars calculation of heat transfer coefficients, which
            yields results from U = 0.5 to U = 9 depending on fluid velocity.
t_PHE           = 0.003;                    % (m)       Thickness of PHE
            plate (standard is 0.4-1.4 mm; modifying to increase channel size
            to decrease P drop)
l_PHE           = 1.1;                      % (m)       Length of PHE plate
            (standard range is 0.4 - 5 m)
w_PHE           = 0.55;                     % (m)       width of PHE plate
            (standard range is 0.07 - 1.2 m)
h_end           = 0.02;                     % (m)       Height of both
            endplates on each end of the stack
A_eff_PHE       = 0.7;                      % ( )       Area efficiency of
            PHE plate. 30% of area per plate is unused, as it is taken up by
            the welded perimeter and inlet/outlet ports.
ff_HE           = 0.04;                     % ( )       Moody friction factor
            for PHEs experiencing turbulent flow. Re in the 10^3 - 10^4
            range. Minimal surface roughness. Source:
            https://www.engineeringtoolbox.com/moody-diagram-d_618.html

%LIQUEFACTION
% MAV
    r_MAV           = 1.3;                  % (m)       radius of the MAV
            oxygen tank
    h_MAV           = 7.7;                  % (m)       height of the MAV
            oxygen tank
    rho_piping_MAV  = 2700;                 % (kg/m3)   density of aluminum
            pipes in the radiator and around the MAV. Aluminum used rather
            than copper per Wes Johnson @ NASA; much lighter weight, decent
            heat transfer, and better match to MAV tank for thermal expansion
            and contraction
% System Inputs
```

```
    H_latent_O2     = 214e3;                % (J/kg)    latent heat of
            vaporization of O2
    A_O2            = 3.85845;              % ( )       Antoine Equation
            coefficient for O2 liquid-vapor curve. Source:
            https://webbook.nist.gov/cgi/cbook.cgi?ID=C7782447&Mask=4&Type=AN
            TOINE&Plot=on
    B_O2            = 325.675;              % ( )       Antoine Equation
            coefficient for O2 liquid-vapor curve. Source:
            https://webbook.nist.gov/cgi/cbook.cgi?ID=C7782447&Mask=4&Type=AN
            TOINE&Plot=on
    C_O2            = -5.667;               % (K)       Antoine Equation
            coefficient for O2 liquid-vapor curve. Source:
            https://webbook.nist.gov/cgi/cbook.cgi?ID=C7782447&Mask=4&Type=AN
            TOINE&Plot=on
    P10             = 100000;               % (Pa)      Pressure of liquid
            oxygen
    Cp10            = 1062;                 % (J/kg-K)  specific isobar heat
            capacity of O2 at 90 K and 1 bar. Great source that can calculate
            this value and more for any cryo temp and pressure:
            https://www.peacesoftware.de/einigewerte/calc_o2.php7
    rho_LO2         = 196.21;               % (kg/m^3)  density of liquid O2
            at 90 K and 1 bar. Great source that can calculate this value and
            more for any cryo temp and pressure:
            https://www.peacesoftware.de/einigewerte/calc_o2.php7
    od_liq_piping   = 0.025;                % (m)       outer diameter of
            pipe. Reference: Wes Johnson @ NASA. recommended 12-25 mm
    t_liq_piping    = 0.002;                % (m)       thickness of pipe in
            liquefaction subsystem
    l_liq_piping    = 2*pi*r_MAV*15;        % (m)       total length of
            piping throughout liquefaction subsystem that is exposed to the
            Mars atmosphere. Calculated based on the pipes wrapping around
            the MAV. Length equal to circumference of MAV multiplied by
            number of coils.
% Radiator
    T_root          = 315;                  % (K)       inlet temperature for
            the radiator working fluid (ammonia). Justification on page 111
            of my notebook. This is an estimated temperature based on the
            neon predicted temperatures in the cryocooler loop. It is fair to
            assume a temperature (rather than calculate it), as many factors
            can be adjusted to achieve the set temperature, including
            compressor power, recuperator area, and heat exchanger size.
    skytemp         = 170;                  % (K)       worst-case Mars sky
            temperature for radiator
    emissivity_r    = 0.92;                 % ( )       emissivity of
            radiator surface (white paint)
    absorptivity_r  = 0.09;                 % ( )       absorptivity of the
            white paint on the radiator surface. The radiator will absorb
            this percentage of incoming heat flux.
    sb              = 5.67e-8;              % (W/m2-K4) Stefan-Boltzmann
            constant
    Cp_NH3          = 4744;                 % (J/kg-K)  specific heat
            capacity of liquid NH3. Gas NH3 = 2175 J/kg-K
    rho_NH3_liq     = 696;                  % (kg/m3)   density of liquid
            ammonia at -33ÀöC and 1 atm
    vel_NH3         = 2;                    % (m/s)     flow rate of ammonia
            through pipe to avoid damaging the pipes. Source:
            https://www.engineeringtoolbox.com/flow-velocity-water-pipes-
            d_385.html?web=1&wdLOR=cE8BB49A4-A0D6-2B4B-BDD8-FD6064B353B9
```

```
    kvisc_NH3       = 0.3e-6;               % (m2/s)    kinematic viscosity
            of liquid ammonia at 4 bar and 260 K. Source:
            https://www.engineeringtoolbox.com/ammonia-dynamic-kinematic-
            viscosity-gas-liquid-pressure-temperature-d_2015.html
    Q_solar         = 400;                  % (W/m2)    heat flux arriving on
            Mars surface (average)
% Radiator Pipe
    d_hp_r          = 0.05;                 % (m)       diameter of heat pipe
            in radiator
    mdot_NH3 = rho_NH3_liq*vel_NH3*pi*(d_hp_r/2)^2;     % (kg/s)    .003 mass
            flow of NH3 coolant in radiator loop
    n_heat_pipes    = 5;                    % ( )       number of heat pipes
            in the radiator
    rho_piping      = 8960;                 % (kg/m3)   density of copper
            pipes in the radiator
% Radiator Fins
    rho_cc_fins     = 2000;                 % (kg/m3)   density of carbon-
            carbon composite grid fins for radiator
    t_radiator      = .01;                  % (m)       thickness of radiator
            fins

%PRESSURE LOSS (CONNECTING FLOW)
R_CO2           = 188.92;                   % (J/kg-K)  source:
            https://www.engineeringtoolbox.com/individual-universal-gas-
            constant-d_588.html
R_O2            = 259.84;                   % (J/kg-K)  source:
            https://www.engineeringtoolbox.com/individual-universal-gas-
            constant-d_588.html
R_excess        = (188.92+296.84)/2;        % (J/kg-K)  R for a 50/50 mixed
            stream of CO/CO2. source:

%CONSTANTS
R               = 8.3145;                   % (J/mol-K) gas constant
F               = 96485.332;                % (C/mol)   Faraday constant

sim Mars_ISRU_Plant_Optimization_Model_v44;

%--------- Display Constraints ---------%

disp(' ');
disp(' ');
disp(' ');
disp('Constraints and associated variable values displayed below.');
disp(' ');

%First set up a vector that tells us which constraints, if any, are
%violated.
n_C = 6;                                    % Number of constraints
C = zeros(n_C,1);                           % Create a zeros vector that
            will store if each constraint is satisfied (1) or violated (0)
C(1) = mdot_O2 > O2_prod_rate;              % Outputs 1 if inequality is
            true, 0 if false. Stores that in the C vector.
C(2) = P5 > 8500;                           % Constraint #2 verification
            (stores 0 if false, 1 if true)
C(3) = V_Nernst < V_app < V_Nernst_C;       % Constraint #3
C(4) = V_Nernst < V_Nernst_C;               % Constraint #4
C(5) = U < 1 && U > 0;                      % Constraint #5
```

```
C(6) = Total_Reliability > 0.80;                % Constraint #6

% Now display the results in black text if constraint was met, and orange
            text if violated
if C(1) == 0
    fprintf(['[\bC1. mdot_O2:       ',num2str(mdot_O2),' kg/hr   !>
            O2_prod_rate: ',num2str(O2_prod_rate),' kg/hr]\b\n']);  %The
            produced oxygen flow rate has to meet or exceed the required
            oxygen production rate
else
    fprintf(['C1. mdot_O2:       ',num2str(mdot_O2),' kg/hr   >
            O2_prod_rate: ',num2str(O2_prod_rate),' kg/hr\n']);  %The
            produced oxygen flow rate has to meet or exceed the required
            oxygen production rate
end
if C(2) == 0
    fprintf(['[\bC2. P5:            ',num2str(P5),' Pa  !>  8500 Pa]\b\n']);
            %P5 has to be higher than the lowest pressure at which SOE can
            function
else
    fprintf(['C2. P5:            ',num2str(P5),' Pa  >  8500 Pa\n']);  %P5
            has to be higher than the lowest pressure at which SOE can
            function
end
if C(3) == 0
    fprintf(['[\bC3. V_Nernst_CO:   ',num2str(V_Nernst),' V      !<  V_app:
            ',num2str(V_app),' V !< V_Nernst_C: ',num2str(V_Nernst_C),'
            V]\b\n']);  %To make oxygen and avoid coking, the applied voltage
            must be more than the nernst potential for CO formation but less
            than the nernst potential for carbon formation
else
    fprintf(['C3. V_Nernst_CO:   ',num2str(V_Nernst),' V      <  V_app:
            ',num2str(V_app),' V < V_Nernst_C: ',num2str(V_Nernst_C),'
            V\n']);  %To make oxygen and avoid coking, the applied voltage
            must be more than the nernst potential for CO formation but less
            than the nernst potential for carbon formation
end
if C(4) == 0
    fprintf(['[\bC4. V_Nernst_CO:   ',num2str(V_Nernst),' V       !<
            V_Nernst_C: ',num2str(V_Nernst_C),' V]\b\n']);  %Utilization
            fraction must be controlled to ensure we do not surpass the
            Boudouard Boundary, where Vnernst for carbon becomes lower than
            Vnernst for oxygen at all conditions
else
    fprintf(['C4. V_Nernst_CO:   ',num2str(V_Nernst),' V      <  V_Nernst_C:
            ',num2str(V_Nernst_C),' V\n']);  %Utilization fraction must be
            controlled to ensure we do not surpass the Boudouard Boundary,
            where Vnernst for carbon becomes lower than Vnernst for oxygen at
            all conditions
end
if C(5) == 0
    fprintf(['[\bC5. Utilization fraction must be between 0 and 1:
            ',num2str(U),']\b\n']);  %U is a fraction between 0 and 1
else
    fprintf(['C5. Utilization fraction must be between 0 and 1:
            ',num2str(U),'\n']);  %U is a fraction between 0 and 1
end
if C(6) == 0
```

```
    fprintf(['[\bC6. System Reliability: ',num2str(Total_Reliability),'   !>
            0.80]\b\n']);               %The system must have a reliability
            of at least the amount specified here.
else
    fprintf(['C6. System Reliability: ',num2str(Total_Reliability),'   >
            0.80\n']);              %The system must have a reliability of
            at least the amount specified here.
end

%--------- Display Main Output Variables ---------%
disp(' ');
disp('System Objectives Output:');
disp(['Total system power:   ',num2str(round(Total_Power,0)),' W']);
disp(['Total system mass:    ',num2str(round(Total_Mass,0)),'  kg']);
disp(['Total system volume:  ',num2str(round(Total_Volume,0)),'    m^3']);
disp(['Total system reliability: ',num2str(Total_Reliability)]);
disp(['Total O2 produced:    ',num2str(round(Total_O2,0)),' kg']);

%Take into account constraints using exterior penalty function method
%We only have equality constraints (care about g(x) which are violated at x)
rhoP = 1e20; %penalty parameter
    %If rhoP is small, phi is easy to minimize but yields large constraint
    %violations
    %If rhoP is large, constraints are all nearly satisfied but
    %optimization problem is numerically ill-conditioned

%First constraint: mdot_O2 (O2 production rate) >= O2_prod_rate (required
%O2 production rate)
g1 = min(mdot_O2-O2_prod_rate,0); %take the lesser of the difference of O2
            production and 0

%Second constraint: P5 >= (100 mbar = 10000 Pa) else SOE may not work
P5min = 8500; %[Pa]
g2 = min(P5-P5min,0);

%Third constraint: V_app for each cell cannot exceed the Nernst potential
%for CO -> C formation at a given U (V_app/Ncells < Vnernst_C)
N_cells = N_cps*N_stacks;
g3 = max(((V_app-V_act*N_cells)/N_cells)-V_Nernst_C,0);

%Fourth constraint: minimize utilization fraction (VnernstCO2<VnernstCO)
g4 = max(V_Nernst-V_Nernst_C,0);

%Fifth constraint: make sure that utilization fraction is < 1
max_utilization = 1;
g5 = max(U-max_utilization,0);

%Sixth constraint: make sure that utilization fraction is > 0
min_utilization = 0;
g6 = min(U-min_utilization,0);

%Seventh constraint: make sure that System Reliability is >
            Total_Reliability_1
Total_Reliability_1 = 0.80;
g7 = min(Total_Reliability - Total_Reliability_1,0);
```

```
%Construct a quadratic penalty function: P
penalty_fun = g1^2 + g2^2 + g3^2 + g4^2 + g5^2 + g6^2 + g7^2;
g = [g1 g2 g3 g4 g5 g6 g7];

%Save workspace outputs as .mat file
save('SimulationOutputs');        %Saves the entire workspace as a .mat file
            for later review

%%%%%%%%%%%%%%%SENSITIVITY STUDY - SAVE DATA OF RELEVANCE%%%%%%%%%%%%%%%%%%
Power = Total_Power;
Mass = Total_Mass;
Reliability = Total_Reliability;
Volume = Total_Volume;

if penalty_fun > 0
    violation = "Y";
    ind = find(g~=0);    %Find values in g where g does not equal 0, aka
            which constraints were violated
else
    violation = "N";
    ind = 0;
end

if record_on == 1
    data =
            {Label,violation,num2str(ind),Power,Mass,Op_months,Reliability,R_
            PS,R_CAC,R_SOE,R_Liq,R_HE,Volume,mdot_in,P2,CAC,A_cell,N_cps,N_st
            acks,T6,P6,V_app,A_HE1,A_HE2,N_CAC,t_liq_pipe_ins,t_liq_MAV_ins,t
            _ins_pipe,t_SOE_ins1,t_SOE_ins2,Blower_numSpareUnits,Cryocooler_n
            umSpareUnits,Valve_numSpareUnits,CACmechanical_numSpareUnits,SOEC
            ell_numSpareUnits,SOEStack_numSpareUnits,Kilopower_numSpareUnits,
            Heatexchanger_numSpareUnits};
    header = {'Label','Violation?', 'Constraint(s) Violated', 'Power',
            'Mass', 'Reliability', 'Volume', 'mdot_in', 'P2', 'CAC',
            'A_cell', 'N_cps', 'N_stacks', 'T6', 'P6', 'V_app', 'A_HE1',
            'A_HE2', 'N_CAC', 't_liq_pipe_ins', 't_liq_MAV_ins',
            't_ins_pipe', 't_SOE_ins1', 't_SOE_ins2', 'Blower_numSpareUnits',
            'Cryocooler_numSpareUnits', 'Valve_numSpareUnits',
            'CACmechanical_numSpareUnits', 'SOECell_numSpareUnits',
            'SOEStack_numSpareUnits', 'Kilopower_numSpareUnits',
            'Heatexchanger_numSpareUnits'};
    filename = strcat('SensitivityStudyIIResults.xlsx');
    writecell(data,filename,'WriteMode','append'); %Exports csv file with ID,
            power, mass, and design variables for each successful iteration
else
end
```

D.2 Simulated Annealing Code

The Simulated Annealing code is a package from Mathworks that was used in an unmodified form for this dissertation.

```
function [xbest,Ebest,xhist]=SA(xo,file_eval,file_perturb,options);
% [xbest,Ebest,xhist]=SA(xo,file_eval,file_perturb,options);
%
% Single Objective Simulated Annealing (SA) Algorithm
%
```

```
% This function is a generic implementation of the single objective
% Simulated Annealing (SA) algorithm first proposed by Kirkpatrick,
% Gelatt and Vecchi. The algorithm tries to improve upon an initial
% configuration, xo, by evaluating perturbed configurations. When the
% system reaches the "frozen" state, the algorithm stops and the best
% configuration and search history are returned. The user can choose
% from one of two cooling schedules: linear or exponential.
%
% Input:
% xo            initial configuration of the system (a row vector)
% file_eval     file name (character string) of configuration evaluator;
%               assumes that E='file_eval'(x) is a legitimate function
%               call; set up function such that (scalar) output E will be
%               minimized.
% file_perturb file name (character string) of configuration perturbator;
%               assumes that xp='fname_perturb'(x) is a legitimate function
%               call. This function creates a "neighboring" configuration.
% options       algorithm option flags. Uses defaults, [ ], if left blank
%    (1)        To - initial system temperature - automatically determined if
%               left blank ([]). To should be set such that the expression
%               exp(-E(xo)/To)>0.99 is true, i.e. the initial system is
            "melted"
%    (2)        Cooling Schedule: linear=1, exponential=[2]
%    (3)        dT Temp. increment, e.g. [dT=0.9] for exp. cooling Tk=dT^k*To,
%               abs. temperature increment for linear cooling (Tk+1=Tk-dT);
%    (4)        neq = equilibrium condition, e.g. number of rearrangements
%               attempted to reach equilibrium at a given temperature, neq=[5]
%    (5)        frozen condition - sets up SA exit criterion
%               nfrozen = non-integer, e.g. 0.1 SA interprets this numbers as
            Tmin,
%               the minimum temperature below which the system is frozen.
%               nfrozen = integer ,e.g. 1,2..  SA interprets this as # of
            successive
%               temperatures for which the number of desired acceptances
            defined
%               under options(4) is not achieved, default: nfrozen=[3]
%    (6)        set to 1 to display diagnostic messages (=[1])
%    (7)        set to 1 to plot progress during annealing (=[0])
%
% Output:
% xbest         Best configuration(s) found during execution - row vector(s)
% Ebest         Energy of best configuration(s) (lowest energy state(s) found)
% xhist         structure containing the convergence history
%   .iter       Iteration number (number of times file_eval was called)
%   .x          current configuration at that iteration
%   .E          current system energy at that iteration
%   .T          current system temperature at that iteration
%   .k          temperature step index k
%   .C          specific heat at the k-th temperature
%   .S          entropy at the k-th temperature
%   .Tnow       temperature at the k-th temperature step
%
% User Manual (article):   SA.pdf
%
% Demos:          SAdemo0 - four atom placement problem
%                 SAdemo1 - demo of SA on MATLAB peaks function
%                 SAdemo2 - demo of SA for Travelling Salesman Problem (TSP)
%                 SAdemo3 - demo of SA for structural topology optimization
```

```
%                SAdemo4 - demo of SA for telescope array placement problem
%
% dWo,(c)  MIT 2004
%
% Ref: Kirkpatrick, S., Gelatt Jr., C.D. and Vecchi, M.P., "Optimization
% by Simulated Annealing", Science, Vol. 220, Number 4598, pp. 671-680, May
% 1983


%check input
if ~isempty(options)
    To=options(1);
    schedule=options(2);
    dT=options(3);
    neq=options(4);
    nfrozen=options(5);
    diagnostics=options(6);
    plotflag=options(7);
else
    % set all options to default
    % To - set initial system temperature
    eval(['Eo=' file_eval '(xo);']);
    To=abs(-Eo/log(0.99));   % set initial temperature such that probablility
            of
    % accepting an inferior solution is initially equal to 0.99
    schedule=2;
    dT=0.9;   % this is the ratio dT=(T_i+1/T_i) for geometrical cooling
    neq=5;   % number of rearrangements accepted at a given T
    nfrozen=3;  % if neq hasn't been reached at nfrozen successive
    % temperatures the system is considered frozen and the SA exits
    diagnostics=1; % display messages
    plotflag=0; %plot convergence
end
%
nmax=neq*round(sqrt(max(size(xo)))); % nmax - maximum number of steps at one
            temperature, while
%                                       trying to establish thermal
            equilibrium
%
if nfrozen==round(nfrozen)
    % nfrozen is integer - look for nfrozen successive temperatures without
    % neq acceptances
    Tmin=0;
else
    Tmin=nfrozen; nfrozen=3;
end



% Step 1 - Show initial configuration
if diagnostics==1
disp('Initial configuration: ')
xo
end

% Step 2 - Evaluate initial configuration
eval(['Eo=' file_eval '(xo);']);
```

```
counter=1;
xnow=xo; Enow=Eo; nnow=1;
xhist(nnow).iter=counter;

xhist(nnow).x=xo;
xhist(nnow).E=Enow;
xhist(nnow).T=To;
%  still need to add .S         current entropy at that iteration
xbest=xnow;
Ebest=Enow;
Tnow=To;
if diagnostics==1
    disp(['Energy of initial configuration Eo: ' num2str(Eo)])
end

if plotflag
    figure(99)
    plot(counter,Enow,'k*');
    hold on
    plot(counter,Enow,'mo')
    xlabel('Iteration Number')
    ylabel('System Energy')
    legend('current configuration','new best configuration')
    title('SA convergence history')
    lastbest=counter;
    drawnow
end

frozen=0;  % exit flag for SA
naccept=1; % number of accepted configurations since last temperature change
Tlast=1;   % counter index of last temperature change
k=1;       % first temperature step
ET=[];     % vector of energies at constant system temperature

% start annealing
while (frozen<nfrozen)&(Tnow>Tmin)

%Step 3 - Perturb xnow to obtain a neighboring solution

if diagnostics
    disp(['Counter: ' num2str(counter) ' Temp: ' num2str(Tnow) ' Perturbing
            configuration'])
end

eval(['xp=' file_perturb '(xnow);']);

%Step 4 - Evaluate perturbed solution
eval(['Ep=' file_eval '(xp);'])
counter=counter+1;

%Step 5 - Metropolis Step

dE=Ep-Enow; % difference in system energy
PdE=exp(-dE/Tnow);
if diagnostics
```

```
    disp(['Counter: ' num2str(counter) ' Temp: ' num2str(Tnow) ' P(dE)= '
            num2str(PdE)])
end

%Step 6 - Acceptance of new solution
if dE<=0 % energy of perturbed solution is lower , automatically accept
    nnow=nnow+1;
    xnow=xp; Enow=Ep;
    xhist(nnow).iter=counter;
    xhist(nnow).x=xp;
    xhist(nnow).E=Ep;
    xhist(nnow).T=Tnow;
    naccept=naccept+1;
   if diagnostics
   disp(['Counter: ' num2str(counter) ' Temp: ' num2str(Tnow)  '
            Automatically accept better configuration (downhill)'])
   end

else
   % energy of perturbed configuration is higher, but might still accept it
   randomnumber01=rand;
    if PdE>randomnumber01
        nnow=nnow+1;
        xnow=xp; Enow=Ep;
        xhist(nnow).iter=counter;
        xhist(nnow).x=xp;
        xhist(nnow).E=Ep;
        xhist(nnow).T=Tnow;
      if diagnostics
       disp(['Counter: ' num2str(counter) ' Temp: ' num2str(Tnow)  ' Accepted
            inferior configuration (uphill)'])
      end

    else
        % keep current configuration
        xnow=xnow;
        Enow=Enow;
      if diagnostics
       disp(['Counter: ' num2str(counter) ' Temp: ' num2str(Tnow)  ' Kept the
            current configuration'])
      end
    end
end
       ET=[ET; Enow];
       if plotflag
       figure(99)
       plot(counter,Enow,'k*');
       drawnow
       end


if Enow<Ebest
    % found a new 'best' configuration
    Ebestlast=Ebest;
    Ebest=Enow;
    xbest=xnow;
    if diagnostics
```

```
        disp(['Counter: ' num2str(counter) ' Temp: ' num2str(Tnow)  ' This is
             a new best configuration'])
    end
    if plotflag
        figure(99)
        plot(counter,Enow,'mo');
        plot([lastbest counter],[Ebestlast Enow],'m-');
        lastbest=counter;
        drawnow
    end
elseif Enow==Ebest
    same=0;
    for ib=1:size(xbest,1)
        if xbest(ib,:)==xnow
             if diagnostics
          disp(['Counter: ' num2str(counter) ' Temp: ' num2str(Tnow)  ' Found
            same best configuration'])
             end
        same=1;
        end
    end

     if same ==0
       Ebestlast=Ebest;
       Ebest=Enow;
       xbest=[xbest ; xnow];
        if diagnostics
          disp(['Counter: ' num2str(counter) ' Temp: ' num2str(Tnow)  ' Found
            another best configuration'])
        end
      if plotflag
       figure(99)
       plot(counter,Enow,'mo');
       plot([lastbest counter],[Ebestlast Enow],'m-');
       lastbest=counter;
       drawnow
      end
    end
end

%Step 7 - Adjust system temperature
Told=Tnow;
if (naccept<neq)&(counter-Tlast)<nmax
    if diagnostics
       disp(['Counter: ' num2str(counter) ' Temp: ' num2str(Tnow)  ' Need to
            reach equilibrium at this temperature'])
    end
    % continue at the same system temperature
elseif (naccept<neq)&(counter-Tlast)>=nmax
    if diagnostics
       disp(['Counter: ' num2str(counter) ' Temp: ' num2str(Tnow)  ' System
            nearly frozen'])
    end

    Eavg=mean(ET);
    Evar=mean(ET.^2);
    C=(Evar-Eavg^2)/Tnow^2;     % specific heat
    S=log(nmax*length(unique(ET))/length(ET));
```

```
    xhist(k).k=k;
    xhist(k).C=C;
    xhist(k).S=S;
    xhist(k).Tnow=Tnow;


    frozen=frozen+1;
    Tlast=counter;
    naccept=0;


    switch schedule
        case 1
            % linear cooling
            Tnow=Tnow-dT;
              if Tnow<0
                  frozen=nfrozen; %system temperature cannot go negative,
            exit
              end
        case 2
            % exponential cooling
              Tnow=dT*Tnow;
        case 3
              Tindex=Tindex+1;
              if Tindex>size(Tuser,1)
                  frozen=nfrozen; % have run through entire user supplied
            cooling schedule
              else
              Tnow=Tuser(Tindex,1);
              neq=Tuser(Tindex,2);
              end
        otherwise
              disp('Erroneous cooling schedule choice - option(2) - illegal')
    end


    k=k+1;

   if plotflag
    figure(98)
    hist(ET); Nh=hist(ET); Nh=max(Nh);
    hold on
    plot([Eavg Eavg]',[0 Nh+1],'k--')
    text(Eavg, Nh+1, ['T=' num2str(Told,2)])
    xlabel('Energy')
    ylabel('Occurences')
    drawnow
  end
    ET=[];

 elseif (naccept==neq)
    if diagnostics
       disp(['Counter: ' num2str(counter) ' Temp: ' num2str(Tnow)  ' System
            reached equilibrium'])
    end
```

```
    Eavg=mean(ET);
    Evar=mean(ET.^2);
    C=(Evar-Eavg^2)/Tnow^2;      % specific heat
    S=log(nmax*length(unique(ET))/length(ET));
    xhist(k).k=k;
    xhist(k).C=C;
    xhist(k).S=S;
    xhist(k).Tnow=Tnow;


    Tlast=counter;
    naccept=0;

    switch schedule
        case 1
            % linear cooling
            Tnow=Tnow-dT;
              if Tnow<0
                  frozen=nfrozen; %system temperature cannot go negative,
            exit
              end
        case 2
            % exponential cooling
              Tnow=dT*Tnow;
        case 3
            % user supplied cooling
              Tindex=Tindex+1;
              if Tindex>size(Tuser,1)
                  frozen=nfrozen; %have run through entire user supplied
            cooling schedule
              else
              Tnow=Tuser(Tindex,1);
              neq=Tuser(Tindex,2);
              end

        otherwise
              disp('Erroneous cooling schedule choice - option(2) - illegal')
    end


     k=k+1;

  if plotflag
        figure(98)
    hist(ET); Nh=hist(ET); Nh=max(Nh);
    hold on
    plot([Eavg Eavg]',[0 Nh+1],'k--')
    text(Eavg, Nh+1, ['T=' num2str(Told,2)])
    xlabel('Energy')
    ylabel('Occurences')
    drawnow
end

  ET=[];
 end
```

```
end %while (frozen<nfrozen)&(Tnow>tmin)

% Reached end of SA
 if plotflag
       figure(97)
       k=k-1;
       for ind=1:k
           S(ind)=xhist(ind).S;
           C(ind)=xhist(ind).C;
           Tnow(ind)=xhist(ind).Tnow;
       end

           plot([1:k],C,'bo')
           hold on
           plot([1:k],S,'ms')
           plot([1:k],log(Tnow),'kd')
           legend('C-specific heat','S-entropy','ln(T)-temperature')
           xlabel('Temperature Step')
           title('Simulated Annealing Evolution')
           plot([1:k],C,'b-')
           plot([1:k],S,'m-')
           plot([1:k],log(Tnow),'k-')

           drawnow

  end

    if diagnostics
       disp(['Counter: ' num2str(counter) ' Temp: ' num2str(Tnow)  ' System
            frozen, SA ended'])
       disp(['Best configuration: '])
       xbest
       disp(['Lowest System Energy: ' num2str(Ebest) ])
    end
```

D.3 Perturbation Function

The perturbation function determines how each design variable is adjusted between simulations during a Simulated Annealing optimization.

```
function [xnext] = perturbMOXIE(xi)

%VERSION II
% This version only perturbs 3 design variables at a time. This will make
% for a much more orderly simulated annealing optimization.

%There are 12 primary design variables:
mdot_in     = xi(1);    %continuous
P2          = xi(2);    %continuous
CAC         = xi(3);    %discrete
A_cell      = xi(4);    %continuous
N_cps       = xi(5);    %integer
N_stacks    = xi(6);    %integer
T6          = xi(7);    %continuous
P6          = xi(8);    %continuous
V_app       = xi(9);    %continuous
```

```
A_HE1       = xi(10);   %continuous
A_HE2       = xi(11);   %continuous
N_CAC       = xi(12);   %integer

%There are also secondary design variables:
t_liq_pipe_ins  = xi(13);    %continuous
t_liq_MAV_ins   = xi(14);    %continuous
t_ins_pipe      = xi(15);    %continuous
t_SOE_ins1      = xi(16);    %continuous
t_SOE_ins2      = xi(17);    %continuous

Blower_numSpareUnits =          xi(18);    %integer
Cryocooler_numSpareUnits =      xi(19);    %integer
Valve_numSpareUnits =           xi(20);    %integer
CACmechanical_numSpareUnits =   xi(21);    %integer
SOECell_numSpareUnits =         xi(22);    %integer
SOEStack_numSpareUnits =        xi(23);    %integer
Kilopower_numSpareUnits =       xi(24);    %integer
Heatexchanger_numSpareUnits =   xi(25);    %integer

%% ------------------------LOGIC TO SELECT VARIABLES-----------------------
%To change the # of variables perturbed, just add or delete extra elements
%to the xp array. The rest of the code should function with changes.
xp(1) = randi(length(xi));    %Randomly select an integer from 1 to the # of
            design variables we have
xp(2) = randi(length(xi));    %Randomly select an integer from 1 to the # of
            design variables we have
xp(3) = randi(length(xi));    %Randomly select an integer from 1 to the # of
            design variables we have
xp                            %Array with the three random integers. These
            are the three variables that will be perturbed.

%% ------------------------CONTINUOUS VARIABLES-----------------------
%Perturb the continuous variables and check that they are within the defined
            ranges
%Create random variable in range [-mdot_in/2, mdot_in/2] and add it to
            current mdot_in

if ismember(1,xp) == 1                                  %Checks if mdot_in is one
            of the variables that should be randomly perturbed this
            simulation. If it is, perturb it, else, skip it.
    disp('mdot_in perturbed')
    coeff_1 = 2*rand()-1;                               %Randomly chooses a
            number between -1 and 1, which we use as a coefficient
    frac_1 = 0.2;                                       %The max fractional
            change that we want to impose on this variable. If 0.05, it will
            be changed by up to +/-5% with each iteration.
    mdot_in_new = mdot_in + mdot_in*frac_1*coeff_1; %Calculates the next
            iteration of this variable. It will decrease or increase by up to
            frac*100%.
    %Check that mdot_in_new lies within mdot_in range: [4 100]
    if (mdot_in_new < 4)
        mdot_in_new = 4;
    elseif (mdot_in_new > 100)
        mdot_in_new = 100;
    end
else
```

```
    mdot_in_new = mdot_in;                          %If this variable was not
            selected to be perturbed this round, keep it at its old value.
end

%Create random variable in range [-P2/2, P2/2] and add it to current P2
if ismember(2,xp) == 1
    disp('P2 perturbed')
    coeff_2 = 2*rand()-1;                           %Randomly chooses a number
            between -1 and 1, which we use as a coefficient
    frac_2 = 0.2;                                   %The max fractional change
            that we want to impose on this variable. If 0.05, it will be
            changed by up to +/-5% with each iteration.
    P2_new = P2 + P2*frac_2*coeff_2;                %Calculates the next
            iteration of this variable. It will decrease or increase by up to
            frac*100%.
    %Check that P2 lies within P2 range: [13300 100000]
    if (P2_new < 13300)                             %COULD EVENTUALLY TURN ALL
            THESE IF STATEMENTS INTO CONSTRAINTS
        P2_new = 13300;
    elseif (P2_new > 100000)
        P2_new = 100000;
    end
else
    P2_new = P2;
end

%Create random variable in range [-A_cell/2, A_cell/2] and add it to current
            A_cell
if ismember(4,xp) == 1
    disp('A_cell perturbed')
    coeff_3 = 2*rand()-1;                           %Randomly chooses a number
            between -1 and 1, which we use as a coefficient
    frac_3 = 0.2;                                   %The max fractional change
            that we want to impose on this variable. If 0.05, it will be
            changed by up to +/-5% with each iteration.
    A_cell_new = A_cell + A_cell*frac_3*coeff_3; %Calculates the next
            iteration of this variable. It will decrease or increase by up to
            frac*100%.
    %Check that A_cell_new lies within A_cell range: [22.5 111]
    if (A_cell_new < 22.5)
        A_cell_new = 22.5;
    elseif (A_cell_new > 111)
        A_cell_new = 111;           %rand = 1, T6 = 1000, so dT6 = 100 - 50 =
            50. (5%). rand = 0, dT6 = -5%.
    end
else
    A_cell_new = A_cell;
end

%Create random variable in range [-T6/2, T6/2] and add it to current T6
if ismember(7,xp) == 1
    disp('T6')
    coeff_4 = 60*rand()-30;                         %Randomly chooses a number
            between -30 and 30, which we use as a coefficient
    T6_new = T6 + coeff_4;                          %Calculates the next
            iteration of this variable.
    %Check that T6_new lies within T6 range: [1023 1123]
    if (T6_new < 1023)
```

```
        T6_new = 1023;
    elseif (T6_new > 1123)
        T6_new = 1123;
    end
else
    T6_new = T6;
end

%Create random variable in range [-P6/2, P6/2] and add it to current P6
if ismember(8,xp) == 1
    disp('P6 perturbed')
    coeff_5 = 2*rand()-1;                          %Randomly chooses a number
            between -1 and 1, which we use as a coefficient
    frac_5 = 0.2;                                  %The max fractional change
            that we want to impose on this variable. If 0.05, it will be
            changed by up to +/-5% with each iteration.
    P6_new = P6 + P6*frac_5*coeff_5;               %Calculates the next
            iteration of this variable. It will decrease or increase by up to
            frac*100%.
    %Check that P6_new lies within P6 range: [5000 200000]
    if (P6_new < 5000)
        P6_new = 5000;
    elseif (P6_new > 200000)
        P6_new = 200000;
    end
else
    P6_new = P6;
end

%Create random variable in range [-V_app/2, V_app/2] and add it to current
            V_app
if ismember(9,xp) == 1
    disp('V_app')
    coeff_6 = 2*rand()-1;                           %Randomly chooses a number
            between -1 and 1, which we use as a coefficient
    frac_6 = 0.05;                                  %The max fractional change
            that we want to impose on this variable.
    V_app_new = V_app + frac_6*coeff_6;    %Calculates the next iteration of
            this variable. It will decrease or increase by up to frac*100%.
    %Check that V_app_new lies within V_app range: [0.8 1.04]
    if (V_app_new < 0.8)
        V_app_new = 0.8;
    elseif (V_app_new > 1.04)
        V_app_new = 1.04;
    end
else
    V_app_new = V_app;
end

%Create random variable in range [-A_HE1/2, A_HE1/2] and add it to current
            A_HE1
if ismember(10,xp) == 1
    disp('A_HE1 perturbed')
    coeff_7 = 2*rand()-1;                          %Randomly chooses a number
            between -1 and 1, which we use as a coefficient
    frac_7 = 0.4;                                  %The max fractional change
            that we want to impose on this variable. If 0.05, it will be
            changed by up to +/-5% with each iteration.
```

```
    A_HE1_new = A_HE1 + A_HE1*frac_7*coeff_7;             %Calculates the
            next iteration of this variable. It will decrease or increase by
            up to frac*100%.
    %Check that A_HE1 lies within A_HE1 range: [0 10]
    if (A_HE1_new < 0)                                    %physical minimum constraint
            on min surface area of Heat Exchanger
        A_HE1_new = 0;
    elseif (A_HE1_new > 10)                              %physical max constraint on
            surface area of Heat Exchanger
        A_HE1_new = 10;
    end
else
    A_HE1_new = A_HE1;
end

%Create random variable in range [-A_HE2/2, A_HE2/2] and add it to current
            A_HE2
if ismember(11,xp) == 1
    disp('A_HE2 perturbed')
    coeff_8 = 2*rand()-1;                                 %Randomly chooses a number
            between -1 and 1, which we use as a coefficient
    frac_8 = 0.4;                                         %The max fractional change
            that we want to impose on this variable. If 0.05, it will be
            changed by up to +/-5% with each iteration.
    A_HE2_new = A_HE2 + A_HE2*frac_8*coeff_8;             %Calculates the
            next iteration of this variable. It will decrease or increase by
            up to frac*100%.
    %Check that A_HE2 lies within A_HE2 range: [0 10]
    if (A_HE2_new < 0)                                    %physical minimum constraint
            on min surface area of Heat Exchanger
        A_HE2_new = 0;
    elseif (A_HE2_new > 10)                              %physical max constraint on
            surface area of Heat Exchanger
        A_HE2_new = 10;
    end
else
    A_HE2_new = A_HE2;
end

%Create random variable in range [-t_liq_pipe_ins/2, t_liq_pipe_ins/2] and
            add it to current t_liq_pipe_ins
if ismember(13,xp) == 1
    disp('t_liq_pipe_ins perturbed')
    coeff_14 = 2*rand()-1;                                %Randomly chooses a number
            between -1 and 1, which we use as a coefficient
    frac_14 = 0.04;                                       %The max fractional change
            that we want to impose on this variable. If 0.05, it will be
            changed by up to +/-5% with each iteration.
    t_liq_pipe_ins_new = t_liq_pipe_ins + frac_14*coeff_14;
            %Calculates the next iteration of this variable. It will decrease
            or increase by up to frac*100%.
    %Check that t_liq_pipe_ins lies within t_liq_pipe_ins range: [0 1]
    if (t_liq_pipe_ins_new < 0)                           %physical minimum
            constraint
        t_liq_pipe_ins_new = 0;
    elseif (t_liq_pipe_ins_new > 1)                       %physical max
            constraint
        t_liq_pipe_ins_new = 1;
```

```
    end
else
    t_liq_pipe_ins_new = t_liq_pipe_ins;
end

%Create random variable in range [-t_liq_MAV_ins/2, t_liq_MAV_ins/2] and add
            it to current t_liq_MAV_ins
if ismember(14,xp) == 1
    disp('t_liq_MAV_ins perturbed')
    coeff_15 = 2*rand()-1;                          %Randomly chooses a number
            between -1 and 1, which we use as a coefficient
    frac_15 = 1;                                    %The max fractional change
            that we want to impose on this variable. If 0.05, it will be
            changed by up to +/-5% with each iteration.
    t_liq_MAV_ins_new = t_liq_MAV_ins + frac_15*coeff_15;
            %Calculates the next iteration of this variable. It will decrease
            or increase by up to frac*100%.
    %Check that t_liq_MAV_ins lies within t_liq_MAV_ins range: [0 0.5]
    if (t_liq_MAV_ins_new < 0)                       %Physical minimum
            constraint
        t_liq_MAV_ins_new = 0;
    elseif (t_liq_MAV_ins_new > 0.5)                  %Physical max constraint
        t_liq_MAV_ins_new = 0.5;
    end
else
    t_liq_MAV_ins_new = t_liq_MAV_ins;
end

%Create random variable in range [-t_ins_pipe/2, t_ins_pipe/2] and add it to
            current t_ins_pipe
if ismember(15,xp) == 1
    disp('t_ins_pipe perturbed')
    coeff_16 = 2*rand()-1;                          %Randomly chooses a number
            between -1 and 1, which we use as a coefficient
    frac_16 = 0.05;                                  %The max fractional change
            that we want to impose on this variable. If 0.05, it will be
            changed by up to +/-5% with each iteration.
    t_ins_pipe_new = t_ins_pipe + frac_16*coeff_16;             %Calculates
            the next iteration of this variable. It will decrease or increase
            by up to frac*100%.
    %Check that t_ins_pipe lies within t_ins_pipe range: [0 1]
    if (t_ins_pipe_new < 0)                          %physical minimum
            constraint
        t_ins_pipe_new = 0;
    elseif (t_ins_pipe_new > 1)                      %physical max constraint
        t_ins_pipe_new = 1;
    end
else
    t_ins_pipe_new = t_ins_pipe;
end

%Create random variable in range [-t_SOE_ins1/2, t_SOE_ins1/2] and add it to
            current t_SOE_ins1
if ismember(16,xp) == 1
    disp('t_SOE_ins1 perturbed')
    coeff_17 = 2*rand()-1;                          %Randomly chooses a number
            between -1 and 1, which we use as a coefficient
```

```
    frac_17 = 0.06;                                 %The max fractional change
            that we want to impose on this variable. If 0.05, it will be
            changed by up to +/-5% with each iteration.
    t_SOE_ins1_new = t_SOE_ins1 + frac_17*coeff_17;             %Calculates
            the next iteration of this variable. It will decrease or increase
            by up to frac*100%.
    %Check that t_SOE_ins1 lies within t_SOE_ins1 range: [0 1]
    if (t_SOE_ins1_new < 0)                           %physical minimum
            constraint
        t_SOE_ins1_new = 0;
    elseif (t_SOE_ins1_new > 1)                     %physical max constraint
        t_SOE_ins1_new = 1;
    end
else
    t_SOE_ins1_new = t_SOE_ins1;
end

%Create random variable in range [-t_SOE_ins2/2, t_SOE_ins2/2] and add it to
            current t_SOE_ins2
if ismember(17,xp) == 1
    disp('t_SOE_ins2 perturbed')
    coeff_18 = 2*rand()-1;                          %Randomly chooses a number
            between -1 and 1, which we use as a coefficient
    frac_18 = 0.06;                                 %The max fractional change
            that we want to impose on this variable. If 0.05, it will be
            changed by up to +/-5% with each iteration.
    t_SOE_ins2_new = t_SOE_ins2 + frac_18*coeff_18;             %Calculates
            the next iteration of this variable. It will decrease or increase
            by up to frac*100%.
    %Check that t_SOE_ins2 lies within t_SOE_ins2 range: [0 1]
    if (t_SOE_ins2_new < 0)                           %physical minimum
            constraint
        t_SOE_ins2_new = 0;
    elseif (t_SOE_ins2_new > 1)                     %physical max constraint
        t_SOE_ins2_new = 1;
    end
else
    t_SOE_ins2_new = t_SOE_ins2;
end


%% ------------------------INTEGER VARIABLES--------------------------
%Next, perturb the integer variables and check that they are
%within the defined ranges, and fix as integers (by rounding)
%N_cps
if ismember(5,xp) == 1
    disp('N_cps perturbed')
    coeff_9 = 2*rand()-1;                           %Randomly chooses a number
            between -1 and 1, which we use as a coefficient
    frac_9 = 0.2;                                   %The max fractional change
            that we want to impose on this variable. If 0.05, it will be
            changed by up to +/-5% with each iteration.
    N_cps_new = N_cps + round(N_cps*frac_9*coeff_9);    %Calculates the next
            iteration of this variable. It will decrease or increase by up to
            frac*100%. Rounded to keep it as an integer.
    %Check that N_cps_new lies within N_cps range: [1 1000]
    if (N_cps_new < 1)
        N_cps_new = 1;
```

```
    elseif (N_cps_new > 1000)
        N_cps_new = 1000;
    end
else
    N_cps_new = N_cps;
end

%N_stacks
if ismember(6,xp) == 1
    disp('N_stacks perturbed')
    coeff_10 = randi(5)-3;                          %Randomly chooses -2, -1,
            0, 1, or 2
    N_stacks_new = N_stacks + coeff_10;             %Calculates the next
            iteration of this variable. It will decrease or increase by up to
            2
    %Check that N_stacks_new lies within N_stacks range: [1 1000]
    if (N_stacks_new < 1)
        N_stacks_new = 1;
    elseif (N_stacks_new > 1000)
        N_stacks_new = 1000;
    end
else
    N_stacks_new = N_stacks;
end

%N_CAC
if ismember(12,xp) == 1
    disp('N_CAC perturbed')
    coeff_12 = randi(5)-3;                          %Randomly chooses -2, -1,
            0, 1, or 2
    N_CAC_new = N_CAC + coeff_12;                   %Calculates the next
            iteration of this variable. It will decrease or increase by up to
            2.
    %Check that N_CAC_new lies within N_CAC range: [1 1000]
    if (N_CAC_new < 1)
        N_CAC_new = 1;
    elseif (N_CAC_new > 1000)
        N_CAC_new = 1000;
    end
else
    N_CAC_new = N_CAC;
end

%Blower_numSpareUnits
if ismember(18,xp) == 1
    disp('Blower_numSpareUnits perturbed')
    coeff_19 = 2*randi(2)-3;                        %Randomly chooses -1 or 1
    Blower_numSpareUnits_new = Blower_numSpareUnits + coeff_19; %Calculates
            the next iteration of this variable. It will decrease or increase
            by 1.
    %Check that Blower_numSpareUnits_new lies within Blower_numSpareUnits
            range: [0 5]
    if (Blower_numSpareUnits_new < 0)
        Blower_numSpareUnits_new = 0;
    elseif (Blower_numSpareUnits_new > 4)
        Blower_numSpareUnits_new = 4;
    end
else
```

```
    Blower_numSpareUnits_new = Blower_numSpareUnits;
end

%Cryocooler_numSpareUnits
if ismember(19,xp) == 1
    disp('Cryocooler_numSpareUnits perturbed')
    coeff_20 = 2*randi(2)-3;                        %Randomly chooses -1 or 1
    Cryocooler_numSpareUnits_new = Cryocooler_numSpareUnits + coeff_20;
            %Calculates the next iteration of this variable. It will decrease
            or increase by 1.
    %Check that Cryocooler_numSpareUnits_new lies within
            Cryocooler_numSpareUnits range: [0 3]
    if (Cryocooler_numSpareUnits_new < 0)
        Cryocooler_numSpareUnits_new = 0;
    elseif (Cryocooler_numSpareUnits_new > 3)
        Cryocooler_numSpareUnits_new = 3;
    end
else
    Cryocooler_numSpareUnits_new = Cryocooler_numSpareUnits;
end

%Valve_numSpareUnits
if ismember(20,xp) == 1
    disp('Valve_numSpareUnits perturbed')
    coeff_21 = randi(5)-3;                          %Randomly chooses -2, -1,
            0, 1, or 2
    Valve_numSpareUnits_new = Valve_numSpareUnits + coeff_21; %Calculates the
            next iteration of this variable. It will decrease or increase by
            up to 2.
    %Check that Valve_numSpareUnits_new lies within Valve_numSpareUnits
            range: [0 20]
    if (Valve_numSpareUnits_new < 0)
        Valve_numSpareUnits_new = 0;
    elseif (Valve_numSpareUnits_new > 20)
        Valve_numSpareUnits_new = 20;
    end
else
    Valve_numSpareUnits_new = Valve_numSpareUnits;
end

%CACmechanical_numSpareUnits
if ismember(21,xp) == 1
    disp('CACmechanical_numSpareUnits perturbed')
    coeff_22 = 2*randi(2)-3;                        %Randomly chooses -1 or 1
    CACmechanical_numSpareUnits_new = CACmechanical_numSpareUnits + coeff_22;
            %Calculates the next iteration of this variable. It will decrease
            or increase by 1.
    %Check that CACmechanical_numSpareUnits_new lies within
            CACmechanical_numSpareUnits range: [0 5]
    if (CACmechanical_numSpareUnits_new < 0)
        CACmechanical_numSpareUnits_new = 0;
    elseif (CACmechanical_numSpareUnits_new > 5)
        CACmechanical_numSpareUnits_new = 5;
    end
else
    CACmechanical_numSpareUnits_new = CACmechanical_numSpareUnits;
end
```

```
%SOECell_numSpareUnits
if ismember(22,xp) == 1
    disp('SOECell_numSpareUnits perturbed')
    coeff_23 = 2*rand()-1;                          %Randomly chooses a number
            between -1 and 1, which we use as a coefficient
    frac_23 = 0.2;                                  %The max fractional change
            that we want to impose on this variable. If 0.05, it will be
            changed by up to +/-5% with each iteration.
    SOECell_numSpareUnits_new = SOECell_numSpareUnits +
            round(SOECell_numSpareUnits*frac_23*coeff_23); %Calculates the
            next iteration of this variable. It will decrease or increase by
            up to frac*100%. Rounded to keep it as an integer.
    %Check that SOECell_numSpareUnits_new lies within SOECell_numSpareUnits
            range: [0 1000]
    if (SOECell_numSpareUnits_new < 0)
        SOECell_numSpareUnits_new = 0;
    elseif (SOECell_numSpareUnits_new > 1000)
        SOECell_numSpareUnits_new = 1000;
    end
else
    SOECell_numSpareUnits_new = SOECell_numSpareUnits;
end

%SOEStack_numSpareUnits
if ismember(23,xp) == 1
    disp('SOEStack_numSpareUnits perturbed')
    coeff_24 = 2*randi(2)-3;                        %Randomly chooses -1 or 1
    SOEStack_numSpareUnits_new = SOEStack_numSpareUnits + coeff_24;
            %Calculates the next iteration of this variable. It will decrease
            or increase by 1.
    %Check that SOEStack_numSpareUnits_new lies within SOEStack_numSpareUnits
            range: [0 10]
    if (SOEStack_numSpareUnits_new < 0)
        SOEStack_numSpareUnits_new = 0;
    elseif (SOEStack_numSpareUnits_new > 10)
        SOEStack_numSpareUnits_new = 10;
    end
else
    SOEStack_numSpareUnits_new = SOEStack_numSpareUnits;
end

%Kilopower_numSpareUnits
if ismember(24,xp) == 1
    disp('Kilopower_numSpareUnits perturbed')
    coeff_26 = 2*randi(2)-3;                        %Randomly chooses -1 or 1
    Kilopower_numSpareUnits_new = Kilopower_numSpareUnits + coeff_26;
            %Calculates the next iteration of this variable. It will decrease
            or increase by 1.
    %Check that Kilopower_numSpareUnits_new lies within
            Kilopower_numSpareUnits range: [0 3]
    if (Kilopower_numSpareUnits_new < 0)
        Kilopower_numSpareUnits_new = 0;
    elseif (Kilopower_numSpareUnits_new > 3)
        Kilopower_numSpareUnits_new = 3;
    end
else
    Kilopower_numSpareUnits_new = Kilopower_numSpareUnits;
```

```
end

%Heatexchanger_numSpareUnits
if ismember(25,xp) == 1
    disp('Heatexchanger_numSpareUnits perturbed')
    coeff_27 = 2*rand()-1;                          %Randomly chooses a number
            between -1 and 1, which we use as a coefficient
    frac_27 = 0.2;                                  %The max fractional change
            that we want to impose on this variable. If 0.05, it will be
            changed by up to +/-5% with each iteration.
    Heatexchanger_numSpareUnits_new = Heatexchanger_numSpareUnits +
            round(Heatexchanger_numSpareUnits*frac_27*coeff_27); %Calculates
            the next iteration of this variable. It will decrease or increase
            by up to frac*100%. Rounded to keep it as an integer.
    %Check that Heatexchanger_numSpareUnits_new lies within
            Heatexchanger_numSpareUnits range: [0 100]
    if (Heatexchanger_numSpareUnits_new < 0)
        Heatexchanger_numSpareUnits_new = 0;
    elseif (Heatexchanger_numSpareUnits_new > 100)
        Heatexchanger_numSpareUnits_new = 100;
    end
else
    Heatexchanger_numSpareUnits_new = Heatexchanger_numSpareUnits;
end


%% ------------------------DISCRETE VARIABLES--------------------------
%Next, choose whether or not to change the discrete variable (CAC)
if ismember(3,xp) == 1
    disp('CAC perturbed')
    random_CAC = randi([1 4],1);        %Randomly selects an integer from 1 to
            4, inclusive, for CAC
    CAC_new = random_CAC;               %Sets the CAC type for the next
            iteration's design vector
else
    CAC_new = CAC;
end

%-------------------------------------------------------------------------
%Define perturbed vector:
xnext = [mdot_in_new, P2_new, CAC_new, A_cell_new, N_cps_new, N_stacks_new,
            ...
    T6_new, P6_new, V_app_new, A_HE1_new, A_HE2_new, N_CAC_new, ...
    t_liq_pipe_ins_new, t_liq_MAV_ins_new, t_ins_pipe_new, t_SOE_ins1_new,
            ...
    t_SOE_ins2_new, Blower_numSpareUnits_new, Cryocooler_numSpareUnits_new,
            ...
    Valve_numSpareUnits_new, CACmechanical_numSpareUnits_new,
            SOECell_numSpareUnits_new, ...
    SOEStack_numSpareUnits_new, Kilopower_numSpareUnits_new,
            Heatexchanger_numSpareUnits_new];

end
```

D.4 Calculate Reliability Function

The calculate reliability function is used to calculate the reliability of each component in BAM.

```
function reliability = calculateReliability(numSpareUnits, totalUnits,
            lambda)
    m = totalUnits - numSpareUnits; % m is the number of running units
    n = totalUnits; % n is the total number of units
    %value = 0;

    a = [0:n-m];
    %for i = 0:n-m % is the redundant units
        numerator = (lambda*m).^a;
            numerator(isinf(numerator)) = 1;    % We run into issues when the
            numerator or denominator equals infinity, as MATLAB does not
            interpret the rest of the calculation correctly. This is a
            workaround.
        denominator = factorial(a);
            denominator(isinf(denominator)) = 1;
        reliability = sum((numerator./denominator)).*exp(-lambda*m);
    %end
    %value = value*exp(-lambda*m);
    % reliability = 1 - value;
end
```

D.5 Radiator Heat Transfer Function

The radiator heat transfer function calculates the heat that must be rejected by the radiator in the liquefaction unit.

```
function heat_rejected =
            rad_heat_trans(d_hp_r,T9,T10,T_root,Q_solar,absorptivity_r,w_fin_
            r,sb,emissivity_r,skytemp,conv_coeff,T_MA,Cp_NH3,mdot_NH3,l_pipe_
            r,n_heat_pipes,rho_NH3_liq,kvisc_NH3)

    % Heat pipe parameters
    circ = d_hp_r*pi();   % surface area (per length) of pipe

    % Flux onto the radiator
    Q_solar_r = Q_solar*absorptivity_r;     % (W/m2) Heat flux absorbed by
            radiator from the sun
    heat_solver = @(x,T) [(Q_solar_r-(circ+2*w_fin_r)*(sb*emissivity_r*(T^4-
            skytemp^4)+conv_coeff*(T-T_MA)))/(Cp_NH3*mdot_NH3)];
    options = odeset('RelTol',1e-6,'AbsTol',1e-6,'MaxStep',.01);
    [~,T] = ode45(heat_solver,[0,l_pipe_r],T_root,options);


    heat_rejected = n_heat_pipes*mdot_NH3*Cp_NH3*(T_root-T(end));
end
```

D.6 Code in Simulink Model

The following sections will list the code used in each subsystem of the BAM Simulink model.

Kilopower

```
function [P_non_el, P_Total, M_PS, V_PS, P_PS] = fcn(P_El, P_CAC, P_SOE,
            P_Liq, ...
```

```
    P_kilopower, m_kilopower, V_kilopower, P_power_regulation, M_kpcable,
            Kilopower_numSpareUnits)

%This function calculates the power, mass, and volume of the Kilopower
%system. It also calculates the total power of the ISRU system, along with
%how many Kilopower units need to be used to achieve that power (assuming
%10 kWe output of each Kilopower unit).

P_Total  = P_El + P_CAC + P_SOE + P_Liq;     % (W)   Total power of the ISRU
            system
P_non_el = P_CAC + P_SOE + P_Liq;            % (W)   This term is used to
            calculate the power of the electronics subsystem. We cannot
            include P_El in this calculation or it creates a run-away
            algebraic loop.

numKiloActive = ceil(P_Total/P_kilopower);   % ( )   # of Kilopower units
            needed to be active at all times to supply enough power for the
            ISRU plant. "ceil" function is used because you can't send a
            fraction of a Kilopower unit.

P_PS     = numKiloActive*P_power_regulation; % (W)   Power consumed by the
            power system itself. Equal to zero because I assume that all
            power regulation and distribution is already included in the mass
            and power numbers for the 10 kWe Kilopower unit. Not confirmed.
M_PS     = (numKiloActive+Kilopower_numSpareUnits)*m_kilopower+M_kpcable; %
            (kg)  Mass of all Kilopower units (active plus spares)
V_PS     = (numKiloActive+Kilopower_numSpareUnits)*V_kilopower; % (kg)  Mass
            of all Kilopower units (active plus spares)
```

CAC

```
function P1f = filterPdrop(P1,deltaP_f)

%This function identifies the pressure drop from the filter. Source:
%Extensibility of MOXIE by D. Rapp.
P1f = P1-deltaP_f;
```

Cryopump

```
function [cryo_blower_power,cryo_blower_mass,cryo_blower_vol] =
            blowercalc(mdot_in,cryo_blower,cryo_blower_eff,blower_spec_mass,b
            lower_spec_vol,cycle_time_cryo,cool_time_cryo)

%Calculates power, mass, and volume of blower fan for cryo system.
%cryo_blower is a J/kg figure that represents the energy needed by a
%typical blower to move one kg of martian gas into the system.
sph = 3600;                                                    % (s)
            Seconds per hour

blower_on_frac = cool_time_cryo/cycle_time_cryo;               % ( )
            Fraction of each pumping cycle that blower is active

cryo_blower_power = cryo_blower*mdot_in/(cryo_blower_eff*sph)*blower_on_frac;
            % (W)   Power draw of blower fan as a function of flow rate
cryo_blower_mass = blower_spec_mass*mdot_in^0.8;     % (kg)  Mass of one
            blower in the system. Uses a scaling law equation since it won't
            scale linearly.
```

```
cryo_blower_vol = blower_spec_vol*mdot_in^0.8;       % (m3)  Volume of one
            blower in the system.


function M_Blower = SparesModifier(M_Blower_active, Blower_numRunningUnits,
            Blower_numSpareUnits)

M_Blower =
            M_Blower_active*(Blower_numRunningUnits+Blower_numSpareUnits)/Blo
            wer_numRunningUnits;

function V_Blower = SparesModifier(V_Blower_active, Blower_numRunningUnits,
            Blower_numSpareUnits)

V_Blower =
            V_Blower_active*(Blower_numRunningUnits+Blower_numSpareUnits)/Blo
            wer_numRunningUnits;


function [P_cryo_CO2_cooling,P_cryo_CO2_deposition,P_CAC_cryo_cooling]=
            frost(cryo_efficiency,
            T1,T_freeze_CO2,H_latent_CO2,mdot_in,Cp1,cool_time_cryo,cycle_tim
            e_cryo)

% This function calculates the power required to cool the incoming CO2 to
% its freezing point and the power for it to solidify into Dry Ice.

sph = 3600;                                              %    Seconds per
            hour

cool_frac = cool_time_cryo/cycle_time_cryo;              % ( ) Fraction of
            each pumping cycle that involves cooling

P_cryo_CO2_cooling = mdot_in*Cp1*(T1-T_freeze_CO2)/sph*cool_frac;   %(W)
            Power required to cool the gas at its incoming temp, T1, to its
            freezing temp, 148 K
P_cryo_CO2_deposition = mdot_in*H_latent_CO2/sph*cool_frac;         %(W)
            Power required to phase change CO2 from gas to solid

P_CAC_cryo_cooling = (P_cryo_CO2_cooling +
            P_cryo_CO2_deposition)/cryo_efficiency;     %(W) Total power to
            cool and deposit CO2 onto cold fins

function P_CAC_cryo_warming =
            defrost(P_cryo_CO2_deposition,T2,T_freeze_CO2,mdot_in,Cp2,heater_
            efficiency,heatloss_efficiency,warm_time_cryo,cycle_time_cryo)

% This function calculates the power required to sublimate the CO2 ice and
% warm it to the required temperature, T2.

sph = 3600;                                              % (sph) Seconds
            per hour

warm_frac = warm_time_cryo/cycle_time_cryo;              % ( ) Fraction of
            each pumping cycle that involves heating
```

```
P_cryo_CO2_deposition;                                          % (W) Power
            required to phase change CO2 from solid to gas
P_cryo_CO2_warming = mdot_in*Cp2*(T2-T_freeze_CO2)/sph*warm_frac;     % (W)
            Power required to warm the newly-sublimated gas to T2. Note that
            as I currently have it modeled, this will be equal to zero
            because the heat input goes towards sublimation, NOT warming the
            gas that is already sublimated. So the gas remains at the
            freezing temperature of CO2.

P_CAC_cryo_warming = (P_cryo_CO2_deposition +
            P_cryo_CO2_warming)/(heater_efficiency*heatloss_efficiency);
            % (W) Total power to cool and deposit CO2 onto cold fins

function [M_CH,M_CC_shell,M_heaters,M_CAC_cryo] = cryoMass(mdot_in, N_CAC)

%This function calculates the mass of the main cryopump body, which
%includes:
%   1. Coldhead
%   2. Cryochamber shell
%   3. Cartridge heaters
%Note that the most significant mass term - that of the cryocooler - is
%calculated in the Liquefaction subsystem, as the cryocooler is shared
%between subsystems.

mdot_s = mdot_in/N_CAC;                                         % (kg/hr) average
            flow rate produced by each cryopump. If you have 2 cryopumps and
            you need 10 kg/hr continuous, each will produce an average of 5
            kg/hr over a long period. Ex: #1 will produce 10 kg/hr for 30
            min, then will go into its freezing phase for 30 min. #2 will
            freeze for 30 min then produce 10 kg/hr for 30 min. So total
            output stays consistent at 10 kg/hr between the two, but each
            only produces an average of 5 kg/hr over an hour.

%Coldhead
ref_CH_mass = 0.34;                                             % (kg)  mass of
            coldhead used in Berg and Shah. Calculated as copper coldhead
            with the stated 2.37 in^3 of volume, producing 1.5 g/min average
            collection. Supports ref_CH_flow amount of CO2.
ref_CH_flow = .09;                                              % (kg/hr) flow rate
            produced by a coldhead in the reference
ex = 0.67;                                                      % ( )     exponent to
            establish scaling law. Chosen somewhat arbitrarily. A value of
            0.67 represents a scaling law of r^3 (volume) over r^2 (area,
            mass, etc.)
M_CH = ref_CH_mass*(mdot_s/ref_CH_flow)^ex;                     % (kg)  mass of
            coldhead used in one cryopump at the flowrate used by each pump.

%Cryochamber Shell
ref_shell_mass = 38;                                            % (kg)  mass of
            cryochamber shell used in Meier et al. Estimated from imagery.
            Assumes 3/16" thick aluminum shell with a radius of 65 cm and
            height of 130 cm. Supports ref_CH_flow amount of CO2. If I wanted
            to be legit, I would calculate shell thickness based on P2 and
            use P2 as an input. Forget flowrate, the only thing it cares
            about is the pressure it will experience, which is P2. That
            involves things like hoop stress though I think.
```

```
ref_shell_flow = 1.1;                                    % (kg/hr) flow rate
            produced by a cryochamber shell in the reference
ex = 0.67;                                               % ( )     exponent to
            establish scaling law. Chosen somewhat arbitrarily. A value of
            0.67 represents a scaling law of r^3 (volume) over r^2 (area,
            mass, etc.)
M_CC_shell = ref_shell_mass*(mdot_s/ref_shell_flow)^ex; % (kg)  mass of
            cryochamber shell used in one cryopump at the flowrate used by
            each pump.

%Cartridge Heaters
ref_heater_mass = 0.5;                                   % (kg)  A 550 W
            cartridge heater has a mass of 0.25 kg (source at end of
            comment). Meier et al. cryocooler required 400 W of cooling, so
            one of these cartridge heaters seems to be in line with what is
            needed per cryocooler. Source:
            https://www.oemheaters.com/product/5196/12-x-7-550w-240v-
            cartridge-
            heater#:~:text=1%2F2%22%20x%207%22%20550W%20240V%20Cartridge%20He
            ater,-SKU%3A%20K330115&text=Weight%3A%200.48%20lb.
ref_heater_flow = 1.1;                                   % (kg/hr) flow rate
            in the reference (Meier et al. 2018)
ex = 0.67;                                               % ( )     exponent to
            establish scaling law. Chosen somewhat arbitrarily. A value of
            0.67 represents a scaling law of r^3 (volume) over r^2 (area,
            mass, etc.)
M_heaters = ref_heater_mass*(mdot_s/ref_heater_flow)^ex;% (kg)  mass of
            cartridge heaters used in one cryopump at the flowrate used by
            each pump.

%Total Masses
M_CAC_cryo_s = M_CH + M_CC_shell + M_heaters;            % (kg)  mass of a
            single cryopump body, excluding cryocooler
M_CAC_cryo = M_CAC_cryo_s*N_CAC;                         % (kg)  mass of all
            cryopumps.

function V_CAC_cryo = cryoVolume(mdot_in, cryo_Volume, N_CAC)

%This function calculates the volume of a cryogenic pumping system for CO2
%acquisition. It is largely based on the design from Meier et al. (2018) at
%NASA.

%A loose approximation will be created to relate inlet mass flow to
%cryocooler volume, as the system will scale with increasing flow.

ref_flowrate = 1.1;                    % (kg/hr) inlet CO2 flow rate of the
            reference cryocooler system (Meier et al. 2018)
ex = 0.67;                             % ( )     exponent to establish scaling
            law. As mdot_in increases, volume will increase sub-linearly
            thanks to economies of scale. This value was picked arbitrarily,
            but with the intent that volume scales with r^3 and mdot scales
            with surface area on the radiator, or r^2. So r^(3/2) = r^1.5, or
            a scaling factor of 1/1.5 = 0.67.
mdot_s = mdot_in/N_CAC;                % (kg/hr) average flow rate produced by
            each cryopump. If you need 10 kg/hr and you have N_CAC = 2
            cryopumps, you need each to produce an average of 5 kg/hr.
```

```
V_CAC_cryo_s = cryo_Volume*(mdot_s/ref_flowrate)^ex;     % (kg)    predicted
            volume of a single cryopump
V_CAC_cryo = V_CAC_cryo_s*N_CAC;                         % (kg)    predicted
            volume of a single cryopump
end


function [cryo_v_power, cryo_v_mass] = fcn(N_CAC, sol_valve_m, check_valve_m,
            sol_valve_p)

% This function calculates the mass and power of the solenoid valves and
% check valves in the cryopump system. It is assumed that each cryopump
% will have three solenoid valves (one on inlet, one on outlet, one on
% exhaust) and one check valve (on outlet, to prevent backflow). Check
% valves do not require power, so only their mass is considered.

cryo_v_power = N_CAC*3*sol_valve_p/2;                    % (W) Power used by
            all solenoid valves in the cryopump system. Divided by 2 because
            only half of the valves are open at any given time. Solenoids
            consume energy when open, but not when closed (in a 'normally-
            closed' valve configuration).
cryo_v_mass = N_CAC*(3*sol_valve_m + 1*check_valve_m); % (kg) Mass of all
            valves in the cryopump system
end


function P_CAC_cryo = fcn(P_blower, P_warming, P_v, cryo_HE_factor)

% This function calculates the total power consumed by the cryopump system.
% Note that N_CAC does not come into play here; regardless of the number of
% cryopumps, the same mass flow rate of CO2 must be moved by the blower,
% frozen out, and warmed back up. So this is independent of N_CAC.
% Note also that the power required of the pump to recirculate
% the working fluid in the cryocooler loop is excluded, as this will be
% calculated in the liquefaction subsystem. The same working fluid loop is
% shared by the cryopump and the liquefaction subsystems.

P_CAC_cryo = cryo_HE_factor*P_warming+P_blower+P_v;   % (W) Total cryopump
            power
```

Mechanical Compressor

```
function [M_CAC_scroll_single,V_CAC_scroll_single,P_CAC_scroll, M_CAC_scroll,
            V_CAC_scroll,T2] = Scroll(mdot_in, P1, P2, T1, N_CAC, gamma, R,
            MW_Mars, eff_ad_scroll)

%Note: these calculations are shown in the engineering paper sketches on
%this page in Simulink. They use 2.7 kg/hr CO2 units to estimate mass and
%volume, assuming we use multiple units in parallel if more than 2.7 kg/hr
%CO2 is needed.

%The power is calculated as the adiabatic compression of a gas divided by
%the compressor's adiabatic efficiency.
```

```
%RETIRED CALCULATION: P_CAC_scroll = 534.5*mdot_in+53.9;     %(W) Power of
            scaled scroll pump, based on linear fit of Air Squared data
sph = 3600;         % (s) Seconds per hour
k = 0.8;            % ( ) Exponential scaling factor for economy of scale
            with mass and volume scaling
M_AS = 28.2;        % (kg) Mass of Air Squared compressor
mdot_AS = 2.7;      % (kg/hr) Mass flow rate of Air Squared compressor
V_AS = 0.343*0.349*0.35;    % (m^3) Volume of Air Squared compressor
mdot = mdot_in/N_CAC;       % (kg/hr) Mass flow rate handled by each
            individual compressor in BAM

M_CAC_scroll_single = M_AS*(mdot/mdot_AS)^k;      % (kg) Mass of a single
            scaled scroll pump, based on 2.7 kg/hr CO2 single-stage units
            from Air Squared interim report 2018
V_CAC_scroll_single = V_AS*(mdot/mdot_AS)^k;      % (m3) Volume of a single
            scaled scroll pump, based on 2.7 kg/hr CO2 single-stage units
            from Air Squared interim report 2018

P_CAC_scroll = T1*mdot_in*R/MW_Mars*(gamma/(gamma-1))*((P2/P1)^((gamma-
            1)/gamma)-1)/eff_ad_scroll/sph;    % (W) Scroll compressor power
            consumption
M_CAC_scroll = M_CAC_scroll_single*N_CAC;   % (kg) Total mass of all active
            mechanical compressors
V_CAC_scroll = V_CAC_scroll_single*N_CAC;   % (kg) Total volume of all active
            mechanical compressors
T2 = T1*(P2/P1)^((gamma-1)/gamma);          % (K)  Outlet temperature of
            compressor. Isentropic assumption (all heat goes into the gas).


function [P_CAC_centr, M_CAC_centr, V_CAC_centr,T2] = Centr(mdot_in, P1, P2,
            T1, f_centr, gamma, R, MW_Mars, eff_ad_centr, P1_IR, P2_IR, k_IR,
            rho_cc_fins)

%The power is calculated as the adiabatic compression of a gas divided by
%the compressor's adiabatic efficiency.

sph = 3600;         % (s) Seconds per hour

P_CAC_centr = T1*mdot_in*R/MW_Mars*(gamma/(gamma-1))*((P2/P1)^((gamma-
            1)/gamma)-1)/eff_ad_centr/sph;    % (W) Scroll compressor power
            consumption
V_CAC_centr = 0.03*((P2/P1)/(P2_IR/P1_IR))^k_IR;        % (m3)  Volume of
            five-stage centrifugal compressor, modified for pressure ratio
M_CAC_centr = f_centr*rho_cc_fins*V_CAC_centr;          % (kg)   Mass of
            five-stage centrifugal compressor, modified for pressure ratio
            via volume

T2 = T1*(P2/P1)^((gamma-1)/gamma);                      % (K)  Outlet
            temperature of compressor. Isentropic assumption (all heat goes
            into the gas).


function M_CAC = SparesModifier(M_CAC_active, CACmechanical_numRunningUnits,
            CACmechanical_numSpareUnits)
```

```
M_CAC =
            M_CAC_active*(CACmechanical_numRunningUnits+CACmechanical_numSpar
            eUnits)/CACmechanical_numRunningUnits;

function V_CAC = SparesModifier(V_CAC_active, CACmechanical_numRunningUnits,
            CACmechanical_numSpareUnits)

V_CAC =
            V_CAC_active*(CACmechanical_numRunningUnits+CACmechanical_numSpar
            eUnits)/CACmechanical_numRunningUnits;
```

Sorption Pump

```
function [sorp_blower_power,sorp_blower_mass,sorp_blower_vol] =
            blowercalc(mdot_in,cryo_blower,cryo_blower_eff,blower_spec_mass,b
            lower_spec_vol)

%Calculates power, mass, and volume of blower fan for cryo system.
%cryo_blower is a J/kg figure that represents the energy needed by a
%typical blower to move one kg of martian gas into the system.
sph = 3600;                                                    % (s)
            Seconds per hour

sorp_blower_power = cryo_blower*mdot_in/(cryo_blower_eff*sph);  % (W)   Power
            draw of blower fan as a function of flow rate.
sorp_blower_mass = blower_spec_mass*mdot_in^0.8;     % (kg)  Mass of one
            blower in the system. Uses a scaling law equation since it won't
            scale linearly.
sorp_blower_vol = blower_spec_vol*mdot_in^0.8;       % (m3)  Volume of one
            blower in the system.

function M_Blower = SparesModifier(M_Blower_active, Blower_numRunningUnits,
            Blower_numSpareUnits)

M_Blower =
            M_Blower_active*(Blower_numRunningUnits+Blower_numSpareUnits)/Blo
            wer_numRunningUnits;

function V_Blower = SparesModifier(V_Blower_active, Blower_numRunningUnits,
            Blower_numSpareUnits)

V_Blower =
            V_Blower_active*(Blower_numRunningUnits+Blower_numSpareUnits)/Blo
            wer_numRunningUnits;


%Mass of CO2 sorption compression

function [sorb_mass,pump_mass] =
            sorption_mass(mdot_O2,cycle_time,mdot_in,loading,sorp_eff2,sorp_m
            ass_factor)

sorb_mass = 1/loading*mdot_in*cycle_time/sorp_eff2; % (kg)  Mass of sorbent
            bed material. Increases as cycle time increases.
pump_mass = sorb_mass*sorp_mass_factor;             % (kg)  Mass of sorbent
            bed plus structure around it. Assumes titanium.
```

```
end


%Volume of CO2 sorption compression
%Source: AIAA-87-1900
%Mass and Power Estimate for Mars In-Situ Propellant production Systems
%Frisbee, JPL, 1987

%mdot is of O2 production rate
function volume = sorption_volume(mdot_O2)

volume_sorbent = 0.0022*mdot_O2*24; % (m3) (multiply by 24 because mdot_O2 in
            Frisbee (1987) assumed kg/day, our mdot_O2 is kg/hr)

volume = 5*volume_sorbent;          % (m3) Total volume of sorption pump.
            Scaling factor of five to account for framing, heating and
            cooling channels, etc.

end


%Mass of CO2 sorption compression
%Source: AIAA-87-1900
%Mass and Power Estimate for Mars In-Situ Propellant production Systems
%Frisbee, JPL, 1987

%mdot is of O2 production rate
function [P_sorption,Q_cool,P_cool,P_heat,T2] =
            sorption_power(mdot_O2,mdot_in,P_MA,P2,sorb_mass,pump_mass,Cp_zeo
            lite,Cp_ti,Cp1,Cp2,CpCv_CO2,T_cold,T1,cycle_time,sorp_eff,cryo_ef
            ficiency)

T_hot = T1*(P2/P_MA)^(1-1/(CpCv_CO2));                          % (K)
            Calculation for desorption temperature based on desired
            desorption pressure (P2)
sph = 3600;                                                     % (sph) Seconds
            per hour
time = (cycle_time/2)*sph;                                      % (s)   Time for
            heating and cooling, each assumed to be half of the cycle time
T_cold = min(T_cold, T1);                                       % (K)   If our
            cold temperature setting is actually warmer than the current
            ambient temperature on Mars, no cooling is needed. Therefore, set
            the "cold" temperature setting equal to the Mars atmosphere.
            Otherwise we start to get negative heats and complex answers.

%Cooling Stage
Q_bed_cool = sorb_mass*Cp_zeolite*(T1-T_cold)/time;             % (W)   Heat
            removal required to cool the sorbent bed from Mars atmospheric
            temperature to the sorption cold temperature (-40 C)
Q_frame_cool = 0.15*pump_mass*Cp_ti*(T1-T_cold)/time;           % (W)   Heat
            removal required to cool a portion of the sorbent bed frame from
            Mars atmospheric temperature to the sorption cold temperature (-
            40 C). It is assumed that ~15% of heat is lost to the titanium
            frame as opposed to being used to heat the sorbent bed and gas.
```

```
Q_gas_cool = mdot_in*Cp1*(T1-T_cold)/sph;                    % (W)   Heat
            removal required to cool the gas from Mars atmospheric
            temperature to the sorption cold temperature
Q_cool = (1-sorp_eff)*(Q_bed_cool+Q_frame_cool+Q_gas_cool)/2; % (W)   Total
            heat removal required to cool the sorption pump. Assumes a
            fraction equal to "sorp_eff" of heat is recovered with each
            cycle. Divided by 2 because the pump is only heating for 1/2 the
            time and cooling for 1/2 the time.
P_cool = Q_cool/cryo_efficiency;                             % (W)   Power
            required for cooling in the sorption pump. Assumes use of the
            shared cryocooler with the liquefaction unit.

%Heating Stage
Q_bed_heat = sorb_mass*Cp_zeolite*(T_hot-T_cold)/time;       % (W)   Heat
            required to warm the sorbent bed from its cold adsorption
            temperature to its hot desorption temperature
Q_frame_heat = 0.15*pump_mass*Cp_ti*(T_hot-T_cold)/time;     % (W)   Heat
            required to warm a portion of the sorbent bed frame from its cold
            adsorption temperature to its hot desorption temperature. It is
            assumed that ~15% of heat is lost to the titanium frame as
            opposed to being used to heat the sorbent bed and gas.
Q_gas_heat = mdot_in*Cp1*(T_hot-T_cold)/sph;                 % (W)   Heat
            required to warm the gas from its cold adsorption temperature to
            its hot desorption temperature
P_heat = (1-sorp_eff)*(Q_bed_heat+Q_frame_heat+Q_gas_heat)/2; % (W)   Heater
            power required to warm the system. Divided by 2 because the pump
            is only heating for 1/2 the time and cooling for 1/2 the time.

%Total Power
P_sorption = P_cool + P_heat;                                % (W)   Total
            power required of the sorption pump for heating and cooling
T2 = T_hot;                                                  % (K)   Output
            temperature of sorption

end
```

SOE

```
function [iASR_temp,Res_cell] = fcn(T6,iASR,Ea,R,A,A_cell)

%   This function converts a baseline iASR (value at 1073 K) into a
            temperature-corrected
%   iASR, which should be used for cell calculations.
iASR_temp = iASR/(A*exp(-Ea/(R*T6)));    %(Ohms-cm^2) temperature-corrected
            intrinsic ASR
Res_cell = iASR_temp/A_cell;             %(Ohms/cell) resistance per SOE cell

function V_Nernst =
            IntegralAvgNernst(T6,PO2,xCO_in,xCO,R,F,VNernstA,VNernstB)


PO2_atm = PO2/101325;       %(atm) Converting pascal to atm for this equation
            (per JJH)
A = 1 / (xCO - xCO_in);     %First term in integral average Nernst potential
            equation
B = xCO*(VNernstA*T6+VNernstB)+R*T6/(4*F)*[xCO*log(abs(PO2_atm*xCO^2/(1-
            xCO)^2))+2*log(abs(1-xCO))];  %CO out term
```

```
C =
            xCO_in*(VNernstA*T6+VNernstB)+R*T6/(4*F)*[xCO_in*log(abs(PO2_atm*
            xCO_in^2/(xCO_in-1)^2))+2*log(abs(1-xCO_in))];  %CO in term

V_Nernst = A * (B - C);     %Piece it all together!

function V_Nernst_C =
            IntegralAvgNernst(T6,P5,PO2,xCO_in,xCO,R,F,VN_CO_A,VN_CO_B,VN_CO_
            C,VN_CO_D)

% This function calculates the Nernst potential for CO -> C(s) + 1/2 O2
% Eric derived this equation from the relationship between electrochemical
% cell potential and change in Gibb's free energy. Confirmed with JJH's
% testing sheets macros.

% 1. Define change in Gibb's free energy at standard state

A = VN_CO_A;                                % See dGO_CO comment for
            explanation
B = VN_CO_B;
C = VN_CO_C;
D = VN_CO_D;
dGo_CO = (A+B*T6+C*T6^2+D*T6^3)*1000;       % Change in Gibb's free energy at
            standard state, as a function of temperature. Source: Joe
            Hartvigsen.

% 2. Calculate average concentration of CO across the cell (assume linear
% increase across cell)

xCO_avg = (xCO_in+xCO)/2;                   % Average concentration of CO on
            the cell

% 3. Calculate Nernst potential

PO2_atm = PO2/101325;                       %(atm) Converting pascal to atm
            for this equation (per JJH)
P5_atm = P5/101325;                         %(atm) Converting pascal to atm
            for this equation (per JJH)

A = dGo_CO / (2*F);                         % First term in integral average
            Nernst potential equation
B = R * T6 / (2*F);                         % Second term in integral average
            Nernst potential equation
C = log(abs((PO2_atm)^(0.5)/(P5_atm*xCO_avg))); % Third term in integral
            average Nernst potential equation

V_Nernst_C = A + B * C;                     %Piece it all together!

function I = CurrentCalc(Res_cell,V_act,V_Nernst,V_app,N_cps,N_stacks,A_Cell)


%Calculate Current from Voltages and Resistance of Cells, assuming all
%cells identical and in series
```

```
Num_cells = N_cps*N_stacks;                 % ( )    Total number of cells,
            assuming all are in series electrically
Resistance = Num_cells*Res_cell;            % (Ohms) Total resistance,
            assuming all cells are in series
                                            % Note: if some are in
                                            % parallel, need to rethink
                                            % this and how I calculate.
% Resistance = iASR/(A_Cell*(N_stacks*N_cps));   %Resistance in parallel?
I_cell = (V_app - V_Nernst - V_act)/Res_cell;  % (A) Amps per cell. V_app is
            the total stack voltage
I = I_cell*Num_cells;   % (A) Total current in the whole system. Analogous to
            adding up O2 production for each cell.

function [P_Electrolysis,V_tn] = fcn(I,T6,F,N_stacks,N_cps)

%This function calculates the thermal neutral voltage of the 2CO2 -> 2CO +
%O2 reaction. It then uses that to calculate the power required for
%electrolysis. Note that this includes the electrical power required to
%drive the reaction (V*I) as well as the make-up power required to heat the
%system after the endothermic reaction consumes some amount of heat.

A = -0.00334;               %(J/K^2) Constant for enthalphy of reaction of
            CO2 reduction, for T range 800 - 1400 K, taken from Meyen thesis
            (no source cited).
B = -0.57737;               %(J/K) Constant for enthalphy of reaction of CO2
            reduction, for T range 800 - 1400 K, taken from Meyen thesis (no
            source cited).
C = 569263.5;               %(J) Constant for enthalphy of reaction of CO2
            reduction, for T range 800 - 1400 K, taken from Meyen thesis (no
            source cited).

delta_H = A*T6^2+B*T6+C;    %(J) Temperature-dependent enthalpy of reaction
            of CO2 reduction to CO and O
n = 4;                      %(-) charge (number of electrons) transferred in
            the reaction as written above

V_tn = delta_H/(n*F);       %(V) Thermal neutral voltage, where the reaction
            is neither endothermic nor exothermic
P_Electrolysis = I*V_tn*N_stacks*N_cps;    %(W) Power required for
            electrolysis of CO2, including make-up heat requirements from the
            reaction being endothermic

function P_Heat_Gas = SOE_Heater_Gas(mdot_in,T5,T6,Cp5,Cp6,heater_eff)

% This function calculates the heating power required to warm the incoming
% Mars gas stream from T5 (Heat Exchanger output) to T6 (SOE setpoint). It
% assumes an inline heater similar to this one:
            https://www.thermaldevices.com/wp-content/uploads/2018/04/Watlow-
            Fluent-Heater-Catalog-Pages.pdf
% Heater efficiency was difficult to find. Assuming minimal heat losses,
% the efficiency is primarily the efficiency of converting from electrical
% energy to thermal energy. This is typically a 100% efficient conversion
% (see https://en.wikipedia.org/wiki/Electric_heating for explanation).

sph = 3600;                 % seconds per hour
Cp_avg = (Cp5+Cp6)/2;       % (J/kg-K) Average heat capacity of the gas between
            T5 and T6 temperatures
```

```
P_Heat_Gas = mdot_in*Cp_avg*(T6-T5)/(sph*heater_eff);   % (W) Power required
            to heat the incoming gas from T5 to T6

function [Q_Heat_Loss, A_inner_shell, A_outer_shell, V_outer_shell] =
            SOE_Heat_Loss(T6,T_MA,N_quadSOE,N_singleSOE,N_cps,t_SOE_ins1,t_SO
            E_ins2,w_quad,l_quad,w_single,l_single,k_efrax_Mars,h_c)

% This function calculates the heat lost from the SOE unit to the ambient
% Mars environment.

f_modules = 1.3;          % ( ) multiplication factor to account for spacing
            between modules
margin = 1.5;             % multiplication factor to account for heat losses
            through piping and electrical interfaces entering and leaving the
            hotbox
% Assumptions:
% 1) The SOE stack is at T6. In reality, the gas is at T6 and so the stack
% material itself may be above T6. We assume it is equal to T6.
% 2) The "layers" in the system are as follows:
%   1. Aerogel insulation between quad/single modules and the inner shell
%   2. Aerogel insulation between the inner shell and outer shell
% 3) We ignore the conduction through the inner and outer shells, as the
% shells are thin compared to the aerogel and much higher in thermal
% conductivity. Thus, they will not be the limiting heat transfer step and
% can be ignored in calculations.
% 4) We assume that regardless of N_stacks or N_cps, the thickness of
% insulation surrounding the modules will be the same. In reality this may
% not be a good assumption (i.e. higher N_stacks = more volume occupied =
% more insulation mass), but it should not impact heat loss significantly.
% Therefore, heat loss will only be dependent on T6.
% 5) A factor of 1.5 is added to the heat loss number to account for heat
% loss through inlet/outlet pipes and electrical ports.

% Calculate configuration of quad and single stack modules
w_num_quad = ceil(sqrt(N_quadSOE));          % ( ) number of quad stack
            modules in the width direction, assuming they are flush against
            one another. If there are 4 quads, we want a 2x2 arrangement. If
            there are 5 quads, we want a 3x2 arrangement. This formula helps
            us calculate the appropriate width for this.

%If we have no quad-stack modules:
if w_num_quad == 0                           % If there are no quad-stack
            modules...
    l_num_quad = 0;                          % ( ) there are zero quad-stack
            modules in the length direction
    if N_singleSOE == 3                      % If number of single stack
            moduels is 3 (i.e. total stacks = exactly 3)
        w_num_single = 2;                    % ( ) we have a 2x2 configuration
            (with one empty slot)
        l_num_single = 2;
    elseif N_singleSOE == 2                  % If number of single stack
            modules is 2 (i.e. total stacks = exactly 2)
        w_num_single = 2;                    % ( ) Do a 2x1 arrangement of
            modules
        l_num_single = 1;
    elseif N_singleSOE == 1                  % If number of single stack
            moduels is 1 (i.e. total stacks = exactly 1)
```

```
        w_num_single = 1;                   % ( ) Do a 1x1 arrangement of
            modules
        l_num_single = 1;
    elseif N_singleSOE == 0                 % If number of single stack
            moduels is 0 (i.e. total stacks = exactly 0)
        w_num_single = 0;
        l_num_single = 0;
    else
        error('Eric, something is wrong with your Electrolysis -> Power Heat
            Loss inputs. It seems you have a strange number of single and
            quad-stack SOE modules.');
    end

%If we do have quad-stack modules:
else                                        % If there ARE quad-stack
            modules
    l_num_quad = ceil(N_quadSOE/w_num_quad);    % ( ) number of quad stack
            modules in the length direction, assuming they are flush against
            one another.
    l_num_single = 0;                       % ( ) we will never have to
            extend the lengthwise direction for single stack modules if we
            have at least one quad-stack module; increasing the width is
            enough to accomodate up to 3 single stack modules, which is the
            max we'd ever have
    if w_num_quad*l_num_quad > N_quadSOE        % if we have a blank slot in
            our arrangement (i.e. 3x2 arrangement but we only have 5 quad
            modules, so sixth slot is open)
        w_num_single = 0;                   % ( ) no extra space is
            needed for single stack modules
    else
        if N_quadSOE >= 3
            if N_singleSOE == 0             % If we have no single
            stacks...
                w_num_single = 0;           % ( ) then we obviously do
            not need to extend the volume for the single stacks!
            else                            % but if we do have single
            stacks...
                w_num_single = 1;               % ( ) we will extend the
            width of the space by the total width of one single stack module.
            Reasoning: if we have at least 3 quad modules, we have at least a
            2x2 configuration. That means that by adding one slot in the
            width direction, we can then stack 3 single modules deep. There
            will be enough space.
            end
        else
            if N_singleSOE == 3             % If we have 3 single stacks
            in addition to our one or two quad-stacks...
                w_num_single = 2;           % ( ) If we have only 1 or 2
            quad SOE stacks, that means we have a 1x1 or 2x1 configuration
            for the quads. For 1 or 2 single stacks, we can get away with
            only extending the width of the hotbox by one single stack width
            length. But if we have 3 single stacks, we have to extend it by 2
            (essentially making a mini 2x2 single stack area)
            elseif N_singleSOE == 0         % If we have zero single
            stacks in addition to our one or two quad-stacks (i.e. we have
            exactly 4 or 8 total stacks)
                w_num_single = 0;
```

```
            elseif N_singleSOE < 3              % If we have either 1 or 2
            single stacks in addition to our 1 or 2 quad-stacks...
                w_num_single = 1;
            else
                error('Eric, something is wrong with your Electrolysis ->
            Power Heat Loss inputs. It seems you have a strange number of
            single and quad-stack SOE modules. This is the second error
            coded.');
            end
        end
    end
end

% w_num_quad
% l_num_quad
% w_num_single
% l_num_single

% Calculate areas that heat will transfer through each layer
w_modules = f_modules*(w_num_quad*w_quad + w_num_single*w_single);      % (m)
            width of all the modules lined up in the hotbox
l_modules = f_modules*(l_num_quad*l_quad + l_num_single*l_single);      % (m)
            length of all the modules lined up in the hotbox
h_modules = f_modules*(0.004*N_cps + 0.05);                             % (m)
            height of the modules based on number of cells per stack and
            OxEon's model. Add 0.05 for endplates.

w_base_i = w_modules + 2*t_SOE_ins1;                            % (m) width of
            the base of the inner shell of the hotbox
l_base_i = l_modules + 2*t_SOE_ins1;                            % (m) width of
            the length of the inner shell of the hotbox
h_i = h_modules + 2*t_SOE_ins1;                                 % (m) height of
            the inner shell of the hotbox

A_base_i = w_base_i*l_base_i;                                   % (m^2) area of
            the base and top of the inner shell
A_side_i = l_base_i*h_i;                                        % (m^2) area of
            two of the sides of the inner shell
A_front_i = w_base_i*h_i;                                       % (m^2) area of
            the front and back sides of the inner shell
A_inner_shell = 2*(A_base_i+A_side_i+A_front_i);                % (m^2) surface
            area of the inner shell

w_base_o = w_base_i + 2*t_SOE_ins2;                             % (m) width of
            the base of the outer shell of the hotbox
l_base_o = l_base_i + 2*t_SOE_ins2;                             % (m) length of
            the base of the outer shell of the hotbox
h_o = h_i + 2*t_SOE_ins2;                                       % (m) height of
            the outer shell of the hotbox

A_base_o = w_base_o*l_base_o;                                   % (m^2) area of
            the base and top of the outer shell
A_side_o = l_base_o*h_o;                                        % (m^2) area of
            two of the sides of the outer shell
A_front_o = w_base_o*h_o;                                       % (m^2) area of
            the front and back sides of the outer shell
```

```
A_outer_shell = 2*(A_base_o+A_side_o+A_front_o);            % (m^2) surface
            area of the outer shell

V_outer_shell = h_o*w_base_o*l_base_o;                      % (m^3) volume of
            the hotbox. Not needed for power calculations, but convenient to
            output here for later volume calculations.
% Calculate thermal resistance through each layer. Source:
            https://community.ptc.com/sejnu66972/attachments/sejnu66972/PTCMa
            thcad/173365/1/1.1%20Heat%20Conduction%20in%20Multilayered%20Wall
            s.pdf
%   - For conduction, R = L/(kA)
%   - For convection, R = 1/(hA)
%   - Total resistance: R = A_T/(Ai/Ri+Ao/Ro)
% Source for calculating heat loss using a V = IR analogy:
            https://celsiainc.com/heat-sink-blog/fundamentals-of-thermal-
            resistance/

R_ins_1 = t_SOE_ins1/(k_efrax_Mars*A_inner_shell);          % (K/W) Thermal
            resistance through the first insulation layer of the SOE hotbox
R_ins_2 = t_SOE_ins2/(k_efrax_Mars*A_outer_shell);          % (K/W) Thermal
            resistance through the second insulation layer of the SOE hotbox
R_conv = 1/(h_c*A_outer_shell);                             % (K/W) Thermal
            resistance for convection from the outer layer of the SOE hotbox
            to the atmosphere

R_total_numerator = (A_inner_shell+A_outer_shell);      % (m^2) Total area of
            all conduction resistances
R_total_den = (A_inner_shell/R_ins_1+A_outer_shell/R_ins_2);   % (m^2-W/K)
            Sum of all Areas divided by Resistances
R_total = R_total_numerator/R_total_den + R_conv;       % (K/W) Total thermal
            resistance of all layers

% Calculate Heat Loss, Q

Q_Heat_Loss = margin*(T6-T_MA)/R_total;                 % (W) Heat loss from
            SOE hotbox to the environment
end

% Determine if heat lost FROM GAS FLOW THROUGH IS SOMETHING I NEED TO
% ACCOUNT FOR HERE!

function P_Compression = Compression(I,P5,P6,T6,R,F)

% Electrochemical compression occurs when the pressure of the anode is
% greater than the pressure of the cathode. The extra work put into the gas
% to compress it across the electrolyte is in the form of extra voltage,
            which
% is calculated as V = (RT/2F)ln(Pa/Pc) according to the MOXIE pre-mission
% special edition publication. P=IV to calculate the power. This was
% confirmed with Joe Hartvigsen at OxEon. It should equate to ~53 mV per
% decade change in pressure.

if P6 > P5
    V = (R*T6/(2*F))*log(P6/P5);    % (V)   Extra voltage needed to compress
            the gas electrochemically from P5 to P6 (cathode pressure to
            anode pressure)
```

```
    P_Compression = I*V;            % (W)   Extra power needed for
            electrochemical compression.
else
    P_Compression = 0;
end

function [N_quadSOE,N_singleSOE] = NumModules(N_stacks)

% This function calculates the number of quad-stack modules and
% single-stack modules required by the SOE system. The function builds as
% many quad-stack modules as possible and then fills the remaining stacks
% as single-stack modules.

N_quadSOE = floor(N_stacks/4);          % Round down to the nearest integer.
            Example: if we have 7 stacks, N_quadSOE = floor(7/4) = 1, so we
            will have 1 quad stack. If we have 3 stacks, N_quadSOE = 0.
N_singleSOE = N_stacks - N_quadSOE*4;   % The remainder of stacks will be
            single stack modules.

function [M_SOE,M_stack,M_stacks,M_ins,M_shells,V_SOE] =
            SOEmass(N_cps,A_cell,A_inner_shell, V_outer_shell, A_outer_shell,
            N_stacks_actual,t_SOE_ins1,t_SOE_ins2,rho_efrax,rho_ti,rhoZ,rhoIC
            ,rhoEP,tZ,tIC,tEP,t8,t10,f_SOE,fEP,fIC)

% This function calculates all of the dimensions, mass and volume of the
% SOE cells, stacks, and enclosures. I have validated the A_cellT, w4, l4,
% h4, and M4 numbers with OxEon data as of February 2021 and they are an
% extremely close match. So the SOE stack mass and volume are on point!

N_EP = ceil(N_cps/100)+1;                               % ( ) number of endplates
            / midplates required, assumed to be required every hundred cells
            plus an extra on the end.
A_cellT = A_cell/(0.0357+0.133*log(A_cell));        % (cm^2) Total cell area,
            derived from active cell area using a logarithmic function based
            on MOXIE (A_cell=22.74, A_cellT=50) and OxEon's larger scale work
            (A_cell=110.8, A_cellT=169). See notebook page 109 for more
            details.

%Calculate Masses
M4 =
            N_cps*A_cellT/100^2*(f_SOE*rhoZ*tZ+rhoIC*tIC*fIC)+rhoEP*tEP*A_cel
            lT/100^2*fEP*N_EP; %(kg) mass of one SOE stack. Includes ScSZ,
            InterConnects, EndPlates every 100 cells, Nickel Felt and Glass
            Seals. Confirmed with OxEon numbers on April 29, 2021. It should
            be ~17.9 kg for a 65 cell stack at 110 cm^2 active area per cell.
M5 = 0;                                                 % (kg) mass of inlet and
            outlet tubes for SOE (assumed to be negligible)
M6 = M4*0.2;                                            % (kg) mass of the
            compression rig surrounding each stack. Should confirm 0.2 number
            with JJH.
M7 = t_SOE_ins1*A_inner_shell*rho_efrax;                % (kg) mass of insulation
            between stacks and inner shell of hotbox. Note this is a slight
            overestimate because I am using the area of the inner shell, when
            in reality the average insulation cross-sectional area is
            slightly less than this. I think this is a good over-estimation,
            however, as I am not accounting for extra insulation that is
            needed to fill in the cracks and crevices of the SOE hotbox.
```

```
M8 = t8*A_inner_shell*rho_ti;                          % (kg) mass of the inner
            hotbox shell, assumed to be made of titanium (lightweight, high
            melting point, low thermal conductivity - all good)
M9 = t_SOE_ins2*A_outer_shell*rho_efrax;               % (kg) mass of insulation
            between inner and outer shell of hotbox. Note this is a slight
            overestimate because I am using the area of the outer shell, when
            in reality the average insulation cross-sectional area is
            slightly less than this. I think this is a good over-estimation,
            however, as I am not accounting for extra insulation that is
            needed to fill in the cracks and crevices of the SOE hotbox.
M10 = t10*A_outer_shell*rho_ti;                        % (kg) mass of the outer
            hotbox shell, assumed to be made of titanium (lightweight, high
            melting point, low thermal conductivity - all good)

%Intermediate Outputs
M_stack = M4+M5+M6;                                    % (kg) mass of one SOE
            stack, including the compression rig and inlet/outlet tubing
M_stacks = N_stacks_actual*M_stack;                    % (kg) mass of all the
            SOE stacks in this design, including compressions rigs and tubing
M_ins = M7+M9;                                         % (kg) mass of both
            layers of insulation in the hotbox
M_shells = M8+M10;                                     % (kg) mass of both
            titanium shells in the hotbox

%Final Outputs
V_SOE = V_outer_shell;                                 % (m3) Volume of the
            hotbox.
M_SOE = N_stacks_actual*(M4+M5+M6)+M7+M8+M9+M10;       % (kg) Mass of the
            hotbox. Includes SOE stacks, endplates, compression rig, two
            layers of Excelfrax insulation, and two layers of titanium
            shells.

function N_stacks_actual = fcn(N_cps,N_stacks,SOECell_numSpareUnits,
            SOEStack_numSpareUnits)

N_cells = SOECell_numSpareUnits + N_cps*N_stacks;                    % ( )
            Number of total SOE cells we have at the start of the mission,
            including spares
N_stacks_actual = ceil(N_cells/N_cps)+SOEStack_numSpareUnits;        % ( )
            Number of stacks, including spares. N_stacks is only the active
            stacks that are actively making oxygen. We need to include all
            stacks.

function MW_mix_in  = fcn(xCO_a,xAr_a,xN2_a,xCO2_a)
% MW_mix = sigma(mole%*weight). Note this is just for one comes in the
% compressor, it does NOT include the recycle system.

MW_mix_in = xCO_a*28.01+xCO2_a*44.01+xAr_a*39.95+xN2_a*28.01;
            %MW of the mix coming in from Mars

end

function ndot_in = mass_to_moles(MW_mix,mdot_in)

%We have our total inlet mass flow rate from the compressor, and we know
%our average molecular weight of the gas. Use these to calculate a total
```

```
%molar inlet flow rate, which we need for other calculations later on.
gpkg = 1000;                %1000 grams per kilogram
sph = 3600;                 %3600 seconds per hour
ndot_in = mdot_in * gpkg / (sph * MW_mix);  %(mol/s) Molar flow rate of gas
            incoming to SOE, currently assuming no recycle.

function [ndot_O2_cell,ndot_O2,mdot_O2,mdot_O2_cell] =
            Curr_to_O2(I,MW_O2,N_cps,N_stacks)

%This function will convert electrical current in SOE to a flow rate of
%oxygen (the two are linked). 2CO2 -> 2CO + O2

F = 96484.56;                               %(C/e) Faraday's constant, in
            Coulombs per mole of electrons
n = 4;                                      %(-) # moles electrons transferred
            w/ one O2 mole
ndot_O2_cell = I/(n*F);                     %(mol/s) Molar flow rate of oxygen
            produced per SOE cell
ndot_O2 = ndot_O2_cell*N_cps*N_stacks;      %(mol/s) Total molar flow rate of
            oxygen produced across all cells in all stacks

sph = 3600;                                 %(-) Number of seconds per hour
mdot_O2 = ndot_O2 * MW_O2 * sph;            %(kg/hr) Total kg/hr of oxygen
            produced across all cells in all stacks
mdot_O2_cell = mdot_O2/(N_cps*N_stacks);    %(kg/hr) Mass flowrate of O2
            leaving each cell

function [ndot_CO_cell,ndot_CO,mdot_CO,mdot_CO_cell] =
            CO_Calc(ndot_O2_cell,ndot_O2,MW_CO,N_cps,N_stacks)

%This function will convert oxygen flowrates into carbon monoxide flowrates.
%oxygen (the two are linked). 2CO2 -> 2CO + O2

sph = 3600;                                 %(-) Number of seconds per hour

ndot_CO_cell = ndot_O2_cell*2;              %(mol/s) Moles of CO produced. 2
            moles CO for every 1 mole O2 per 2CO2 -> 2CO + O2
ndot_CO = ndot_O2*2;                        %(mol/s) Same reasoning as above
mdot_CO = ndot_CO * MW_CO * sph;            %(kg/hr) Total kg/hr of oxygen
            produced across all cells in all stacks
mdot_CO_cell = mdot_CO/(N_cps*N_stacks);    %(kg/hr) Mass flowrate of CO
            leaving each cell

function [ndot_Ar,ndot_N2,mdot_Ar,mdot_N2] =
            Inert_Flows(ndot_in,xAr_a,xN2_a,MW_Ar,MW_N2)

%This function will convert the incoming molar fraction of Argon and
%Nitrogen to molar flowrates and mass flowrates of each.

ndot_Ar = ndot_in * xAr_a;                  %(mol/s) Total molar flowrate of
            Argon gas throughout the system
ndot_N2 = ndot_in * xN2_a;                  %(mol/s) Total molar flowrate of
            Nitrogen gas throughout the system

sph = 3600;                                 %(-) Number of seconds per hour
```

```
mdot_Ar = ndot_Ar*MW_Ar*sph;                %(kg/hr) Total mass flowrate of
            Argon throughout the system
mdot_N2 = ndot_N2*MW_N2*sph;                %(kg/hr) Total mass flowrate of
            Argon throughout the system

function [ndot_CO2,ndot_CO2_cell,mdot_CO2,mdot_CO2_cell] =
            CO2_Calc(ndot_in,xCO2_a,MW_CO2,ndot_CO,N_cps,N_stacks)

%This function will take the inlet flowrate of CO2 and subtract the amount
%of CO2 that was converted to CO to yield the outlet CO2 flowrates from
%SOE.

ndot_CO2_in = ndot_in * xCO2_a;             %(mol/s) Molar flowrate of CO2
            coming into SOE
ndot_CO2 = ndot_CO2_in - ndot_CO;           %(mol/s) Molar flowrate of CO2
            leaving SOE
ndot_CO2_cell = ndot_CO2/(N_cps*N_stacks); %(mol/s) Molar flowrate of CO2
            leaving each cell

sph = 3600;                                 %(-) Number of seconds per hour
mdot_CO2 = ndot_CO2 * MW_CO2 * sph;         %(kg/hr) Total kg/hr of carbon
            dioxide produced across all cells in all stacks
mdot_CO2_cell = mdot_CO2/(N_cps*N_stacks); %(kg/hr) Mass flowrate of CO2
            leaving each cell

function [xCO,xN2,xAr,xCO2,ndot_total] =
            molefractions(ndot_CO,ndot_N2,ndot_Ar,ndot_CO2)

% This function will convert the molar flowrates leaving the SOE cathode into
            mole
% fractions, as these fractions are used in calculations such as the Nernst
% potential.
ndot_total = ndot_CO+ndot_N2+ndot_Ar+ndot_CO2; % sum of all molar flowrates
            leaving SOE

xCO = ndot_CO/ndot_total;       % mole fraction of CO in the outlet stream of
            SOE cathode exhaust
xN2 = ndot_N2/ndot_total;
xAr = ndot_Ar/ndot_total;
xCO2 = ndot_CO2/ndot_total;

function [ndot_CO_r,ndot_N2_r,ndot_Ar_r,ndot_CO2_r,ndot_r] =
            recycleflowrate(ndot_CO,ndot_N2,ndot_Ar,ndot_CO2,ndot_out,rec_fra
            c)

% This function calculates the Molar Flowrates of the Recycle Stream (mol/s)

ndot_CO_r = ndot_CO*rec_frac;       %(mol/s) molar flow rate of CO in the
            recycle stream
ndot_N2_r = ndot_N2*rec_frac;
ndot_Ar_r = ndot_Ar*rec_frac;
ndot_CO2_r = ndot_CO2*rec_frac;

ndot_r = ndot_out * rec_frac;       %(mol/s) total molar flow rate of the
            recycle stream
```

```
function [mdot_CO_r,mdot_N2_r,mdot_Ar_r,mdot_CO2_r,mdot_r] =
            recycleflowrate(ndot_CO_r,ndot_N2_r,ndot_Ar_r,ndot_CO2_r,MW_CO,MW
            _N2,MW_Ar,MW_CO2)

% This function calculates the Molar Flowrates of the Recycle Stream (mol/s)

sph = 3600;                          % seconds per hour

mdot_CO_r = ndot_CO_r*sph*MW_CO;       %(kg/hr) mass flow rate of CO in the
            recycle stream
mdot_N2_r = ndot_N2_r*sph*MW_N2;
mdot_Ar_r = ndot_Ar_r*sph*MW_Ar;
mdot_CO2_r = ndot_CO2_r*sph*MW_CO2;

mdot_r = mdot_CO_r+mdot_N2_r+mdot_Ar_r+mdot_CO2_r;       %(kg/hr) total mass
            flow rate of the recycle stream

function xCO_in = COin(xCO_a,xCO,ndot_in,ndot_r)
xCO_r = xCO;        %Simply reminding myself that all mole fractions of gases
            in the recycle stream equal those in the cathode exhaust stream
xCO_in = (xCO_a*ndot_in + xCO_r*ndot_r) / (ndot_in+ndot_r);  %Mole fraction
            of CO into SOE equals the weighted sum of mole fractions of CO in
            the ambient air and in the recycle stream

function U = UtilizationRate(xCO2_a,xCO,xCO_in)

% Calculate utilization fraction of CO2 from inlet of SOE to outlet of SOE.

U = (xCO-xCO_in)/xCO2_a;

function [P11, deltaP_SOE, deltaP_SOE_channels, deltaP_SOE_outlet] =
            deltaP_SOE(P5,mdot_in,A_cell,ff_SOE,h_SOE,rho5,N_cps,N_stacks,Di,
            d_SOE)
%   This function calculates the pressure drop across an SOE cell. It is
%   based on the model generated at OxEon by Mukul and shared with Eric by
%   Joe Hartvigsen in September, 2020.

%   The basic underlying equation is the same as that of a pressure drop
%   across a pipe: deltaP = f*(L/D)*(rho/2)*v^2. D, the diameter, is
%   modified for a rectangular channel.

%   I verified this matches the model from OxEon when I fix the two errors
%   from OxEon in their model (see "Pressure drop calcs across SOE - Oxeon
%   and Eric.xlsx" for more information). So even though it is a tiny
%   pressure drop, this seems to be correct.

%%  Calculate intermediate values

sph = 3600;                                    % (sph)     Seconds per Hour

l_SOE = 0.000568*A_cell+0.0501;                % (m)       Length of average
            channel in SOE cell, based on cell size. Formula created as a
            linear relationship between measured channel length in big and
            small MOXIE cells.
w_SOE = 0.00001816*A_cell+0.0005878;           % (m)       Width of one
            channel in SOE cell, based on cell size. Formula created as a
```

```
            linear relationship between measured channel width in big and
            small MOXIE cells.
num_channels = ceil(0.1362*A_cell+12.9);       % (m)       Number of channels
            in SOE cell across flow path direction, based on cell size.
            Formula created as a linear relationship between measured number
            of channels in big and small MOXIE cells.

P = 2*w_SOE + 2*h_SOE;                         % (m)       Perimeter of one
            SOE channel
A = w_SOE * h_SOE;                             % (m^2)     Cross-sectional
            area of one SOE channel
mdot_cell = mdot_in/(N_cps*N_stacks);          % (kg/hr)   Mass flow rate
            seen by an individual cell
Qv = mdot_cell / (sph * num_channels) / rho5;  % (m^3/s)   Volumetric flow
            rate of gas in one SOE channel
v = Qv / A;                                    % (m/s)     Gas velocity in
            the channel
kvis = 52e-6;                                  % (m2/s)    Kinematic
            viscosity of CO2 at 800 K and 1 bar. Not perfect for pressure,
            but a decent estimate. Source: table halfway down at:
            https://www.engineeringtoolbox.com/carbon-dioxide-dynamic-
            kinematic-viscosity-temperature-pressure-d_2074.html
Re = v*w_SOE/kvis;                             % ( )       Reynolds number
            for the flow. Laminar if Re < 2320.

%%  Calculate equivalent length for P drop exiting SOE into outlet
% This function will calculate the pressure drop from the SOE cathode
% exhaust as it exits the SOE flow channels and moves into the SOE cathode
% exit tube. It is expected by JJH that this will be significantly higher
% of a pressure drop than that across the cells themselves.

% This is modeled as a reducer with a sudden contraction, as the SOE flow
% channels exit into the outlet plenum. Source:
            https://www.enggcyclopedia.com/2019/04/reducer-k-value/

K = max(0.5*(1-Di^2/(d_SOE*N_cps)^2),0);% ( )   K factor for calculating
            equivalent pressure drop for a sudden contraction in piping.
            Source: https://www.enggcyclopedia.com/2019/04/reducer-k-value/
l_eq = K*(d_SOE*N_cps)/ff_SOE;          % (m)   Equivalent length of pressure
            drop

l_total = l_SOE+l_eq;                   % (m)   Total equivalent length of
            the pipe

%%  Delta-P Calculation

deltaP_SOE_channels = ff_SOE*l_SOE*P/(4*A)*(rho5*v^2/2);     % (Pa)
            Pressure drop across each channel in SOE (same for all, so no
            need to multiply by number of channels)
deltaP_SOE_outlet = ff_SOE*l_eq*P/(4*A)*(rho5*v^2/2);        % (Pa)
            Pressure drop from SOE channels into outlet cathode plenum pipe

deltaP_SOE = deltaP_SOE_channels+deltaP_SOE_outlet;          % (Pa)
            Total pressure drop across SOE channels and into outlet plenum
```

```
P11 = P5 - deltaP_SOE;                                          % (Pa)      The
            exit pressure of the cathode exhaust stream as it leaves the
            cell, prior to it entering the cathode exhaust tubing (which will
            incur its own separate pressure drop)

end
```

Heat Exchanger

The heat exchanger uses a modified version of an existing heat exchanger code from Mathworks. It calculates the temperature changes and heat transfer that takes place within the modeled heat exchangers.

```
function
            [T_hot_out,T_cold_out,P_HE1,M_HE1,V_HE1,effectiveness,N_plates1]=
            HeatExchanger(m_dot_hot,c_p_hot,T_hot_in,m_dot_cold,c_p_cold,T_co
            ld_in,U,A_HE1,A_eff_PHE,t_PHE,w_PHE,l_PHE,density_inc,h_end)
% AUTHOR: grabbed from MathWorks File Exchange:
            https://www.mathworks.com/matlabcentral/fileexchange/46303-heat-
            exchanger-solver
%
            [T_hot_out,T_cold_out]=HeatExchanger(c_p_hot,m_dot_hot,T_hot_in,c
            _p_cold,m_dot_cold,T_cold_in,U,A,HE_Type);
% This function calculates the outlet temperatures of a heat exchanger
% using Epsilon-NTU method. This function uses effectiveness.m as a
% function and should have access to that function.
%
% The inputs are as follows:
% Hot Flow: c_p_hot, m_dot_hot, T_hot_in.
% Cold Flow: c_p_cold, m_dot_cold, T_cold_in.
% Heat exchanger design parameters: U,A, HE_Type.
%
% HE_Type defines the type of heat exchanger: (see reference)
%   'Parallel Flow'
%   'Counter Flow'
%   'One Shell Pass'
%   'N Shell Pass'
%   'Cross Both Unmixed'
%   'Cross Cmax Mixed'
%   'Cross Cmin Mixed'
%
% Reference:
% Frank P. Incropera, Introduction to heat transfer. New York:Wiley, 1985,
            Section 11.4.
% Programmer: Seyyed Ali Hedayat Mofidi (seyyed4li@yahoo.com)

%HE_Type = 'Counter Flow';   %HE_Type defines the type of heat exchange

%%  Calculate Heat Capacity Rates
sph = 3600;                             % ( ) seconds per hour
C_hot = m_dot_hot*c_p_hot/sph;          % (W/K) heat capacity rate of the hot
            stream
C_cold = m_dot_cold*c_p_cold/sph;       % (W/K) heat capacity rate of the cold
            stream
C_min = min(C_hot,C_cold);              % (W/K) finds the flow with lower heat
            capacity rate.
```

```
C_max = max(C_hot,C_cold);          % (W/K) finds the flow with higher heat
            capacity rate.
C_r=C_min/C_max;                    % ( ) ratio of min heat capacity to max
            heat capacity

%% Calculate Number of Transfer Units (NTUs)
NTU = U*A_HE1/C_min;                % ( ) number of transer units of the heat
            exchanger. Higher Area = higher NTU = higher effectiveness = more
            heat transferred

%% Calculate Effectiveness
%epsilon = effectiveness (NTU,C_r,HE_Type);         Katie: calculate
            effectiveness inside THIS function, since I don't know how to
            call another Matlab function from within a Matlab Function block
            in Simulink
%Code taken from effectiveness.m
% epsilon = f (NTU,C_r)
%
% Regardless of heat exchanger type, if C_r=0, either hot flow is
% condensing (means no change in T_hot) or cold flow is evaporating (no
% change in T_cold), therefore if C_max =inf its temperature does not change.
%
% HE_Type defines the type of heat exchanger: (see reference)
%   'Parallel Flow'
%   'Counter Flow'
%   'One Shell Pass'
%   'N Shell Pass'
%   'Cross Both Unmixed'
%   'Cross Cmax Mixed'
%   'Cross Cmin Mixed'
%
% Reference:
% Frank P. Incropera, Introduction to heat transfer. New York:Wiley, 1985,
            Section 11.4.
% Programmer: Seyyed Ali Hedayat Mofidi (seyyed4li@yahoo.com)

% ===== Calculating effectiveness (epsilon) =====
if C_r==1
    effectiveness = NTU/(1+NTU);        % ( ) Not strictly needed, as the
            actual equation for effectiveness below would simplify to this
            equation when C_r equals 1
else
    effectiveness = (1-exp(-NTU*(1-C_r)))/(1-C_r*exp(-NTU*(1-C_r)));
end

%  Calculate Heat Transfer
q_max = C_min*(T_hot_in-T_cold_in);      % (W) Maximum heat transfer that
            would occur in an infinitely long counterflow heat exchanger
            where the fluid with the lower specific heat capacity rate
            achieves the maximum possible temperature difference.
q = effectiveness * q_max;                      % (W) Actual heat transfer
            rate in our system.

%% Calculate Outlet Temperatures
T_hot_out = T_hot_in - q/C_hot;         % (K)
T_cold_out = T_cold_in + q/C_cold;      % (K)
```

```
%% Calculate Objectives - Plate Heat Exchanger
A_plate = l_PHE*w_PHE;                  % (m2)  Area of each PHE plate,
            including welded perimeter
N_plates1 = A_HE1/A_plate*1/A_eff_PHE;   % ( )   Number of plates needed to
            build out the full active heat exchange area specified by A_HE1
            design variable

if A_HE1 == 0                           % ( )   Have to put this clause into
            effect, else a non-existent heat exchanger would still register
            mass and volume due to the endplates
    P_HE1 = 0;
    V_HE1 = 0;
    M_HE1 = 0;
else
    P_HE1 = 2*q;                                % (W)   Power savings through use
            of the heat exchanger. Multiplied by two because we benefit from
            not having to heat the stream that warms up AND we benefit from
            not having to cool the stream that cools down.
    V_HE1 = (N_plates1*t_PHE+h_end)*1.5*w_PHE*1.5*l_PHE;  % (m3) Volume of
            the heat exchanger, including endplates. 1.5 multiples are for
            bracketing and bolts surrounding the plates.
    M_HE1 = density_inc*(V_HE1/1.5^2)*0.3;          % (kg)  Mass of heat
            exchanger. Assumes it is a solid block of Inconel, with 70% cut
            out as channels and dead space. Divide by 1.5*1.5 to remove the
            additional space factored into the volume calculation for
            railings and bolts (which do not contribute significantly to the
            mass).
end

end

function
            [T_hot_out,T_cold_out,P_HE2,M_HE2,V_HE2,effectiveness2,N_plates2]
            =HeatExchanger(m_dot_hot,c_p_hot,T_hot_in,m_dot_cold,c_p_cold,T_c
            old_in,U,A_HE2,A_eff_PHE,t_PHE,w_PHE,l_PHE,density_inc,h_end)
% AUTHOR: grabbed from MathWorks File Exchange:
            https://www.mathworks.com/matlabcentral/fileexchange/46303-heat-
            exchanger-solver
%
            [T_hot_out,T_cold_out]=HeatExchanger(c_p_hot,m_dot_hot,T_hot_in,c
            _p_cold,m_dot_cold,T_cold_in,U,A,HE_Type);
% This function calculates the outlet temperatures of a heat exchanger
% using Epsilon-NTU method. This function uses effectiveness.m as a
% function and should have access to that function.
%
% The inputs are as follows:
% Hot Flow: c_p_hot, m_dot_hot, T_hot_in.
% Cold Flow: c_p_cold, m_dot_cold, T_cold_in.
% Heat exchanger design parameters: U,A, HE_Type.
%
% HE_Type defines the type of heat exchanger: (see reference)
%   'Parallel Flow'
%   'Counter Flow'
%   'One Shell Pass'
%   'N Shell Pass'
%   'Cross Both Unmixed'
%   'Cross Cmax Mixed'
%   'Cross Cmin Mixed'
```

```
%
% Reference:
% Frank P. Incropera, Introduction to heat transfer. New York:Wiley, 1985,
            Section 11.4.
% Programmer: Seyyed Ali Hedayat Mofidi (seyyed4li@yahoo.com)

%HE_Type = 'Counter Flow';   %HE_Type defines the type of heat exchange

%%  Calculate Heat Capacity Rates
sph = 3600;                             % ( ) seconds per hour
C_hot = m_dot_hot*c_p_hot/sph;          % (W/K) heat capacity rate of the hot
            stream
C_cold = m_dot_cold*c_p_cold/sph;       % (W/K) heat capacity rate of the cold
            stream
C_min = min(C_hot,C_cold);              % (W/K) finds the flow with lower heat
            capacity rate.
C_max = max(C_hot,C_cold);              % (W/K) finds the flow with higher heat
            capacity rate.
C_r=C_min/C_max;                        % ( ) ratio of min heat capacity to max
            heat capacity

%% Calculate Number of Transfer Units (NTUs)
NTU = U*A_HE2/C_min;                    % ( ) number of transer units of the heat
            exchanger. Higher Area = higher NTU = higher effectiveness = more
            heat transferred

%% Calculate Effectiveness
%epsilon = effectiveness (NTU,C_r,HE_Type);         Katie: calculate
            effectiveness inside THIS function, since I don't know how to
            call another Matlab function from within a Matlab Function block
            in Simulink
%Code taken from effectiveness.m
% epsilon = f (NTU,C_r)
%
% Regardless of heat exchanger type, if C_r=0, either hot flow is
% condensing (means no change in T_hot) or cold flow is evaporating (no
% change in T_cold), therefore if C_max =inf its temperature does not change.
%
% HE_Type defines the type of heat exchanger: (see reference)
%   'Parallel Flow'
%   'Counter Flow'
%   'One Shell Pass'
%   'N Shell Pass'
%   'Cross Both Unmixed'
%   'Cross Cmax Mixed'
%   'Cross Cmin Mixed'
%
% Reference:
% Frank P. Incropera, Introduction to heat transfer. New York:Wiley, 1985,
            Section 11.4.
% Programmer: Seyyed Ali Hedayat Mofidi (seyyed4li@yahoo.com)

% ===== Calculating effectiveness (epsilon) =====
if C_r==1
    effectiveness2 = NTU/(1+NTU);
else
    effectiveness2 = (1-exp(-NTU*(1-C_r)))/(1-C_r*exp(-NTU*(1-C_r)));
```

```
end

%%  Calculate Heat Transfer
q_max = C_min*(T_hot_in-T_cold_in);      % (W) Maximum heat transfer that
            would occur in an infinitely long counterflow heat exchanger
            where the fluid with the lower specific heat capacity rate
            achieves the maximum possible temperature difference.
q = effectiveness2 * q_max;                     % (W) Actual heat transfer
            rate in our system.

%% Calculate Outlet Temperatures
T_hot_out = T_hot_in - q/C_hot;          % (K)
T_cold_out = T_cold_in + q/C_cold;       % (K)

%% Calculate Objectives - Plate Heat Exchanger
A_plate = l_PHE*w_PHE;                   % (m2)  Area of each PHE plate,
            including welded perimeter
N_plates2 = A_HE2/A_plate*1/A_eff_PHE;   % ( )   Number of plates needed to
            build out the full active heat exchange area specified by A_HE1
            design variable

if A_HE2 == 0                            % ( )   Have to put this clause into
            effect, else a non-existent heat exchanger would still register
            mass and volume due to the endplates
    P_HE2 = 0;
    V_HE2 = 0;
    M_HE2 = 0;
else
    P_HE2 = 2*q;                                % (W)   Power savings through use
            of the heat exchanger. Multiplied by two because we benefit from
            not having to heat the stream that warms up AND we benefit from
            not having to cool the stream that cools down.
    V_HE2 = (N_plates2*t_PHE+h_end)*1.5*w_PHE*1.5*l_PHE;  % (m3) Volume of
            the heat exchanger, including endplates. 1.5 multiples are for
            bracketing and bolts surrounding the plates.
    M_HE2 = density_inc*(V_HE2/1.5^2)*0.3;          % (kg)  Mass of heat
            exchanger. Assumes it is a solid block of Inconel, with 70% cut
            out as channels and dead space. Divide by 1.5*1.5 to remove the
            additional space factored into the volume calculation for
            railings and bolts (which do not contribute significantly to the
            mass).
end

end

function [P4,P8,P13,dP_HE_1c,dP_HE_1h,dP_HE_2c,dP_HE_2h] =
            deltaP_HE(P3,P7,P12,t_PHE,l_PHE,w_PHE,N_plates1,N_plates2,mdot_in
            ,mdot_O2,mdot_excess,rho3,rho7,rho12,ff_HE)
%   This function calculates the pressure drop across the heat exchanger.
%   It is based on this source:
            https://www.hindawi.com/journals/ijce/2019/3693657/

%   The basic underlying equation is the same as that of a pressure drop
%   across a pipe: deltaP = f*(L/D)*(rho/2)*v^2. L is the effective length
%   of the plate heat exchanger in its entirety (not just one plate).

%   Heat Exchanger 1 is the hot anode stream heat exchanger
```

```
%   Heat Exchanger 2 is the hot cathode stream heat exchanger

%%  Calculate intermediate values

sph = 3600;                                         % (sph)     Seconds per Hour

%   Lengths
D = t_PHE;                                          % (m)       Equivalent
            diameter of flow channels between plates
l_HE1 = N_plates1*l_PHE/2;                          % (m)       Effective length
            of heat exchanger 1, aka the length the fluid travels. Equal to
            the length it travels across one plate multiplied by the number
            of plates. Divided by two, as each fluid only passes across
            every-other plate.
l_HE2 = N_plates2*l_PHE/2;                          % (m)       Effective length
            of heat exchanger, aka the length the fluid travels. Equal to the
            length it travels across one plate multiplied by the number of
            plates. Divided by two, as each fluid only passes across every-
            other plate.

%   Cross Sectional Areas
A_1 = D*w_PHE;                                      % (m)       Cross-sectional
            area of the plate where fluid flows in heat exchanger 1. Equal to
            the height of the PHE channels multiplied by the width.
A_2 = D*w_PHE;                                      % (m)       Cross-sectional
            area of the plate where fluid flows in heat exchanger 2. Equal to
            the height of the PHE channels multiplied by the width.

%   Densities
rho_1c = rho3/7;                                    % (kg/m3)   Density of gas in
            heat exchanger 1 on the cold side (this should actually be rho4,
            but this creates an unsolveable algebraic loop. Instead, look at
            past simulations and realize that rho4 is typically ~rho3/7)
rho_2c = rho3;                                      % (kg/m3)   Density of gas in
            heat exchanger 2 on the cold side (assumed to be equal to inlet
            density, though in reality it will change along length of heat
            exchanger)
rho_1h = (rho7+rho7*7)/2;                           % (kg/m3)   Density of gas in
            heat exchanger 1 on the hot side (this should actually be the
            average of rho7 and rho8, but this creates an unsolveable
            algebraic loop. Instead, look at past simulations and realize
            rho8 is typically ~rho7*7)
rho_2h = rho12;                                     % (kg/m3)   Density of gas in
            heat exchanger 2 on the hot side

%   Flow Rates
Q_1c = mdot_in/(sph*rho_1c);                        % (m^3/s)   Volumetric flow
            rate of gas in heat exchanger 1 on the cold side
Q_2c = mdot_in/(sph*rho_2c);                        % (m^3/s)   Volumetric flow
            rate of gas in heat exchanger 2 on the cold side
Q_1h = mdot_O2/(sph*rho_1h);                        % (m^3/s)   Volumetric flow
            rate of gas in heat exchanger 1 on the hot side
Q_2h = mdot_excess/(sph*rho_2h);                    % (m^3/s)   Volumetric flow
            rate of gas in heat exchanger 2 on the hot side

%   Velocities
```

```
v_1c = Q_1c/A_1;                                    % (m/s)     Velocity of gas
            in heat exchanger 1 on the cold side
v_2c = Q_2c/A_2;                                    % (m/s)     Velocity of gas
            in heat exchanger 2 on the cold side
v_1h = Q_1h/A_1;                                    % (m/s)     Velocity of gas
            in heat exchanger 1 on the hot side
v_2h = Q_2h/A_2;                                    % (m/s)     Velocity of gas
            in heat exchanger 2 on the hot side


%%  Delta-P Calculation

dP_HE_1c = ff_HE*(l_HE1/D)*(rho_1c*v_1c^2/2);       % (Pa)      Pressure drop
            across heat exchanger 1 for cold stream (inlet CO2)
dP_HE_2c = ff_HE*(l_HE2/D)*(rho_2c*v_2c^2/2);       % (Pa)      Pressure drop
            across heat exchanger 2 for cold stream (inlet CO2)
dP_HE_1h = ff_HE*(l_HE1/D)*(rho_1h*v_1h^2/2);       % (Pa)      Pressure drop
            across heat exchanger 1 for hot stream (SOE anode exhaust)
dP_HE_2h = ff_HE*(l_HE2/D)*(rho_2h*v_2h^2/2);       % (Pa)      Pressure drop
            across heat exchanger 2 for hot stream (SOE cathode exhaust)

P4 = max(P3 - dP_HE_2c - dP_HE_1c,1);                 % (Pa)      Pressure of
            inlet CO2 stream after passing through both heat exchangers
P8 = max(P7 - dP_HE_1h,1);                          % (Pa)      Pressure of
            SOE anode exhaust (oxygen) after passing through the heat
            exchanger
P13 = max(P12 - dP_HE_2h,1);                        % (Pa)      Pressure of
            SOE cathode exhaust after passing through the heat exchanger

end

function M_HE = SparesModifier(M_HE_active, Heatexchanger_numRunningUnits,
            Heatexchanger_numSpareUnits)

M_HE =
            M_HE_active*(Heatexchanger_numRunningUnits+Heatexchanger_numSpare
            Units)/Heatexchanger_numRunningUnits;

function V_HE = SparesModifier(V_HE_active, Heatexchanger_numRunningUnits,
            Heatexchanger_numSpareUnits)

V_HE =
            V_HE_active*(Heatexchanger_numRunningUnits+Heatexchanger_numSpare
            Units)/Heatexchanger_numRunningUnits;
```

Liquefaction

The liquefaction code includes all heat transfer equations and sizing for the radiator, cryocooler, and MAV piping and insulation.

```
function [Q_pipe, M_pipe, V_pipe] = fcn(rho_piping_MAV, rho_efrax,
            od_liq_piping, t_liq_piping, l_liq_piping,
            t_liq_pipe_ins,k_pipe,k_efrax_Mars,h_c,T_MA,T10,t_liq_MAV_ins,r_M
            AV,h_MAV)

% This function calculates the mass and volume of the piping and valving
```

```
% that wrap around the MAV as well as the connecting piping and valving
% between the MAV - cryocooler - radiator system. It also calculates the
% heat "lost" out of the pipes and MAV tank. Keep in mind this will be a
% negative value, so it is really calculating how much heat seeps into the
% MAV and piping from the Mars environment.

% Calculate power loss through piping and insulation
%   Source: An Introduction to Mass and Heat Transfer by Stanley Middleman,
%   Chapters 10 - 12. Primarily Chapter 10 used.

% Calculate radii
r1  = od_liq_piping/2;          %(m) Outer radius of pipe, inside insulation
ri  = r1-t_liq_piping;          %(m) Inner radius of pipe
r2  = r1+t_liq_pipe_ins;        %(m) Outer radius of insulation on pipe

% 1. Calculate Biot number to determine if heat loss is controlled by
% convection or internal conduction.

if r1 == r2          % If there is no insulation
    k_c = k_pipe;    %(W/m-K) Thermal conductivity is the thermal
            conductivity of the bare pipe
else                 % Otherwise, if there is insulation,
    k_c = k_efrax_Mars;     %(W/m-K) thermal conductivity is the thermal
            conductivity of the insulation (since insulation is what
            ultimately limits the heat transfer via conduction).
end
Bi  = h_c*r2/k_c;    %(-) Biot number, a measure of the effects of conduction
            vs. convection

% 2. Calculate heat loss through the pipe and out of the insulation

Q_liq_pipes = 2*pi*l_liq_piping/5*(T10-
            T_MA)/(log(r1/ri)/k_pipe+log(r2/r1)/k_efrax_Mars+1/(r2*h_c));
            %(W) Heat lost through pipe and insulation to Mars environment.
            Equation 10.2.30 in source above. Does conduction through both
            materials and convection to the environment. Ignores convection
            for our gas to the interior pipe wall for some reason. Divided by
            5 because most of the pipe in this subsystem is that which is
            wrapped around the MAV, which is covered in MAV insulation. So
            the heat loss there is already accounted for in the MAV
            insulation heat loss calculations a few lines below.

% 3. Calculate heat loss out of the MAV tank insulation. Model the MAV as a
% long cylinder.
r_MAV = r_MAV;                  % (m) radius of the MAV. Ignore thickness of
            MAV tank; assume conduction through it is negligible compared to
            conduction through the insulation and convection to Mars
r2_MAV = r_MAV+t_liq_MAV_ins;   % (m) radius of the MAV plus insulation
h_MAV = h_MAV;                  % (m) height of the MAV tank

Q_liq_MAV_sides = 2*pi*h_MAV*(T10-
            T_MA)/(log(r2_MAV/r_MAV)/k_efrax_Mars+1/(r2_MAV*h_c));    % (W)
            Heat lost through pipe and insulation to Mars environment.
            Equation 10.2.30 in source above. Does conduction through both
            materials and convection to the environment. Ignores convection
            for our gas to the interior pipe wall for some reason.
```

```
Q_liq_MAV = Q_liq_MAV_sides*(1+2*pi*r2_MAV^2/(2*pi*r2_MAV*h_MAV));
            % (W) Total heat lost out of the sides and the top and bottom of
            the MAV (take heat lost out of the sides and multiply by a factor
            that increases the area to include the top and bottom of the
            cylindrical tank as well)

Q_pipe = Q_liq_pipes + Q_liq_MAV; % (W) Total heat lost (or gained) by the
            piping and MAV tank in the liquefaction subsystem

% Calculate mass of valves, piping, and insulation in the liquefaction system
M_valves = 5;                                          % (kg)  Mass of all
            valves in the liquefaction system (estimate)
CSA_piping = pi*(od_liq_piping/2)^2-pi*((od_liq_piping-2*t_liq_piping)/2)^2;
            % (m^2) Cross sectional area of the piping
CSA_ins = pi*((od_liq_piping+2*t_liq_pipe_ins)/2)^2-pi*(od_liq_piping/2)^2;
            % (m^2) Cross sectional area of the insulation
M_piping = rho_piping_MAV*l_liq_piping*CSA_piping;      % (kg)   Mass of
            piping
M_ins1 = rho_efrax*l_liq_piping/5*CSA_ins;             % (kg)   Mass of
            insulation around piping. Divided by 5 because the piping is
            primarily the piping wrapped around the MAV. The bottom half of
            that pipe will be in contact with the MAV wall to conduct heat.
            The sides of it will be covered with MAV insulation, the mass of
            which is already calculated. So only the top portion of the
            pipes, maybe 1/5 of the surface area, needs extra insulation
            covering it.
M_ins2 = pi*(r2_MAV^2-r_MAV^2)*h_MAV*rho_efrax+pi*r2_MAV^2*
            t_liq_MAV_ins*rho_efrax;       % (kg)   Mass of insulation around
            MAV tank sides and top of tank
M_ins = M_ins1 + M_ins2;

M_pipe = M_valves + M_piping + M_ins;                  % (kg)      Total mass of
            piping and valves in the liquefaction system

% Calculate volume of valves and piping in the liquefaction system
V_pipe = 0;                       % (m3)      Note: Volume is set to zero for
            this because all piping will be within the envelope of the larger
            units
end

%calculate the cooling load

function [Wcool,P_liquefy_O2] = calc_Wcool(mdot_O2,Cp_O2,H_latent_O2,T9,T10)

%% Frisbee (1987) calculation of cooling load (Wcool), which helps us
            calculate mass and volume of liquefaction unit based on his
            scaling laws. Should eventually swap this for an actual
            calculation probably, like I did for power.
if mdot_O2 < 0
    mdot_O2 = -mdot_O2;
end

Wcool = 3.941*mdot_O2*24 + 0.592*(mdot_O2*24)^(2/3);  %Frisbee et al. 1987,
            cooling load (W), multiplying by 24 because their scaling laws
            were based on kg/day for mdot
```

```
%% Directly calculating cooling load for oxygen liquefaction rather than
            using Frisbee's calculation.
% NOTE: There are two heat requirements for the liquefaction: one is the
% actual liquefaction power to cool and liquefy gaseous oxygen, the second
% is the parasitic heat loss from the liquefier and tanks. I think the
% second might be out of scope for the project, since we don't take into
% account the long-term storage of the cryogenic oxygen.

sph = 3600;     %Seconds per hour
P_cool_O2 = mdot_O2*Cp_O2*(T9-T10)/sph;        %(W) Power required to cool
            the gas at its incoming temp, T9, to its boiling point
P_liquefy = mdot_O2*H_latent_O2/sph;        %(W) Power required to phase
            change O2 from gas to liquid

P_liquefy_O2 = P_cool_O2 + P_liquefy;     %(W) Total power to cool and
            liquefy O2

end

%Source: AIAA-87-1900
%Mass and Power Estimate for Mars In-Situ Propellant production Systems
%Frisbee, JPL, 1987

function P_cc  = power_liquefaction(cryo_efficiency, Q_pipe, P_liquefy_O2,
            P_sorp_cooling, P_cryo_CO2_deposition, P_cryo_CO2_cooling,
            cryo_HE_factor)

% Cooling load plus the heat leaks experienced by the MAV and pipe divided by
            efficiency to determine power consumption by
% liquefaction unit.
P_cc =
            (Q_pipe+P_liquefy_O2+P_sorp_cooling+cryo_HE_factor*P_cryo_CO2_coo
            ling+P_cryo_CO2_deposition)/cryo_efficiency;    % (W) Power
            requirement of liquefaction unit. Includes cooling loads from
            cryopump and sorption pump.

end

function [M_cc, V_cc, P_total_cool] = fcn(P_liquefy_O2, cryo_HE_factor,
            P_cryo_CO2_cooling, P_cryo_CO2_deposition, P_sorp_cooling)

% This function calculates the mass and volume of the turbo-Brayton
% cryocooler as part of the refrigeration cycle of the liquefaction
% subsystem.

P_total_cool = P_liquefy_O2 + cryo_HE_factor*(P_cryo_CO2_cooling +
            P_cryo_CO2_deposition) + P_sorp_cooling;   % (W) Total cooling
            lift required of the cryocooler. Equal to the power to cool and
            liquefy O2 summed with the power to cool and solidify CO2 (in the
            event that the cryopump is used in the CAC system) or the power
            to cool CO2 (in the event that the sorption pump is used in the
            CAC system)
M_sp_cc = 3.9985*P_total_cool^(-0.404);     % (kg/W)    System specific mass
            of the cryocooler as a function of cooling lift, extrapolated
            from Zagarola & McCormick (2005) and calculated using a power
            regression fit (see Cryocooler Mass Equation excel workbook for
```

```
            exact equation). Ends up being around 0.5 kg/W, which seems
            reasonable to me (see table in section 4.5 of my dissertation -
            Cryocooler power and sizing.)
M_cc = M_sp_cc*P_total_cool;                % (kg)      Mass of the
            cryocooler as a function of cooling lift.
V_cc = 0.052*P_total_cool^(0.596);          % (m^3)     Volume of the
            cryocooler as a function of cooling lift.
                                            % Zagarola & McCormick (2005)
            demonstrated that volume and mass scale in the same way for
            cryocoolers.
                                            % I calculated the pre-
            exponential constant based on my (random) estimate that a
            cryocooler for my full-scale design would be about 3'x3'x3' in
            dimensions.
                                            % This is a total guess based on
            pictures I saw in a few cryocooler studies.
                                            % I may need to refine this if I
            find any baseline cryocooler volume measurements in papers.
end

function M_CC = SparesModifier(M_CC_active, Cryocooler_numRunningUnits,
            Cryocooler_numSpareUnits)

M_CC =
            M_CC_active*(Cryocooler_numRunningUnits+Cryocooler_numSpareUnits)
            /Cryocooler_numRunningUnits;

function V_CC = SparesModifier(V_CC_active, Cryocooler_numRunningUnits,
            Cryocooler_numSpareUnits)

V_CC =
            V_CC_active*(Cryocooler_numRunningUnits+Cryocooler_numSpareUnits)
            /Cryocooler_numRunningUnits;

function Q_radiator_req = fcn(P_liquefy_O2, P_cc)

% This function calculates the total heat that must be rejected by the
% radiator. With how we have defined the efficiency of the cryocooler and
% the power required of it, the heat rejected by the radiator equals the
% cryocooler input power PLUS the heat picked up by the cooling fluid when
% it liquefies oxygen.

% I went back and forth on this for a while and even asked my ChemE
% undergrad friends, because it seems like 100% of the input cryocooler
% power would NOT go into the gas itself and thus would not all have to be
% dissipated by the radiator. However, the turbine credits and compressor
            debits are
% taken into account by the cryo_efficiency term that I used to calculate
% P_cc. So I do not take compressor efficiency into account here, else I
% will be double counting it.

Q_radiator_req = P_liquefy_O2 + P_cc;       % (W) Total heat that must be
            rejected by the radiator.
end
```

```
function
            [total_radiator_power_rejected,mass_radiator,area_radiator,vol_ra
            diator] =
            mass_radiator(Q_radiator_req,time,d_hp_r,T9,T10,T_root,Q_solar,ab
            sorptivity_r,sb,emissivity_r,skytemp,h_c,T_MA,Cp_NH3,mdot_NH3,n_h
            eat_pipes,rho_NH3_liq,kvisc_NH3,t_radiator,t_liq_piping,rho_pipin
            g,rho_cc_fins)
%% Calculates the dimensions and mass of a radiator given heat rejection
            requirements
    coder.extrinsic('rad_heat_trans');
    total_radiator_power_rejected = double(0);
    if time < .5 % start delay to avoid infinite loops
        total_radiator_power_rejected = 0;
        area_radiator = 0; % (m^2) total cross-sectional area of radiator
        mass_radiator = 0; % (kg) total mass of radiator
        vol_radiator = 0;  % (m^3) volume of radiator
    else
        low_x_radiator = 0.1;      % (m) length of radiator fluid pipe
        high_x_radiator = 50;
        low_y_radiator = 0.1;      % (m) width of radiator fins
        high_y_radiator = 50;
        max = high_x_radiator;     % variable to be used for exit criteria of
            while loop below
        l_pipe_r = (low_x_radiator+high_x_radiator)/2;
        w_fin_r = (low_y_radiator+high_y_radiator)/2;
        total_radiator_power_rejected =
            rad_heat_trans(d_hp_r,T9,T10,T_root,Q_solar,absorptivity_r,w_fin_
            r,sb,emissivity_r,skytemp,h_c,T_MA,Cp_NH3,mdot_NH3,l_pipe_r,n_hea
            t_pipes,rho_NH3_liq,kvisc_NH3);   %Call external function to
            calculate heat rejected for one pipe/fin combo
%% binary search algorithm to find appropriate dimensions
        tol = 20;           % (W) Tolerance (how close my radiator heat
            rejection should be to the required heat rejection before exiting
            the loop below
        count_max = 300;    % ( ) Maximum iterations of while loop below
            before it exits and thorws an error
        count = 0;          % ( ) Initialize count sequence
        while abs(total_radiator_power_rejected - Q_radiator_req) > tol &&
            count < count_max && l_pipe_r < max
            count = count + 1;          % ( ) Increment the count!
            if total_radiator_power_rejected < Q_radiator_req   %If we aren't
            rejecting enough heat, increase length of pipe and width of fin
                low_x_radiator = l_pipe_r;
                low_y_radiator = w_fin_r;

            elseif total_radiator_power_rejected > Q_radiator_req %If we are
            rejecting too much heat, decrease length of pipe and width of fin
                high_x_radiator = l_pipe_r;
                high_y_radiator = w_fin_r;
            end
            l_pipe_r = (low_x_radiator+high_x_radiator)/2;
            w_fin_r = (low_y_radiator+high_y_radiator)/2;
            total_radiator_power_rejected =
            rad_heat_trans(d_hp_r,T9,T10,T_root,Q_solar,absorptivity_r,w_fin_
            r,sb,emissivity_r,skytemp,h_c,T_MA,Cp_NH3,mdot_NH3,l_pipe_r,n_hea
            t_pipes,rho_NH3_liq,kvisc_NH3);  % (W) Recalculate heat rejected
            by the radiator
        end
```

```
        if count >= count_max           % ( ) Let the user know that the
            solution did not converge
            count
            count_max
            total_radiator_power_rejected
            Q_radiator_req
            error('An error has occured - radiator power rejection
            calculation in Liquefaction->Radiator->Radiation Function block
            did not converge prior to hitting the maximum specified
            iterations');
        else
        end
        area_radiator = (2*w_fin_r+pi*d_hp_r)*l_pipe_r;     % (m^2) Surface
            area of the radiator, including the fins and the piping surface
            area
        mass_radiator =
            (2*w_fin_r*t_radiator*l_pipe_r*rho_cc_fins)+pi*d_hp_r*t_liq_pipin
            g*l_pipe_r*rho_piping;     % (kg)  calculates mass based on
            density of aluminum and carbon-carbon composite
        vol_radiator = (2*w_fin_r)*l_pipe_r*t_radiator +
            pi*(d_hp_r/2)^2*l_pipe_r;   % (m^3) Volume of radiator in its
            deployed state, including volume of grid fins plus volume of the
            pipe
    end
end
```

Reliability

The reliability code includes all reliability calculations for BAM components, including those modified by design variables.

```
function
[rel_blower_init,rel_Blower,rel_Cryocooler_init,rel_Cryocooler,rel_CACmechani
cal_init,rel_CACmechanical_int,rel_CACmechanical,rel_SOEStack_init,rel_SOESta
ck,rel_SOECell_init,rel_SOECell_int,rel_SOECell,rel_Valve,rel_Kilopower,rel_H
eatexchanger,rel_CAC_cryo,rel_CAC_mech,rel_CAC_sorp,rel_SOE,rel_Liq,rel_HE,re
l_Pow,rel_SYS_cryo,rel_SYS_mech,rel_SYS_sorp,Blower_numRunningUnits,Cryocoole
r_numRunningUnits, Valve_numRunningUnits, CACmechanical_numRunningUnits,
SOECell_numRunningUnits, SOEStack_numRunningUnits, Kilopower_numRunningUnits,
Heatexchanger_numRunningUnits]...
    = ReliabilityCalculator(MissionLength, mdot_in, P_total_cool, P2, N_cps,
P5, P6, Vnernst_C, N_CAC, V_app, Blower_numSpareUnits,
Cryocooler_numSpareUnits, Valve_numSpareUnits, CACmechanical_numSpareUnits,
SOECell_numSpareUnits, SOEStack_numSpareUnits, Kilopower_numSpareUnits,
Heatexchanger_numSpareUnits)

%% FailureRatesEstimator estimates failure rates of MOXIE subsystem
%
% Reference documents-
%   1. Mean Time Between Failure NASA Reference Document (Appendix C):
https://core.ac.uk/download/pdf/4947189.pdf
%   2. Poisson Distribution CDF Formula (right side):
https://en.wikipedia.org/wiki/Poisson_distribution
%   3. Compressor lifetimes: http://seedengr.com/CompressorLongevity.pdf
%   4. Kilopower lifetime:
https://ntrs.nasa.gov/api/citations/20170011067/downloads/20170011067.pdf
```

```
%   5. Plate Heat Exchangers: http://www.gesmex.com/en/products/service-and-
spareparts
%   6. Reliability equation-
https://reliabilityanalyticstoolkit.appspot.com/static/redundancy_equations_f
or_calculating_reliability.pdf
%   7. Elango and Joe (OxEon), verbally communicated on 10/7/2021
%
% Aug 28th, 2021
% Eric Hinterman and Piyush Khopkar

% Terminology
%   1. MTBF= (hr) Mean Time Between Failures (MTBF) for the system
%   2. numSpareUnits = Number of redundant units on top of the primary
unit(s)
%   3. lambda = mission length * (1/MTBF)
%   4. rel = reliability

%% Load External Functions and set variables that use those functions to type
double
    coder.extrinsic('calculateReliability');

    rel_blower_init         = double(0);
    rel_Cryocooler_init     = double(0);
    rel_CACmechanical_init  = double(0);
    rel_SOEStack_init       = double(0);
    rel_SOECell_init        = double(0);
    rel_Valve               = double(0);
    rel_Kilopower           = double(0);
    rel_Heatexchanger       = double(0);

%% Component Inputs
% Component = blower
Blower_numRunningUnits      = 2;
Blower_totalUnits           = Blower_numSpareUnits + Blower_numRunningUnits;
Blower_MTBF                 = 129700;   % Reference Document 1
Blower_lambda               = MissionLength * (1/Blower_MTBF);

% Component =  cryocooler
Cryocooler_numRunningUnits  = 3;
Cryocooler_totalUnits       = Cryocooler_numSpareUnits +
Cryocooler_numRunningUnits;
Cryocooler_MTBF             = 129700;   %Reference Document 1
Cryocooler_lambda           = MissionLength * (1/Cryocooler_MTBF);

% Component =  valve
Valve_numRunningUnits       = 20;
Valve_totalUnits            = Valve_numSpareUnits + Valve_numRunningUnits;
Valve_MTBF                  = 300000;   %Reference Document 1
Valve_lambda                = MissionLength * (1/Valve_MTBF);

% Component =  CACmechanical
CACmechanical_numRunningUnits = N_CAC;
CACmechanical_totalUnits    = CACmechanical_numSpareUnits +
CACmechanical_numRunningUnits;
CACmechanical_MTBF          = 46800;    %Reference Document 3
CACmechanical_lambda        = MissionLength * (1/CACmechanical_MTBF);
```

```
% Component =  SOECell
SOECell_numRunningUnits     = 165;
SOECell_totalUnits          = SOECell_numSpareUnits +
SOECell_numRunningUnits;
SOECell_MTBF                = 15000;    % (hr) Reference 7
SOECell_lambda              = MissionLength * (1/SOECell_MTBF);

% Component =  SOEStack
SOEStack_numRunningUnits    = 3;       %Number of STACKs of SOE cells
SOEStack_totalUnits         = SOEStack_numSpareUnits +
SOEStack_numRunningUnits;
SOEStack_MTBF               = 3000000; %Randomly selected this. Really the
SOE stack shouldn't fail unless it gets too tall and loses strength. So this
number is less important than the modification based on N_CPS below.
SOEStack_lambda             = MissionLength * (1/SOEStack_MTBF);

% Component =  kilopower
Kilopower_numRunningUnits   = 3;
Kilopower_totalUnits        = Kilopower_numSpareUnits +
Kilopower_numRunningUnits;
Kilopower_MTBF              = 175200;   %Reference Document 4
Kilopower_lambda            = MissionLength * (1/Kilopower_MTBF);

% Component =  heatexchanger
Heatexchanger_numRunningUnits = 100;
Heatexchanger_totalUnits    = Heatexchanger_numSpareUnits +
Heatexchanger_numRunningUnits;
Heatexchanger_MTBF          = 219000;   %Reference Document 5
Heatexchanger_lambda        = MissionLength * (1/Heatexchanger_MTBF);

%%  Reliability of Components
%   Take the correct output of the CDF to give the probability of that
%   component succeeding for the entire mission, given "n" number
%   of redundant units.

rel_blower_init           = calculateReliability(Blower_numSpareUnits,
Blower_totalUnits, Blower_lambda);      %mdot_in
    mdot_in_o= 15;  % _o meaning a baseline value
    if mdot_in <= mdot_in_o
        % We are multiplying 1-rel with the ratio for shrinking the failure
rate. Idea is if
        % mdot_in is less than mdot_in_o, that impliest the blower should
        % last longer than what is being calculated in reliability earlier.
        b = 1;                      % Exponential term to scale the effect of
the design variable on reliability calculations. Higher "b" means higher
impact of the design variable.
        rel_Blower  = rel_blower_init + (1-rel_blower_init)*((mdot_in_o-
mdot_in)/mdot_in_o)^(1/b);
    else
        % We are multiplying the ratio by rel but not by 1-rel, for
        % extending the failure rate.
        b = 0.1;                    % Exponential term to scale the effect
of the design variable on reliability calculations. Higher "b" means higher
impact of the design variable.
        rel_Blower  = rel_blower_init -
rel_blower_init*(mdot_in/(mdot_in+mdot_in_o))^(1/b);
    end
```

```
rel_Cryocooler_init       = calculateReliability(Cryocooler_numSpareUnits,
Cryocooler_totalUnits, Cryocooler_lambda);    %temperatures, Q_cooling (heat
pulled out of CO2, which really includes temperature if you think about it)
    P_total_cool_o= 2000;        % (W)
     if P_total_cool <= P_total_cool_o
        b = 1;                        % Exponential term to scale the effect of
the design variable on reliability calculations. Higher "b" means higher
impact of the design variable.
        rel_Cryocooler  = rel_Cryocooler_init + (1-
rel_Cryocooler_init)*((P_total_cool_o-P_total_cool)/P_total_cool_o)^(1/b);
     else
        b = .08;                      % Exponential term to scale the effect of
the design variable on reliability calculations. Higher "b" means higher
impact of the design variable.
        rel_Cryocooler  = rel_Cryocooler_init -
rel_Cryocooler_init*(P_total_cool/(P_total_cool+P_total_cool_o))^(1/b);
    end

rel_CACmechanical_init    = calculateReliability(CACmechanical_numSpareUnits,
CACmechanical_totalUnits, CACmechanical_lambda); %mdot_in, N_CAC (already
taken into account with m-of-n), P2
    P2_o = 20000;               % (Pa)
    mdot_in_o= 15;
    if P2 <= P2_o       % First modify it based on P2
         b = 1;                       % Exponential term to scale the effect
of the design variable on reliability calculations. Higher "b" means higher
impact of the design variable.
        rel_CACmechanical_int  = rel_CACmechanical_init + (1-
rel_CACmechanical_init)*((P2_o-P2)/P2_o)^(1/b);
    else
         b = .06;                     % Exponential term to scale the effect
of the design variable on reliability calculations. Higher "b" means higher
impact of the design variable.
        rel_CACmechanical_int  = rel_CACmechanical_init -
rel_CACmechanical_init*(P2/(P2+P2_o))^(1/b);
    end

    if mdot_in <= mdot_in_o         % Then modify it based on mdot_in
        b = 1;                        % Exponential term to scale the effect of
the design variable on reliability calculations. Higher "b" means higher
impact of the design variable.
        rel_CACmechanical  = rel_CACmechanical_int + (1-
rel_CACmechanical_int)*((mdot_in_o-mdot_in)/mdot_in_o)^(1/b);
    else
        b = .1;                       % Exponential term to scale the effect of
the design variable on reliability calculations. Higher "b" means higher
impact of the design variable.
        rel_CACmechanical  = rel_CACmechanical_int -
rel_CACmechanical_int*(mdot_in/(mdot_in+mdot_in_o))^(1/b);
    end

rel_SOEStack_init         = calculateReliability(SOEStack_numSpareUnits,
SOEStack_totalUnits, SOEStack_lambda); %N_cps, does not depend on N_stacks,
as that is already taken into account with m-of-n calculations
    N_cps_o = 65;               % (Cells per stack) Number of cells per SOE
stack
```

```
    if N_cps <= N_cps_o         % Modify it based on N_cps
        b = 1;                      % Exponential term to scale the effect of
the design variable on reliability calculations. Higher "b" means higher
impact of the design variable.
        rel_SOEStack  = rel_SOEStack_init + (1-rel_SOEStack_init)*((N_cps_o-
N_cps)/N_cps_o)^(1/b);
    else
        b = .13;                    % Exponential term to scale the effect of
the design variable on reliability calculations. Higher "b" means higher
impact of the design variable.
        rel_SOEStack  = rel_SOEStack_init -
rel_SOEStack_init*(N_cps/(N_cps+N_cps_o))^(1/b);
    end

rel_SOECell_init          = calculateReliability(SOECell_numSpareUnits,
SOECell_totalUnits, SOECell_lambda); %voltage (Nernst closest approach)
Vnernst_C-V_app, P5-P6, NOT N_cps as it is already taken into account with m-
of-n
    P5_P6_o = 0.1;              % (Bar) Pressure differential from cathode
to anode
    P5_P6 = abs(P5-P6)/100000;   % (Bar) Absolute value because a delta-P is
a delta-P regardless of signs. 100000 converts Pa to bar.
    if P5_P6 <= P5_P6_o          % Modify it based on deltaP
        b = .55;                    % Exponential term to scale the effect of
the design variable on reliability calculations. Higher "b" means higher
impact of the design variable.
        rel_SOECell_int  = rel_SOECell_init + (1-rel_SOECell_init)*((P5_P6_o-
P5_P6)/P5_P6_o)^(1/b);
    else
        b = .08;                    % Exponential term to scale the effect of
the design variable on reliability calculations. Higher "b" means higher
impact of the design variable.
        rel_SOECell_int  = rel_SOECell_init -
rel_SOECell_init*(P5_P6/(P5_P6+P5_P6_o))^(1/b);
    end
    Vnernst_Vapp_o = 0.1;     % (V) Vnernst_C-V_app. Average voltage
difference between applied voltage and Nernst voltage for carbon formation
    Vnernst_Vapp = max(Vnernst_C-V_app,0);              % (V) Max because if
this goes negative, we run into issues with the reliability calculation going
imaginary.
    if Vnernst_Vapp < Vnernst_Vapp_o          % Modify it based on deltaV
        b = .15;                    % Exponential term to scale the effect of
the design variable on reliability calculations. Higher "b" means higher
impact of the design variable.
        % replace b with tunning parameter
        rel_SOECell  = rel_SOECell_int -
rel_SOECell_int*(Vnernst_Vapp_o/(Vnernst_Vapp+Vnernst_Vapp_o))^(1/b);
    else
        b = .48;                    % Exponential term to scale the effect of
the design variable on reliability calculations. Higher "b" means higher
impact of the design variable.
        rel_SOECell  = rel_SOECell_int + (1-rel_SOECell_int)*((Vnernst_Vapp-
Vnernst_Vapp_o)/Vnernst_Vapp)^(1/b);
    end

rel_Valve           = calculateReliability(Valve_numSpareUnits,
Valve_totalUnits, Valve_lambda);   %number of valves, already taken into
account with m-of-n
```

```
rel_Kilopower        = calculateReliability(Kilopower_numSpareUnits,
Kilopower_totalUnits, Kilopower_lambda); %
rel_Heatexchanger    = calculateReliability(Heatexchanger_numSpareUnits,
Heatexchanger_totalUnits, Heatexchanger_lambda); %no modification needed
rel_sorp             = 0.95; % ( ) Sorption pumping needs to take a hit on
reliability due to its inherent complexity. This design uses a rapid cycle,
microchannel design. This will require over 300,000 thermal cycles over one
mission and hundreds of intricate cooling/heating channels.

%%  Success Rates of Subsystems
rel_CAC_cryo     = rel_Blower*rel_Cryocooler*rel_Valve;              % ( )
success rate of the cryopump CAC system
rel_CAC_mech     = rel_CACmechanical;                               % ( )
success rate of the mechanical CAC system
rel_CAC_sorp     = rel_Blower*rel_Cryocooler*rel_Valve*rel_sorp;     % ( )
success rate of the sorption CAC system
rel_SOE          = rel_SOECell*rel_SOEStack;                        % ( )
success rate of the entire SOE system
rel_Liq          = rel_Cryocooler;                                  % ( )
success rate of the liquefaction system
rel_HE           = rel_Heatexchanger;                               % ( )
success rate of the heat exchanger system
rel_Pow          = rel_Kilopower;                                   % ( )
success rate of the kilopower system

%%  Success Rate of Total System
rel_SYS_cryo = rel_CAC_cryo*rel_SOE*rel_Liq*rel_HE*rel_Pow;
% ( )   success rate of the entire atmospheric ISRU plant system with the
cryogenic pump as the CAC
rel_SYS_mech = rel_CAC_mech*rel_SOE*rel_Liq*rel_HE*rel_Pow;
% ( )   success rate of the entire atmospheric ISRU plant system with the
cryogenic pump as the CAC
rel_SYS_sorp = rel_CAC_sorp*rel_SOE*rel_Liq*rel_HE*rel_Pow;
% ( )   success rate of the entire atmospheric ISRU plant system with the
cryogenic pump as the CAC

end
```

Connecting Pipes and Insulation

The connecting pipes and insulation code includes the mass, volume, and heat transfer calculations of the piping and insulation segments that connect each subsystem in BAM.

```
% This function calculates the boiling point of oxygen as a function of
% pressure. If oxygen is liquefied below 1 bar, it must be cooled to a
% lower temperature and thus will take more power. The Antoine Equation is
% used for this calculation. Its coefficients and a plot of P vs. T for
% oxygen are found here:
            https://webbook.nist.gov/cgi/cbook.cgi?ID=C7782447&Mask=4&Type=AN
            TOINE&Plot=on

function T10 = OxLiqTemp(A_O2, B_O2, C_O2, P9)

P9_bar = P9/10^5;                        % (bar) Convert P9 from Pa to bar
```

```
T10 = B_O2/(A_O2-log10(P9_bar))-C_O2;   % (K)   Boiling point / condensation
            point of oxygen at the specified pressure

function mConnectingFlow = mass_pipes(density_pipe,density_ins, Di, Do, Dins,
            Lpipe)

%Calculate the mass of the connecting flow pipes
%Calculate cross-sectional area (m2) based on dimensions
CS_area_pipe = pi()*(Do/2)^2 - pi()*(Di/2)^2;
CS_area_ins = pi()*(Dins/2)^2 - pi()*(Do/2)^2;

%Calculate volumes (m3) based on dimensions provided
V_pipe = CS_area_pipe*Lpipe;
V_ins = CS_area_ins*Lpipe;

%Calculate mass (kg) based on volume and density
mPipe = V_pipe*density_pipe;
mIns  = V_ins*density_ins;

%Add mass of pipe and insulation together
mPiping = mPipe+mIns;

%This is the mass for ONE piping section, but there are 5 (CAC->HE, HE->SOE,
            SOEa->HE, SOEc->HE, HE->Liq)
mConnectingFlow = 5*mPiping;


function [Cp1,Cp2,Cp3,Cp4,Cp5,Cp6,Cp7,Cp8,Cp9,Cp10,Cp11,Cp12,Cp13] =
            fcn(T1,T2,T3,T4,T5,T6,T7,T8,T9,Cp10,T11,T12,T13,CO2_coef,O2_coef,
            CO_coef,N2_coef,MarsMix_coef,mdot_cath_Ar,mdot_cath_N2,mdot_cath_
            CO,mdot_cath_CO2)
% This function calculates the specific heat capacity (Cp) for every stream
% in the ISRU system. These values are dependent on temperature and
% composition.

% Mars inlet streams
Cp1 = sum(MarsMix_coef.*[T1^3 T1^2 T1 1]');          % (J/kg-K) Cp of Mars
            atmosphere at T1
Cp2 = sum(MarsMix_coef.*[T2^3 T2^2 T2 1]');          % (J/kg-K) Cp of Mars
            atmosphere gas at T2
Cp3 = sum(MarsMix_coef.*[T3^3 T3^2 T3 1]');          % (J/kg-K) Cp of Mars
            atmosphere gas at T3
Cp4 = sum(MarsMix_coef.*[T4^3 T4^2 T4 1]');          % (J/kg-K) Cp of Mars
            atmosphere gas at T4
Cp5 = sum(MarsMix_coef.*[T5^3 T5^2 T5 1]');          % (J/kg-K) Cp of Mars
            atmosphere gas at T5

% Oxygen streams
Cp6 = sum(O2_coef.*[T6^4 T6^3 T6^2 T6 1]');          % (J/kg-K) Cp of oxygen
            at T6
Cp7 = sum(O2_coef.*[T7^4 T7^3 T7^2 T7 1]');          % (J/kg-K) Cp of oxygen
            at T7
Cp8 = sum(O2_coef.*[T8^4 T8^3 T8^2 T8 1]');          % (J/kg-K) Cp of oxygen
            at T8
Cp9 = sum(O2_coef.*[T9^4 T9^3 T9^2 T9 1]');          % (J/kg-K) Cp of oxygen
            at T9
```

```
Cp10 = Cp10;                                          % (J/kg-K) Cp of oxygen
            at 90 K and 1 bar. Great source that can calculate this value and
            more for any cryo temp and pressure:
            https://www.peacesoftware.de/einigewerte/calc_o2.php7

% Cathode exhaust streams
%  - This is a bit more complex than the others; first calculate the
% individual Cp of each constituent (N2, Ar, CO, CO2) and then combine
% based on mass fractions. Cp_total = xCO*Cp_CO+xAr*Cp_Ar+...
%  - Assume Cp_Ar = 0.5*Cp_N2 since I cannot find reliable data for Argon Cp
            as a
% function of temperature. Source:
            https://www.engineeringtoolbox.com/specific-heat-capacity-gases-
            d_159.html

mdot_total = mdot_cath_CO2 + mdot_cath_CO + mdot_cath_N2 + mdot_cath_Ar;
            % (kg/hr) Total mass flow rate of all constituents in cathode
            exhaust
mass_frac = [mdot_cath_CO2 mdot_cath_CO mdot_cath_N2
            mdot_cath_Ar]./mdot_total;     % ( ) Calculating all mass
            fractions and putting them in a vector

Cp11_CO2 = sum(CO2_coef.*[T11^3 T11^2 T11 1]');      % (J/kg-K) Cp of CO2 at
            T11
Cp11_CO = sum(CO_coef.*[T11^4 T11^3 T11^2 T11 1]');  % (J/kg-K) Cp of CO at
            T11
Cp11_N2 = sum(N2_coef.*[T11^3 T11^2 T11 1]');        % (J/kg-K) Cp of N2 at
            T11
Cp11_Ar = 0.5*Cp11_N2;                               % (J/kg-K) Assumed Cp of
            Ar at T11
Cp11_all = [Cp11_CO2 Cp11_CO Cp11_N2 Cp11_Ar];       % (J/kg-K) Putting all
            Cps in one matrix for location 11
Cp11 = sum(mass_frac.*Cp11_all);                     % (J/kg-K) Cp of cathode
            exhaust at T11

Cp12_CO2 = sum(CO2_coef.*[T12^3 T12^2 T12 1]');      % (J/kg-K) Cp of CO2 at
            T12
Cp12_CO = sum(CO_coef.*[T12^4 T12^3 T12^2 T12 1]');  % (J/kg-K) Cp of CO at
            T12
Cp12_N2 = sum(N2_coef.*[T12^3 T12^2 T12 1]');        % (J/kg-K) Cp of N2 at
            T12
Cp12_Ar = 0.5*Cp12_N2;                               % (J/kg-K) Assumed Cp of
            Ar at T12
Cp12_all = [Cp12_CO2 Cp12_CO Cp12_N2 Cp12_Ar];       % (J/kg-K) Putting all
            Cps in one matrix for location 12
Cp12 = sum(mass_frac.*Cp12_all);                     % (J/kg-K) Cp of cathode
            exhaust stream at T12

Cp13_CO2 = sum(CO2_coef.*[T13^3 T13^2 T13 1]');      % (J/kg-K) Cp of CO2 at
            T13
Cp13_CO = sum(CO_coef.*[T13^4 T13^3 T13^2 T13 1]');  % (J/kg-K) Cp of CO at
            T13
Cp13_N2 = sum(N2_coef.*[T13^3 T13^2 T13 1]');        % (J/kg-K) Cp of N2 at
            T13
Cp13_Ar = 0.5*Cp13_N2;                               % (J/kg-K) Assumed Cp of
            Ar at T13
```

```
Cp13_all = [Cp13_CO2 Cp13_CO Cp13_N2 Cp13_Ar];       % (J/kg-K) Putting all
            Cps in one matrix for location 13
Cp13 = sum(mass_frac.*Cp13_all);                     % (J/kg-K) Cp of cathode
            exhaust stream at T13
end


function rho13 = rho13(P13,T13,R)

%Calculate the fluid density using ideal gas law
rho13 = P13/(R*T13);                %(kgO2/m3)

function [T3, dT23] = temp_loss(mdot_in, T2, Lpipe, Tmars, Do, Di, Dins,
            k_pipe, k_ins, h_c, Cp2)

%Source: An Introduction to Mass and Heat Transfer by Stanley Middleman,
%Chapters 10 - 12. Primarily Chapter 10 used.

%calculate radii
r1  = Do/2;          %(m) Outer radius of pipe, inside insulation
ri  = Di/2;          %(m) Inner radius of pipe
r2  = Dins/2;        %(m) Outer radius of insulation on pipe

% 1. Calculate Biot number to determine if heat loss is controlled by
% convection or internal conduction.

if r1 == r2          % If there is no insulation
    k_c = k_pipe;    %(W/m-K) Thermal conductivity is the thermal
            conductivity of the bare pipe
else                 % Otherwise, if there is insulation,
    k_c = k_ins;     %(W/m-K) thermal conductivity is the thermal
            conductivity of the insulation (since insulation is what
            ultimately limits the heat transfer via conduction).
end
Bi  = h_c*r2/k_c;    %(-) Biot number, a measure of the effects of conduction
            vs. convection

% 2. If Biot >> 1, heat loss is controlled by conduction. If Biot << 1,
% heat loss is controlled by convection. Calculate heat loss via conduction
% and convection through the copper pipe and the aerogel insulation.

Q = 2*pi*Lpipe*(T2-Tmars)/(log(r1/ri)/k_pipe + log(r2/r1)/k_ins+1/(r2*h_c));
            %(W) Heat lost through pipe and insulation to Mars environment.
            Equation 10.2.30 in source above. Does conduction through both
            materials and convection to the environment. Ignores convection
            for our gas to the interior pipe wall for some reason.


% 3. Calculate temperature drop of the gas based on that heat loss

T3 = T2 - (Q/(mdot_in*Cp2));      %(K) Temperature at end of pipe based on
            heat loss. Eq: Q = mdot*Cp*(T1-T2). Ensure Cp is in units of
            mass, not moles.

% 4. Iterate to obtain final T. Take average T in the pipe, re-do step #2.
```

```
% Then take the new heat loss and re-do step #3. Iterate until T2 stop
% changing significantly.

T3_o = T2;                          %Just temporarily setting Tout_original
            to something for the initial comparison in two lines.
i = 0;
while abs(T3 - T3_o) > .01          %Sets a tolerance. It will move past this
            loop once the temperature stops changing and it converges to a
            solution.
    i = i+1;
    Tavg = (T3+T3_o)/2;             %Average temperature in pipe from inlet to
            outlet.
    T3_o = T3;                      %Define T_out at beginning of calculation
    Q = 2*pi*Lpipe*(Tavg-Tmars)/(log(r1/ri)/k_pipe +
            log(r2/r1)/k_ins+1/(r2*h_c));  %(W) Heat lost through pipe and
            insulation to Mars environment. Equation 10.2.30 in source above.
            Does conduction through both materials and convection to the
            environment. Ignores convection for our gas to the interior pipe
            wall for some reason.
    T3 = T2 - (Q/(mdot_in*Cp2));  %(K) Temperature at end of pipe based on
            heat loss
end

dT23 = T3-T2;                       % (K) Final temperature change across
            this section of pipe

end

function [T5, dT45] = temp_loss(mdot_in, T4, Lpipe, Tmars, Do, Di, Dins,
            k_pipe, k_ins, h_c, Cp4)

%Source: An Introduction to Mass and Heat Transfer by Stanley Middleman,
%Chapters 10 - 12. Primarily Chapter 10 used.

%calculate radii
r1  = Do/2;          %(m) Outer radius of pipe, inside insulation
ri  = Di/2;          %(m) Inner radius of pipe
r2  = Dins/2;        %(m) Outer radius of insulation on pipe

% 1. Calculate Biot number to determine if heat loss is controlled by
% convection or internal conduction.

if r1 == r2          % If there is no insulation
    k_c = k_pipe;    %(W/m-K) Thermal conductivity is the thermal
            conductivity of the bare pipe
else                 % Otherwise, if there is insulation,
    k_c = k_ins;     %(W/m-K) thermal conductivity is the thermal
            conductivity of the insulation (since insulation is what
            ultimately limits the heat transfer via conduction).
end
Bi  = h_c*r2/k_c;    %(-) Biot number, a measure of the effects of conduction
            vs. convection

% 2. If Biot >> 1, heat loss is controlled by conduction. If Biot << 1,
% heat loss is controlled by convection. Calculate heat loss via conduction
% and convection through the copper pipe and the aerogel insulation.
```

```
Q = 2*pi*Lpipe*(T4-Tmars)/(log(r1/ri)/k_pipe+log(r2/r1)/k_ins+1/(r2*h_c));
            %(W) Heat lost through pipe and insulation to Mars environment.
            Equation 10.2.30 in source above. Does conduction through both
            materials and convection to the environment. Ignores convection
            for our gas to the interior pipe wall for some reason.

% 3. Calculate temperature drop of the gas based on that heat loss

T5 = T4 - (Q/(mdot_in*Cp4));      %(K) Temperature at end of pipe based on
            heat loss. Eq: Q = mdot*Cp*(T1-T2). Ensure Cp is in units of
            mass, not moles.

% 4. Iterate to obtain final T. Take average T in the pipe, re-do step #2.
% Then take the new heat loss and re-do step #3. Iterate until T2 stop
% changing significantly.

T5_o = T4;                        %Just temporarily setting Tout_original to
            something for the initial comparison in two lines.
i = 0;
while abs(T5 - T5_o) > .01        %Sets a tolerance. It will move past this
            loop once the temperature stops changing and it converges to a
            solution.
    i = i+1;
    Tavg = (T5+T5_o)/2;           %Average temperature in pipe from inlet to
            outlet.
    T5_o = T5;                    %Define T_out at beginning of calculation
    Q = 2*pi*Lpipe*(Tavg-Tmars)/(log(r1/ri)/k_pipe +
            log(r2/r1)/k_ins+1/(r2*h_c));  %(W) Heat lost through pipe and
            insulation to Mars environment. Equation 10.2.30 in source above.
            Does conduction through both materials and convection to the
            environment. Ignores convection for our gas to the interior pipe
            wall for some reason.
    T5 = T4 - (Q/(mdot_in*Cp4));  %(K) Temperature at end of pipe based on
            heat loss
end

dT45 = T5-T4;                     % (K) Final temperature change across this
            section of pipe

end

function [T7, dT67] = temp_loss(mdot_in, T6, Lpipe, Tmars, Do, Di, Dins,
            k_pipe, k_ins, h_c, Cp6)

%Source: An Introduction to Mass and Heat Transfer by Stanley Middleman,
%Chapters 10 - 12. Primarily Chapter 10 used.

%calculate radii
r1  = Do/2;          %(m) Outer radius of pipe, inside insulation
ri  = Di/2;          %(m) Inner radius of pipe
r2  = Dins/2;        %(m) Outer radius of insulation on pipe

% 1. Calculate Biot number to determine if heat loss is controlled by
% convection or internal conduction.
```

```
if r1 == r2          % If there is no insulation
    k_c = k_pipe;    %(W/m-K) Thermal conductivity is the thermal
            conductivity of the bare pipe
else                 % Otherwise, if there is insulation,
    k_c = k_ins;     %(W/m-K) thermal conductivity is the thermal
            conductivity of the insulation (since insulation is what
            ultimately limits the heat transfer via conduction).
end
Bi  = h_c*r2/k_c;    %(-) Biot number, a measure of the effects of conduction
            vs. convection

% 2. If Biot >> 1, heat loss is controlled by conduction. If Biot << 1,
% heat loss is controlled by convection. Calculate heat loss via conduction
% and convection through the copper pipe and the aerogel insulation.

Q = 2*pi*Lpipe*(T6-Tmars)/(log(r1/ri)/k_pipe + log(r2/r1)/k_ins+1/(r2*h_c));
            %(W) Heat lost through pipe and insulation to Mars environment.
            Equation 10.2.30 in source above. Does conduction through both
            materials and convection to the environment. Ignores convection
            for our gas to the interior pipe wall for some reason.


% 3. Calculate temperature drop of the gas based on that heat loss

T7 = T6 - (Q/(mdot_in*Cp6));      %(K) Temperature at end of pipe based on
            heat loss. Eq: Q = mdot*Cp*(T1-T2). Ensure Cp is in units of
            mass, not moles.

% 4. Iterate to obtain final T. Take average T in the pipe, re-do step #2.
% Then take the new heat loss and re-do step #3. Iterate until T2 stop
% changing significantly.

T7_o = T6;                          %Just temporarily setting Tout_original
            to something for the initial comparison in two lines.
i = 0;
while abs(T7 - T7_o) > .01          %Sets a tolerance. It will move past this
            loop once the temperature stops changing and it converges to a
            solution.
    i = i+1;
    Tavg = (T7+T7_o)/2;             %Average temperature in pipe from inlet to
            outlet.
    T7_o = T7;                      %Define T_out at beginning of calculation
    Q = 2*pi*Lpipe*(Tavg-Tmars)/(log(r1/ri)/k_pipe +
            log(r2/r1)/k_ins+1/(r2*h_c));  %(W) Heat lost through pipe and
            insulation to Mars environment. Equation 10.2.30 in source above.
            Does conduction through both materials and convection to the
            environment. Ignores convection for our gas to the interior pipe
            wall for some reason.
    T7 = T6 - (Q/(mdot_in*Cp6));  %(K) Temperature at end of pipe based on
            heat loss
end

dT67 = T7-T6;                       % (K) Final temperature change across
            this section of pipe

end
```

```
function [T9, dT89] = temp_loss(mdot_in, T8, Lpipe, Tmars, Do, Di, Dins,
            k_pipe, k_ins, h_c, Cp8)

%Source: An Introduction to Mass and Heat Transfer by Stanley Middleman,
%Chapters 10 - 12. Primarily Chapter 10 used.

%calculate radii
r1  = Do/2;          %(m) Outer radius of pipe, inside insulation
ri  = Di/2;          %(m) Inner radius of pipe
r2  = Dins/2;        %(m) Outer radius of insulation on pipe

% 1. Calculate Biot number to determine if heat loss is controlled by
% convection or internal conduction.

if r1 == r2          % If there is no insulation
    k_c = k_pipe;    %(W/m-K) Thermal conductivity is the thermal
            conductivity of the bare pipe
else                 % Otherwise, if there is insulation,
    k_c = k_ins;     %(W/m-K) thermal conductivity is the thermal
            conductivity of the insulation (since insulation is what
            ultimately limits the heat transfer via conduction).
end
Bi  = h_c*r2/k_c;    %(-) Biot number, a measure of the effects of conduction
            vs. convection

% 2. If Biot >> 1, heat loss is controlled by conduction. If Biot << 1,
% heat loss is controlled by convection. Calculate heat loss via conduction
% and convection through the copper pipe and the aerogel insulation.

Q = 2*pi*Lpipe*(T8-Tmars)/(log(r1/ri)/k_pipe + log(r2/r1)/k_ins+1/(r2*h_c));
            %(W) Heat lost through pipe and insulation to Mars environment.
            Equation 10.2.30 in source above. Does conduction through both
            materials and convection to the environment. Ignores convection
            for our gas to the interior pipe wall for some reason.


% 3. Calculate temperature drop of the gas based on that heat loss

T9 = T8 - (Q/(mdot_in*Cp8));      %(K) Temperature at end of pipe based on
            heat loss. Eq: Q = mdot*Cp*(T1-T2). Ensure Cp is in units of
            mass, not moles.

% 4. Iterate to obtain final T. Take average T in the pipe, re-do step #2.
% Then take the new heat loss and re-do step #3. Iterate until T2 stop
% changing significantly.

T9_o = T8;                          %Just temporarily setting Tout_original
            to something for the initial comparison in two lines.
i = 0;
while abs(T9 - T9_o) > .01         %Sets a tolerance. It will move past this
            loop once the temperature stops changing and it converges to a
            solution.
    i = i+1;                            %To track the # of iterations if
            desired (display i if so).
```

```
    Tavg = (T9+T9_o)/2;            %Average temperature in pipe from inlet to
           outlet.
    T9_o = T9;                     %Define T_out at beginning of calculation
    Q = 2*pi*Lpipe*(Tavg-Tmars)/(log(r1/ri)/k_pipe +
           log(r2/r1)/k_ins+1/(r2*h_c));  %(W) Heat lost through pipe and
           insulation to Mars environment. Equation 10.2.30 in source above.
           Does conduction through both materials and convection to the
           environment. Ignores convection for our gas to the interior pipe
           wall for some reason.
    T9 = T8 - (Q/(mdot_in*Cp8));  %(K) Temperature at end of pipe based on
           heat loss
end

dT89 = T9-T8;                       % (K) Final temperature change across
           this section of pipe

end

function [T12, dT1112] = temp_loss(mdot_in, T11, Lpipe, Tmars, Do, Di, Dins,
           k_pipe, k_ins, h_c, Cp11)

%Source: An Introduction to Mass and Heat Transfer by Stanley Middleman,
%Chapters 10 - 12. Primarily Chapter 10 used.

%calculate radii
r1  = Do/2;          %(m) Outer radius of pipe, inside insulation
ri  = Di/2;          %(m) Inner radius of pipe
r2  = Dins/2;        %(m) Outer radius of insulation on pipe

% 1. Calculate Biot number to determine if heat loss is controlled by
% convection or internal conduction.

if r1 == r2          % If there is no insulation
    k_c = k_pipe;    %(W/m-K) Thermal conductivity is the thermal
           conductivity of the bare pipe
else                 % Otherwise, if there is insulation,
    k_c = k_ins;     %(W/m-K) thermal conductivity is the thermal
           conductivity of the insulation (since insulation is what
           ultimately limits the heat transfer via conduction).
end
Bi  = h_c*r2/k_c;    %(-) Biot number, a measure of the effects of conduction
           vs. convection

% 2. If Biot >> 1, heat loss is controlled by conduction. If Biot << 1,
% heat loss is controlled by convection. Calculate heat loss via conduction
% and convection through the copper pipe and the aerogel insulation.

Q = 2*pi*Lpipe*(T11-Tmars)/(log(r1/ri)/k_pipe + log(r2/r1)/k_ins+1/(r2*h_c));
           %(W) Heat lost through pipe and insulation to Mars environment.
           Equation 10.2.30 in source above. Does conduction through both
           materials and convection to the environment. Ignores convection
           for our gas to the interior pipe wall for some reason.


% 3. Calculate temperature drop of the gas based on that heat loss
```

```
T12 = T11 - (Q/(mdot_in*Cp11));      %(K) Temperature at end of pipe based on
            heat loss. Eq: Q = mdot*Cp*(T1-T2).

% 4. Iterate to obtain final T. Take average T in the pipe, re-do step #2.
% Then take the new heat loss and re-do step #3. Iterate until T2 stop
% changing significantly.

T12_o = T11;                          %Just temporarily setting Tout_original
            to something for the initial comparison in two lines.
i = 0;
while abs(T12 - T12_o) > .01         %Sets a tolerance. It will move past
            this loop once the temperature stops changing and it converges to
            a solution.
    i = i+1;                           %To track the # of iterations if
            desired (display i if so).
    Tavg = (T12+T12_o)/2;            %Average temperature in pipe from inlet
            to outlet.
    T12_o = T12;                     %Define T_out at beginning of
            calculation
    Q = 2*pi*Lpipe*(Tavg-Tmars)/(log(r1/ri)/k_pipe +
            log(r2/r1)/k_ins+1/(r2*h_c));  %(W) Heat lost through pipe and
            insulation to Mars environment. Equation 10.2.30 in source above.
            Does conduction through both materials and convection to the
            environment. Ignores convection for our gas to the interior pipe
            wall for some reason.
    T12 = T11 - (Q/(mdot_in*Cp11));  %(K) Temperature at end of pipe based on
            heat loss
end

dT1112 = T12-T11;                     % (K) Final temperature change across
            this section of pipe

end


function [P3, dP23, rho2, vel2, Re2, rho3, vel3, Re3] = pressure_loss(P2, T2,
            T3, Lpipe, R, mdot, Di)

%Source:
            https://www.engineersedge.com/fluid_flow/pressure_drop/pressure_d
            rop.htm
%Note: May need to add in a scalar that increases dP for bends in the
%pipes, as this assumes a straight pipe. Elbows cause P drops.

%1. Calculate the fluid density using ideal gas law
rho2 = P2/(R*T2);        %(kgO2/m3)

%2. Calculate cross-sectional area
A = pi()*(Di/2)^2;              %(m^2)

%3. Calculate flow velocity using mass flow rate conversion
sph = 3600;                           %seconds per hour
vel2 = (mdot/rho2)/(sph*A); %(m/s) flow velocity  kg/hr * m3/kg  m3/hr

%4. Calculate Reynold's number and friction coefficient of pipe
```

```
kvis2 = 8.472e-6*100000/P2;     %(m2/s) Kinematic viscosity of CO2 at 300 K
            and 1 bar, corrected for pressure (viscosity roughly doubles as
            pressure is cut in half). Not perfect for pressure, but a decent
            estimate. Source: table halfway down at:
            https://www.engineeringtoolbox.com/carbon-dioxide-dynamic-
            kinematic-viscosity-temperature-pressure-d_2074.html
Re2 = vel2*Di/kvis2;            %Reynolds number for the flow. Laminar if Re
            < 2320.
if Re2 < 2320                    %Laminar flow if Re < 2320, turbulent if
            not. Source at top of page gives different equations for lambda
            depending on Re.
    lambda = 64/Re2;            %Friction factor of pipe under laminar flow
            conditions
else
    lambda = 0.1;               %Worst-case friction factor for turbulent
            flow conditions. Source: Moody Diagram,
            https://www.engineersedge.com/graphics/moodys-diagram.png
end


%5. Put it all together to calculate the loss in pressure due to frictional
            losses
dP23 = lambda*(Lpipe/Di)*(rho2/2)*(vel2^2); % (Pa) velocities have to be high
            or small diameter for friction to have large impact

P3 = P2 - dP23;

%6. Now back-calculate gas density, exit velocity, amd Reynold's number
rho3 = P3/(R*T3);               %(kgO2/m3)
vel3 = (mdot/rho3)/(sph*A);     %(m/s) flow velocity  kg/hr * m3/kg  m3/hr
kvis3 = 8.472e-6*100000/P3;     %(m2/s) Kinematic viscosity of CO2 at 300 K
            and 1 bar, corrected for pressure (viscosity roughly doubles as
            pressure is cut in half). Not perfect for pressure, but a decent
            estimate. Source: table halfway down at:
            https://www.engineeringtoolbox.com/carbon-dioxide-dynamic-
            kinematic-viscosity-temperature-pressure-d_2074.html
Re3 = vel3*Di/kvis3;            %Reynold's number for the flow. Laminar if Re
            < 2320.

end

function [P5, dP45, rho4, vel4, Re4, rho5, vel5, Re5] = pressure_loss(P4, T4,
            T5, Lpipe, R, mdot,Di)

%Source:
            https://www.engineersedge.com/fluid_flow/pressure_drop/pressure_d
            rop.htm
%Note: May need to add in a scalar that increases dP for bends in the
%pipes, as this assumes a straight pipe. Elbows cause P drops.

%1. Calculate the fluid density using ideal gas law
rho4 = P4/(R*T4);        %(kgO2/m3)

%2. Calculate cross-sectional area
A = pi()*(Di/2)^2;              %(m^2)
```

```
%3. Calculate flow velocity using mass flow rate conversion
sph = 3600;                                 %seconds per hour
vel4 = (mdot/rho4)/(sph*A); %(m/s) flow velocity  kg/hr * m3/kg  m3/hr

%4. Calculate Reynold's number and friction coefficient of pipe
kvis4 = 36.68e-6*100000/P4;     %(m2/s) Kinematic viscosity of CO2 at 650 K
            and 1 bar, corrected for pressure (viscosity roughly doubles as
            pressure is cut in half). Not perfect for pressure, but a decent
            estimate. Source: table halfway down at:
            https://www.engineeringtoolbox.com/carbon-dioxide-dynamic-
            kinematic-viscosity-temperature-pressure-d_2074.html
Re4 = vel4*Di/kvis4;            %Reynold's number for the flow. Laminar if
            Re < 2320.
if Re4 < 2320                   %Laminar flow if Re < 2320, turbulent if
            not. Source at top of page gives different equations for lambda
            depending on Re.
    lambda = 64/Re4;            %Friction factor of pipe under laminar flow
            conditions
else
    lambda = 0.1;               %Worst-case friction factor for turbulent
            flow conditions. Source: Moody Diagram,
            https://www.engineersedge.com/graphics/moodys-diagram.png
end

%5. Put it all together to calculate the loss in pressure due to frictional
            losses
dP45 = lambda*(Lpipe/Di)*(rho4/2)*(vel4^2); %  (Pa) velocities have to be
            high or small diameter for friction to have large impact

P5 = P4 - dP45;

%6. Now back-calculate gas density, exit velocity, amd Reynold's number
rho5 = P5/(R*T5);               %(kgO2/m3)
vel5 = (mdot/rho5)/(sph*A);     %(m/s) flow velocity  kg/hr * m3/kg  m3/hr
kvis5 = 36.68e-6*100000/P5;     %(m2/s) Kinematic viscosity of CO2 at 650 K
            and 1 bar, corrected for pressure (viscosity roughly doubles as
            pressure is cut in half). Not perfect for pressure, but a decent
            estimate. Source: table halfway down at:
            https://www.engineeringtoolbox.com/carbon-dioxide-dynamic-
            kinematic-viscosity-temperature-pressure-d_2074.html
Re5 = vel5*Di/kvis5;            %Reynold's number for the flow. Laminar if Re
            < 2320.

end

function [P7, dP67, rho6, vel6, Re6, rho7, vel7, Re7] = pressure_loss(P6, T6,
            T7, Lpipe, R, mdot,Di)

%Source:
            https://www.engineersedge.com/fluid_flow/pressure_drop/pressure_d
            rop.htm
%Note: May need to add in a scalar that increases dP for bends in the
%pipes, as this assumes a straight pipe. Elbows cause P drops.

%1. Calculate the fluid density using ideal gas law
rho6 = P6/(R*T6);        %(kgO2/m3)
```

```
%2. Calculate cross-sectional area
A = pi()*(Di/2)^2;              %(m^2)

%3. Calculate flow velocity using mass flow rate conversion
sph = 3600;                              %seconds per hour
vel6 = (mdot/rho6)/(sph*A); %(m/s) flow velocity  kg/hr * m3/kg  m3/hr

%4. Calculate Reynold's number and friction coefficient of pipe
kvis6 = 127.7e-6;                 %(m2/s) Kinematic viscosity of oxygen at
            1000 K and 1 bar. Not perfect for pressure, but a decent
            estimate. Source: table halfway down at:
            https://www.engineeringtoolbox.com/oxygen-O2-dynamic-kinematic-
            viscosity-temperature-pressure-d_2081.html
Re6 = vel6*Di/kvis6;     %Reynold's number for the flow. Laminar if Re <
            2320.
if Re6 < 2320                     %Laminar flow if Re < 2320, turbulent if
            not. Source at top of page gives different equations for lambda
            depending on Re.
    lambda = 64/Re6;              %Friction factor of pipe under laminar flow
            conditions
else
    lambda = 0.1;                 %Worst-case friction factor for turbulent
            flow conditions. Source: Moody Diagram,
            https://www.engineersedge.com/graphics/moodys-diagram.png
end


%5. Put it all together to calculate the loss in pressure due to frictional
            losses
dP67 = lambda*(Lpipe/Di)*(rho6/2)*(vel6^2); % (Pa) velocities have to be high
            or small diameter for friction to have large impact

P7 = P6 - dP67;

%6. Now back-calculate gas density, exit velocity, amd Reynold's number
rho7 = P7/(R*T7);                %(kgO2/m3)
vel7 = (mdot/rho7)/(sph*A);      %(m/s) flow velocity  kg/hr * m3/kg  m3/hr
kvis7 = 127.7e-6;                 %(m2/s) Kinematic viscosity of oxygen at
            1000 K and 1 bar. Not perfect for pressure, but a decent
            estimate. Source: table halfway down at:
            https://www.engineeringtoolbox.com/oxygen-O2-dynamic-kinematic-
            viscosity-temperature-pressure-d_2081.html
Re7 = vel7*Di/kvis7;             %Reynold's number for the flow. Laminar if Re
            < 2320.

end

function [P9, dP89, rho8, vel8, Re8, rho9, vel9, Re9] = pressure_loss(P8, T8,
            T9, Lpipe, R, mdot, Di)

%Source:
            https://www.engineersedge.com/fluid_flow/pressure_drop/pressure_d
            rop.htm
%Note: May need to add in a scalar that increases dP for bends in the
%pipes, as this assumes a straight pipe. Elbows cause P drops.
```

```
%1. Calculate the fluid density using ideal gas law
rho8 = P8/(R*T8);        %(kgO2/m3)

%2. Calculate cross-sectional area
A = pi()*(Di/2)^2;            %(m^2)

%3. Calculate flow velocity using mass flow rate conversion
sph = 3600;                              %seconds per hour
vel8 = (mdot/rho8)/(sph*A); %(m/s) flow velocity  kg/hr * m3/kg  m3/hr

%4. Calculate Reynold's number and friction coefficient of pipe
kvis8 = 26.86e-6;                %(m2/s) Kinematic viscosity of oxygen at 400
            K and 1 bar. Not perfect for pressure, but a decent estimate.
            Source: table halfway down at:
            https://www.engineeringtoolbox.com/oxygen-O2-dynamic-kinematic-
            viscosity-temperature-pressure-d_2081.html
Re8 = vel8*Di/kvis8;     % Reynold's number for the flow. Laminar if Re <
            2320.
if Re8 < 2320                    %Laminar flow if Re < 2320, turbulent if
            not. Source at top of page gives different equations for lambda
            depending on Re.
    lambda = 64/Re8;             %Friction factor of pipe under laminar flow
            conditions
else
    lambda = 0.1;                %Worst-case friction factor for turbulent
            flow conditions. Source: Moody Diagram,
            https://www.engineersedge.com/graphics/moodys-diagram.png
end


%5. Put it all together to calculate the loss in pressure due to frictional
            losses
dP89 = lambda*(Lpipe/Di)*(rho8/2)*(vel8^2); % (Pa) velocities have to be high
            or small diameter for friction to have large impact

P9 = P8 - dP89;

%6. Now back-calculate gas density, exit velocity, amd Reynold's number
rho9 = P9/(R*T9);                %(kgO2/m3)
vel9 = (mdot/rho9)/(sph*A);      %(m/s) flow velocity  kg/hr * m3/kg  m3/hr
kvis9 = 26.86e-6;                %(m2/s) Kinematic viscosity of oxygen at 400
            K and 1 bar. Not perfect for pressure, but a decent estimate.
            Source: table halfway down at:
            https://www.engineeringtoolbox.com/oxygen-O2-dynamic-kinematic-
            viscosity-temperature-pressure-d_2081.html
Re9 = vel9*Di/kvis9;             %Reynold's number for the flow. Laminar if Re
            < 2320.

end

function [P12, dP1112, rho11, vel11, Re11, rho12, vel12, Re12] =
            pressure_loss(P11, T11, T12, Lpipe, R, mdot, Di)
```

```
%Source:
            https://www.engineersedge.com/fluid_flow/pressure_drop/pressure_d
            rop.htm
%Note: May need to add in a scalar that increases dP for bends in the
%pipes, as this assumes a straight pipe. Elbows cause P drops.

%1. Calculate the fluid density using ideal gas law
rho11 = P11/(R*T11);                %(kgO2/m3)

%2. Calculate cross-sectional area
A = pi()*(Di/2)^2;                  %(m^2)

%3. Calculate flow velocity using mass flow rate conversion
sph = 3600;                              %seconds per hour
vel11 = (mdot/rho11)/(sph*A);       %(m/s) flow velocity  kg/hr * m3/kg  m3/hr

%4. Calculate Reynold's number and friction coefficient of pipe
kvis11 = 53.38e-6*100000/P11;       %(m2/s) Kinematic viscosity of CO2 at 800
            K and 1 bar, corrected for pressure (viscosity roughly doubles as
            pressure is cut in half). CO aligns with CO2 for the most part,
            so this is a fair estimate for a mixed stream. Not perfect for
            pressure, but a decent estimate. Source: extrapolated from table
            halfway down at: https://www.engineeringtoolbox.com/carbon-
            dioxide-dynamic-kinematic-viscosity-temperature-pressure-
            d_2074.html
Re11 = vel11*Di/kvis11;             % Reynold's number for the flow. Laminar
            if Re < 2320.
if Re11 < 2320                     %Laminar flow if Re < 2320, turbulent if
            not. Source at top of page gives different equations for lambda
            depending on Re.
    lambda = 64/Re11;              %Friction factor of pipe under laminar flow
            conditions
else
    lambda = 0.1;                 %Worst-case friction factor for turbulent
            flow conditions. Source: Moody Diagram,
            https://www.engineersedge.com/graphics/moodys-diagram.png
end


%5. Put it all together to calculate the loss in pressure due to frictional
            losses
dP1112 = lambda*(Lpipe/Di)*(rho11/2)*(vel11^2); % (Pa) velocities have to be
            high or small diameter for friction to have large impact

P12 = max(P11 - dP1112,0);

%6. Now back-calculate gas density, exit velocity, amd Reynold's number
rho12 = P12/(R*T12);                %(kgO2/m3)
vel12 = (mdot/rho12)/(sph*A);       %(m/s) flow velocity  kg/hr * m3/kg / m2
kvis12 = 53.38e-6*100000/P12;       %(m2/s) Kinematic viscosity of CO2 at 800
            K and 1 bar, corrected for pressure (viscosity roughly doubles as
            pressure is cut in half). Not perfect for pressure, but a decent
            estimate. Source: extrapolated from table halfway down at:
            https://www.engineeringtoolbox.com/carbon-dioxide-dynamic-
            kinematic-viscosity-temperature-pressure-d_2074.html
Re12 = vel12*Di/kvis12;             %Reynold's number for the flow. Laminar if
            Re < 2320.
```

```
end
```

Congratulations on making it to the end of this dissertation. I grant you a 10% discount on a ticket to Mars and thank you for your time.

References

1 Sanders, G. B. (2000). ISRU: An Overview of NASA's Current Development Activities and Long-Term Goals. *38th Aerospace Sciences Meeting*.

2 Kleinhenz, J. E., & Paz, A. (2017). An ISRU Propellant Production System to Fully Fuel a Mars Ascent Vehicle. *AIAA SciTech Forum,* DOI: 10.2514/6.2017-0423.

3 Franz, B. P. & Villarreal, J. K. (2015). Survey of Perchlorate Extraction and Potential Uses on Mars. *AIAA SPACE 2015 Conference and Exposition.*

4 Meyen, F. (2017). System Modeling, Design, and Control of the Mars Oxygen In-Situ Resource Utilization Experiment (MOXIE) and Implications for Atmospheric ISRU Processing Plants. *Doctor of Philosophy Thesis. Massachusetts Institute of Technology Department of Aeronautics and Astronautics*.

5 Liu, T., & Wu, Z. (2015). Modeling of Top Scroll Profile Using Equidistant-Curve Approach for a Scroll Compressor. *Mathematical Problems in Engineering, 2015:* 1-8.

6 O'Brien, J. E., Stoots, C. M., Herring, J. S., & Hawkes, G. L. (2006). Hydrogen Production from Nuclear Energy via High Temperature Electrolysis. *The 1st Energy Center Hydrogen Initiative Symposium, Purdue University*. https://digital.library.unt.edu/ark:/67531/metadc877829/m2/1/high_res_d/911703.pdf

7 Laguna-Bercero, M. A., Kilner, J. A., & Skiner, S. J. (2011). Development of oxygen electrodes for reversible solid oxide fuel cells with Scandia stabilized zirconia electrolytes. *Solid State Ionics, 192*(1)*,* 501-504. https://doi.org/10.1016/j.ssi.2010.01.003

8 *Chromium alloys – Chromium.* (2017). Plansee. https://www.plansee.com/en/materials/chromium.html

9 Passaro, R. E., & Williams, K. (1980). Non-dispersive infrared gas analyzer. *United States Patent #US4346296A*

10 Howell, E. (2012). *First Spacecraft to Mars*. Space.com. https://www.space.com/18787-mariner-4.html

11 Blasius, K. R., Cutts, J. A., Guest, J. E., & Masursky, H. (1977). Geology of the Valles Marineris: First analysis of imaging from the Viking 1 Orbiter Primary Mission. *Journal of Geophysical Research, 82*(28), 4067-4091. https://agupubs.onlinelibrary.wiley.com/doi/full/10.1029/JS082i028p04067

12 Klein, H. P. (1978). The Viking biological experiments on Mars. *Icarus, 34* (3), 666-674. https://doi.org/10.1016/0019-1035(78)90053-2

13 Klein, H. P. (1979). The Viking mission and the search for life on Mars. *Reviews of Geophysics.* https://doi.org/10.1029/RG017i007p01655

14 Smith, P. H., Tamppari, L. K., Arvidson, R. E., Bass, D., Blaney, D., Boynton, W. V…Zent, A. P. (2009). H_2O at the Phoenix Landing Site. *Science, 325*(5936), 58-61. http://science.sciencemag.org/content/325/5936/58

15 Eisen, H.J., Wen, L.C., Hickey, G., & Braun, D. F. (1998). Sojourner Mars Rover Thermal Performance. *Journal of Aerospace, 107*(1), 697-707.

16 Economou, T. (2001). Chemical analyses of Martian soil and rocks obtained by the Pathfinder Alpha Proton X-ray spectrometer. *Radiation Physics and Chemistry, 61*(3-6), 191-197.

17 Squyres, S. W., Knoll, A. H., Arvidson, R. E., Clark, B. C., Grotzinger, J. P., Jolliff, B. L…Yen, A. S. (2006). Two Years at Meridiani Planum: Results from the Opportunity Rover. *Science, 313*(5792), 1403-1407. http://science.sciencemag.org/content/313/5792/1403

18 Webster, C. R., Mahaffy, P. R., Atreya, S. K., Flesch, G. J., Mischna, M. A., Meslin, P…Lemmon, M. T. (2015). Mars methane detection and variability at Gale crater. *Science, 347*(6220), 415-417. http://science.sciencemag.org/content/347/6220/415.full

19 Williams, R. M., Grotzinger, J. P., Dietrich, W. E., Gupta, S., Sumner, D. Y., Wiens, R. C…Deen, R. G. (2013). Martian Fluvial Conglomerates at Gale Crater. *Science, 340*(6136), 1068-1072. http://science.sciencemag.org/content/340/6136/1068.full

20 Ming, D. W., Archer, P. D., Glavin, D. P., Eigenbrode, J. L., Franz, H. B., Sutter, B…Yingst, R. A. (2014). Volatile and Organic Compositions of Sedimentary Rocks in Yellowknife Bay, Gale Crater, Mars. *Science 343*(6169). http://science.sciencemag.org/content/343/6169/1245267.full

21 Arunan, S., & Satish, R. (2015). Mars Orbiter Mission spacecraft and its challenges. *Current Science, 109*(6), 1061-1069.

22 Jorge, V. et al. (2006). ExoMars – searching for life on the Red Planet. *ESA Bulletin No. 126,* 16-23.

23 Landis, G. A., & Linne, D. L. (2001). Mars Rocket Vehicle Using In Situ Propellants. *Journal of Spacecraft and Rockets, 38*(5), 730-735.

24 Values depicted on Earth-Mars graphic provided by Diane Linne, NASA Glenn Research Center. Values in the table provided by the Jet Propulsion Laboratory.

25 Sanders, G.B., et al. (2015). Mars ISRU for Production of Mission Critical Consumables – Options, Recent Studies, and Current State of the Art. *AIAA SPACE 2015, 4458.*

26 Owen, T. et al. (1977). The Composition of the Atmosphere at the Surface of Mars. *Journal of Geophysical Research, 82*(28), 4635-4639.

27 Ash, R. L., Dowler, W. L., & Varsi, G. (1978). Feasibility of rocket propellant production on Mars. *Acta Astronautica, 5*(9), 705-724. http://www.sciencedirect.com/science/article/pii/0094576578900498

28 Drake, B. G. (2009). Human Exploration of Mars: Design Reference Architecture 5.0. N.J.S. Center. Washington, D.C. NASA.

29 Rapp, D. (2015). *Human Mission to Mars*. Praxis/Springer Publishing Co.

30 Williams, D. R. (2018). *Viking Mission to Mars*. NASA. https://nssdc.gsfc.nasa.gov/planetary/viking.html

31 Soffen, G. A. (1977). The Viking Project. *Journal of Geophysical Research, 82*(28), 3959-3970.

32 Hill, P.G., & Peterson, C.R. (1965). *Mechanics and thermodynamics of propulsion.* https://books.google.com/books/about/Mechanics_and_thermodynamics_of_propulsi.html?id=gHlTAAAAMAAJ

33 Falcon 9 & Falcon Heavy. (2017). *SpaceX.* http://www.spaceflightinsider.com/hangar/falcon/

34 Romohalli, K., Lawton, E., & Ash, R. (1989). Recent Concepts in Missions to Mars: Extraterrestrial Processes. *Journal of Propulsion and Power, 5*(2), 181-187. https://arc.aiaa.org/doi/pdfplus/10.2514/3.23134

35 Hoffman, S. J., Andrews, A., Joosten, B. K., & Watts, K. (2017). A Water-Rich Mars Surface Mission Scenario. *IEEE Aerospace Conference, 978-1-5090-1613.*

36 Beaty, D. W. et al. (2016). Some strategic considerations related to the potential use of water resource deposits on Mars by future human explorers. *ASCE Earth and Space Conference, Orlando, FL*.

37 Benson, T. et al. (2014). IceCube Enhanced Hot Water Drill Functional Description. *Annals of Glaciology, 55*(68)*,* 105-114. DOI: 10.3189/2014AoG68A032.

38 Sridhar, K. R., Finn, J. E., & Kliss, M. H. (2000). In-situ resource utilization technologies for Mars life support systems. *Advanced Space Resources, 25*(2)*,* 249-255.

39 Zubrin, R. (1996). *The Case for Mars.* New York City, NY: Simon & Schuster. Pages 16, 157, 165.

40 Sanders, J. B., & Kaplan, D. I. (1998). Mars ISPP Precursor (MIP): The First Flight Demonstration of In-Situ Propellant Production. *AIAA.* DOI: 10.2514/6.1998-3306.

41 Kaplan, D. I. et al. (2001). The Mars In-situ-propellant-production Precursor (MIP) Flight Demonstration. *Presented at Mars 2001: Integrated Science in Preparation for Sample Return and Human Exploration*, Lunar and Planetary Institute, Houston, TX.

42 Kaplan, D. I. et al. (2000). The 2001 Mars In-situ-propellant-production Precursor (MIP) Flight Demonstration: Project Objectives and Qualification Test Results. *AIAA-2000-5145.* DOI: 10.2514/6.2000-5145.

43 Hoffman, S. J., & Kaplan, D. I. (1997). Human Exploration of Mars: The Reference Mission of the NASA Mars Exploration Study Team. *NASA Special Publication 6107.*

44 Weaver, D. B. Duke, M. B., & Roberts, B. B. (1993). Mars Exploration Strategies: A Reference Design Mission. *International Astronautical Congress, 93-Q.1.383.*

45 Mueller, R. P. et al. (2015). Regolith Advanced Surface Systems Operations Robot (RASSOR) 2.0. *ASCE Earth & Space*.

46 Abbud-Madrid, A. et al. (2016). Report of the Mars Water In-Situ Resource Utilization (ISRU) Planning (M-WIP) Study.

47 Sanders, G. B., & Larson, W. E. (2015). Final review of analog field campaigns for In Situ Resource Utilization technology and capability maturation. *Advances in Space Research, 55*(10)*,* 2381-2404.

48 Sanders, G. B. (2011). Comparison of Lunar and Mars In-Situ Resource Utilization for Future Robotic and Human Missions. *AIAA Aerospace Sciences Meeting, 2011-120.*

49 Andrews, D. et al. (2014). Introducing the Resource Prospector (RP) Mission. *AIAA SPACE Forum*.

50 Nernst, W. (1899). On the electrolytic conduction of solid bodies at high temperatures. *Z. Electrochem, 6*(2), 41-43.

51 Minh, N. Q. (1999). Centenary of Nernst's discovery of zirconia electrolytes – review of zirconia-based electrochemical technologies. *Electrochemical Society Proceedings, 99-19.*

52 Sridhar, K. R., & Foerstner, R. (2000). Regenerative Solid Oxide Fuel Cells for Mars Exploration. *Journal of Propulsion and Power, 16*(6), 1105-1111.

53 Ioacomini, C. S., & Sridhar, K. R. Electrolyzer Power Requirements for Oxidizer Production on Mars. *Journal of Propulsion and Power, 21*(6), 1062-1068.

54 Ash et al. (1982). Autonomous oxygen production for a Mars return vehicle. *International Astronautical Congress.*

55 Richter, R. (1981). Basic Investigation into the Production of Oxygen in a Solid Electrolyte Process. *AIAA 16th Thermophysics Conference*. DOI: 10.2514/6.1981-1175.

56 Suitor, J. W. et al. (1987). Development of an Alternate Oxygen Production Source Using a Zirconia Solid Electrolyte Membrane. *Jet Propulsion Lab. Paper D-4320*.

57 Tao, G., Sridhar, K. R., & Chan, C. L. (2004). Study of carbon dioxide electrolysis at electrode/electrolyte interface: Part I. Pt/YSZ interface. *Solid State Ionics*, *175*(1-4), 615-619.

58 Tao, G., Sridhar, K. R., & Chan, C. L. (2004). Study of carbon dioxide electrolysis at electrode/electrolyte interface: Part II. Pt-YSZ cermet/YSZ interface. *Solid State Ionics, 175*(1-4), 621-624.

59 Colvin, J., Schallhorn, P., & Ramohalli, K. (1992). Full System Engineering Design and Operation of an Oxygen Plant. *Journal of Propulsion and Power, 8*(5), 1103-1108.

60 Sridhar, K. R., & Vaniman, B. T. (1997). Oxygen production on Mars using solid oxide electrolysis. *Solid State Ionics, 93*(304), 321-328.

61 Sridhar, K. R., Iacomini, C. S. & Finn, J. E. (2004). Combined H_2O/CO_2 Solid Oxide Electrolysis for Mars In Situ Resource Utilization. *Journal of Propulsion and Power, 20*(5), 892-901.

62 Hartvigsen, J. et al. (2017). Oxygen Production from Mars Atmosphere Carbon Dioxide Using Solid Oxide Electrolysis. *ECS Trans., 78*(1), 2953-2963.

63 O'Brien, J. E. et al. (2005). Performance Measurement of Solid-Oxide Electrolysis Cells for Hydrogen Production. *Journal of Electrochemical Energy Conversion and Storage, 2*(3), 156-163.

64 Zhang, X. et al. (2013). Improved durability of SOEC stacks for high temperature electrolysis. *International Journal of Hydrogen Energy, 38*(1), 20-28.

65 Hartvigsen, J. et al. (2008). Carbon Dioxide Recycling by High Temperature Co-electrolysis and Hydrocarbon Synthesis. *ECS Trans., 12*(1).

66 Elangovan, S. & Hartvigsen, J. J. (2011). Efficient reversible electrodes for solid oxide electrolyzer cells. *US Patent #: US7976686B2*.

67 Hartvigsen, J. J. et al. (2015). Challenges of Solid Oxide Electrolysis for Production of Fuel and Oxygen From Mars Atmospheric CO_2. *ECS Transactions, 68*(1) 3563-3583.

68 Mustard, J. F. et al. (2013). Appendices to the Report of the Mars 2020 Science Definition Team. *Mars Exploration Program Analysis Group (MEPAG)*.

69 Rapp, D. et al. (2015). The Mars Oxygen ISRU Experiment (MOXIE) on the Mars 2020 Rover. *AIAA SPACE Forum*. DOI: 10.2514/6.2015-4561.

70 Elangovan, S. et al. (2011). Materials for Solid Oxide Electrolysis Cells. *ECS Trans., 35*(1), 2875-2882.

71 O'Brien, J. E. et al. (2006). Hydrogen production performance of a 10-cell planar solid-oxide electrolysis stack. *Journal of Fuel Cell Science and Technology, 3*(2), 213-219.

72 Osada, N., Uchida, H. & Watanabe, M. (2006). Polarization behavior of SDC cathode with highly dispersed Ni catalysts for solid oxide electrolysis cells. *Journal of the electrochemical Society, 153*(5), A816-A820.

73 Lahijani, P. et al. (2015). Conversion of the greenhouse gas CO_2 to the fuel gas CO via the Boudouard reaction: A review. *Renewable and Sustainable Energy Reviews 41*, 615-632.

74 Frisbee, R. H. (1987). Mass and Power Estimates for Martian In-Situ Propellant Production Systems. *AIAA Propulsion Conference*. DOI: 10.2514/6.1987-1900.

75 Hartvigsen, J. J. (2020). Private communication with OxEon.

76 Hartvigsen, J. J. (2019). Private communication with OxEon.

77 Colvin, J. et al. (1991). Propellant Production on Mars: Single Cell Oxygen Production Test Bed. *AIAA 27th Joint Propulsion Conference*. DOI: 10.2514/6.1991-2444.

78 Agui, J. H. (2016). Filter Media Tests Under Simulated Martian Atmospheric Conditions. *ASCE Earth and Space Conference*. DOI: 10.1061/9780784479971.

79 Agui, J. H. (2019). A Scroll Filter System for In-Situ Resource Utilization CO_2 Acquisition of the Martian Atmosphere. *Space Resources Roundtable*. Report #GRC-E-DAA-TN69432.

80 Phillips, J. R. et al. (2016). Martian atmospheric dust mitigation for ISRU intakes via electrostatic precipitation. *15th Biennial ASCE Conference on Engineering, Science, and Operations in Challenging Environments*.

81 McClean, J. B. et al. (2018). Dust Loading and Pressure Drop of Fibrous Filters for Atmospheric In-Situ Resource Utilisation on Mars 2020. *European Planetary Science Congress*, Vol. 12.

82 Pich, J. (1971). Pressure characteristics of fibrous aerosol filters. *Journal of Colloid and Interface Science, 37*, 912-917. DOI: 10.1016/0021-9797(71)90372-9.

83 Lewis, S. R. et al. (1999). A climate database for Mars. *Journal of Geophysical Research, 104*(E10), 24177-24194.

84 Muscatello, A. C. et al. (2011). Mars Atmospheric Capture and Gas Separation. *AIAA SPACE 2011 Conference & Expedition*.

85 Muscatello, A. C. et al. (2011). Evaluation of Mars CO_2 Capture and Gas Separation Technologies. *AIAA SPACE 2011*.

86 Hinterman, E. D. (2018). System Modeling, Graphical User Interface Development, and Sensors Testing for the Mars Oxygen In-Situ Resource Utilization Experiment (MOXIE). *Master's of Science Thesis. Massachusetts Institute of Technology Department of Aeronautics and Astronautics*. June, 2018.

87 Zubrin, R. M., Baker, D. A. & Gwynne, O. (1991). Mars Direct: A Simple, Robust, and Cost Effective Architecture for the Space Exploration Initiative. *29th Aerospace Sciences Meeting*.

88 Kieffer, H. H. et al. (1976). Martian North Pole Summer Temperatures: Dirty Water Ice. *Science, 194*(4271), 1344-1346.

89 Kieffer, H. H. et al. (1976). Soil and Surface Temperatures at the Viking Landing Sites. *Science, 194*(4271), 1341-1344.

90 Din, F. (1962). Thermodynamic Functions of Gases, Volume 1: Ammonia, Carbon Dioxide and Carbon Monoxide. *Butterworth, London*.

91 Clark, L. D., Payne, K. S., & Trevathan, J. R. (2001). Carbon Dioxide Collection and Purification System for Mars. *AIAA Space 2001 Conference and Exposition*. Report #: JSC-CN-7018.

92 Muscatello, A., Devor, R., & Captain, J. (2014). Atmospheric Processing Module for Mars Propellant Production. *Earth and Space 2014*.

93 Muscatello, A. C., & Santiago-Maldonado, E. (2012). Mars In Situ Resource Utilization Technology Evaluation. *AIAA Aerospace Sciences Meeting*.

94 Frisbee, R. H., French Jr., J. R., & Lawton, E. A. (1987). A New Look At Oxygen Production On Mars – In-Situ Propellant Production (ISPP). *AIAA Aerospace Sciences Meeting*. DOI: 10.2514/6.1987-236.

95 Sridhar, K. R., Finn, J. E., & McKay, C. P. (1996). Martian Atmosphere Utilization by Temperature-Swing Adsorption. *26th International Conference on Environmental Systems*.

96 Brooks, K. (2012). Microchannel Rapid Temperature Swing Adsorption of CO_2 for Methane Production. *AIChE Annual Meeting, Conference Presentation*.

97 Brooks, K. et al. (2006). Development of a microchannel in situ propellant production system. *AIP Conference Proceedings, 813*(1), 1111-1121.

98 Johnson, K. R. et al. (2000). Sorbent Bed Acquisition and Compression of Carbon Dioxide from the Mars Atmosphere. *30th International Conference on Environmental Systems*.

99 Rapp, D. et al. (1997). Adsorption compressor for acquisition and compression of atmospheric CO_2 on Mars. *AIAA*.

100 Ash, R. L. et al. (1986). Elements of Oxygen Production Systems Using Martian Atmosphere. *AIAA 22nd Joint Propulsion Conference*.

101 Mueller, P., & Durrant, T. (1999). Cryogenic propellant liquefaction and storage for a precursor to a human Mars mission. *Cryogenics 39,* 1021-2028.

102 Hauser, D. M., Johnson, W. L., & Sutherlin, S. G. (2016). Liquefaction and Storage of In-Situ Oxygen on the Surface of Mars. *8th Symposium on Space Resource Utilization*.

103 Johnson, W. L. et al. (2018). Comparison of oxygen liquefaction methods for use on the Martian surface. *Cryogenics 90,* 60-69.

104 Desai, P., Hauser, D., & Sutherlin, S. (2017). Mars Propellant Liquefaction and Storage Performance Modeling Using Thermal Desktop with an Integrated Cryocooler Model.

105 Mac Knight, A., & Schipper, L. Assessment of Liquefaction/Refrigeration of Mars In Situ Propellant. *AlliedSignal Aerospace Systems & Equipment*.

106 Rapp, D. (2019). Extensibility of the MOXIE ISRU Demonstration. *Internal MOXIE Science Team Document Draft, 55*.

107 Rucker, M. A., et al. (2016). Solar Versus Fission Surface Power for Mars. *AIAA Space Forum 2016, AIAA2016-5452*. DOI: 10.1109/AERO.2017.7943946.

108 Palac, D. et al. (2016). Nuclear Systems Kilopower Overview. *Nuclear and Emerging Technologies for Space (NETS) 2016*, Report #GRC-E-DAA-TN29740.

109 Gibson, M. A., et al. (2017). NASA's Kilopower reactor development and the path to higher power missions. *IEEE Aerospace Conference*.

110 Rucker, M. A. (2015). Integrated Surface Power Strategy for Mars. *Nuclear and Emerging Technologies for Space (NETS) 2015*, Report #JSC-CN-32561.

111 Mueller, R. P. et al. (2015). Opportunities and Strategies for Testing and Infusion of ISRU in the Evolvable Mars Campaign. *AIAA SPACE 2015 Conference*.

112 Hecht, M. et al. (2017). The latest from MOXIE. *Internal MOXIE Science Team Presentation*.

113 Hartvigsen, J. J., Elangovan, S., & Lyman, F. (2018). MOXIE Development Driven Prospects For ISRU and Atmosphere Revitalization. *International Conference on Environmental Systems*.

114 Forget, F. et al. (1999). Improved general circulation models of the Martian atmosphere from the surface to above 80 km. *Journal of Geophysical Research – Planets, 104*(E10), 24155-24175.

115 Millour, F. et al. (2018). The Mars Climate Database (Version 5.3).

116 Hecht, M. et al. (2020). Mars Oxygen ISRU Experiment (MOXIE). *Pre-mission Special Publication*.

117 Meyen, F. E., Hecht, M. H., & Hoffman, J. A. (2016). Thermodynamic model of Mars Oxygen ISRU Experiment (MOXIE). *Acta Astronautica, 129*, 82-87.

118 Hinterman, E. D. (2020). Simulating oxygen production on Mars for the Mars Oxygen In-Situ Resource Utilization Experiment. *Acta Astronautica, 170*, 678-685.

119 Milobar, D. G., Hartvigsen, J. J., & Elangovan, S. (2015). A techno-economic model of a solid oxide electrolysis system. *The Royal Society of Chemistry,* DOI: 10.1039/c5fd00015g

120 Polsgrove, T. et al. (2015). Mars Ascent Vehicle Design for Human Exploration. *AIAA Space 2015 Conference and Exposition.*

121 Drake, B. G., Hoffman S. J., & Beaty, D. W. (2010). Human exploration of Mars, design reference architecture 5.0. *Aerospace Conference, 2010 IEEE*.

122 Drake, B. G., & Watts, D. D. (2014). Human Exploration of Mars Design Reference Architecture 5.0, Addendum #2.

123 Michalewicz, Z. (1994). Genetic Algorithms + Data Structures = Evolution Programs, 2nd Ed. *Springer-Verlag, New York.*

124 Chepko, A. B. et al. (2008). A Modeling Framework for Applying Discrete Optimization to System Architecture Selection and Application to In-Situ Resource Utilization. *AIAA/ISSMO Multidisciplinary Analysis and Optimization Conference.*

125 De Weck, O. (2004). System Optimization with Simulated Annealing (SA). *MIT Course Material*.

126 Willcox, K. & Wakayama, S. (2003). Simultaneous optimization of a multiple-aircraft family. *Journal of Aircraft, 40*(4), 616-622.

127 Papalambros, P.Y. & Wilde, D.J. (2000). Principles of optimal design: modeling and computation. *Cambridge University Press.*

128 Mayborne, M., Kosoko-Thorodds, M. & Cardenas, N. (2021). MIT Undergraduate Research Contributors.

129 Air Squared Acceptance Tests, DR2 FM Unit. Air Squared. *Internal MOXIE documentation.*

130 Berg, J., Iannetti, A., & Hasseeb, H. (2019). Experimental Configuration and Preliminary Results of Testing a Rapid Cycle Adsorption Pump for Martian CO_2 Acquisition. *49th International Conference on Environmental Systems.*

131 Berg, J., & Shah, M. (2018). CO_2 Cryofreezer Coldhead and Cycle Design Insights for Mars ISRU.

132 Legacy in Flow Controls. (2022). *Marotta*. https://marotta.com/products/flow-controls/

133 Ling, A.L., & Mulyandasari, V. (2011). Compressor Selection and Sizing (Engineering Design Guideline). *KLM Technology Group*.

134 Heinrich, M. (2016). Genetic Optimization of Turbomachinery Components using the Volute of a Transonic Centrifugal Compressor as a Case Study. *Technische Universitat Bergakademie Freiberg.*

135 Brown, R.N. (1997). Compressors: Selection and sizing. *Gulf Professional Publishing*. 3-4.

136 Oswald, J. (2020). MIT Undergraduate Research Contributor.

137 Wilson, J. (2020). Compressor Test Results – Two Stage Unit. *Internal Presentation.*

138 Cho, Y., Lee, B., & Lee, J. (1996). Development of high efficiency scroll compressor for packane air conditioners.

139 Lada, G. (2020). *Centrifugal Compressor Modeling for Mars Applications, voluntary consulting work.* Ingersoll Rand Nash.

140 Wilson, J. (2018). High Capacity Multi-Stage Scroll Compressor for Mars Atmosphere Acquisition. *Air Squared, Inc. NASA SBIR Phase II.*

141 Brooks, K.P. et al. (2006). Microchannel In Situ Propellant Production System Project Final Report. *Battelle – Pacific Northwest Division Rept. PNWD-3670.*

142 Linne, D.L. et al. (2013). Demonstration of Critical Systems for Propellant Production on Mars for Science and Exploration Missions. *51st AIAA Aerospace Sciences Meeting.*

143 Rapp, D. (2018). *Use of Extraterrestrial Resources for Human Space Missions to Moon or Mars*. Springer.

144 Rapp, D., Karlmann, P. B., Clark, D. L., & Carr, C. M. (1997). Adsorption Pump for Acquisition and Compression of Atmospheric CO_2 on Mars.

145 Finn J. E., Mulloth, L. M., & Borchers, B. A. (2000). Performance of Adsorption-Based CO_2 Acquisition Hardware for Mars ISRU. *30th International Conference on Environmental Systems.*

146 Brooks, K.P., Rassat, S.D., & TeGrotenhuis, W.E. (2005). Development of a Microchannel *In Situ* Propellant Production System. *Pacific Northwest National Laboratory*.

147 Hasseeb, H. & Iannetti, A. (2017). A System Level Mass and Energy Calculation for a Temperature Swing Adsorption Pump used for In-Situ Resource Utilization (ISRU) on Mars. *TFAWS 2017.*

148 Clark, D. L. Mars Atmospheric Acquisition and Compression System – Initial Results. *Lockheed Martin Astronautics ISRU III Technical Interchange Meeting*.

149 Excelfrax 1800 Board. (2021). *Unifrax.* http://www.unifrax.com/product/excelfrax-1800-board/

150 Fricke, J. & Caps, R. (2004). 4.3.2 *Aerogels for Thermal Insulation*. Springer Science, New York.

151 Hecht, M. et al. (2021). Mars Oxygen ISRU Experiment (MOXIE). *Space Science Reviews, 217*.

152 Dickson, D. et al. (2020). Optimization of an Electrolysis System for Production of Rocket Fuel from Lunar Ice. *IEEE Aerospace.*

153 Plachta, D. W., Johnson, W. L., & Feller, J. R. (2016). Zero boil-off system testing. *Cryogenics*, *74*, 88-94.

154 Plachta, D. (2004). Results of an Advanced Development Zero Boil-Off Cryogenic Propellant Storage Test. *AIAA Joint Propulsion Conference.*

155 Zagarola, M. V., Cragin, K. J., Hill, R.W., & J. A. McCormick. (2021). Efficiency Improvements for Turbo-Brayton Cryocoolers for Space. *International Cryocooler Conference.*

156 Breedlove, J., Cragin, K., & Zagarola, M. (2014). Testing of a two-stage 10 k turbo-Brayton cryocooler for space applications. *Cryocoolers*, *18*, 445-452.

157 Meier, A. J. et al. (2018). Full-Scale CO_2 Freezer Project Developments for Mars Atmospheric Acquisition. *AIAA SPACE and Astronautics Forum and Exposition*.

158 Chowdhury, A. A. (2020). *Minus Eighty-Degree Laboratory Freezer for ISS (MELFI).* NASA Life Sciences Data Archive. https://lsda.jsc.nasa.gov/Hardware/hardw/1218

159 Hoh, B. (2020). MIT Undergraduate Research Contributor.

160 Johnson, K. R., & Brinza, D. E. (2000). The Mars Thermal Environment and Radiator Characterization (MTERC) Experiment (No. 2000-01-2402). *SAE Technical Paper*.

161 Swift, W. L., Cheng, E., Zagarola, M. V., & Dolan, F. X. (2003). On-Orbit Operating Experience with the NICMOS Cryocooler—First Year. *Proceedings of the TDW*, 19-20.

162 Kempenaar, J., Novak, K., Redmond, M., Farias, E., Singh, K., & Wagner, M. (2018). Detailed Surface Thermal Design of the Mars 2020 Rover. *48th International Conference on Environmental Systems.*

163 Gaier, J., Perez-Davis, M., Rutledge, S., Hotes, D., & Olle, R. (1991). Effects of dust accumulation and removal on radiator surfaces on Mars. DOI:10.2172/10181280

164 Zagarola, M. V., & McCormick, J. A. (2006). High-capacity turbo-Brayton cryocoolers for space applications. *Cryogenics 46,* 169-175.

165 Augustynowicz, S. D., J. E. Fesmire, & J. P. Wikstrom. (1999). Cryogenic insulation systems. *20th International congress of refrigeration Sydney*. No. 2000-1147.

166 Fesmire, J. E., Augustynowicz, S. D., & Scholtens, B. E. (2008). Robust multilayer insulation for cryogenic systems. *AIP Conference Proceedings, 985*(1).

167 Johnson, W. L. et al. (2021). Cryogenic Insulation Solutions for the Surface of Mars with Its Unique Environments. *Symposium on Performance, Properties and Resiliency of Thermal Insulations.*

168 Oxygen Antoine Equation Parameters. (2021). *National Institute of Standards and Technology.* https://webbook.nist.gov/cgi/cbook.cgi?ID=C7782447&Mask=4&Type=ANTOINE&Plot=on

169 Maximum Flow Velocities in Water Systems. (2003). Engineering ToolBox. https://www.engineeringtoolbox.com/flow-velocity-water-pipes-d_385.html

170 Saari, J. Heat Exchanger Dimensioning. *Lappeenranta University of Technology.*

171 Incropera, F. P., & Dewitt, D. P. (2001). *Introduction to Heat Transfer.* John Wiley & Sons. Pages 623-632.

172 Vesely, W. E. (2011). Probabilistic risk assessment. *System Health Management: With Aerospace Applications,* 253-263.

173 U. S. Nuclear Regulatory Commission. (1975). Reactor Safety Study, an Assessment of Accident Risks in U.S. Nuclear Power Plants. *WASH-1400, NUREG-75/014.*

174 Pate-Cornell, E., & Dillon, R. (2001). Probabilistic risk analysis for the NASA space shuttle: a brief history and current work. *Reliability Engineering and System Safety, 74* 345-352.

175 Buchbinder, B. (1990). The NASA Risk Management Program. *AIAA Space Programs and Technologies Conference.* DOI: 10.2514/6.1990-3769.

176 Slay et al. (1987). Space Shuttle Risk Assessment Proof-of-Concept Study, Auxiliary Power Unit and Hydraulic Power Unit Analysis Report. *McDonnell Douglas Corp.*

177 Apostolakis, G. E. (2004). How Useful is Quantitative Risk Assessment? *Risk Analysis, 24*(3), 515-520.

178 Lewis, H. W. et al. (1978). Risk Assessment Review Group Report to the U.S. Nuclear Regulatory Commission. *Report, NUREG/CR-0400*. Washington, DC: U.S. Nuclear Regulatory Commission.

179 Kastenberg, W. E. et al. (1988). Findings of the Peer Review Panel on the Draft Reactor Risk Reference Document. *Report, NUEG/CR-5113.* Washington, DC: U.S. Nuclear Regulatory Commission.

180 Apostolakis, G. E. et al. (2002). Report of the Independent Peer Review Panel on the Probabilistic Risk Assessment of the International Space Station, Phase II – Stage 7a Configuration. *Prepared for NASA Headquarters, Office of Safety and Mission Assurance.*

181 Garrick, J. B. (1988). The Approach to Risk Analysis in Three Industries: Nuclear Power, Space Systems, and Chemical Process. *Reliability Engineering and System Safety, 23,* 195-205.

182 Sherwin, D. J., & Bossche, A. (1993). Standby redundancy. The Reliability, Availability and Productiveness of Systems. *Springer, Dordrecht*. DOI: https://doi.org/10.1007/978-94-011-1582-7_4.

183 Hanford, A. J. (2006). Advanced Life Support Baseline Values and Assumptions Document. *NASA/CR.*

184 Compressor Longevity. (2000). ThermaCom. https://seedengr.com/CompressorLongevity.pdf

185 Hartvigsen, J. J., & Elangovan, E. (2021). Private communication with OxEon.

186 Service and parts for plate heat exchangers. (2021). Gesmex. https://gesmex.com/service-and-spareparts

187 Bernadet, L., Gousseau, G., Chatroux, A., Laurencin, J., Mauvy, F., & Reytier, M. (2015). Influence of pressure on solid oxide electrolysis cells investigated by experimental and modeling approach. *International Journal of Hydrogen Energy 40,* 12918-12928.

188 Henke, M., Willich, C., Kallo, J., & Friedrich, K. A. (2014). Theoretical study on pressurized operation of solid oxide electrolysis cells. *International Journal of Hydrogen Energy 39,* 12434-12439.

189 Jensen, S. H., Sun, X., Ebbesen, S. D., Knibbe, R., & Mogensen, M. (2010). Hydrogen and synthetic fuel production using pressurized solid oxide electrolysis cells. *International Journal of Hydrogen Energy, 35,* 9544-9549.

190 Treybal, R.E. (1980). Mass Transfer Operations. *New York, 466*. 24-31.

191 Hartvigsen, J. J., & Elangovan, E. (2021). Private communication with OxEon.

192 Ni, M., Leung, M. K., and Leung, D. Y. (2006). A modeling study on concentration overpotentials of a reversible solid oxide fuel cell. *Journal of Power Sources, 163,* 460-466.

193 Falcon User's Guide. (2021). SpaceX. https://spacex.com/media/falcon-users-guide-2021-09.pdf

194 Non-dominates Points. (2022). MATLAB Central File Exchange. https://www.mathworks.com/matlabcentral/fileexchange/40287-non-dominates-points

195 Bussey, B., & Hoffman, S. J. (2016, March). Human Mars landing site and impacts on Mars surface operations. *2016 IEEE Aerospace Conference*, 1-21.

196 Arnaudo, P., Castaldi, M., Quadri, L. & Sangiorgio, V. A. (2021). Mars Ascent Vehicle Operations (MAV-Ops). *Alta Scuola Politecnica Multidisciplinary Project.*

197 Sanders, G. B., Trevathan, J. R., Peters, T. A., & Baird, R. S. (2000). Preparing for Robotic & Human Exploration Missions Which Incorporate In-Situ Resource Utilization. *Space 2000 Conference and Exposition.*

198 Carbon Dioxide Gas - Specific Heat (2005). Engineering ToolBox. https://www.engineeringtoolbox.com/carbon-dioxide-d_974.html

199 Oxygen Gas – Specific Heat (2005). Engineering ToolBox. https://www.engineeringtoolbox.com/oxygen-d_978.html

200 Nitrogen – Specific Heat. (2005). Engineering ToolBox. https://www.engineeringtoolbox.com/nitrogen-d_977.html

201 Carbon Monoxide – Specific Heat. (2005). Engineering ToolBox. https://www.engineeringtoolbox.com/carbon-monoxide-d_975.html

202 Specific Heat and Individual Gas Constants of Gases. (2003). Engineering ToolBox. https://www.engineeringtoolbox.com/specific-heat-capacity-gases-d_159.html

203 Moody Diagram. (2003). Engineering ToolBox. https://www.engineeringtoolbox.com/moody-diagram-d_618.html

204 Fans – Efficiency and Power Consumption. (2003). Engineering ToolBox. https://www.engineeringtoolbox.com/fans-efficiency-power-consumption-d_197.html

205 Middleman, S. (1998). An Introduction to Mass and Heat Transfer. *Wiley.* Chapters 10-12.

206 Kilopower. (2016). *NASA*. https://ntrs.nasa.gov/api/citations/20160012354/downloads/20160012354.pdf?attachment=true